Investigation of Host Proteostasis Dependencies to Inhibit RNA Virus Infection

by

Katherine Mandy Almasy

Dissertation

Submitted to the Faculty of the

Graduate School of Vanderbilt University

in partial fulfillment of the requirements

for the degree of

DOCTOR OF PHILOSOPHY

in

Chemistry

June 30, 2022

Nashville, Tennessee, USA

Approved:

Lars Plate, PhD

Renã A.S. Robinson, PhD

David W. Wright, PhD

Suman R. Das, PhD

To my father, my first and favorite teacher, and in whose memory I try to smile every day.

Acknowledgements

This dissertation would not have been possible without the support of a village. First and foremost, I am grateful to Lars for allowing me to be one of the founding members of his lab in 2017. As much as he must have trusted me to take me as a student, I have trusted him to be my guide on this journey and he has gone above and beyond what I could have asked. Even having a general sense of what graduate school would entail, I had no idea how much I would grow as both a scientist and a person during this experience, and I am better in both regards for having had Lars as a mentor. His kindness, excitement during the good times, patience during the slow times, and passion for science gave me confidence that I could not have made it through graduate school without. Likewise, I feel incredibly fortunate to have been surrounded with such supportive coworkers turned friends over the last 5 years. I couldn't have imagined the changes and experiences Madison and I would have while watching the lab change and grow, but I'm grateful to have shared this experience with him. Jonathan's name shows up multiple times in this dissertation for good reason- his scientific curiosity, sense of humor, and partnership on all things virus related have made such a positive impact on my time in the lab.

I am also grateful to the other members of my committee; Dr. Renã Robinson, Dr. David Wright, and Dr. Suman Das, for their invaluable feedback during meetings and presentations. They were patient with me when my eyes were bigger than my scientific capabilities, and I always felt supported and like they were rooting for me to succeed. I have also been fortunate to have worked with several talented rotation students, many of whose names appear in this dissertation and on manuscripts because of their contributions on various projects. Their work opened up doors for me to continue asking questions and finding answers, and I am grateful for their time and talent. Likewise, I am grateful to those funding sources who made doing this work possible; startup funds from Vanderbilt University, R35 GM133552 (Plate) and T32 AI112541 (Skaar, Chemical Biology of Infectious Diseases) from the NIH, the Vanderbilt Institute of Chemical Biology, the National

Science Foundation Graduate Research Fellowship program, and Pfizer Viral Vaccines R&D for hosting me as an intern (sponsored by the CBID T32 and Vanderbilt Institute for Infection, Immunology, and Inflammation) during one of the busiest put perhaps most exciting times of the company's existence.

My academic career has been influenced by many; I am thankful to have had excellent educators from my beginnings in Durham Public Schools, especially those in the International Baccalaureate Program at Hillside High School. The chemistry department at NC State was full of professors willing to give me a chance, and I would not be here without the leaps of faith Dr. Jonathan Lindsey and later Dr. Gavin Williams took to allow me to work as an undergraduate in their labs. In Gavin's lab, Dr. Sam Carpenter was instrumental in helping me build confidence in myself, and I am fortunate to have had her as a role model as a woman in science. Dr. Jeremiah Feducia has also been incredibly influential supporting whatever path I've happened to be on at any given moment, and most importantly reminds me that your love of science can be just as big as your sense of humor. The Goodnight Scholars Program at NC State, through all the highs and lows that undergraduate brought, was and continues to be a major source of support and inspires my desire to make the world a better place.

I would be very little, scientifically or otherwise, without the support of my friends and family. The friends I gained through the IB program at Hillside continue to be a tremendous source of support, especially now that I've finally written something longer than that Invisible Man portfolio from junior year. My friends from NC State, whether from the honors village or the chemistry department or the Goodnight Scholars Program, remind me that school doesn't have to be all work and no play, and that achievements feel best when you can celebrate them with those you care about. That has continued into graduate school, where I feel fortunate to have found communities on campus and off that have kept me sane through an intensive program and a global pandemic. The persistence of KEY conferences, especially SYP and Winterlight, has kept me centered in faith and reminded me that God's love is eternal and uncompromising. Alli, Allie, and Kara have always

inspired me to become the best version of myself, and I am grateful for their friendship over the many, many years we have known each other.

My partner, Dustin, has been the brightest light in my life since the moment I met him. The number of smiles he puts on my face is too large to count, and his support during the last portion of research and the writing of this dissertation have meant more than I could ever put in words.

Lastly, I am most thankful and grateful for my mother and sister, who have been my rocks since day 1 of this and every journey I have taken, and who are the foundations on which any of my achievements stand. If I have made them proud, this whole journey was worth it.

TABLE OF CONTENTS

LIST OF ABBREVIATIONS

ACE2	Angiotensin-converting enzyme 2
AGC	Automatic gain control
AMP	Adenosine monophosphate
AP-MS	Affinity purification-mass spectrometry
ATF(#)	Activating transcription factor (#)
ATP	Adenosine triphosphate
BME	Beta-mercaptoethanol
BSA	Bovine serum albumin
BTTAA	2-(4-((Bis((1-(tert-butyl)-1H-1,2,3-triazol-4-yl)methyl)amino)methyl)-1H-1,2,3-triazol-1-yl)acetic acid
bZIP	Basic leucine zipper
cDNA	Complementary DNA
CMV	Cytomegalovirus
CO_2	Carbon dioxide
CoV	Coronavirus
Cp-A7	Ceapin-A7
DENV	Dengue virus
(dd)DHFR	(Degradation domain) Dihydrofolate reductase
DMEM	Dulbecco’s modified Eagle’s medium
DMSO	Dimethyl sulfoxide
DMV	Double membrane vesicle
DNA	Deoxyribonucleic acid
dsRNA	Double stranded RNA
EDTA	Ethylenediaminetetraacetic acid
ER	Endoplasmic reticulum
ERAD	ER-associated degradation
FBS	Fetal bovine serum
FDR	False discovery rate
FFA	Focus forming assay

GO	Gene ontology
H_2O_2	Hydrogen peroxide
HCD	Higher energy C-trap dissociation
HEPES	2-(4-2-hydroxyethyl)piperazin-1-yl)ethanesulfonic acid
HIV	Human immunodeficiency virus
hpi	hours post infection
HRP	Horseradish peroxidase
IC50	50% inhibitory concentration
IP	Immunoprecipitation
IRE1	Inositol requiring enzyme 1
ISG	Interferon-stimulated gene
LC-MS/MS	Liquid chromatography-mass spectrometry/mass spectrometry
LMNG	Lauryl maltose neopentyl glycol
MERS	Middle East respiratory syndrome
MHV	Murine hepatitis virus
MOI	Multiplicity of infection
mRNA	Messenger ribonucleic acid
MudPIT	Multidimensional peptide identification technology
NaCl	Sodium chloride
NCE	Normalized collision energy
NS(#)	Flavivirus non-structural protein
nsp(#)	Coronavirus non-structural protein
OST	Oligosaccharyl transferase
(D)PBS	(Dulbecco's) Phosphate buffered saline
PDI	Protein disulfide isomerase
PPI(s)	Protein-protein interaction(s)
ppm	Parts per million
PERK	PKR-like ER kinase
RIPA	Radioimmunoprecipitation assay
qPCR	Quantitative polymerase chain reaction

RNA	Ribonucleic acid
rRNA	Ribosomal RNA
SARS	Severe acute respiratory syndrome
SCX	Strong cation exchange
SDS-PAGE	Sodium dodecyl sulfate-polyacrylamide gel electrophoresis
shRNA	Small hairpin RNA
TBST	Tris-buffered saline + 0.1% Tween-20
TCEP	Tris(2-carboxyethyl)phosphine
Tg	Thapsigargin
Tm	Tunicamycin
TMP	Trimethoprim
TMT	Tandem mass tag
TNI	Tris, NaCl, Igepal CA-630
Tris	Tris(hydroxymethyl)aminomethane
UPR	Unfolded protein response
vRNA	Viral RNA
Xbp1s	X-box binding protein 1, spliced
YFV	Yellow Fever virus
ZIKV	Zika virus

LIST OF FIGURES

LIST OF TABLES

CHAPTER 1: Exploiting viral dependencies: Identifying and targeting host endoplasmic reticulum functions to prevent infection

1.1 Role of the ER in protein homeostasis and in viral infections

Although viruses vary widely in size, shape, genome composition, and host reservoirs, among the ubiquitous traits of these obligate parasites are the ability and need to rewire the cellular networks of their host to facilitate their own replication[1,2]. Hijacking of these networks is required throughout each stage of the viral life cycle; host factors are needed to assist in entry/release of the viral genome, replication and transcription/translation of the genome, assembly and maturation of new progeny virions, and egress of the newly synthesized virions from the cell[3,4]. One critical cellular compartment for many viruses is the endoplasmic reticulum (ER), which for many viruses can play diverse roles in many stages of the viral life cycle[5–7]. The organelle itself is highly dynamic; its tubular (rough ER) or sheet-like (smooth ER) structures are constantly being structurally rearranged, dealing with a changing composition of lipids and proteins both on the surface and within the lumen[8–11].

All secreted and membrane proteins, encompassing about 30% of the human proteome, are folded, glycosylated, and otherwise processed in the ER[12]. Among the types proteins found in the ER are N-glycosylation machinery, protein disulfide isomerases, and numerous heat shock proteins (Hsps) responsible for recognition, binding, and refolding of misfolded substrates to prevent aggregation of those client proteins[13]. Collectively, these proteins are referred to as the proteostasis or protein folding network (**Figure 1.1**). A typical ER substrate is recognized via a hydrophobic signal sequence at the N-terminus of the protein, which is subsequently bound by the signal recognition particle and results in the ribosome being directed to the ER membrane to translocate the nascent polypeptide across the ER membrane via the Sec61 translocon[14].

In case any of these quality control systems fail, the ER uses several mechanisms to dispose of misfolded or aggregated ER proteins, as well as more generally respond to misfolding stress

within the organelle. Endoplasmic reticulum-associated degradation (ERAD), is used to mark a single protein substrate for degradation via ubiquitination to route towards the proteasome[15,16]. For larger aggregates, autophagy of a portion of the ER (colloquially referred to as ERphagy) is used to remove the aggregate from the ER[17]. When an abundance of misfolded proteins or aggregates are present, the ER activates any or all branches of the unfolded protein response, a stress pathway meant to increase the folding capacity of the ER as well as slow substrate entry in an attempt to alleviate the protein folding stress[18].

Aberrant proteostasis pathology has been implicated in a number of different disease states, particularly those related to neurodegenerative diseases linked with aging and protein aggregation such as Parkinson's or Alzheimer's[19–22]. For this reason, targeting of the proteostasis network for therapeutic purposes has been a long standing goal.

Many virus families use the ER, either structurally or functionally, to facilitate their own replication cycles. Positive-sense RNA viruses use the ER to form replication organelles of some variety; flaviviruses create invaginations within the ER and form convoluted membranes and vesicle packets, while hepatitis C and severe acute respiratory syndrome virus create double membrane vesicles to serve as replication organelles[23–25]. Studies have shown this remodeling to be essential for viral replication, reiterating the importance of this structural perturbation within the viral life cycle[26]. Various negative sense RNA, double stranded RNA, and DNA viruses have been shown to form inclusion bodies, which are also thought to derive from ER membranes[27,28]. Overall, extensive remodeling of the ER by viruses suggests that ways to modulate the proteostasis network to block this remodeling may be a viable therapeutic strategy.

Pharmacological modulators of the proteostasis network have been investigated as potential therapeutics for various diseases, from protein aggregation diseases to cystic fibrosis[29–32]. As it becomes increasingly apparent that targeting of ER proteins may serve therapeutic purposes across a wide range of diseases states, several approaches have been utilized to investigate the dependencies of virus strains or families on proteostasis machinery to add to the utility of this

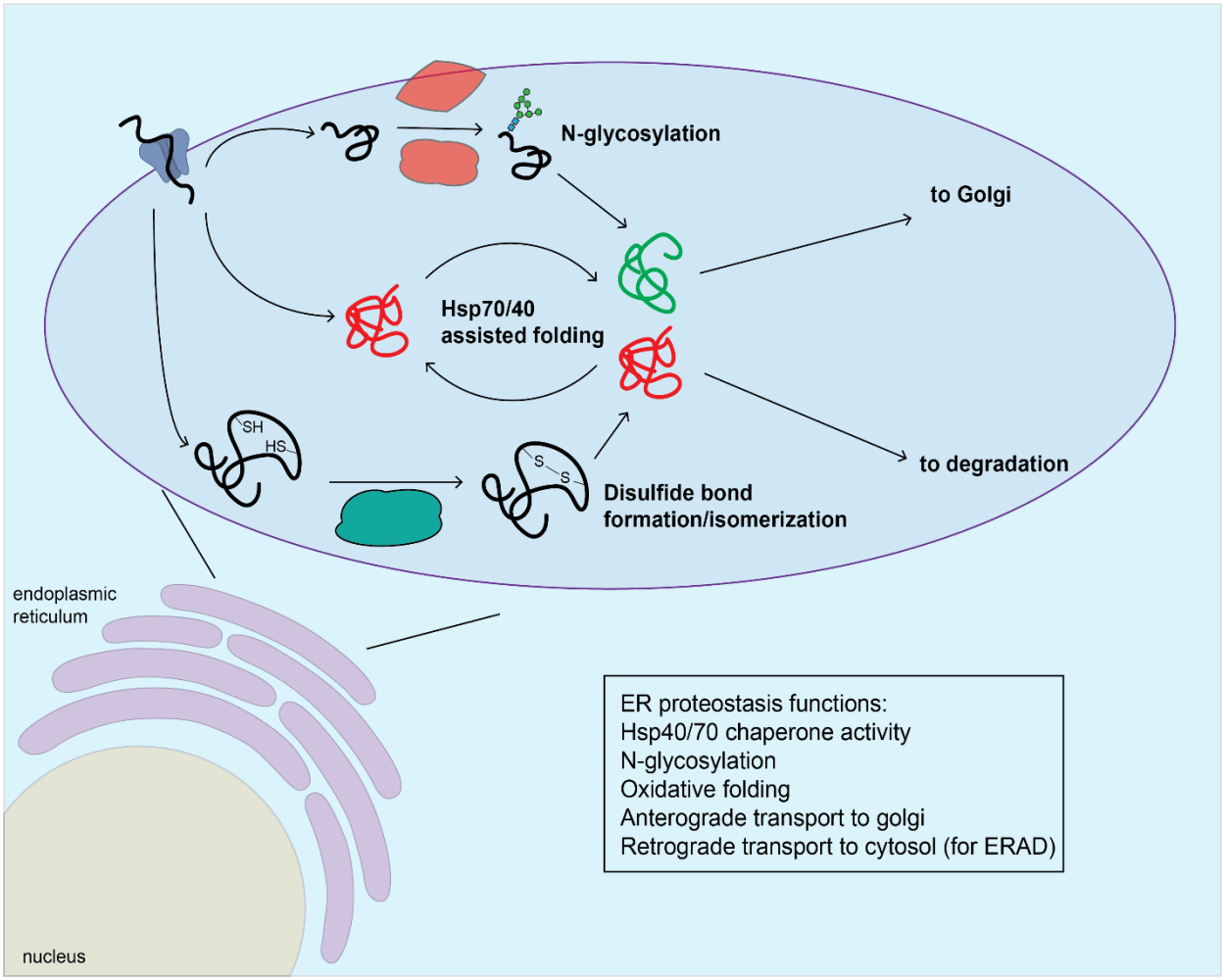

Figure 1.1. The proteostasis network. Protein folding in the ER consists of a wide variety of functions to ensure a protein takes its properly folded state. N-glycosylation can take place co- or post-translationally, Hsp70, 40, and even 90 chaperones prevent aggregation of substrates, and disulfide bond formation aids in assisting a protein's tertiary structure formation. Properly folded substrates are sent to the Golgi for further processing, while misfolded substrates may be degraded by ERAD or ERphagy.

work. This indirect targeting of viral replication via modulation of cellular processes is commonly known as 'host-directed' therapy and harbors several potential advantages over the targeting of viral proteins directly[33,34]. Virus mutational rates are known to be incredibly high relative to any living organism, including bacteria. For reference, higher eukaryotes (including humans) have a genomic mutation rate of approximately 10^{-10} per nucleotide per replication cycle. Bacteria mutate about 10x as quickly, approximately 10^{-9} per nucleotide per mutation cycle. For RNA viruses, this

rate can be as high as 10^{-4}, or 100,000x more often than bacterial genomes[35,36]. This makes viruses particularly susceptible to the development of resistance via simple mutation, thus rendering the binding of any drug ineffective. Since host proteins are outside the genetic and mutational control of the virus, any drug targeting a host process would likely remain outside the scope of resistance development. Secondly, by targeting host processes required by one virus, any related viruses would likely utilize similar processes, thus creating a broad-spectrum antiviral agent[34,37].

The idea of host-directed therapies is not new, and in fact is already in practice. Interferon, a component of the innate immune system, can be delivered to patients to boost function of the patient's own immune system, and assist in upregulating expression of antiviral genes[38,39]. Closer to the topic of this review, cyclophilin inhibitors have been shown to be effective in cases of human immunodeficiency virus (HIV) and hepatitis C virus (HCV) infections and may be effective in further exploration with other viruses known to utilize cyclophilins in their replication cycles[40–44].

This chapter will highlight the exploration of host-centered protein folding modulators which have been under investigation as antiviral compounds. Specific focus will be given towards ER proteostasis dependencies, which are still underexplored as targets for antiviral interventions.

1.2 Identifying host-virus interactions with the protein folding network

To narrow down a list of targets required for viral replication, it is necessary to understand how viral proteins and host proteins interact. Importantly, selection of targets for host-directed therapies must engage proteins without disrupting important endogenous function of these proteins within the cell or organism (to avoid viability and/or toxicity concerns). These dependencies may be elucidated in numerous ways; gain or loss-of-function screens, affinity purification of viral proteins, or proximity labeling of nearby proteins.

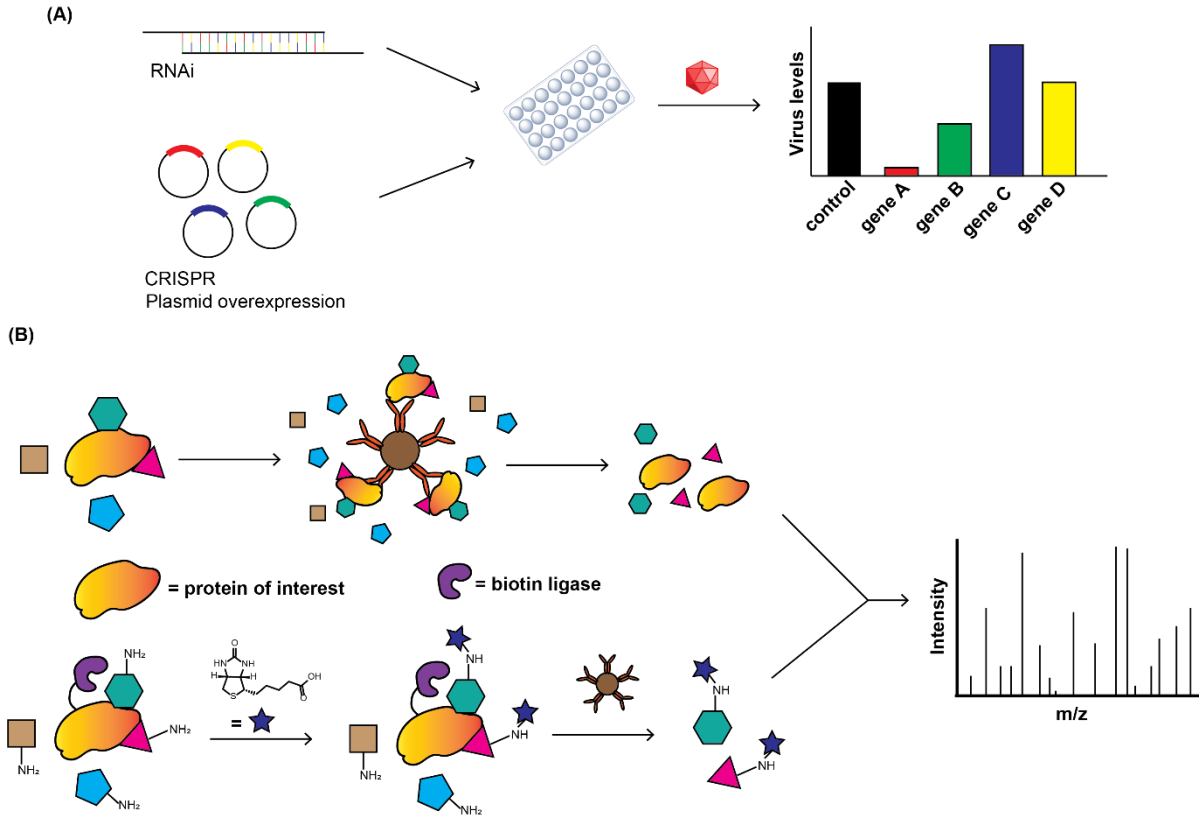

Figure 1.2. Methods for identifying virus-host interactions. (A) RNAi (top) or plasmid (bottom) libraries can be used to determine the effects on virus levels when genes are knocked down or overexpressed, respectively. (B) Affinity purification (top) or proximity labeling (bottom) approaches allow for the isolation of a protein's interactors via direct purification or attachment of an affinity handle to interactors respectivel, and those interactors can be identified using mass spectrometry.

1.2.1 Whole genome gain or loss-of-function screens

CRISPR/Cas9 and RNAi have both provided high-throughput methods for observing the role of knockout or knockdown of host proteins on viral replication in cell culture models. While not identifying interactions directly between proteins (although this data may be combined with AP-MS data as discussed below), these methods provide ways to quantify the effects of perturbing host function on viral replication[45–47]. Such screens also provide information about which proteins serve as proviral factors assisting in replication vs. those that serve as antiviral factors inhibiting infection. A whole-genome screen for gain and loss of function observations with Chikungunya virus was used to identify inhibitors of specific proteins as broad-spectrum antivirals[48]. Another

CRISPR study on flaviviruses revealed that IFI6, an interferon stimulated gene upregulated during viral infection, is an ER-localized protein that interacts with an Hsp70 chaperone in the ER lumen and prevents the formation of convoluted membranes and vesicle packets needed for flavivirus replication[49]. Interestingly, IFI6 does not affect replication of viruses that require double membrane vesicle formation, such as hepatitis C virus, since it does not affect formation of DMVs specifically[45,50–52]. Several recent studies have used knockdown screens to identify host factors required for the replication of SARS-CoV-2, the causative agent of COVID-19[45,53].

The contrast to a genetic knockdown screen would be overexpression of single proteins to monitor effects on virus replication, and this has also been performed. A gain-of-function screen using overexpression constructs identified TMEM120A as an antiviral factor during Zika infection as a result of STING activation[54]. A study by Schoggins et al. overexpressed specific interferon-stimulated genes (ISGs) to monitor effects on several human viruses, including chikungunya and several members of the Flaviviridae family[55]. A further screen used CRISPR/dCas9 as a method to overexpress single proteins and identify B4GALNT2 as an anti-pan-influenza factor[52].

1.2.2 Mass spectrometry-based identification of virus-host interactions

To uncover direct interactions between host and viral proteins, several groups have employed the use of affinity purification-mass spectrometry (AP-MS) techniques to isolate a bait protein (typically, but not always a viral protein) and its interactors. At the beginning of the COVID-19 pandemic, Gordon et al. used AP-MS to identify interactors of many SARS-CoV-2 proteins, and further showed that subsequent infection of cells treated with modulators of these interactors in some cases led to decreased viral propagation within cells[56]. Drug repurposing, though outside the scope of this review, is another strategy that has regained renewed attention during the COVID-19 pandemic. Soon to follow were studies comparing the interactors of SARS-CoV-2 to those of homologous coronavirus proteins, from both pathogenic strains such as SARS-CoV and endemic common cold strains such as hCoV-OC43[57–59]. Importantly, host-directed therapies were

later shown to be effective against emerging variants of SARS-CoV-2, indicating the conservation of intracellular interactions even as pathogenesis and transmission of these variants change[60].

Proximity approaches such as BioID and APEX labeling have also been used; these tag single viral proteins with biotin ligases, which then attach biotin to nearby proteins or interactors. These proteins can then be isolated and identified using western blot or mass spectrometry. Both techniques possess advantages and disadvantages; while proximity labeling is more promiscuous, it often aids in the identification of transient or weaker interactions as compared to traditional AP-MS. Several studies employed this method to determine the interactomes of SARS-CoV-2[61,62]. These studies largely use BioID, which tags a protein of interest with a biotin ligase; upon biotin addition to culture media, all proteins within approximately 10nm are labeled with biotin. These proteins can then be later isolated using a streptavidin pulldown[63]. This protocol has also been used to study Epstein-Barr virus Latent Membrane Protein 1, and the method was published as a suggested way to study Herpes Simplex Virus proteins[64,65].

Constraints on viral proteins often make insertion of affinity tags into replicating virus difficult, especially in cases where the genome consists of polyproteins that require individual proteins to retain specific N or C termini for protease cleavage. Heaton et al. performed transposon mutagenesis to insert random epitopes into influenza A viral proteins within the context of the full length genome. After rescuing those viruses which survived the insertion, the authors then replaced those random epitopes with affinity tags for AP-MS. They then utilized these infectious reporter viruses, which spanned 8 of the 10 viral proteins, and investigated interactions with the proteostasis network, specifically the Sec61 translocon[66]. Similar processes have been done with DENV, using transposon mutagenesis to explore the tolerance of insertions into the viral genome followed by functional analysis of interactions using an affinity-tagged replicating virus system[67,68]. In another case, Hafirassou et al. deleted three structural proteins from the DENV genome, allowing the N-terminal nonstructural protein (NS1) to be tagged without interfering with protease cleavage sites, but leaving the replication complex essentially intact with the presence of all non-

structural proteins. This allowed for identification of the NS1 interactome in a pseudo-infection context, an advantage over single protein expression. As expected, given that NS1 is a secreted protein this interactome was enriched with factors localized to the ER, as well as many localized to the mitochondria.

For viruses where single proteins are expressed in various open reading frames, these considerations are less of a factor, as the termini are more easily tagged without concerns for disrupting protease cleavage sites. A study which tagged the human cytomegalovirus protein pUL13 identified extensive interactions with ER and mitochondrial proteins[69].

1.3 Perturbing host-virus interactions with the protein folding network to block replication

1.3.1 Glycosylation & glycan modification

Glycosylation is immensely important in several viral surface proteins. For example, the Env protein of HIV (specifically the gp120 subunit) is approximately 50% glycan by weight[70]. The glycosylation patterns have been highly studied in an attempt to understand how they may influence the binding of neutralizing antibodies to specific epitopes on the envelope protein for development of vaccine candidates[71]. Of course, the requirements for any of these processes to occur is that the glycans must be correctly installed and modified on the viral proteins. As noted in the introduction, the ER is responsible for facilitating N-glycosylation at N-X-S/T motifs on nascent peptides. This glycosylation is performed by either of two catalytic subunits of the oligosaccharyl transferase (OST) complex containing catalytic subunits STT3A and STT3B[72]. Post-installation, the initial high-mannose glycan is trimmed in the ER to remove terminal glucose residues. During and after binding by any of several lectin chaperones or glycosyltransferases/glucosidases, the protein is further modified and sent to the Golgi for further modification or signaled for degradation by the proteasome (**Figure 1.3**)[73,74]. The activity of these enzymes can be competitively inhibited by iminosugars, which are sugar mimetics where the cyclic oxygen is replaced by a nitrogen atom. Clinically, iminosugars are already used for the

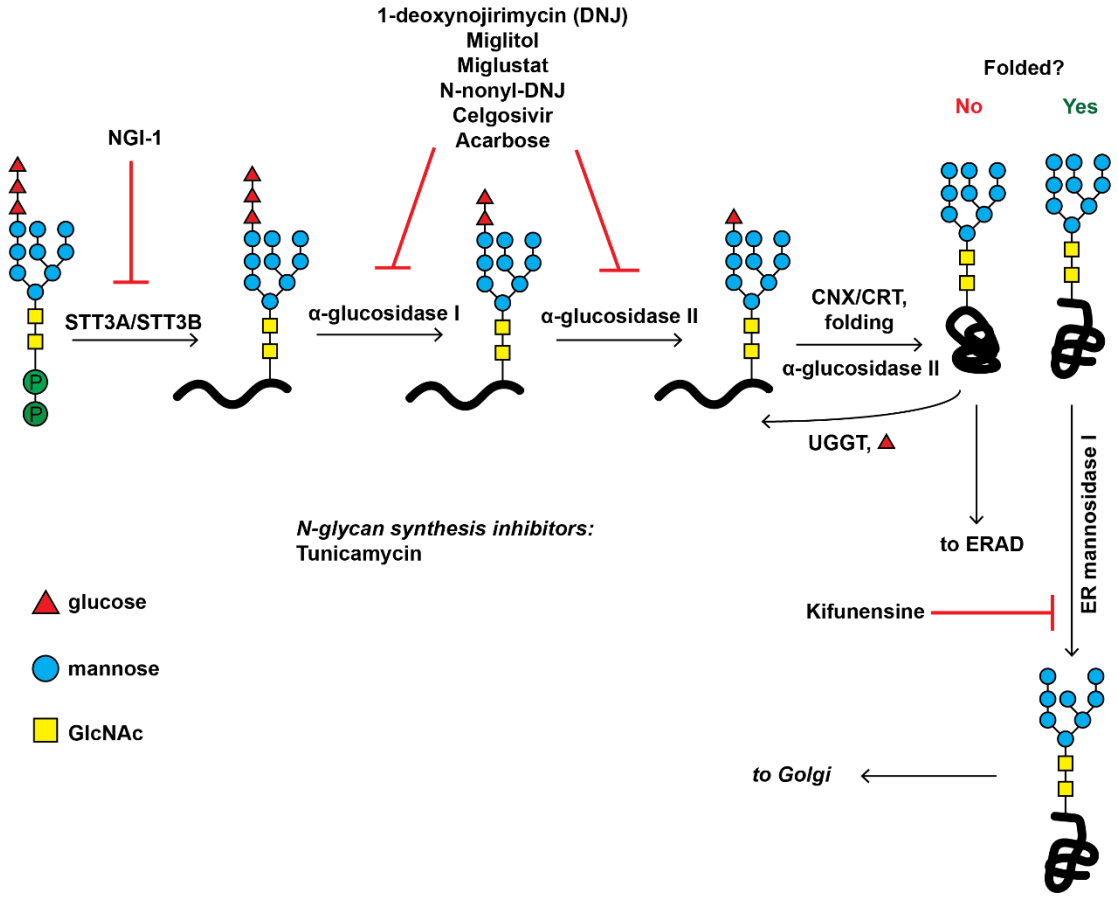

Figure 1.3. N-glycan installation and modification in the ER. After synthesis of the N-glycan on an ER-resident lipid, the oligosaccharyl transfer complex transfers the glycan to an asparagine residue co- or post-translationally using STT3A or STT3B. Glucosidases trim the proximal glucose residues, and the protein shuttles through the calnexin/calreticulin cycle until properly folded, at which point ER mannosidase I removes a single mannose residue to signal forward translocation. If a protein is not folded, it is translocated to the cytosol for ERAD.

treatment of type I Gaucher disease and/or Neimann-Pick disease type C (depending on the regulatory authority of the country), validating these as therapeutic intervention points[75,76].

ER α-glucosidases I and II carry out the initial polysaccharide trimming, removing the first and second terminal glucose residues respectively from the branched chain. Iminosugars that target these enzymes such as the one clinically approved for the diseases listed above have been shown to inhibit the replication of several different viruses, including flaviviruses, influenza viruses, and retroviruses[77–79]. However, these glucosidases may be bypassed via the action of Golgi endo-α-1,2-mannosidase (MANEA), a regulator of independent glycoprotein maturation pathway. A

structure of this enzyme was published by Sobala et al., as well as the structure in complex with inhibitors under investigation as further antiviral drugs[80].

Tunicamycin, which inhibits N-glycan synthesis, has also been used to inhibit viral infections[81].

Intriguingly, non-catalytic functions of the OST have been implicated in flavivirus infection[46]. A CRISPR screen initially identified STT3A and STT3B as host dependency factors required for viral replication; however, further studies showed the function of STT3B in DENV replication to be as a stabilizer for the non-catalytic subunit of MAGT1, where a CXXC motif is required for DENV propagation (see 'Oxidative Folding' section)[82]. This would suggest that in addition to disrupting just host-virus protein-protein interactions, interruption of certain host-host protein-protein interactions may also be an aid in inhibiting virus replication.

1.3.2 Oxidative folding

The endoplasmic reticulum, unlike the cytosol, is an oxidative environment[83]. This means the ER lumen, with the assistance of dedicated disulfide isomerases and other oxidative enzymes, is able to facilitate the formation of disulfide bonds within and between client proteins. Protein disulfide isomerases (PDIs) catalyze the oxidation of two free cysteine residues to disulfides or facilitate the rearrangement of disulfide bonds. PDIs comprise a class of ~20 enzymes which each contain at least one thioredoxin domain characterized by an active site CXXC motif[84]. Disulfide bond formation is crucial for ensuring proper folding and stabilization of most secretory proteins, hence several viruses rely on proper PDI-mediated disulfide bond formation to form progeny virions during replication. For example, the dengue virus envelope protein is known to contain disulfide bonds that link homodimers together. Various PDIs have been shown to be necessary for specific viral infections, such as the requirement for PDIA3 in the influenza A life cycle, specifically in the maturation of the HA protein into its native structure[85,86]. PDIA3 (ERp57) is also closely connected to the lectin chaperone cycle through interactions with calreticulin and calnexin, thereby linking glycan-mediated folding to oxidative folding[86]. PDIA3 may also be targeted for inhibiting proper

folding of the fusion F protein in paramyxovirus infection[87]. Another protein disulfide isomerase, PDIA4, has been shown to be necessary for uncoating of the genome uncoating of astroviruses[88]. Disulfide bonds may also mediate protein-protein interactions, such as those between the coronavirus spike protein and envelope protein. Langsjoen et al. showed that modulators of PDIs and other thioredoxin-domain containing proteins lowered extracellular plaque-forming units (PFUs) of chikungunya virus while not affecting viral RNA levels intracellularly, presumably affecting the structure of progeny virions[89]. Although the mechanism was not known at the time, PDI inhibition was shown in an older study by Ryser et al. to adversely affect the ability of HIV to bind to its cognate receptor[90]. Interestingly, this implies a functional role of PDI at the cell surface in virus infection- the localization of PDI at the cell surface was known, but its varying roles in viral infection make this a broader target for inhibiting replication. A follow up study by Fenouillet et al. identified the mechanism of this interaction, showing PDI is required for envelope-mediated membrane fusion after binding to the CD4 receptor[91].

In specific cases, secondary infection with a virus (or primary infection after vaccination) can lead to antibody dependent-enhancement, whereby antibodies from a primary infection bind but do not neutralize virions from a secondary infection, instead dissociating after phagocytosis by a macrophage and leading to subsequent infection of that macrophage[92,93]. With dengue virus, this has also been shown to be correlated with antibody titer levels post-infection. A protein disulfide isomerase inhibitor was shown to specifically block ADE of infection in human monocytic cells[94].

1.3.3 ERAD

Endoplasmic reticulum-associated degradation (ERAD) is the system responsible for hydrolysis and degradation of terminally misfolded protein clients within the ER. Herpesviruses have been shown to hijack this system by suppression of the cellular immune response, ubiquitinating and causing degradation of loaded MHC-I complexes which are en route to the cell surface for antigen display[95]. Flaviviruses use this system for selective degradation of a subset of membrane-bound

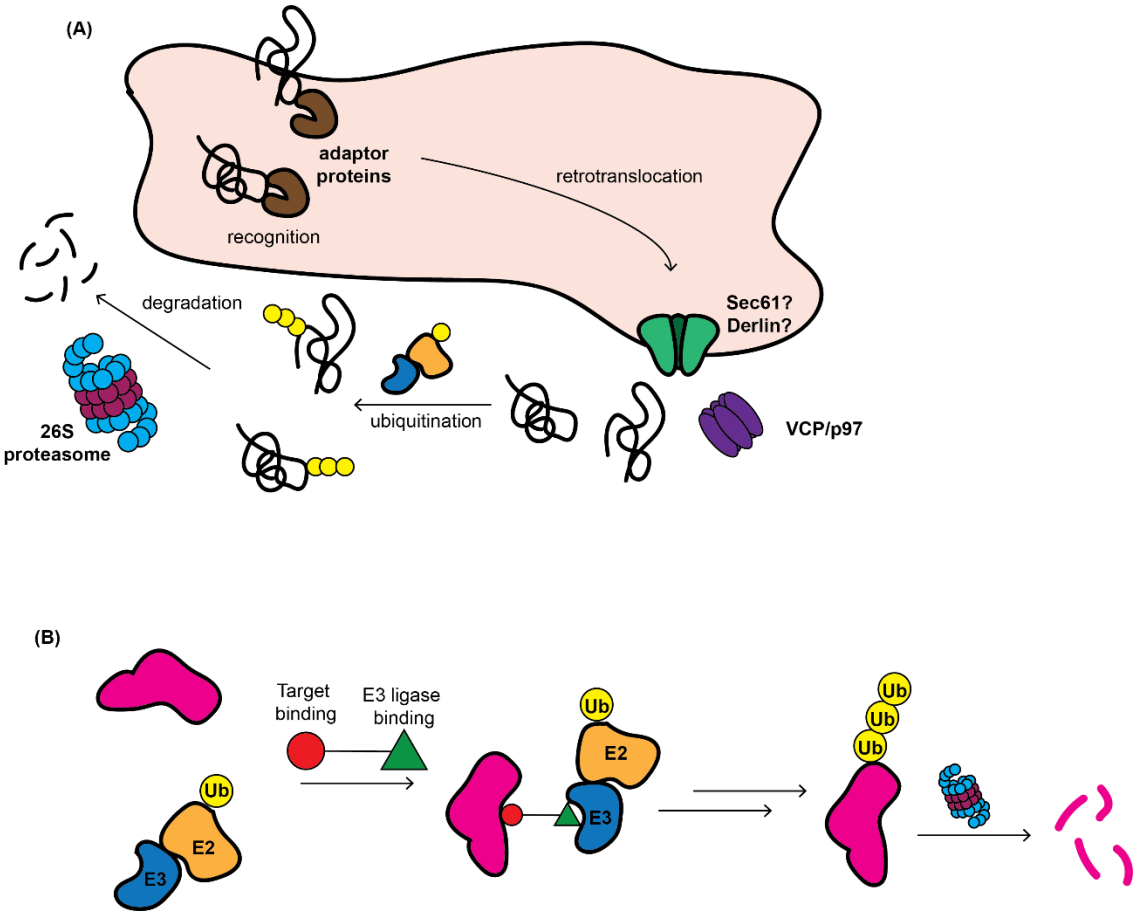

Figure 1.4. ERAD and PROTACs. (A) Misfolded protein substrates are detected and prevented from proceeding in the secretory pathway; instead, they are delivered for retrotranslocation to the cytosol and degraded by the 26S proteasome. (B) PROTACS combine a drug targeting a protein of interest with a drug targeting an E3 ligase; bringing these two proteins in proximity causes ubiquitination and subsequent degradation of the target protein.

nonstructural proteins, to ensure the presence of a correct ratio of structural to non-structural proteins during replication[96].

After recognition of these misfolded proteins, the p97/VCP (vasolin containing protein) retrotranslocation complex binds the client protein and retrotranslocates it to the cytosol. The ATPase activity of VCP has been shown to be essential for formation of DENV replication organelles via interaction with NS4B. Pharmacologic inhibition of this ATPase activity prevents replication of the virus[97].

In addition to ERAD machinery being used by viruses, PROteolysis TArgeting Chimeras (PROTACs) have been developed to selectively degrade host factors needed for viral replication. Hahn et al. showed selective degradation of cyclin-dependent kinase 9 led to inhibition of cytomegalovirus (CMV) and SARS-CoV-2, while not affecting the replication of other viruses such as Varicella Zoster Virus (VZV) and Zika[98]. A second study showed that a PROTAC linking indomethacin with an E3 ligase targeting compound showed pan-coronavirus activity. This activity was hypothesized to be through disruption of the interaction between nsp7 and PGES-2, a prostaglandin E synthase[99]. Another strategy fuses peptide sequences instead of small molecules; Montrose and Krissansen fused two domains of the hepatitis B X-protein (an oligomerization domain and an instability domain) together along with a cell penetrating peptide. As the oligomerization domain bound another molecule of the X-protein, the instability domain leads to ubiquitination and degradation of the complex[100]. While not always directly targeting host-virus interactions, this perturbation of a host protein has nonetheless proven an effective method of controlling host biology to compromise viral replication.

1.3.4 The Unfolded Protein Response

As noted earlier, the UPR is a three-pronged stress response pathway that leads to the upregulation of chaperones, lipid biosynthesis, and other folding factors (through the IRE1/XBP1s arms), as well as feeding into the integrated stress response to temporarily attenuate translation (via the PERK arm)[18]. Many viruses have been shown to upregulate these pathways, including flaviviruses and coronaviruses, as their proteins are translated and hijack the chaperone pathways normally reserved for host client proteins[101,102]. This UPR activation is typically mild, presumably as the virus attempts to control any clearance that may occur as a result of prolonged ER stress. Additionally, prolonged or intense ER stress induces apoptosis, and thus mild activation subverts these paths to maintain cell viability[18,103].

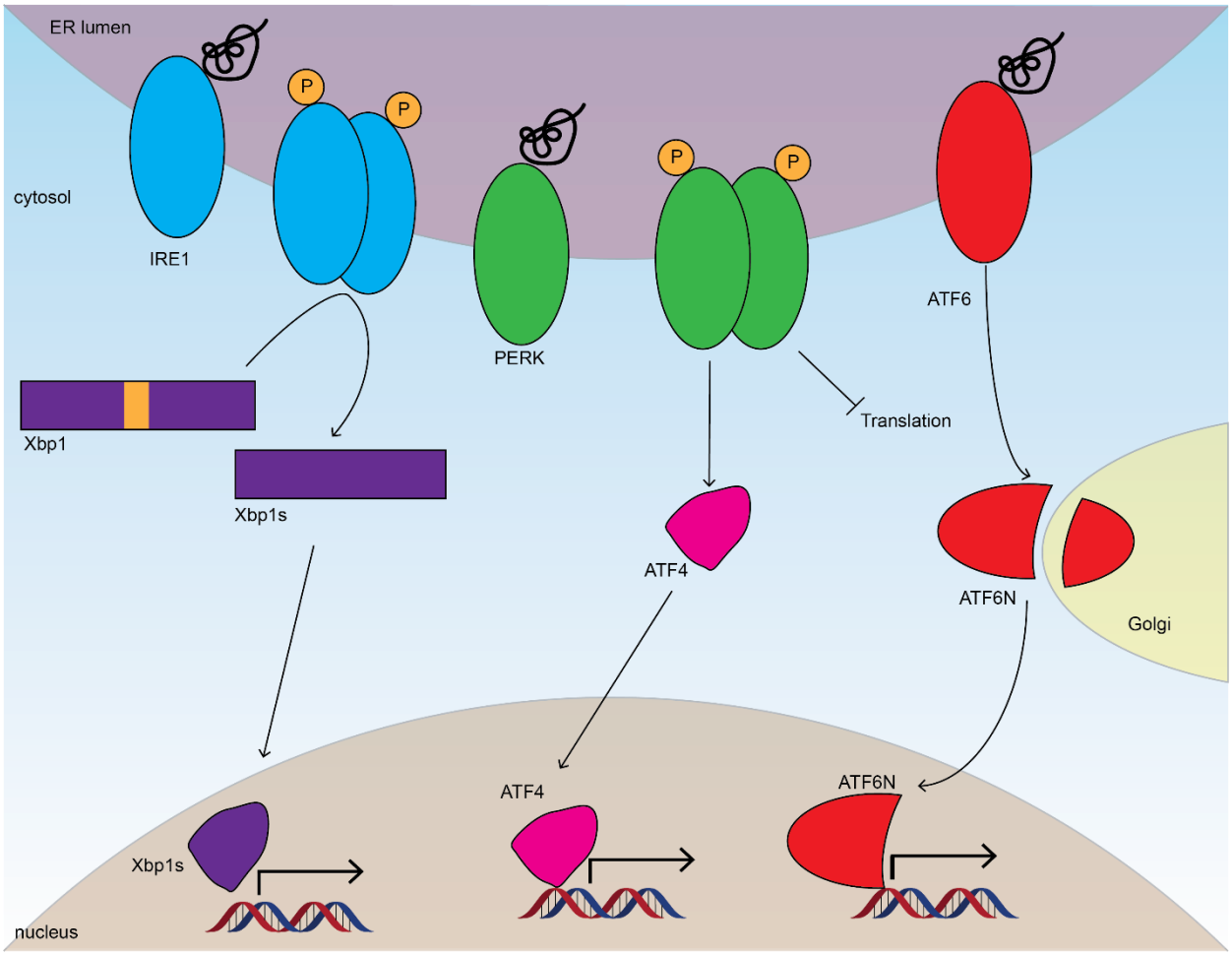

Figure 1.5. The unfolded protein response. Three transmembrane sensors sit across the ER membrane. On dissociation of binding immunoglobulin protein from the sensor (shown in black), activation by dimerization or disulfide bond isomerization causes downstream effects leading to upregulation of reporter genes for each branch.

The UPR has become an increasingly interesting pharmacologic target because of its dysregulation in many disease states. Small molecule modulators of UPR signaling have effects ranging from control of cardiac damage after stress to control of diabetes and obesity[104–106]. Several viruses have been shown to activate the UPR, while several others have been known to suppress activation[103,107]. UPR modulation has been studied in the context of single protein overexpression, as well as in the context of live infection. For a more detailed discussion of how different virus families manipulate the UPR, see the review by Prasad and Greber[107].

Our lab recently showed that a compound initially designed as an activator of the ATF6 arm of the UPR was able to inhibit DENV and ZIKV infection in cell culture models, though this activity was shown to be independent of ATF6 activity and rather relied on covalent modification of thiols on largely ER resident proteins[108].

A combination of UPR inhibitors was shown to inhibit both murine hepatitis virus (MHV) and SARS-CoV-2 infection in cell models. Inhibitors of the PERK and ATF6 branches were effective on their own, a combination treatment was shown to be the most effective[109]. Another study by Sims et al. showed inhibition of PERK using the small molecule AMG PERK 44 resulted in a decrease in MERS-CoV replication in in primary human lung cells[110]. A combination of UPR inhibitors was also shown to have anti-ZIKV effects in human lung cells; PERK inhibition on its own showed no effects, but ATF6 inhibition using Ceapin-A7 did. Co-treatment of the two was able to further inhibit infection, suggesting synergistic action is required for the activity of the PERK inhibitor. 4-phenylbutyric acid inhibits ATF6 and PERK while potentiating IRE1 activity, and this combination was also sufficient to inhibit ZIKV replication[111].

Contrarily, activation of the UPR using pharmacologic thiopurines was shown to affect influenza A virus maturation without affecting intracellular viral RNA levels[112]. Global UPR activation with Brefeldin A (a trafficking inhibitor), tunicamycin (an N-glycosylation inhibitor), or thapsigargin (a SERCA ATPase inhibitor) also inhibited rhinovirus replication in airway epithelial cells[81]. Thapsigargin was also shown to inhibit replication of three different coronavirus strains (hCoV-229E, MERS-CoV, SARS-CoV-2) in various cell types[113]. A broader study showed it to be effective against additional respiratory viruses, namely influenza A and respiratory syncytial virus[114]. Therapeutic use of thapsigargin is limited due to its extremely high cytotoxicity; however, less-toxic derivatives and prodrug variants are being explored[115].

1.3.5 Other proteostasis factors

The sections above provide a broad but not all-encompassing overview of the ways in which proteostasis modulation has been used to inhibit replication of several classes of viruses. Among

other pathways targeted are translation and the translocon machinery, as noted in the influenza virus interactome study above. Some cotransational processes such as glycosylation have already been discussed, but other less studied processes such as proline hydroxylation have also been shown to be essential for viral replication (flaviviruses in this case)[116].

Furthermore, inhibition of GRP94, an ER-resident Hsp90-like protein, was shown to inhibit dengue and Zika virus replication in Huh7 cells[117].

1.4 Summary and Conclusions

This review summarizes some of the ways in which virus-host interactions are identified, with particular focus on those interactions of viral proteins with host endoplasmic reticulum machinery. The endoplasmic reticulum, as a hub for protein folding within the cell, provides many chaperones that viruses have evolved to utilize within their own replication cycles.

We then examine the ways in which these interactions or dependencies may be targeted using host-directed therapies in order to inhibit viral replication. The two largest advantages posited by this method, as opposed to traditional direct-acting antiviral therapy, are avoiding the high mutational rates of viruses, as well as targeting conserved host factors to create a broad-spectrum antiviral compound. However, other concerns must be addressed before many of these compounds are utilized in a therapeutic capacity, including validation of *in vivo* efficacy while avoiding toxicity to the host. Additionally, although it is harder for viruses to evolve resistance to host-centered therapeutics, the possibility still exists. Newcastle disease virus on long term propagation was shown to acquire resistance to thapsigargin[118]. Similarly, an inhibitor of MNK1, which is effective against buffalopox virus, becomes ineffective after multiple passages[119]. Thus, caution must be taken to monitor resistance development even with host-centered molecules.

1.5 Scope of dissertation

This dissertation outlines the work I have conducted in furthering our understanding of the ways in which viruses interact with host cells and begins exploring how these dependencies can be exploited for the pursuit of new antiviral targets. This work approaches the problem from two sides: 1) identifying the interactions protein-protein interactions that take place during viral infections with the intention of understanding their importance, and 2) using small molecules that disrupt known interactions with the intention of discovering their specific targets. This chapter has outlined some of the known relationships of viruses with the endoplasmic reticulum protein folding network, concluding that these interactions are extensive and encompass several classes and functions of proteins. With an interest in these proteostasis interactions, particularly those related to the unfolded protein response, chapter 2 explores the effects of UPR regulators on flavivirus infection. These regulators, which are all recently discovered molecules, were designed to be able to preferentially activate or inhibit the IRE1 and ATF6 branches of the UPR. Chapter 2 answers the question of how modulating these pathways affects viral replication. Of these regulators, the ATF6 activator **147** was the only one that showed effects on viral replication. These effects are further investigated in chapter 3, where I show the antiviral effects are independent of ATF6 activation, but rather dependent on covalent targeting of free thiols, namely cysteine residues on ER resident proteins. Although the specific targets of **147** responsible for the antiviral activity are still unknown, the molecule possesses broad-spectrum activity against several dengue and Zika strains. In chapter 4, I explore the effects of a structurally similar molecule, **263**. This was another compound discovered in the initial screen for ATF6 activators[120]. Given the structural similarities between **263** and **147**, I hypothesized that the mechanisms of action may be similar. However, we show that this is not the case and the covalent protein targets are different. Similarly to **147**, the targets of **263** responsible for the antiviral activity remain unknown.

Chapter 5 then begins exploring the interactions of coronavirus non-structural proteins with the host cell; this project began as the COVID-19 pandemic reached the United States, and our lab

gained an interest in determining how the interactions of SARS-CoV-2 proteins are similar or different to those of homologous proteins from other coronavirus strains. We begin with nsp2 and nsp4. Nsp2 is a non-conserved protein that is dispensable for replication, while nsp4 is more conserved and forms an integral part of the double-membrane vesicles, which are characteristic of and necessary for replication of the viral genome. Several interactors are conserved between SARS-CoV-1 and SARS-CoV-2 nsp2, and between SARS-CoV-1, SARS-CoV-2, and hCoV-OC43 nsp4 homologs. However, several unique interactions are also seen with each homolog, and exploring these differential interactions may explain some of the unique pathogenesis seen with each strain. Followup studies show these interactors are enriched for proteins found at mitochondria-associated ER membranes. In chapter 6, we study the host interactions of coronavirus nsp3, a large, multi-domain protein that required truncations in order to express. We truncate the protein into three parts and study homologs from five different coronavirus strains; the three noted above, in addition to MERS-CoV and hCoV-229E. Similarly to the nsp2/nsp4 study, we show both conserved interactions and unique interactions, though almost no interactions were seen that were common to all five coronavirus strains. We discovered that the nsp3 N-terminal fragment (nsp3.1) interacted with the UPR sensor ATF6, and follow-up studies have shown that nsp3.1 from SARS-CoV-2 is able to modulate the ATF6 stress response. Lastly, chapter 7 summarizes my work as well as exploring ongoing experiments and provides ideas on how the work may continue.

Overall, this work contributes to our understanding of how virus hijack signaling pathways within cells to facilitate their own replication cycles and opens the possibility to targeting some of these interactions for therapeutic purposes.

1.6 References

(1) Neufeldt, C. J.; Cortese, M.; Acosta, E. G.; Bartenschlager, R. Rewiring Cellular Networks by Members of the Flaviviridae Family. *Nat. Rev. Microbiol.* **2018**, *16* (3), 125–142. https://doi.org/10.1038/NRMICRO.2017.170.

(2) Belov, G. A.; Van Kuppeveld, F. J. (+)RNA Viruses Rewire Cellular Pathways to Build Replication Organelles. *Curr. Opin. Virol.* **2012**, *2* (6), 740–747. https://doi.org/10.1016/J.COVIRO.2012.09.006.

(3) Taguwa, S.; Maringer, K.; Li, X.; Bernal-Rubio, D.; Rauch, J. N.; Gestwicki, J. E.; Andino, R.; Fernandez-Sesma, A.; Frydman, J. Defining Hsp70 Subnetworks in Dengue Virus Replication Reveals Key Vulnerability in Flavivirus Infection. *Cell* **2015**, *163* (5), 1108–1123. https://doi.org/10.1016/J.CELL.2015.10.046/ATTACHMENT/DD2A8D18-BB22-4E83-8D1D-06E377EAF788/MMC1.PDF.

(4) Taguwa, S.; Yeh, M. Te; Rainbolt, T. K.; Nayak, A.; Shao, H.; Gestwicki, J. E.; Andino, R.; Frydman, J. Zika Virus Dependence on Host Hsp70 Provides a Protective Strategy against Infection and Disease. *Cell Rep.* **2019**, *26* (4), 906-920.e3. https://doi.org/10.1016/J.CELREP.2018.12.095/ATTACHMENT/0C673173-7F84-4B6E-946B-0B1FFF72CE80/MMC1.PDF.

(5) Ravindran, M. S.; Bagchi, P.; Cunningham, C. N.; Tsai, B. Opportunistic Intruders: How Viruses Orchestrate ER Functions to Infect Cells. *Nat. Rev. Microbiol.* **2016**, *14* (7), 407–420. https://doi.org/10.1038/nrmicro.2016.60.

(6) Inoue, T.; Tsai, B. How Viruses Use the Endoplasmic Reticulum for Entry, Replication, and Assembly. *Cold Spring Harb. Perspect. Biol.* **2013**, *5* (1), a013250. https://doi.org/10.1101/CSHPERSPECT.A013250.

(7) Gillespie, L. K.; Hoenen, A.; Morgan, G.; Mackenzie, J. M. The Endoplasmic Reticulum Provides the Membrane Platform for Biogenesis of the Flavivirus Replication Complex. *J. Virol.* **2010**, *84* (20), 10438–10447. https://doi.org/10.1128/JVI.00986-10/SUPPL_FILE/SUPPL__FIG____MOVIE_LEGENDS.DOC.

(8) Espadas, J.; Pendin, D.; Bocanegra, R.; Escalada, A.; Misticoni, G.; Trevisan, T.; Velasco del Olmo, A.; Montagna, A.; Bova, S.; Ibarra, B.; Kuzmin, P. I.; Bashkirov, P. V.; Shnyrova, A. V.; Frolov, V. A.; Daga, A. Dynamic Constriction and Fission of Endoplasmic Reticulum Membranes by Reticulon. *Nat. Commun.* **2019**, *10* (1), 1–11. https://doi.org/10.1038/s41467-019-13327-7.

(9) Shibata, Y.; Voeltz, G. K.; Rapoport, T. A. Rough Sheets and Smooth Tubules. *Cell* **2006**, *126* (3), 435–439. https://doi.org/10.1016/J.CELL.2006.07.019.

(10) Parashar, S.; Chidambaram, R.; Chen, S.; Liem, C. R.; Griffis, E.; Lambert, G. G.; Shaner, N. C.; Wortham, M.; Hay, J. C.; Ferro-Novick, S. Endoplasmic Reticulum Tubules Limit the Size of Misfolded Protein Condensates. *Elife* **2021**, *10*. https://doi.org/10.7554/ELIFE.71642.

(11) Puhka, M.; Joensuu, M.; Vihinen, H.; Belevich, I.; Jokitalo, E. Progressive Sheet-to-Tubule Transformation Is a General Mechanism for Endoplasmic Reticulum Partitioning in Dividing Mammalian Cells. *Mol. Biol. Cell* **2012**, *23* (13), 2424–2432. https://doi.org/10.1091/MBC.E10-12-0950/ASSET/IMAGES/LARGE/2424FIG9.JPEG.

(12) Benham, A. M. Protein Secretion and the Endoplasmic Reticulum. *Cold Spring Harb. Perspect. Biol.* **2012**, *4* (8), a012872. https://doi.org/10.1101/CSHPERSPECT.A012872.

(13) Speckhart, K.; Williams, J. M.; Tsai, B. How DNA and RNA Viruses Exploit Host Chaperones to Promote Infection. *Viruses* **2021**, *13* (6), 958. https://doi.org/10.3390/V13060958.

(14) Akopian, D.; Shen, K.; Zhang, X.; Shan, S. O. Signal Recognition Particle: An Essential Protein-Targeting Machine. *Annu. Rev. Biochem.* **2013**, *82*, 693–721.

https://doi.org/10.1146/ANNUREV-BIOCHEM-072711-164732.

(15) Meusser, B.; Hirsch, C.; Jarosch, E.; Sommer, T. ERAD: The Long Road to Destruction. *Nat. Cell Biol.* **2005**, *7* (8), 766–772. https://doi.org/10.1038/ncb0805-766.

(16) Das, P.; Dudley, J. P. How Viruses Use the VCP/P97 ATPase Molecular Machine. *Viruses* **2021**, *13* (9), 1881. https://doi.org/10.3390/V13091881.

(17) Chino, H.; Mizushima, N. ER-Phagy: Quality Control and Turnover of Endoplasmic Reticulum. *Trends Cell Biol.* **2020**, *30* (5), 384–398. https://doi.org/10.1016/J.TCB.2020.02.001.

(18) Walter, P.; Ron, D. The Unfolded Protein Response: From Stress Pathway to Homeostatic Regulation. *Science (80-.).* **2011**, *334* (6059), 1081–1086. https://doi.org/10.1126/SCIENCE.1209038/ASSET/238BD530-CE66-4C19-BA32-FC13641E3646/ASSETS/GRAPHIC/334_1081_F3.JPEG.

(19) Gonzalez-Teuber, V.; Albert-Gasco, H.; Auyeung, V. C.; Papa, F. R.; Mallucci, G. R.; Hetz, C. Small Molecules to Improve ER Proteostasis in Disease. *Trends Pharmacol. Sci.* **2019**, *40* (9), 684–695. https://doi.org/10.1016/J.TIPS.2019.07.003.

(20) Kurtishi, A.; Rosen, B.; Patil, K. S.; Alves, G. W.; Møller, S. G. Cellular Proteostasis in Neurodegeneration. *Mol. Neurobiol.* **2019**, *56* (5), 3676–3689. https://doi.org/10.1007/S12035-018-1334-Z/FIGURES/3.

(21) Hipp, M. S.; Kasturi, P.; Hartl, F. U. The Proteostasis Network and Its Decline in Ageing. *Nat. Rev. Mol. Cell Biol.* **2019**, *20* (7), 421–435. https://doi.org/10.1038/s41580-019-0101-y.

(22) Klaips, C. L.; Jayaraj, G. G.; Hartl, F. U. Pathways of Cellular Proteostasis in Aging and Disease. *J. Cell Biol.* **2018**, *217* (1), 51–63. https://doi.org/10.1083/JCB.201709072.

(23) Welsch, S.; Miller, S.; Romero-Brey, I.; Merz, A.; Bleck, C. K. E.; Walther, P.; Fuller, S. D.; Antony, C.; Krijnse-Locker, J.; Bartenschlager, R. Composition and Three-Dimensional Architecture of the Dengue Virus Replication and Assembly Sites. *Cell Host Microbe* **2009**, *5* (4), 365–375. https://doi.org/10.1016/J.CHOM.2009.03.007.

(24) Romero-Brey, I.; Merz, A.; Chiramel, A.; Lee, J. Y.; Chlanda, P.; Haselman, U.; Santarella-Mellwig, R.; Habermann, A.; Hoppe, S.; Kallis, S.; Walther, P.; Antony, C.; Krijnse-Locker, J.; Bartenschlager, R. Three-Dimensional Architecture and Biogenesis of Membrane Structures Associated with Hepatitis C Virus Replication. *PLOS Pathog.* **2012**, *8* (12), e1003056. https://doi.org/10.1371/JOURNAL.PPAT.1003056.

(25) Wolff, G.; Limpens, R. W. A. L.; Zevenhoven-Dobbe, J. C.; Laugks, U.; Zheng, S.; de Jong, A. W. M.; Koning, R. I.; Agard, D. A.; Grünewald, K.; Koster, A. J.; Snijder, E. J.; Bárcena, M. A Molecular Pore Spans the Double Membrane of the Coronavirus Replication Organelle. *Science (80-.).* **2020**, *369* (6509), 1395–1398. https://doi.org/10.1126/SCIENCE.ABD3629/SUPPL_FILE/ABD3629_WOLFF_SM.PDF.

(26) Ci, Y.; Liu, Z. Y.; Zhang, N. N.; Niu, Y.; Yang, Y.; Xu, C.; Yang, W.; Qin, C. F.; Shi, L. Zika NS1-Induced ER Remodeling Is Essential for Viral Replication. *J. Cell Biol.* **2020**, *219* (2). https://doi.org/10.1083/JCB.201903062/133534.

(27) Netherton, C.; Moffat, K.; Brooks, E.; Wileman, T. A Guide to Viral Inclusions, Membrane Rearrangements, Factories, and Viroplasm Produced During Virus Replication. *Adv. Virus Res.* **2007**, *70*, 101–182. https://doi.org/10.1016/S0065-3527(07)70004-0.

(28) Dolnik, O.; Gerresheim, G. K.; Biedenkopf, N. New Perspectives on the Biogenesis of

Viral Inclusion Bodies in Negative-Sense RNA Virus Infections. *Cells* **2021**, *10* (6), 1460. https://doi.org/10.3390/CELLS10061460.

(29) Plate, L.; Wiseman, R. L. Regulating Secretory Proteostasis through the Unfolded Protein Response: From Function to Therapy. *Trends Cell Biol.* **2017**, *27* (10), 722–737. https://doi.org/10.1016/J.TCB.2017.05.006.

(30) Grandjean, J. M. D.; Luke Wiseman, R. Small Molecule Strategies to Harness the Unfolded Protein Response: Where Do We Go from Here? *J. Biol. Chem.* **2020**, *295* (46), 15692–15711. https://doi.org/10.1074/JBC.REV120.010218.

(31) Labbadia, J.; Morimoto, R. I. The Biology of Proteostasis in Aging and Disease. *Annu. Rev. Biochem.* **2015**, *84*, 435–464. https://doi.org/10.1146/ANNUREV-BIOCHEM-060614-033955.

(32) Brusa, I.; Sondo, E.; Falchi, F.; Pedemonte, N.; Roberti, M.; Cavalli, A. Proteostasis Regulators in Cystic Fibrosis: Current Development and Future Perspectives. *J. Med. Chem.* **2022**, *65* (7), 5212–5243. https://doi.org/10.1021/ACS.JMEDCHEM.1C01897.

(33) Mahajan, S.; Choudhary, S.; Kumar, P.; Tomar, S. Antiviral Strategies Targeting Host Factors and Mechanisms Obliging +ssRNA Viral Pathogens. *Bioorg. Med. Chem.* **2021**, *46*, 116356. https://doi.org/10.1016/J.BMC.2021.116356.

(34) Kumar, N.; Sharma, S.; Kumar, R.; Tripathi, B. N.; Barua, S.; Ly, H.; Rouse, B. T. Host-Directed Antiviral Therapy. *Clin. Microbiol. Rev.* **2020**, *33* (3). https://doi.org/10.1128/CMR.00168-19/ASSET/155DF052-ACD0-479E-B444-67ABFB9E2044/ASSETS/GRAPHIC/CMR.00168-19-F0003.GIF.

(35) Duffy, S. Why Are RNA Virus Mutation Rates so Damn High? *PLOS Biol.* **2018**, *16* (8), e3000003. https://doi.org/10.1371/JOURNAL.PBIO.3000003.

(36) Gago, S.; Elena, S. F.; Flores, R.; Sanjuán, R. Extremely High Mutation Rate of a Hammerhead Viroid. *Science (80-.).* **2009**, *323* (5919), 1308. https://doi.org/10.1126/SCIENCE.1169202/SUPPL_FILE/GAGO.SOM.PDF.

(37) Geller, R.; Taguwa, S.; Frydman, J. Broad Action of Hsp90 as a Host Chaperone Required for Viral Replication. *Biochim. Biophys. Acta - Mol. Cell Res.* **2012**, *1823* (3), 698–706. https://doi.org/10.1016/J.BBAMCR.2011.11.007.

(38) Katze, M. G.; He, Y.; Gale, M. Viruses and Interferon: A Fight for Supremacy. *Nat. Rev. Immunol.* **2002**, *2* (9), 675–687. https://doi.org/10.1038/nri888.

(39) Lin, F. ching; Young, H. A. Interferons: Success in Anti-Viral Immunotherapy. *Cytokine Growth Factor Rev.* **2014**, *25* (4), 369–376. https://doi.org/10.1016/J.CYTOGFR.2014.07.015.

(40) Gallay, P. A. Cyclophilin Inhibitors: A Novel Class of Promising Host-Targeting Anti-HCV Agents. *Immunol. Res.* **2012**, *52* (3), 200–210. https://doi.org/10.1007/S12026-011-8263-5/FIGURES/2.

(41) Ptak, R. G.; Gallay, P. A.; Jochmans, D.; Halestrap, A. P.; Ruegg, U. T.; Pallansch, L. A.; Bobardt, M. D.; De Béthune, M. P.; Neyts, J.; De Clercq, E.; Dumont, J. M.; Scalfaro, P.; Besseghir, K.; Wenger, R. M.; Rosenwirth, B. Inhibition of Human Immunodeficiency Virus Type 1 Replication in Human Cells by Debio-025, a Novel Cyclophilin Binding Agent. *Antimicrob. Agents Chemother.* **2008**, *52* (4), 1302–1317. https://doi.org/10.1128/AAC.01324-07/SUPPL_FILE/SUPPLEMENT_TABLE.PDF.

(42) Ahmed-Belkacem, A.; Colliandre, L.; Ahnou, N.; Nevers, Q.; Gelin, M.; Bessin, Y.; Brillet,

R.; Cala, O.; Douguet, D.; Bourguet, W.; Krimm, I.; Pawlotsky, J. M.; Guichou, J. F. Fragment-Based Discovery of a New Family of Non-Peptidic Small-Molecule Cyclophilin Inhibitors with Potent Antiviral Activities. *Nat. Commun.* **2016**, *7* (1), 1–11. https://doi.org/10.1038/ncomms12777.

(43) Colpitts, C. C.; Ridewood, S.; Schneiderman, B.; Warne, J.; Tabata, K.; Ng, C. F.; Bartenschlager, R.; Selwood, D. L.; Towers, G. J. Hepatitis C Virus Exploits Cyclophilin a to Evade PKR. *Elife* **2020**, *9*, 1–25. https://doi.org/10.7554/ELIFE.52237.

(44) Nevers, Q.; Ruiz, I.; Ahnou, N.; Donati, F.; Brillet, R.; Softic, L.; Chazal, M.; Jouvenet, N.; Fourati, S.; Baudesson, C.; Bruscella, P.; Gelin, M.; Guichou, J. F.; Pawlotsky, J. M.; Ahmed-Belkacem, A. Characterization of the Anti-Hepatitis C Virus Activity of New Nonpeptidic Small-Molecule Cyclophilin Inhibitors with the Potential for Broad Anti-Flaviviridae Activity. *Antimicrob. Agents Chemother.* **2018**, *62* (7). https://doi.org/10.1128/AAC.00126-18/SUPPL_FILE/ZAC007187285S1.PDF.

(45) Wang, R.; Simoneau, C. R.; Kulsuptrakul, J.; Bouhaddou, M.; Travisano, K. A.; Hayashi, J. M.; Carlson-Stevermer, J.; Zengel, J. R.; Richards, C. M.; Fozouni, P.; Oki, J.; Rodriguez, L.; Joehnk, B.; Walcott, K.; Holden, K.; Sil, A.; Carette, J. E.; Krogan, N. J.; Ott, M.; Puschnik, A. S. Genetic Screens Identify Host Factors for SARS-CoV-2 and Common Cold Coronaviruses. *Cell* **2021**, *184* (1), 106-119.e14. https://doi.org/10.1016/J.CELL.2020.12.004/ATTACHMENT/6132394D-27BB-4E30-92C2-8C0A4D8878CC/MMC5.XLSX.

(46) Marceau, C. D.; Puschnik, A. S.; Majzoub, K.; Ooi, Y. S.; Brewer, S. M.; Fuchs, G.; Swaminathan, K.; Mata, M. A.; Elias, J. E.; Sarnow, P.; Carette, J. E. Genetic Dissection of Flaviviridae Host Factors through Genome-Scale CRISPR Screens. *Nature* **2016**, *535* (7610), 159–163. https://doi.org/10.1038/nature18631.

(47) Han, J.; Perez, J. T.; Chen, C.; Li, Y.; Benitez, A.; Kandasamy, M.; Lee, Y.; Andrade, J.; tenOever, B.; Manicassamy, B. Genome-Wide CRISPR/Cas9 Screen Identifies Host Factors Essential for Influenza Virus Replication. *Cell Rep.* **2018**, *23* (2), 596–607. https://doi.org/10.1016/J.CELREP.2018.03.045.

(48) Karlas, A.; Berre, S.; Couderc, T.; Varjak, M.; Braun, P.; Meyer, M.; Gangneux, N.; Karo-Astover, L.; Weege, F.; Raftery, M.; Schönrich, G.; Klemm, U.; Wurzlbauer, A.; Bracher, F.; Merits, A.; Meyer, T. F.; Lecuit, M. A Human Genome-Wide Loss-of-Function Screen Identifies Effective Chikungunya Antiviral Drugs. *Nat. Commun.* **2016**, *7* (1), 1–14. https://doi.org/10.1038/ncomms11320.

(49) Richardson, R. B.; Ohlson, M. B.; Eitson, J. L.; Kumar, A.; McDougal, M. B.; Boys, I. N.; Mar, K. B.; De La Cruz-Rivera, P. C.; Douglas, C.; Konopka, G.; Xing, C.; Schoggins, J. W. A CRISPR Screen Identifies IFI6 as an ER-Resident Interferon Effector That Blocks Flavivirus Replication. *Nat. Microbiol.* **2018**, *3* (11), 1214–1223. https://doi.org/10.1038/s41564-018-0244-1.

(50) Daniloski, Z.; Jordan, T. X.; Wessels, H. H.; Hoagland, D. A.; Kasela, S.; Legut, M.; Maniatis, S.; Mimitou, E. P.; Lu, L.; Geller, E.; Danziger, O.; Rosenberg, B. R.; Phatnani, H.; Smibert, P.; Lappalainen, T.; tenOever, B. R.; Sanjana, N. E. Identification of Required Host Factors for SARS-CoV-2 Infection in Human Cells. *Cell* **2021**, *184* (1), 92-105.e16. https://doi.org/10.1016/J.CELL.2020.10.030.

(51) Wei, J.; Alfajaro, M. M.; DeWeirdt, P. C.; Hanna, R. E.; Lu-Culligan, W. J.; Cai, W. L.; Strine, M. S.; Zhang, S. M.; Graziano, V. R.; Schmitz, C. O.; Chen, J. S.; Mankowski, M. C.; Filler, R. B.; Ravindra, N. G.; Gasque, V.; de Miguel, F. J.; Patil, A.; Chen, H.;

Oguntuyo, K. Y.; Abriola, L.; Surovtseva, Y. V.; Orchard, R. C.; Lee, B.; Lindenbach, B. D.; Politi, K.; van Dijk, D.; Kadoch, C.; Simon, M. D.; Yan, Q.; Doench, J. G.; Wilen, C. B. Genome-Wide CRISPR Screens Reveal Host Factors Critical for SARS-CoV-2 Infection. *Cell* **2021**, *184* (1), 76-91.e13. https://doi.org/10.1016/J.CELL.2020.10.028.

(52) Heaton, B. E.; Kennedy, E. M.; Dumm, R. E.; Harding, A. T.; Sacco, M. T.; Sachs, D.; Heaton, N. S. A CRISPR Activation Screen Identifies a Pan-Avian Influenza Virus Inhibitory Host Factor. *Cell Rep.* **2017**, *20* (7), 1503–1512. https://doi.org/10.1016/J.CELREP.2017.07.060.

(53) Jones, C. E.; Tan, W. S.; Grey, F.; Hughes, D. J. Discovering Antiviral Restriction Factors and Pathways Using Genetic Screens. *J. Gen. Virol.* **2021**, *102*, 1603. https://doi.org/10.1099/jgv.0.001603.

(54) Li, S.; Qian, N.; Jiang, C.; Zu, W.; Liang, A.; Li, M.; Elledge, S. J.; Tan, X. Gain-of-Function Genetic Screening Identifies the Antiviral Function of TMEM120A via STING Activation. *Nat. Commun.* **2022**, *13* (1), 1–12. https://doi.org/10.1038/s41467-021-27670-1.

(55) Schoggins, J. W.; Wilson, S. J.; Panis, M.; Murphy, M. Y.; Jones, C. T.; Bieniasz, P.; Rice, C. M. A Diverse Range of Gene Products Are Effectors of the Type I Interferon Antiviral Response. *Nature* **2011**, *472* (7344), 481–485. https://doi.org/10.1038/nature09907.

(56) Gordon, D. E.; Jang, G. M.; Bouhaddou, M.; Xu, J.; Obernier, K.; White, K. M.; O'Meara, M. J.; Rezelj, V. V.; Guo, J. Z.; Swaney, D. L.; Tummino, T. A.; Hüttenhain, R.; Kaake, R. M.; Richards, A. L.; Tutuncuoglu, B.; Foussard, H.; Batra, J.; Haas, K.; Modak, M.; Kim, M.; Haas, P.; Polacco, B. J.; Braberg, H.; Fabius, J. M.; Eckhardt, M.; Soucheray, M.; Bennett, M. J.; Cakir, M.; McGregor, M. J.; Li, Q.; Meyer, B.; Roesch, F.; Vallet, T.; Mac Kain, A.; Miorin, L.; Moreno, E.; Naing, Z. Z. C.; Zhou, Y.; Peng, S.; Shi, Y.; Zhang, Z.; Shen, W.; Kirby, I. T.; Melnyk, J. E.; Chorba, J. S.; Lou, K.; Dai, S. A.; Barrio-Hernandez, I.; Memon, D.; Hernandez-Armenta, C.; Lyu, J.; Mathy, C. J. P.; Perica, T.; Pilla, K. B.; Ganesan, S. J.; Saltzberg, D. J.; Rakesh, R.; Liu, X.; Rosenthal, S. B.; Calviello, L.; Venkataramanan, S.; Liboy-Lugo, J.; Lin, Y.; Huang, X. P.; Liu, Y. F.; Wankowicz, S. A.; Bohn, M.; Safari, M.; Ugur, F. S.; Koh, C.; Savar, N. S.; Tran, Q. D.; Shengjuler, D.; Fletcher, S. J.; O'Neal, M. C.; Cai, Y.; Chang, J. C. J.; Broadhurst, D. J.; Klippsten, S.; Sharp, P. P.; Wenzell, N. A.; Kuzuoglu-Ozturk, D.; Wang, H. Y.; Trenker, R.; Young, J. M.; Cavero, D. A.; Hiatt, J.; Roth, T. L.; Rathore, U.; Subramanian, A.; Noack, J.; Hubert, M.; Stroud, R. M.; Frankel, A. D.; Rosenberg, O. S.; Verba, K. A.; Agard, D. A.; Ott, M.; Emerman, M.; Jura, N.; von Zastrow, M.; Verdin, E.; Ashworth, A.; Schwartz, O.; D'Enfert, C.; Mukherjee, S.; Jacobson, M.; Malik, H. S.; Fujimori, D. G.; Ideker, T.; Craik, C. S.; Floor, S. N.; Fraser, J. S.; Gross, J. D.; Sali, A.; Roth, B. L.; Ruggero, D.; Taunton, J.; Kortemme, T.; Beltrao, P.; Vignuzzi, M.; García-Sastre, A.; Shokat, K. M.; Shoichet, B. K.; Krogan, N. J. A SARS-CoV-2 Protein Interaction Map Reveals Targets for Drug Repurposing. *Nature* **2020**, *583* (7816), 459–468. https://doi.org/10.1038/s41586-020-2286-9.

(57) Gordon, D. E.; Hiatt, J.; Bouhaddou, M.; Rezelj, V. V.; Ulferts, S.; Braberg, H.; Jureka, A. S.; Obernier, K.; Guo, J. Z.; Batra, J.; Kaake, R. M.; Weckstein, A. R.; Owens, T. W.; Gupta, M.; Pourmal, S.; Titus, E. W.; Cakir, M.; Soucheray, M.; McGregor, M.; Cakir, Z.; Jang, G.; O'Meara, M. J.; Tummino, T. A.; Zhang, Z.; Foussard, H.; Rojc, A.; Zhou, Y.; Kuchenov, D.; Hüttenhain, R.; Xu, J.; Eckhardt, M.; Swaney, D. L.; Fabius, J. M.; Ummadi, M.; Tutuncuoglu, B.; Rathore, U.; Modak, M.; Haas, P.; Haas, K. M.; Naing, Z. Z. C.; Pulido, E. H.; Shi, Y.; Barrio-Hernandez, I.; Memon, D.; Petsalaki, E.; Dunham, A.;

Marrero, M. C.; Burke, D.; Koh, C.; Vallet, T.; Silvas, J. A.; Azumaya, C. M.; Billesbølle, C.; Brilot, A. F.; Campbell, M. G.; Diallo, A.; Dickinson, M. S.; Diwanji, D.; Herrera, N.; Hoppe, N.; Kratochvil, H. T.; Liu, Y.; Merz, G. E.; Moritz, M.; Nguyen, H. C.; Nowotny, C.; Puchades, C.; Rizo, A. N.; Schulze-Gahmen, U.; Smith, A. M.; Sun, M.; Young, I. D.; Zhao, J.; Asarnow, D.; Biel, J.; Bowen, A.; Braxton, J. R.; Chen, J.; Chio, C. M.; Chio, U. S.; Deshpande, I.; Doan, L.; Faust, B.; Flores, S.; Jin, M.; Kim, K.; Lam, V. L.; Li, F.; Li, J.; Li, Y. L.; Li, Y.; Liu, X.; Lo, M.; Lopez, K. E.; Melo, A. A.; Moss, F. R.; Nguyen, P.; Paulino, J.; Pawar, K. I.; Peters, J. K.; Pospiech, T. H.; Safari, M.; Sangwan, S.; Schaefer, K.; Thomas, P. V.; Thwin, A. C.; Trenker, R.; Tse, E.; Tsui, T. K. M.; Wang, F.; Whitis, N.; Yu, Z.; Zhang, K.; Zhang, Y.; Zhou, F.; Saltzberg, D.; Hodder, A. J.; Shun-Shion, A. S.; Williams, D. M.; White, K. M.; Rosales, R.; Kehrer, T.; Miorin, L.; Moreno, E.; Patel, A. H.; Rihn, S.; Khalid, M. M.; Vallejo-Gracia, A.; Fozouni, P.; Simoneau, C. R.; Roth, T. L.; Wu, D.; Karim, M. A.; Ghoussaini, M.; Dunham, I.; Berardi, F.; Weigang, S.; Chazal, M.; Park, J.; Logue, J.; McGrath, M.; Weston, S.; Haupt, R.; Hastie, C. J.; Elliott, M.; Brown, F.; Burness, K. A.; Reid, E.; Dorward, M.; Johnson, C.; Wilkinson, S. G.; Geyer, A.; Giesel, D. M.; Baillie, C.; Raggett, S.; Leech, H.; Toth, R.; Goodman, N.; Keough, K. C.; Lind, A. L.; Klesh, R. J.; Hemphill, K. R.; Carlson-Stevermer, J.; Oki, J.; Holden, K.; Maures, T.; Pollard, K. S.; Sali, A.; Agard, D. A.; Cheng, Y.; Fraser, J. S.; Frost, A.; Jura, N.; Kortemme, T.; Manglik, A.; Southworth, D. R.; Stroud, R. M.; Alessi, D. R.; Davies, P.; Frieman, M. B.; Ideker, T.; Abate, C.; Jouvenet, N.; Kochs, G.; Shoichet, B.; Ott, M.; Palmarini, M.; Shokat, K. M.; García-Sastre, A.; Rassen, J. A.; Grosse, R.; Rosenberg, O. S.; Verba, K. A.; Basler, C. F.; Vignuzzi, M.; Peden, A. A.; Beltrao, P.; Krogan, N. J. Comparative Host-Coronavirus Protein Interaction Networks Reveal Pan-Viral Disease Mechanisms. *Science (80-.).* **2020**, *370* (6521). https://doi.org/10.1126/SCIENCE.ABE9403.

(58) Davies, J. P.; Almasy, K. M.; McDonald, E. F.; Plate, L. Comparative Multiplexed Interactomics of SARS-CoV-2 and Homologous Coronavirus Nonstructural Proteins Identifies Unique and Shared Host-Cell Dependencies. *ACS Infect. Dis.* **2020**, *6* (12), 3174–3189. https://doi.org/10.1021/ACSINFECDIS.0C00500/SUPPL_FILE/ID0C00500_SI_007.XLSX.

(59) Almasy, K. M.; Davies, J. P.; Plate, L. Comparative Host Interactomes of the SARS-CoV-2 Nonstructural Protein 3 and Human Coronavirus Homologs. *Mol. Cell. Proteomics* **2021**, *20*, 100120. https://doi.org/10.1016/J.MCPRO.2021.100120/ATTACHMENT/DC696480-9DA5-4D88-B4F1-9CCBDB68C498/MMC9.XLSX.

(60) Reuschl, A.-K.; Thorne, L. G.; Zuliani-Alvarez, L.; Bouhaddou, M.; Obernier, K.; Hiatt, J.; Soucheray, M.; Turner, J.; Fabius, J. M.; Nguyen, G. T.; Swaney, D. L.; Rosales, R.; White, K. M.; Avilés, P.; Kirby, I. T.; Melnyk, J. E.; Shi, Y.; Zhang, Z.; Shokat, K. M.; García-Sastre, A.; Jolly, C.; Towers, G. J.; Krogan, N. J. Host-Directed Therapies against Early-Lineage SARS-CoV-2 Retain Efficacy against B.1.1.7 Variant. *bioRxiv* **2021**, *10*, 2021.01.24.427991. https://doi.org/10.1101/2021.01.24.427991.

(61) Liu, X.; Huuskonen, S.; Laitinen, T.; Redchuk, T.; Bogacheva, M.; Salokas, K.; Pöhner, I.; Öhman, T.; Tonduru, A. K.; Hassinen, A.; Gawriyski, L.; Keskitalo, S.; Vartiainen, M. K.; Pieti€ Ainen, V.; Poso, A.; Varjosalo, M. SARS-CoV-2–Host Proteome Interactions for Antiviral Drug Discovery. *Mol. Syst. Biol.* **2021**, *17* (11), e10396. https://doi.org/10.15252/MSB.202110396.

(62) Samavarchi-Tehrani, P.; Abdouni, H.; Knight, J. D. R.; Astori, A.; Samson, R.; Lin, Z.-Y.;

Kim, D.-K.; Knapp, J. J.; St-Germain, J.; Go, C. D.; Larsen, B.; Wong, C. J.; Cassonnet, P.; Demeret, C.; Jacob, Y.; Roth, F. P.; Raught, B.; Gingras, A.-C. A SARS-CoV-2 – Host Proximity Interactome. *bioRxiv* **2020**, 2020.09.03.282103. https://doi.org/10.1101/2020.09.03.282103.

(63) Roux, K. J.; Kim, D. I.; Burke, B.; May, D. G. BioID: A Screen for Protein-Protein Interactions. *Curr. Protoc. Protein Sci.* **2018**, *91* (1), 19.23.1-19.23.15. https://doi.org/10.1002/CPPS.51.

(64) Rider, M. A.; Cheerathodi, M. R.; Hurwitz, S. N.; Nkosi, D.; Howell, L. A.; Tremblay, D. C.; Liu, X.; Zhu, F.; Meckes, D. G. The Interactome of EBV LMP1 Evaluated by Proximity-Based BioID Approach. *Virology* **2018**, *516*, 55–70. https://doi.org/10.1016/J.VIROL.2017.12.033.

(65) Cheerathodi, M. R.; Meckes, D. G. *BioID Combined with Mass Spectrometry to Study Herpesvirus Protein–Protein Interaction Networks*; Humana, New York, NY, 2020; Vol. 2060. https://doi.org/10.1007/978-1-4939-9814-2_19.

(66) Heaton, N. S.; Moshkina, N.; Fenouil, R.; Gardner, T. J.; Aguirre, S.; Shah, P. S.; Zhao, N.; Manganaro, L.; Hultquist, J. F.; Noel, J.; Sachs, D. H.; Hamilton, J.; Leon, P. E.; Chawdury, A.; Tripathi, S.; Melegari, C.; Campisi, L.; Hai, R.; Metreveli, G.; Gamarnik, A. V.; García-Sastre, A.; Greenbaum, B.; Simon, V.; Fernandez-Sesma, A.; Krogan, N. J.; Mulder, L. C. F.; van Bakel, H.; Tortorella, D.; Taunton, J.; Palese, P.; Marazzi, I. Targeting Viral Proteostasis Limits Influenza Virus, HIV, and Dengue Virus Infection. *Immunity* **2016**, *44* (1), 46–58. https://doi.org/10.1016/J.IMMUNI.2015.12.017/ATTACHMENT/B62B1AE8-90BD-4162-97C6-9016405107BA/MMC5.XLSX.

(67) Eyre, N. S.; Johnson, S. M.; Eltahla, A. A.; Aloi, M.; Aloia, A. L.; Mcdevitt, C. A.; Bull, R. A.; Beard, M. R. Genome-Wide Mutagenesis of Dengue Virus Reveals Plasticity of the NS1 Protein and Enables Generation of Infectious Tagged Reporter Viruses. *J. Virol.* **2017**, *91* (23). https://doi.org/10.1128/JVI.01455-17.

(68) Perry, J. W.; Chen, Y.; Speliotes, E.; Tai, A. W. Functional Analysis of the Dengue Virus Genome Using an Insertional Mutagenesis Screen. *J. Virol.* **2018**, *92* (7), 2085–2102. https://doi.org/10.1128/JVI.02085-17/SUPPL_FILE/ZJV007183411SD1.XLSX.

(69) Betsinger, C. N.; Jankowski, C. S. R.; Hofstadter, W. A.; Federspiel, J. D.; Otter, C. J.; Jean Beltran, P. M.; Cristea, I. M. The Human Cytomegalovirus Protein PUL13 Targets Mitochondrial Cristae Architecture to Increase Cellular Respiration during Infection. *Proc. Natl. Acad. Sci. U. S. A.* **2021**, *118* (32). https://doi.org/10.1073/PNAS.2101675118/SUPPL_FILE/PNAS.2101675118.SM01.MP4.

(70) Shen, R.; Raska, M.; Bimczok, D.; Novak, J.; Smith, P. D. HIV-1 Envelope Glycan Moieties Modulate HIV-1 Transmission. *J. Virol.* **2014**, *88* (24), 14258–14267. https://doi.org/10.1128/JVI.02164-14/ASSET/83462AE8-A7FD-4626-99B9-94C646D7EA3F/ASSETS/GRAPHIC/ZJV9990998210007.JPEG.

(71) Seabright, G. E.; Doores, K. J.; Burton, D. R.; Crispin, M. Protein and Glycan Mimicry in HIV Vaccine Design. *J. Mol. Biol.* **2019**, *431* (12), 2223–2247. https://doi.org/10.1016/J.JMB.2019.04.016.

(72) Ruiz-Canada, C.; Kelleher, D. J.; Gilmore, R. Cotranslational and Posttranslational N-Glycosylation of Polypeptides by Distinct Mammalian OST Isoforms. *Cell* **2009**, *136* (2), 272–283. https://doi.org/10.1016/J.CELL.2008.11.047/ATTACHMENT/D5AF7078-5BDF-4DC8-8D92-795AD6775737/MMC1.PDF.

(73) Aebi, M.; Bernasconi, R.; Clerc, S.; Molinari, M. N-Glycan Structures: Recognition and Processing in the ER. *Trends Biochem. Sci.* **2010**, *35* (2), 74–82. https://doi.org/10.1016/J.TIBS.2009.10.001.

(74) Ruddock, L. W.; Molinari, M. N-Glycan Processing in ER Quality Control. *J. Cell Sci.* **2006**, *119* (21), 4373–4380. https://doi.org/10.1242/JCS.03225.

(75) Pineda, M.; Walterfang, M.; Patterson, M. C. Miglustat in Niemann-Pick Disease Type C Patients: A Review. *Orphanet J. Rare Dis.* **2018**, *13* (1), 1–21. https://doi.org/10.1186/S13023-018-0844-0.

(76) Ficicioglu, C. Review of Miglustat for Clinical Management in Gaucher Disease Type 1. *Ther. Clin. Risk Manag.* **2008**, *4* (2), 425–431. https://doi.org/10.2147/TCRM.S6865.

(77) Rajasekharan, S.; Bonotto, R. M.; Alves, L. N.; Kazungu, Y.; Poggianella, M.; Martinez-Orellana, P.; Skoko, N.; Polez, S.; Marcello, A. Inhibitors of Protein Glycosylation Are Active against the Coronavirus Severe Acute Respiratory Syndrome Coronavirus SARS-CoV-2. *Viruses* **2021**, *13* (5), 808. https://doi.org/10.3390/V13050808.

(78) Yan, L.; Yin, Z.; Niu, L.; Shao, J.; Chen, H.; Li, X. Synthesis of Pentacyclic Iminosugars with Constrained Butterfly-like Conformation and Their HIV-RT Inhibitory Activity. *Bioorg. Med. Chem. Lett.* **2018**, *28* (3), 425–428. https://doi.org/10.1016/J.BMCL.2017.12.025.

(79) Warfield, K. L.; Alonzi, D. S.; Hill, J. C.; Caputo, A. T.; Roversi, P.; Kiappes, J. L.; Sheets, N.; Duchars, M.; Dwek, R. A.; Biggins, J.; Barnard, D.; Shresta, S.; Treston, A. M.; Zitzmann, N. Targeting Endoplasmic Reticulum α-Glucosidase i with a Single-Dose Iminosugar Treatment Protects against Lethal Influenza and Dengue Virus Infections. *J. Med. Chem.* **2020**, *63* (8), 4205–4214. https://doi.org/10.1021/ACS.JMEDCHEM.0C00067/SUPPL_FILE/JM0C00067_SI_002.CSV.

(80) Sobala, L. F.; Fernandes, P. Z.; Hakki, Z.; Thompson, A. J.; Howe, J. D.; Hill, M.; Zitzmann, N.; Davies, S.; Stamataki, Z.; Butters, T. D.; Alonzi, D. S.; Williams, S. J.; Davies, G. J. Structure of Human Endo-a-1,2-Mannosidase (MANEA), an Antiviral Host-Glycosylation Target. *Proc. Natl. Acad. Sci. U. S. A.* **2020**, *117* (47), 29595–29601. https://doi.org/10.1073/PNAS.2013620117/-/DCSUPPLEMENTAL.

(81) Schögler, A.; Caliaro, O.; Brügger, M.; Oliveira Esteves, B. I.; Nita, I.; Gazdhar, A.; Geiser, T.; Alves, M. P. Modulation of the Unfolded Protein Response Pathway as an Antiviral Approach in Airway Epithelial Cells. *Antiviral Res.* **2018**, *162*, 44–50. https://doi.org/10.1016/j.antiviral.2018.12.007.

(82) Lin, D. L.; Cherepanova, N. A.; Bozzacco, L.; Macdonald, M. R.; Gilmore, R.; Tai, A. W. Dengue Virus Hijacks a Noncanonical Oxidoreductase Function of a Cellular Oligosaccharyltransferase Complex. *MBio* **2017**, *8* (4). https://doi.org/10.1128/MBIO.00939-17/SUPPL_FILE/MBO004173397ST2.DOCX.

(83) Go, Y. M.; Jones, D. P. Redox Compartmentalization in Eukaryotic Cells. *Biochim. Biophys. Acta - Gen. Subj.* **2008**, *1780* (11), 1273–1290. https://doi.org/10.1016/J.BBAGEN.2008.01.011.

(84) Horibe, T.; Gomi, M.; Iguchi, D.; Ito, H.; Kitamura, Y.; Masuoka, T.; Tsujimoto, I.; Kimura, T.; Kikuchi, M. Different Contributions of the Three CXXC Motifs of Human Protein-Disulfide Isomerase-Related Protein to Isomerase Activity and Oxidative Refolding. *J. Biol. Chem.* **2004**, *279* (6), 4604–4611. https://doi.org/10.1074/JBC.M310922200.

(85) Chamberlain, N.; Korwin-Mihavics, B. R.; Nakada, E. M.; Bruno, S. R.; Heppner, D. E.;

Chapman, D. G.; Hoffman, S. M.; van der Vliet, A.; Suratt, B. T.; Dienz, O.; Alcorn, J. F.; Anathy, V. Lung Epithelial Protein Disulfide Isomerase A3 (PDIA3) Plays an Important Role in Influenza Infection, Inflammation, and Airway Mechanics. *Redox Biol.* **2019**, *22*, 101129. https://doi.org/10.1016/J.REDOX.2019.101129.

(86) Mahmood, F.; Xu, R.; Awan, M. U. N.; Song, Y.; Han, Q.; Xia, X.; Zhang, J. PDIA3: Structure, Functions and Its Potential Role in Viral Infections. *Biomed. Pharmacother.* **2021**, *143*, 112110. https://doi.org/10.1016/J.BIOPHA.2021.112110.

(87) Piacentini, S.; La Frazia, S.; Riccio, A.; Pedersen, J. Z.; Topai, A.; Nicolotti, O.; Rossignol, J. F.; Santoro, M. G. Nitazoxanide Inhibits Paramyxovirus Replication by Targeting the Fusion Protein Folding: Role of Glycoprotein-Specific Thiol Oxidoreductase ERp57. *Sci. Rep.* **2018**, *8* (1), 1–14. https://doi.org/10.1038/s41598-018-28172-9.

(88) Aguilar-Hernández, N.; Meyer, L.; López, S.; Dubois, R. M.; Arias, C. F. Protein Disulfide Isomerase A4 Is Involved in Genome Uncoating during Human Astrovirus Cell Entry. *Viruses* **2020**, *13* (1), 53. https://doi.org/10.3390/V13010053.

(89) Langsjoen, R. M.; Auguste, A. J.; Rossi, S. L.; Roundy, C. M.; Penate, H. N.; Kastis, M.; Schnizlein, M. K.; Le, K. C.; Haller, S. L.; Chen, R.; Watowich, S. J.; Weaver, S. C. Host Oxidative Folding Pathways Offer Novel Anti-Chikungunya Virus Drug Targets with Broad Spectrum Potential. *Antiviral Res.* **2017**, *143*, 246–251. https://doi.org/10.1016/J.ANTIVIRAL.2017.04.014.

(90) Ryser, H. J. P.; Levy, E. M.; Mandel, R.; DiSciullo, G. J. Inhibition of Human Immunodeficiency Virus Infection by Agents That Interfere with Thiol-Disulfide Interchange upon Virus-Receptor Interaction. *Proc. Natl. Acad. Sci. U. S. A.* **1994**, *91* (10), 4559–4563. https://doi.org/10.1073/PNAS.91.10.4559.

(91) Fenouillet, E.; Barbouche, R.; Courageot, J.; Miquelis, R. The Catalytic Activity of Protein Disulfide Isomerase Is Involved in Human Immunodeficiency Virus Envelope–Mediated Membrane Fusion after CD4 Cell Binding. *J. Infect. Dis.* **2001**, *183* (5), 744–752. https://doi.org/10.1086/318823.

(92) Halstead, S. B. Neutralization and Antibody-Dependent Enhancement of Dengue Viruses. *Adv. Virus Res.* **2003**, *60*, 421–467. https://doi.org/10.1016/S0065-3527(03)60011-4.

(93) Katzelnick, L. C.; Gresh, L.; Halloran, M. E.; Mercado, J. C.; Kuan, G.; Gordon, A.; Balmaseda, A.; Harris, E. Antibody-Dependent Enhancement of Severe Dengue Disease in Humans. *Science (80-.).* **2017**, *358* (6365), 929–932. https://doi.org/10.1126/SCIENCE.AAN6836/SUPPL_FILE/AAN6836_KATZELNICK_SM.PDF.

(94) Rawarak, N.; Suttitheptumrong, A.; Reamtong, O.; Boonnak, K.; Pattanakitsakul, S. nga. Protein Disulfide Isomerase Inhibitor Suppresses Viral Replication and Production during Antibody-Dependent Enhancement of Dengue Virus Infection in Human Monocytic Cells. *Viruses* **2019**, *11* (2), 155. https://doi.org/10.3390/V11020155.

(95) Orr, M. T.; Edelmann, K. H.; Vieira, J.; Corey, L.; Raulet, D. H.; Wilson, C. B. Inhibition of MHC Class I Is a Virulence Factor in Herpes Simplex Virus Infection of Mice. *PLOS Pathog.* **2005**, *1* (1), e7. https://doi.org/10.1371/JOURNAL.PPAT.0010007.

(96) Tabata, K.; Arakawa, M.; Ishida, K.; Kobayashi, M.; Nara, A.; Sugimoto, T.; Okada, T.; Mori, K.; Morita, E. Endoplasmic Reticulum-Associated Degradation Controls Virus Protein Homeostasis, Which Is Required for Flavivirus Propagation. *J. Virol.* **2021**, *95* (15). https://doi.org/10.1128/JVI.02234-20/SUPPL_FILE/JVI.02234-20-S0001.PDF.

(97) Mazeaud, C.; Anton, A.; Pahmeier, F.; Sow, A. A.; Cerikan, B.; Freppel, W.; Cortese, M.; Bartenschlager, R.; Chatel-Chaix, L. The Biogenesis of Dengue Virus Replication Organelles Requires the ATPase Activity of Valosin-Containing Protein. *Viruses* **2021**, *13* (10), 2092. https://doi.org/10.3390/V13102092/S1.

(98) Hahn, F.; Hamilton, S. T.; Wangen, C.; Wild, M.; Kicuntod, J.; Brückner, N.; Follett, J. E. L.; Herrmann, L.; Kheimar, A.; Kaufer, B. B.; Rawlinson, W. D.; Tsogoeva, S. B.; Marschall, M. Development of a PROTAC-Based Targeting Strategy Provides a Mechanistically Unique Mode of Anti-Cytomegalovirus Activity. *Int. J. Mol. Sci.* **2021**, *22* (23), 12858. https://doi.org/10.3390/IJMS222312858.

(99) Desantis, J.; Mercorelli, B.; Celegato, M.; Croci, F.; Bazzacco, A.; Baroni, M.; Siragusa, L.; Cruciani, G.; Loregian, A.; Goracci, L. Indomethacin-Based PROTACs as Pan-Coronavirus Antiviral Agents. *Eur. J. Med. Chem.* **2021**, *226*, 113814. https://doi.org/10.1016/J.EJMECH.2021.113814.

(100) Montrose, K.; Krissansen, G. W. Design of a PROTAC That Antagonizes and Destroys the Cancer-Forming X-Protein of the Hepatitis B Virus. *Biochem. Biophys. Res. Commun.* **2014**, *453* (4), 735–740. https://doi.org/10.1016/J.BBRC.2014.10.006.

(101) Peña, J.; Harris, E. Dengue Virus Modulates the Unfolded Protein Response in a Time-Dependent Manner. *J. Biol. Chem.* **2011**, *286* (16), 14226–14236. https://doi.org/10.1074/JBC.M111.222703/ATTACHMENT/26D81C6A-EC37-478A-8216-AE9671042F97/MMC1.PDF.

(102) Xue, M.; Feng, L. The Role of Unfolded Protein Response in Coronavirus Infection and Its Implications for Drug Design. *Front. Microbiol.* **2021**, *12*, 4123. https://doi.org/10.3389/FMICB.2021.808593/BIBTEX.

(103) Li, S.; Kong, L.; Yu, X. The Expanding Roles of Endoplasmic Reticulum Stress in Virus Replication and Pathogenesis. *Crit. Rev. Microbiol.* **2015**, *41* (2), 150–164. https://doi.org/10.3109/1040841X.2013.813899.

(104) Rius, B.; Mesgarzadeh, J. S.; Romine, I. C.; Paxman, R. J.; Kelly, J. W.; Wiseman, R. L. Pharmacologic Targeting of Plasma Cell Endoplasmic Reticulum Proteostasis to Reduce Amyloidogenic Light Chain Secretion. *Blood Adv.* **2021**, *5* (4), 1037–1049. https://doi.org/10.1182/BLOODADVANCES.2020002813.

(105) Marrocco, V.; Tran, T.; Zhu, S.; Choi, S. H.; Gamo, A. M.; Li, S.; Fu, Q.; Cunado, M. D.; Roland, J.; Hull, M.; Nguyen-Tran, V.; Joseph, S.; Chatterjee, A. K.; Rogers, N.; Tremblay, M. S.; Shen, W. A Small Molecule UPR Modulator for Diabetes Identified by High Throughput Screening. *Acta Pharm. Sin. B* **2021**, *11* (12), 3983–3993. https://doi.org/10.1016/J.APSB.2021.05.018.

(106) Hetz, C.; Axten, J. M.; Patterson, J. B. Pharmacological Targeting of the Unfolded Protein Response for Disease Intervention. *Nat. Chem. Biol.* **2019**, *15* (8), 764–775. https://doi.org/10.1038/s41589-019-0326-2.

(107) Prasad, V.; Greber, U. F. The Endoplasmic Reticulum Unfolded Protein Response – Homeostasis, Cell Death and Evolution in Virus Infections. *FEMS Microbiol. Rev.* **2021**, *45* (5), 1–19. https://doi.org/10.1093/FEMSRE/FUAB016.

(108) Almasy, K. M.; Davies, J. P.; Lisy, S. M.; Tirgar, R.; Tran, S. C.; Plate, L. Small-Molecule Endoplasmic Reticulum Proteostasis Regulator Acts as a Broad-Spectrum Inhibitor of Dengue and Zika Virus Infections. *Proc. Natl. Acad. Sci. U. S. A.* **2021**, *118* (3). https://doi.org/10.1073/PNAS.2012209118/-/DCSUPPLEMENTAL.

(109) Echavarría-Consuegra, L.; Cook, G. M.; Busnadiego, I.; Lefèvre, C.; Keep, S.; Brown, K.; Doyle, N.; Dowgier, G.; Franaszek, K.; Moore, N. A.; Siddell, S. G.; Bickerton, E.; Hale, B. G.; Firth, A. E.; Brierley, I.; Irigoyen, N. Manipulation of the Unfolded Protein Response: A Pharmacological Strategy against Coronavirus Infection. *PLOS Pathog.* **2021**, *17* (6), e1009644. https://doi.org/10.1371/JOURNAL.PPAT.1009644.

(110) Sims, A. C.; Mitchell, H. D.; Gralinski, L. E.; Kyle, J. E.; Burnum-Johnson, K. E.; Lam, M.; Fulcher, M. L.; West, A.; Smith, R. D.; Randell, S. H.; Metz, T. O.; Sheahan, T. P.; Waters, K. M.; Baric, R. S. Unfolded Protein Response Inhibition Reduces Middle East Respiratory Syndrome Coronavirus-Induced Acute Lung Injury. *MBio* **2021**, *12* (4). https://doi.org/10.1128/MBIO.01572-21/SUPPL_FILE/MBIO.01572-21-ST002.XLSX.

(111) Mufrrih, M.; Chen, B.; Chan, S.-W. Zika Virus Induces an Atypical Tripartite Unfolded Protein Response with Sustained Sensor and Transient Effector Activation and a Blunted BiP Response. *mSphere* **2021**, *6* (3). https://doi.org/10.1128/MSPHERE.00361-21/ASSET/6D7B8F67-3303-4851-B3C6-6D378D7512AC/ASSETS/IMAGES/LARGE/MSPHERE.00361-21-F012.JPG.

(112) Slaine, P. D.; Kleer, M.; Duguay, B. A.; Pringle, E. S.; Kadijk, E.; Ying, S.; Balgi, A.; Roberge, M.; McCormick, C.; Khaperskyy, D. A. Thiopurines Activate an Antiviral Unfolded Protein Response That Blocks Influenza A Virus Glycoprotein Accumulation. *J. Virol.* **2021**, *95* (11). https://doi.org/10.1128/JVI.00453-21/ASSET/7759755A-D4C4-4055-80A2-88AF5A701CE4/ASSETS/IMAGES/LARGE/JVI.00453-21-F0008.JPG.

(113) Shaban, M. S.; Müller, C.; Mayr-Buro, C.; Weiser, H.; Meier-Soelch, J.; Albert, B. V.; Weber, A.; Linne, U.; Hain, T.; Babayev, I.; Karl, N.; Hofmann, N.; Becker, S.; Herold, S.; Schmitz, M. L.; Ziebuhr, J.; Kracht, M. Multi-Level Inhibition of Coronavirus Replication by Chemical ER Stress. *Nat. Commun.* **2021**, *12* (1), 1–20. https://doi.org/10.1038/s41467-021-25551-1.

(114) Al-Beltagi, S.; Preda, C. A.; Goulding, L. V.; James, J.; Pu, J.; Skinner, P.; Jiang, Z.; Wang, B. L.; Yang, J.; Banyard, A. C.; Mellits, K. H.; Gershkovich, P.; Hayes, C. J.; Nguyen-Van-tam, J.; Brown, I. H.; Liu, J.; Chang, K. C. Thapsigargin Is a Broad-Spectrum Inhibitor of Major Human Respiratory Viruses: Coronavirus, Respiratory Syncytial Virus and Influenza A Virus. *Viruses* **2021**, *13* (2), 234. https://doi.org/10.3390/V13020234.

(115) Jaskulska, A.; Janecka, A. E.; Gach-Janczak, K. Thapsigargin—From Traditional Medicine to Anticancer Drug. *Int. J. Mol. Sci.* **2020**, *22* (1), 4. https://doi.org/10.3390/IJMS22010004.

(116) Aviner, R.; Li, K. H.; Frydman, J.; Andino, R. Cotranslational Prolyl Hydroxylation Is Essential for Flavivirus Biogenesis. *Nature* **2021**, *596* (7873), 558–564. https://doi.org/10.1038/s41586-021-03851-2.

(117) Rothan, H. A.; Zhong, Y.; Sanborn, M. A.; Teoh, T. C.; Ruan, J.; Yusof, R.; Hang, J.; Henderson, M. J.; Fang, S. Small Molecule Grp94 Inhibitors Block Dengue and Zika Virus Replication. *Antiviral Res.* **2019**, *171*, 104590. https://doi.org/10.1016/J.ANTIVIRAL.2019.104590.

(118) Kumar, N.; Khandelwal, N.; Kumar, R.; Chander, Y.; Rawat, K. D.; Chaubey, K. K.; Sharma, S.; Singh, S. V.; Riyesh, T.; Tripathi, B. N.; Barua, S. Inhibitor of Sarco/Endoplasmic Reticulum Calcium-ATPase Impairs Multiple Steps of Paramyxovirus Replication. *Front. Microbiol.* **2019**, 209. https://doi.org/10.3389/FMICB.2019.00209/BIBTEX.

(119) Kumar, R.; Khandelwal, N.; Chander, Y.; Riyesh, T.; Tripathi, B. N.; Kashyap, S. K.; Barua, S.; Maherchandani, S.; Kumar, N. MNK1 Inhibitor as an Antiviral Agent Suppresses Buffalopox Virus Protein Synthesis. *Antiviral Res.* **2018**, *160*, 126–136. https://doi.org/10.1016/J.ANTIVIRAL.2018.10.022.

(120) Plate, L.; Cooley, C. B.; Chen, J. J.; Paxman, R. J.; Gallagher, C. M.; Madoux, F.; Genereux, J. C.; Dobbs, W.; Garza, D.; Spicer, T. P.; Scampavia, L.; Brown, S. J.; Rosen, H.; Powers, E. T.; Walter, P.; Hodder, P.; Luke Wiseman, R.; Kelly, J. W. Small Molecule Proteostasis Regulators That Reprogram the ER to Reduce Extracellular Protein Aggregation. *Elife* **2016**, *5*. https://doi.org/10.7554/ELIFE.15550.

CHAPTER 2: Characterizing unfolded protein response modulators in Huh7 cells and measuring their ability to impair flavivirus infection

2.1 Introduction

Flaviviruses are a class of positive-sense, single stranded RNA viruses that include dengue, Zika, and yellow fever. While the yellow fever vaccine has been one of the most reliable and successful vaccines developed, no other widespread vaccination options exist for flaviviruses, which is surprising given that half the world's population is estimated to be at risk of dengue infection[1]. Additionally, no therapeutics exist for the treatment of flavivirus infection, though several efforts have been made to characterize and develop direct-acting antiviral compounds[2,3].

To begin investigating dependencies of flaviviruses on host machinery, we focused on the endoplasmic reticulum, an organelle basally used as a hub for host protein folding[4]. Specifically,

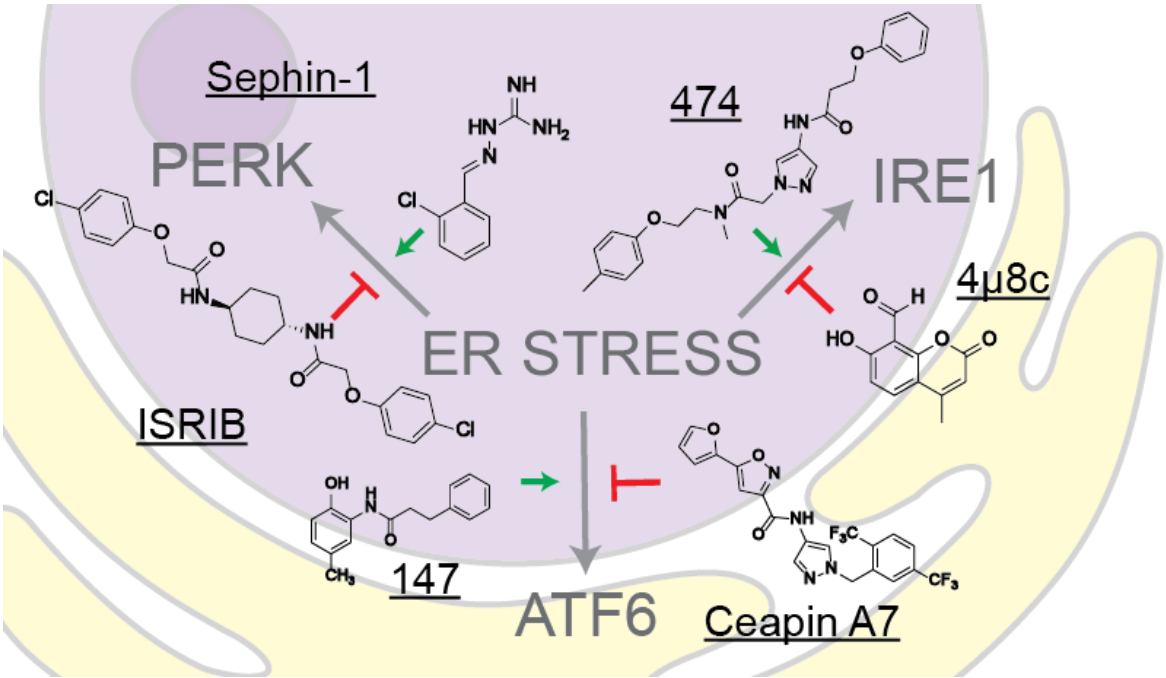

Figure 2.1 Small molecules can selectively regulate UPR branches. The above structures show the small molecules designed to activate or inhibit (green/red symbols respectively) the three branches of the unfolded protein response. The molecules for regulation of IRE1 and ATF6 will be discussed further.

we took advantage of the observation that DENV infection selectively modulates the unfolded protein response, a stress response pathway intended to return the cell to a homeostatic state under conditions of increased protein folding load or stress from the buildup of unfolded proteins or if prolonged ER stress persists, induce apoptosis.[5].

The UPR consists of three branches; PERK, IRE1/XBP1s (referred to as IRE1 from hereon) and ATF6. Each of these three branches is ultimately responsible for upregulating distinct but overlapping functional outputs in order to increase the folding capacity of the ER and/or decrease cellular translation rates in order to allow the cell to play catch-up on a current protein folding load[6].

We began with the selection of four molecules that activate or inhibit the IRE1 and ATF6 branches of the UPR (**Figure 2.1**). All of these molecules are recently discovered, and provide a novel method of selectively regulating each of these branches[7–10].

The UPR branches are named after the transmembrane sensors that localize inside of the ER membrane and are able to direct communication between sensing stress in the ER lumen and relay the response to the cytosol or other organelles[6]. On the ER luminal side, under non-stressed conditions, these transmembrane sensors are bound by binding immunoglobulin protein (BiP, also referred to as GRP78). BiP is the sole ER luminal Hsp70 chaperone that, upon sensing an accumulation of unfolded proteins, will dissociate from the UPR sensor in an attempt to correct the misfolding. This dissociation is what thought to initiate the cascade of UPR activation, though alternative mechanisms have been proposed[11–14].

BiP dissociation from PERK induces dimerization and autophosphorylation, which leads to full activation of its kinase domain. This domain then phosphorylates eukaryotic initiation factor 2α, which results in translational attenuation via the ribosome[15–17]. Counterintuitively, this leads to the selective translation of specific transcripts containing upstream open reading frames (uORFs), one of which is activating transcription factor 4 (ATF4)[17,18]. ATF4 protein trafficks to the nucleus and upregulates specific targets, two of which are CHOP and GADD34[19]. CHOP is another

transcription factor which begins a further cascade of upregulating components of apoptosis; thus, prolonged PERK activation leads to this mechanism of controlled cell death. GADD34/PPP1R15A is the regulator which closes the negative feedback loop, serving as a specific regulatory subunint of the protein phosphatase 1 complex that dephosphorylates eIF2α and allows translation to resume normally[20]. The phosphorylation of eIF2α marks the intersection of the UPR with the integrated stress response (ISR), which is a broader cellular response activated under a range of physiological changes or stimuli[21]. Due to the interplay between these two pathways, small molecules have been developed to study the ISR at large, some of which bind PERK directly[22]. Sephin-1, an ISR 'activator', works via inhibition of the GADD34 phosphatase subunit, thus prolonging eIF2α phosphorylation[10]. ISRIB, short for integrated stress response inhibitor, works by enhancing activity or eIF2B, another component of the initiation complex. The activity enhancement is able to counteract the phosphorylation of eIF2α and prevent the translation attenuation[9].

In a similar fashion, BiP dissociation from IRE1 also causes dimerization and autophosphorylation of this sensor[12,23]. However, in this instance an endonuclease domain within IRE1 is activated after phosphorylation. The endonuclease domain degrades selective mRNA substrates via regulated IRE1-dependent decay (RIDD), but also cleaves a 26 nucleotide sequence from the mRNA of the X-box binding protein 1 (XBP1)[24–26]. This non-canonical splicing event causes a frameshift, and results in translation of an alternate protein product labeled as XBP1s. XBP1s is a transcription factor that upregulates some chaperones and other folding factors, but also upregulates genes involved in lipid biosynthesis and ER-associated degradation to increase overall folding capacity and help rid the organelle of misfolded proteins[27]. Inhibitors of both the kinase and endonuclease domains of IRE1 have been discovered and characterized[28–30].

The last sensor is ATF6, whose mechanism of activation is less defined than either PERK or IRE1. ATF6 is localized in the ER membrane as an oligomer, with intramolecular disulfide bonds linking monomers together. After BiP dissociation, these oligomers are reduced to a specifically

linked dimer, and these dimers of ATF6 are trafficked to the Golgi apparatus[31,32]. Here, ATF6 is cleaved by S1P and S2P proteases to release a cytosolic active transcription factor, which traffics to the nucleus and again upregulates chaperones and other folding factors which help restore protein homeostasis[33]. The two compounds designed to preferentially modulate this pathway are the activator **147** and the inhibitor Ceapin-A7[7,8]. **147** was discovered in a high-throughput screen that looked at ATF6 activation at both the transcript and protein levels, and selected molecules which initially enhanced activation of a luciferase under the ERSE (BiP) promoter (indicative of ATF6 cleavage), while counterscreening against those molecules which also activated XBP1. Several other molecules were looked at as potential candidates after both screens, including compound **263**, which will be discussed in chapter 4 in this dissertation. A follow-up study showed that this compound does not bind ATF6 directly, but rather targets protein disulfide isomerases, which are hypothesized to control the oligomeric state of ATF6 in the membrane via oxidation and reduction of disulfide bonds[34]. Ceapin-A7 prevents trafficking of ATF6 from the ER membrane to the Golgi apparatus, thus inhibiting its ability to form a functional transcription factor[35]. It does this by tethering the cytosolic domain of the sensor to a second transmembrane protein, ABCD3, found within the membrane of the peroxisome[36].

This chapter details efforts to characterize the selectivity of the ATF6 and IRE1 modulators in Huh7 cells, later used as a model system for flavivirus infection. After characterization, these modulators were tested in viral infections to monitor the effects of modulation of ATF6 and IRE1 modulation on viral replication.

2.2 Results

2.2.1 Measuring effects of UPR regulators in Huh7 cells

Previous efforts in characterizing each of the UPR regulators had taken place in a variety of cell lines, but Huh7 cells were not among them. Huh7 cells are a commonly used model for flavivirus infections, and thus confirming the specificity (or otherwise observing pathway effects) was an

important checkpoint. At this point, the structures and functions of **147**, the IRE1 inhibitor **4μ8c**, and Ceapin-A7 were known. Studies on the preferential IRE1 activator **474/IXA4** (referred to hereon as **474**) studies had not yet been released, and thus data from this molecule is excluded from these studies.

Initial **4μ8c** experiments tested the molecule over a various range of concentrations, and the ability of the drug to inhibit XBP1 splicing was dose-dependent[29]. To determine the optimal concentration for use in Huh7 cells, cells were seeded into 12-well dishes and treated with 0.5 μM final concentration thapsigargin (Tg), a universal UPR activator, or DMSO as a control[37]. Wells treated with thapsigargin were then treated with increasing concentrations of **4μ8c** in DMSO. After 6 hours, samples were harvested for RT-PCR and qPCR to measure effects on *XBP1* splicing. cDNA was synthesized from the collected RNA for each sample and a PCR product of the *XBP1* gene was amplified using primers that spanned the splice site (**Table A2.1**, splice site is nucleotides 494-519 of the coding sequence), thus creating two products with 26 nucleotide difference. These products were separated on a 3% agarose gel, which provided the resolution to visualize two bands; one slightly above 200 bp, and one slightly below (**Figure 2.2**). These bands correspond to the unspliced and spliced products respectively. Under basal conditions (no thapsigargin or other ER stress), the majority of *XBP1* mRNA remains unspliced. After thapsigargin addition, these conditions are reversed and a significant portion becomes

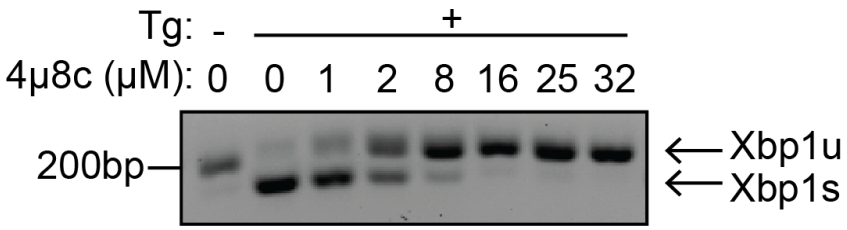

Figure 2.2. XBP1 splicing inhibition by 4μ8c is dose-dependent. Samples were treated with the indicated compounds (thapsigargin, where indicated, was dosed at 0.5 μM) for 6 hours. RNA was isolated, and the complimentary cDNA was synthesized and separated on an agarose gel. Upper band represents unspliced mRNA, lower band represents excision of 26bp after UPR activation. Saturated pixels not shown.

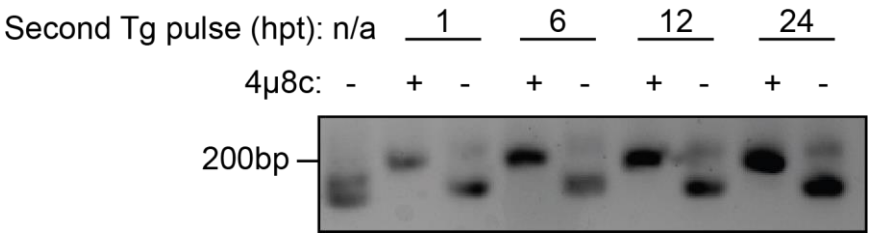

Figure 2.3. XBP1 splicing inhibition by 4μ8c lasts at least 24 hours. Cells were treated with thapsigargin and 4μ8c (where indicated) simultaneously. A second dose of thapsigargin was given at the indicated hour post treatment (hpt). Levels of XBP1 splicing were measured 6 hours after the second treatment by RT-PCR. Saturated pixels not shown.

spliced. As the dose of **4μ8c** increases, the splicing ratio decreases; by 32 μM, no splicing is seen. Thus, 32 μM was chosen as the concentration for later experiments; experiments down to 16 μM would likely have also given valid results, as the majority of splicing is inhibited at this concentration.

A second *XBP1* splicing assay was performed to determine how long the effects of **4μ8c** last in Huh7 cells. If a compound is quickly metabolized or otherwise disappears from the intracellular space, the effects on its target should not be expected to last a long time. To test this in Huh7 cells, samples were treated with a pulse of 0.5 μM thapsigargin, with or without **4μ8c**. After the initial treatment, sequences of wells were treated with a second pulse of thapsigargin, pairing a **4μ8c** treated and untreated well. If **4μ8c** levels in the cell were sufficiently reduced, this second pulse of thapsigargin would result in an increase in splicing due to the decreased availability of the endonuclease inhibitor. However, even when the second pulse came 24 hours after the first, little splicing was seen in the presence of **4μ8c** (**Figure 2.3**). Attempts to extend the timecourse were unsuccessful, likely due to the high toxicity of thapsigargin.

A similar experiment was performed with Ceapin-A7, the ATF6 inhibitor. Because an mRNA splicing event does not occur as with XBP1, a further downstream event needs to be measured. In this case, quantification of *HspA5*, a marker selective for ATF6, was used[27]. Again, samples were treated with thapsigargin with or without Ceapin-A7. A second pulse of thapsigargin was added at the indicated hour post treatment, and transcription was measured 6 hours post-

treatment. Similarly to the results with **4μ8c**, Ceapin-A7 was able to inhibit ATF6 activation up to 24 hours post treatment (**Figure 2.4**). The BiP upregulation at the 6 hours post treatment timepoint even in the presence of Ceapin-A7 was unexpected, and given the continued effect at 12 and 24 hours post treatment suggests Ceapin-A7 was aberrantly omitted from the sample.

After ensuring that the molecules are effective during the length of times required for infection experiments, a more general exploration of the selectivity of these molecules for each UPR branch was carried out. Although designed for inhibition or activation of a single branch, it is conceivable that this selectivity may vary slightly from cell line to cell line. To characterize the effects on reporter gene levels of each compound, a combination of qPCR and proteomics was used. Reporter genes were chosen based on studies by Shoulders et al., and Grandjean et al., characterizing genes upregulated by a single stress pathway (so as to avoid genes upregulated by multiple branches)[27,38]. To measure changes at the transcript/mRNA level, Huh7 cells were treated with the indicated compounds and harvested 6 hours post-treatment for qPCR or RT-PCR

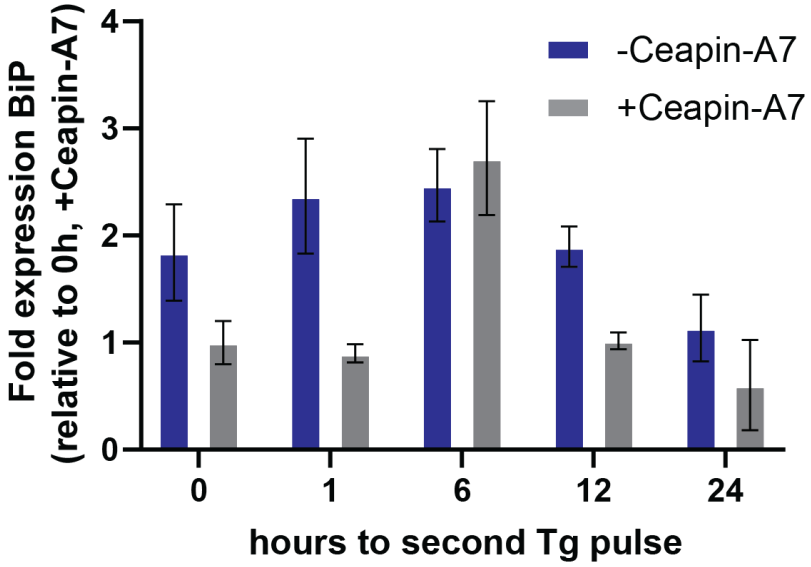

Figure 2.4. ATF6 inhibition by Ceapin-A7 lasts 24 hours. Cells were treated with thapsigargin and Ceapin-A7 (where indicated) simultaneously. A second dose of thapsigargin was given at the indicated hour post treatment (hpt). Levels of *HspA5* as an ATF6 reporter gene were measured 6 hours after the second treatment by qPCR.

to measure *XBP1* splicing. To measure changes at the translational/protein level, which is downstream of transcription, a timepoint of 20 hours post-treatment was used.

When examining transcript levels after treatment with each molecule, a discrepancy was observed between expected and experimental results. First, *XBP1* splicing was measured using the same assay as outlined in **Figures 2.2** and **2.3**. Thapsigargin was used as a universal UPR activator to measure upregulation of all three branches. **Figure 2.5** shows the results of examining *XBP1* splicing in the presence of single compounds or combination treatments; **RP22** was used as an inactive analog of **147**, and Ceapin-A5 as an inactive analog of Ceapin-A7. As expected, addition of thapsigargin induced a large amount of XBP1 splicing, which was reversed by **4μ8c** but not Ceapin-A7. However, **147** also appeared to induce a significant amount of splicing, indicating it may possess IRE1 activating potential as well as ATF6 activating potential in the Huh7 cell line. This splicing was not reversed by Ceapin-A7 but it was inhibited by the IRE1 inhibitor **4μ8c**.

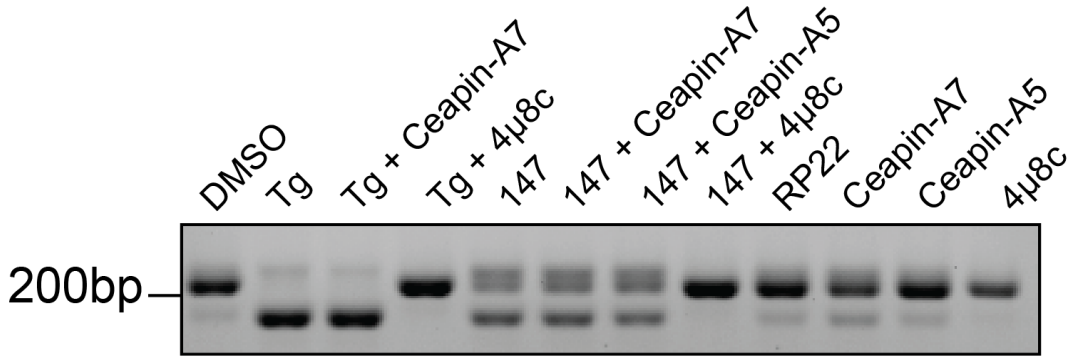

Figure 2.5. Selectivity of small molecules for XBP1s. Cells were treated with the indicated compounds and harvested 6 hours post-treatment. RT-PCR was performed using primers spanning the XBP1 splice site and samples were run on a 3% agarose gel at 80V for approximately 1 hour.

For qPCR experiments to measure reporter gene levels of each branch, *CHOP* was used as a PERK marker (it should be noted this gene may also respond to ATF6 activation), *HspA5* as an ATF6 marker, and Erdj4 as an IRE1 marker. RiboP was used as a housekeeping gene and all transcripts were normalized to the level in each sample.

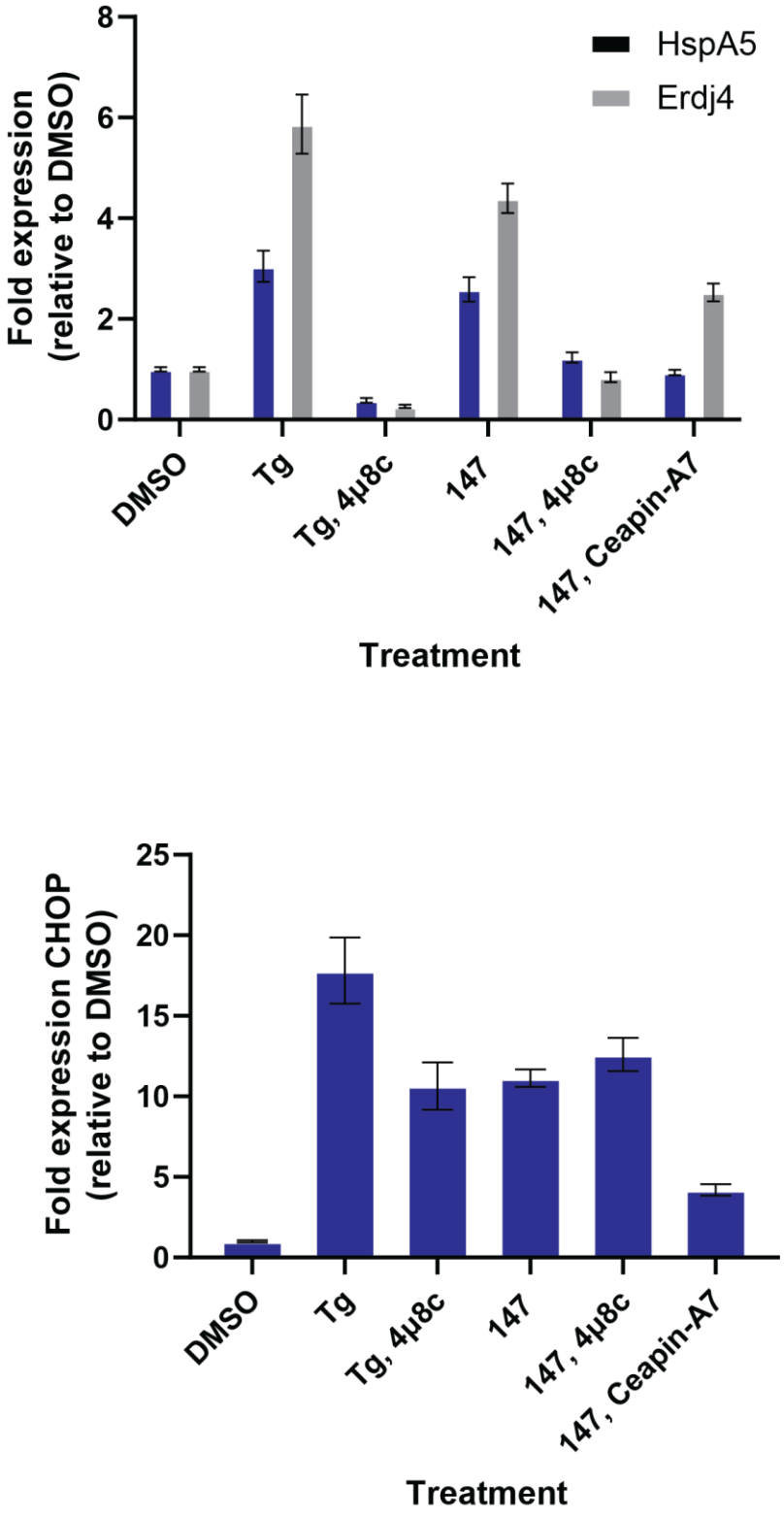

Figure 2.6. Selectivity of small molecules by qPCR. Cells were treated with the indicated compounds for 6 hours. RNA was harvested, cDNA was synthesized from 500ng cellular RNA, and qPCR primers for the genes listed above were used for amplification. Primers listed in **Table A2.1**.

When measuring *CHOP* levels, which were the most drastically changed in each of the treatments compared to background, thapsigargin and **147** both resulted in a greater than a 10 fold increase in expression (with Tg inducing closer to 20 fold). This was expected with thapsigargin, the global activator, but not with **147**, which should be selective for ATF6 and thus levels should not be as high. **4μ8c** was able to reduce levels of expression in the Tg treated samples, but not the **147** treated samples. Ceapin-A7, on the other hand, did reduce *CHOP* expression in the presence of **147** (**Figure 2.6**).

As expected, *HspA5* levels were raised in both the Tg and **147** treated sample. **4μ8c** was able to attenuate this increase in both cases, suggesting it is capable of reversing ATF6 activation. **Ceapin-A7** was also able to reduce *HspA5* levels, to a greater extent than **4μ8c**. However, **Ceapin-A7** was also able to reduce expression levels of *Erdj4*, a marker intended to be selective for IRE1.

2.2.2 Effects of IRE1 and ATF6 inhibitors on DENV infection

Given that DENV upregulates the IRE1 and ATF6 branches of the UPR, our initial hypothesis was that inhibition of these branches using small molecules would lead to deleterious effects on virus replication. Intriguingly, in the initial study knockout of either ATF6 or XBP1 did not affect replication of the virus. Knockout of IRE1, however, did lead to a decrease in replication; this implicates a function of IRE1 other than XBP1 splicing being important in the DENV life cycle[5]. In this study, an endonuclease inhibitor was used to specifically inhibit the RNA splicing/degradation function of IRE1, while in theory leaving the kinase domain active. Huh7 cells were seeded and infected with DENV2 strain BID-V533 at MOI 3 for 3 hours. Inoculum was removed, cells were washed, and media containing DMSO or 32 μM **4μ8c** was added. Cells were harvested between 12 and 60 hours post-infection at 12 hour intervals. Lysate was used to compare viral protein levels between samples, and media was collected to evaluate infectious viral titer. At 12 hours, neither viral protein nor viral titers were observed. This is likely too early in the replication cycle

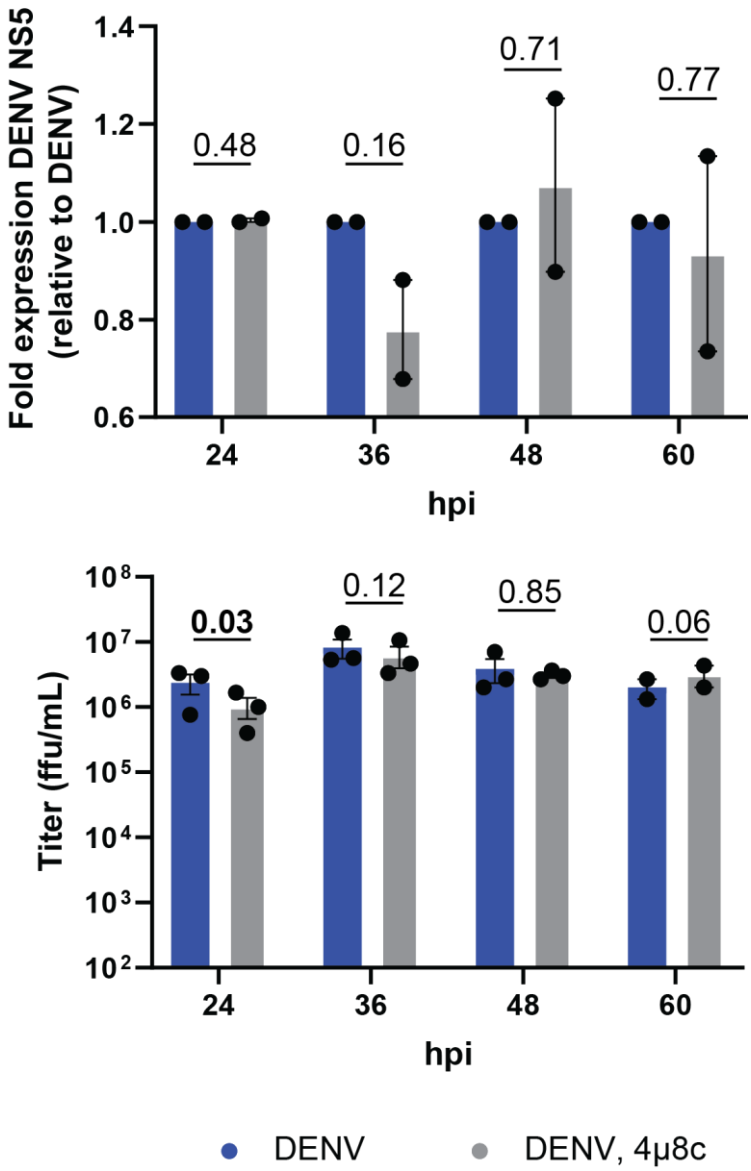

Figure 2.7. Effects of 4μ8c on the viral life cycle. Samples were infected with DENV2 BID-V533 for 3 hours. After infection, inoculum was removed, cells were washed, and media containing DMSO or 32 μM 4μ8c was added. Cells were harvested at the indicated intervals post-infection; samples were also taken at 12 hours, but no signal was observed at the titer or protein level.

(approximately 24 hours) for output to be monitored, or a more sensitive assay would need to be used to obtain measurements. At all timepoints, no effect on viral protein levels was seen, suggesting the molecule does not affect production of the viral polyprotein. At most timepoints, no effect on viral titer was seen either. However, a small reduction in titer, approximately 50% was seen at the 24 hour timepoint (**Figure 2.7**). The selectivity for a decrease in titer but not

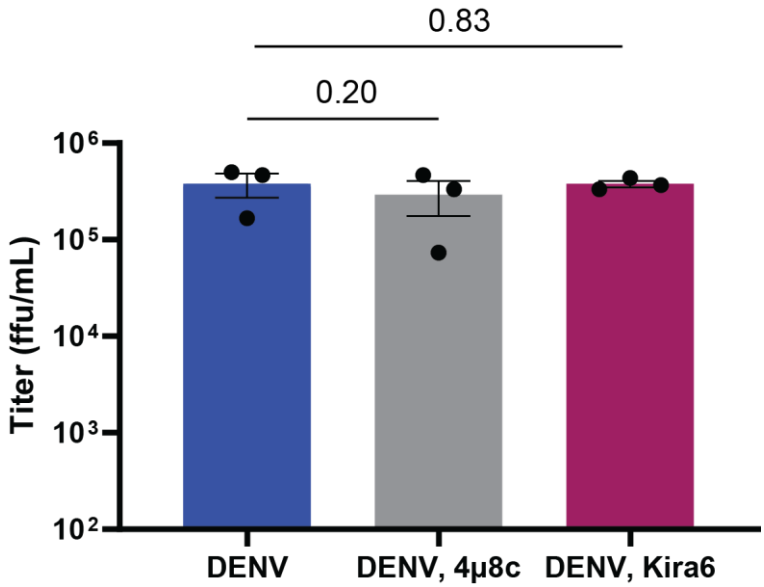

Figure 2.8. Viral titers after treatment with IRE1 inhibitors. Cells were pre-treated with inhibitors for 16 hours, prior to infection with DENV2 BID-V533 for 3 hours. Inoculum was removed, cells were washed, and media and treatments were replaced. Media was collected for focus forming assay 24 hours post infection. No significant differences in titers seen.

protein suggested a mechanism by which assembly and secretion of progeny virions was affected; however, with a small effect, this needed to be confirmed.

To confirm the effect seen with **4μ8c**, another inhibitor of the IRE1 endonuclease domain was used, **Kira6**[28]. This time, the 24 hour timepoint was used as a representative sample, rather than completing the entire timecourse, since this is where effects were initially seen with **4μ8c**. This time, no effects were seen with either molecule (**Figure 2.8**), leading to the conclusion that the endonuclease domain of IRE1 and/or subsequent activation of downstream UPR reporter genes is not necessary for flavivirus infection. Notably, the significant change with **4μ8c** observed in initial experiments was not seen again, even with a pre-treatment step added.

Experiments were repeated with the ATF6 inhibitor Ceapin-A7. Given that ATF6 knockout did not affect viral replication in Peña and Harris, it was hypothesized that the addition of this molecule would not have a significant effect on viral titers. This proved to be true, as both protein and titer levels were unaffected by Ceapin-A7 up to 60 hours post infection (**Figure 2.9**).

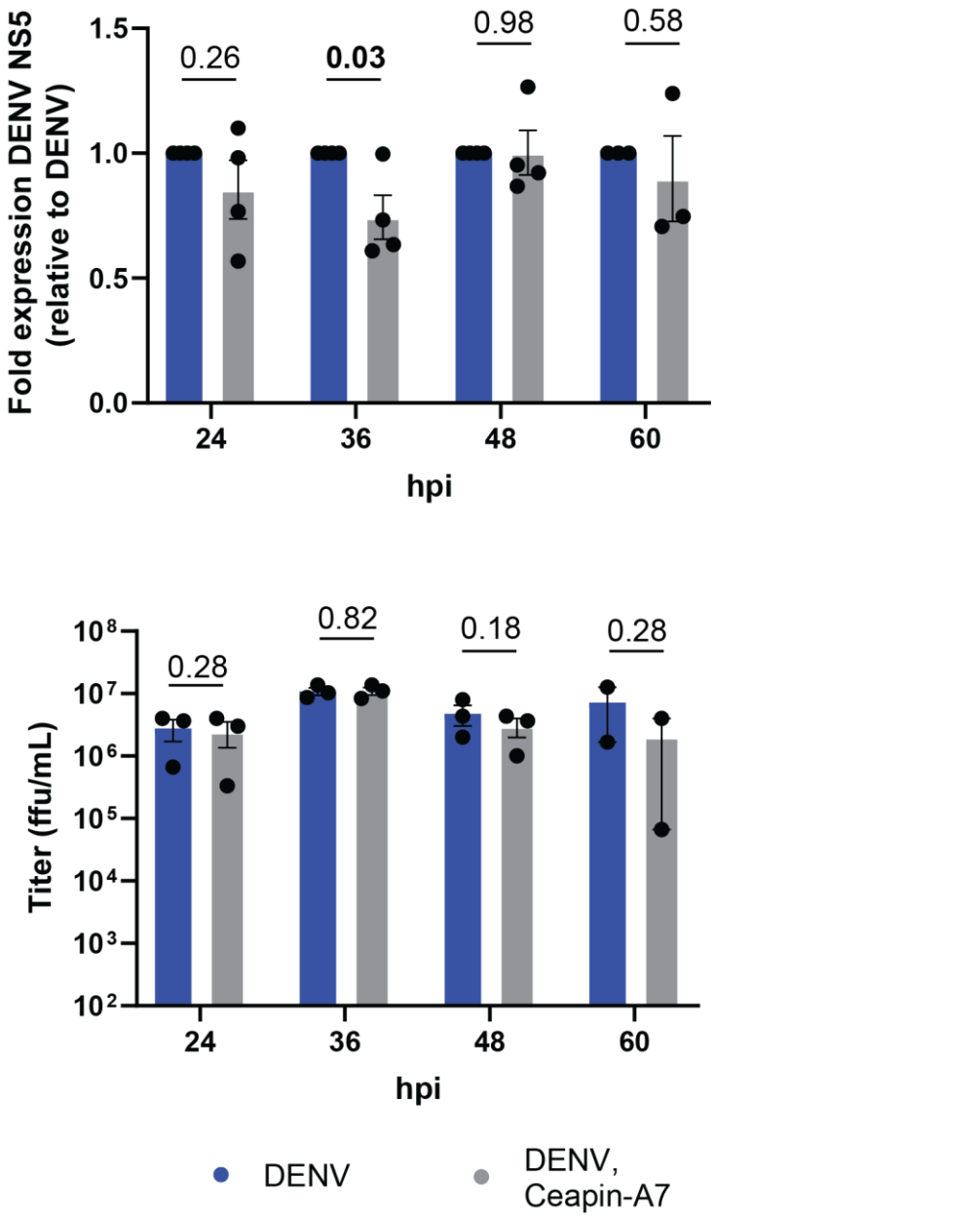

Figure 2.9. Effects of Ceapin-A7 on the viral life cycle. Samples were infected with DENV2 BID-V533 for 3 hours. After infection, inoculum was removed, cells were washed, and media containing 6 µM Ceapin-A5 or 6 µM Ceapin-A7 was added. Cells were harvested at the indicated intervals post-infection; samples were also taken at 12 hours, but no signal was observed at the titer or protein level.

2.2.3 Effects of IRE1 and ATF6 activators on DENV infection

Although the inhibitors were initially of interest, given the availability of complementary activators of the IRE1 and ATF6 branches we were also intrigued to characterize the effects of these

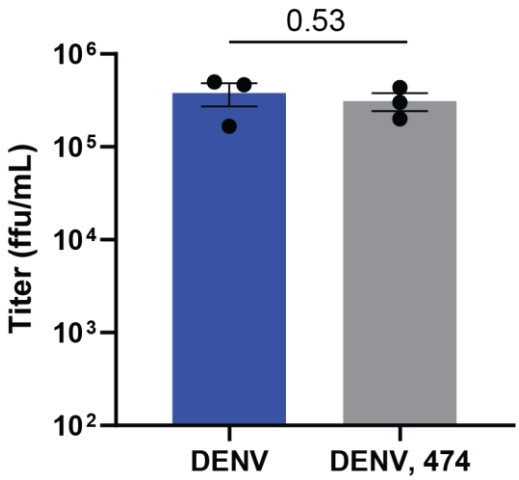

Figure 2.10. Effect of IRE1 activator 474 on DENV infection. Samples were pre-treated with 10 µM 474 or DMSO and infected with DENV2 BID-V533 for 3 hours. After infection, inoculum was removed, cells were washed, and media containing DMSO or 10 µM 474 was added. Media samples were collected for focus forming assay 24 hours post infection.

molecules on viral infection. Previously, selective activation of each UPR branch was not possible; an 'activator' of the PERK branch was available, but this worked by inhibition of the GADD34 phosphatase rather than direct activation of PERK itself[10].

Given that DENV upregulates the IRE1 and ATF6 UPR branches, we hypothesized that treatment with pharmacologic activators may enhance viral infection, leading to increased protein and titer levels. To test this hypothesis, we pre-treated Huh7 cells with 10 µM **474** or **147** before infection with DENV2 strain BID-V533 at an MOI of 3 for 3 hours. **474** showed no effect on viral titers 24 hours post-infection (**Figure 2.10**); initial experiments by a rotation student (data not shown) indicated that it may increase titers, as was hypothesized, but this data was not reproducible in later experiments shown here.

When the treatments were repeated with **147**, a remarkable decrease in titer was observed at 24 hours, and up to 36 hours post-infection (**Figure 2.11**). This decrease neared 2 orders of magnitude, or a 99% reduction in virus levels. The change at the protein level was still significant, but on the order of a ~75% decrease instead of maintaining two orders of magnitude. After this

observation, **147** became the topic of focus for this portion of the dissertation project, and the effects of this molecule are much further discussed in chapter 3.

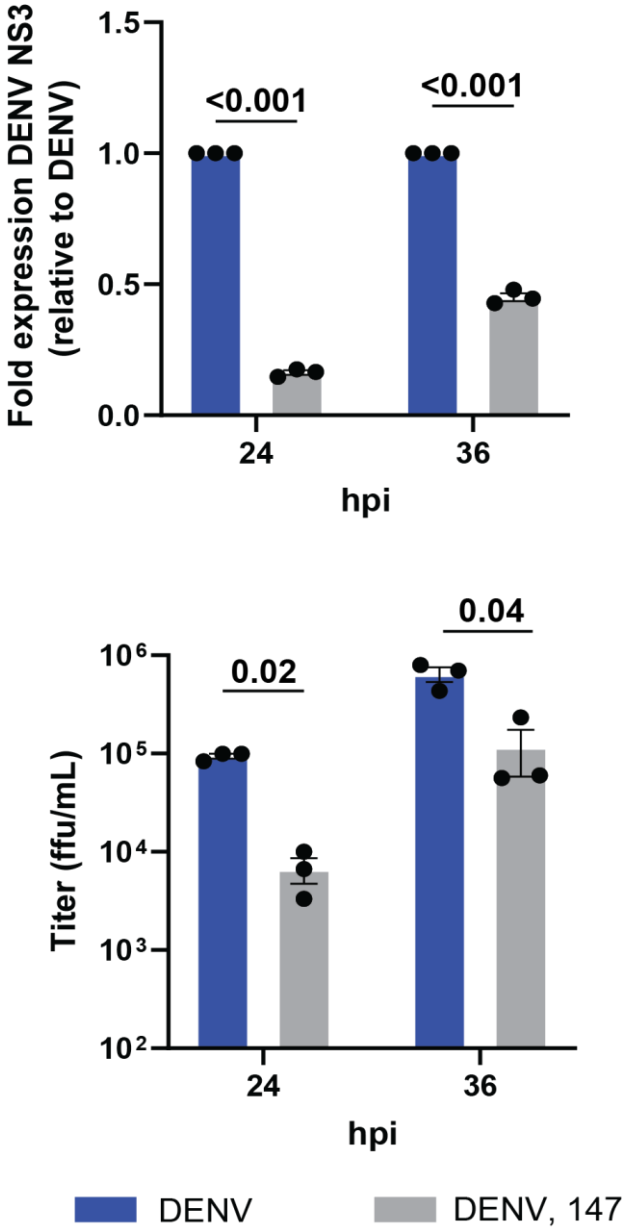

Figure 2.11. Effect of ATF6 activator 147 on DENV infection. Samples were pre-treated with 10 µM 147 or DMSO and infected with DENV2 BID-V533 for 3 hours. After infection, inoculum was removed, cells were washed, and media containing DMSO or 10 µM 147 was added.

2.3 Discussion

Our interest in using these pharmacologic agents to inhibit flavivirus infection came from the initial observation that DENV upregulates the IRE1 and ATF6 branches of the UPR, and thus further pharmacologic manipulation may be able to perturb the replication cycle of the virus either by inhibition or enhancement. To this end, we selected four recently characterized small molecules, one activator and inhibitor each of the IRE1 and ATF6 branches. Our work began by determining the effects of these molecules on each UPR branch to determine the dose and duration of effect, as well as if the selectivity for each branch held in Huh7 cells. The dose and duration experiments were performed on **4μ8c** specifically; we observed complete inhibition of XBP1 splicing at 32 μM, which led to the selection of this dose as the concentration for later viral infection experiments. At this dose, we also observe effects through at least 24 hours after a single treatment, as monitored by co-treatment with a UPR activator over the course of those 24 hours. However, experiments could conceivably be done at a lower dose of **4μ8c**, as a significant amount of splicing was inhibited at 16 μM. This may be a wise option, given the later observations that the 32 μM dose was able to inhibit activation of other UPR branches, namely ATF6, as well. While it is not surprising that lower activation of ATF6 targets was seen, given the extensive crosstalk and overlap in gene upregulation between the ATF6 and IRE1 branches, if the goal is selective modulation of each branch the current conditions did not meet the true goal. Ultimately, no effects on viral replication were seen with **4μ8c** treatment in Huh7 cells. These results were supported by trials with a different IRE1 endonuclease inhibitor, **Kira6**, which also showed no effects on viral replication. Given the experiments in Peña and Harris, which saw no effect on viral replication in an XBP1 knockout model compared to a wild-type, it is conceivable that the endonuclease function of IRE1 is simply not important for viral infection, and that activation of this pathway is simply a result of infection rather than a necessity for the virus[5]. Future experiments could instead use an inhibitor of the kinase domain of IRE1 rather than inhibitors of the endonuclease domain, such as APY29[39,40].

When examining selectivity of the other modulators available at the time, broad UPR activity was observed rather than specific modulation. Initially, **Ceapin-A7** appeared to be the most specific of the molecules, with no XBP1 splicing inhibition observed between activator control and the addition of **Ceapin-A7**. However, a qPCR for Erdj4 did show it was able to inhibit expression of this gene, used as an IRE1 marker, in the presence of **147** (which should be ATF6 selective, but does not appear to be). It is possible that in Huh7 cells, Erdj4 expression levels are increased in response to both IRE1 and ATF6 activation, and **Ceapin-A7** is inhibiting expression due only to ATF6 activation. Testing of **Ceapin-A7** response against a broader gene set would reveal more insight into its true selectivity in this cell line. As noted, **4μ8c** also showed an ability to inhibit ATF6 activation, as noted by the lower expression levels of BiP/HspA5 in the qPCR experiments compared to the activated controls. Again, lowering the concentration of the compound used may make this compound more selective. Since no effects were seen against viral infection, the point may be moot in this context, but should be kept in mind when using this compound for other purposes in Huh7 cells.

The ATF6 activator **147** also lacked selectivity in this cell line; by qPCR, increased expression of both HspA5 (expected, an ATF6 marker) and Erdj4 (unexpected, an IRE1 marker) was seen. As discussed above, the increased expression of Erdj4 may be due to the gene's lack of selectivity in Huh7 cells, rather than the lack of selectivity of the molecule. However, **147** also increased XBP1 splicing in these cells, which is a direct marker of IRE1 activation. Additionally, a significant increase in CHOP levels were observed, which is a marker for PERK activation. Again, it is possible that CHOP is less of a selective PERK marker in these cells than in others, and caution should be taken to make conclusions based on a single gene. However, later experiments using mass spectrometry to measure global protein changes suggest the activation was not localized to specific genes in each branch, and general activation of all three branches was seen (**Figure A2.1**). In addition, strong activation of the oxidative stress response (OSR) was seen, though later experiments by a rotation student using an OSR activator suggested this was likely not

responsible for the antiviral effects of **147** (data not shown)[1]. The global proteomics experiment also suggested **Ceapin-A7** may be able to slightly suppress IRE1 gene activation as well (**Figure A2.1**).

The PERK modulators ISRIB and Sephin-1 were not tested in these experiments, partially due to additional considerations of timing and assays that would be needed to measure activation. PERK is typically the first UPR branch to respond after ER stress, and so for purposes of timing earlier than 6 hours (for transcript) or 20 hours (for protein) may be needed. To this extent, levels of phosphorylated PERK or phosphorylated eIF2α may be used to monitor the most upstream events of pathway activation. With these considerations in mind, the PERK regulators may be used for similar experiments as described here, and their effects on viral replication may be measured.

Given the exciting results seen with **147**, this compound was chosen for further studies on the effects of flavivirus infection in Huh7 cells, and these results will be discussed in chapter 3.

2.4 Materials and Methods

Chemicals and resources

All compounds were kept as 1000x stocks in DMSO (0.1% final concentration DMSO for cellular treatments). 147 and **474** were used at 10 µM, **4µ8c** was used at 32 µM, and **Ceapin-A7** was used at 6 µM. Kira6 was used at 10 µM.

Cell culture and virus infections

Cells were maintained in Dulbecco's Modified Eagle's Medium (DMEM) with high glucose and supplemented with 10% fetal bovine serum (FBS), 1% penicillin/streptomycin, and 1% glutamine. Huh7 and Vero cells were kept at 37°C, 5% CO_2. C6/36 cells were kept at 28°C, 5% CO_2.

[1] Experiments performed by Henry Schares

For experimental infections of cell lines, media was removed from cells and DENV was added at MOI 3 for 3 hours. After infection, inoculum was removed, cells were washed with DPBS, and media containing chemical compounds or DMSO was added for the remainder of the experiment. Huh7 cells were obtained from ATCC. Vero and C6/36 cells were a gift from Dr. Tom Voss of the virology core at the Vanderbilt Vaccine Center. Cells were regularly tested for mycoplasma.

Viral Focus Forming Assay

Confluent Vero cells in 96 well plates were inoculated with 10-fold serial dilutions of DENV in BA-1 diluent (1xM199 media, 5% BSA, 1x L-glutamine, 1x penicillin-streptomycin, 0.04% sodium bicarbonate, 50mM Tris) for 2 hours. The cells were overlayed with a 1:1 mixture of 2x nutrient overlay (2x Earle's Balanced Salt solution, 2x Ye-Lah Medium, 4% FBS, 0.4% sodium bicarbonate, 0.1 mg/mL gentamycin, 0.5 mg/mL amphotericin B) and 2.4% methylcellulose in water. After 3 days, overlay was removed, and cells were fixed in ice-cold 85% acetone for 30 minutes. Infectious foci were stained with a primary mouse anti-pan-flavivirus 4G2 antibody (1:1000 in 5% BSA, TBST) and secondary anti-mouse HRP-conjugated secondary antibody (1:1000 in 2.5% milk, TBST. Foci were visualized using 400 µL 8 mg/mL 3-amino-9-ethyl-carbazole in 10 mL 50 mM sodium acetate and 4 µL 30% H_2O_2 for 15-45 minutes or until staining was visible.

Virus

DENV2 strain BID-V533 was a gift from Dr. Tom Voss of the Vanderbilt Vaccine Center. For passaging, C6/36 or Vero cells were infected at MOI 0.1. Six days (C6/36) or three days (Vero) post-infection, culture supernatant was harvested and cell debris was pelleted at 3700xg for 10 minutes. Cleared supernatant was combined with 23% FBS and mixture was frozen in 1 mL aliquots at -80°C.

XBP1 splicing assay

RNA was prepared from plates directly using the Zymo Quick-RNA miniprep kit. cDNA was synthesized from 500 ng total cellular RNA using random primers, oligo-dT primers, and Promega

M-MLV reverse transcriptase. Primers for XBP1 spanning the splicing site (**Table A2.1**) were used to amplify cDNA, and relative quantification was performed by separating the short and long products on a 3% agarose gel at 80V for 1 hour.

SDS-PAGE gels and immunoblotting

Cell pellets were lysed in RIPA buffer (50 mM Tris pH 7.5, 150 mM NaCl, 0.1% SDS, 1% Triton-X-100, 0.5% sodium deoxycholate) + Roche cOmplete protease inhibitor. Cells were left on ice for at least 10 minutes, and lysate was cleared at 17,000xg for 10 minutes. Cleared lysates were transferred to new tubes and normalized gel samples were prepared. Samples were separated on SDS-PAGE gels and transferred to PVDF membranes using standard settings on the TransBlot Turbo (BioRad). Blots were blocked in 5% milk in TBST for 30 minutes at room temperature or 4°C overnight. Primaries were added for 2 hours at room temperature or 4°C overnight. Primary antibodies were used at 1:1000 unless otherwise indicated; secondary antibodies were used at 1:10,000 unless otherwise indicated.

Quantitative RT-PCR

RNA was prepared from cell pellets using the Zymo Quick-RNA miniprep kit. cDNA was synthesized from 500 ng total cellular RNA using random primers, oligo-DT primers, and Promega M-MLV reverse transcriptase. qPCR analysis was performed using Bio-Rad iTaq Universal SYBR Green Supermix combined with primers for genes of interest. Reactions were run in 96 well plates on a Bio-Rad CFX instrument. Conditions used for amplification were 95°C, 2 minutes (initial denaturation followed by 45 repeats of 95°C, 10s/60°C, 30s (denaturation/annealing/extension). A melting curve was generated in 0.5°C increments from 65°C to 95°C. Cq values were calculated by the CFX Maestro software. For relative gene expression measurements, samples were normalized to a housekeeping gene (RiboP or GAPDH). All measurements were performed in technical duplicate on a single plate.

Mass Spectrometry Sample Preparation

Protein lysate from DENV infected and non-infected Huh7 cells (for whole cell lysate samples, 20 µg of protein as measured using Bio-Rad protein assay dye reagent) was aliquoted and purified using methanol/chloroform precipitation. Protein was resuspended in 3 µL 1% Rapigest (Waters) and diluted with water and 0.5 M HEPES. Proteins were reduced with 5 mM TCEP (Thermo Scientific) and alkylated with 10 mM iodoacetamide (Sigma). Proteins were digested in trypsin (Thermo Scientific) overnight at 37ºC shaking at 750 rpm. Peptides were labeled for 1 hour at room temperature using 11-plex tandem mass tag (TMT) reagents (Thermo Scientific) resuspended in acetonitrile. Labeling reactions were quenched with 0.4% ammonium bicarbonate for 1 hour at room temperature. Samples were combined and acidified to pH 2 by addition of 5% formic acid. Pooled samples were concentrated using a SpeedVac and resuspended in 94.9% water/5% acetonitrile/0.1% formic acid. Rapigest cleavage products were pelleted by centrifugation at 14,000xg for 30 minutes.

Mass Spectrometry Data Acquisition

Up to 10 µg of digested peptides were loaded onto a triphasic column filled sequentially with 1.5 or 2.5 cm layers of 5 µm 100 Å C18 resin (Phenomenex), Luna 5 µm 100 Å SCX resin (Phenomenex) and a second layer of C18 resin using a high-pressure chamber. The column was washed for 30 minutes in 95% water/5% acetonitrile/0.1% formic acid (buffer A) and attached to an Ultimate 3000 nano LC system connected to a 20 cm, 100 µm ID fused-silica microcapillary column with a laser-pulled tip filled with 3 µm 100 Å C18 resin (Phenomenex). Mass spectrometry was carried out on a Q-Exactive HF (ThermoFisher). MuDPIT analysis was performed with 10 µL sequential injections of 0 - 100% buffer C (500 mM ammonium acetate, diluted in buffer A), each injection increasing by 10%, followed by an injection of 90% buffer C/10% buffer B (100% acetonitrile/1% formic acid). Peptides were separated on a 90 min gradient from 5% to 40% buffer B at a flow rate of 500nL/min, followed by a 5 min ramp to 60 - 80% buffer B. Electrospray ionization was performed from the tip of the microcapillary column at a voltage of 2.2 kV with an ion transfer tube temperature of 275 ºC. Data-dependent mass spectra were collected by

performing a full scan from 300 – 1800 m/z at a resolution of 120,000 and AGC target of 1e6. Tandem mass spectrometry was performed using TopN from each full scan using HCD collision energy of NCE 38, isolation window of 0.7, with automatic maximum injection time, a resolution of 45,000, fixed first mass of 110 m/z, and dynamic exclusion of 10s.

Mass Spectrometry Data Analysis

Peptide and protein identification, and TMT reporter ion quantification was analyzed using Proteome Discover 2.4. Searches were carried out with the SEQUEST node using a human proteome database (UniProt) with DENV proteins added manually and the following parameters: 20ppm precursor mass tolerance, minimum peptide length of 6 amino acids, trypsin cleavage with a maximum of 2 missed cleavages, static modifications of +57.0215Da (carbamidomethylation at C) and +229.1629 (TMT/11plex), and dynamic modifications of +15.995 (oxidation at M), N-terminal methionine loss (-131.040), and N-terminal acetylation (+42.011). Search results were filtered with Percolator using a decoy database of reversed sequences with a peptide false discovery rate of 1% and a minimum of 2 peptides for protein identification. TMT intensities were quantified using the reporter ion quantification node with TMT intensities from each channel being normalized using the total peptide amount, quantitative value correction enabled to correct for TMT impurities, and co-isolation threshold set to 25%. Intensities for each protein were calculated by summing the intensities of each peptide. A reference TMT channel of pooled samples was included for scaling of protein abundances across multiple mass spectrometry runs.

2.5 References

(1) Bhatt, S.; Gething, P. W.; Brady, O. J.; Messina, J. P.; Farlow, A. W.; Moyes, C. L.; Drake, J. M.; Brownstein, J. S.; Hoen, A. G.; Sankoh, O.; Myers, M. F.; George, D. B.; Jaenisch, T.; William Wint, G. R.; Simmons, C. P.; Scott, T. W.; Farrar, J. J.; Hay, S. I. The Global Distribution and Burden of Dengue. *Nature* **2013**, *496* (7446), 504–507. https://doi.org/10.1038/nature12060.

(2) Zhao, R.; Wang, M.; Cao, J.; Shen, J.; Zhou, X.; Wang, D.; Cao, J. Flavivirus: From Structure to Therapeutics Development. *Life* **2021**, *11* (7), 615. https://doi.org/10.3390/LIFE11070615.

(3) García, L. L.; Padilla, L.; Castaño, J. C. Inhibitors Compounds of the Flavivirus Replication Process. *Virol. J.* **2017**, *14* (1), 1–12. https://doi.org/10.1186/S12985-017-

0761-1/TABLES/1.

(4) Braakman, I.; Hebert, D. N. Protein Folding in the Endoplasmic Reticulum. *Cold Spring Harb. Perspect. Biol.* **2013**, *5* (5), a013201. https://doi.org/10.1101/CSHPERSPECT.A013201.

(5) Peña, J.; Harris, E. Dengue Virus Modulates the Unfolded Protein Response in a Time-Dependent Manner. *J. Biol. Chem.* **2011**, *286* (16), 14226–14236. https://doi.org/10.1074/JBC.M111.222703/ATTACHMENT/26D81C6A-EC37-478A-8216-AE9671042F97/MMC1.PDF.

(6) Walter, P.; Ron, D. The Unfolded Protein Response: From Stress Pathway to Homeostatic Regulation. *Science (80-.).* **2011**, *334* (6059), 1081–1086. https://doi.org/10.1126/SCIENCE.1209038/ASSET/238BD530-CE66-4C19-BA32-FC13641E3646/ASSETS/GRAPHIC/334_1081_F3.JPEG.

(7) Gallagher, C. M.; Garri, C.; Cain, E. L.; Ang, K. K. H.; Wilson, C. G.; Chen, S.; Hearn, B. R.; Jaishankar, P.; Aranda-Diaz, A.; Arkin, M. R.; Renslo, A. R.; Walter, P. Ceapins Are a New Class of Unfolded Protein Response Inhibitors, Selectively Targeting the ATF6α Branch. *Elife* **2016**, *5*. https://doi.org/10.7554/ELIFE.11878.

(8) Plate, L.; Cooley, C. B.; Chen, J. J.; Paxman, R. J.; Gallagher, C. M.; Madoux, F.; Genereux, J. C.; Dobbs, W.; Garza, D.; Spicer, T. P.; Scampavia, L.; Brown, S. J.; Rosen, H.; Powers, E. T.; Walter, P.; Hodder, P.; Luke Wiseman, R.; Kelly, J. W. Small Molecule Proteostasis Regulators That Reprogram the ER to Reduce Extracellular Protein Aggregation. *Elife* **2016**, *5*. https://doi.org/10.7554/ELIFE.15550.

(9) Sidrauski, C.; Acosta-Alvear, D.; Khoutorsky, A.; Vedantham, P.; Hearn, B. R.; Li, H.; Gamache, K.; Gallagher, C. M.; Ang, K. K. H.; Wilson, C.; Okreglak, V.; Ashkenazi, A.; Hann, B.; Nader, K.; Arkin, M. R.; Renslo, A. R.; Sonenberg, N.; Walter, P. Pharmacological Brake-Release of MRNA Translation Enhances Cognitive Memory. *Elife* **2013**, *2013* (2). https://doi.org/10.7554/ELIFE.00498.

(10) Das, I.; Krzyzosiak, A.; Schneider, K.; Wrabetz, L.; D'Antonio, M.; Barry, N.; Sigurdardottir, A.; Bertolotti, A. Preventing Proteostasis Diseases by Selective Inhibition of a Phosphatase Regulatory Subunit. *Science (80-.).* **2015**, *348* (6231), 239–242. https://doi.org/10.1126/SCIENCE.AAA4484/SUPPL_FILE/DAS-SM.PDF.

(11) Shen, J.; Chen, X.; Hendershot, L.; Prywes, R. ER Stress Regulation of ATF6 Localization by Dissociation of BiP/GRP78 Binding and Unmasking of Golgi Localization Signals. *Dev. Cell* **2002**, *3* (1), 99–111. https://doi.org/10.1016/S1534-5807(02)00203-4.

(12) Han, X.; Zhou, J.; Zhang, P.; Song, F.; Jiang, R.; Li, M.; Xia, F.; Guo, F. J. IRE1α Dissociates with BiP and Inhibits ER Stress-Mediated Apoptosis in Cartilage Development. *Cell. Signal.* **2013**, *25* (11), 2136–2146. https://doi.org/10.1016/J.CELLSIG.2013.06.011.

(13) Bertolotti, A.; Zhang, Y.; Hendershot, L. M.; Harding, H. P.; Ron, D. Dynamic Interaction of BiP and ER Stress Transducers in the Unfolded-Protein Response. *Nat. Cell Biol.* **2000**, *2* (6), 326–332. https://doi.org/10.1038/35014014.

(14) Adams, C. J.; Kopp, M. C.; Larburu, N.; Nowak, P. R.; Ali, M. M. U. Structure and Molecular Mechanism of ER Stress Signaling by the Unfolded Protein Response Signal Activator IRE1. *Front. Mol. Biosci.* **2019**, *6*, 11. https://doi.org/10.3389/FMOLB.2019.00011/BIBTEX.

(15) Ma, K.; Vattem, K. M.; Wek, R. C. Dimerization and Release of Molecular Chaperone

Inhibition Facilitate Activation of Eukaryotic Initiation Factor-2 Kinase in Response to Endoplasmic Reticulum Stress. *J. Biol. Chem.* **2002**, *277* (21), 18728–18735. https://doi.org/10.1074/JBC.M200903200.

(16) Harding, H. P.; Zhang, Y.; Ron, D. Protein Translation and Folding Are Coupled by an Endoplasmic-Reticulum-Resident Kinase. *Nature* **1999**, *397* (6716), 271–274. https://doi.org/10.1038/16729.

(17) Harding, H. P.; Novoa, I.; Zhang, Y.; Zeng, H.; Wek, R.; Schapira, M.; Ron, D. Regulated Translation Initiation Controls Stress-Induced Gene Expression in Mammalian Cells. *Mol. Cell* **2000**, *6* (5), 1099–1108. https://doi.org/10.1016/S1097-2765(00)00108-8.

(18) Vattem, K. M.; Wek, R. C. Reinitiation Involving Upstream ORFs Regulates ATF4 MRNA Translation in Mammalian Cells. *Proc. Natl. Acad. Sci. U. S. A.* **2004**, *101* (31), 11269–11274. https://doi.org/10.1073/PNAS.0400541101/ASSET/86AC6DFB-7D14-475E-B5D2-460B21596D7C/ASSETS/GRAPHIC/ZPQ0310455790005.JPEG.

(19) Marciniak, S. J.; Yun, C. Y.; Oyadomari, S.; Novoa, I.; Zhang, Y.; Jungreis, R.; Nagata, K.; Harding, H. P.; Ron, D. CHOP Induces Death by Promoting Protein Synthesis and Oxidation in the Stressed Endoplasmic Reticulum. *Genes Dev.* **2004**, *18* (24), 3066–3077. https://doi.org/10.1101/GAD.1250704.

(20) Novoa, I.; Zeng, H.; Harding, H. P.; Ron, D.; Neibert, D. W.; Hollander, M. C.; Luethy, J. D.; Papathanasiou, M.; Fragoli, J.; Holbrook, N. J.; Hoffman-Lieberman, B. Feedback Inhibition of the Unfolded Protein Response by GADD34-Mediated Dephosphorylation of EIF2α. *J. Cell Biol.* **2001**, *153* (5), 1011–1022. https://doi.org/10.1083/JCB.153.5.1011.

(21) Pakos-Zebrucka, K.; Koryga, I.; Mnich, K.; Ljujic, M.; Samali, A.; Gorman, A. M. The Integrated Stress Response. *EMBO Rep.* **2016**, *17* (10), 1374–1395. https://doi.org/10.15252/EMBR.201642195.

(22) Grandjean, J. M. D.; Luke Wiseman, R. Small Molecule Strategies to Harness the Unfolded Protein Response: Where Do We Go from Here? *J. Biol. Chem.* **2020**, *295* (46), 15692–15711. https://doi.org/10.1074/JBC.REV120.010218.

(23) Zhou, J.; Liu, C. Y.; Back, S. H.; Clark, R. L.; Peisach, D.; Xu, Z.; Kaufman, R. J. The Crystal Structure of Human IRE1 Luminal Domain Reveals a Conserved Dimerization Interface Required for Activation of the Unfolded Protein Response. *Proc. Natl. Acad. Sci. U. S. A.* **2006**, *103* (39), 14343–14348. https://doi.org/10.1073/PNAS.0606480103/SUPPL_FILE/06480TABLE2.PDF.

(24) Uemura, A.; Oku, M.; Mori, K.; Yoshida, H. Unconventional Splicing of XBP1 MRNA Occurs in the Cytoplasm during the Mammalian Unfolded Protein Response. *J. Cell Sci.* **2009**, *122* (16), 2877–2886. https://doi.org/10.1242/JCS.040584.

(25) Calfon, M.; Zeng, H.; Urano, F.; Till, J. H.; Hubbard, S. R.; Harding, H. P.; Clark, S. G.; Ron, D. IRE1 Couples Endoplasmic Reticulum Load to Secretory Capacity by Processing the XBP-1 MRNA. *Nature* **2002**, *415* (6867), 92–96. https://doi.org/10.1038/415092a.

(26) Maurel, M.; Chevet, E.; Tavernier, J.; Gerlo, S. Getting RIDD of RNA: IRE1 in Cell Fate Regulation. *Trends Biochem. Sci.* **2014**, *39* (5), 245–254. https://doi.org/10.1016/J.TIBS.2014.02.008.

(27) Shoulders, M. D.; Ryno, L. M.; Genereux, J. C.; Moresco, J. J.; Tu, P. G.; Wu, C.; Yates, J. R.; Su, A. I.; Kelly, J. W.; Wiseman, R. L. Stress-Independent Activation of XBP1s and/or ATF6 Reveals Three Functionally Diverse ER Proteostasis Environments. *Cell Rep.* **2013**, *3* (4), 1279–1292. https://doi.org/10.1016/J.CELREP.2013.03.024.

(28) Ghosh, R.; Wang, L.; Wang, E. S.; Perera, B. G. K.; Igbaria, A.; Morita, S.; Prado, K.; Thamsen, M.; Caswell, D.; Macias, H.; Weiberth, K. F.; Gliedt, M. J.; Alavi, M. V.; Hari, S. B.; Mitra, A. K.; Bhhatarai, B.; Schürer, S. C.; Snapp, E. L.; Gould, D. B.; German, M. S.; Backes, B. J.; Maly, D. J.; Oakes, S. A.; Papa, F. R. Allosteric Inhibition of the IRE1α RNase Preserves Cell Viability and Function during Endoplasmic Reticulum Stress. *Cell* **2014**, *158* (3), 534–548. https://doi.org/10.1016/J.CELL.2014.07.002.

(29) Cross, B. C. S.; Bond, P. J.; Sadowski, P. G.; Jha, B. K.; Zak, J.; Goodman, J. M.; Silverman, R. H.; Neubert, T. A.; Baxendale, I. R.; Ron, D.; Harding, H. P. The Molecular Basis for Selective Inhibition of Unconventional MRNA Splicing by an IRE1-Binding Small Molecule. *Proc. Natl. Acad. Sci. U. S. A.* **2012**, *109* (15). https://doi.org/10.1073/PNAS.1115623109/SUPPL_FILE/SM02.MPG.

(30) Grandjean, J. M. D.; Madhavan, A.; Cech, L.; Seguinot, B. O.; Paxman, R. J.; Smith, E.; Scampavia, L.; Powers, E. T.; Cooley, C. B.; Plate, L.; Spicer, T. P.; Kelly, J. W.; Wiseman, R. L. Pharmacologic IRE1/XBP1s Activation Confers Targeted ER Proteostasis Reprogramming. *Nat. Chem. Biol.* **2020**, *16* (10), 1052–1061. https://doi.org/10.1038/s41589-020-0584-z.

(31) Oka, O. B. V.; Pierre, A. S.; Pringle, M. A.; Tungkum, W.; Cao, Z.; Fleming, B.; Bulleid, N. J. Activation of the UPR Sensor ATF6α Is Regulated by Its Redox-Dependent Dimerization and ER Retention by ERp18. *Proc. Natl. Acad. Sci. U. S. A.* **2022**, *119* (12). https://doi.org/10.1073/PNAS.2122657119/SUPPL_FILE/PNAS.2122657119.SAPP01.PDF.

(32) Oka, O. B.; Lith, M. van; Rudolf, J.; Tungkum, W.; Pringle, M. A.; Bulleid, N. J. ERp18 Regulates Activation of ATF6α during Unfolded Protein Response. *EMBO J.* **2019**, *38* (15), e100990. https://doi.org/10.15252/EMBJ.2018100990.

(33) Ye, J.; Rawson, R. B.; Komuro, R.; Chen, X.; Davé, U. P.; Prywes, R.; Brown, M. S.; Goldstein, J. L. ER Stress Induces Cleavage of Membrane-Bound ATF6 by the Same Proteases That Process SREBPs. *Mol. Cell* **2000**, *6* (6), 1355–1364. https://doi.org/10.1016/S1097-2765(00)00133-7.

(34) Paxman, R.; Plate, L.; Blackwood, E. A.; Glembotski, C.; Powers, E. T.; Wiseman, R. L.; Kelly, J. W. Pharmacologic ATF6 Activating Compounds Are Metabolically Activated to Selectively Modify Endoplasmic Reticulum Proteins. *Elife* **2018**, *7*. https://doi.org/10.7554/ELIFE.37168.

(35) Gallagher, C. M.; Walter, P. Ceapins Inhibit ATF6α Signaling by Selectively Preventing Transport of ATF6α to the Golgi Apparatus during ER Stress. *Elife* **2016**, *5*. https://doi.org/10.7554/ELIFE.11880.

(36) Torres, S. E.; Gallagher, C. M.; Plate, L.; Gupta, M.; Liem, C. R.; Guo, X.; Tian, R.; Stroud, R. M.; Kampmann, M.; Weissman, J. S.; Walter, P. Ceapins Block the Unfolded Protein Response Sensor Atf6α by Inducing a Neomorphic Inter-Organelle Tether. *Elife* **2019**, *8*. https://doi.org/10.7554/ELIFE.46595.

(37) Jaskulska, A.; Janecka, A. E.; Gach-Janczak, K. Thapsigargin—From Traditional Medicine to Anticancer Drug. *Int. J. Mol. Sci.* **2021**, *22* (1), 4. https://doi.org/10.3390/IJMS22010004.

(38) Grandjean, J. M. D.; Plate, L.; Morimoto, R. I.; Bollong, M. J.; Powers, E. T.; Luke Wiseman, R. Deconvoluting Stress-Responsive Proteostasis Signaling Pathways for Pharmacologic Activation Using Targeted RNA Sequencing. *ACS Chem. Biol.* **2019**, *14* (4), 784–795.

https://doi.org/10.1021/ACSCHEMBIO.9B00134/SUPPL_FILE/CB9B00134_SI_004.XLSX.

(39) Wang, L.; Perera, B. G. K.; Hari, S. B.; Bhhatarai, B.; Backes, B. J.; Seeliger, M. A.; Schürer, S. C.; Oakes, S. A.; Papa, F. R.; Maly, D. J. Divergent Allosteric Control of the IRE1α Endoribonuclease Using Kinase Inhibitors. *Nat. Chem. Biol.* **2012**, *8* (12), 982–989. https://doi.org/10.1038/nchembio.1094.

(40) Korennykh, A. V.; Egea, P. F.; Korostelev, A. A.; Finer-Moore, J.; Zhang, C.; Shokat, K. M.; Stroud, R. M.; Walter, P. The Unfolded Protein Response Signals through High-Order Assembly of Ire1. *Nature* **2008**, *457* (7230), 687–693. https://doi.org/10.1038/nature07661.

CHAPTER 3: ER proteostasis regulator 147 acts as a broad-spectrum inhibitor of dengue and Zika virus infections

This chapter is adapted, with permission from journal and co-authors, from Almasy, K.M., Davies, J.P, Lisy, S.M., Tirgar, R., Tran., S.C., and Plate, L., *Proceedings of the National Academy of Sciences*, **2021**, 118 (3) e 2012209118; https://doi.org/10.1073/pnas.2012209118.

3.1 Introduction

Flaviviruses are significant human pathogens that cause widespread mortality around the world. The genus encompasses several arthropod-borne viruses including Dengue (DENV), Yellow Fever (YFV), and Zika (ZIKV)[1–3]. These viruses pose serious public health threats, particularly as increased global travel and climate change have caused an increase in the spread of both the virus and their mosquito vectors (*A. albopictus* and *A. aegypti*)[4,5]. It is estimated that 53% of the world population lives in areas suitable for dengue transmission resulting in 50-100 million dengue infections per year, of which 500,000 proceed to dengue hemorrhagic fever and 22,000 are fatal[1,6]. ZIKV infection has been linked to serious neurological defects, including Guillain-Barré syndrome and microcephaly in newborns[7]. While ZIKV diagnoses were relatively rare until the early 2000s, the 2015–2016 pandemic in the Americas highlighted the potential for rapid spread of the disease vectors [3].

Vaccines currently exist for only a limited range of flaviviruses[8]. The first DENV vaccine, Dengvaxia, was approved by the FDA in early 2019[9]. However, its use remains limited to children with confirmed prior infection. In addition, no post-exposure therapeutic options are available for patients infected with these viruses; current treatments only attempt to alleviate the symptoms[10–12]. Antiviral strategies often focus on directly targeting viral proteins. For instance, while molecules inhibiting the flavivirus RNA-dependent RNA polymerase NS5 or the protease NS3 have been identified, the high mutation rate of the virus allows for resistance to be developed quickly[10,13,14].

One increasing area of exploration for alternative therapeutic approaches is the targeting of host factors that are critical for virus propagation[15]. As these proteins are not under genetic control of the virus, development of resistance is much less likely[16–18]. In addition, host-targeted therapeutics should be effective as broad-spectrum antivirals instead of targeting a single virus[19–21].

Flaviviruses contain a genome of positive-sense, single stranded RNA (+ssRNA) approximately 11kbp in size. The viruses replicate and assemble around the endoplasmic reticulum (ER) membrane[22]. As the genome is translated after entry into the cell, the single polyprotein is inserted into the ER membrane and is co- and post-translationally processed into three structural (capsid, pre-membrane, and envelope) and seven nonstructural (NS1, NS2A, NS2B, NS3, NS4A, NS4B, NS5) proteins[23]. The host proteostasis network has been implicated in the maintenance of individual viral proteins and virus evolution[20,24–26]. The proteostasis network is comprised of chaperones, co-chaperones and other protein quality control factors that control protein folding, assembly, post-translational modification, trafficking, and degradation. Genetic screens have identified many proteostasis factors as essential for DENV replication, including several components of the oligosaccharyl transferase (OST) complex, as well as the ER membrane protein complex[27–30]. Aside from promoting biogenesis of viral proteins, these components also have additional roles in organizing viral replication centers at the ER membrane[28,29,31]. Additionally, diverse cellular chaperone and co-chaperone systems are required for all stages of the viral life cycle, including virus entry and disassembly, folding of individual viral proteins, as well as assembly and egress of new virions[21,32,33]. Pharmacologic inhibition of proteostasis factors, including the OST as well as cytosolic Hsp70 and Hsp90 chaperones, has been shown to be an effective strategy to reduce flavivirus infection in cell models[19,21,33–36].

As flavivirus replication and polyprotein translation occurs at the ER membrane, infection results in expansion of the ER and remodeling of the ER proteostasis environment [31,37,38]. DENV infection leads to modulation of the unfolded protein response (UPR), the adaptive stress response that

remodels the ER proteostasis environment to counter stress caused by accumulation of misfolded proteins[39,40]. The UPR consists of three overlapping but distinct signaling branches downstream of the stress-sensing receptors IRE1 (inositol-requiring enzyme 1), ATF6 (activating transcription factor 6), and PERK (Protein kinase R-like ER kinase)[41,42]. The first two branches primarily control the upregulation of chaperones and other proteostasis factors to expand the protein folding capacity of the ER. The PERK branch is responsible for translational attenuation via phosphorylation of eukaryotic initiation factor 2 alpha (eIF2a) and subsequent activation of the integrated stress response. DENV has been shown to upregulate the IRE1/XBP1s and ATF6 branches of the UPR, while suppressing activation of the PERK branch[39].

Given the dependencies of DENV and other flaviviruses on UPR modulation and an enhanced ER proteostasis environment in the host cells during infection, we sought to explore whether these dependencies can be perturbed pharmacologically to impair viral infection. Pharmacologic remodeling of ER proteostasis pathways has become an attractive strategy at correcting imbalances associated with diverse phenotypes related to protein stress and misfolding without affecting endogenous protein maturation or causing toxicity[43–47]. In particular, compound **147**, which was developed as a preferential activator of the ATF6 pathway, has broadly beneficial effects at reducing secretion of amyloidogenic proteins and protecting against oxidative organ damage from ischemia/reperfusion[43,46].

Here, we demonstrate that ER proteostasis remodeling by compound **147** serves as an effective strategy to reduce flavivirus infection. We determine that **147** reduces viral replication but particularly lowers the infectivity of secreted virions. The replication and assembly defect is surprisingly not mediated through activation of ATF6. Instead, the activity is mediated by upstream covalent modifications of protein targets by **147.** Prior work identified protein disulfide isomerases (PDIs) as critical targets for the **147**-dependent ATF6 activation[48], however, our data suggests PDIs are not fully responsible for the antiviral activity. Finally, we show that **147** treatment can reduce proliferation of multiple DENV serotypes and several ZIKV strains, demonstrating that the

pharmacologic agent could be a broadly effective strategy against flaviviruses and other viruses that depend on ER proteostasis processes.

3.2 Results

3.2.1 A Selective Modulator of the ATF6 Pathway Impairs Dengue Virus Infection

DENV is known to activate the UPR in infected host cells and was previously found to specifically upregulate the ATF6 and IRE1/XBP1s signaling arms, which transcriptionally upregulate ER protein quality control factors and adjust proteostasis capacity (**Figure 3.1A**)[39,49]. To confirm the activation of ER proteostasis pathways by DENV, we performed an infection time-course with DENV serotype 2 (DENV2) in Huh7 liver carcinoma cells and measured transcript levels of an ATF6-regulated gene (*PDIA4*) and an XBP1s-regulated gene (*ERDJ4*) by qPCR. Both *PDIA4* and *ERDJ4* transcripts exhibited a time-dependent induction in response to DENV2 infection (**Figure 3.1B**). The late onset of UPR activation and degree transcript and protein induction was consistent with prior studies in other cell lines[39]. While a similar time-dependent upregulation of ATF6 and XBP1s-regulated protein products could be observed by western blot, the upregulation of individual proteins was variable (**Figure A3.1A-B**). To more broadly understand how DENV regulates the proteostasis network in Huh7 cells, we performed quantitative proteomics analysis at 24 and 36 hours post infection (hpi) with DENV2 to quantify global changes in protein expression (**Figure A3.1C-D**). We found that DENV2 activated specific factors involved in ER proteostasis maintenance, such as DNAJC10, BiP, SRPRB, and HYOU1. We also filtered previously defined genesets consisting of ~20 specific genes for each of the UPR signaling branches to quantify the cumulative activation of ER proteostasis pathways (**Figure 3.1C**)[50]. This analysis indicated a mild stimulation of ATF6 and XBP1s-regulated proteins, while PERK-regulated proteins remained largely unchanged. In contrast, we did not observe upregulation of cytosolic proteostasis factors that are under control of the heat shock response (HSR)[51]. Overall,

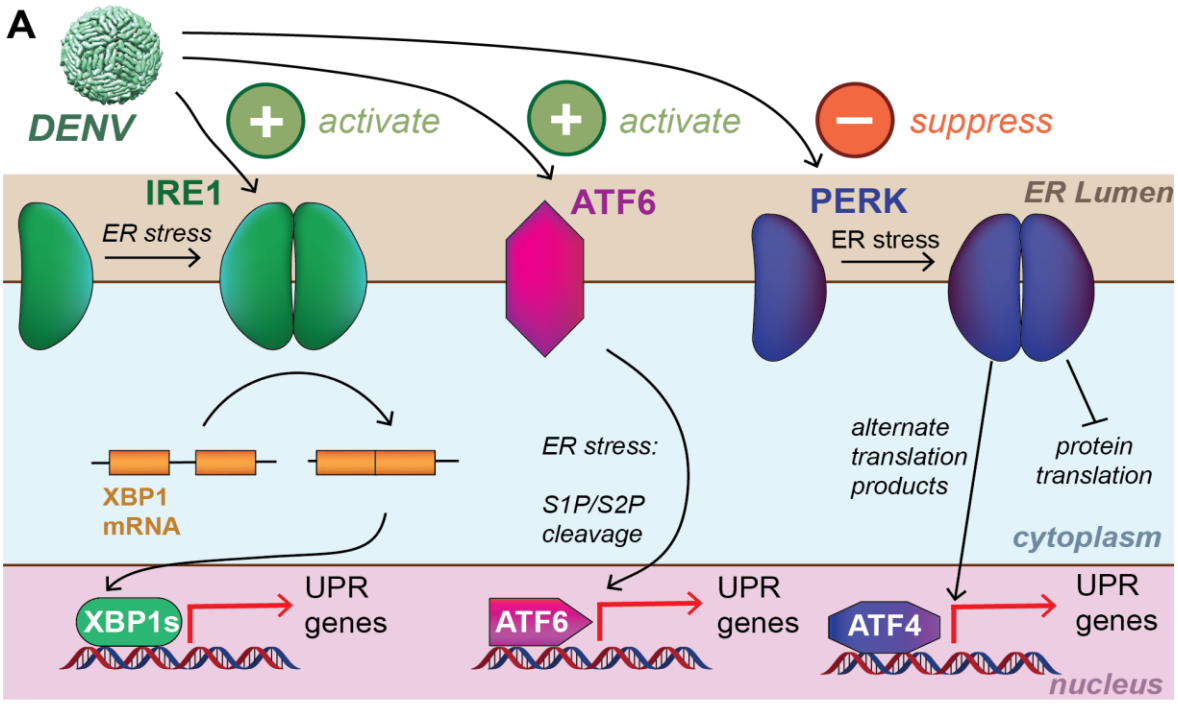
A
DENV
activate
activate
suppress
IRE1
ER stress
ATF6
PERK
ER stress
ER Lumen
XBP1
mRNA
ER stress:
S1P/S2P
cleavage
alternate
translation
products
protein
translation
cytoplasm
XBP1s
UPR
genes
ATF6
UPR
genes
ATF4
UPR
genes
nucleus

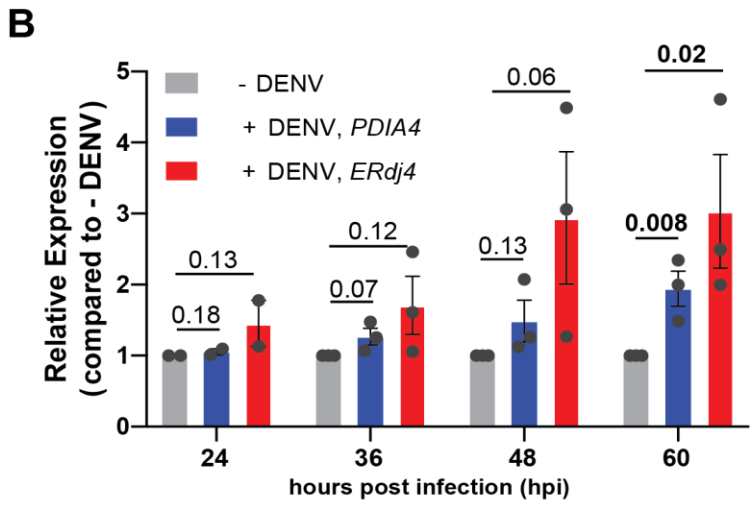
B
- DENV
+ DENV, PDIA4
+ DENV, ERdj4
Relative Expression
(compared to - DENV)
0.18
0.13
0.07
0.12
0.13
0.06
0.008
0.02
24
36
48
60
hours post infection (hpi)

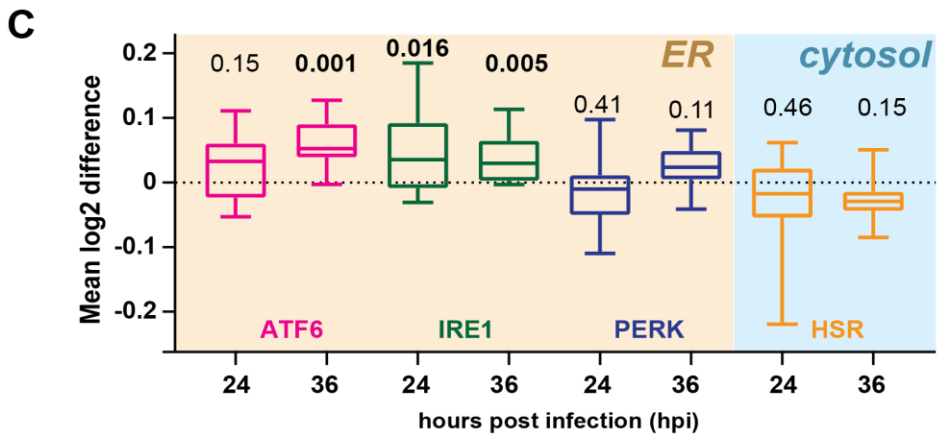
C
Mean log2 difference
0.15
0.001
0.016
0.005
0.41
0.11
0.46
0.15
ER
cytosol
ATF6
IRE1
PERK
HSR
24
36
hours post infection (hpi)

Figure 3.1. DENV infection activates the ER Unfolded Protein Response (UPR).

A. Schematic overview of the UPR showing the three signaling branches: IRE1/XBP1s, PERK, and ATF6. ER protein misfolding stress induces dimerization of IRE1 and PERK, followed by autophosphorylation and activation of downstream signaling pathways. ER stress activation of ATF6 results in trafficking to the Golgi and proteolytic cleavage by S1/S2 proteases. Prior work showed that DENV increased activity of the IRE1/XBP1s and ATF6 branches, while simultaneously preventing activation of the PERK branch (as indicated at the top) (39).
B. Time course of qPCR data showing transcriptional upregulation of an IRE1/XBP1s target (*ERdj4*) and an ATF6 target (*PDIA4*) in response to DENV activation (MOI 3) in Huh7 cells. Error bars shows SEM from 2 to 3 biological replicates and p-values from two-tailed unpaired student t-tests are displayed.
C. Box plots of proteomics data showing the aggregate upregulation of IRE1/XBP1s and ATF6 protein targets at 24 and 36 hpi. PERK and cytosolic heat-shock response (HSR) targets are not affected. Huh7 cells were infected with DENV (MOI 3) for 24h or 36h. Genesets for UPR and HSR pathways were defined based on prior transcriptional profiles [50]. p-values from two-tailed Wilcoxon signed rank tests are indicated. Cell-wide proteomics data comparing DENV infected to non-infected Huh7 cells is shown in **Figure A3.1C-D**.

our results confirm that DENV2 preferentially remodels ER proteostasis pathways through ATF6 and IRE1/XBP1s-dependent upregulation of specific chaperones and protein folding factors.

Considering the dependencies of DENV and other flaviviruses on UPR activation, we determined the impact of the proteostasis regulators **147** (a preferential activator of the ATF6 branch), and Ceapin-A7 (**Cp-A7**) (a selective inhibitor of the ATF6 branch) on DENV infection (**Figure 3.2A**). We pretreated Huh7 cells with the respective compounds 16 hours prior to infection by DENV2 to induce or inhibit UPR-dependent proteostasis remodeling, and we retreated immediately after infection. Quantification of DENV viral titers by a focus forming assay demonstrated a significant reduction in infection with compound **147** at 24 and 36 hpi (**Figure 3.2B**). In contrast, **Cp-A7** treatment only resulted in a small reduction in viral titers at 24 hpi but the infection recovered at 36 hpi. Consistent with experiments in other cell lines, treatment with **Cp-A7** did not induce a large amount of cell toxicity. Compound **147** at 10 μM caused a small reduction (approximate 20%) in cell proliferation when quantifying ATP levels by CellTiter-Glo (**Figure A3.2A**)[46]. We conducted dose-response studies with **147** demonstrating that the compound was effective at reducing DENV proteins at an IC50 of approximately 1 μM (**Figure A3.2B**). Cell viability was maintained

above 90% at this concentration (**Figure A3.2C**). To determine if this viability change was a result of active cell death, we measured the increase in caspase activity induced by DENV, **147**, or the combination of both to quantify apoptosis induction (**Figure A3.2D**). On their own, DENV and **147** did not stimulate an increase in caspase activity while the combined DENV infection with **147** treatment (above 3 µM) led to a very mild 1.5-fold increase in caspase activity. However, this induction was much lower than with short treatment of the known caspase activator staurosporin (**Figure A3.2D**), indicating that any change in ATP levels is likely due to cytostatic activity, rather than a cell-death mediated pathway. These results demonstrate that modulation of the ER proteostasis network with the preferential ATF6 activator **147** could represent an effective strategy to impair DENV2 infection.

The ER plays critical roles in several stages of the viral life cycle including replication of viral RNA at replication centers on the cytosolic side of the ER membrane, translation and proteolytic processing of the viral polyprotein in the ER membrane, as well as the folding, assembly and secretion of new virions[53,54]. To determine at what stage in the viral life cycle the compound treatment impaired viral propagation, we investigated the impact of compound **147** on viral RNA (vRNA) and protein levels at different time points post infection (**Figure 3.2C-D**). The replicative cycle of DENV lasts approximately 24 h; therefore the 12 and 24 hpi time points corresponds to initial infection, while the 36 hpi time point includes reinfection. Quantification of vRNA by qPCR indicated a modest but significant reduction of 50% at 24 hpi, which was attenuated to 30% reduction at 36 hpi (**Figure 3.2E**). Western blot quantification of NS3 and NS5 viral protein in Huh7 cell lysates from DENV2 infected cells showed a 35-80 % reduction in viral non-structural proteins in response to **147** treatment (**Figure 3.2F, Figure A3.2E**). This highlighted that the ER proteostasis regulator exerted a more pronounced effect on viral protein production relative to replication of vRNA. In contrast, infectious viral titers showed a far greater reduction reaching 98% at 12 hpi and sustaining 80% reduction at 36 hpi (**Figure 3.2G**). We confirmed that reduction

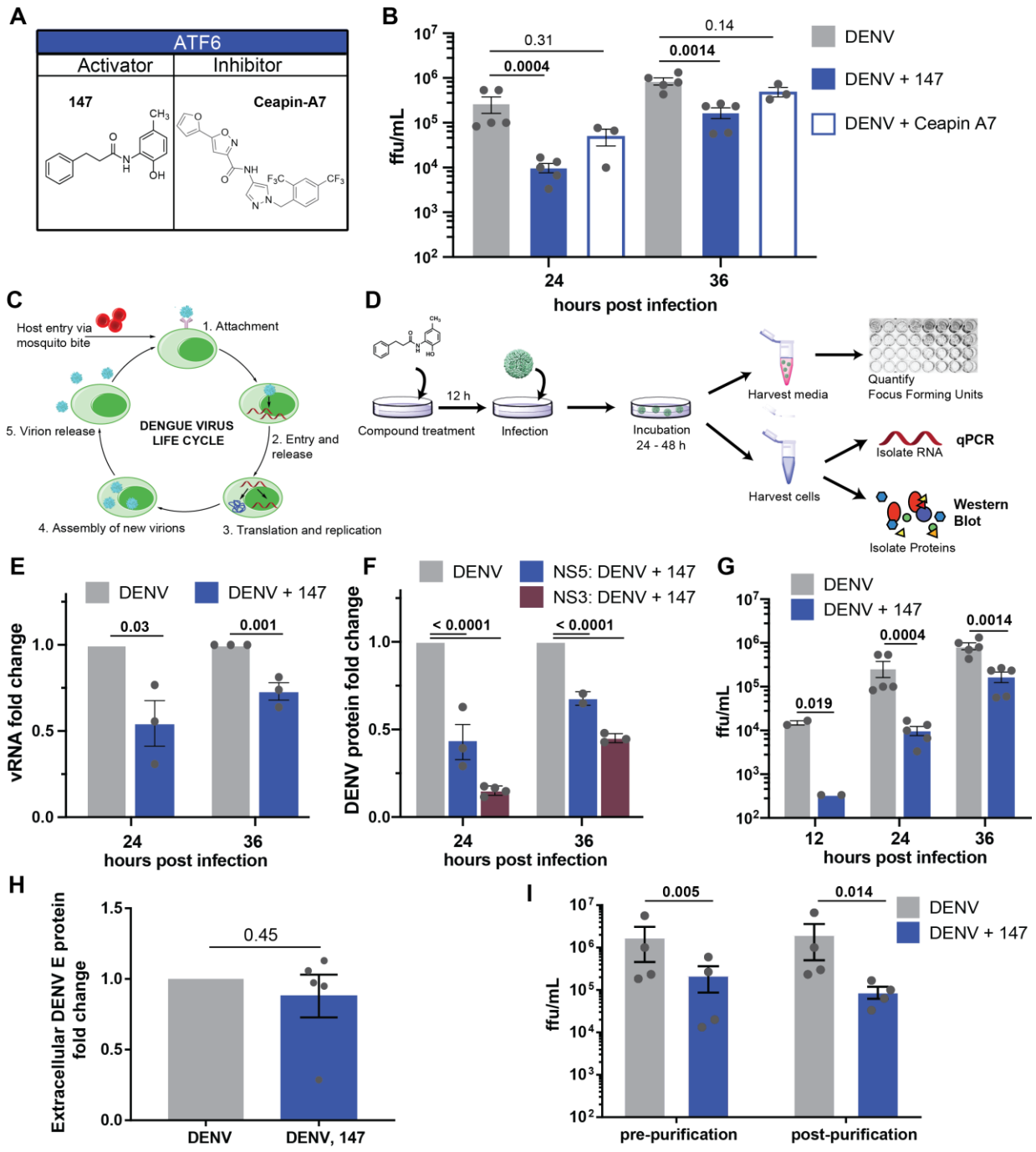

Figure 3.2. Treatment with small molecule 147 reduces viral RNA, protein, and titer levels.

A. Chemical structures of small molecule ATF6 activator **147** and ATF6 inhibitor **Ceapin-A7 (Cp-A7)**.

B. Focus forming assay to quantify changes in Dengue infection in response to treatment with ATF6 modulator compounds. Huh7 cells were treated with compounds, and 16 h later infected with DENV-2 BID-V533 at a MOI of 3 for 3 hours. Media and treatments were replaced, and cells and media were harvested at indicated timepoints and virus focus forming units (ffu/mL) quantified. Error bars show SEM and p-values from ratio paired t-tests are indicated.

C. Schematic of the flavivirus life cycle. After attachment of the virus to a cellular receptor and clathrin-mediated endocytosis, fusion of the envelope protein with the endosome causes release of the capsid and RNA genome. The positive sense genome is then translated, providing the machinery to begin forming replication pockets at the ER membrane. Once sufficient proteins are available, new virions are assembled, trafficked through the Golgi network, and released into the extracellular space.
D. Experimental workflow for quantifying viral RNA, viral protein and titer levels. After pretreatment with compound **147**, cells are infected, retreated with **147**, and left for harvesting at later timepoints. Media samples are taken to quantify ffu; cellular samples taken to quantify vRNA by qPCR or viral proteins by Western Blot/proteomics analysis.
E. Bar graph showing reduction in viral RNA in response to **147** treatment as outlined in **D** 24 and 36 hpi. Error bars correspond to SEM of 3 biological replicates and p-values from unpaired t-tests are shown.
F. Bar graph showing reduction in NS3 and NS5 viral protein levels in response to **147** treatment as outlined in **D** 24 and 36 hpi. Error bars correspond to SEM from 2 to 3 biological replicates per protein and p-values from unpaired t-tests are shown. Representative western blots are shown in **Figure A3.2E**.
G. Bar graph showing reduction DENV viral titers in response to **147** treatment as outlined in **D** 24 and 36 hpi. Error bars correspond to SEM from 2 to 5 biological replicates and p-values from ratio paired t-tests are shown.
H. Quantification of envelope (E) protein from extracellular virus showing that **147** does not reduce viral structural proteins levels. Secreted virions (24 hpi) were purified and concentrated from the media by ultracentrifugation on a sucrose cushion. The same volume of sample was analyzed by SDS-PAGE and western blots (representative blot of E and prM proteins shown in Figure S2J). Error bars correspond to SEM from 5 biological replicates and p-value from unpaired t-tests are shown.
I. Bar graph showing reduction DENV viral titers in response to **147** treatment 24 hpi as pre- and post-purification as described in **H**. Error bars correspond to SEM from 4 biological replicates and p-values from ratio paired t-tests are shown.

in viral proteins is sustained 48 hpi and that renewed treatment with **147** 24 hpi does not further reduce viral propagation (**Figure A3.2F**).

The intensified effect of **147** on viral titers compared to vRNA and protein levels suggests that the compound predominantly acts on a stage subsequent to translation of viral proteins, which would be consistent with disruption of viral maturation or secretion pathways through modulation of ER proteostasis. We confirmed that **147** did not impair viral entry. Omission of the pretreatment prior to infection and treatment of Huh7 cells with the compound only after infection still resulted in a comparable reduction in viral protein and titers, confirming that the compound must act at a post-entry stage (**Figure A3.2G-J**).

To further disentangle the mechanism by which **147** may be impairing viral assembly and egress, we compared the reduction in intracellular vs. extracellular viral protein levels by Western Blot. Extracellular virus secreted into the media was concentrated 24 hpi by ultracentrifugation. While the reduction of nonstructural protein levels intracellularly was up to 80% (**Figure 3.2F**, **Figure A3.2E**), matching the decrease seen with non-structural proteins, no decrease was observed in the extracellular structural protein levels (E and prM, **Figure 3.2H**, **Figure A3.2K**). Importantly, the reduction in secreted structural protein levels is markedly less than the observed ~95% reduction in infectious titer levels observed from the same samples. These combined findings suggest that **147** is affecting DENV assembly and/or secretion in a way that may lead to secretion of non-infectious virions. To support this mechanism, we performed qPCR on the purified extracellular virus samples to measure if there was a change in RNA similar to the change in titer. In support of the assembly defect, this reduction in extracellular vRNA was much smaller than the reduction in titers and not statistically significant (**Figure A3.2L**). This data suggests that the reduction in titer is not simply due to the presence of empty virions in the supernatant.

3.2.2 Inhibition of DENV infection by 147 is only partially dependent on ATF6

Given that flavivirus infection activates the ATF6 pathway, it seemed surprising that pre-activation could reduce viral propagation. We therefore sought to investigate whether ATF6 activation and induction of ATF6-targeted proteostasis factors was required for the **147**-dependent inhibition of DENV infection. We first confirmed by qPCR and quantitative Western blot analysis that treatment with **147** activated the ATF6 regulated gene *HSPA5* (*BiP*) in Huh7 cells (**Figure A3.3A**). To probe the impact of ATF6 activation on the compound activity, we took advantage of the ATF6 inhibitor **Cp-A7,** which inhibits ATF6[55,56]. **Cp-A7** mediates a neomorphic interaction between ATF6 and the peroxisomal membrane protein ABCD3, keeping ATF6 in a trafficking-incompetent oligomeric state, which cannot be activated by **147** (**Figure 3.3A**)[57]. We confirmed by qPCR and Western blot that co-treatment with **147** and **Cp-A7** could attenuate the **147**-dependent induction of ATF6

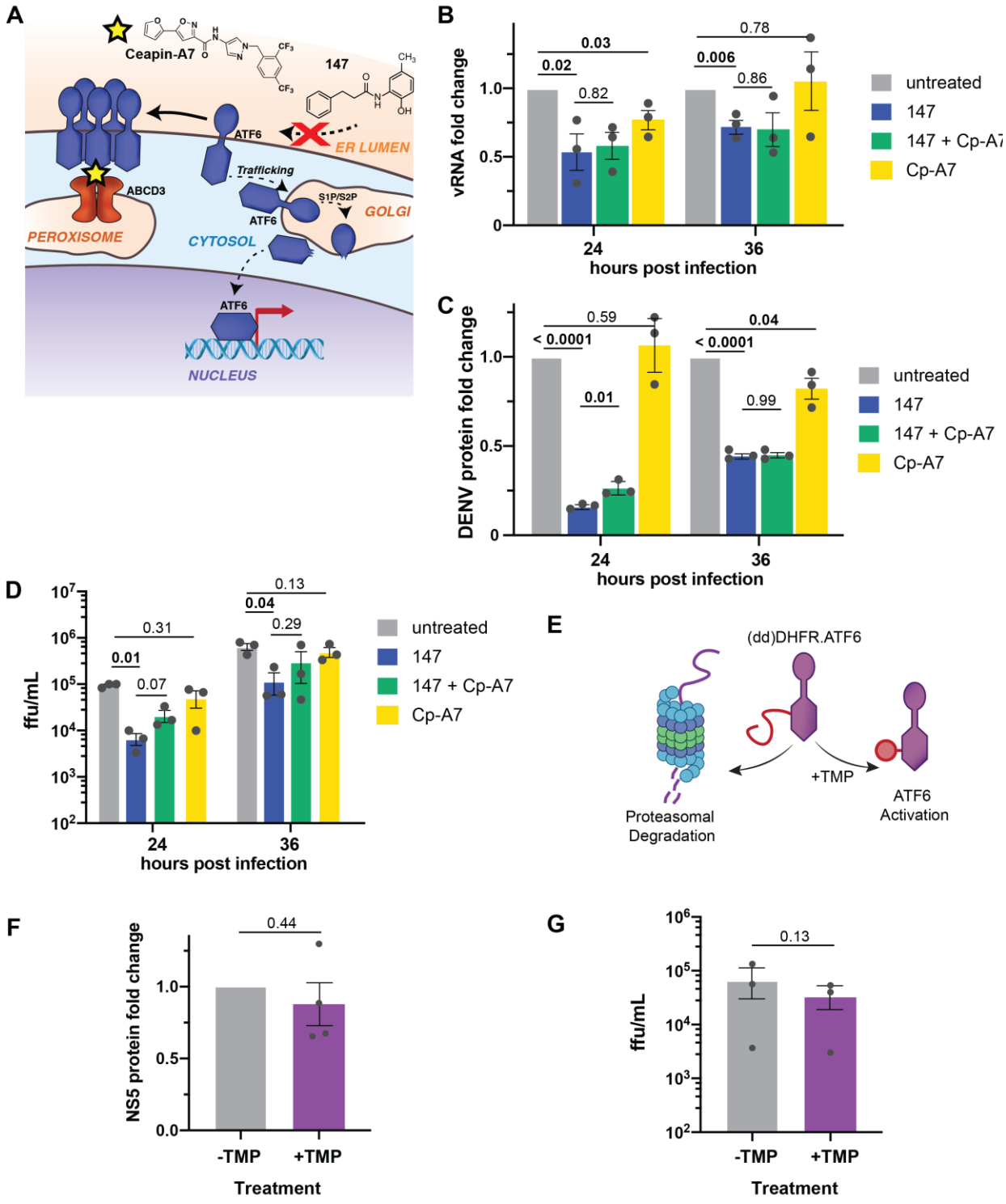

Figure 3.3. ATF6 inhibition does not attenuate the 147-mediated reduction in DENV replication.

A. **Ceapin-A7** (**Cp-A7**) acts as an ATF6 inhibitor downstream of **147** by tethering inactive ATF6 to the peroxisomal membrane protein ABCD3 preventing ATF6 trafficking to the Golgi and activation through S1/S2 cleavage.

B. Bar graph showing the reduction in vRNA levels in response to **147** and **Cp-A7** treatment measured by qPCR in Huh7 cells infected with DENV as outlined in **Figure 3.2D**. **Cp-A7** does not attenuate the **147**-mediate reduction. Error bars correspond to SEM from 3 biological replicates and p-values from unpaired t-tests are shown.
C. Bar graph showing the reduction in NS3 viral protein levels in response to **147** and **Cp-A7** treatment measured by Western blot in Huh7 cells infected with DENV as outlined in **Figure 3.2D**. **Cp-A7** does not attenuate the **147**-mediate reduction. Error bars correspond to SEM from 3 biological replicates and p-values from unpaired t-tests are shown. Representative western blots are shown in **Figure 3.2E**.
D. Bar graph showing the reduction in DENV viral titers in response to **147** and **Cp-A7** treatment in Huh7 cells infected with DENV as outlined in **Figure 3.2D**. **Cp-A7** only minimally attenuates the **147**-mediate reduction at 24 hpi. Error bars correspond to SEM from 3 biological replicates and p-values from paired ratio t-tests are shown.
E. Schematic of the destabilized-domain (dd)DHFR.ATF6 construct, which is constitutively degraded in the absence of the stabilizing ligand trimethoprim (TMP). TMP addition leads to accumulation of ATF6 and transcriptional activation of ATF6 target genes.
F. Graph showing NS5 viral protein levels in DENV infected Huh7 cells that were transiently transfected with ddDHFR.ATF6. ATF6 was activated through addition of TMP 16 hours prior to DENV infection (MOI 3). Data points were collected 24 hpi. Error bars correspond to SEM from 3 biological replicates and p-value from unpaired t-tests is shown. Representative western blots are shown in **Figure A3.3G**.
G. Graph showing DENV viral titers in infected Huh7 cells that were transiently transfected with ddDHFR.ATF6. ATF6 was activated through addition of TMP 16 hours prior to DENV infection (MOI 3) and DENV ffu were quantified 24 hpi. Error bars correspond to SEM from 3 biological replicates and p-value from ratio paired t-tests is shown.

target genes in Huh7 cells (**Figure A3.3A-B**). Furthermore, quantitative proteomics data of cell-wide expression changes confirmed the reduced induction of larger set of ATF6 target genes (**Figure A3.3C**). We then investigated the addition of **Cp-A7** on the **147**-mediated reduction of DENV propagation. Co-treatment of **Cp-A7** did not diminish the reduction in vRNA or NS3 protein (**Figure 3.3B-C**). Furthermore, the addition of **Cp-A7** only partially recovered the DENV2 viral titers at 24 hpi (**Figure 3.3D**). These results highlight that the reduction in viral titers could not be fully attributed to the **147**-mediated induction of ATF6 target genes. To further probe whether the reduced viral propagation could be ascribed to activation of the ATF6 pathway, we took advantage of an orthogonal chemical genetic approach to selectively induce the ATF6 pathway independent of global ER stress. We transiently transfected a destabilized domain (dd)DHFR.ATF6 construct into Huh7 cells. This construct is constitutively degraded in the absence of a small molecule ligand, but can be stabilized through addition of trimethoprim (TMP) leading to accumulation of DHFR.ATF6 and selective induction of ATF6-regulated genes (**Figure 3.3E**)[49]. We confirmed

TMP-dependent upregulation of ATF6-regulated targets BiP, PDIA4, and GRP94 in Huh7 cells (**Figure A3.3D-F**). Next, we pre-treated Huh7 cells with TMP to stabilize ddDHFR.ATF6, infected cells with DENV2, and quantified propagation of the virus by monitoring viral protein levels by Western blot and measuring infectious titers. Chemical genetic ATF6 activation did not lead to a measurable reduction in viral protein levels (**Figure 3.3F, Figure A3.3G**). At the same time, a moderate decrease in viral titers could be observed, but this reduction in viral propagation was much lower than seen with **147** treatment (**Figure 3.3G**). Together, the results from ATF6 inhibition and chemical-genetic ATF6 activation indicate that induction of ATF6-regulated ER proteostasis factors does not impact vRNA replication or production of viral proteins, and only partially accounts for the reduction in DENV2 viral titers.

3.2.3 Reduced DENV propagation requires 147 to covalently target protein thiols

Considering that reduced viral propagation in response to **147** was only partially mediated by ATF6 activation, we sought to explore other mechanisms of how the molecule could impair the virus. Previous studies showed that **147** is a prodrug and requires metabolic activation in cells to generate a reactive *p*-quinone methide that can then form protein adducts with reactive cysteine residues (**Figure 3.4A**)[46,48,58]. In several cell types, ER-resident protein disulfide isomerases (PDIs) were identified as the common protein targets of **147**, and this modulation of PDIs was linked to the activation of ATF6[48]. To explore whether covalent targeting of reactive thiols by **147** is required for the reduction in DENV propagation, we blocked the covalent modifications through addition of an excess of the small-molecule thiol 2-mercaptoethanol (BME) to the cells treated with **147** (**Figure 3.4A**). We confirmed that this addition did not impair cell viability (**Figure A3.4B**), and that BME alone only had a minimal effect on NS3 viral protein levels (**Figure A3.4A**). When BME was added to DENV infected cells that were treated with **147**, this resulted in a partial to complete recovery of viral proteins at 24 and 36 hpi, respectively (**Figure 3.4B, Figure A3.4C**). Similarly, the reduction in DENV2 viral titers was attenuated by the addition of BME (**Figure 3.4C**).

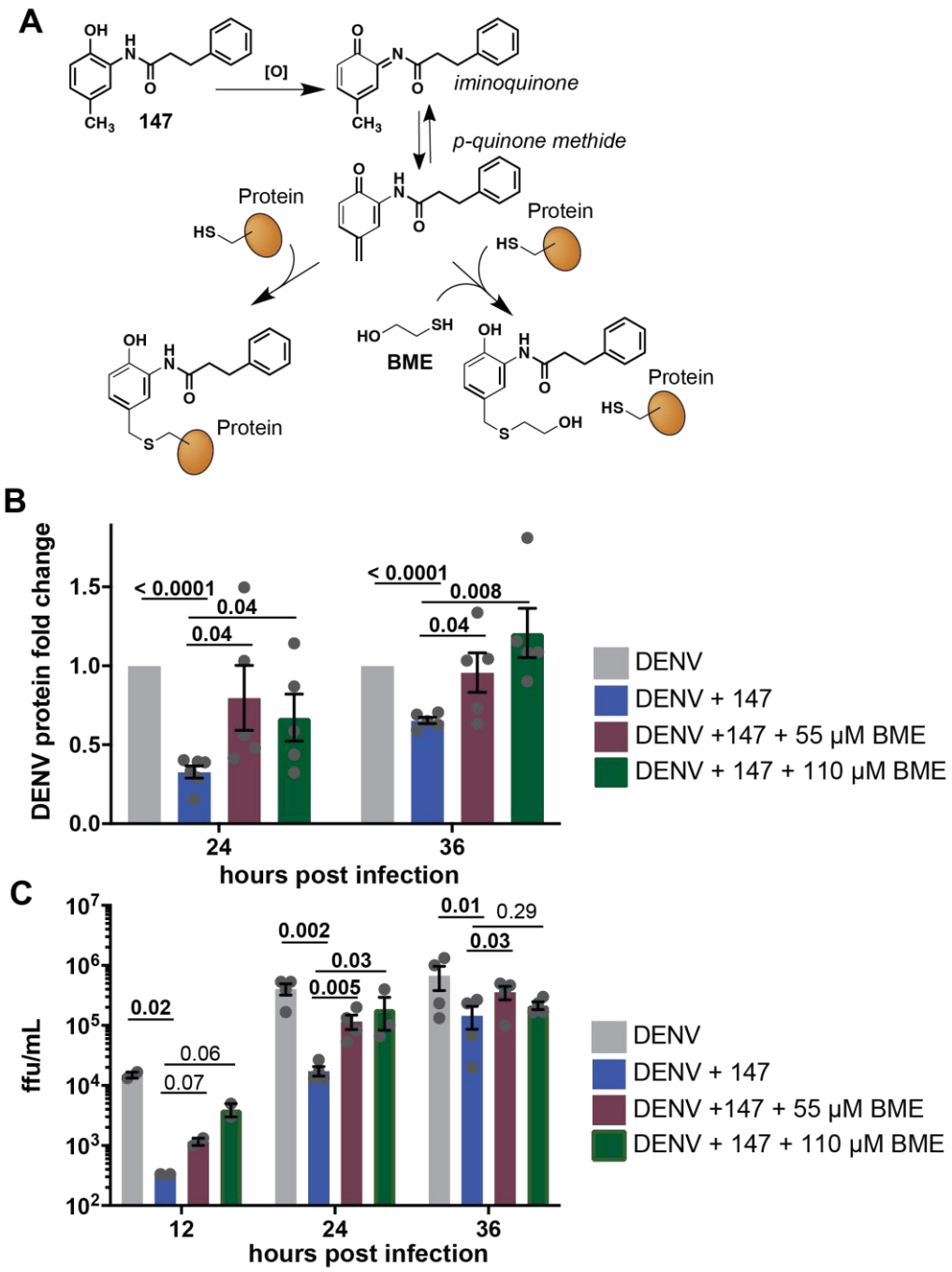

Figure 3.4. 147-mediated reduction in DENV infection is sensitive to small molecule thiols.

A. Schematic outlining the metabolic activation mechanisms of **147**. After oxidation by P450 enzymes, the generated *p*-quinone methide can react with thiol nucleophiles such as cysteine residues on cellular protein targets. Addition of exogenous free thiols such as 2-mercaptoethanol (BME) can quench the active form of **147** before it reacts with protein targets.

B. Graph showing reduction in DENV NS3, NS5 or E protein levels in response to **147** treatment and addition of BME. Huh7 cells were pretreated with **147** and indicated concentrations of BME 16 hours prior to DENV infection (MOI 3) and immediately after

infection. Protein levels were quantified by Western blot. Error bars show SEM and p-values from unpaired t-tests are shown. Representative western blot is shown in **Figure A3.4C**.

C. Bar graph showing DENV viral titer levels in response to **147** treatment and rescue through addition of BME. Huh7 cells were pretreated with **147** and indicated concentrations of BME 16 hours prior to DENV infection (MOI 3) and immediately after infection, and viral ffu were quantified by a focus forming assay. Error bars show SEM and p-values from ratio paired t-tests are shown.

These results indicate that the targeting of cellular thiol groups is required for the inhibition of virus propagation.

We next explored whether targeting of specific PDI proteins by **147** was required for the reduced viral replication. Previous studies determined the covalent targets of **147** in HEK293T, HepG2, and ALLC plasma cells[48]. However, it was conceivable that the metabolic activation mechanism differs in cell types and could result in alternative targets. We therefore determined whether **147** could similarly target PDIs in Huh7 cells. We took advantage of the active analog **147-20**, which contains an alkyne handle that enables further Click chemistry derivatization with desthiobiotin after protein labeling, followed by isolation of the targeted proteins on streptavidin resin (**Figure 3.5A**). The desthiobiotin probe also contained a TAMRA fluorophore that allowed gel-based visualization of the targeted proteins (**Figure 3.5B**). We confirmed that **147-20** retained activity reducing DENV titer levels and NS3 protein levels in infected cells (**Figure A3.5A-C**). In contrast, treatment with **147-4**, an inactive analog where generation of the quinone methide is blocked by the trifluoromethyl group, did not reduce infection. We probed for the presence of specific PDIs (PDIA4, PDIA1, PDIA6), which were identified as **147** targets in other cell lines. These proteins were clearly detectable at molecular weights of prominent labeled bands that were competed by **147**, confirming them as targets in Huh7 cells (**Figure 3.5B, Figure A3.5D**)[48]. In DENV-infected cells that were treated with **147-20**, no additional labeled protein bands were observed, indicating that viral proteins are not directly targeted by the compound (**Figure A3.5E**).

Considering the targeting of multiple PDI enzymes, we were interested in whether the inhibition of PDIs could have an important role in the reduction of viral propagation. We created stable

knockdown cell lines of several PDIs using shRNAs (**Figure A3.5F**). These cell lines were then infected with DENV2 and treated with **147** to assess the effect of PDI knockdown on propagation of the virus. Individual knockdown of *PDIA1* (*P4HB*)*, PDIA4*, or *PDIA6* did not result in a decrease in viral titers indicating that none of these individual PDIs are essential for viral propagation (**Figure A3.5G**). Only knockdown of *PDIA3* resulted in a small reduction in viral titers. While knockdown for some of the PDIs was mild, **147** has been shown to incompletely target these proteins with approximately 25% of PDIA4 was labeled[48]. Thus, even mild knockdown of the proteins should be sufficient to mimic the incomplete targeting by **147**. Next, we measured viral infections in the knockdown cell lines in the presence of **147** to determine whether particular PDIs are required for the **147**-mediated virus inhibition. We observed no measurable attenuation in the reduced viral titers with any single PDI knockdown, including the *PDIA3* knockdown, suggesting that no individual PDIs are responsible for the **147**-mediated effect (**Figure A3.5G**).

To further explore whether PDI inhibition could be responsible for the reduction in DENV infection, we took advantage of several published small-molecule inhibitors of PDIA1 (**Figure 3.5C**)[59–61]. Importantly, these molecules display different degrees of specificity towards PDIA1 relative to other PDIs, mirroring the polypharmacology observed with **147**. We profiled the specific PDIs targeted by the compounds in Huh7 cells by modifying the alkyne handles on the molecule with a fluorophore. **KSC-34** displayed the greatest preference for PDIA1, while **Rb-11-ca** also labeled PDIA4, PDIA6, and several other proteins (**Figure S3.5H**). This is consistent with observations in other cell types and the development of **KSC-34** as a more specific derivative of **Rb-11-ca**[60]. **16F16** does not contain an alkyne handle but previous studies show even broader reactivity towards PDIs than **Rb-11-ca**[61]. We then tested the effect of the compounds on DENV2 infection in Huh7 cells using the same treatment regime as for **147**. **KSC-34** and **16F16** were unable to reduce viral NS3 protein levels (**Figure 3.5D, Figure A3.5J**). **Rb-11-ca** was able to lower viral protein production by 40%; however, this reduction did not translate into lower viral titers (**Figure**

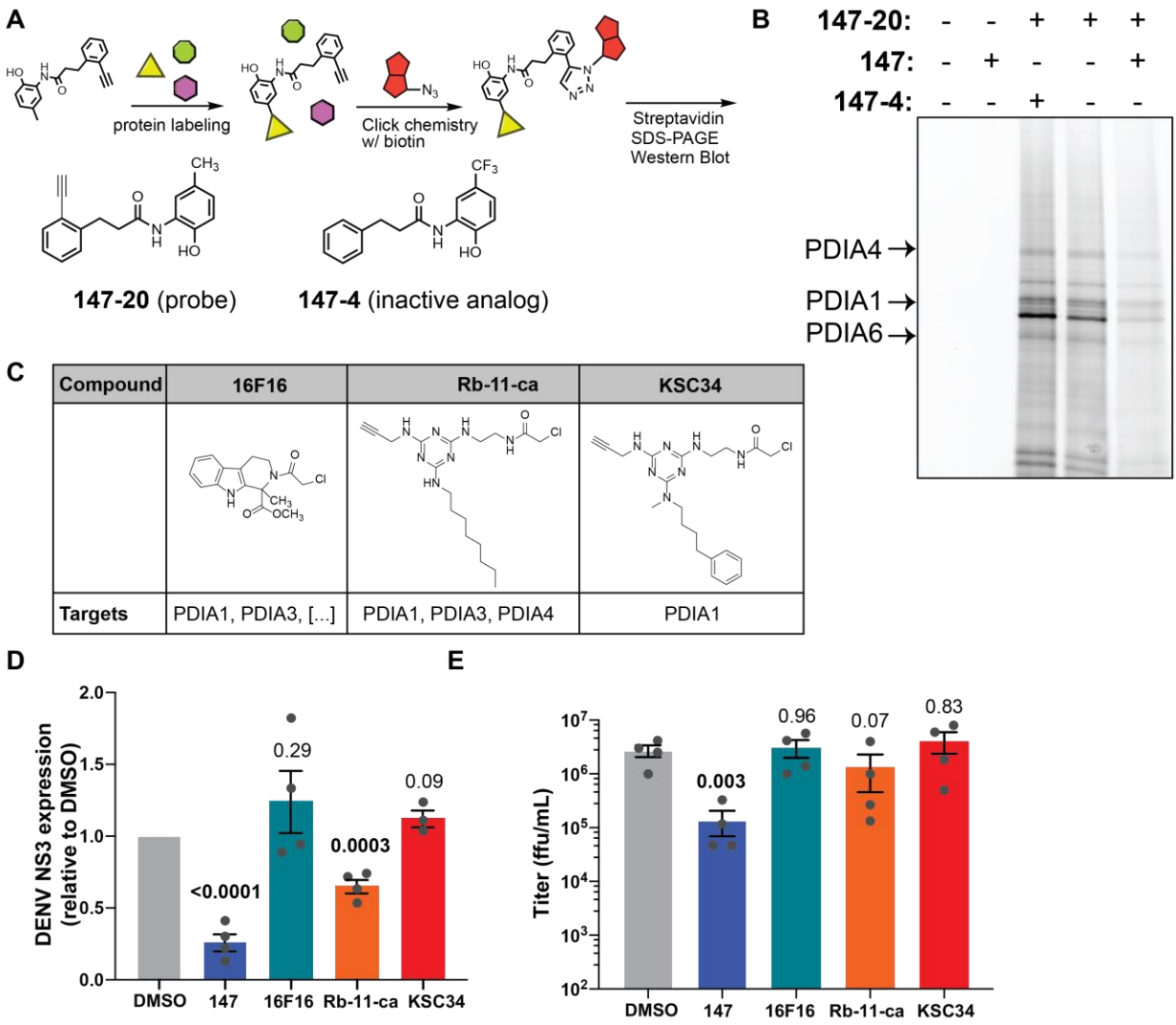

Figure 3.5. **Modification of individual protein disulfide isomerases by 147 is not sufficient to reduce viral infection.**

A. Illustration of the chemoproteomic workflow for target identification using chemical derivatives of **147**. Cells are treated with **147-20**, an alkyne analog of 147 which retains activity and can covalently label proteins as outlined in **Figure 3.4A**. The alkyne handle enables derivatization with either a fluorophore or biotin azide for detection or affinity purification of protein targets. **147-4** is an inactive analog of **147** used to determine specificity in competition experiments.

B. Fluorescence SDS-PAGE image identifying proteins labeled by **147-20** in Huh7 cells. Huh7 cells were treated with **147-20** (3μM) and 3-fold excess competitor (active **147**, or inactive **147-4**) for 18 hours. Labeled proteins in cell lysates were derivatized with a TAMRA-desthiobiotin azide, proteins resolved on SDS-PAGE and a fluorescence image of the gel is shown. The pattern of labeled proteins reveals similar targets as seen in other cell lines [48]. The location of PDIA4, PDIA6, and PDIA1/P4HB is indicated. **Figure A3.5D** shows images of Western blot overlays probing for individual PDI targets.

C. Table showing chemical structures of PDI inhibitors **16F16**, **Rb-11-ca**, and **KSC-34** and their target selectivity for PDI isoforms.

D. Graph quantifying DENV NS3 protein levels in Huh7 cells in response to treatment with small molecule PDI inhibitors. Huh7 cells were treated with **147** or PDI inhibitors 16 hours prior to DENV infection (MOI 3) and NS3 protein levels were quantified by Western blot 24 hpi. Only **147** and **Rb-11-ca** treatment lead to a significant reduction in viral protein. Error bars show SEM and p-values from unpaired t-tests are shown. Representative western blots shown in **Figure A3.5J**.
E. Graph showing DENV viral titers in Huh7 cells treated with **147** or PDI inhibitors. Cells were treated with the corresponding molecules for 16 hours prior to DENV infection (MOI 3). Viral ffu were quantified 24 hpi by focus forming assay. Only **147** treatment reduces viral titers. Error bars show SEM and p-values from ratio paired t-tests are shown.

3.5E). Reduction in viral protein levels with **Rb-11-ca** could be attributed to compound toxicity, as we observed a 40% reduction in cell proliferation (**Figure A3.5I**). These results indicate that targeting of individual PDIs is not solely responsible for the reduced viral titers by **147** and that these existing PDI inhibitors are not effective at inhibiting DENV replication.

To identify additional mechanisms that could contribute to the **147**-mediated reduction in DENV viral propagation, we turned to untargeted quantitative proteomics of the affinity-enriched samples to identify additional protein targets. We used tandem mass tags for relative quantification of proteins in the **147-20** enriched samples relative to the competition samples (**147-20** treated with 3-fold excess **147**) (**Figure 3.6A**). This analysis confirmed that PDIs were the most highly enriched proteins that were covalently targeted by **147-20** (**Figure 3.6B, Figure A3.6A**). While labeling of PDIA4, PDIA6, and PDIA1 was confirmed above, we identified additional targeted PDIs (TXNDC5, PDIA3, TMX1) and two other highly enriched protein targets (GSTO1 and ALDH1A1). We compared these targets to previous datasets of **147-20** targets in HEK293T, HepG2, and ALMC-2 plasma cells (**Figure 3.6C, Figure A3.6B**)[48]. The additional proteins were targets specific to Huh7 cells and were not observed in other cell types, suggesting that they could have a unique role in the reduction in virus propagation in the Huh7 cells. To determine if targeting of any of these novel proteins could be responsible for the effects of **147**, we similarly created stable knockdown cell lines of *GSTO1, ALDH1A1, TXNDC5 and TMX1* using lentiviral delivery of shRNA. We validated knockdown by Western Blot (**Figure A3.6C**) and subsequently repeated

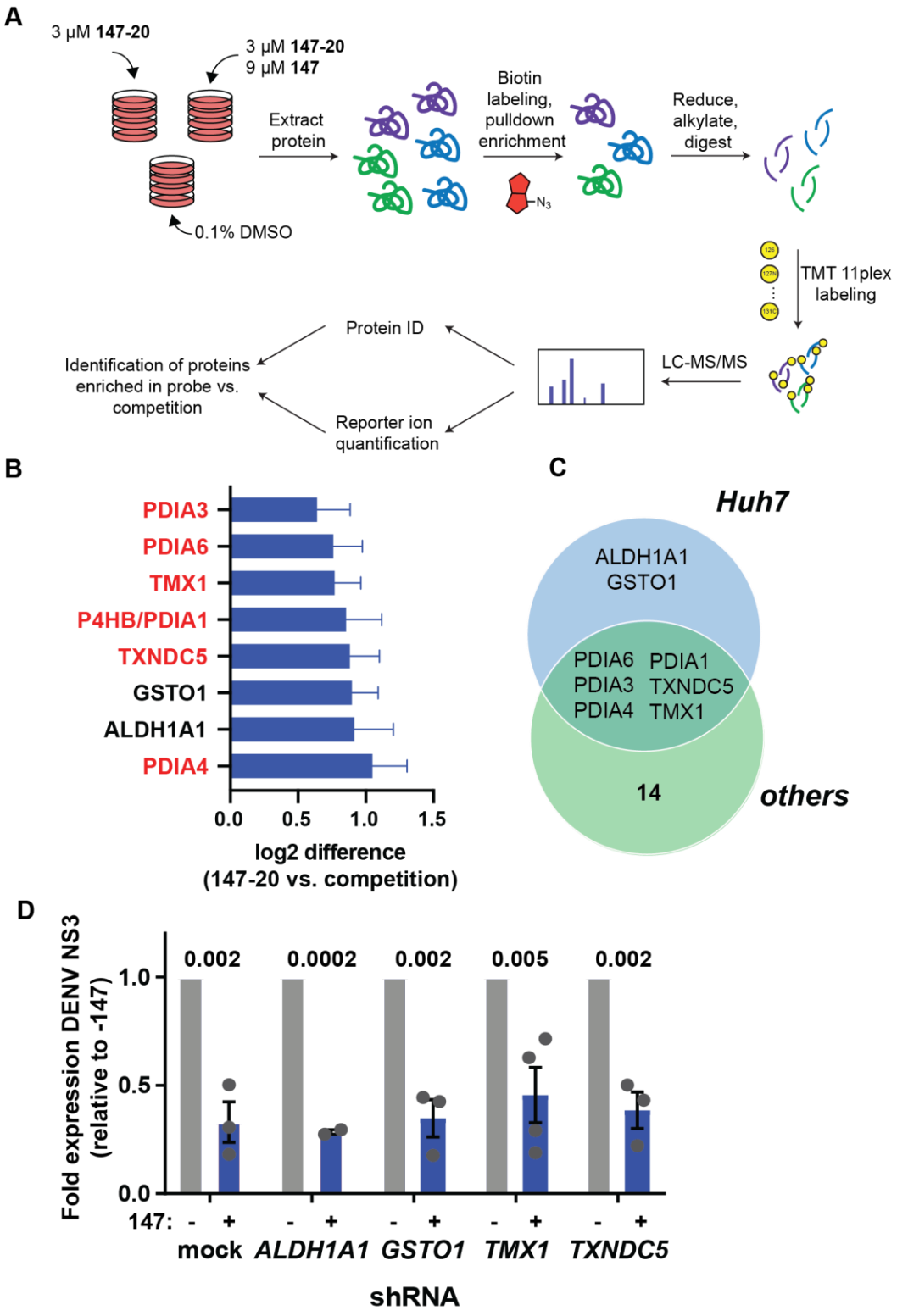

Figure 3.6. **Identification of covalent protein targets of 147 in Huh7 cells.**

A. Illustration of the workflow for the chemoproteomic target identification. Huh7 cells were treated with 3μM **147-20** alone or in competition with 9μM **147** for 18 hours. Cell lysates were labeled with a TAMRA-desthiobiotin probe, labeled proteins were isolated on

streptavidin beads, eluted and digested with trypsin. Individual samples were then labeled with tandem mass tags, pooled and subjected to LC-MS/MS for identification of proteins and quantitative comparison of proteins in the **147-20** treated compared to the **147-20**/**147** competition.

B. Graph showing the most highly enriched proteins targets in the **147-20** treated samples compared to the competition with **147**. The full data is shown in **Figure A3.6A**. High-confidence targets were filtered that displayed a log2 enrichment ratio greater than two standard deviations of the distribution of enrichment ratios across four biological replicates.
C. Venn diagram showing the comparison of high-confidence protein targets of **147-20** in Huh7 cells and other cells lines (HEK293T, HepG2 and ALMC-2) identified in a prior study (Paxman et al, 2018). **Figure A3.6B** shows the overlapping targets with individual cell lines.
D. Bar graph showing reduction in DENV NS3 protein levels in response to **147** treatment in Huh7 knockdown cell cells *ALDH1A1*, *GSTO1*, *TNXDC5* and *TMX1*. Stable shRNA knockdown cell lines were generated by lentivirus transduced with a pool of 2-3 shRNAs for each target. Knockdown was validated by western blot (**Figure A3.6C**). Representative western blot is shown in **Figure A3.6E**.

the infection experiments to determine if knockdown of any single protein attenuated viral replication. No individual knockdown of these protein was sufficient to attenuate the **147**-mediated reduction in DENV virus proteins (**Figure 3.6D**). Furthermore, all knockdowns produced similar DENV titers (**Figure A3.6D**) as the mock transduced control. All cell lines retained sensitivity to **147** treatment to reduce viral propagation. Overall, these results showed that the **147**-mediated DENV inhibition is unlikely to be mediated by a single protein target.

3.2.4 Compound 147 is effective against other DENV strains and Zika virus

Studies until this point were carried out with Dengue serotype 2 BID-V533 (isolated in 2005 in Nicaragua) in Huh7 cells. To determine the scope of **147** antiviral activity, we tested the effect against DENV2 propagation in HepG2 cells, another liver carcinoma cell line commonly used as an infection model. Prior data also showed that **147** treatment is non-toxic in HepG2 cells and can reduce amyloidogenic protein secretion[46]. When testing the impact on DENV titers in HepG2 cells, **147** treatment resulted in a significant reduction in DENV propagation 48 hpi (**Figure 3.7A**). A similar decrease in protein levels was also detected (**Figure A3.7A**). Next, we proceeded to test whether the compound could be more broadly effective against other DENV strains. We tested

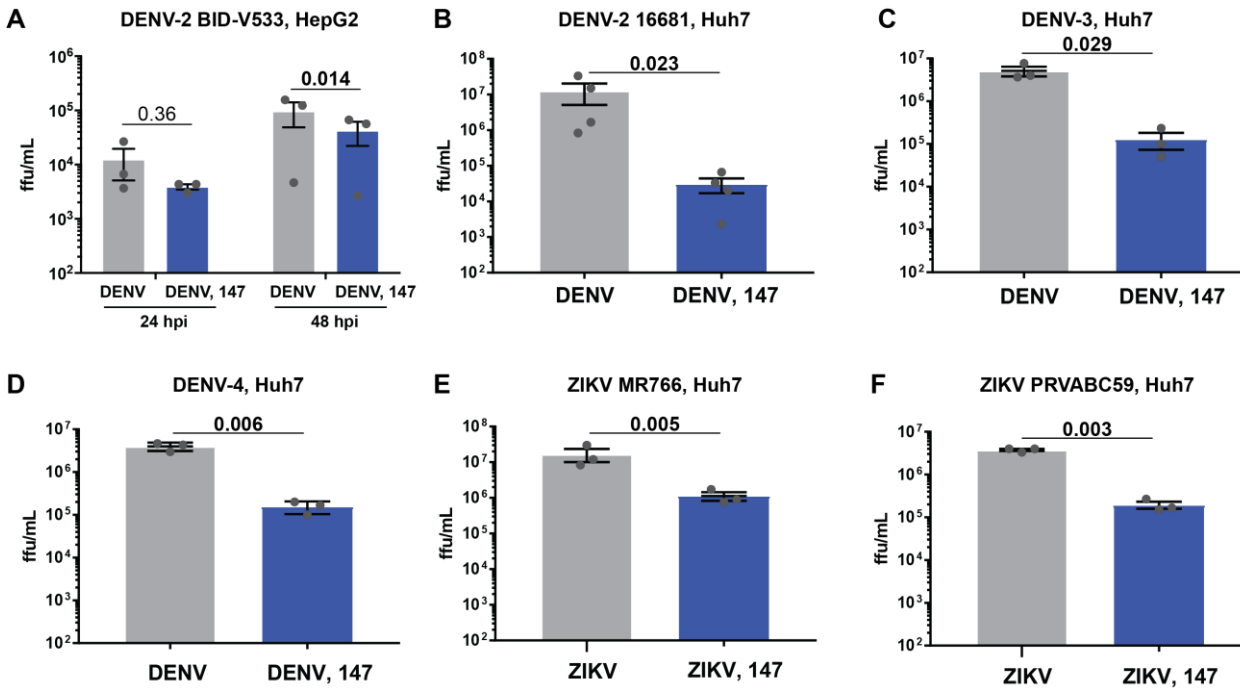

Figure 3.7. Compound 147 can reduce infection of multiple DENV strains, serotypes, as well as Zika virus.

A. Reduction of DENV2 infection in response to **147** in HepG2 liver carcinoma cells. HepG2 cells were pretreated with **147** (10μM) for 16 hours prior to infection with DENV-2 BID-V533 (MOI 3). Viral titers were determined 24 and 48 hpi by focus forming assays.

B. Graph showing reduction in infection with DENV serotype 2 strain 16681 (isolated in Thailand in 1984) in response to treatment with compound **147**. Prior studies were carried out with DENV-2 BID-V533 (Nicaragua). Huh7 cells were pretreated with compound **147** (10μM) 16 hrs prior to DENV infection (MOI 3) and viral titers were determined 24 hpi.

C.–D. Treatment with **147** reduces infection of DENV serotype 3 and 4. Huh7 were pretreated with **147** (10μM) for 16 hours prior to infection with DENV-3 Philippines/H87/1956 (**C**) or DENV-4 H241 (**D**) (MOI 3). Viral titers were determined 24 hpi by focus forming assays.

E.–F. Compound **147** is similarly active at reducing infection of Zika virus. Huh7 cells were pretreated with **147** (10μM) for 16 hours prior to infection with ZIKV strain MR766 (**E**) or ZIKV strain PRVABC59 (**F**). Viral titers were determined 24 hours hpi by focus forming assay. All error bars show SEM from 3 biological replicates and p-values from ratio paired t-tests are shown.

147 against a different DENV2 strain (16681, isolated in 1984 in Thailand) as well as against strains from DENV serotypes 3 and 4[62]. Treatment with compound **147** was able to reduce viral titers consistently greater than 95% (**Figure 3.7B–D**) and protein levels were similarly reduced

(**Figure A3.7B**). Finally, we sought to test whether compound **147** could be useful to treat other flaviviruses. We measured the effect against two different strains of Zika virus; MR766 (isolated from Eastern Africa in the 1950s), and PRVABC59 (isolated from Puerto Rico in 2015)[63,64]. The molecule displayed similar activity at reducing ZIKV titers and protein levels for both strains (**Figure 3.7E-F, Figure A3.7C-D**). Similar to earlier effects with DENV2 strain BID-V533, a small reduction in cell proliferation was seen with 10 µM **147** treatment during virus infection (**Figure A3.7E**). To validate the observed antiviral effects were independent of the viability reduction, we repeated the experiments at 1 µM **147**, the approximate IC50 observed in **Figure A3.2B**. At this concentration, we observed cell proliferation above 90% with **147** treatment in the context of infection with each virus. As expected, the lower 1 µM dose of **147** resulted in a muted antiviral effect, but ZIKV MR766 still showed significant inhibition on treatment with **147 (Figure A3.7F-J)**. These results provide evidence that compound **147** is broadly active against multiple flaviviruses in multiple cell lines, thus facilitating its potential application as an extensive host-centered antiviral agent.

3.3 Discussion

The continued health burden from arbovirus infections, such as dengue and Zika, combined with the lack of effective vaccines and therapeutics against these viruses, highlights a need for the development of new antiviral strategies. Therapeutic methods which target host factors required for viral propagation provide a path unlikely to elicit drug resistance and may act broadly across several virus species[17,18,20]. However, a challenge remains to target host factors that selectively impair viral replication without causing toxicity to the host cell and infected organism. Prior studies with **147** have already indicated that the compound has broad potential to safely ameliorate proteostasis imbalances that are associated a variety of disease conditions[43,46]. The compound is effective at reducing the secretion and aggregation of amyloidogenic proteins, such as immunoglobulin light chains and transthyretin[46]. In addition, selective remodeling of ER

proteostasis pathways through an ATF6-dependent mechanism by **147** was shown to prevent oxidative organ damage in mouse models of ischemia/reperfusion[43]. The same study also showed that **147** could be safely administered to mice through IV injections and was able to activate ER proteostasis pathways in multiple tissues, including liver, kidney and heart[43]. Here, we expand the therapeutic utility of compound **147** by establishing that the small molecule serves as a promising strategy to target multiple flaviviruses without causing significant toxicity in the host cell.

Treatment with the small molecule proteostasis regulator **147** had the most profound effect on viral titer levels, indicating that the compound was most active at preventing the assembly and secretion of mature infectious virions. This is consistent with the compound targeting critical proteostasis processes that could be required for production of infectious virions and are thus, crucial to the viral life cycle[32,33]. To support this mechanism, we found little to no reduction in extracellular virus structural protein levels, in contrast to intracellular protein levels which were reduced by up to 80% and extracellular viral titers which were reduced by ~95%. A possible explanation for this observation is that while similar numbers of virions are being secreted from the cell, these virions possess some structural defect that leave them unable to infect cells. **147** had mild cytostatic effects in Huh7 cells at the higher doses, but other antiviral effects persisted at lower doses where cell proliferation was not impacted. Importantly, prior studies showed that **147** is generally non-toxic in multiple cell lines and well tolerated in mice[43,46].

While **147** was designed as a preferential activator of the ATF6 branch of the UPR, we found that ATF6 activation did not mediate the antiviral effect. The ATF6 inhibitor **Cp-A7** on its own also did not reduce virus infection, which is consistent with prior knockout of ATF6 not affecting DENV propagation[39]. These results prompted us to examine alternative mechanisms for the antiviral effects by investigating the specific protein targets of **147**. Prior work showed that **147** is a prodrug that is metabolically oxidized to an iminoquinone or quinone methide, which covalently targets nucleophilic cysteine residues on cellular protein[46,48,58]. We showed that the metabolic activation mechanism and covalent targeting of reactive thiols is similarly required to reduce virus infection.

Furthermore, chemoproteomic target identification in Huh7 cells identified a similar set of PDIs, including PDIA1, PDIA4, and PDIA6, as **147** targets in this cell line. However, knockdown of individual PDIs was not sufficient to reduce viral titers suggesting that these individual PDIs are not responsible for the inhibition of viral infection.

We addressed whether inhibition of multiple PDIs could be required by testing the effect of existing PDI inhibitors that display varying selectivity towards PDIA1/P4HB and additional PDIs also modified by **147**. None of the PDI inhibitor compounds significantly reduced DENV viral titers, suggesting that **147** elicits its antiviral activity through an alternative mechanism of action. Importantly, one of the compounds, **Rb-11-ca,** exhibited considerably more toxicity in Huh7 cells, even at the highest concentration that we tested for **147**. Toxicity has also been observed for other PDI inhibitors[65]. This further highlights the unique properties of compound **147.** The low toxicity could be explained by previous observations showing that less than 25% of the PDIA4 pool is labeled by the compound, indicating that PDIs are not globally inhibited by the molecule[48]. Furthermore, endogenous protein secretion and formation of disulfide bonds in secreted proteins, including fully assembled immunoglobulins, are not affected by **147** [46]. This lack of perturbation to normal proteostasis processes and selective inhibition of viral propagation makes **147** an ideal candidate for a host-centered antiviral strategy.

To address whether alternative protein targets besides the most prominent PDIs could be responsible for reduction in virus propagation, we compared our identified targets in Huh7 cells to the prior list of covalently modified proteins in other cell lines[48]. In addition to the PDIs studied above, additional members of the PDI family were identified (TXNDC5, TMX1), as well as two unique proteins that were identified only in Huh7 cells: ALDH1A1 and GSTO1. However, knockdown of these proteins was also insufficient to recapitulate the reduction in viral replication induced by **147**. These studies highlight the unique polypharmacology needed for **147**'s antiviral effects which likely requires a combinations of protein targets.

The recent COVID-19 pandemic has refocused attention to the need for broad-spectrum antiviral agents that could inhibit future virus threats[13]. Targeting essential host pathways that are commonly hijacked by virus infection without causing significant host toxicity is recognized as one important strategy to combat future infection with unknown pathogens. We determined that compound **147** has broad antiviral activity against multiple DENV strains and serotypes and that the compound is also effective against multiple ZIKV strains. These results highlight broad utility of the proteostasis regulator compound to reduce flavivirus infection by targeting conserved host cell processes that are commonly exploited by the virus. Our results here now provide an entirely new therapeutic application of **147** as a broad antiviral agent to reduce flavivirus infections.

3.4 Materials and Methods

Chemicals and Resources

All compounds except 2-mercaptoethanol (BME) were kept as 1000x stocks in DMSO (0.1% final concentration DMSO for cellular treatments). BME was directly diluted from a 55 mM DPBS stock. **147**, **147-4**, **147-20**, and **16F16** were used at 10 µM unless otherwise noted. **Rb-11-ca** was used at 20 µM. **KSC-34** was used at 5 µM. **Ceapin-A7** was used at 6 µM. Thapsigargin was used at 0.5 µg/mL. All other resources are listed in **Table S1**.

Cell culture and virus infections

Cells were maintained in Dulbecco's Modified Eagle's Medium (DMEM) with high glucose and supplemented with 10% fetal bovine serum (FBS), 1% penicillin/streptomycin, and 1% glutamine. All cell lines except C6/36 were kept at 37ºC, 5% CO_2. C6/36 cells were kept at 28ºC, 5% CO_2. For experimental infections of cell lines, media was removed from cells and virus was added at MOI 3 (DENV) for 3 hours or MOI 0.5 for 1 hour (ZIKV) (unless otherwise noted). Inoculum was removed, cells were washed, and media containing chemical compounds or DMSO was added for the remainder of the experiment. Huh7 and HepG2 cells were obtained from ATCC. Vero and

C6/36 cells were a kind gift from Dr. Tom Voss of the virology core at the Vanderbilt Vaccine Center. Cells were tested monthly for mycoplasma contamination.

Viral Focus Forming Assay

Confluent Vero cells in 96 well plates were inoculated with 10-fold serial dilutions of DENV or ZIKV in BA-1 diluent (1xM199 media, 5% BSA, 1x L-glutamine, 1x penicillin/streptomycin, 0.04% sodium bicarbonate, 50 mM Tris) for 2 hours. The cells were overlaid with a 1:1 mixture of 2x nutrient overlay (2x Earle's Balanced Salt Solution, 2x Ye-Lah Medium, 4% FBS, 0.4% sodium bicarbonate, 0.1 mg/mL gentamycin, 0.5 mg/mL amphotericin B) + 2.4% methylcellulose in water. After 2 days (ZIKV, DENV3, DENV4) or 3 days (DENV2), overlay was removed, and cells were fixed in ice cold 85% acetone for 30 minutes. Infectious foci were stained with a primary pan-flavivirus 4G2 antibody (1:1000 in 5% BSA, TBST) and secondary HRP antibody (1:1000 in 5% milk, TBST), then visualized using 400 µL 8 mg/mL 3-amino-9-ethylcarbazole (Sigma) in 10 mL 50 mM sodium acetate (Fisher) + 4 µL 30% H_2O_2 (Fisher) and exposed for 15-45 minutes until foci were visible.

Viruses

DENV: DENV2 strain BID-V533 was a generous gift from Dr. Tom Voss of the Vanderbilt Vaccine Center. Strain 16681 was generated from a cDNA clone in pD2/ic-30p NBX that was a generous gift from Dr. Claire Huang at the Center for Disease Control. DENV-3 and DENV-4 strains were obtained from BEI Resources. For passaging, C6/36 or Vero cells were infected at MOI 0.1. Six days (C6/36) or three days (Vero) post-infection, culture supernatant was harvested and cell debris was pelleted at 3700xg for 10 minutes. Cleared supernatant was combined with 23% FBS and mixture was frozen as 1 mL aliquots at -80ºC.

For experimental infections of cell lines, media was removed from cells and virus was added at MOI 3 for 3 hours (unless otherwise noted). Inoculum was removed, cells were washed, and media containing compounds or DMSO was added for the remainder of the experiment. Strain 16681 was generated from a cDNA clone[62]. Plasmid DNA was transformed into DH5α cells and

purified by miniprep (Zymo Research). DNA was ethanol/sodium acetate precipitated for purification and concentration. Plasmid DNA was digested using XbaI (NEB) to cut upstream of the T7 promoter. A MEGAScript T7 in vitro transcription kit (Invitrogen) was used to obtain viral RNA, which was then transfected into Huh7 cells using the TransIT mRNA transfection reagent (Mirus). Virus stocks were amplified as indicated above.

ZIKV: Strains MR766 and PRVABC59 were obtained from ATCC. For passaging, Vero cells were infected at MOI 0.05. Three days post-infection, culture supernatant was harvested and cell debris was pelleted at 3700xg for 10 minutes. Cleared supernatant was used as virus stock and stored at -80ºC. For experimental infections of cell lines, media was removed from cells and virus was added at MOI 0.5 for 1 hour. Inoculum was removed, cells were washed, and media containing compounds or DMSO was added for the remainder of the experiment.

Lentivirus: The 3rd generation system was used for production. Respective shRNA plasmids were transfected into HEK293T cells together with lentivirus packaging plasmids RRG, VSVG, and Rev using the calcium phosphate method as described[48]. Media was changed 20 hours post-transfection. Supernatants were collected 3 days post transfection, and cleared at 3700xg for 10 minutes. To generate respective shRNA stable knockdown cell lines in Huh7 cells, lentiviruses prepared with pools of 2-3 shRNAs per target were added to Huh7 cells and media containing 4 µg/mL final concentration polybrene. Selection proceeded for 1 week under puromycin (5 µg/mL). Successful knockdown was confirmed by Western Blot.

SDS-PAGE Gels and Immunoblotting

Cell pellets were lysed in RIPA buffer (50 mM Tris pH 7.5, 150 mM NaCl, 0.1% SDS, 1% Triton-X-100, 0.5% sodium deoxycholate) + Roche cOmplete protease inhibitor. Cells were left on ice for at least 10 minutes and lysate was cleared at 17,000xg for 10 minutes. Cleared lysate concentrations were normalized and gel samples were separated by SDS-PAGE. Gels were transferred to PVDF membranes using standard settings on the TransBlot Turbo (BioRad). Blots were blocked in 5% non-fat dry milk in Tris-buffered saline (TBST, 50mM Tris pH 7.4, 150mM

NaCl, 0.1 % Tween-20) for 30 minutes before applying antibodies. Primary antibodies (in 5% BSA, TBST) were applied at room temperature for 2 hours or at 4ºC overnight. Secondary antibodies (in 5% milk, TBST) were applied at room temperature for 30 minutes or at 4ºC for 1 hour. Primary antibodies were used at dilutions indicated in **Table A3.1**; all secondary antibodies were used at a 1:10,000 dilution.

Quantitative RT-PCR

RNA was prepared from cell pellets using the Zymo Quick-RNA miniprep kit. cDNA was synthesized from 500 ng total cellular RNA using random primers (IDT), oligo-dT primers (IDT), and Promega M-MLV reverse transcriptase. qPCR analysis was performed using Bio-Rad iTaq Universal SYBR Green Supermix combined with primers for genes of interest (listed below) and reaction were run in 96-well plates on a Bio-Rad CFX qPCR instrument. Conditions used for amplification were 95ºC, 2 minutes, 45 repeats of 95ºC, 10s and 60ºC, 30s. A melting curve was generated in 0.5ºC intervals from 65ºC to 95ºC. C_q values were calculated by the BioRad CFX Maestro software. Transcripts were normalized to a housekeeping gene (either RiboP or GAPDH), except in the case of extracellular viral RNA quantification. All measurements were performed in technical duplicate; each of these duplicates was treated as a single measurement for the final average, except extracellular viral RNA quantification where the values were pooled. Data was analyzed using the BioRad CFX Maestro software.

Cell Viability & Caspase Activity Assays

Cell viability was determined using the CellTiter-Glo reagent (Promega). Huh7 cells were seeded into 96 well plates and treated with 100x dilutions of compounds in culture media. 16 hours after treatment, media was removed and cells were infected as described above (for -DENV samples, no virus was added). Media was replaced 24 hours after infection and 100 µL Cell Titer Glo reagent was added and luminescence was measured for each well on a Synergy HT plate reader. To assess the level of caspase 3/7 activation in Huh7 cells upon **147** treatment, we used the EnzCheck Caspase-3 Assay Kit #2 (ThermoFisher, E-13184). In brief, Huh7 cells were treated

with DMSO or 1, 3, or 10 µM **147** for 14-16 hours pre-infection. Cells were then either mock or DENV2 infected (MOI 3) and retreated with DMSO or **147** for an additional 24 hpi. Treatment with 1 µM staurosporin for 12 hours pre-harvest was used as a positive control for caspase activation. Cells were harvested and lysed per kit instructions on ice for 30 min. Cell lysates were then treated with DMSO or 20 µM Ac-DEVD-CHO inhibitor for 10 min at room temperature before addition of 25 µM Z-DEVD-R110 substrate solution. Samples were incubated at room temperature for 20 h and measured for fluorescence (excitation/emission 496/520 nm). Caspase activation was calculated by taking the difference in fluorescence between Ac-DEVD-CHO inhibitor and DMSO treated paired lysates and normalized to DMSO, mock infected samples. For all samples, n = 6, except 1 µM 147, mock or DENV2 infected (n = 3).

Enrichment of Covalent Protein Targets

Huh7 cells were treated with 3 µM **147-20** or a combination of 3 µM **147-20** and 9 µM **147**. Cells were harvested 16-18 hours post-treatment and lysed as described above. Click chemistry using 100 µM Cy5 azide or TAMRA desthiobiotin azide was performed with 1.6 mM BTTAA, 0.8 mM copper sulfate, and 5 mM sodium ascorbate for 1 hour at 37ºC, shaking at 500 rpm. All reagents were purchased from Click Chemistry Tools. For detection, samples from Cy5 reactions were run directly on SDS-PAGE gels for analysis. For enrichment of proteins, excess reagents were removed via methanol/chloroform precipitation; protein was washed twice with methanol before resuspension in 6 M urea. Samples were diluted in PBS and added to pre-washed (in PBS) streptavidin agarose beads (Thermo Scientific). Pulldowns were rotated for 1 hour at room temperature. Supernatant was removed and beads were washed six times in PBS and 1% SDS. Samples were eluted two times by incubation with 50 mM biotin, pH 7.2, in 1% SDS (PBS) for 10 minutes.

Mass Spectrometry Sample Preparation

Protein lysate from DENV infected and non-infected Huh7 cells (for whole cell lysate samples, 10 µg of protein as measured using Bio-Rad protein assay dye reagent) was aliquoted and purified

using methanol/chloroform precipitation. Streptavidin-enriched samples for target identification were used without normalization and purified by methanol/chloroform precipitation. Mass spectrometry samples were prepared as described previously[43]. Briefly, protein was resuspended in 3 µL 1% Rapigest (Waters) and diluted with water and 0.5 M HEPES. Proteins were reduced with 5 mM TCEP (Thermo Scientific) and subsequently alkylated with 10 mM iodoacetamide (Sigma). Proteins were digested in sequencing-grade trypsin (Thermo Scientific) overnight at 37ºC while shaking at 750 rpm. Peptides were labeled for 1 hour at room temperature using 11-plex tandem mass tag (TMT) reagents (Thermo Scientific) resuspended in 40% acetonitrile. Labeling reactions were quenched with 0.4% ammonium bicarbonate for 1 hour at room temperature. Samples were combined and acidified to pH 2 by addition of 5% formic acid. Pooled samples were concentrated using a SpeedVac and resuspended in 94.9% water/5% acetonitrile/0.1% formic acid. Rapigest cleavage products were pelleted by centrifugation at 14,000xg for 30 minutes.

Mass Spectrometry Data Acquisition

Digested peptides (up to 20 µg) were loaded onto a triphasic column filled sequentially with 1.5 or 2.5 cm layers of 5 µm 100 Å C18 resin (Phenomenex), Luna 5 µm 100 Å strong cation exchange resin (Phenomenex) and a second layer of C18 resin using a high pressure chamber[66]. The column was washed for 30 minutes in 95% water/5% acetonitrile/0.1% formic acid (buffer A) and attached to an Ultimate 3000 nano LC system connected to a 20 cm, 100 µm ID fused-silica microcapillary column with a laser-pulled tip filled with 3 µm 100 Å C18 resin (Phenomenex). Mass spectrometry was carried out on a Q-Exactive HF or an Exploris 480 instrument (ThermoFisher). For whole cell lysate samples, multidimensional peptide identification technology (MuDPIT) analysis was performed with 10 µL sequential injections of 0-100% buffer C (500 mM ammonium acetate, diluted in buffer A), each injection increasing by 10%, followed by an injection of 90% buffer C/10% buffer B (100% acetonitrile/1% formic acid). For target ID samples, only the 0, 10, 20, 40, 60, 80, 100 and 90%C/10%B injections were carried out. Peptides were separated on a

90 min gradient from 5%-40% buffer B at a flow rate of 500nL/min, followed by a 5 min ramp to 60-80% buffer B. Electrospray ionization was performed from the tip of the microcapillary column at a voltage of 2.2 kV with an ion transfer tube temperature of 275º C. Data-dependent mass spectra were collected by performing a full scan from 300 – 1800 m/z (Q-Exactive HF) or 375 – 1500 (Exploris 480) at a resolution of 120,000 and AGC target of 1e6. Tandem mass spectrometry was performed using TopN (15 cycles, Q-Exactive) or TopSpeed (3 sec, Exploris 480) from each full scan using HCD collision energy of NCE 38 (Q-Exactive HF) or NCE 36 (Exploris 480), isolation window of 0.7 (Q-Exactive HF) or 0.4 (Exploris 480), with automatic maximum injection time, a resolution of 45,000 (Q-Exactive HF) or 30,000 + TurboTMT setting (Exploris 480), fixed first mass of 110 m/z, and dynamic exclusion of 10s (Q-Exactive HF) or 45s (Exploris 480).

Mass Spectrometry Data Analysis

Peptide and protein identification, and TMT reporter ion quantification was analyzed using Proteome Discover 2.4. Searches were carried out with the SEQUEST node using a human proteome database (UniProt) with DENV proteins added manually and the following parameters: 20ppm precursor mass tolerance, minimum peptide length of 6 amino acids, trypsin cleavage with a maximum of 2 missed cleavages, static modifications of +57.0215Da (carbamidomethylation at C) and +229.1629 (TMT6/11plex), and dynamic modification of +15.995 (oxidation at M), N-terminal methionine loss (-131.040), and N-terminal acetylation (+42.011). Search results were filtered with Percolator using a decoy database of reversed sequences with a peptide false discovery rate of 1% and a minimum of 2 peptides for protein identification. TMT intensities were quantified using the reporter ion quantification node with TMT intensities from each channel being normalized using the total peptide amount, quantitative value correction enabled to correct for TMT impurities, and co-isolation threshold set to 25%. Intensities for each protein were calculated by summing the intensities of each peptide. A reference TMT channel of pooled samples was included for scaling of protein abundances across multiple mass spectrometry runs. For Target ID samples, Proteome Discoverer searches were identical to the whole cell lysate searches,

except the normalization of TMT intensities was omitted in the reporter ion quantification node. Log2 transformations were performed on all TMT reporter ion intensities, and averages were determined for four **147-20** replicates and the four **147-20/147** competition replicates. Fold enrichment was determined as the log2 fold difference of the two averages. The log2 fold enrichment was fitted to a gaussian distribution and targets were defined as proteins with log2 fold difference greater than two standard deviations.

Purification and Concentration of Virus Media

Virus was purified using a modified version of a previously published protocol[67]. In brief, virus-containing media (9 mL) was layered on top of 3 mL of sterile-filtered 20% w/v sucrose and spun at 167,000 x g (Sorvall Surespin 630) for 3 hours at 4ºC to pellet virus. Media supernatant and sucrose were carefully removed and virus pellet was briefly air-dried for 10 minutes before resuspension in 100 µL ice-cold 5 mM HEPES, pH 7.9

Data availability

All data is either included in the dissertation or associated paper or is available upon request.

3.5 References

(1) Bhatt, S.; Gething, P. W.; Brady, O. J.; Messina, J. P.; Farlow, A. W.; Moyes, C. L.; Drake, J. M.; Brownstein, J. S.; Hoen, A. G.; Sankoh, O.; Myers, M. F.; George, D. B.; Jaenisch, T.; Wint, G. R. W.; Simmons, C. P.; Scott, T. W.; Farrar, J. J.; Hay, S. I. The Global Distribution and Burden of Dengue. *Nature* **2013**, *496* (7446), 504–507. https://doi.org/10.1038/nature12060.

(2) Daep, C. A.; Munoz-Jordan, J. L.; Eugenin, E. A. Flaviviruses, an Expanding Threat in Public Health: Focus on Dengue, West Nile, and Japanese Encephalitis Virus. *J Neurovirol* **2014**, *20* (6), 539–560. https://doi.org/10.1007/s13365-014-0285-z.

(3) Weaver, S. C.; Costa, F.; Garcia-Blanco, M. A.; Ko, A. I.; Ribeiro, G. S.; Saade, G.; Shi, P. Y.; Vasilakis, N. Zika Virus: History, Emergence, Biology, and Prospects for Control. *Antivir. Res* **2016**, *130*, 69–80. https://doi.org/10.1016/j.antiviral.2016.03.010.

(4) Tatem, A. J.; Huang, Z.; Das, A.; Qi, Q.; Roth, J.; Qiu, Y. Air Travel and Vector-Borne Disease Movement. *Parasitology* **2012**, *139* (14), 1816–1830. https://doi.org/10.1017/S0031182012000352.

(5) Whitehorn, J.; Yacoub, S. Global Warming and Arboviral Infections. *Clin. Med. (Northfield. Il).* **2019**, *19* (2), 149–152.

(6) Messina, J. P.; Brady, O. J.; Golding, N.; Kraemer, M. U. G.; Wint, G. R. W.; Ray, S. E.; Pigott, D. M.; Shearer, F. M.; Johnson, K.; Earl, L.; Marczak, L. B.; Shirude, S.; Davis Weaver, N.; Gilbert, M.; Velayudhan, R.; Jones, P.; Jaenisch, T.; Scott, T. W.; Reiner Jr., R. C.; Hay, S. I. The Current and Future Global Distribution and Population at Risk of Dengue. *Nat Microbiol* **2019**, *4* (9), 1508–1515. https://doi.org/10.1038/s41564-019-0476-8.

(7) Mendez, N.; Oviedo-Pastrana, M.; Mattar, S.; Caicedo-Castro, I.; Arrieta, G. Zika Virus Disease, Microcephaly and Guillain-Barre Syndrome in Colombia: Epidemiological Situation during 21 Months of the Zika Virus Outbreak, 2015-2017. *Arch Public Heal.* **2017**, *75*, 65. https://doi.org/10.1186/s13690-017-0233-5.

(8) Collins, M. H.; Metz, S. W. Progress and Works in Progress: Update on Flavivirus Vaccine Development. *Clin Ther* **2017**, *39* (8), 1519–1536. https://doi.org/10.1016/j.clinthera.2017.07.001.

(9) Thomas, S. J.; Yoon, I. K. A Review of Dengvaxia: Development to Deployment. *Hum Vaccin Immunother* **2019**, *15* (10), 2295–2314. https://doi.org/10.1080/21645515.2019.1658503.

(10) Bernatchez, J. A.; Tran, L. T.; Li, J.; Luan, Y.; Siqueira-Neto, J. L.; Li, R. Drugs for the Treatment of Zika Virus Infection. *J Med Chem* **2020**, *63* (2), 470–489. https://doi.org/10.1021/acs.jmedchem.9b00775.

(11) Lim, S. P. Dengue Drug Discovery: Progress, Challenges, and Outlook. *Antivir. Res* **2019**, *163*, 156–178.

(12) Lim, S. P.; Wang, Q. Y.; Noble, C. G.; Chen, Y. L.; Dong B., H. Z.; Yokokawa, F.; Nilar, S.; Smith, P.; Beer, D.; Lescar, J.; Shi, P. Y. Ten Years of Dengue Drug Discovery: Progress and Prospects. *Antivir. Res* **2013**, *100* (2), 500–519.

(13) Carrasco-Hernandez, R.; Jacome, R.; Lopez Vidal, Y.; Ponce de Leon, S. Are RNA Viruses Candidate Agents for the Next Global Pandemic? A Review. *ILAR J* **2017**, *58* (3), 343–358. https://doi.org/10.1093/ilar/ilx026.

(14) Garcia, L. L.; Padilla, L.; Castano, J. C. Inhibitors Compounds of the Flavivirus Replication Process. *Virol J* **2017**, *14* (1), 95. https://doi.org/10.1186/s12985-017-0761-1.

(15) Kaufmann, S. H. E.; Dorhoi, A.; Hotchkiss, R. S.; Bartenschlager, R. Host-Directed Therapies for Bacterial and Viral Infections. *Nat Rev Drug Discov* **2018**, *17* (1), 35–56. https://doi.org/10.1038/nrd.2017.162.

(16) De Clercq, E. Three Decades of Antiviral Drugs. *Nat. Rev. Drug Discov.* **2007**, *6*, 941.

(17) Geller, R.; Andino, R.; Frydman, J. Hsp90 Inhibitors Exhibit Resistance-Free Antiviral Activity against Respiratory Syncytial Virus. *PLoS One* **2013**, *8* (2), e56762. https://doi.org/10.1371/journal.pone.0056762.

(18) Geller, R.; Vignuzzi, M.; Andino, R.; Frydman, J. Evolutionary Constraints on Chaperone-Mediated Folding Provide an Antiviral Approach Refractory to Development of Drug Resistance. *Genes Dev* **2007**, *21* (2), 195–205. https://doi.org/10.1101/gad.1505307.

(19) Taguwa, S.; Maringer, K.; Li, X.; Bernal-Rubio, D.; Rauch, J. N.; Gestwicki, J. E.; Andino, R.; Fernandez-Sesma, A.; Frydman, J. Defining Hsp70 Subnetworks in Dengue Virus Replication Reveals Key Vulnerability in Flavivirus Infection. *Cell* **2015**, *163* (5), 1108–1123. https://doi.org/10.1016/j.cell.2015.10.046.

(20) Aviner, R.; Frydman, J. Proteostasis in Viral Infection: Unfolding the Complex Virus–Chaperone Interplay. *Cold Spring Harb. Perspect. Biol.* **2020**, *12* (3), a034090. https://doi.org/10.1101/cshperspect.a034090.

(21) Taguwa, S.; Yeh, M. T.; Rainbolt, T. K.; Nayak, A.; Shao, H.; Gestwicki, J. E.; Andino, R.; Frydman, J. Zika Virus Dependence on Host Hsp70 Provides a Protective Strategy against Infection and Disease. *Cell Rep* **2019**, *26* (4), 906-920 e3. https://doi.org/10.1016/j.celrep.2018.12.095.

(22) Apte-Sengupta, S.; Sirohi, D.; Kuhn, R. J. Coupling of Replication and Assembly in Flaviviruses. *Curr. Opin. Virol.* **2014**, *9*, 134–142. https://doi.org/10.1016/j.coviro.2014.09.020.

(23) Perera, R.; Kuhn, R. J. Structural Proteomics of Dengue Virus. *Curr. Opin. Microbiol.* **2008**, *11* (4), 369–377. https://doi.org/10.1016/j.mib.2008.06.004.

(24) Ravindran, M. S. Molecular Chaperones: From Proteostasis to Pathogenesis. *FEBS J* **2018**, *285* (18), 3353–3361. https://doi.org/10.1111/febs.14576.

(25) Phillips, A. M.; Gonzalez, L. O.; Nekongo, E. E.; Ponomarenko, A. I.; McHugh, S. M.; Butty, V. L.; Levine, S. S.; Lin, Y. S.; Mirny, L. A.; Shoulders, M. D. Host Proteostasis Modulates Influenza Evolution. *Elife* **2017**, *6*. https://doi.org/10.7554/eLife.28652.

(26) Reid, D. W.; Campos, R. K.; Child, J. R.; Zheng, T.; Chan, K. W. K.; Bradrick, S. S.; Vasudevan, S. G.; Garcia-Blanco, M. A.; Nicchitta, C. V. Dengue Virus Selectively Annexes Endoplasmic Reticulum-Associated Translation Machinery as a Strategy for Co-Opting Host Cell Protein Synthesis. *J Virol* **2018**, *92* (7). https://doi.org/10.1128/JVI.01766-17.

(27) Lin, D. L.; Inoue, T.; Chen, Y. J.; Chang, A.; Tsai, B.; Tai, A. W. The ER Membrane Protein Complex Promotes Biogenesis of Dengue and Zika Virus Non-Structural Multi-Pass Transmembrane Proteins to Support Infection. *Cell Rep.* **2019**, *27* (6), 1666-1674.e4. https://doi.org/10.1016/j.celrep.2019.04.051.

(28) Marceau, C. D.; Puschnik, A. S.; Majzoub, K.; Ooi, Y. S.; Brewer, S. M.; Fuchs, G.; Swaminathan, K.; Mata, M. A.; Elias, J. E.; Sarnow, P.; Carette, J. E. Genetic Dissection of Flaviviridae Host Factors through Genome-Scale CRISPR Screens. *Nature* **2016**, *535* (7610), 159–163. https://doi.org/10.1038/nature18631.

(29) Ngo, A. M.; Shurtleff, M. J.; Popova, K. D.; Kulsuptrakul, J.; Weissman, J. S.; Puschnik, A. S. The ER Membrane Protein Complex Is Required to Ensure Correct Topology and Stable Expression of Flavivirus Polyproteins. *Elife* **2019**, *8*. https://doi.org/10.7554/eLife.48469.

(30) Savidis, G.; McDougall, W. M.; Meraner, P.; Perreira, J. M.; Portmann, J. M.; Trincucci, G.; John, S. P.; Aker, A. M.; Renzette, N.; Robbins, D. R.; Guo, Z.; Green, S.; Kowalik, T. F.; Brass, A. L. Identification of Zika Virus and Dengue Virus Dependency Factors Using Functional Genomics. *Cell Rep.* **2016**, *16* (1), 232–246. https://doi.org/10.1016/j.celrep.2016.06.028.

(31) Rothan, H. A.; Kumar, M. Role of Endoplasmic Reticulum-Associated Proteins in Flavivirus Replication and Assembly Complexes. *Pathogens* **2019**, *8* (3). https://doi.org/10.3390/pathogens8030148.

(32) Fischl, W.; Bartenschlager, R. Exploitation of Cellular Pathways by Dengue Virus. *Curr*

Opin Microbiol **2011**, *14* (4), 470–475. https://doi.org/10.1016/j.mib.2011.07.012.

(33) Heaton, N. S.; Moshkina, N.; Fenouil, R.; Gardner, T. J.; Aguirre, S.; Shah, P. S.; Zhao, N.; Manganaro, L.; Hultquist, J. F.; Noel, J.; Sachs, D. H.; Hamilton, J.; Leon, P. E.; Chawdury, A.; Tripathi, S.; Melegari, C.; Campisi, L.; Hai, R.; Metreveli, G.; Gamarnik, A. V.; Garcia-Sastre, A.; Greenbaum, B.; Simon, V.; Fernandez-Sesma, A.; Krogan, N. J.; Mulder, L. C. F. F.; van Bakel, H.; Tortorella, D.; Taunton, J.; Palese, P.; Marazzi, I.; García-Sastre, A.; Greenbaum, B.; Simon, V.; Fernandez-Sesma, A.; Krogan, N. J.; Mulder, L. C. F. F.; van Bakel, H.; Tortorella, D.; Taunton, J.; Palese, P.; Marazzi, I. Targeting Viral Proteostasis Limits Influenza Virus, HIV, and Dengue Virus Infection. *Immunity* **2016**, *44* (1), 46–58. https://doi.org/10.1016/j.immuni.2015.12.017.

(34) Howe, M. K.; Speer, B. L.; Hughes, P. F.; Loiselle, D. R.; Vasudevan, S.; Haystead, T. A. An Inducible Heat Shock Protein 70 Small Molecule Inhibitor Demonstrates Anti-Dengue Virus Activity, Validating Hsp70 as a Host Antiviral Target. *Antivir. Res* **2016**, *130*, 81–92. https://doi.org/10.1016/j.antiviral.2016.03.017.

(35) Yang, J.; Xu, Y.; Yan, Y.; Li, W.; Zhao, L.; Dai, Q.; Li, Y.; Li, S.; Zhong, J.; Cao, R.; Zhong, W. Small Molecule Inhibitor of ATPase Activity of HSP70 as a Broad-Spectrum Inhibitor against Flavivirus Infections. *ACS Infect Dis* **2020**, *6* (5), 832–843. https://doi.org/10.1021/acsinfecdis.9b00376.

(36) Puschnik, A. S.; Marceau, C. D.; Ooi, Y. S.; Majzoub, K.; Rinis, N.; Contessa, J. N.; Carette, J. E. A Small-Molecule Oligosaccharyltransferase Inhibitor with Pan-Flaviviral Activity. *Cell Rep.* **2017**, *21* (11), 3032–3039. https://doi.org/10.1016/j.celrep.2017.11.054.

(37) Stohlman, S. A.; Wisseman, C. L.; Eylar, O. R.; Silverman, D. J. Dengue Virus-Induced Modifications of HOst Cell Membranes. *J. Virol.* **1975**, *16* (4), 1017–1026.

(38) Ravindran, M. S.; Bagchi, P.; Cunningham, C. N.; Tsai, B. Opportunistic Intruders: How Viruses Orchestrate ER Functions to Infect Cells. *Nat. Rev. Microbiol.* **2016**, *14* (7), 407–420. https://doi.org/10.1038/nrmicro.2016.60.

(39) Peña, J.; Harris, E. Dengue Virus Modulates the Unfolded Protein Response in a Time-Dependent Manner. *J. Biol. Chem.* **2011**, *286* (16), 14226–14236. https://doi.org/10.1074/jbc.M111.222703.

(40) Perera, N.; Miller, J. L.; Zitzmann, N. The Role of the Unfolded Protein Response in Dengue Virus Pathogenesis. *Cell Microbiol* **2017**, *19* (5). https://doi.org/10.1111/cmi.12734.

(41) Walter, P.; Ron, D. The Unfolded Protein Response: From Stress Pathway to Homeostatic Regulation. *Science (80-.).* **2011**, *334* (November), 1081–1086. https://doi.org/10.1152/physrev.00001.2011.

(42) Shoulders, M. D.; Ryno, L. M.; Genereux, J. C.; Moresco, J. J.; Tu, P. G.; Wu, C.; Yates, J. R.; Su, A. I.; Kelly, J. W.; Wiseman, R. L. Stress-Independent Activation of XBP1s and/or ATF6 Reveals Three Functionally Diverse ER Proteostasis Environments. *Cell Rep.* **2013**, *3* (4), 1279–1292. https://doi.org/10.1016/j.celrep.2013.03.024.

(43) Blackwood, E. A.; Azizi, K.; Thuerauf, D. J.; Paxman, R. J.; Plate, L.; Kelly, J. W.; Wiseman, R. L.; Glembotski, C. C. Pharmacologic ATF6 Activation Confers Global Protection in Widespread Disease Models by Reprograming Cellular Proteostasis. *Nat Commun* **2019**, *10* (1), 187. https://doi.org/10.1038/s41467-018-08129-2.

(44) Chen, J. J.; Genereux, J. C.; Qu, S.; Hulleman, J. D.; Shoulders, M. D.; Wiseman, R. L. ATF6 Activation Reduces the Secretion and Extracellular Aggregation of Destabilized Variants of an Amyloidogenic Protein. *Chem Biol* **2014**, *21* (11), 1564–1574. https://doi.org/10.1016/j.chembiol.2014.09.009.

(45) Cooley, C. B.; Ryno, L. M.; Plate, L.; Morgan, G. J.; Hulleman, J. D.; Kelly, J. W.; Wiseman, R. L. Unfolded Protein Response Activation Reduces Secretion and Extracellular Aggregation of Amyloidogenic Immunoglobulin Light Chain. *Proc Natl Acad Sci U S A* **2014**, *111* (36), 13046–13051. https://doi.org/10.1073/pnas.1406050111.

(46) Plate, L.; Cooley, C. B.; Chen, J. J.; Paxman, R. J.; Gallagher, C. M.; Madoux, F.; Genereux, J. C.; Dobbs, W.; Garza, D.; Spicer, T. P.; Scampavia, L.; Brown, S. J.; Rosen, H.; Powers, E. T.; Walter, P.; Hodder, P.; Wiseman, L.; Kelly, J. W.; Wiseman, R. L.; Kelly, J. W. Small Molecule Proteostasis Regulators That Reprogram the ER to Reduce Extracellular Protein Aggregation. *Elife* **2016**, *5* (2016JULY), 1–26. https://doi.org/10.7554/eLife.15550.

(47) Kroeger, H.; Grimsey, N.; Paxman, R.; Chiang, W. C.; Plate, L.; Jones, Y.; Shaw, P. X.; Trejo, J. A.; Tsang, S. H.; Powers, E.; Kelly, J. W.; Luke Wiseman, R.; Lin, J. H. The Unfolded Protein Response Regulator ATF6 Promotes Mesodermal Differentiation. *Sci. Signal.* **2018**, *11* (517). https://doi.org/10.1126/scisignal.aan5785.

(48) Paxman, R.; Plate, L.; Blackwood, E. A.; Glembotski, C.; Powers, E. T.; Wiseman, R. L.; Kelly, J. W. Pharmacologic ATF6 Activating Compounds Are Metabolically Activated to Selectively Modify Endoplasmic Reticulum Proteins. *Elife* **2018**, *7*. https://doi.org/10.7554/eLife.37168.

(49) Shoulders, M. D.; Ryno, L. M.; Genereux, J. C.; Moresco, J. J.; Tu, P. G.; Wu, C.; Yates, J. R.; Su, A. I.; Kelly, J. W.; Wiseman, R. L. Stress-Independent Activation of XBP1s and/or ATF6 Reveals Three Functionally Diverse ER Proteostasis Environments. *Cell Rep.* **2013**, *3* (4), 1279–1292. https://doi.org/10.1016/j.celrep.2013.03.024.

(50) Grandjean, J. M. D.; Plate, L.; Morimoto, R. I.; Bollong, M. J.; Powers, E. T.; Wiseman, R. L. Deconvoluting Stress-Responsive Proteostasis Signaling Pathways for Pharmacologic Activation Using Targeted RNA Sequencing. *ACS Chem Biol* **2019**, *14* (4), 784–795. https://doi.org/10.1021/acschembio.9b00134.

(51) Vabulas, R. M.; Raychaudhuri, S.; Hayer-Hartl, M.; Hartl, F. U. Protein Folding in the Cytoplasm and the Heat Shock Response. *Cold Spring Harb Perspect Biol* **2010**, *2* (12), a004390. https://doi.org/10.1101/cshperspect.a004390.

(52) Pena, J.; Harris, E. Dengue Virus Modulates the Unfolded Protein Response in a Time-Dependent Manner. *J Biol Chem* **2011**, *286* (16), 14226–14236. https://doi.org/10.1074/jbc.M111.222703.

(53) Li, M. Y.; Grandadam, M.; Kwok, K.; Lagache, T.; Siu, Y. L.; Zhang, J. S.; Sayteng, K.; Kudelko, M.; Qin, C. F.; Olivo-Marin, J. C.; Bruzzone, R.; Wang, P. G. KDEL Receptors Assist Dengue Virus Exit from the Endoplasmic Reticulum. *Cell Rep* **2015**, *10* (9), 1496–1507. https://doi.org/10.1016/j.celrep.2015.02.021.

(54) Neufeldt, C. J.; Cortese, M.; Acosta, E. G.; Bartenschlager, R. Rewiring Cellular Networks by Members of the Flaviviridae Family. *Nature Reviews Microbiology*. Nature Publishing Group February 12, 2018, pp 125–142. https://doi.org/10.1038/nrmicro.2017.170.

(55) Gallagher, C. M.; Garri, C.; Cain, E. L.; Ang, K. K.; Wilson, C. G.; Chen, S.; Hearn, B. R.;

Jaishankar, P.; Aranda-Diaz, A.; Arkin, M. R.; Renslo, A. R.; Walter, P. Ceapins Are a New Class of Unfolded Protein Response Inhibitors, Selectively Targeting the ATF6alpha Branch. *Elife* **2016**, *5*. https://doi.org/10.7554/eLife.11878.

(56) Gallagher, C. M.; Walter, P. Ceapins Inhibit ATF6alpha Signaling by Selectively Preventing Transport of ATF6alpha to the Golgi Apparatus during ER Stress. *Elife* **2016**, *5*. https://doi.org/10.7554/eLife.11880.

(57) Torres, S. E.; Gallagher, C. M.; Plate, L.; Gupta, M.; Liem, C. R.; Guo, X.; Tian, R.; Stroud, R. M.; Kampmann, M.; Weissman, J. S.; Walter, P. Ceapins Block the Unfolded Protein Response Sensor ATF6alpha by Inducing a Neomorphic Inter-Organelle Tether. *Elife* **2019**, *8*. https://doi.org/10.7554/eLife.46595.

(58) Palmer, J. E.; Brietske, B. M.; Bate, T. C.; Blackwood, E. A.; Garg, M.; Glembotski, C. C.; Cooley, C. B. Reactive Oxygen Species (ROS)-Activatable Prodrug for Selective Activation of ATF6 after Ischemia/Reperfusion Injury. *ACS Med Chem Lett* **2020**, *11* (3), 292–297. https://doi.org/10.1021/acsmedchemlett.9b00299.

(59) Banerjee, R.; Pace, N. J.; Brown, D. R.; Weerapana, E. 1,3,5-Triazine as a Modular Scaffold for Covalent Inhibitors with Streamlined Target Identification. *J Am Chem Soc* **2013**, *135* (7), 2497–2500. https://doi.org/10.1021/ja400427e.

(60) Cole, K. S.; Grandjean, J. M. D.; Chen, K.; Witt, C. H.; O'Day, J.; Shoulders, M. D.; Wiseman, R. L.; Weerapana, E. Characterization of an A-Site Selective Protein Disulfide Isomerase A1 Inhibitor. *Biochemistry* **2018**, *57* (13), 2035–2043. https://doi.org/10.1021/acs.biochem.8b00178.

(61) Hoffstrom, B. G.; Kaplan, A.; Letso, R.; Schmid, R. S.; Turmel, G. J.; Lo, D. C.; Stockwell, B. R. Inhibitors of Protein Disulfide Isomerase Supress Apoptosis Induced by Misfolded Proteins. *Nat. Chem. Biol.* **2010**, *6*, 900–906.

(62) Kinney, R. M.; Butrapet, S.; Chang, G.-J. J.; Tsuchiya, K. R.; Roehrig, J. T.; Bhamarapravati, N.; Gubler, D. J. Construction of Infectious CDNA Clones for Dengue 2 Virus: Strain 16681 and Its Attenuated Vaccine Derivative, Strain PDK-53. *Virology* **1997**, *230* (2), 300–308. https://doi.org/10.1006/VIRO.1997.8500.

(63) Dick, G. W. A.; Kitchen, S. F. Zika Virus (I). Isolations and Serological Specificity. *Trans. R. Soc. Trop. Med. Hygeine* **1952**, *46* (5), 509–520.

(64) Lanciotti, R. S.; Lambert, A. J.; Holodniy, M.; Saavedra, S.; Signor Ldel, C. Phylogeny of Zika Virus in Western Hemisphere, 2015. *Emerg Infect Dis* **2016**, *22* (5), 933–935. https://doi.org/10.3201/eid2205.160065.

(65) Langsjoen, R. M.; Auguste, A. J.; Rossi, S. L.; Roundy, C. M.; Penate, H. N.; Kastis, M.; Schnizlein, M. K.; Le, K. C.; Haller, S. L.; Chen, R.; Watowich, S. J.; Weaver, S. C. Host Oxidative Folding Pathways Offer Novel Anti-Chikungunya Virus Drug Targets with Broad Spectrum Potential. *Antiviral Res.* **2017**, *143*, 246–251. https://doi.org/10.1016/j.antiviral.2017.04.014.

(66) Fonslow, B. R.; Niessen, S. M.; Singh, M.; Wong, C. C.; Xu, T.; Carvalho, P. C.; Choi, J.; Park, S. K.; Yates 3rd, J. R. Single-Step Inline Hydroxyapatite Enrichment Facilitates Identification and Quantitation of Phosphopeptides from Mass-Limited Proteomes with MudPIT. *J Proteome Res* **2012**, *11* (5), 2697–2709. https://doi.org/10.1021/pr300200x.

(67) Jensen, S. M.; Nguyen, C. T.; Jewett, J. C. A Gradient-Free Method for the Purification of

Infective Dengue Virus for Protein-Level Investigations. *J. Virol. Methods* **2016**, *235*, 125–130. https://doi.org/10.1016/j.jviromet.2016.05.017.

CHAPTER 4: ER proteostasis regulator 263 acts as a broad-spectrum inhibitor of dengue and Zika virus infections

This chapter is adapted from a manuscript to be submitted for publication by Almasy, K.M., Mansueto, A.J., and Plate., L.

4.1 Introduction

As highlighted by the COVID-19 pandemic, new therapies are needed to treat current and future outbreaks of viral diseases. Among such families are the flaviviruses, a genus of Group IV viruses (genome of positive-sense, single-stranded RNA) which include Dengue virus (DENV), Zika virus (ZIKV), West Nile Virus (WNV) and Yellow Fever virus (YFV). These mosquito-borne pathogens currently pose a significant threat to public health, with close to half the world's population proposed to live under risk of DENV infection[1,2]. DENV is known to cause hemorrhagic fever, particularly during secondary infection due to antibody-dependent enhancement[3,4].

Despite the prevalence and increasing occurrence of these viruses, no current therapeutics exist to fight flavivirus infections[5,6]. Most current small-molecule treatments only address the underlying symptoms, and do not interfere with the viruses themselves. Antiviral strategies often focus on inhibition of viral enzymes, otherwise known as direct-acting antivirals (DAAs). For flaviviruses, work largely focuses on small molecules inhibiting the NS3 protease and NS5 polymerase[7]. Molecules effective against these enzymes have been discovered and characterized but are not currently in use[8–11]. One limitation seen often with molecules that engage with viral proteins is the rapid development of resistance due to the ability of the viral genome to quickly mutate, decreasing the binding affinity of the small molecule with the protein[12]. An increasing area of exploration takes the alternative approach of identifying and targeting host factors essential for viral replication, aiming to disrupt protein-protein interactions necessary for the viral life cycle. As these host factors are not under direct genetic control of the virus, mutations leading to a

disruption in binding should be far less common. Additionally, should these host factors be required for replication of one or more entire families of viruses, these compounds could be use as broad-spectrum antivirals rather than targeting a single virus[13,14].

As noted, flaviviruses contain a genome of positive-sense, single-stranded RNA. After receptor-mediated entry, the genomes are translated, and the resultant viral proteins remodel the interior of the cell to assist in replication of the genome and packaging of progeny virions. Both viruses concentrate this replication and assembly process in and around the endoplasmic reticulum (ER), which also serves as a protein folding center for the host cell itself[15–17]. The host protein homeostasis (or proteostasis) network has been heavily implicated in the flavivirus life cycle, and several screens have identified specific dependencies of viral replication on diverse proteostasis factors[18–21]. In addition, DENV infections cause upregulation of the ATF6 and IRE1 branches of the ER unfolded protein response (UPR), a stress response pathway initiated by the presence of misfolded protein buildup within the ER[22,23]. Pharmacologic modulation of the proteostasis network, for instance with inhibitors of Hsp70 and the oligosaccharyl transfer complex (OST), can prevent flavivirus replication in both cellular and mouse models[24–26]. Additionally, our recent study showed an ER proteostasis modulator, compound **147**, serves as an effective inhibitor of DENV and ZIKV replication[27].

Pharmacologic modulation of ER proteostasis pathways has become an increasingly utilized strategy to correct protein folding imbalances associated with diverse disease phenotypes. Importantly, this correction occurs without affecting endogenous protein function or causing toxicity[28–32]. Compound **147**, in addition to serving as an effective antiviral, has been shown to reduce secretion of amyloidogenic light chain proteins as well as preventing organ damage after oxidative injury during ischemia/reperfusion[33,34]. Given the broad utility of **147**, we wanted to explore if compound **263**, a structurally similar molecule, possessed similar antiviral qualities. **263** was initially discovered in the same high-throughput screen which identified **147** as an activator of the ATF6 branch of the UPR[35]. While the mechanism of **263** is less defined than that of **147**,

the structural similarities led us to believe the targets of the molecule, and therefore the antiviral mechanisms would be largely similar. Our results show that **263** does indeed harbor antiviral effects, with an EC_{50} and maximum effect size comparable to those of **147**. However, target enrichment studies using a competition-based chemoproteomics approach suggest that the targets of the molecules may only overlap partially. Additional experiments were directed at delineating the molecular mechanism of the molecule demonstrating that unlike **147**, **263** does not function through covalent modification of cysteine residues. Overall, these results show that the proteostasis modulator **263** possesses antiviral effects which work by a different mechanism than **147**.

4.2 Results

4.2.1 Compound 263 inhibits DENV2 replication in Huh7 cells

Compound **147** was initially reported as a regulator of the ATF6 branch of the unfolded protein response[35]. Previously, we reported **147** as an effective anti-flavivirus compound effective across several strains of DENV and ZIKV[27]. We showed that this activity was dependent on a 2-amino-*p*-cresol moiety, which is oxidized to give an active quinone methide to serve as an electrophile for nucleophilic attack by free cysteine residues on host proteins. Given the active moiety of the molecule, we examined whether a similarly reactive moiety on a different molecule would retain anti-DENV and ZIKV activity. In the initial high-throughput screen for **147**, a compound bearing a similar functional group was discovered, compound **263** (**Figure 4.1a**)[35]. Instead of a 2-amino-*p*-cresol moiety, **263** bears a benzylidene hydrazine (or hydrazone) functional group (**Figure 4.1a**). Both groups are readily oxidized to a para- (**147**) or ortho- (**263**) quinone methide forming a highly active electrophile. Given the similarity in reactivity, we sought to determine if **263** would possess comparable effects inhibiting flavivirus replication. To examine the effects at different stages of the viral life cycle, a combination of assays was used to measure intracellular viral RNA (genome

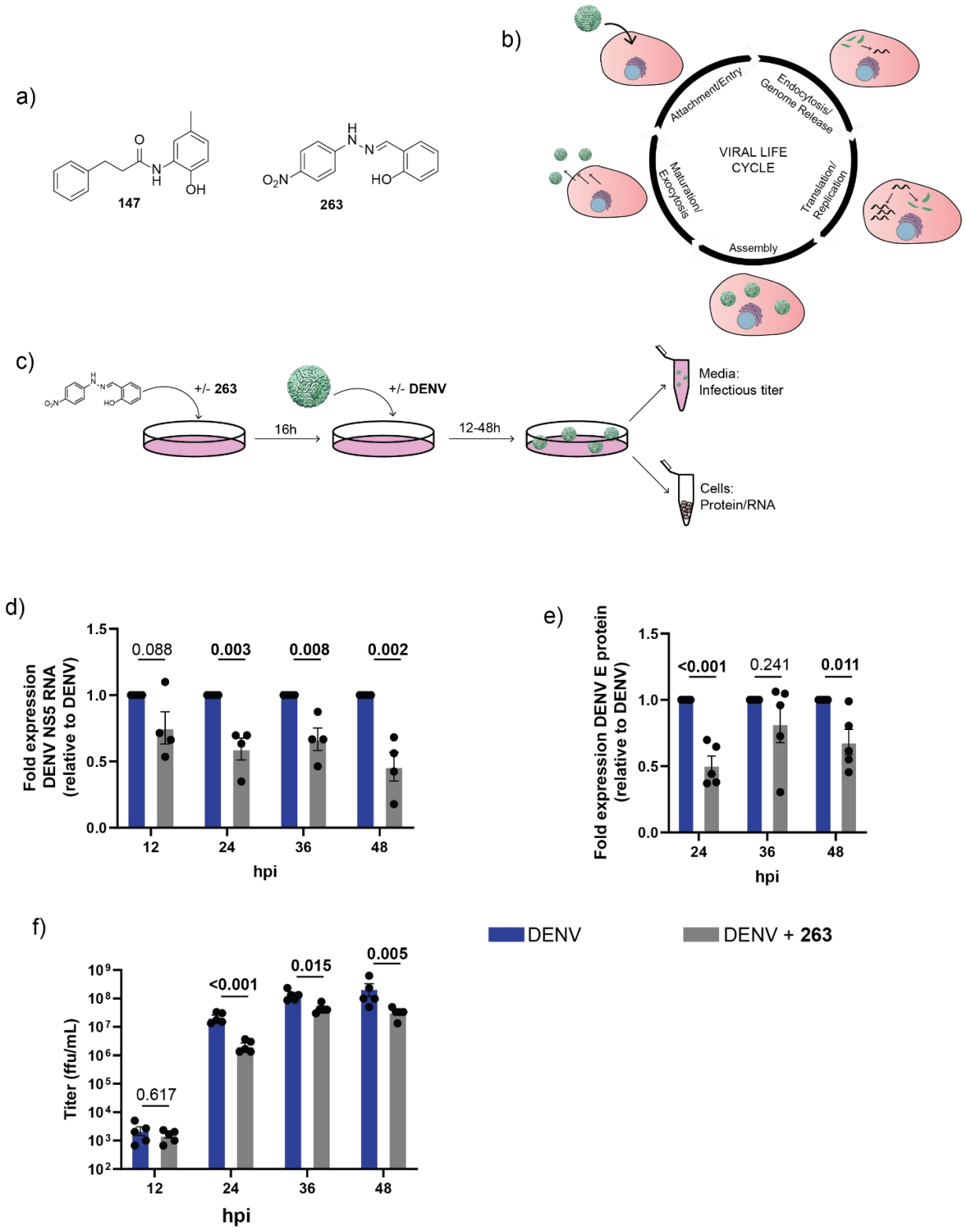

Figure 4.1. 263 inhibits DENV2 propagation in Huh7 cells. a) Structures of compounds 147 (left) and **263** (right), the two proteostasis regulators of interest. b) DENV life cycle. After entry to the cell via clathrin-mediated endocytosis, the genome is uncoated, translated into a single

polypeptide in and around the ER membrane, and cleaved into its individual proteins. Formation of the viral replication complex allows for replication of the RNA genome; some copies are translated, while others are eventually packaged into progeny virions as enough copies of the structural proteins become available. Maturation and egress through the trans-Golgi network leads to the release of the newly assembled virons. c) Huh7 cells were pre-treated with indicated concentrations of **263** for 16h before each experiment; cells were infected with DENV for 12-48 hours, with samples collected every 12 hours to measure viral RNA or protein levels intracellularly, and viral titers extracellularly. d) Quantification of reduction in viral RNA as measured by qPCR. Statistics reflect student's unpaired t-test, with the untreated control at each timepoint set to an RNA expression level of 1. e) Quantification of reduction in intracellular viral protein levels as measured by western blot. Statistics reflect student's unpaired t-test, with the untreated control at each timepoint set to a protein expression level of 1. f) Absolute quantification of viral titers as measured by focus forming assay. Statistics reflect student's paired ratio t-test.

replication) and protein (viral protein translation) levels, as well as extracellular infectious titer levels (**Figure 4.1b**). Huh7 cells were seeded and treated with 2.5 µM **263** or a DMSO control. 16 hours post-infection, cells were infected with DENV serotype 2 strain 16681 (generated from a cDNA clone[36]) at a multiplicity of infection (MOI) of 3, or mock infected with a media control. Infection proceeded for 3 hours, at which point the inoculum was removed and replaced with fresh media and compounds. Timepoints were taken every 12 hours up to 48 hours post-infection (hpi) to determine the effects **263** had on viral replication. 12 hours marks the earliest stage of progeny virion release, while 24 hours and beyond mark peak viral production[37]. Cells were harvested for RNA (via qPCR) and protein (via western blot) quantification, while the media was saved to measure extracellular virus infectious titers (**Figure 1c**). At 12 hpi, low titers and RNA levels were measured, but protein levels at this timepoint were too low to be detected by western blot, showing the low abundance of the virus at this stage. To this point, no significant differences were seen between treated and untreated samples. However, the 24 hour timepoint revealed differences between the two conditions. RNA levels were reduced approximately 50% across the 24, 36, and 48 hour timepoints in the **263** treated samples versus the control, all three of which were significant at the $p<0.05$ level (**Figure 4.1d**). By western blot, we again observed an approximately 50% decrease in viral protein levels 24 hours post-infection in the **263** treated samples compared to the DMSO treated control, and measurable differences were also observed at the 48 hour

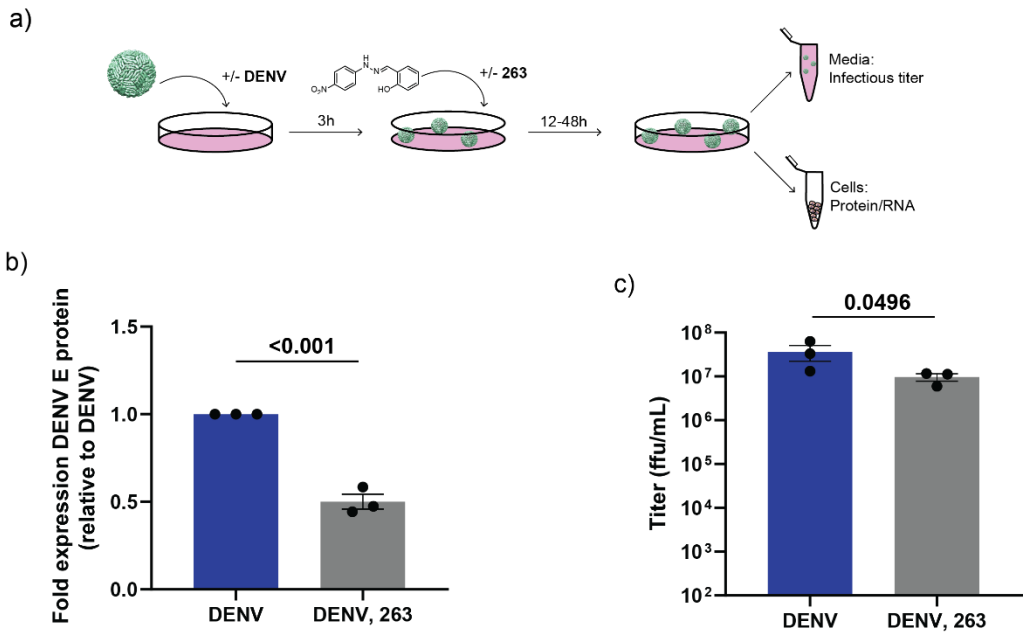

Figure 4.2. Eliminating pre-treatment step does not attenuate effects of 263. a) Experimental design for determining if **263** affects viral entry. Similar to Figure 1c, but without the step of pre-treating prior to infection. b) Quantification of western blots showing DENV E protein in vehicle control vs. 263 treated cells. Representative blot is shown in Figure A4.2. c) Graph showing absolute titers of vehicle vs **263** treatment, following experimental scheme shown in a.

timepoint. The 36 hour timepoint produced more variable results, and no statistical significance was observed (**Figure 4.1e, Figure A4.1**). Extracellular infectious titers were the most affected at the same timepoints; measured levels were reduced by just over 90% at the 24 hour timepoint, indicating that the molecule predominantly affects the viral assembly/packaging/egress stage. We also observe that minimal recovery of viral replication takes place over time; by 48hpi, titers are still significantly lowered in the **263** treated cells compared to the untreated control (**Figure 4.1f**). To further investigate the timing of the antiviral effects, we eliminated the pre-treatment of the cells (**Figure 4.2a**) to test if **263** affected viral entry. Given that the largest impact was observed on infectious titers, we hypothesized that the molecule should acts largely at a post-translational step and thus the pre-treatment step would be unnecessary. Consistent with this notion, we found that the pre-treatment step prior to infection was not necessary for **263** to lower protein or titer levels (**Figure 4.2b-c, Figure A4.2**), indicating the molecule acts at a post-viral entry stage.

Having observed these same effects with **147**, we next tested if the reduction in viral titers corresponded to less viral protein being secreted, or as with **147**, reduction in titers was independent of total viral protein secretion. Virus containing media was collected from either DMSO or **263** treated infected cells 24 hours post-infection, virus particles were purified via ultracentrifugation, inactivated, and protein levels were measured via western blot (**Figure 4.3a**). Samples treated with **263** reproducibly showed lower extracellular envelope protein levels (**Figure 4.3b-c, Figure A4.3**). The reduction of protein levels was comparable to the magnitude reduction seen at the titer level (80-90%), suggesting the lower infectious titer is due to less progeny virions virions. Additionally, qPCR was performed to measure any differences in RNA levels between treated and untreated purified virus samples (**Figure 4.3d**). The **263** treated samples consistently contained lower levels of RNA than the DMSO treated samples, although this difference did not reach statistical significance due to high variability in measured RNA amounts. We conducted dose-response studies to study how the antiviral effect and the toxicity of the molecule changed with concentration. The dose-response curve indicated an EC50 value of approximately 7.5 μM; however, a significant reduction in cell viability is seen at this concentration. The 2.5 μM concentration, on the other hand, still produced reproducibly significant reductions in viral titer with a viability above 70%. These viability results held true whether or not the cells were infected with virus (**Figure A4.4, Figure A4.5)**.

While **263** was shown to be effective up to 48 hours post-infection, the effects of the molecule began to wane over time, expectedly as the drug is metabolized and rendered inactive. To examine how readministration of the drug may result in continued viral inhibition, we treated cells as above, while readministering the drug every 24 hours up to 72 hours post infection. As noted above, the single treatment was enough to result in a significant decrease up to 48 hours post infection; however, re-administration of the drug at 24 hours post infection resulted in an additional decrease compared to the sample treated only once (**Figure A4.6**).

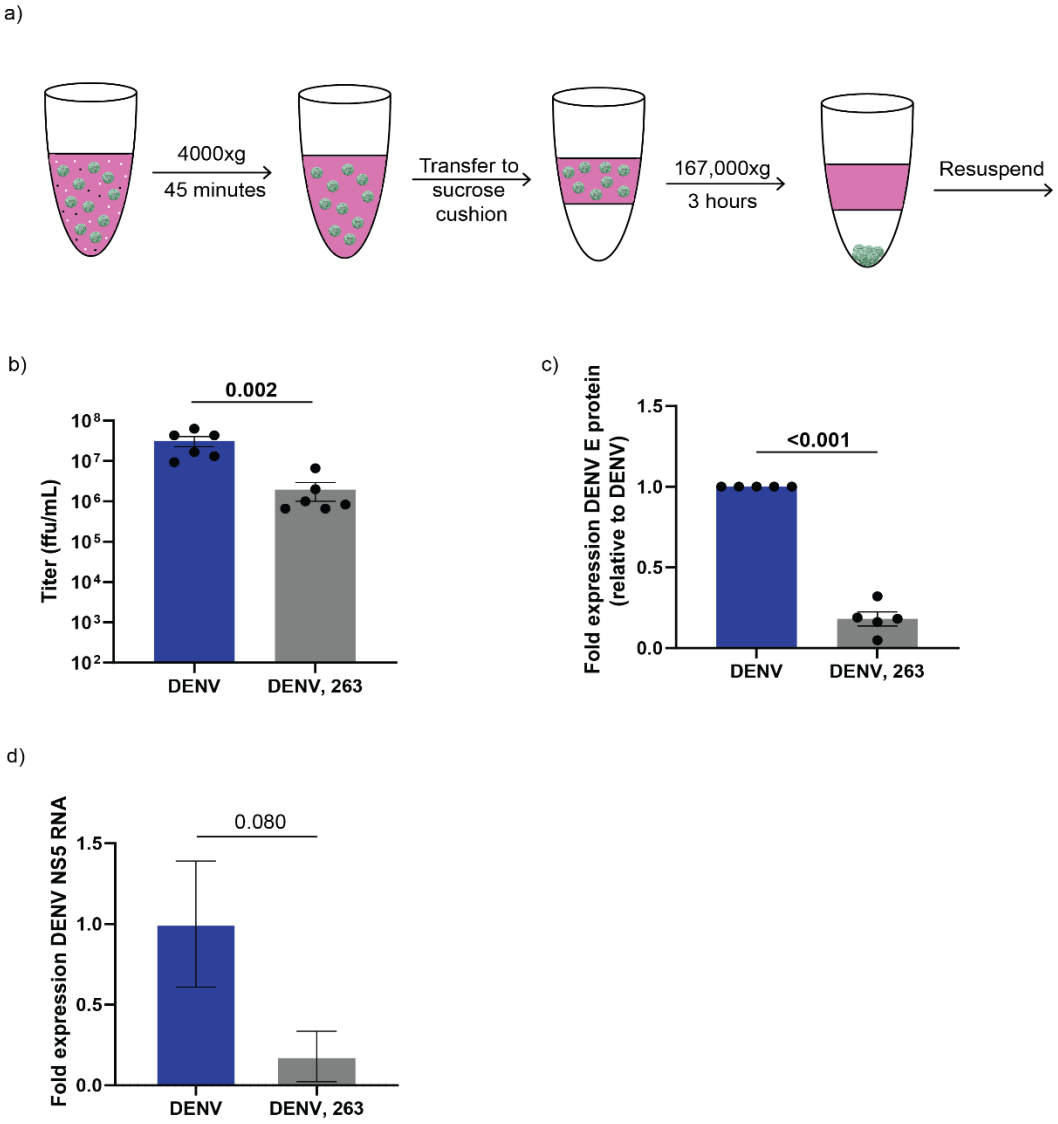

Figure 4.3. Purification of DENV supernatant in 263 treated samples shows decrease in secreted viral protein levels. a) Scheme for purification of DENV. Media is collected from infected cells and cleared on a benchtop centrifuge at 4000xg for 45 minutes. Samples are then ultracentrifuged on a 20% sucrose cushion for 3 hours at 167000xg. Supernatant is removed, pellets are left to dry, and virus is resuspended in buffer and prepared for western blot analysis. b) Post-purification titers of DMSO vs **263** treated samples, showing difference in titer is maintained during the purification process. c) Western blot analysis of purified DENV E protein post-purification. A reduction of 80-90% is observed, eclipsing the difference observed intracellularly and matching the reduction in titers. Representative western blot is shown in Figure A4.3. d) qPCR data from DMSO vs **263** treated virus post-purification.

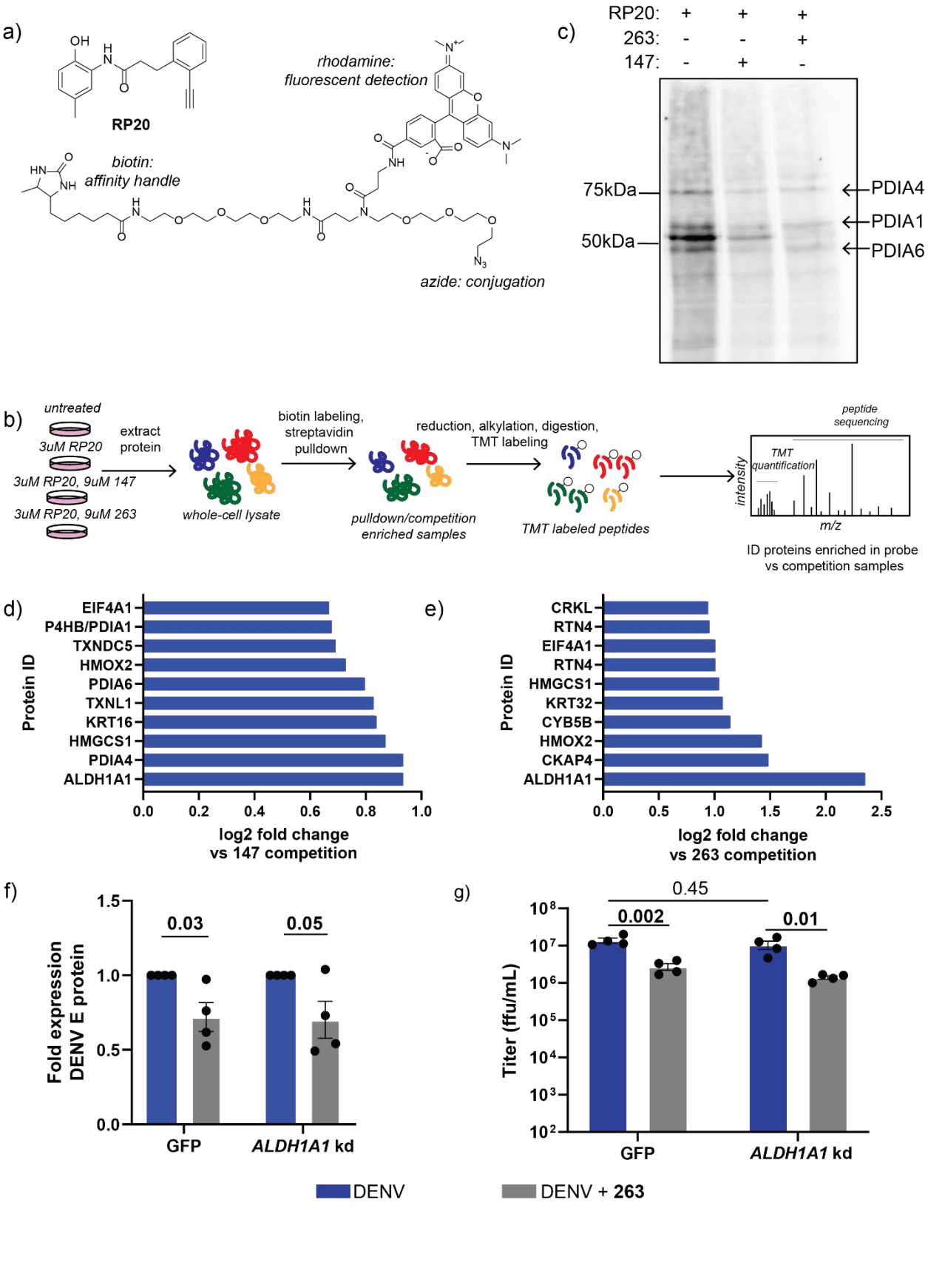
a)
RP20
rhodamine:
fluorescent detection
biotin:
affinity handle
azide: conjugation
c)
RP20: + + +
263: - - +
147: - + -
75kDa
50kDa
PDIA4
PDIA1
PDIA6
b)
untreated
3uM RP20
3uM RP20, 9uM 147
3uM RP20, 9uM 263
extract protein
whole-cell lysate
biotin labeling, streptavidin pulldown
pulldown/competition enriched samples
reduction, alkylation, digestion, TMT labeling
TMT labeled peptides
peptide sequencing
TMT quantification
intensity
m/z
ID proteins enriched in probe vs competition samples
d)
Protein ID
EIF4A1
P4HB/PDIA1
TXNDC5
HMOX2
PDIA6
TXNL1
KRT16
HMGCS1
PDIA4
ALDH1A1
0.0 0.2 0.4 0.6 0.8 1.0
log2 fold change vs 147 competition
e)
Protein ID
CRKL
RTN4
EIF4A1
RTN4
HMGCS1
KRT32
CYB5B
HMOX2
CKAP4
ALDH1A1
0.0 0.5 1.0 1.5 2.0 2.5
log2 fold change vs 263 competition
f)
Fold expression DENV E protein
0.03
0.05
GFP
ALDH1A1 kd
g)
0.45
0.002
0.01
Titer (ffu/mL)
GFP
ALDH1A1 kd
DENV
DENV + 263

Figure 4.4. Indirect target ID suggests differing mechanism of 263. a) Structures of alkyne-labeled **147** variant used in pulldown experiments (**147-20**) and trifunctional probe used for simultaneous CuAAC click chemistry, detection, and pulldown. b) Target ID experiment workflow. Cells were treated with **147-20** alone, or in competition with an excess of **147** or **263**. For pulldown experiments, lysates were 'clicked' with trifunctional probe and **147-20** labeled proteins were isolated using streptavidin. TMT labeling and quantitative proteomics of pulldown vs competition samples revealed targets competitively labeled by **147** or **263** respectively. c) Fluorescent western blot of **147-20** treated lysates, with **147** and **263** competitions. PDIs were blotted for as a known target of **147**. The band between PDIA1 and PDIA6 was later identified as ALDH1A1. d) Quantification of targets most enriched in **147-20** pulldown vs. competition with **147**. e) Quantification of targets most enriched in **147-20** pulldown vs. competition with **263**. f) Effects of 263 in cell line with *ALDH1A1* knocked down vs. GFP/mock control cells. Representative western blot (including knockdown efficacy) shown in Figure A4.8. g) Absolute titers in *ALDH1A1* knockdown cell lines and GFP/mock control cells.

At 72 hours post-infection, this difference in the samples treated once vs repeated treatments became more apparent, indicating that re-administration of the drug is a viable strategy for sustained inhibition of viral replication. Additionally, by 72 hours, the media quality of the untreated DENV-infected samples was visibly compromised. As **263** causes a decrease in cell viability, the lower cell population in these wells likely allowed the media quality to remain higher, increasing virion stability and therefore infectious titer (**Figure A4.6**).

4.2.2 Target ID using 147 analogues suggests protein targets are different than 147

Given the similarity between the phenotypes of **147** and **263** treatment against DENV, paired with the resemblance of oxidizable moieties in the compound structures, sought to determine if the molecules target similar host proteins. Prior investigations of **147**, as well as our recent study in Huh7 cells, showed the primary targets of **147** are protein disulfide isomerases (PDIs)[27,38]. PDIs were the predominant class of proteins labeled by **147** as measured by a competition assay between an alkyne-substituted derivative of **147** (**147-20, Figure 4.4a**) and the parent compound. While neither structure-activity relationship data nor an alkyne-labeled derivative are available for **263**, we took advantage of the fact that the molecules are expected to have similar covalent targets and conducted an analogous competition experiment between **147-20**, **147,** and **263**.

Huh7 cells were treated with 3 µM **147-20**, 3 µM **147-20** and 9 µM **147**, or 3 µM **147-20** and 9 µM **263** (**Figure 4.4b**). In the **147-20** samples, target proteins are covalently labeled by the alkyne-containing compound via the mechanism highlighted in **Figure 4.1a**. Modified proteins can subsequently be labeled via click chemistry with a TAMRA-desthiobiotin-azide compound and enriched with a streptavidin pulldown to then be visualized via SDS-PAGE/western blot (**Figure 4.4c**) or identified via mass spectrometry. In the cotreatments, the 3-fold excess of the parent compounds **147** or **263** will compete with **147-20** binding to specific targets, thus less labeling of targets should occur in these samples. This competition workflow is routinely employed to distinguish specific targets that rely on distinct interactions with the probe compound versus high-abundance background binding partners[39,40].

After pulldown, samples were reduced, alkylated, and digested overnight. Using TMTpro reagents, 16 samples were labeled with isobaric tags and combined into a single mass spectrometry run, with LC separation using multidimensional peptide identification technology (MudPIT). As validation of the competition experiment, we confirmed observation of PDIs as the predominant targets of **147** (**Figure 4.4d**). However, these enrichments were not seen in the **263** competition samples. This implies **263** did not compete off the PDIs as initially expected (**Figure 4.4e**). A small number of targets overlapped as enriched between the **147** and **263** competition experiments, but no PDIs were observed in the **263** dataset. One protein, ALDH1A1, was identified as the top target of both compounds. Interestingly, a much stronger 6-fold enrichment was observed in the probe vs. competition with **263**, while only a 2-fold enrichment was observed in the probe vs. competition experiment for **147**, suggesting **263** more effectively binds ALDH1A1 than does **147**. We previously showed that shRNA knockdown of *ALDH1A1* does not impact viral replication[27]. To validate this point, we generated a stable ALDH1A1 shRNA knockdown cell line (**Figure A4.8**), infected the cells with DENV and treated with either DMSO or **263**. The cell line retained sensitivity to **263** treatment, as titers were significantly lower when **263** was added to the samples. As expected, knockdown of ALDH1A1 did not, on its own, cause a reduction in viral

protein or titers (**Figure 4.4f-g, Figure A4.8**). Overall, the lack of overlap between the targets competed off by **263** compared to **147** suggests the targets of the two molecules in Huh7 cells are more divergent than initially anticipated.

4.2.3 Antiviral effects of 263 are not thiol or P450 dependent

Considering the divergence in covalent targets of **263** and **147**, it seemed plausible that the compounds exert their antiviral activities through distinct mechanisms. **147** is oxidized by P450 enzymes to yield an ortho-quinone imine, which tautomerizes to a paraquinone methide, the active electrophilic species (**Figure 4.5a**)[38,41]. Inhibition of the oxidation step with resveratrol (a broad-spectrum P450 inhibitor) or competition of the nucleophilic addition step with beta-mercaptoethanol) resulted in restoration of viral titers. With **263**, we hypothesized that P450 oxidation of the molecule would lead to the formation of an ortho-quinone methide, which would subsequently provide an electrophile to be attacked by nucleophilic residues on target proteins (**Figure 4.5b**). However, given the divergent covalent targets despite similar antiviral activities of the two compounds, we sought to test whether the metabolic activation and nucleophilic attack was required for the antiviral activity of 263. We therefore explored two possible ways to disrupt the oxidation/nucleophilic attack mechanism; both have been shown to attenuate the effects of **147**[27,38].

First, cells were treated with DMSO, 2.5 μM **263**, or a combination of 2.5 μM **263** and 55 μM or 110 μM β-mercaptoethanol (BME). Excess BME will quench the nucleophilic addition step, leaving the protein targets unmodified. However, we found that BME addition failed to attenuate the antiviral effects of **263**, suggesting covalent modification of thiols is not required for the mechanism of action (**Figure 4.5c-d, Figure A4.10**). Secondly, cells were treated with DMSO, 2.5 μM **263**, or a combination of 2.5 μM **263** and 10 μM resveratrol, a broad-spectrum cytochrome P450 inhibitor. Co-treatment with resveratrol blocks any P450-mediated oxidation required if **263** to test if metabolic activation us needed for antiviral activity. In experiments with **147**, resveratrol

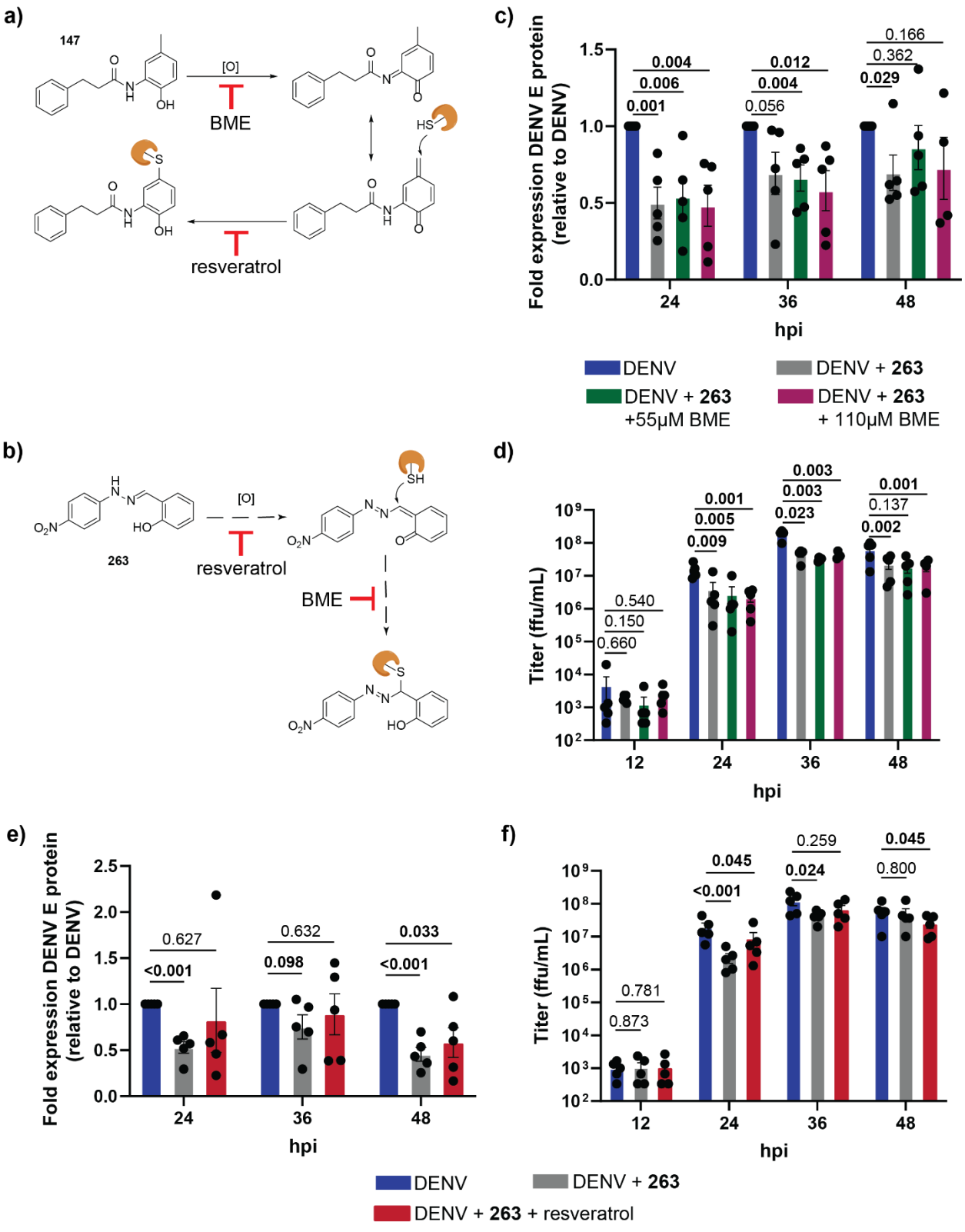

Figure 4.5. 263 does not work via a thiol-dependent mechanism. a) Mechanism of action of **147**- the compound is oxidized and tautomerizes to the active electrophilic species, which is

available for covalent modification by sulfhydryl groups on free cysteine residues of proteins. b) Hypothesized mechanism of **263** effect, based on similarities between para-cresol moiety on **147** and benzylidene hydrazine group on **263**. c) Protein levels of virus-infected samples treated with DMSO, **263**, and varying concentrations of beta-mercaptoethanol. Representative western blot is shown in Figure S10. d) Absolute titers of virus-infected samples treated with DMSO, **263**, and varying concentrations of beta-mercaptoethanol. e) Protein levels of virus-infected cells treated with DMSO, **263**, and resveratrol. Representative western blot is shown in Figure S10. f) Absolute titers of virus-infected samples treated with DMSO, **263**, and resveratrol.

reproducibly blocked the effects of the molecule and a significant recovery in virus titer was observed. In experiments with **263**, results were less consistent, but viral titer was generally not significantly different from either the untreated or treated samples (the exception being at 48 hpi, where viral titer in the co-treated sample was still significantly lower than the untreated sample) (**Figure 4.5e-f, Figure A4.10**). No changes in cell viability were observed on co-treatment of **263** with either of the aforementioned compounds (**Figure A4.9**).

4.2.4 Compound 263 is effective against several flaviviruses

It is hypothesized that host-centered antivirals often possess broad activity against related viruses. We therefore tested **263** across a larger panel of flaviviruses. Studies until this point were conducted with DENV2 strain 16681, a Thailand isolate, in Huh7 cells. Experiments with DENV3 strain Philippines/H87/1956 and DENV4 strain H241 in Huh7 showed similar effects. Titer reduction 24 hours post infection was consistently around 90% (**Figure 4.6a-b**). To show effectiveness against multiple flaviviruses, we tried using **263** against two different strains of Zika virus; strain MR766, isolated in the 1950s, and strain PRVABC59, from the recent 2015 outbreak in Puerto Rico. Again, the molecule displayed effectiveness at reducing viral titers >90% 24 hours post-infection (**Figure 4.6c-d**), and these same effects were seen at the protein level (**Figure S4.11**).

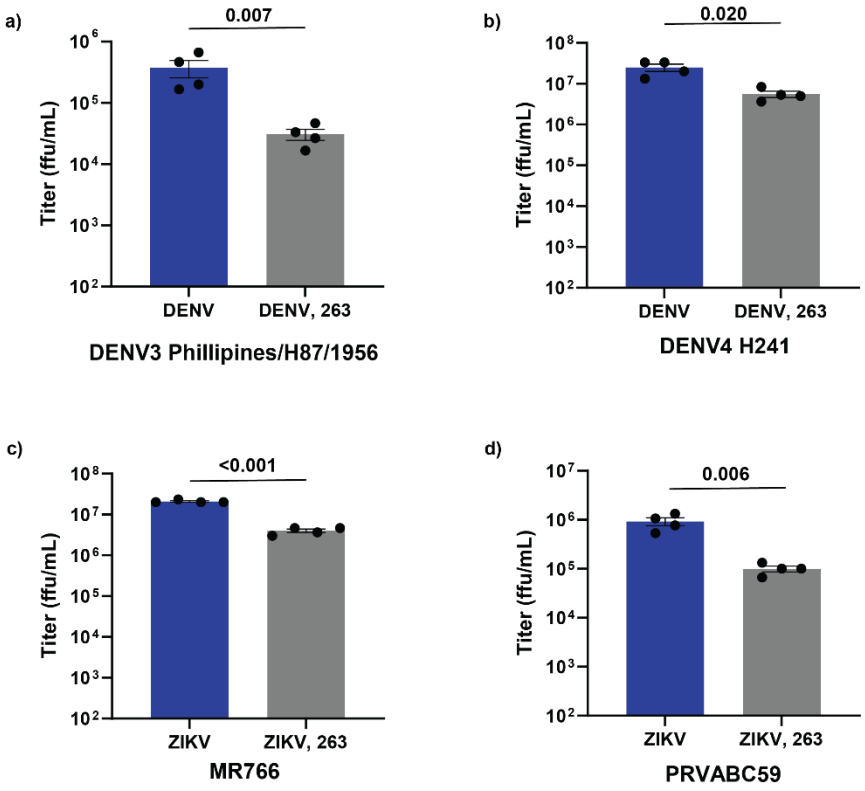

Figure 4.6. 263 is effective against multiple DENV and ZIKV strains. a) Absolute titers of DENV serotype 3 strain Philippines/H87/1956 samples treated with DMSO or **263**. b) Absolute titers of DENV serotype 4 strain H241 samples treated with DMSO or **263**. c) Absolute titers of ZIKV strain MR766 samples treated with DMSO or **263**. d) Absolute titers of ZIKV strain PRVABC59 treated with DMSO or **263**.

4.3 Discussion

The COVID-19 pandemic has highlighted the need for the development of new, effective, antiviral therapies. Ideally, therapies developed for existing virus strains could be applied to future viruses or outbreaks as well. The development of host-centered antivirals, which would target cellular protein factors required for virus propagation, is an attractive strategy for this purpose, and additionally would likely have the advantage of avoiding the development of resistant viral strains by targeting proteins outside the genetic control of the virus. Our work focuses on utilizing pharmacologic modulators of the human ER proteostasis network to identify protein folding factors required for the replication of multiple viruses. Previously, we showed that **147**, a proteostasis regulator effective at reducing secretion of amyloidogenic proteins and preventing cardiac

damage in mouse models of ischemia/reperfusion, also served as an effective antiviral against both dengue and Zika virus [33,34]. Here, we explore the antiviral activity of compound **263**, a molecule structurally related to **147** and shown to have some of the same phenotypic effects with regards to proteostasis regulation[35]. We thus sought to test a) if **263** would possess similar antiviral effects, and b) if the effects were a result of similar mechanisms and targeting.

Treatment of DENV-infected cells with **263** produced generally similar effects to what was seen with **147**. With an EC50 of approximately 2.5 µM, the molecule was up to 90% effective at reducing viral titers 24 hours post-infection. While the magnitude of inhibition was greatest for infectious titers, we also observed a ~50% reduction in intracellular viral RNA and protein levels at the same timepoint. Believing that this pointed to **263** causing a defect in viral assembly or secretion, we measured the total extracellular protein content in DMSO vs. **263** treated cells and showed that the overall amount of viral protein secreted decreases, largely matching the percentage reduction seen in the extracellular viral titers. This indicates that the reduction in titer can be completely explained by a reduction in secretion of viral proteins, rather than secretion of incorrectly folded or otherwise aberrant protein species. Further studies may be done to highlight where specifically in the packaging and assembly process the molecule is exerting an effect.

Believing that the structural similarities between the two molecules would be enough to direct the targeting in similar directions, we utilized an alkyne-labeled variant of **147** in competition with either **263** or the true parent compound **147** to investigate which **147-20** targets were competed off by an excess of either compound. While not a true target ID scheme for **263**, we believed this would give us information on how similar the targeting of the two compounds was. Surprisingly, the overlap was very small. The competition experiment with **147** led expectedly to the ID of protein disulfide isomerases; none of these proteins were among the most competed off by **263**. The most prominent taret for each molecule was ALDH1A1. We previously showed that shRNA knockdown of *ALDH1A1* was not sufficient to mimic **147** treatment in Huh7 cells, and here show that these cells also retain **263** sensitivity. However, previous research shows that benzylidine

hydrazines (otherwise called hydrazones) do possess the potential to be oxidized; one study outlined the ability of these molecules to scavenge free radicals[42]. An additional study showed that an aldehyde dehydrogenase was one of the enzymes found in yeast responsible for metabolism of these compounds[43]. This could indicate another member of the ALDH family is responsible for the antiviral activity, or otherwise for metabolism of the compounds in liver cells, where dehydrogenase enzymes are highly expressed[44]. Other commonly labeled targets for **263** and **147** were HMG-CoA reductase (HMGCS1) and constitutive heme oxygenase 2 (HMOX2). The role of cholesterol biosynthesis or oxidative stress in DENV propagationcould be further studied.

Considering that the covalent targets were different between the two molecules, we investigated whether the molecular mechanism of **263** was similar to that of **147**. **147** requires P450 oxidation to form the active quinone methide, at which point free thiols are covalently modified after binding the electrophilic functional group. We blocked P450 oxidation with resveratrol and intercepted the nucleophilic attack step with beta-mercaptoethanol. These same experiments with **263** did not attenuate the antiviral effects, indicating that the molecule works by a completely different mechanism, and does not require covalent modification of cysteine residues on protein targets. Considering this fact, the mechanism by which **263** appeared to compete for binding with **147-20** targets raises questions about how these two molecules bind some of the same proteins (or at the very least, ALDH1A1). While outside the scope of this study, this may suggest the benzylidene hydrazine is somewhat relevant for non-antiviral functions of the molecule, or, as suggested, targets of **147** may be responsible for metabolism of **263**.

Finally, we tested **263** across a panel of flaviviruses. Consistent with our expectation that a host-centered antiviral agents should have broad spectrum activity against multiple viruses, the compound exerted similar effects against two strains of Zika, and three serotypes of DENV (DENV2, DENV3, DENV4). This continues to highlight the potential of protein folding modulators as potential anti-flavivirus drugs, a model pathway being increasingly explored.

4.4 Materials and methods

Cell culture

Huh7 and Vero cells were maintained in Dulbecco's Modified Eagle's Medium (DMEM) with high glucose and supplemented with 10% fetal bovine serum, 1% penicillin/streptomycin, and 1% glutamine. Cells were kept at 37°C, 5% CO_2.

Virus infections

For flavivirus infection of cell lines, media was removed from cells and virus was added at MOI 3 for 3 hours (DENV) or MOI 0.5 for 1 hour (ZIKV), unless otherwise noted.

Inoculum was removed, cells were washed, and media containing chemical treatments or DMSO was added for the remainder of the experiment.

Virus maintenance

DENV: DENV2 strain 16681 was generated from a cDNA clone in PD2/ic-30p from Dr. Claire Huang at the United States Centers for Disease Control. DENV3 and DENV4 were obtained from BEI resources. For passaging, Vero cells were infected at an MOI of 0.1 in DMEM supplemented with 1% penicillin/streptomycin, 1% glutamine, and 2% fetal bovine serum. Two days post-infection, culture supernatant was harvested and cell debris was pelleted at 4000xg for 10 minutes. Cleared media was frozen as 1-1.5mL aliquots at -80°C.

ZIKV: ZIKV MR766 and ZIKV PRVABC59 were obtained from ATCC. For passaging, Vero cells were infected at an MOI of 0.05 in DMEM supplemented with 1% penicillin/streptomycin, 1% glutamine, and 2% fetal bovine serum. Two days post-infection, culture supernatant was harvested and cell debris was pelleted at 4000xg for 10 minutes. Cleared media was frozen as 1-1.5mL aliquots at -80°C.

Lentivirus: A 3rd generation lentivirus system was used for production. Packaging plasmids were a combination of 3 shRNAs for ALDH1A1 knockdown, or a mitochondrial GFP as a mock control. Packaging plasmids and structural plasmids Rev, RRE, and VSVG were cotransfected into HEK293T cells using a calcium phosphate method. Media was changed 20 hours post-

transfection, and supernatant containing lentivirus was collected 48 hours after changing media. Lentivirus-containing media was cleared for 10 minutes at 4000xg, and sterile filtered using a 0.45 micron syringe filter. Lentiviruses were transduced onto Huh7 cells in media containing 4 µg/mL final concentration polybrene. Selection began 1 day post-transduction under 5 µg/mL puromycin and proceeded for one week before knockdown was confirmed by western blot.

Flavivirus quantification by focus forming assay

Confluent Vero cells in 96 well plates were inoculated with serial dilutions (10-fold) of DENV or ZIKV in BA-1 diluent (M199 media, 5% bovine serum albumin, 1x glutamine/penicillin/streptomycin, 0.04% sodium bicarbonate, 50 mM Tris) for 2 hours. 110 L of a 1:1 mixture of nutrient overlay (2x Earle's Balanced Salt Solution, 2x Ye-Lah medium, 4% fetal bovine serum, 0.4% sodium bicarbonate, 0.1 mg/mL gentamycin, 0.5 mg/mL fungizone) and 2.4% methycellulose in water. After 2 days (ZIKV, DENV3, DENV4) or 3 days (DENV2), overlay was removed and cells were fixed with ice cold 85% acetone for 30 minutes. Foci were stained with a primary pan-flavivirus antibody (clone 4G2, 1:1000 in 5% BSA) followed by a secondary HRP-conjugated antibody (1:1000 in 5% milk, TBST), and visualized using a solution of 8 mg/mL 3-amino-9-ethylcarbazole in 50 mM sodium acetate with 0.00012% hydrogen peroxide for 15-45 minutes until foci were visible.

SDS-PAGE gels and immunoblotting

Cell pellets were lysed in RIPA buffer (50 mM Tris pH 7.5, 150 mM NaCl, 0.1% SDS, 1% Triton-X100, 0.5% sodium deoxycholate) supplemented with Roche cOmplete protease inhibitor. Cells were left on ice for 10 minutes, and lysate was cleared at 21.1xg for 20 minutes. Cleared lysate concentrations were normalized using Bio-Rad Protein Assay Dye, and normalized gel samples were separated by SDS-PAGE gel at 175V. Gels were transferred to PVDF membranes using mixed molecular weight settings on the TransBlot Turbo. Antibodies used are listed in **Table A4.1**.

Quantitative Polymerase Chain Reaction (qPCR)

RNA was isolated from cell samples or purified virus using the Zymo Quick RNA miniprep kit. cDNA was synthesized from 500ng cellular RNA or the maximum allowed purified virus RNA using random hexamer and oligo-dT primers from IDT and Promega M-MLV reverse transcriptase. Primers specific to DENV NS5 and GAPDH are listed in Table S1, and reactions were performed using BioRad iTaq Universal SYBR green supermix on a BioRad CFX qPCR instrument. Conditions used for amplification were 95°C, 2 minutes for initial denaturation followed by 45 cycles of 95°C/10s and 60°C/30s. A melting curve was generated in 0.5°C intervals from 65°C to 95°C. C_q values were generated by the BioRad CFX Maestro software. For cellular RNA, $\Delta\Delta C_q$ values were calculated after normalization of samples to GAPDH expression. For purified virus RNA, ΔC_q values were calculated.

Cell viability assays

Cell viability was determined using the Cell Titer Glo reagent from Promega. Huh7 cells were seeded into 96 well plates and treated with 100x dilutions of compound in culture media. 16 hours after treatment, media was removed, and cells were infected as noted earlier. Media was replaced 24 hours post infection, and 100 µL prepared Cell Titer Glo reagent was added. Luminescence was measured on a Synergy HT plate reader.

*Enrichment/competition of covalent protein targets with **147-20***

Huh7 cells were treated with DMSO, 3 µM **147-20**, 3 µM **147-20** and 9 µM **147**, or 3 µM **147-20** and 9 µM **263**. Cells were harvested 24 hours post-treatment and lysed as indicated above. Lysates were normalized to 1 mg/mL for click reactions. Click reactions contained lysate, 100 µM TAMRA desthiobiotin azide, 1.6mM BTTAA, 0.8mM copper sulfate (all purchased from Click Chemistry Tools), and 5mM sodium ascorbate and were run for 1 hour at 37°C under vigorous shaking. For detection, samples were prepared for and run on SDS-PAGE gels as described above. For enrichment, excess reagent was removed by chloroform/methanol/water precipitation (1:3:1) and protein pellets were washed with methanol before resuspension in 6M urea in 1% SDS. Samples were diluted in PBS and added to pre-washed streptavidin agarose beads.

Pulldowns were rotated for 1 hour at room temperature. Supernatants were removed and beads were washed 6x in PBS with 1% SDS. Bound proteins were eluted in 2 rounds of 50 mM biotin, pH 7.2 in 1% SDS in PBS for 10 minutes each.

Mass Spectrometry (MS) Sample Preparation

Samples from pulldowns were directly precipitated using chloroform/methanol/water (1:3:1) and protein pellets were washed twice in methanol. Dried samples were resuspended in 1% Rapigest (Waters). Proteins were reduced with 5mM TCEP in 0.5M HEPES, then alkylated with 10mM iodoacetamide. Proteins were digested overnight at 37°C with 0.5µg sequencing-grade trypsin (Thermo Scientific) while shaking. Peptides were labeled for 1 hour at room temperature with TMTpro reagents (Thermo Scientific) in 40% acetonitrile. Reactions were quenched for 1 hour with the addition of 0.4% ammonium bicarbonate. Samples were combined, acidified to pH 2 using approximately 5% formic acid. Collected samples were acidified using a SpeedVac and resuspended in 95% water/5% acetonitrile/0.1% formic acid and pH adjusted to 2 if necessary. Rapigest cleavage products were pelleted by centrifugation at 18,800xg for 45 minutes.

MS Data Acquisition

1/2 to 1/3 of each pulldown was loaded onto a triphasic column 1.5cm layers of 5 µm 100Å C18 resin, Luna 5 µm 100 Å strong cation exchange resin (both from Phenomenex), and a second layer of C18 resin using a high-pressure chamber. Loaded columns were washed in 95% water/5% acetonitrile/0.1% formic acid (buffer A) for 30 minutes prior to attachment to an Ultimate 3000 nano liquid chromatography system connected to a 20cm, 100µm inner diameter fused-silica microcapillary column with a laser-pulled tip filled with 3µM 100 Å C18 resin (Phenomenex). Data acquisition was carried out on a Thermo Exploris 480 instrument using multidimensional peptide identification technology (MuDPIT). Separation was performed using sequential 10µL injections of 0, 10, 20, 40, 60, 80, and 100% buffer C (500mM ammonium acetate, diluted in buffer A) followed by an injection of 90% buffer C/10% buffer A (100% acetonitrile/0,1% formic acid). Separation occurred over a 90 minute gradient from 4-40% buffer B, followed by a 5 minute

gradient of 40-80% buffer B. Electrospray ionization was performed from the tip of the microcapillary at 2.2kV with an ion transfer tube of 275°C. Data-dependent spectra were collected with a full scan from 375-1500 m/z at an orbitrap resolution of 120k and an AGC target of 100%. Tandem mass spectra were collected using a TopSpeed (3s) method from each full scan (dynamic exclusion 10s) using a HCD normalized collision energy of 36%, an isolation window of 0.4 m/z, an AGC target of 200%, a resolution of 30k with TurboTMT, and a fixed first mass of 110 m/z.

MS Data Analysis

Protein/peptide identification and reporter ion quantification were performed using Proteome Discoverer 2.4. Searches were carried out with SEQUEST using a SwissProt human proteome database (ID=9606) with DENV proteins added manually. The following parameters were used: 20ppm precursor mass tolerance, peptide length 6-144 amino acids, trypsin cleavage with a maximum of 2 missed cleavage points, static modifications of carbamidomethylation at C (+57.0215Da) and TMTpro at N-termini and K (+304.207Da), dynamic modification of oxidation at M (+15.995Da). Search results were filtered using Percolator with a false discovery rate of 0.01 (strict) and 0.05 (relaxed). A minimum of 2 peptides were required for protein ID. For quantification, unique and razor peptides were used and a co-isolation threshold of 50% was used. TMT intensities were not normalized prior to abundance ratio calculations. Intensities for individual proteins were calculated by summing the intensities of individual peptides. Fold enrichment is expressed as the log2 fold change of the abundance ratios between the pulldown and competition samples for the **147** and **263** competitions respectively.

Concentration and purification of flavivirus media

Virus was purified as previously described [27,45]. Briefly, virus-containing media was layered on 20% w/v sucrose and spun for 3 hours at 4°C, 167000xg. Media and sucrose layers were removed, virus pellet was air-dried and resuspended in 5 mM HEPES, pH 7.9.

4.5 References

(1) Bhatt, S.; Gething, P. W.; Brady, O. J.; Messina, J. P.; Farlow, A. W.; Moyes, C. L.; Drake, J. M.; Brownstein, J. S.; Hoen, A. G.; Sankoh, O.; Myers, M. F.; George, D. B.; Jaenisch, T.; William Wint, G. R.; Simmons, C. P.; Scott, T. W.; Farrar, J. J.; Hay, S. I. The Global Distribution and Burden of Dengue. *Nature* **2013**, *496* (7446), 504–507. https://doi.org/10.1038/nature12060.

(2) Messina, J. P.; Brady, O. J.; Golding, N.; Kraemer, M. U. G.; Wint, G. R. W.; Ray, S. E.; Pigott, D. M.; Shearer, F. M.; Johnson, K.; Earl, L.; Marczak, L. B.; Shirude, S.; Davis Weaver, N.; Gilbert, M.; Velayudhan, R.; Jones, P.; Jaenisch, T.; Scott, T. W.; Reiner, R. C.; Hay, S. I. The Current and Future Global Distribution and Population at Risk of Dengue. *Nat. Microbiol.* **2019**, *4* (9), 1508–1515. https://doi.org/10.1038/s41564-019-0476-8.

(3) Gubler, D. J. Dengue and Dengue Hemorrhagic Fever. *Clin. Microbiol. Rev.* **1998**, *11* (3), 480–496. https://doi.org/10.1128/CMR.11.3.480/ASSET/16E450CB-BFB4-4AC3-9FB6-BEA6B902602D/ASSETS/GRAPHIC/CM0380020005.JPEG.

(4) Guzman, M. G.; Alvarez, M.; Halstead, S. B. Secondary Infection as a Risk Factor for Dengue Hemorrhagic Fever/Dengue Shock Syndrome: An Historical Perspective and Role of Antibody-Dependent Enhancement of Infection. *Arch. Virol. 2013 1587* **2013**, *158* (7), 1445–1459. https://doi.org/10.1007/S00705-013-1645-3.

(5) Simmons, C. P.; Farrar, J. J.; Van Vinh Chau, N.; Wills, B. Dengue. *N. Engl. J. Med.* **2012**, *366* (15), 1423–1432. https://doi.org/10.1056/NEJMRA1110265/SUPPL_FILE/NEJMRA1110265_DISCLOSURES.PDF.

(6) Zhao, R.; Wang, M.; Cao, J.; Shen, J.; Zhou, X.; Wang, D.; Cao, J. Flavivirus: From Structure to Therapeutics Development. *Life* **2021**, *11* (7), 615. https://doi.org/10.3390/LIFE11070615.

(7) Obi, J. O.; Gutiérrez-Barbosa, H.; Chua, J. V; Deredge, D. J.; Gutiérrez-Barbosa, J. O. ; Chua, H. ;; Deredge, J. V. ; Current Trends and Limitations in Dengue Antiviral Research. *Trop. Med. Infect. Dis. 2021, Vol. 6, Page 180* **2021**, *6* (4), 180. https://doi.org/10.3390/TROPICALMED6040180.

(8) Steuer, C.; Gege, C.; Fischl, W.; Heinonen, K. H.; Bartenschlager, R.; Klein, C. D. Synthesis and Biological Evaluation of α-Ketoamides as Inhibitors of the Dengue Virus Protease with Antiviral Activity in Cell-Culture. *Bioorg. Med. Chem.* **2011**, *19* (13), 4067–4074. https://doi.org/10.1016/J.BMC.2011.05.015.

(9) Luo, D.; Vasudevan, S. G.; Lescar, J. The Flavivirus NS2B–NS3 Protease–Helicase as a Target for Antiviral Drug Development. *Antiviral Res.* **2015**, *118*, 148–158. https://doi.org/10.1016/J.ANTIVIRAL.2015.03.014.

(10) Lim, S. P.; Noble, C. G.; Seh, C. C.; Soh, T. S.; El Sahili, A.; Chan, G. K. Y.; Lescar, J.; Arora, R.; Benson, T.; Nilar, S.; Manjunatha, U.; Wan, K. F.; Dong, H.; Xie, X.; Shi, P. Y.; Yokokawa, F. Potent Allosteric Dengue Virus NS5 Polymerase Inhibitors: Mechanism of Action and Resistance Profiling. *PLOS Pathog.* **2016**, *12* (8), e1005737. https://doi.org/10.1371/JOURNAL.PPAT.1005737.

(11) Benmansour, F.; Trist, I.; Coutard, B.; Decroly, E.; Querat, G.; Brancale, A.; Barral, K. Discovery of Novel Dengue Virus NS5 Methyltransferase Non-Nucleoside Inhibitors by Fragment-Based Drug Design. *Eur. J. Med. Chem.* **2017**, *125*, 865–880.

https://doi.org/10.1016/J.EJMECH.2016.10.007.

(12) Duffy, S. Why Are RNA Virus Mutation Rates so Damn High? *PLOS Biol.* **2018**, *16* (8), e3000003. https://doi.org/10.1371/JOURNAL.PBIO.3000003.

(13) Lin, K.; Gallay, P. Curing a Viral Infection by Targeting the Host: The Example of Cyclophilin Inhibitors. *Antiviral Res.* **2013**, *99* (1), 68–77. https://doi.org/10.1016/J.ANTIVIRAL.2013.03.020.

(14) Kumar, N.; Sharma, S.; Kumar, R.; Tripathi, B. N.; Barua, S.; Ly, H.; Rouse, B. T. Host-Directed Antiviral Therapy. *Clin. Microbiol. Rev.* **2020**, *33* (3). https://doi.org/10.1128/CMR.00168-19/ASSET/155DF052-ACD0-479E-B444-67ABFB9E2044/ASSETS/GRAPHIC/CMR.00168-19-F0003.GIF.

(15) Perera, R.; Kuhn, R. J. Structural Proteomics of Dengue Virus. *Curr. Opin. Microbiol.* **2008**, *11* (4), 369–377. https://doi.org/10.1016/J.MIB.2008.06.004.

(16) Apte-Sengupta, S.; Sirohi, D.; Kuhn, R. J. Coupling of Replication and Assembly in Flaviviruses. *Curr. Opin. Virol.* **2014**, *9*, 134–142. https://doi.org/10.1016/J.COVIRO.2014.09.020.

(17) Braakman, I.; Hebert, D. N. Protein Folding in the Endoplasmic Reticulum. *Cold Spring Harb. Perspect. Biol.* **2013**, *5* (5), a013201. https://doi.org/10.1101/CSHPERSPECT.A013201.

(18) Marceau, C. D.; Puschnik, A. S.; Majzoub, K.; Ooi, Y. S.; Brewer, S. M.; Fuchs, G.; Swaminathan, K.; Mata, M. A.; Elias, J. E.; Sarnow, P.; Carette, J. E. Genetic Dissection of Flaviviridae Host Factors through Genome-Scale CRISPR Screens. *Nature* **2016**, *535* (7610), 159–163. https://doi.org/10.1038/nature18631.

(19) Lin, D. L.; Cherepanova, N. A.; Bozzacco, L.; Macdonald, M. R.; Gilmore, R.; Tai, A. W. Dengue Virus Hijacks a Noncanonical Oxidoreductase Function of a Cellular Oligosaccharyltransferase Complex. *MBio* **2017**, *8* (4). https://doi.org/10.1128/MBIO.00939-17/SUPPL_FILE/MBO004173397ST2.DOCX.

(20) Reid, D. W.; Campos, R. K.; Child, J. R.; Zheng, T.; Chan, K. W. K.; Bradrick, S. S.; Vasudevan, S. G.; Garcia-Blanco, M. A.; Nicchitta, C. V. Dengue Virus Selectively Annexes Endoplasmic Reticulum-Associated Translation Machinery as a Strategy for Co-Opting Host Cell Protein Synthesis. *J. Virol.* **2018**, *92* (7), 1766–1783. https://doi.org/10.1128/JVI.01766-17/SUPPL_FILE/ZJV007183404SD4.XLSX.

(21) Hafirassou, M. L.; Meertens, L.; Umaña-Diaz, C.; Labeau, A.; Dejarnac, O.; Bonnet-Madin, L.; Kümmerer, B. M.; Delaugerre, C.; Roingeard, P.; Vidalain, P. O.; Amara, A. A Global Interactome Map of the Dengue Virus NS1 Identifies Virus Restriction and Dependency Host Factors. *Cell Rep.* **2017**, *21* (13), 3900–3913. https://doi.org/10.1016/J.CELREP.2017.11.094.

(22) Peña, J.; Harris, E. Dengue Virus Modulates the Unfolded Protein Response in a Time-Dependent Manner. *J. Biol. Chem.* **2011**, *286* (16), 14226–14236. https://doi.org/10.1074/JBC.M111.222703/ATTACHMENT/26D81C6A-EC37-478A-8216-AE9671042F97/MMC1.PDF.

(23) Perera, N.; Miller, J. L.; Zitzmann, N. The Role of the Unfolded Protein Response in Dengue Virus Pathogenesis. *Cell. Microbiol.* **2017**, *19* (5), e12734. https://doi.org/10.1111/CMI.12734.

(24) Taguwa, S.; Maringer, K.; Li, X.; Bernal-Rubio, D.; Rauch, J. N.; Gestwicki, J. E.; Andino, R.; Fernandez-Sesma, A.; Frydman, J. Defining Hsp70 Subnetworks in Dengue Virus

Replication Reveals Key Vulnerability in Flavivirus Infection. *Cell* **2015**, *163* (5), 1108–1123. https://doi.org/10.1016/J.CELL.2015.10.046.

(25) Taguwa, S.; Yeh, M. Te; Rainbolt, T. K.; Nayak, A.; Shao, H.; Gestwicki, J. E.; Andino, R.; Frydman, J. Zika Virus Dependence on Host Hsp70 Provides a Protective Strategy against Infection and Disease. *Cell Rep.* **2019**, *26* (4), 906-920.e3. https://doi.org/10.1016/J.CELREP.2018.12.095.

(26) Puschnik, A. S.; Marceau, C. D.; Ooi, Y. S.; Majzoub, K.; Rinis, N.; Contessa, J. N.; Carette, J. E. A Small-Molecule Oligosaccharyltransferase Inhibitor with Pan-Flaviviral Activity. *Cell Rep.* **2017**, *21* (11), 3032–3039. https://doi.org/10.1016/J.CELREP.2017.11.054.

(27) Almasy, K. M.; Davies, J. P.; Lisy, S. M.; Tirgar, R.; Tran, S. C.; Plate, L. Small-Molecule Endoplasmic Reticulum Proteostasis Regulator Acts as a Broad-Spectrum Inhibitor of Dengue and Zika Virus Infections. *Proc. Natl. Acad. Sci. U. S. A.* **2021**, *118* (3). https://doi.org/10.1073/PNAS.2012209118/-/DCSUPPLEMENTAL.

(28) Gonzalez-Teuber, V.; Albert-Gasco, H.; Auyeung, V. C.; Papa, F. R.; Mallucci, G. R.; Hetz, C. Small Molecules to Improve ER Proteostasis in Disease. *Trends Pharmacol. Sci.* **2019**, *40* (9), 684–695. https://doi.org/10.1016/J.TIPS.2019.07.003.

(29) Njomen, E.; Tepe, J. J. Proteasome Activation as a New Therapeutic Approach To Target Proteotoxic Disorders. *J. Med. Chem.* **2019**, *62* (14), 6469–6481. https://doi.org/10.1021/ACS.JMEDCHEM.9B00101.

(30) Vilas, A.; Yuste-Checa, P.; Gallego, D.; Desviat, L. R.; Ugarte, M.; Pérez-Cerda, C.; Gámez, A.; Pérez, B. Proteostasis Regulators as Potential Rescuers of PMM2 Activity. *Biochim. Biophys. Acta - Mol. Basis Dis.* **2020**, *1866* (7), 165777. https://doi.org/10.1016/J.BBADIS.2020.165777.

(31) Davis, A. K.; Pratt, W. B.; Lieberman, A. P.; Osawa, Y. Targeting Hsp70 Facilitated Protein Quality Control for Treatment of Polyglutamine Diseases. *Cell. Mol. Life Sci.* **2019**, *77* (6), 977–996. https://doi.org/10.1007/S00018-019-03302-2.

(32) Hanrahan, J. W.; Sato, Y.; Carlile, G. W.; Jansen, G.; Young, J. C.; Thomas, D. Y. Cystic Fibrosis: Proteostatic Correctors of CFTR Trafficking and Alternative Therapeutic Targets. *Expert Opin. Ther. Targets* **2019**, *23* (8), 711–724. https://doi.org/10.1080/14728222.2019.1628948.

(33) Rius, B.; Mesgarzadeh, J. S.; Romine, I. C.; Paxman, R. J.; Kelly, J. W.; Wiseman, R. L. Pharmacologic Targeting of Plasma Cell Endoplasmic Reticulum Proteostasis to Reduce Amyloidogenic Light Chain Secretion. *Blood Adv.* **2021**, *5* (4), 1037–1049. https://doi.org/10.1182/BLOODADVANCES.2020002813.

(34) Blackwood, E. A.; Azizi, K.; Thuerauf, D. J.; Paxman, R. J.; Plate, L.; Kelly, J. W.; Wiseman, R. L.; Glembotski, C. C. Pharmacologic ATF6 Activation Confers Global Protection in Widespread Disease Models by Reprograming Cellular Proteostasis. *Nat. Commun.* **2019**, *10* (1), 1–16. https://doi.org/10.1038/s41467-018-08129-2.

(35) Plate, L.; Cooley, C. B.; Chen, J. J.; Paxman, R. J.; Gallagher, C. M.; Madoux, F.; Genereux, J. C.; Dobbs, W.; Garza, D.; Spicer, T. P.; Scampavia, L.; Brown, S. J.; Rosen, H.; Powers, E. T.; Walter, P.; Hodder, P.; Luke Wiseman, R.; Kelly, J. W. Small Molecule Proteostasis Regulators That Reprogram the ER to Reduce Extracellular Protein Aggregation. *Elife* **2016**, *5*. https://doi.org/10.7554/ELIFE.15550.

(36) Kinney, R. M.; Butrapet, S.; Chang, G.-J. J.; Tsuchiya, K. R.; Roehrig, J. T.;

Bhamarapravati, N.; Gubler, D. J. Construction of Infectious CDNA Clones for Dengue 2 Virus: Strain 16681 and Its Attenuated Vaccine Derivative, Strain PDK-53. *Virology* **1997**, *230* (2), 300–308. https://doi.org/10.1006/VIRO.1997.8500.

(37) Brinton, M. A. Replication of Flaviviruses. In *The Togaviridae and Flaviviridae*; Schlesinger, S., Schlesinger, M. J., Eds.; Springer: Boston, MA, 1986; pp 327--374.

(38) Paxman, R.; Plate, L.; Blackwood, E. A.; Glembotski, C.; Powers, E. T.; Wiseman, R. L.; Kelly, J. W. Pharmacologic ATF6 Activating Compounds Are Metabolically Activated to Selectively Modify Endoplasmic Reticulum Proteins. *Elife* **2018**, *7*. https://doi.org/10.7554/ELIFE.37168.

(39) Leung, D.; Hardouin, C.; Boger, D. L.; Cravatt, B. F. Discovering Potent and Selective Reversible Inhibitors of Enzymes in Complex Proteomes. *Nat. Biotechnol.* **2003**, *21* (6), 687–691. https://doi.org/10.1038/nbt826.

(40) Moellering, R. E.; Cravatt, B. F. How Chemoproteomics Can Enable Drug Discovery and Development. *Chem. Biol.* **2012**, *19* (1), 11–22. https://doi.org/10.1016/J.CHEMBIOL.2012.01.001.

(41) Palmer, J. E.; Brietske, B. M.; Bate, T. C.; Blackwood, E. A.; Garg, M.; Glembotski, C. C.; Cooley, C. B. Reactive Oxygen Species (ROS)-Activatable Prodrug for Selective Activation of ATF6 after Ischemia/Reperfusion Injury. *ACS Med. Chem. Lett.* **2020**, *11* (3), 292–297. https://doi.org/10.1021/ACSMEDCHEMLETT.9B00299/SUPPL_FILE/ML9B00299_SI_001.PDF.

(42) Sersen, F.; Gregan, F.; Kotora, P.; Kmetova, J.; Filo, J.; Loos, D.; Gregan, J. Synthesis and Free Radical Scavenging Activity of New Hydroxybenzylidene Hydrazines. *Molecules* **2017**, *22* (6), 894. https://doi.org/10.3390/MOLECULES22060894.

(43) Itoh, H.; Suzuta, T.; Hoshino, T.; Takaya, N. Novel Dehydrogenase Catalyzes Oxidative Hydrolysis of Carbon-Nitrogen Double Bonds for Hydrazone Degradation. *J. Biol. Chem.* **2008**, *283* (9), 5790–5800. https://doi.org/10.1074/JBC.M709027200/ATTACHMENT/2DB501A3-DB30-44BF-AECD-0E14C7287909/MMC1.PDF.

(44) Crabb, D. W.; Matsumoto, M.; Chang, D.; You, M. Overview of the Role of Alcohol Dehydrogenase and Aldehyde Dehydrogenase and Their Variants in the Genesis of Alcohol-Related Pathology. *Proc. Nutr. Soc.* **2004**, *63* (1), 49–63. https://doi.org/10.1079/PNS2003327.

(45) Jensen, S. M.; Nguyen, C. T.; Jewett, J. C. A Gradient-Free Method for the Purification of Infective Dengue Virus for Protein-Level Investigations. *J. Virol. Methods* **2016**, *235*, 125–130. https://doi.org/10.1016/J.JVIROMET.2016.05.017.

CHAPTER 5: Comparative multiplexed interactomics of SARS-CoV-2 and homologous coronavirus nonstructural proteins identifies unique and shared host-cell dependencies

This chapter is adapted, with permission from journal and co-authors, from Davies, J.P.*, Almasy, K.M.*, McDonald, E.F., and Plate L., *ACS Infectious Diseases,* **2020**, 6(12), 3174-3189.
*authors contributed equally

5.1 Introduction

Coronaviruses (CoVs) are positive single-stranded RNA viruses capable of causing human disease with a range of severity. While some strains, such as endemic hCoV-OC43, cause milder common-cold like symptoms, other strains are associated with more severe pathogenesis and higher lethality, including SARS-CoV-1 (emerged in 2002), MERS-CoV (in 2012), and most recently SARS-CoV-2, the causative agent of COVID-19[1,2]. Despite the relevance of CoVs for human health, our understanding of the factors governing their divergent pathogenicity remains incomplete. Pathogenicity may be mediated by a variety of factors, including different specificities and affinity for different cell surface receptors such as angiotensin-converting enzyme 2 (ACE2) for SARS-CoV-1 and SARS-CoV-2[1,3] or 9-*O*-acetylated sialic acid for hCoV-OC43[4]. CoV strains also engage a variety of host immune processes in infected cells. Pathogenic strains more strongly interfere with interferon I signaling[4,5] and induce apoptosis and pyroptosis[6–9]. Ensembles of virus-host protein-protein interactions (PPIs) orchestrate the reprogramming of these processes during infection.

Coronaviruses possess the largest known RNA viral genomes, approximately 30kbp in length. The 5’ 20 kb region of the genome encodes for two open reading frames (orf1a/1ab) that produce 16 non-structural proteins (nsp1-nsp16) needed to form the viral replication complex, while the 3’ proximal region encodes for the structural proteins and several accessory factors with varying roles (**Figure 5.1A**). Previous protein-protein interaction studies of individual CoV proteins have

shed light on their functions in the infected host cells and putative roles during pathogenesis. Yeast-two hybrid studies of coronavirus proteins have identified intraviral interactions[10] and interactions between nsp1 and immunophilins[11], and a proximity-labeling approach was used to determine host proteins concentrated in sites of replication[12].

Affinity purification-mass spectrometry (AP-MS) is a powerful tool to study virus-host interactions and has been used extensively to examine how viruses reorganize host cells[13–16]. A prior AP-MS study of SARS-CoV-1 nsp2 identified multiple host interactors including prohibitin 1/2 (PHB1/2)[17]. Most notably, Gordon et al. recently profiled host interactors for 26 SARS-CoV-2 proteins[18]. While these studies enabled important insight on individual viral protein functions, they focused on single CoV strains, limiting direct cross-strain comparisons.

Here, we sought to profile and compare the host interaction profiles of nsps from multiple hCoVs, namely hCoV-OC43, SARS-CoV-1, and SARS-CoV-2. Through comparative interactomics, we identify both conserved and unique interactors across various strains. Notably, quantitative analysis of interaction enrichment enables nuanced differentiation between shared interactions for each coronavirus protein. Through this approach we discovered both conserved and novel functions of viral proteins and the pathways by which they manipulate cellular processes. Comparisons across strains may also provide clues into the evolutionary arms race between virus and host proteins to hijack or protect protein-protein interfaces[19]**.** Additionally, identified host dependencies can potentially be exploited as targets for host-directed antiviral therapeutics.

In particular, we focus on the host interactors of nsp2 and nsp4. Nsp2 has been suggested to play a role in modifying the host cell environment, although its precise function remains unknown[17]. Nsp2 is dispensable for infection in SARS-CoV-1 [20] and has pronounced amino acid sequence differences across coronavirus strains (**Figure 5.1B, Figure A5.1A**). Additionally, early sequence analysis of SARS-CoV-2 identified regions of positive selection pressure in nsp2[21]. Given the variability of sequence across strains and the ambiguous function, a comparison of interaction profiles across strains can yield insights into the role of nsp2. In contrast, the role of nsp4, a

transmembrane glycoprotein, is better defined, most notably in formation of the double-membrane vesicles associated with replication complexes[22,23]. Unlike nsp2, nsp4 has a high degree of sequence similarity across human coronavirus strains (**Figure 5.1B, Figure A5.1B**).

In this study, we use affinity purification-proteomics to identify interactors of nsp2 from two human coronaviruses (SARS-CoV-1 and SARS-CoV-2) and interactors of nsp4 from three strains (OC43, SARS-CoV-1, and SARS-CoV-2). Quantitative comparative analysis of nsp2 interactors identifies common protein binding partners, including the ERLIN1/2 complex and prohibitin complex involved in regulation of mitochondrial function and calcium flux at ER-mitochondrial contact sites. We also identify overlapping nsp4 interactors, including *N*-linked glycosylation machinery, UPR associated factors, and anti-viral innate immune signaling proteins. Unique interactors of different nsp4 homologs include E3 ubiquitin ligase complexes for SARS-CoV-1, and ER homeostasis factors for SARS-CoV-2. In particular, we found nsp2 and nsp4 interactors are strongly enriched for mitochondria-associated ER membranes (MAM) factors, suggesting a potential mechanism to affect calcium homeostasis and other host processes at these organelle contact sites.

5.2 Results

5.2.1 Design and validation of expression of CoV nsp2 and nsp4 constructs for affinity purification

The two main open reading frames of the CoV viral genome, orf1a and orf1ab, encode for 16 non-structural proteins which perform a variety of tasks during the infection cycle (**Figure 5.1A**). We focus our analysis on two of these proteins, nsp2 and nsp4. Nsp2 is a less functionally-well understood protein with less than 70% amino acid sequence identity between the SARS-CoV-1 and SARS-CoV-2 homologs (**Figure 5.1B, Figure A5.1A**). Nsp4 is a component of the CoV replication complex that is 80% identical between SARS strains, but only 42% between SARS and OC43 strains, a less clinically severe human CoV (**Figure 5.1B, Figure A5.1B**).

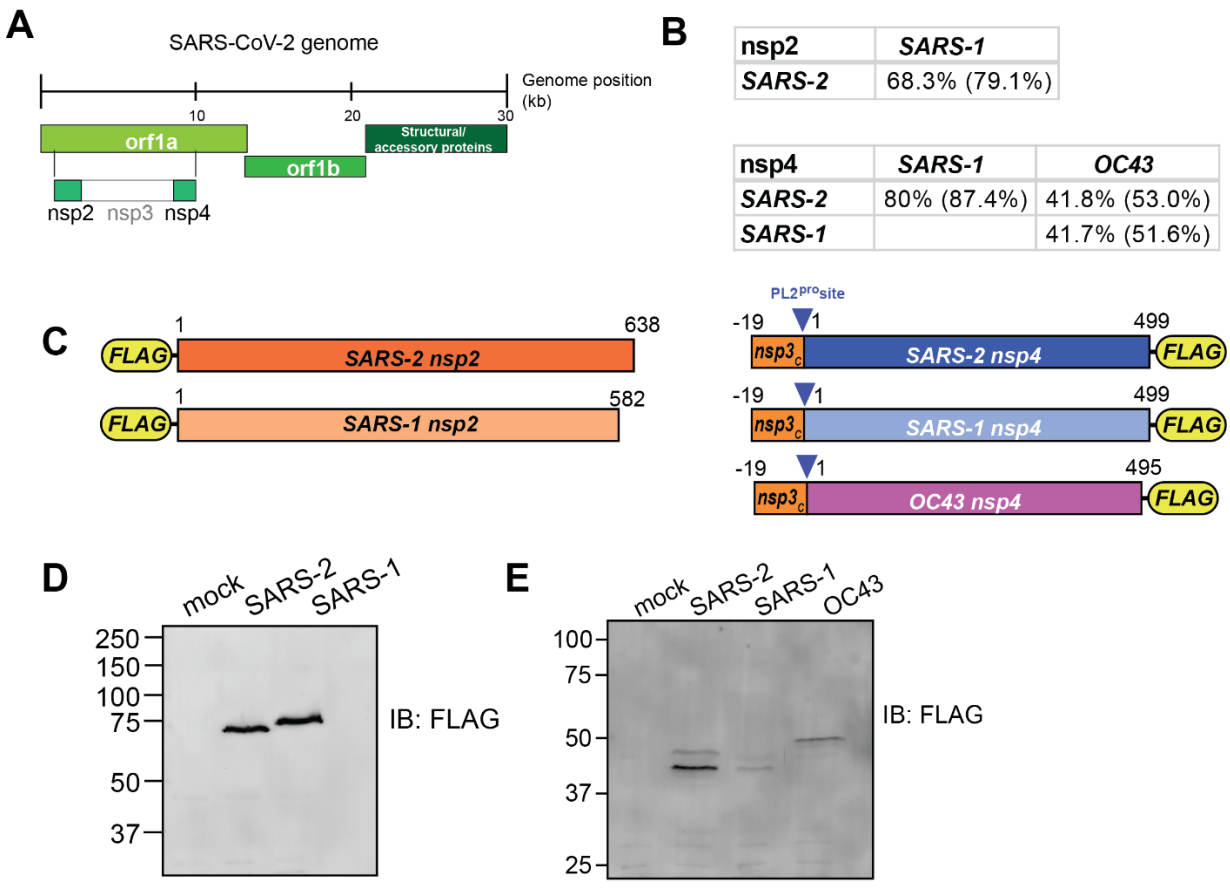

Figure 5.1. Design and validation of expression of CoV nsp2 and nsp4 constructs for affinity purification.
(A) Schematic of SARS-CoV-2 genome organization.
(B) Amino acid sequence identity and similarity (in parentheses) for comparisons of nsp2 and nsp4 homologs. Sequence alignments are shown in Figure S1A-B.
(C) Nsp2 and nsp4 FLAG-tagged construct designs. Nsp2 constructs contain an N-terminal FLAG-tag. Nsp4 constructs contain a 19 amino acid leader sequence from nsp3 at the N-terminus, including the $PL2^{pro}$ cleavage site, along with a C-terminal FLAG-tag.
(D-E) Western blot of nsp2 and nsp4 homologs expressed in HEK293T cells. Cells were transiently transfected with FLAG-nsp2 (D) or nsp4-FLAG (E). Proteins were detected using an anti-FLAG antibody.

To compare the virus-host protein-protein interactions of nsp2 and nsp4 across multiple CoV strains, we designed FLAG-tagged expression constructs for affinity purification (**Figure 5.1C**). SARS-CoV-1 and SARS-CoV-2 nsp2 constructs contain an N-terminal FLAG-tag, while the SARS-CoV-1, SARS-CoV-2, and OC43 nsp4 constructs contain a C-terminal FLAG-tag. In addition, nsp4 constructs contain a 19 amino acid leader sequence corresponding to the C-

terminus of nsp3, which includes the nsp3-PL2^{pro} cleavage site necessary for proper nsp4 translocation into the ER membrane as has been shown previously[24,25]. Improper membrane insertion would likely alter the observed interactome as compared to the native state.

Protein constructs were transiently transfected into HEK293T cells and proteins were detected by immunoblotting for the FLAG-tag. While HEK293T cells are not representative of the primary physiological target tissue, these cells are permissive to infection, and were able to recapitulate strong interactors expected in lung tissue in a prior SARS-CoV-2 interactome study[18]. The nsp2 constructs were detectable as a single protein band at the expected molecular weight **(Figure 5.1D**), while nsp4 constructs displayed two distinct bands at a lower size than its expected molecular weight (**Figure 5.1E**). This lower apparent molecular weight was previously reported and the different bands likely correspond to different glycosylation states[18]. To ensure nsp4 is expressed fully and the detected products do not correspond to a truncated protein, we immunopurified the protein using FLAG-agarose beads and analyzed the purified protein by LC-MS. We detected peptide fragments spanning the N- and C-termini with overall sequence coverage of up to 62% (**Figure A5.1C-E**) confirming expression of the full proteins.

5.2.2 Affinity purification-mass spectrometry identifies nsp2 interactors

To identify host cell interaction partners of the distinct CoV non-structural proteins, we employed an affinity purification-mass spectrometry workflow (**Figure 5.2A**). The protein constructs were expressed in HEK293T cells, gently lysed in mild detergent buffer, and co-immunopurified from whole cell lysates using anti-FLAG agarose beads. Virus-host protein complexes were then reduced, alkylated, and trypsin digested. Importantly, we used tandem mass tag (TMT)-based multiplexing using TMTpro 16plex or TMT11plex for relative quantification of protein abundances. For this purpose, 4–6 co-immunoprecipitation (Co-IP) replicates for respective nsp2 homologs were pooled into a single MS run. Co-IPs from mock GFP transfected cells were included to differentiate non-specific background proteins (**Figure 5.2B**). Overall, the data set included three

individual MS runs containing 34 co-IP (SARS-CoV-2 n = 13; SARS-CoV-1 n = 9; GFP (mock) n = 12) (**Figure A5.2A**).

We first determined interactors of the individual nsp2 homologs by comparing the log-transformed TMT intensity differences for prey proteins between bait and GFP samples (**Figure 5.2C-D**). We optimized variable cutoffs for high- and medium-confidence interactors based on their magnitude of enrichment compared to the GFP samples and confidence as defined by adjusted p-values (**Figure 5.2C-D, Figure A5.2B-C**). Using the most stringent cutoff, we identified 6 and 11 high-confidence interactors for SARS-CoV-2 and SARS-CoV-1 nsp2 respectively (**Figure 5.2C-D**). Including medium-confidence interactors, we identified 20 nsp2 interactors for each homolog, including four overlapping proteins, ERLIN1, ERLIN2, RNF170, and TMEM199 (**Figure 5.2E**).

Gene enrichment analysis shows nsp2 interactors are involved in a number of host cell processes, including metabolic processing and transport (**Figure A5.3A**). A number of these interactors are membrane-associated proteins in the ER and nucleus (**Figure A5.3B**). Detailed comparisons of gene set enrichments for individual nsp2 homologs revealed several pathways preferentially enriched for SARS-CoV-1, such as mitochondrial calcium ion transport, protein deacetylation, and negative regulation of gene expression (**Figure A5.3C**). We confirmed by immunofluorescence that SARS-CoV-1 and SARS-CoV-2 nsp2 are largely localized perinuclear and co-localize partially with the ER marker PDIA4 (**Figure A5.3D**).

To validate our findings, we cross referenced our data set with previous coronavirus interactomics studies. A prior study of SARS-CoV-1 nsp2 identified 11 host interactors, five of which overlap with our SARS-CoV-1 list, including GIGYF2, PHB, PHB2, STOML2, and EIF4E2[17]. We also cross referenced our interactors with a recently published SARS-CoV-2 interactomics data set[18]. Interestingly, we identified 18 new interactors, though several of these share secondary interactions with the proteins identified by Gordon et al. (**Figure A5.4**). In addition, we cross referenced our host interactor data set with tissue- and cell line-specific protein expression data

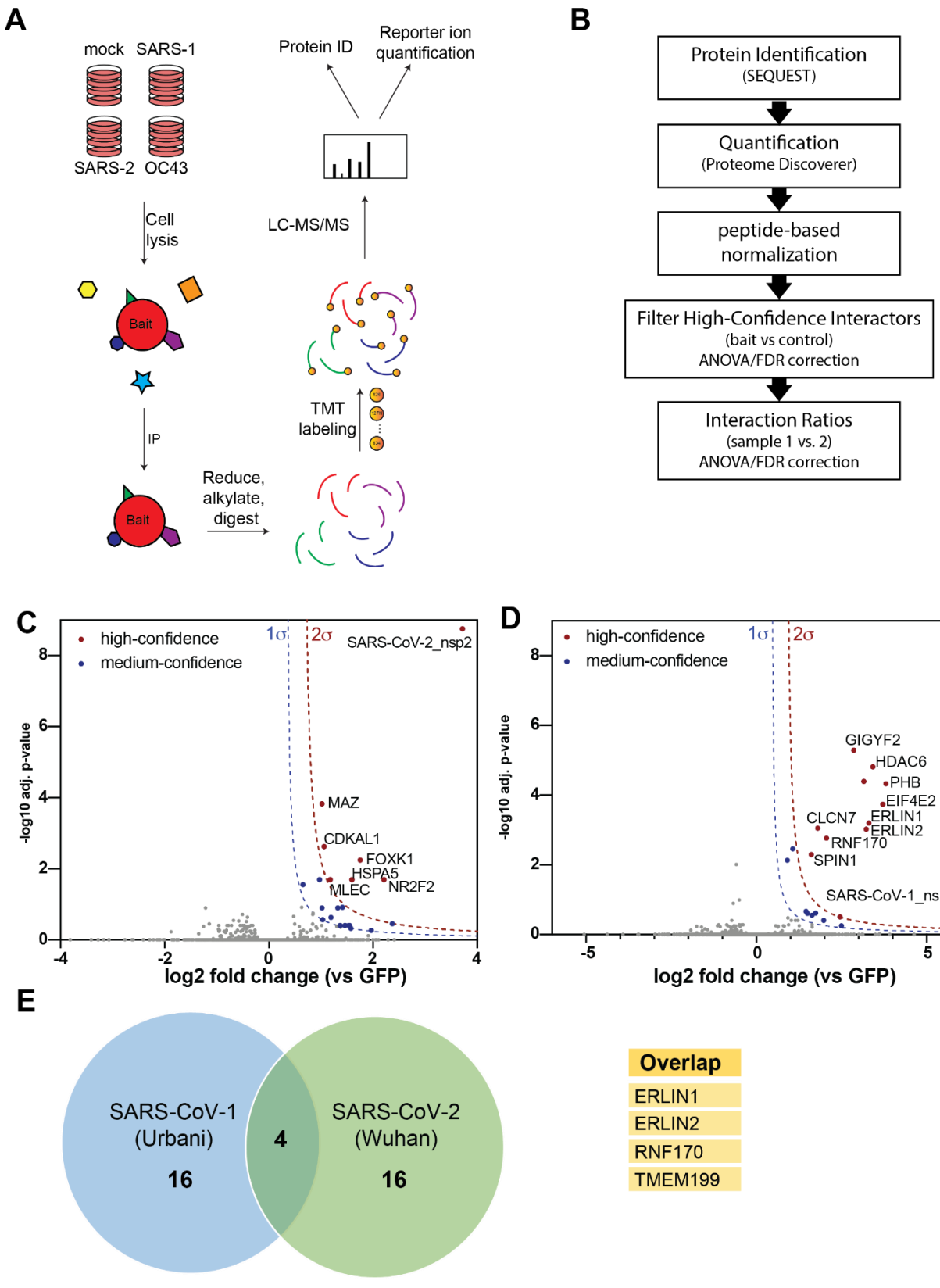
A
mock
SARS-1
SARS-2
OC43
Cell lysis
Bait
IP
Bait
Reduce, alkylate, digest
TMT labeling
LC-MS/MS
Protein ID
Reporter ion quantification
B
Protein Identification
(SEQUEST)
Quantification
(Proteome Discoverer)
peptide-based normalization
Filter High-Confidence Interactors
(bait vs control)
ANOVA/FDR correction
Interaction Ratios
(sample 1 vs. 2)
ANOVA/FDR correction
C
high-confidence
medium-confidence
1σ
2σ
SARS-CoV-2_nsp2
MAZ
CDKAL1
FOXK1
HSPA5
MLEC
NR2F2
-log10 adj. p-value
log2 fold change (vs GFP)
D
high-confidence
medium-confidence
1σ
2σ
GIGYF2
HDAC6
PHB
EIF4E2
CLCN7
ERLIN1
ERLIN2
RNF170
SPIN1
SARS-CoV-1_nsp2
-log10 adj. p-value
log2 fold change (vs GFP)
E
SARS-CoV-1
(Urbani)
16
4
SARS-CoV-2
(Wuhan)
16
Overlap
ERLIN1
ERLIN2
RNF170
TMEM199

Figure 5.2. Affinity purification-mass spectrometry identifies nsp2 interactors.
(A) General AP-MS workflow to quantitatively determine interactors of viral nsp homolog. HEK293T cells are transfected with FLAG-tagged expression constructs of nsps as bait or GFP (mock) and lysed. Bait proteins are immunoprecipitated (IP) along with interacting proteins, reduced, alkylated, and tryptic digested. Peptides are then tandem-mass tag (TMT) labeled, pooled, and analyzed by LC-MS/MS for identification and quantification.
(B) Data processing workflow. Peptide spectra are identified and matched to corresponding proteins (SEQUEST HT), then quantified based on TMT reporter ion intensity (Proteome Discoverer 2.4). High confidence interactors are filtered by comparing bait vs control. Interaction ratios between bait homologs are determined (log2 fold change) and adjusted p-value calculated using ANOVA.
(C-D) Volcano plot of SARS-CoV-2 nsp2 (C) and SARS-CoV-1 nsp2 (D) datasets to identify medium- and high-confidence interactors. Plotted are log2 TMT intensity fold changes for proteins between nsp2 bait channels and GFP mock transfections versus -log10 adjusted p-values. Curves for the variable cutoffs used to define high-confidence (red) or medium confidence (blue) interactors are shown. $1\sigma = 0.5$ for (C), $1\sigma = 0.43$ for (D).
(E) Venn diagram comparing high-confidence interactors between nsp2 homologs. Sixteen unique proteins were identified each, while four proteins overlapped both data sets (listed in adjacent table).

sets to determine interactor expression levels in tissues associated with primary infection (**Figure A5.5**)[26–28]. We find that expression of identified interactors is enriched in lung and upper aerodigestive tissues in multiple proteomics datasets, confirming the relevance of these factors to coronavirus tropism.

5.2.3 Quantitative comparison of SARS-CoV-1 and SARS-CoV-2 interactors

Apart from determining nsp2 host cell interactors, we sought to understand to what degree interactions vary between SARS-CoV-1 and SARS-CoV-2. Our multiplexed analysis enabled direct comparison of TMT intensities between the SARS-CoV-1 and SARS-CoV-2 nsp2 Co-IPs (Figure 5.3A). We validated that nsp2 bait levels are largely invariable across the replicates, enabling the direct comparison of prey protein intensities (Figure A5.2D). We find a subset of interactors are clearly enriched for SARS-CoV-1, including GIGYF2, HDAC8, EIF432, and PHB2 (Figure 5.3A). In contrast, several other interactors are enriched more strongly for SARS-CoV-2, for instance FOXK1 and NR2F2.

We performed unbiased hierarchical clustering of the enrichment intensities to group the nsp2 interactors in an unbiased way. This analysis yielded four distinct clusters. Clusters 1 and 2 contained shared interactors between SARS-CoV-1 and SARS-CoV-2 nsp2. On the other hand, clusters 3 and cluster 4 contained proteins that bound exclusively to either SARS-CoV-2 or SARS-CoV-1, respectively (**Figure 5.3B**). To better visualize the relationship between shared and unique nsp2 interactors, we constructed a network plot (**Figure 5.3C**). We also included experimentally validated secondary interactions from the STRING database to group shared and unique interactors into functionally relevant subclusters.

Several of these subclusters are shared between SARS-CoV-1 and SARS-CoV-2 nsp2, for instance one including STOML2, PHB, PHB2, VDAC2. These proteins were previously shown to interact and upregulate formation of metabolically active mitochondrial membranes[29]. Another subcluster involves ERLIN1, ERLIN2, and RNF170, which form a known complex regulating ubiquitination and degradation of inositol 1,4,5-triphosphate receptors (IP_3Rs), which in turn are channels regulating Ca^{2+} signaling from the ER to the mitochondria. Consistent with this, we detect mitochondrial calcium ion transmembrane transport as one of the unique biological processes associated with SARS-CoV-1 nsp2, but not SARS-CoV-2 (**Figure A5.3C**). Interestingly, ERLIN1 and ERLIN2 show stronger interactions with SARS-CoV-1 nsp2 than with SARS-CoV-2, indicating some strain-specific preference, which was confirmed by western blot analysis of homolog co-IPs (**Figure A5.6A**). Additional shared interactors include a subunit of the vacuolar ATPase (ATP6AP1) and a regulatory protein (TMEM199), supporting a common role for nsp2 to influence lysosomal processes. Finally, we observe one cytosolic and one ER-resident Hsp70 chaperone (HSPA8, HSPA5) as shared interactors, highlighting their role in nsp2 folding and biogenesis. Unique SARS-CoV-2 interactors include FOXK1 and NR2F2, both of which are anti-viral transcription factors induced in response to other viruses[30,31]. We also observe an exonuclease regulator of endosomal nucleic acid sensing (PLD3)[32], a transcription factor associated with the influenza humoral response (MAZ)[33,34], and a DNA-binding protein implicated

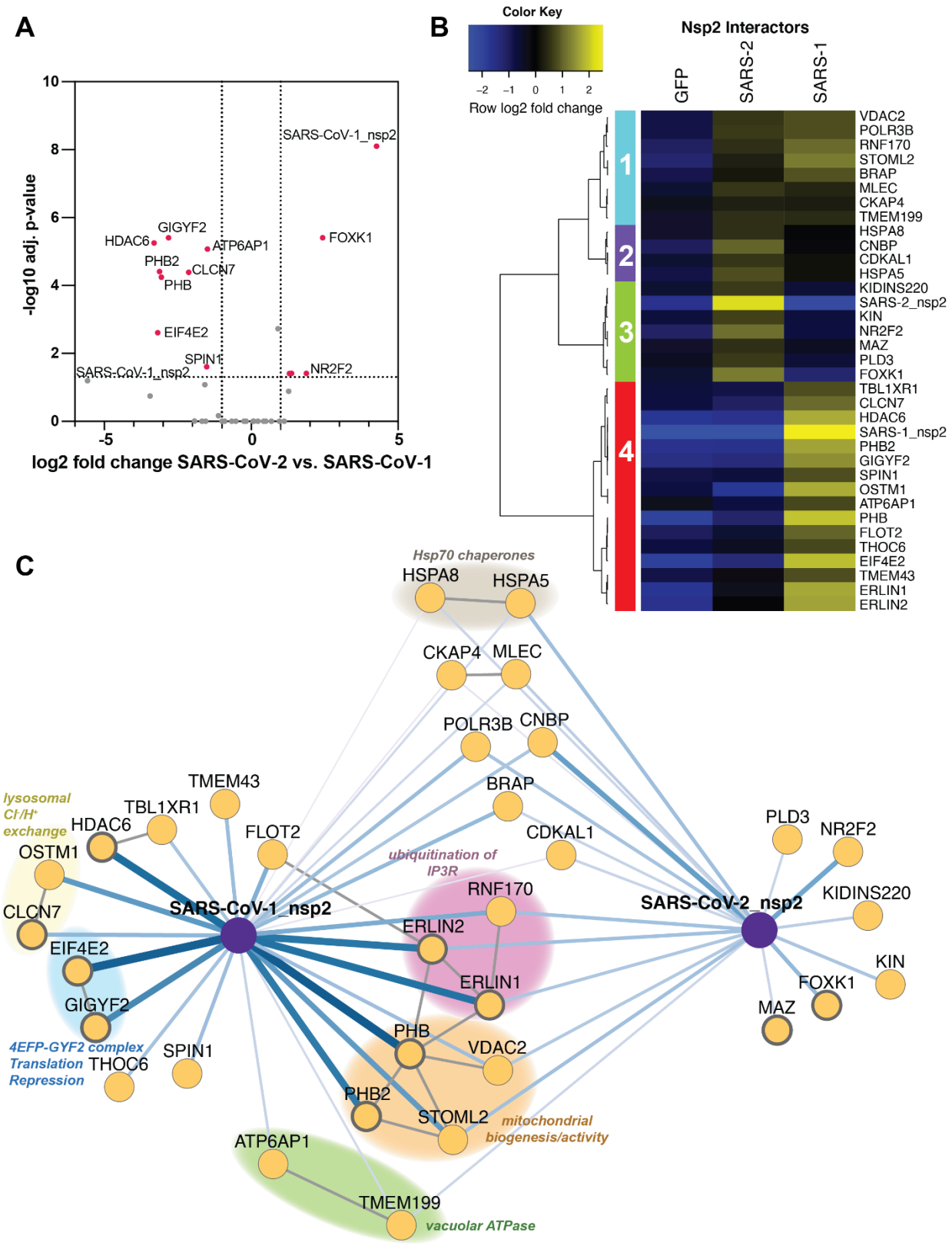
A
-log10 adj. p-value
log2 fold change SARS-CoV-2 vs. SARS-CoV-1
SARS-CoV-1_nsp2
FOXK1
GIGYF2
HDAC6
ATP6AP1
PHB2
CLCN7
PHB
EIF4E2
SPIN1
NR2F2
B
Color Key
Row log2 fold change
Nsp2 Interactors
GFP
SARS-2
SARS-1
VDAC2
POLR3B
RNF170
STOML2
BRAP
MLEC
CKAP4
TMEM199
HSPA8
CNBP
CDKAL1
HSPA5
KIDINS220
SARS-2_nsp2
KIN
NR2F2
MAZ
PLD3
FOXK1
TBL1XR1
CLCN7
HDAC6
SARS-1_nsp2
PHB2
GIGYF2
SPIN1
OSTM1
ATP6AP1
PHB
FLOT2
THOC6
EIF4E2
TMEM43
ERLIN1
ERLIN2
C
Hsp70 chaperones
HSPA8
HSPA5
CKAP4
MLEC
POLR3B
CNBP
BRAP
CDKAL1
TMEM43
TBL1XR1
HDAC6
FLOT2
lysosomal Cl-/H+ exchange
OSTM1
CLCN7
EIF4E2
GIGYF2
4EFP-GYF2 complex Translation Repression
THOC6
SPIN1
SARS-CoV-1_nsp2
ubiquitination of IP3R
RNF170
ERLIN2
ERLIN1
PHB
VDAC2
PHB2
STOML2
mitochondrial biogenesis/activity
ATP6AP1
TMEM199
vacuolar ATPase
SARS-CoV-2_nsp2
PLD3
NR2F2
KIDINS220
KIN
FOXK1
MAZ

Figure 5.3. Quantitative comparison of SARS-CoV-1 and SARS-CoV-2 nsp2 interactors.
(A) Volcano plot comparing interactions between nsp2 homolog from SARS-CoV-1 and SARS-CoV-2. Only high- and medium confidence interactors of nsp2 are shown. Highlighted proteins meet the filter criteria of adjusted p-value <0.05 and | log2 fold change | >1.
(B) Heatmap comparing the enrichment of SARS-CoV-1 and SARS-CoV-2 nsp2 interactors compared to GFP control. log2 fold change is color-coded and centered by row (blue low, yellow high enrichment). Hierarchical clustering using Ward's method shown on the left was carried out on euclidean distances of log2 fold changes scaled by row. Clusters 1 and 2 corresponds to shared interactors of SARS-CoV-1 and -2 nsp2, while cluster 3 and 4 for are unique interactors for SARS-CoV-2 and SARS-CoV-1 nsp2, respectively.
(C) Protein-protein interaction (PPI) network map of nsp2 homologs. Blue lines indicate viral-host PPIs, where line width corresponds to fold enrichment compared to the GFP control. Grey lines indicate annotated host-host PPIs in STRING (score >0.75). Groups of interactors with a common functional role are highlighted.

in B cell class switching (KIN or KIN17)[35]. In contrast, the list of unique SARS-CoV-1 interactors includes components of the 4EFP-GYF2 translation repression complex (GYGYF2, EIF4E2), lysosomal ion channels involved in chloride/proton ion exchange (CLCN7, OSTM1), and the cytosolic histone deacetylase 6 (HDAC6). While SARS-CoV-1 interactors GIGYF2 and EIF4E2 were also identified in the recent SARS-CoV-2 nsp2 dataset[18], it is clear from our quantitative comparison that enrichment of this complex with SARS-CoV-2 nsp2 is much weaker than with SARS-CoV-1 nsp2.

5.2.4 Comparative profiling of CoV nsp4 interactions

We extended our comparative analysis of host cell interactors to another CoV non-structural protein nsp4 involved in the replication complex. We applied the same AP-MS workflow used to identify nsp2 interactors (**Figure 5.2A**). In addition to SARS-CoV-1 and SARS-CoV-2 nsp4, we also included the hCoV-OC43 nsp4 construct. With this addition, we sought to probe the protein-protein interactions that differentiate strains causing severe pathogenesis versus non-severe. To this end, four co-immunoprecipitation replicates of respective nsp4 homologs were pooled into a single MS run, along with mock GFP transfected cells to differentiate non-specific background

proteins (**Figure 5.2B**). The full data set included three individual MS runs, containing 40 Co-IPs (SARS-CoV-2 n = 12; SARS-CoV-1 n = 8; OC43 = 8; GFP (mock) n = 12) (**Figure A5.7A**).

As previously described, we optimized variable cutoffs for high- and medium-confidence interactors based on their magnitude enrichment compared to GFP samples (**Figure 5.4A, Figure A5.7B-C**). We identified 29, 20, and 13 high-confidence interactors for SARS-CoV-2, SARS-CoV-1, and OC43 respectively using the most stringent cutoff. Including medium-confidence interactors, we identified 86, 126, and 93 nsp4 interactors for SARS-CoV-2, SARS-CoV-1, and OC43 nsp4 homologs respectively. Comparisons of high-confidence interactors yielded 17 shared interactors between all strains (**Figure 5.4B**) or 30 medium-confidence shared interactions (**Figure A5.7D**).

Similarly to our analysis of nsp2, we compared our data set with previously published nsp4 interactomics data, including the recently published study of the SARS-CoV-2 interactome[18], and find there is relatively little overlap between our identified SARS-CoV-2 nsp4 interactors and published nsp4 interactomics data (**Figure A5.8**). This discrepancy could be attributed to the nsp4 constructs in our study including the N-terminal residues of nsp3, which were added to ensure proper localization and prevent the hydrophobic N-terminal region of nsp4 to serve as signal sequence[24]. For further validation, we determined interactor expression levels in human tissues and find interactors are enriched in tissues relevant to coronavirus tropism (**Figure A5.5**)[26–28].

Analysis of GO-terms associated with the nsp4 interactors showed multiple enriched biological processes, such as cell organization and biogenesis, transport, and metabolic processes (**Figure A5.9A**). Interestingly, several shared SARS nsp4 interactors are associated with cell death, cellular communication, and cell differentiation. Shared interactors of all three strains are predominantly ER-membrane associated proteins, while many SARS-CoV-1 and OC43 specific interactors are annotated as nuclear-localized (**Figure A5.9B**). Comparisons of gene set enrichment analysis between strains indicate the ERAD pathway is significantly enriched for in STRING (score >0.75). Groups of interactors with a common functional role are highlighted.

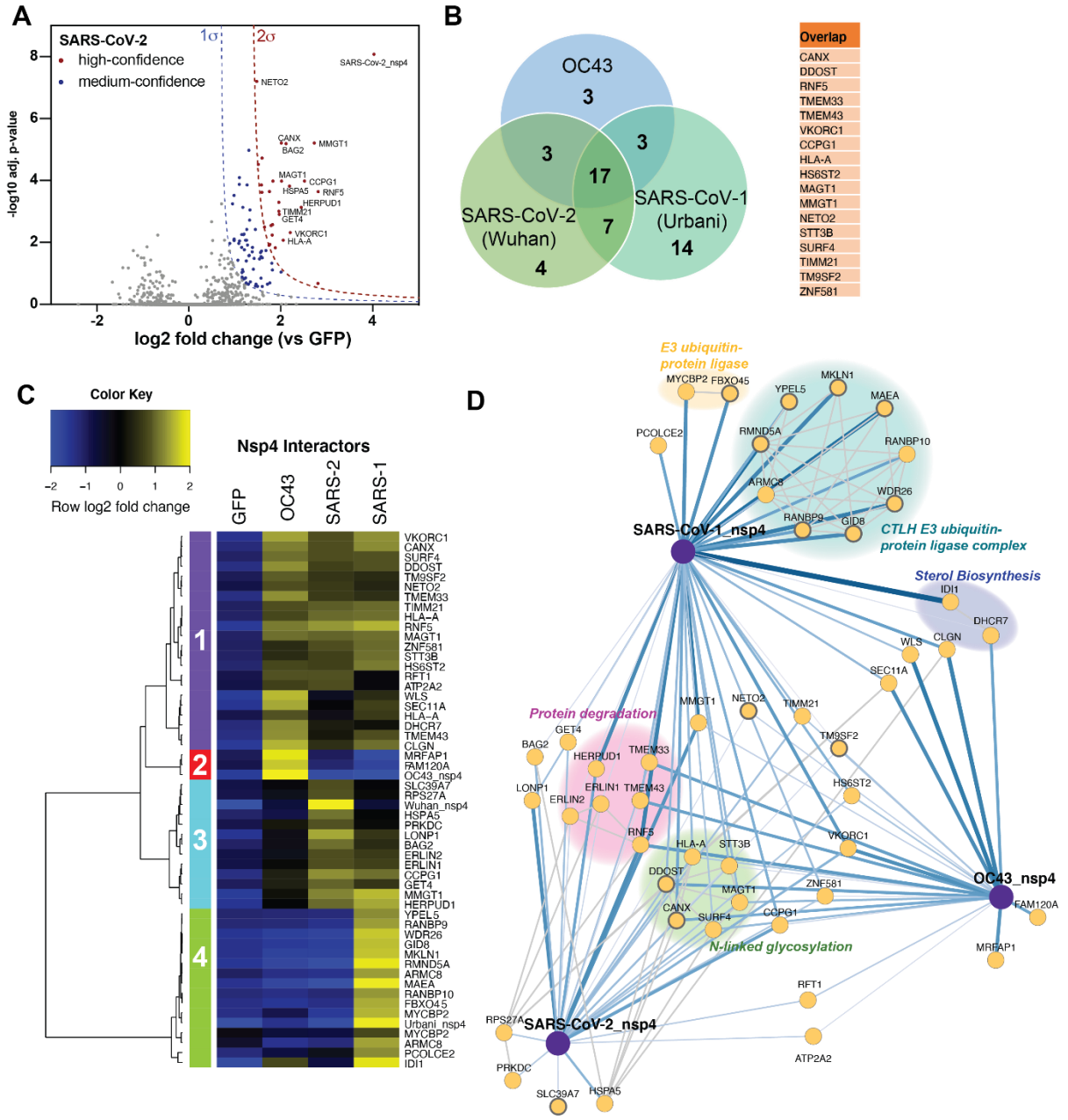

Figure 5.4. Comparative profiling of nsp4 interactions.

(A) Volcano plot of the SARS-CoV-2 nsp4 datasets to identify medium- and high-confidence interactors. Plotted are log2 TMT intensity differences for proteins between nsp4 bait channels and GFP mock transfections versus -log10 adjusted p-values. Curves for the variable cutoffs used to define high-confidence (red) or medium confidence (blue) interactors are shown. 1σ = 0.66. Equivalent volcano plot for SARS-CoV-1 and OC43 nsp4 are shown in Figure S5B-C.
(B) Venn diagram of interactors from nsp4 homologs. Overlapping nsp4 interactors between all strains are listed in the adjacent table.

(C) Heatmap comparing the enrichment of interactors for the different nsp4 homologs. log2 fold change is color-coded and centered by row (blue low, yellow high enrichment). Hierarchical clustering using Ward's method shown on the left was carried out on euclidean distances of log2 fold changes scaled by row. Clusters 1 corresponds to shared interactors of SARS-CoV-1, -2, and OC43 nsp4. Cluster 2, and 4 contain unique interactors for OC43 and SARS-CoV-1 nsp4, respectively, while cluster 3 contains shared interactors of SARS-CoV-1 and SARS-CoV-2.
(D) Protein-protein interaction (PPI) network map of interactors of nsp4 homolog. Blue lines indicate measured viral-host PPIs, where line width corresponds to fold enrichment compared to the GFP control. Grey lines indicate annotated host-host PPIs.

SARS strains, most strongly for SARS-CoV-1 (**Figure A5.9C**). Ubiquitin-dependent protein catabolic processes and ER mannose trimming are also strongly enriched for SARS-CoV-1. In general, processes strongly enriched for SARS-CoV-1 are less enriched for SARS-CoV-2, and to an even lesser extend for OC43.

Our multiplexed analysis of nsp4 homolog Co-IPs enabled direct comparison across strains (**Figure A5.10A-C**). We validated that nsp4 bait levels were mostly similar across replicates, allowing for direct comparison of bait protein intensities (**Figure A5.10D**). Unbiased hierarchical clustering of enrichment intensities to group nsp4 interactors yielded four distinct clusters. Clusters 1 contained common interactors of all nsp4 homologs (**Figure 5.4C**), while cluster 3 contains shared interactors of SARS-CoV-2, SARS-CoV-1 nsp4 that displayed weaker enrichment with OC43. In contrast, cluster 2 and 4 contained unique interactors enriched for OC43 and SARS-CoV-1 nsp4, respectively. To visualize functionally relevant subclusters of shared and unique nsp4 interactors, we constructed a network plot, including high-confidence interactions (score >0.75) from the String database (**Figure 5.4D**). Inclusion of all median-confidence interactors of the nsp4 homologs yielded a similar clustering and network organization (**Figures A5.10E, A5.11**).

We identified several common interactors across all three nsp4 homologs. These include components of UPR signaling (TMEM33) and ER-phagy (CCPG1). We also identify RNF5, an ER-localized E3 ubiquitin ligase known to modulate anti-viral innate immune signaling[36,37], and

VKORC1, which reduces Vitamin K, a key cofactor for several coagulation factor proteins[38]. Not surprisingly, given that nsp4 is a glycosylated protein, we also identify several members of the *N*-linked glycosylation machinery (STT3B, MAGT1, CANX, DDOST) (**Figure 5.4D**) in all three strains.

We identified several shared interactors between SARS-CoV-1 and SARS-CoV-2 that were absent in OC43. These include the ERLIN1/2 complex, LONP1, HERPUD1, GET4, and BAG2, all of which are involved in a facet of ER homeostasis, proteostasis or trafficking (**Figure 5.4D**). We validated the interactions of nsp4 constructs with ERLIN2 and CANX by Co-IP, and confirmed that ERLIN2 enriches significantly more strongly with SARS-CoV-1 and -2 compared to OC43, while CANX interacts with all three homologs (**Figure S6A**). The ERLIN1/2 complex was also identified in the nsp2 data set (**Figure 5.3B-C**) and shows comparable enrichment values between SARS-CoV-1 and SARS-CoV-2. Interestingly, the other four overlapping interactors all exhibit increased enrichment for SARS-CoV-2 versus SARS-CoV-1. LONP1 is a mitochondrial peptidase responsible for removing the majority of damaged mitochondrial proteins via proteolysis. The unfolded protein response (UPR) induces HERPUD1 expression, which is involved in the ER-associated degradation pathway (ERAD) to maintain ER homeostasis [39]. BAG2 serves as a co-chaperone for HSP70 chaperones, acting as a nucleotide exchange factor to regulate chaperone-client interactions through modulating HSP70 ATPase rates [40], while GET4 is part of a complex driving trafficking of tail-anchored proteins to the ER [41].

We observed shared interactors between OC43 and SARS-CoV-2, such as the *N*-glycosylation factor RFT1 [42,43] and a sarcoplasmic/endoplasmic reticulum calcium ATPase (SERCA – ATP2A2)[44]. In addition, we identified shared interactors between OC43 and SARS-CoV-1, including a regulator of UPR-mediated apoptosis (WLS or GPR177)[45], a member of the signal peptidase complex (SEC11A) [46], and factors involved in cholesterol synthesis (IDI1, DHCR7)[47–50]. WLS, SEC11A, and DHRC7 exhibited higher enrichment for OC43, whereas IDI1 was more

greatly enriched for SARS-CoV-1. Consistent with this observation, we identified sterol metabolic process as one of the unique processes enriched for OC43 nsp4.

In addition to shared interactors, we found several unique interactors for SARS-CoV-2, including the monoubiquitin-ribosomal fusion protein (RPS27A), a Golgi/ER-resident zinc receptor that has been shown to regulate TNF receptor trafficking and necroptosis (SLC39A7), and the ER-resident Hsp70 chaperone BiP (HSPA5). The latter two play distinct roles in regulating ER homeostasis and proteostasis. In contrast, only two unique OC43 nsp4 interactors were identified: a target of the NEDD8-Cullin E3 ligase pathway (MRFAP1)[51] and FAM120A, an RNA-binding protein found to serve as a scaffolding protein for the IL13 signaling pathway (**Figure A5.10B-C**)[52,53]. Both of these proteins are localized to the nucleus (**Figure A5.9B**). Lastly, we identified a large cluster of unique SARS-CoV-1 nsp4 interactors that compose the CTLH E3 ubiquitin ligase complex (Figure 4D). This nuclear complex maintains cell proliferation rates, likely through the ubiquitination of the transcription factor Hbp1, a negative regulator of cell proliferation[54]. This complex is highly enriched for SARS-CoV-1 specifically, presenting one of the most profound differences in interaction profile (**Figure A5.8A,C**). This specificity of engagement was validated through co-IP and western blot (**Figure A5.6A-B**). We confirmed that only SARS-CoV-1 nsp4 co-purified with several of CTLH components (MKLN1, WDR26, RANBP9).

The fact that both OC43 and SARS-CoV-1 nsp4 displayed prominent interactions with nuclear proteins prompted us to evaluate the cellular localization of the protein by immunofluorescence. We detected perinuclear puncti for all constructs which partially co-localized with the ER marker PDIA4 (**Figure A5.12**), consistent with prior studies[22]. However, for SARS-CoV-1 and OC43 nsp4, we also detected measurable signal in the nucleus, supporting a nuclear function and the observed interactions with proteins in the nucleus.

5.2.5 Enrichment of mitochondria-associated membrane proteins as nsp2 and nsp4 interactors

In our evaluation of cellular compartment GO-terms, we noticed that nsp2 and nsp4 interactors are enriched in membranes of the endoplasmic reticulum and the mitochondria (**Figures A5.3B, A5.9B**). ERLIN1/2 and RNF170 form an E3 ubiquitin ligase complex known to localize to the interface between the ER and mitochondria, regions termed mitochondria-associated membranes (MAMs). Jonathan Davies, co-first author, and Eli mcDonaldtherefore probed our data set for any other MAMs-associated nsp2 and nsp4 interactors. He cross-referenced our interactor lists with three published data sets that specifically characterized the MAMs proteome[55–57].

He then performed subcellular fractionation and probed for the presence of viral proteins in MAMs fractions, and after confirming this localization has performed follow-up work in characterizing the role of these proteins in viral infection. Given that many of the interactors are involved in calcium regulation across the membranes of the organelles, he is now pursuing how coronavirus infection or overexpression of nsp2/4 constructs alters mitochondrial morphology and calcium homeostasis in cells.

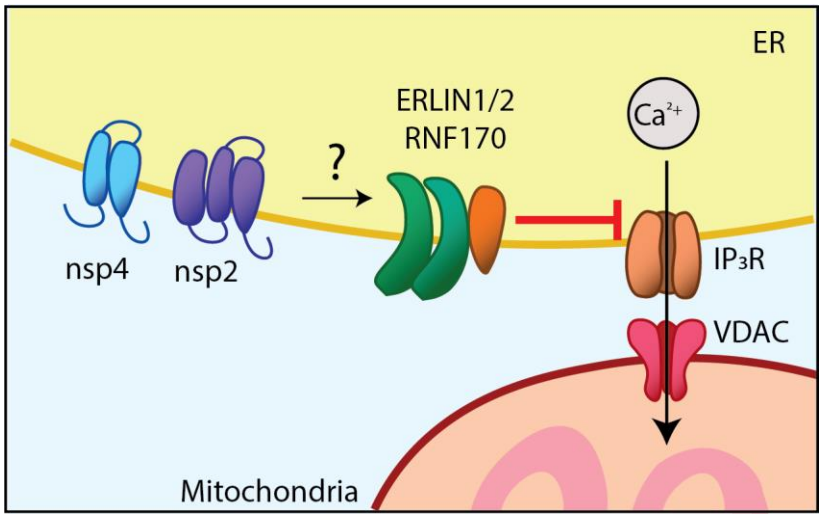

Figure 5.5. Enrichment of mitochondria-associated membrane (MAM) proteins as nsp2 and nsp4 interactors. Proposed model for how SARS-CoV nsp2 and nsp4 utilize ERLIN1/2 and interacting protein factors to regulate ER Ca^{2+} signaling at MAMs.

5.3 Discussion

Our analysis enables both the identification of interactors for SARS-CoV-1, SARS-CoV-2, and OC43 homologs of nsp2 and nsp4, and comparative quantitative enrichment to differentiate between shared and unique host cell binding partners. We acknowledge the limitations of using transiently transfected viral proteins for AP-MS. Viral infection results in a collection of both protein-protein and RNA-protein interactions and our approach cannot account for how these events influence the interactions of nsp2 and nsp4. However, given the logistical barriers to handling BSL-3 viruses, paired with the urgency of the current pandemic, our workflow is an efficient system to perform comparative analysis and generate a shortlist of interactors to prioritize for further investigation.

We identify several nsp2 interactors shared across SARS strains, including STOML2, and prohibitins (PHB and PHB2), which were previously identified as interacting with SARS-CoV-1[17]. These proteins work in tandem to induce formation of metabolically active mitochondrial membranes to regulate mitochondrial biogenesis. Increased levels of STOML2 are associated with increased ATP production and reduced apoptosis induction[29]. This conserved interaction for SARS strains presents an avenue for nsp2 to increase mitochondrial metabolism and stall apoptosis to maintain a pro-viral cellular environment. Additionally, STOML2 has been found to play a key role in stabilizing hepatitis C virus replication complexes[58] and PHB has been shown to promote entry of both Chikungunya virus[59] and enterovirus 71[60]. These factors may prove effective pan-RNA virus targets for host-directed therapies. We also attempted to extend the comparative analysis to OC43 nsp2. However, this construct did not express detectable protein, which could be due to much lower homology to SARS-CoV-2 and SARS-CoV-1 than for other non-structural proteins.

For nsp4, we identify multiple unique SARS-CoV-1 interactors, most notably members of the CTLH E3 ubiquitin ligase complex. This complex is known to regulate levels of Hbp1, a negative regulator of proliferative genes[54] and was previously shown to interact with the dengue viral

protein NS2B3[15], implicating this complex as a target for RNA viruses to influence cell proliferation. We also identified the FBXO45-MYCBP2 E3 ubiquitin ligase complex, which has been shown to prevent cell death in mitosis [61]. Together, this may support a role in SARS-CoV-1 nsp4 co-opting host ubiquitin complexes to extend cell viability during infection to promote viral replication. During resubmission, Gordon et al. published a comparative coronavirus interaction network confirming the SARS-CoV-1 specific interactions with the CTLH E3 ligase complex[62].

Furthermore, we find components of the cholesterol biosynthesis pathway, IDI1 and DHCR7, which were specifically enriched for SARS-CoV-1 and OC43 nsp4 respectively. IDI1 has been shown to be downregulated by host cells in response to CMV-infection-induced interferons[47] and is upregulated by both HIV and HCV during infection[48,49]. DHCR7 is downregulated during RNA virus infection in macrophages to promote IRF3 signaling and IFN-1 production. Moreover, inhibition of DHCR7 aids in clearance of multiple RNA viruses[50]. These previous findings indicate that interactions with IDI1 and DHCR7 may provide means for coronaviruses to counteract anti-viral responses. Interestingly, these interactions with the aforementioned E3 ligase complexes and cholesterol biogenesis factors are not enriched for SARS-CoV-2 nsp4, implying that SARS-CoV-2 pathogenesis may not require these interactions.

As a whole, it appears that SARS-CoV-2 homologs differ from SARS-CoV-1 not by gaining new interactions, but rather by losing network nodes. This is emphasized in the gene enrichment analysis of nsp2 and nsp4 (**Figure A5.3C, A5.9C**), in which multiple pathways are more strongly enriched for SARS-CoV-1, as well as in the nsp4 interactome (**Figure 5.4C-D**), particularly with the absence of E3 ligase complex interactions for SARS-CoV-2. It will be important to investigate potential functional implications of the engagement of the E3 ubiquitin ligase, as well innate immune signaling factors on CoV infections and the course of pathogenicity for the divergent strains.

To gain functional insights into which nsp2 and nsp4 interactions may have an impact on CoV infection, we mined recently published data from a genome wide CRISPR knockout screen and

a targeted siRNA knockdown/CRISPR knockout screen of SARS-CoV-2 interactors (**Figure S13A-B**)[62,63]. The comprehensive genome wide dataset by Heaton et al. conducted in A549 lung cancer cells identified that knockout of several of the proteostasis components (BAG2, DDOST), as well as ERLIN1 and ERLIN2 enhanced cell survival in the presence of SARS-CoV-2, suggesting that these factors may have an anti-viral function (**Figure A5.13A**). When comparing the more limited siRNA knockdown data in A549 cells and CRISPR knockout data in Caco2 colorectal cancer cells, ATP6AP1 stood out as hampering SARS-CoV-2 infection in both cell models supporting a pro-viral role (**Figure A5.13B**)[62]. ATP6AP1/Ac45 is a critical accessory subunit to facilitate the assembly of the vacuolar ATPase in support of lysosome function and autophagy playing a role in viral infection[64]. Future functional genomic screens will be necessary to evaluate the role of other interactors on CoV infection and evaluate differential roles for the distinct strains.

A particularly noteworthy finding is the identification of 17 mitochondria-associated membrane factors in the combined nsp2 and nsp4 datasets, based on cross-referencing interactors with previously published proteomics studies of MAMs proteins[55-57]. Given the prominence of these interactions, it is tempting to speculate that nsp2 and nsp4 localize to MAMs and influence processes at these important organelle contact sites (**Figure 5**). MAMs are nodes for innate immune signaling and apoptosis pathways, both of which are common targets for viral manipulation.

In particular, we identify the E3 ubiquitin ligase RNF5 interacting with all nsp4 homologs. RNF5 targets STING for degradation, which stabilizes retinoic acid-inducible gene-I (RIG-I) and mitochondrial antiviral-signaling protein (MAVS) interactions at MAMs, thereby inducing inteferon-1 and -3 production via IRF3 and NF-κB signaling[36-37]. RIG-I is one of the main viral RNA genome sensors in host cells; therefore, it is possible that nsp4 increases targeting of RNF5 to MAMs to inhibit downstream signaling of RIG-1.

We also identify the ERLIN1/2 complex in both nsp2 and nsp4 data sets. In the nsp2 interaction network, the complex is associated with a different E3 ligase, RNF170. RNF170 has been shown to inhibit innate immune signaling by targeting TLR3 for degradation, thereby blocking IRF3 and NF-κB signaling pathways[65]. In addition, ERLIN1/2 acts in concert with RNF170 to target the inositol-1,4,5-triphophate receptor (IP_3R) for degradation via polyubiquination[66]. IP_3R is an ER-resident Ca^{2+} channel integral in the formation of MAMs[67,68]. Calcium flux at MAMs has been shown to increase mitochondrial calcium uptake, which increases ATP production, thereby benefitting active viral replication[69]. Indeed, several other viruses have been shown to influence ER Ca^{2+} exchange. For instance, the Hepatitis C viral protein, NS5A, promotes degradation of IP_3R3 to limit apoptosis induction triggered by persistent Ca^{2+} signaling at MAMs[70] or the human cytomegalovirus protein, vMIA, which increases ER Ca^{2+} export at MAMs through IP_3R into the mitochondria[72]. Previous studies have shown the SARS-CoV-1 E protein acts as a channel to leak ER calcium stores during infection[71], but to our knowledge, no such features have been attributed to either nsp2 or nsp4. Thus, manipulation of ER Ca^{2+} signaling via IP_3R regulation may represent a novel method by which coronaviruses manipulate mitochondrial function. Additionally, a recent study found that IP_3R3 is significantly upregulated during SARS-CoV-2 infection[72] (**Figure A5.13C**). Further studies will be important to evaluate whether ER calcium exchange and mitochondrial metabolism could impact coronavirus infection.

5.4 Methods

Protein expression constructs

Coding sequences for nsp2 and nsp4 were obtained from GenBank (MN908947 SARS-CoV-2 isolate Wuhan-Hu-1; AY278741 SARS-CoV-1 Urbani; NC_006213 hCoV OC43 strain ATCC VR-759). Human codon optimized sequences were designed, genes synthesized, and cloned into pcDNA3.1-(+)-C-DYK (nsp4) to append a C-terminal FLAG tag, or into pcDNA3.1-(+)-N-DYK (nsp2) to append an N-terminal FLAG tag (GenScript).

Cell culture and transfection

HEK293T cells were maintained in Dulbecco's Modified Eagle's Medium (DMEM) with high glucose and supplemented with 10% fetal bovine serum (FBS), 1% penicillin/streptomycin, and 1% glutamine. Cells were kept at 37°C, 5% CO2. Generally, 2 x 10^6 cells were seeded into 10cm dishes. 24 hours post-seeding, cells were transfected with 5µg nsp2, nsp4, or fluorescent control DNA constructs in pcDNA3.1-(+)-C/N-DYK vectors using a calcium phosphate method. Media was exchanged 16 hours post-transfection, and cells were harvested 24 hours after changing media.

Immunoprecipitation

Cells were collected and washed with PBS. Immunoprecipitation samples were lysed by resuspension in TNI buffer (50 mM Tris pH 7.5, 150mM NaCl, 0.5% IGEPAL-CA-630) with Roche cOmplete protease inhibitor on ice for at least 10 minutes, followed by sonication in a room temperature water bath for 10 minutes. Lysates were cleared by centrifugation at 17,000 x g for 10-20 minutes. Sepharose 4B resin (Sigma) and G1 anti-DYKDDDDK resin (GenScript) were pre-washed 4x with the respective lysis buffer for each sample. Protein concentrations in cleared lysates were normalized using BioRad Protein Assay Dye and added to 15 µL Sepharose 4B resin for 1 hour, rocking at 4°C. Resin was collected by centrifugation for 5-10 minutes at 400 x g and pre-cleared supernatant was added directly to 15 µL G1 anti-DYKDDDDK resin and rocked at 4°C overnight. The next day, supernatant was removed and resin was washed 4 times with the respective lysis buffer. Bound proteins were eluted with the addition of modified 3x Laemelli buffer (62.5 mM Tris, 6% SDS) for 30 minutes at room temperature followed by 15 minutes at 37°C, followed by a second elution for 5-15 minutes at 37°C. 10% of elution was set aside for SDS-PAGE and silver staining to confirm immunoprecipitation efficiency, and the remainder was prepared for mass spectrometry. Silver staining was performed using a Pierce Silver Stain kit (Thermo Scientific). Separate biological replicates of co-immunoprecipitated lysates were identically processed, in which inputs and elutions were normalized and run on SDS-PAGE gel,

transferred to PVDF membrane, and blotted for various host interactors using the following antibodies (1:1000 dilutions): anti-FLAG (Sigma-Aldrich, F1804), anti-calnexin (GeneTex, GTX109669), anti-muskelin (Santa Cruz Biotechnology, SC-398956) anti-ERLIN2 (Sigma-Aldrich, HPA002025), and anti-GAPDH (GeneTex, GTX627408) as a loading control.

Tandem Mass Tag sample preparation

Sample preparation was carried out as described[73]. Briefly, eluted proteins were precipitated in methanol/chloroform/water (3:1:3), washed twice in methanol, and protein pellets were air dried. Pellets were resuspended in 1% Rapigest SF (Waters), reduced, and alkylated. Proteins were digested in trypsin-LysC overnight. Digested peptides were labeled using TMT 11-plex or TMTpro 16-plex reagents (Thermo Scientific), pooled, and acidified using formic acid. Cleaved Rapigest was removed by centrifugation of samples at 17,000 x g for 30 min.

MudPIT liquid chromatography-mass spectrometry analysis

Triphasic MudPIT microcolumn were prepared as described[74]. Individual pooled TMT proteomics samples were directly loaded onto the microcolumns using a high-pressure chamber followed by a wash with 5% acetonitrile, 0.1% formic acid in water (v/v) for 30 min. Peptides were analyzed by liquid chromatography-mass spectrometry on an Exploris 480 in line with an Ultimate 3000 nanoLC system (Thermo Fisher). The MudPIT microcolumns were installed on a column switching valve on the nanoLC systems followed by 20 cm fused silica microcapillary column (ID 100µm) ending in a laser-pulled tip filled with Aqua C18, 3µm, 100 Å resin (Phenomenex). MudPIT runs were carried out by 10µL sequential injection of 0, 10, 20, 40, 60, 80, 100 % buffer C (500mM ammonium acetate, 94.9% water, 5% acetonitrile, 0.1% formic acid), followed by a final injection of 90% C, 10% buffer B (99.9% acetonitrile, 0.1% formic acid v/v). Each injection was followed by a 130 min gradient using a flow rate of 500nL/min (0 – 6 min: 2% buffer B, 8 min: 5% B, 100 min: 35% B, 105min: 65% B, 106 – 113 min: 85% B, 113 – 130 min: 2% B). Electrospray ionization was performed directly from the tip of the microcapillary column using a spray voltage of 2.2 kV, ion transfer tube temperature of 275ºC and RF Lens of 40%. MS1 spectra were collected using

the following settings: scan range 400 – 1600 m/z, 120,000 resolution, AGC target 300%, and automatic injection times. Data-dependent tandem mass spectra were obtained using the following settings: monoisotopic peak selection mode: peptide, included charge state 2 – 7, TopSpeed method (3s cycle time), isolation window 0.4 m/z, HCD fragmentation using a normalized collision energy of 32, resolution 45,000, AGC target 200%, automatic injection times, and dynamic exclusion (20 ppm window) set to 60 s.

Experimental layout and data analysis

The nsp2 AP-MS experiments included three individual MS runs combining 34 Co-AP samples (SARS-CoV-2 n = 13; SARS-CoV-1 n = 9; GFP (mock) n = 12). Samples were distributed to TMTpro 16plex or TMT11plex channels as outlined in Figure A5.2A. The nsp4 AP-MS experiments consisted of three individual MS runs, containing 40 Co-IPs (SARS-CoV-2 n = 12; SARS-CoV-1 n = 8; OC43 = 8; GFP (mock) n = 12). Samples were distributed to TMTpro 16plex channels as outlined in Figure A5.5A. Identification and quantification of peptides and proteins were carried out in Proteome Discoverer 2.4 (Thermo Fisher) using a SwissProt human database (Tax ID 9606, release date 11/23/2019). CoV nsp2 and nsp4 protein sequences were added manually. Searches were conducted in Sequest HT using the following setting: Trypsin cleavage with max. 2 missed cleavage sites, minimum peptide length 6, precursor mass tolerance 20 ppm, fragment mass tolerance 0.02 Da, dynamic modifications: Met oxidation (+15.995 Da), Protein N-terminal Met loss (-131.040 Da), Protein N-terminal acetylation (+42.011 Da), static modifications: Cys carbamidomethylation (+57.021 Da), TMTpro or TMT6plex at Lys and N-termini (+304.207 Da for TMTpro or +229.163 for TMT6plex). Peptide IDs were filtered using the Percolator node using an FDR target of 0.01. Proteins were filtered based on a 0.01 FDR requiring two peptide IDs per protein, and protein groups were created according to a strict parsimony principle. TMT reporter ions were quantified using the reporter ion quantification considering unique and razor peptides and excluding peptides with co-isolation interference greater than 25%. Peptide abundances were normalized based on total peptide amounts in each channel assuming similar

levels of background signal in the APs. Protein quantification roll-up used all quantified peptides. Pairwise ratios between conditions were calculated based on total protein abundances and ANOVA on individual proteins was used to test for changes in abundances and to report adjusted p-values.

To filter high-confidence interactors of individual CoV nsp proteins, we used a variable filter combining log2 fold enrichment and adjusted p-value according to a published method[75]. Briefly, the histogram of log2 protein abundance fold changes between nsp-transfected versus mock-transfected groups were fitted to a gaussian curve using a nonlinear least square fit to determine the standard deviation σ (see Figure A5.2B-C). Fold change cutoffs for high-confidence and medium-confidence interactors were based on 2 σ, or 1 σ, respectively. For actual cutoffs taking into consideration adjusted p-values, we utilized a hyperbolic curve $y > c / (x - x_0)$, where y is the adj. p-value, x the log2 fold change, x_0 corresponds to the standard deviation cutoff (2σ or 1σ), and c is the curvature (c = 0.4 for 1 σ, and 0.8 for 2 σ, **Figures A5.C-D, 5.4A, A5.7B-C**).

The mass spectrometry proteomics data have been deposited to the ProteomeXchange Consortium via the PRIDE[76] partner repository with the dataset identifier PXD022017.

Gene set enrichment analysis

GO-term categories for biological processes and cellular components for interactors were based on assignment in the Proteome Discoverer Protein Annotation node. Gene set enrichment analysis was conducted in EnrichR[77]. The analysis was conducted separately for sets of interactors of individual nsp2 or nsp4 homologs and GO-terms for biological processes were filtered by adjusted p-values <0.1. Redundant GO-terms were grouped manually based on overlapping genes in related terms.

Network plots and identification of overlapping interactions with published data

Extended and overlapping interactomes between novel interactors identified in this study and previously published interactors[18] were generated by scraping the top n interactors of each

primary prey protein on the STRING database using the python API. We established an extended secondary interactome by searching for the top 20 and top 30 STRING db interactors of the nsp4 primary interactors and nsp2 interactors respectively using limit parameter in STRING API and searching against the human proteome (species 9606). We then compared the extended interactomes of our data with the previously published data by dropping any secondary interactors that did not appear in both data sets. Next, we concatenated the primary interactors from our data, the primary interactors from the published data, and the overlapping secondary interactors into a single data frame. Finally, we searched the overlapping secondary interactors against the STRING database human proteome to determine interactors between secondary interactors with a threshold of greater than 50% likelihood in the experimental score category. The results were plotted in Cytoscape.

Immunofluorescence confocal microscopy

HEK293T cells were cultured on glass-bottom culture dishes (MatTek, P35G-0-14-C) and transfected with CoV expression constructs as previously described. Cells were fixed with 4% paraformaldehyde-PBS, washed thrice with PBS, then permeabilized in 0.2% Triton-X (in PBS). After three PBS washes, cells were blocked in PBS with 1% BSA with 0.1% Saponin (blocking buffer). After blocking, cells were incubated with anti-PDIA4 primary antibody (Protein Tech, 14712-1-AP) in blocking buffer (1:1000 dilution) for 1 hour at 37°C. After three PBS washes, cells were incubated with AlexFluor 488-conjugated anti-rabbit goat antibody (ThermoFisher, A-11008) in blocking buffer (1:500 dilution) at room temperature for 30 min. Cells were then stained with M2 FLAG primary antibody (SigmaAldrich, F1804) and AlexFluor 594-conjugated anti-mouse goat antibody (ThermoFisher, A-11005) using the same conditions. Cells were then mounted in Prolong Gold with DAPI stain (ThermoFisher, P36935). Cells were imaged using an LSM-880 confocal microscope (Zeiss) and images were merged using Image J software.

5.5 References

(1) Fehr, A. R.; Perlman, S. Coronaviruses: An Overview of Their Replication and Pathogenesis. *Methods Mol. Biol.* **2015**, *1282*, 1. https://doi.org/10.1007/978-1-4939-2438-7_1.

(2) *Novel Coronavirus (2019-NCoV) Situation Report 1*; 2020, 1-7.

(3) Hoffmann, M.; Kleine-Weber, H.; Schroeder, S.; Mü, M. A.; Drosten, C.; Pö, S. SARS-CoV-2 Cell Entry Depends on ACE2 and TMPRSS2 and Is Blocked by a Clinically Proven Protease Inhibitor. *Cell* **2020**, *181*, 271–280. https://doi.org/10.1016/j.cell.2020.02.052.

(4) Perlman, S.; Netland, J. Coronaviruses Post-SARS: Update on Replication and Pathogenesis. *Nature Reviews Microbiology*. 2009, pp 439–450. https://doi.org/10.1038/nrmicro2147.

(5) Blanco-Melo, D.; Nilsson-Payant, B. E.; Liu, W.-C.; Lim, J. K.; Albrecht, R. A.; Tenoever, B. R. SARS-CoV-2 Infection Induces Low IFN-I and-III Levels with a Moderate ISG Response. *Cell* **2020**, 1-10 https://doi.org/10.1016/j.cell.2020.04.026.

(6) Fung, T. S.; Liu, D. X. Coronavirus Infection, ER Stress, Apoptosis and Innate Immunity. *Frontiers in Microbiology*. Frontiers Research Foundation June 17, 2014, p 296. https://doi.org/10.3389/fmicb.2014.00296.

(7) Tan, Y.-X.; Tan, T. H. P.; Lee, M. J.-R.; Tham, P.-Y.; Gunalan, V.; Druce, J.; Birch, C.; Catton, M.; Fu, N. Y.; Yu, V. C.; Tan, Y.-J. Induction of Apoptosis by the Severe Acute Respiratory Syndrome Coronavirus 7a Protein Is Dependent on Its Interaction with the Bcl-XL Protein. *J. Virol.* **2007**, *81* (12), 6346–6355. https://doi.org/10.1128/jvi.00090-07.

(8) Yeung, M. L.; Yao, Y.; Jia, L.; Chan, J. F. W.; Chan, K. H.; Cheung, K. F.; Chen, H.; Poon, V. K. M.; Tsang, A. K. L.; To, K. K. W.; Yiu, M. K.; Teng, J. L. L.; Chu, H.; Zhou, J.; Zhang, Q.; Deng, W.; Lau, S. K. P.; Lau, J. Y. N.; Woo, P. C. Y.; Chan, T. M.; Yung, S.; Zheng, B. J.; Jin, D. Y.; Mathieson, P. W.; Qin, C.; Yuen, K. Y. MERS Coronavirus Induces Apoptosis in Kidney and Lung by Upregulating Smad7 and FGF2. *Nat. Microbiol.* **2016**, *1* (3), 1–8. https://doi.org/10.1038/nmicrobiol.2016.4.

(9) Yue, Y.; Nabar, N. R.; Shi, C. S.; Kamenyeva, O.; Xiao, X.; Hwang, I. Y.; Wang, M.; Kehrl, J. H. SARS-Coronavirus Open Reading Frame-3a Drives Multimodal Necrotic Cell Death. *Cell Death Dis.* **2018**, *9* (9), 1–15. https://doi.org/10.1038/s41419-018-0917-y.

(10) von Brunn, A.; Teepe, C.; Simpson, J. C.; Pepperkok, R.; Friedel, C. C.; Zimmer, R.; Roberts, R.; Baric, R.; Haas, J. Analysis of Intraviral Protein-Protein Interactions of the SARS Coronavirus ORFeome. *PLoS One* **2007**, *2* (5), e459. https://doi.org/10.1371/journal.pone.0000459.

(11) Pfefferle, S.; Schö Pf, J.; Kö Gl, M.; Friedel, C. C.; Mü Ller, M. A.; Carbajo-Lozoya, J.; Stellberger, T.; Von Dall'armi, E.; Herzog, P.; Kallies, S.; Niemeyer, D.; Ditt, V.; Kuri, T.; Zü St, R.; Pumpor, K.; Hilgenfeld, R.; Schwarz, F.; Zimmer, R.; Steffen, I.; Weber, F.; Thiel, V.; Herrler, G.; Thiel, H.-J. R.; Schwegmann-Weßels, C.; Pö Hlmann 10, S.; Rgen Haas, J.; Drosten, C.; Von Brunn, A. The SARS-Coronavirus-Host Interactome: Identification of Cyclophilins as Target for Pan-Coronavirus Inhibitors. **2011**, 1-15 https://doi.org/10.1371/journal.ppat.1002331.

(12) V'kovski, P.; Gerber, M.; Kelly, J.; Pfaender, S.; Ebert, N.; Braga Lagache, S.; Simillion, C.; Portmann, J.; Stalder, H.; Gaschen, V.; Bruggmann, R.; Stoffel, M. H.; Heller, M.; Dijkman, R.; Thiel, V. Determination of Host Proteins Composing the Microenvironment of Coronavirus Replicase Complexes by Proximity-Labeling. *Elife* **2019**, *8*. https://doi.org/10.7554/eLife.42037.

(13) Jean Beltran, P. M.; Cook, K. C.; Cristea, I. M. Exploring and Exploiting Proteome Organization during Viral Infection. *J. Virol.* **2017**, *91* (18) 1-9. https://doi.org/10.1128/jvi.00268-17.

(14) Hashimoto, Y.; Sheng, X.; Murray-Nerger, L. A.; Cristea, I. M. Temporal Dynamics of Protein Complex Formation and Dissociation during Human Cytomegalovirus Infection. *Nat. Commun.* **2020**, *11* (1) 1-10. https://doi.org/10.1038/s41467-020-14586-5.

(15) Shah, P. S.; Link, N.; Jang, G. M.; Sharp, P. P.; Zhu, T.; Swaney, D. L.; Johnson, J. R.; Von Dollen, J.; Ramage, H. R.; Satkamp, L.; Newton, B.; Hüttenhain, R.; Petit, M. J.; Baum, T.; Everitt, A.; Laufman, O.; Tassetto, M.; Shales, M.; Stevenson, E.; Iglesias, G. N.; Shokat, L.; Tripathi, S.; Balasubramaniam, V.; Webb, L. G.; Aguirre, S.; Willsey, A. J.; Garcia-Sastre, A.; Pollard, K. S.; Cherry, S.; Gamarnik, A. V.; Marazzi, I.; Taunton, J.; Fernandez-Sesma, A.; Bellen, H. J.; Andino, R.; Krogan, N. J. Comparative Flavivirus-Host Protein Interaction Mapping Reveals Mechanisms of Dengue and Zika Virus Pathogenesis. *Cell* **2018**, *175* (7), 1931-1945.e18. https://doi.org/10.1016/j.cell.2018.11.028.

(16) Nicod, C.; Banaei-Esfahani, A.; Collins, B. C. Elucidation of Host–Pathogen Protein–Protein Interactions to Uncover Mechanisms of Host Cell Rewiring. *Curr. Opin. Microbiol.* **2017**, *39*, 7–15. https://doi.org/10.1016/j.mib.2017.07.005.

(17) Cornillez-Ty, C. T.; Liao, L.; Yates, J. R.; III; Kuhn, P.; Buchmeier, M. J. Severe Acute Respiratory Syndrome Coronavirus Nonstructural Protein 2 Interacts with a Host Protein Complex Involved in Mitochondrial Biogenesis and Intracellular Signaling. *J. Virol.* **2009**, *83* (19), 10314-10318. https://doi.org/10.1128/JVI.00842-09.

(18) Gordon, D. E.; Jang, G. M.; Bouhaddou, M.; Xu, J.; Obernier, K.; White, K. M.; O'Meara, M. J.; Rezelj, V. V.; Guo, J. Z.; Swaney, D. L.; Tummino, T. A.; Huettenhain, R.; Kaake, R. M.; Richards, A. L.; Tutuncuoglu, B.; Foussard, H.; Batra, J.; Haas, K.; Modak, M.; Kim, M.; Haas, P.; Polacco, B. J.; Braberg, H.; Fabius, J. M.; Eckhardt, M.; Soucheray, M.; Bennett, M. J.; Cakir, M.; McGregor, M. J.; Li, Q.; Meyer, B.; Roesch, F.; Vallet, T.; Mac Kain, A.; Miorin, L.; Moreno, E.; Naing, Z. Z. C.; Zhou, Y.; Peng, S.; Shi, Y.; Zhang, Z.; Shen, W.; Kirby, I. T.; Melnyk, J. E.; Chorba, J. S.; Lou, K.; Dai, S. A.; Barrio-Hernandez, I.; Memon, D.; Hernandez-Armenta, C.; Lyu, J.; Mathy, C. J. P.; Perica, T.; Pilla, K. B.; Ganesan, S. J.; Saltzberg, D. J.; Rakesh, R.; Liu, X.; Rosenthal, S. B.; Calviello, L.; Venkataramanan, S.; Liboy-Lugo, J.; Lin, Y.; Huang, X. P.; Liu, Y. F.; Wankowicz, S. A.; Bohn, M.; Safari, M.; Ugur, F. S.; Koh, C.; Savar, N. S.; Tran, Q. D.; Shengjuler, D.; Fletcher, S. J.; O'Neal, M. C.; Cai, Y.; Chang, J. C. J.; Broadhurst, D. J.; Klippsten, S.; Sharp, P. P.; Wenzell, N. A.; Kuzuoglu, D.; Wang, H. Y.; Trenker, R.; Young, J. M.; Cavero, D. A.; Hiatt, J.; Roth, T. L.; Rathore, U.; Subramanian, A.; Noack, J.; Hubert, M.; Stroud, R. M.; Frankel, A. D.; Rosenberg, O. S.; Verba, K. A.; Agard, D. A.; Ott, M.; Emerman, M.; Jura, N.; von Zastrow, M.; Verdin, E.; Ashworth, A.; Schwartz, O.; D'Enfert, C.; Mukherjee, S.; Jacobson, M.; Malik, H. S.; Fujimori, D. G.; Ideker, T.; Craik,

C. S.; Floor, S. N.; Fraser, J. S.; Gross, J. D.; Sali, A.; Roth, B. L.; Ruggero, D.; Taunton, J.; Kortemme, T.; Beltrao, P.; Vignuzzi, M.; García-Sastre, A.; Shokat, K. M.; Shoichet, B. K.; Krogan, N. J. A SARS-CoV-2 Protein Interaction Map Reveals Targets for Drug Repurposing. *Nature* **2020**, 459-468. https://doi.org/10.1038/s41586-020-2286-9.

(19) Brito, A. F.; Pinney, J. W. Protein-Protein Interactions in Virus-Host Systems. *Front. Microbiol.* **2017**, *8* (AUG), 1-11. https://doi.org/10.3389/fmicb.2017.01557.

(20) Graham, R. L.; Sims, A. C.; Brockway, S. M.; Baric, R. S.; Denison, M. R. The Nsp2 Replicase Proteins of Murine Hepatitis Virus and Severe Acute Respiratory Syndrome Coronavirus Are Dispensable for Viral Replication. *J. Virol.* **2005**, *79* (21), 13399–13411. https://doi.org/10.1128/JVI.79.21.13399-13411.2005.

(21) Angeletti, S.; Benvenuto, D.; Bianchi, M.; Giovanetti, M.; Pascarella, S.; Ciccozzi, M. COVID-2019: The Role of the Nsp2 and Nsp3 in Its Pathogenesis. *J. Med. Virol.* **2020**, 0–3. https://doi.org/10.1002/jmv.25719.

(22) Oostra, M.; te Lintelo, E. G.; Deijs, M.; Verheije, M. H.; Rottier, P. J. M.; de Haan, C. A. M. Localization and Membrane Topology of Coronavirus Nonstructural Protein 4: Involvement of the Early Secretory Pathway in Replication. *J. Virol.* **2007**, *81* (22), 12323–12336. https://doi.org/10.1128/jvi.01506-07.

(23) Gadlage, M. J.; Sparks, J. S.; Beachboard, D. C.; Cox, R. G.; Doyle, J. D.; Stobart, C. C.; Denison, M. R. Murine Hepatitis Virus Nonstructural Protein 4 Regulates Virus-Induced Membrane Modifications and Replication Complex Function. *J. Virol.* **2010**, *84* (1), 280–290. https://doi.org/10.1128/jvi.01772-09.

(24) Oudshoorn, D.; Rijs, K.; Limpens, R. W. A. L.; Groen, K.; Koster, A. J.; Snijder, E. J.; Kikkert, M.; Bárcena, M. Expression and Cleavage of Middle East Respiratory Syndrome Coronavirus Nsp3-4 Polyprotein Induce the Formation of Double-Membrane Vesicles That Mimic Those Associated with Coronaviral RNA Replication. *MBio* **2017**, *8* (6) 1-7. https://doi.org/10.1128/mBio.01658-17.

(25) Kanjanahaluethai, A.; Chen, Z.; Jukneliene, D.; Baker, S. C. Membrane Topology of Murine Coronavirus Replicase Nonstructural Protein 3. *Virology* **2007**, *361* (2), 391–401. https://doi.org/10.1016/j.virol.2006.12.009.

(26) Nusinow, D. P.; Szpyt, J.; Ghandi, M.; Rose, C. M.; McDonald, E. R.; Kalocsay, M.; Jané-Valbuena, J.; Gelfand, E.; Schweppe, D. K.; Jedrychowski, M.; Golji, J.; Porter, D. A.; Rejtar, T.; Wang, Y. K.; Kryukov, G. V.; Stegmeier, F.; Erickson, B. K.; Garraway, L. A.; Sellers, W. R.; Gygi, S. P. Quantitative Proteomics of the Cancer Cell Line Encyclopedia. *Cell* **2020**, *180* (2), 387-402.e16. https://doi.org/10.1016/j.cell.2019.12.023.

(27) Jiang, L.; Wang, M.; Lin, S.; Jian, R.; Li, X.; Chan, J.; Dong, G.; Fang, H.; Robinson, A. E.; Aguet, F.; Anand, S.; Ardlie, K. G.; Gabriel, S.; Getz, G.; Graubert, A.; Hadley, K.; Handsaker, R. E.; Huang, K. H.; Kashin, S.; MacArthur, D. G.; Meier, S. R.; Nedzel, J. L.; Nguyen, D. Y.; Segrè, A. V.; Todres, E.; Balliu, B.; Barbeira, A. N.; Battle, A.; Bonazzola, R.; Brown, A.; Brown, C. D.; Castel, S. E.; Conrad, D.; Cotter, D. J.; Cox, N.; Das, S.; de Goede, O. M.; Dermitzakis, E. T.; Engelhardt, B. E.; Eskin, E.; Eulalio, T. Y.; Ferraro, N. M.; Flynn, E.; Fresard, L.; Gamazon, E. R.; Garrido-Martín, D.; Gay, N. R.; Guigó, R.; Hamel, A. R.; He, Y.; Hoffman, P. J.; Hormozdiari, F.; Hou, L.; Im, H. K.; Jo, B.; Kasela, S.; Kellis, M.; Kim-Hellmuth, S.; Kwong, A.; Lappalainen, T.; Li, X.; Liang, Y.; Mangul, S.;

Mohammadi, P.; Montgomery, S. B.; Muñoz-Aguirre, M.; Nachun, D. C.; Nobel, A. B.; Oliva, M.; Park, Y. S.; Park, Y.; Parsana, P.; Reverter, F.; Rouhana, J. M.; Sabatti, C.; Saha, A.; Skol, A. D.; Stephens, M.; Stranger, B. E.; Strober, B. J.; Teran, N. A.; Viñuela, A.; Wang, G.; Wen, X.; Wright, F.; Wucher, V.; Zou, Y.; Ferreira, P. G.; Li, G.; Melé, M.; Yeger-Lotem, E.; Barcus, M. E.; Bradbury, D.; Krubit, T.; McLean, J. A.; Qi, L.; Robinson, K.; Roche, N. V.; Smith, A. M.; Sobin, L.; Tabor, D. E.; Undale, A.; Bridge, J.; Brigham, L. E.; Foster, B. A.; Gillard, B. M.; Hasz, R.; Hunter, M.; Johns, C.; Johnson, M.; Karasik, E.; Kopen, G.; Leinweber, W. F.; McDonald, A.; Moser, M. T.; Myer, K.; Ramsey, K. D.; Roe, B.; Shad, S.; Thomas, J. A.; Walters, G.; Washington, M.; Wheeler, J.; Jewell, S. D.; Rohrer, D. C.; Valley, D. R.; Davis, D. A.; Mash, D. C.; Branton, P. A.; Barker, L. K.; Gardiner, H. M.; Mosavel, M.; Siminoff, L. A.; Flicek, P.; Haeussler, M.; Juettemann, T.; Kent, W. J.; Lee, C. M.; Powell, C. C.; Rosenbloom, K. R.; Ruffier, M.; Sheppard, D.; Taylor, K.; Trevanion, S. J.; Zerbino, D. R.; Abell, N. S.; Akey, J.; Chen, L.; Demanelis, K.; Doherty, J. A.; Feinberg, A. P.; Hansen, K. D.; Hickey, P. F.; Jasmine, F.; Kaul, R.; Kibriya, M. G.; Li, J. B.; Li, Q.; Linder, S. E.; Pierce, B. L.; Rizzardi, L. F.; Smith, K. S.; Stamatoyannopoulos, J.; Tang, H.; Carithers, L. J.; Guan, P.; Koester, S. E.; Little, A. R.; Moore, H. M.; Nierras, C. R.; Rao, A. K.; Vaught, J. B.; Volpi, S.; Snyder, M. P. A Quantitative Proteome Map of the Human Body. *Cell* **2020**, *183* (1), 269-283.e19. https://doi.org/10.1016/j.cell.2020.08.036.

(28) Wang, D.; Eraslan, B.; Wieland, T.; Hallström, B.; Hopf, T.; Zolg, D. P.; Zecha, J.; Asplund, A.; Li, L.; Meng, C.; Frejno, M.; Schmidt, T.; Schnatbaum, K.; Wilhelm, M.; Ponten, F.; Uhlen, M.; Gagneur, J.; Hahne, H.; Kuster, B. A Deep Proteome and Transcriptome Abundance Atlas of 29 Healthy Human Tissues. *Mol. Syst. Biol.* **2019**, *15*, 1-16 (2). https://doi.org/10.15252/msb.20188503.

(29) Christie, D. A.; Lemke, C. D.; Elias, I. M.; Chau, L. A.; Kirchhof, M. G.; Li, B.; Ball, E. H.; Dunn, S. D.; Hatch, G. M.; Madrenas, J. Stomatin-Like Protein 2 Binds Cardiolipin and Regulates Mitochondrial Biogenesis and Function. *Mol. Cell. Biol.* **2011**, *31* (18), 3845–3856. https://doi.org/10.1128/mcb.05393-11.

(30) Panda, D.; Gold, B.; Tartell, M. A.; Rausch, K.; Casas-Tinto, S.; Cherry, S. The Transcription Factor FoxK Participates with Nup98 to Regulate Antiviral Gene Expression. *MBio* **2015**, *6* (2) 1-10. https://doi.org/10.1128/mBio.02509-14.

(31) Yenamandra, S. P. Expression Profile of Nuclear Receptors Upon Epstein -- Barr Virus Induced B Cell Transformation. *Exp. Oncol.* **2009**, *31* (2), 92–96.

(32) Gavin, A. L.; Huang, D.; Huber, C.; Mårtensson, A.; Tardif, V.; Skog, P. D.; Blane, T. R.; Thinnes, T. C.; Osborn, K.; Chong, H. S.; Kargaran, F.; Kimm, P.; Zeitjian, A.; Sielski, R. L.; Briggs, M.; Schulz, S. R.; Zarpellon, A.; Cravatt, B.; Pang, E. S.; Teijaro, J.; de la Torre, J. C.; O'Keeffe, M.; Hochrein, H.; Damme, M.; Teyton, L.; Lawson, B. R.; Nemazee, D. PLD3 and PLD4 Are Single-Stranded Acid Exonucleases That Regulate Endosomal Nucleic-Acid Sensing. *Nat. Immunol.* **2018**, *19* (9), 942–953. https://doi.org/10.1038/s41590-018-0179-y.

(33) Parks, C. L.; Shenk, T. Activation of the Adenovirus Major Late Promoter by Transcription Factors MAZ and Sp1. *J. Virol.* **1997**, *71* (12), 9600–9607. https://doi.org/10.1128/jvi.71.12.9600-9607.1997.

(34) Ovsyannikova, I. G.; Salk, H. M.; Kennedy, R. B.; Haralambieva, I. H.; Zimmermann, M.

T.; Grill, D. E.; Oberg, A. L.; Poland, G. A. Gene Signatures Associated with Adaptive Humoral Immunity Following Seasonal Influenza A/H1N1 Vaccination. *Genes Immun.* **2016**, *17* (7), 371–379. https://doi.org/10.1038/gene.2016.34.

(35) Le, M. X.; Haddad, D.; Ling, A. K.; Li, C.; So, C. C.; Chopra, A.; Hu, R.; Angulo, J. F.; Moffat, J.; Martin, A. Kin17 Facilitates Multiple Double-Strand Break Repair Pathways That Govern B Cell Class Switching. *Sci. Rep.* **2016**, *6*, 1-13. https://doi.org/10.1038/srep37215.

(36) Zhong, B.; Zhang, L.; Lei, C.; Li, Y.; Mao, A. P.; Yang, Y.; Wang, Y. Y.; Zhang, X. L.; Shu, H. B. The Ubiquitin Ligase RNF5 Regulates Antiviral Responses by Mediating Degradation of the Adaptor Protein MITA. *Immunity* **2009**, *30* (3), 397–407. https://doi.org/10.1016/j.immuni.2009.01.008.

(37) Fenech, E. J.; Lari, F.; Charles, P. D.; Fischer, R.; Laétitia-Thézénas, M.; Bagola, K.; Paton, A. W.; Paton, J. C.; Gyrd-Hansen, M.; Kessler, B. M.; Christianson, J. C. Interaction Mapping of Endoplasmic Reticulum Ubiquitin Ligases Identifies Modulators of Innate Immune Signalling. *Elife* **2020**, 1-29. https://doi.org/10.1101/2020.03.18.993998.

(38) Owen, R. P.; Gong, L.; Sagreiya, H.; Klein, T. E.; Altman, R. B. VKORC1 Pharmacogenomics Summary. *Pharmacogenetics and Genomics*. NIH Public Access October 2010, pp 642–644. https://doi.org/10.1097/FPC.0b013e32833433b6.

(39) Ho, D. V.; Chan, J. Y. Induction of Herpud1 Expression by ER Stress Is Regulated by Nrf1. *FEBS Lett.* **2015**, *589* (5), 615–620. https://doi.org/10.1016/j.febslet.2015.01.026.

(40) Qin, L.; Guo, J.; Zheng, Q.; Zhang, H. BAG2 Structure, Function and Involvement in Disease. *Cellular and Molecular Biology Letters*. 1-11. BioMed Central Ltd. September 20, 2016. https://doi.org/10.1186/s11658-016-0020-2.

(41) Chartron, J. W.; Suloway, C. J. M.; Zaslaver, M.; Clemons, W. M. Structural Characterization of the Get4/Get5 Complex and Its Interaction with Get3. *Proc. Natl. Acad. Sci. U. S. A.* **2010**, *107* (27), 12127–12132. https://doi.org/10.1073/pnas.1006036107.

(42) Gottier, P.; Gonzalez-Salgado, A.; Menon, A. K.; Liu, Y. C.; Acosta-Serrano, A.; Bütikofer, P. RFT1 Protein Affects Glycosylphosphatidylinositol (GPI) Anchor Glycosylation. *J. Biol. Chem.* **2017**, *292* (3), 1103–1111. https://doi.org/10.1074/jbc.M116.758367.

(43) Haeuptle, M. A.; Pujol, F. M.; Neupert, C.; Winchester, B.; Kastaniotis, A. J. J.; Aebi, M.; Hennet, T. Human RFT1 Deficiency Leads to a Disorder of N-Linked Glycosylation. *Am. J. Hum. Genet.* **2008**, *82* (3), 600–606. https://doi.org/10.1016/j.ajhg.2007.12.021.

(44) Papp, B.; Brouland, J. P.; Arbabian, A.; Gélébart, P.; Kovács, T.; Bobe, R.; Enouf, J.; Varin-Blank, N.; Apáti, Á. Endoplasmic Reticulum Calcium Pumps and Cancer Cell Differentiation. *Biomolecules*. MDPI AG 2012, pp 165–186. https://doi.org/10.3390/biom2010165.

(45) Seo, J.; Lee, S. H.; Park, S. Y.; Jeong, M. H.; Lee, S. Y.; Kim, M. J.; Yoo, J. Y.; Jang, S.; Choi, K. C.; Yoon, Ho G. GPR177 Promotes Gastric Cancer Proliferation by Suppressing Endoplasmic Reticulum Stress-Induced Cell Death. *J. Cell. Biochem.* **2019**, *120* (2), 2532–2539. https://doi.org/10.1002/jcb.27545.

(46) Cui, J.; Chen, W.; Sun, J.; Guo, H.; Madley, R.; Xiong, Y.; Pan, X.; Wang, H.; Tai, A. W.;

Weiss, M. A.; Arvan, P.; Liu, M. Competitive Inhibition of the Endoplasmic Reticulum Signal Peptidase by Non-Cleavable Mutant Preprotein Cargos. *J. Biol. Chem.* **2015**, *290* (47), 28131–28140. https://doi.org/10.1074/jbc.M115.692350.

(47) Blanc, M.; Hsieh, W. Y.; Robertson, K. A.; Watterson, S.; Shui, G.; Lacaze, P.; Khondoker, M.; Dickinson, P.; Sing, G.; Rodríguez-Martín, S.; Phelan, P.; Forster, T.; Strobl, B.; Müller, M.; Riemersma, R.; Osborne, T.; Wenk, M. R.; Angulo, A.; Ghazal, P. Host Defense against Viral Infection Involves Interferon Mediated Down-Regulation of Sterol Biosynthesis. *PLoS Biol.* **2011**, *9* (3). 1-19 https://doi.org/10.1371/journal.pbio.1000598.

(48) van 't Wout, A. B.; Swain, J. V.; Schindler, M.; Rao, U.; Pathmajeyan, M. S.; Mullins, J. I.; Kirchhoff, F. Nef Induces Multiple Genes Involved in Cholesterol Synthesis and Uptake in Human Immunodeficiency Virus Type 1-Infected T Cells. *J. Virol.* **2005**, *79* (15), 10053–10058. https://doi.org/10.1128/jvi.79.15.10053-10058.2005.

(49) Diamond, D. L.; Syder, A. J.; Jacobs, J. M.; Sorensen, C. M.; Walters, K. A.; Proll, S. C.; McDermott, J. E.; Gritsenko, M. A.; Zhang, Q.; Zhao, R.; Metz, T. O.; Camp, D. G.; Waters, K. M.; Smith, R. D.; Rice, C. M.; Katze, M. G. Temporal Proteome and Lipidome Profiles Reveal Hepatitis C Virus-Associated Reprogramming of Hepatocellular Metabolism and Bioenergetics. *PLoS Pathog.* **2010**, *6* (1) 1-18. https://doi.org/10.1371/journal.ppat.1000719.

(50) Xiao, J.; Li, W.; Zheng, X.; Qi, L.; Wang, H.; Zhang, C.; Wan, X.; Zheng, Y.; Zhong, R.; Zhou, X.; Lu, Y.; Li, Z.; Qiu, Y.; Liu, C.; Zhang, F.; Zhang, Y.; Xu, X.; Yang, Z.; Chen, H.; Zhai, Q.; Wei, B.; Wang, H. Targeting 7-Dehydrocholesterol Reductase Integrates Cholesterol Metabolism and IRF3 Activation to Eliminate Infection. *Immunity* **2020**, *52* (1), 109-122.e6. https://doi.org/10.1016/j.immuni.2019.11.015.

(51) Larance, M.; Kirkwood, K. J.; Xirodimas, D. P.; Lundberg, E.; Uhlen, M.; Lamond, A. I. Characterization of MRFAP1 Turnover and Interactions Downstream of the NEDD8 Pathway. *Mol. Cell. Proteomics* **2012**, *11* (3) 1-11. https://doi.org/10.1074/mcp.M111.014407.

(52) Kelly, T. J.; Suzuki, H. I.; Zamudio, J. R.; Suzuki, M.; Sharp, P. A. Sequestration of MicroRNA-Mediated Target Repression by the Ago2-Associated RNA-Binding Protein FAM120A. *RNA* **2019**, *25* (10), 1291–1297. https://doi.org/10.1261/rna.071621.119.

(53) Bartolomé, R. A.; García-Palmero, I.; Torres, S.; López-Lucendo, M.; Balyasnikova, I. V.; Casal, J. I. IL13 Receptor A2 Signaling Requires a Scaffold Protein, FAM120A, to Activate the FAK and PI3K Pathways in Colon Cancer Metastasis. *Cancer Res.* **2015**, *75* (12), 2434–2444. https://doi.org/10.1158/0008-5472.CAN-14-3650.

(54) Lampert, F.; Stafa, D.; Goga, A.; Soste, M. V.; Gilberto, S.; Olieric, N.; Picotti, P.; Stoffel, M.; Peter, M. The Multi-Subunit GID/CTLH E3 Ubiquitin Ligase Promotes Cell Proliferation and Targets the Transcription Factor Hbp1 for Degradation. *Elife* **2018**, *7*, 1-23. https://doi.org/10.7554/eLife.35528.

(55) Cho, K. F.; Branon, T. C.; Rajeev, S.; Svinkina, T.; Udeshi, N. D.; Thoudam, T.; Kwak, C.; Rhee, H.-W.; Lee, I.-K.; Carr, S. A.; Ting, A. Y.; Chan, M.; Biohub, Z.; Francisco, S. Split-TurboID Enables Contact-Dependent Proximity Labeling in Cells. *PNAS* **2020** 1-12 https://doi.org/10.1073/pnas.1919528117/-/DCSupplemental.

(56) Kwak, C.; Shin, S.; Park, J.-S.; Jung, M.; Thi My Nhung, T.; Kang, M.-G.; Lee, C.; Kwon, T.-H.; Ki Park, S.; Young Mun, J.; Kim, J.-S.; Rhee, H.-W. Contact-ID, a Tool for Profiling Organelle Contact Sites, Reveals Regulatory Proteins of Mitochondrial-Associated Membrane Formation. *PNAS* **2020** 1-12. https://doi.org/10.1073/pnas.1916584117/-/DCSupplemental.

(57) Carreras-Sureda, A.; Jaña, F.; Urra, H.; Durand, S.; Mortenson, D. E.; Sagredo, A.; Bustos, G.; Hazari, Y.; Ramos-Fernández, E.; Sassano, M. L.; Pihán, P.; van Vliet, A. R.; González-Quiroz, M.; Torres, A. K.; Tapia-Rojas, C.; Kerkhofs, M.; Vicente, R.; Kaufman, R. J.; Inestrosa, N. C.; Gonzalez-Billault, C.; Wiseman, R. L.; Agostinis, P.; Bultynck, G.; Court, F. A.; Kroemer, G.; Cárdenas, J. C.; Hetz, C. Non-Canonical Function of IRE1α Determines Mitochondria-Associated Endoplasmic Reticulum Composition to Control Calcium Transfer and Bioenergetics. *Nat. Cell Biol.* **2019**, *21* (6), 755–767. https://doi.org/10.1038/s41556-019-0329-y.

(58) Kim, J. H.; Rhee, J. K.; Ahn, D. G.; Kim, K. P.; Oh, J. W. Interaction of Stomatin with Hepatitis C Virus RNA Polymerase Stabilizes the Viral RNA Replicase Complexes on Detergent-Resistant Membranes. *J. Microbiol. Biotechnol.* **2014**, *24* (12), 1744–1754. https://doi.org/10.4014/jmb.1409.09063.

(59) Wintachai, P.; Wikan, N.; Kuadkitkan, A.; Jaimipuk, T.; Ubol, S.; Pulmanausahakul, R.; Auewarakul, P.; Kasinrerk, W.; Weng, W. Y.; Panyasrivanit, M.; Paemanee, A.; Kittisenachai, S.; Roytrakul, S.; Smith, D. R. Identification of Prohibitin as a Chikungunya Virus Receptor Protein. *J. Med. Virol.* **2012**, *84* (11), 1757–1770. https://doi.org/10.1002/jmv.23403.

(60) Too, I. H. K.; Bonne, I.; Tan, E. L.; Chu, J. J. H.; Alonso, S. Prohibitin Plays a Critical Role in Enterovirus 71 Neuropathogenesis. *PLoS Pathog.* **2018**, *14* (1) 1-29. https://doi.org/10.1371/journal.ppat.1006778.

(61) Richter, K. T.; Kschonsak, Y. T.; Vodicska, B.; Hoffmann, I. FBXO45-MYCBP2 Regulates Mitotic Cell Fate by Targeting FBXW7 for Degradation. *Cell Death Differ.* **2020**, *27* (2), 758–772. https://doi.org/10.1038/s41418-019-0385-7.

(62) Gordon, D. E.; Hiatt, J.; Bouhaddou, M.; Rezelj, V. V; Ulferts, S.; Braberg, H.; Jureka, A. S.; Obernier, K.; Guo, J. Z.; Batra, J.; Kaake, R. M.; Weckstein, A. R.; Owens, T. W.; Gupta, M.; Pourmal, S.; Titus, E. W.; Cakir, M.; Soucheray, M.; McGregor, M.; Cakir, Z.; Jang, G.; O, M. J.; Tummino, T. A.; Zhang, Z.; Foussard, H.; Rojc, A.; Zhou, Y.; Kuchenov, D.; Hüttenhain, R.; Xu, J.; Eckhardt, M.; Swaney, D. L.; Fabius, J. M.; Ummadi, M.; Tutuncuoglu, B.; Rathore, U.; Modak, M.; Haas, P.; Haas, K. M.; Zar Chi Naing, Z.; Pulido, E. H.; Shi, Y.; Barrio-Hernandez, I.; Memon, D.; Petsalaki, E.; Dunham, A.; Correa Marrero, M.; Burke, D.; Koh, C.; Vallet, T.; Silvas, J. A.; Azumaya, C. M.; Billesbølle, C.; Brilot, A. F.; Campbell, M. G.; Diallo, A.; Sasha Dickinson, M.; Diwanji, D.; Herrera, N.; Hoppe, N.; Kratochvil, H. T.; Liu, Y.; Merz, G. E.; Moritz, M.; Nguyen, H. C.; Nowotny, C.; Puchades, C.; Rizo, A. N.; Schulze-Gahmen, U.; Smith, A. M.; Sun, M.; Young, I. D.; Zhao, J.; Asarnow, D.; Biel, J.; Bowen, A.; Braxton, J. R.; Chen, J.; Chio, C. M.; Seng Chio, U.; Deshpande, I.; Doan, L.; Faust, B.; Flores, S.; Jin, M.; Kim, K.; Lam, V. L.; Li, F.; Li, J.; Li, Y.-L.; Li, Y.; Liu, X.; Lo, M.; Lopez, K. E.; Melo, A. A.; Moss III, F. R.; Nguyen, P.; Paulino, J.; Ishwar Pawar, K.; Peters, J. K.; Pospiech Jr, T. H.; Safari, M.; Sangwan, S.; Schaefer, K.; Thomas, P. V; Thwin, A. C.; Trenker, R.; Tse, E.; Kin Martin

Tsui, T.; Wang, F.; Whitis, N.; Yu, Z.; Zhang, K.; Zhang, Y.; Zhou, F.; Saltzberg, D.; Moreno, E.; Patel, A. H.; Rihn, S.; Khalid, M. M.; Vallejo-Gracia, A.; Fozouni, P.; Simoneau, C. R.; Roth, T. L.; Wu, D.; Anisul Karim, M.; Ghoussaini, M.; Dunham, I.; Berardi, F.; Weigang, S.; Chazal, M.; Park, J.; Logue, J.; McGrath, M.; Weston, S.; Haupt, R.; James Hastie, C.; Elliott, M.; Brown, F.; Burness, K. A.; Reid, E.; Dorward, M.; Johnson, C.; Wilkinson, S. G.; Geyer, A.; Giesel, D. M.; Baillie, C.; Raggett, S.; Leech, H.; Toth, R.; Goodman, N.; Keough, K. C.; Lind, A. L.; Consortium, Z.; Klesh, R. J.; Hemphill, K. R.; Carlson-Stevermer, J.; Oki, J.; Holden, K.; Maures, T.; Pollard, K. S.; Basler, C. F.; Vignuzzi, M.; Peden, A. A.; Beltrao, P.; Krogan, N. J. Comparative Host-Coronavirus Protein Interaction Networks Reveal Pan-Viral Disease Mechanisms. *Science (80-.).* **2020**, *22*, 14, 1-30. https://doi.org/10.1126/science.abe9403.

(63) Heaton, B. E.; Trimarco, J. D.; Hamele, C. E.; Harding, A. T.; Tata, A.; Zhu, X.; Tata, P. R.; Smith, C. M.; Heaton, N. S. SRSF Protein Kinases 1 and 2 Are Essential Host Factors for Human Coronaviruses Including SARS-CoV-2. *bioRxiv* **2020**, 2020.08.14.251207. https://doi.org/10.1101/2020.08.14.251207.

(64) Abbas, Y. M.; Wu, D.; Bueler, S. A.; Robinson, C. V.; Rubinstein, J. L. Structure of V-ATPase from the Mammalian Brain. *Science* **2020** Vol. 367, 1240-1246. https://doi.org/10.1126/science.aba1120.

(65) Song, X.; Liu, S.; Wang, W.; Ma, Z.; Cao, X.; Jiang, M. E3 Ubiquitin Ligase RNF170 Inhibits Innate Immune Responses by Targeting and Degrading TLR3 in Murine Cells. *Cell. Mol. Immunol.* **2019**. 865-874. https://doi.org/10.1038/s41423-019-0236-y.

(66) Lu, J. P.; Wang, Y.; Sliter, D. A.; Pearce, M. M. P.; Wojcikiewicz, R. J. H. RNF170 Protein, an Endoplasmic Reticulum Membrane Ubiquitin Ligase, Mediates Inositol 1,4,5-Trisphosphate Receptor Ubiquitination and Degradation. *J. Biol. Chem.* **2011**, *286* (27), 24426–24433. https://doi.org/10.1074/jbc.M111.251983.

(67) Berridge, M. J. Inositol Trisphosphate and Calcium Signalling. *Nature* **1993,** *361*, 315-325.

(68) Bartok, A.; Weaver, D.; Golenár, T.; Nichtova, Z.; Katona, M.; Bánsághi, S.; Alzayady, K. J.; Thomas, V. K.; Ando, H.; Mikoshiba, K.; Joseph, S. K.; Yule, D. I.; Csordás, G.; Hajnóczky, G. IP3 Receptor Isoforms Differently Regulate ER-Mitochondrial Contacts and Local Calcium Transfer. *Nat. Commun.* **2019**, *10* (1), 1–14. https://doi.org/10.1038/s41467-019-11646-3.

(69) Missiroli, S.; Patergnani, S.; Caroccia, N.; Pedriali, G.; Perrone, M.; Previati, M.; Wieckowski, M. R.; Giorgi, C. Mitochondria-Associated Membranes (MAMs) and Inflammation. *Cell Death Dis.* **2018** (329) 1-14.. https://doi.org/10.1038/s41419-017-0027-2.

(70) Kuchay, S.; Saeed, M.; Giorgi, C.; Li, J.; Hoffmann, H. H.; Pinton, P.; Rice, C. M.; Pagano, M. NS5A Promotes Constitutive Degradation of IP3R3 to Counteract Apoptosis Induced by Hepatitis C Virus. *Cell Rep.* **2018**, *25* (4), 833-840.e3. https://doi.org/10.1016/j.celrep.2018.09.088.

(71) Nieto-Torres, J. L.; Verdiá-Báguena, C.; Jimenez-Guardeño, J. M.; Regla-Nava, J. A.; Castaño-Rodriguez, C.; Fernandez-Delgado, R.; Torres, J.; Aguilella, V. M.; Enjuanes, L. Severe Acute Respiratory Syndrome Coronavirus E Protein Transports Calcium Ions and

Activates the NLRP3 Inflammasome. *Virology* **2015** (485) 330-339. https://doi.org/10.1016/j.virol.2015.08.010.

(72) Bojkova, D.; Klann, K.; Koch, B.; Widera, M.; Krause, D.; Ciesek, S.; Cinatl, J.; Münch, C. Proteomics of SARS-CoV-2-Infected Host Cells Reveals Therapy Targets. *Nature* **2020**, *583*, 469-472. https://doi.org/10.1038/s41586-020-2332-7.

(73) Wright, M. T.; Kouba, L.; Plate, L. Thyroglobulin Interactome Profiling Uncovers Molecular Mechanisms of Thyroid Dyshormonogenesis. https://doi.org/10.1101/2020.04.08.032482.

(74) Fonslow, B. R.; Niessen, S. M.; Singh, M.; Wong, C. C.; Xu, T.; Carvalho, P. C.; Choi, J.; Park, S. K.; Yates 3rd, J. R. Single-Step Inline Hydroxyapatite Enrichment Facilitates Identification and Quantitation of Phosphopeptides from Mass-Limited Proteomes with MudPIT. *J Proteome Res* **2012**, *11* (5), 2697–2709. https://doi.org/10.1021/pr300200x.

(75) Keilhauer, E. C.; Hein, M. Y.; Mann, M. Accurate Protein Complex Retrieval by Affinity Enrichment Mass Spectrometry (AE-MS) Rather than Affinity Purification Mass Spectrometry (AP-MS). *Mol. Cell. Proteomics* **2015**, *14* (1), 120–135. https://doi.org/10.1074/mcp.M114.041012.

(76) Perez-Riverol, Y.; Csordas, A.; Bai, J.; Bernal-Llinares, M.; Hewapathirana, S.; Kundu, D. J.; Inuganti, A.; Griss, J.; Mayer, G.; Eisenacher, M.; Pérez, E.; Uszkoreit, J.; Pfeuffer, J.; Sachsenberg, T.; Yilmaz, Ş.; Tiwary, S.; Cox, J.; Audain, E.; Walzer, M.; Jarnuczak, A. F.; Ternent, T.; Brazma, A.; Vizcaíno, J. A. The PRIDE Database and Related Tools and Resources in 2019: Improving Support for Quantification Data. *Nucleic Acids Res.* **2019**, *47* (D1), D442–D450. https://doi.org/10.1093/nar/gky1106.

(77) Kuleshov, M. V; Jones, M. R.; Rouillard, A. D.; Fernandez, N. F.; Duan, Q.; Wang, Z.; Koplev, S.; Jenkins, S. L.; Jagodnik, K. M.; Lachmann, A.; Mcdermott, M. G.; Monteiro, C. D.; Gundersen, G. W.; Ma'ayan, A. Enrichr: A Comprehensive Gene Set Enrichment Analysis Web Server 2016 Update. *Nucleic Acids Res.* **2016**, *44*, W90-W97. https://doi.org/10.1093/nar/gkw377.

(78) Bozidis, P.; Williamson, C. D.; Colberg-Poley, A. M. Isolation of Endoplasmic Reticulum, Mitochondria, and Mitochondria-Associated Membrane Fractions from Transfected Cells and from Human Cytomegalovirus-Infected Primary Fibroblasts. *Curr. Protoc. Cell Biol.* **2007**, *37* (1), 3.27.1-3.27.23. https://doi.org/10.1002/0471143030.cb0327s37.

CHAPTER 6: Comparative host interactomes of the SARS-CoV-2 nonstructural protein 3 and human coronavirus homologs

This chapter is adapted, with permission from journals and co-authors, from Almasy, K.M.*, Davies, J.P.*., and Plate, L., *Molecular and Cellular Proteomics*, **2021**, 20 (100120), https://doi.org/10.1016/j.mcpro.2021.100120.

*authors contributed equally

6.1 Introduction

Coronaviruses are a family of positive-sense, single-stranded RNA viruses that typically cause upper respiratory infection in humans. Four endemic strains have been characterized that cause symptoms resembling those of the common cold. However, since 2002, three more pathogenic strains have emerged: SARS-CoV in 2002, MERS-CoV in 2012, and SARS-CoV-2, the causative agent of COVID-19, in 2019[1–5]. Some of the differences in pathogenicity can be attributed to differential receptor binding, for example, SARS-CoV and SARS-CoV-2 utilize the angiotensin converting enzyme 2 (ACE2) receptor, while 229E (a common-cold causing strain) uses the human aminopeptidase N receptor[5–7]. At the same time, the engagement of viral proteins with different host proteins or complexes within infected cells is equally critical to understand changes in pathogenicity. These engagements alter the native protein-protein interaction (PPI) architecture of the cell and have been shown to perform various pro-viral functions such as suppression of the type I interferon system for immune evasion purposes[8–10].

The coronavirus genome is among the largest RNA virus genomes, at approximately 30 kilobase pairs in length. The 3’ third of the genome encodes for the four structural proteins used to construct new virions, as well as several accessory factors shown to be important for pathogenesis. The 5’ two thirds of the genome consist of two open reading frames (orf1a and orf1b) that encode for sixteen non-structural proteins (nsps) that perform a number of functions

throughout the viral life cycle, including replication and proofreading of the RNA genome and formation of the replication-transcription complex. The largest of these proteins, at approximately 2000 amino acids, is nsp3. Nsp3 is a large multi-domain protein, of which the papain-like-protease ($PL2^{Pro}$) domain has been most closely studied. In addition to autoproteolysis of the viral polyprotein, the $PL2^{Pro}$ domains possess both deubiquitinase and deISGylation activities[11–13]. Additionally, nsp3 in complex with nsp4 and nsp6 has been shown to be sufficient for formation of the double-membraned vesicles (DMVs) implicated in the CoV replication cycle[14,15]. Expression of the C-terminus of nsp3 and full-length nsp4, while not enough to induce DMV formation, does cause zippering of the ER membrane[16]. However, role(s) of nsp3 outside of the $PL2^{Pro}$ remain less well understood[17].

Herein, we focused our analysis on four nsp3 homologs from the genus betacoronavirus (hCoV-OC43, MERS-CoV, SARS-CoV, SARS-CoV-2) and one homolog from the genus alphacoronavirus (hCoV-229E). Within the betacoronaviruses, hCoV-OC43 is from clade A, SARS-CoV and SARS-CoV-2 are from clade B, and MERS-CoV is from clade C. The domain organization of nsp3 varies widely among coronavirus genera, and even from strain to strain. Despite the differences, ten regions are conserved across all coronavirus variants: two ubiquitin-like domains (UBLs), a glutamic acid-rich domain, protease domain, two transmembrane regions separated by an ER ectodomain, and two C-terminal Y domains (**Figure A6.1**).

Affinity purification-mass spectrometry (AP-MS) has been used extensively to characterize the coronavirus interactome, including in two large studies by Gordon et al. to characterize the SARS-CoV-2 host protein interactions and compare these to the SARS-CoV and MERS-CoV interactomes[18,19]. Another study compared the interactomes of isolated SARS-CoV and SARS-CoV-2 $PL2^{pro}$ domains[11]. However, the remaining parts of nsp3 have been missing from SARS-CoV-2 interactome studies thus far, likely because their complex topology and large size makes expression of the protein difficult. To circumvent this problem, we divided the nsp3 protein into three fragments based on earlier interrogation of the SARS intraviral interactome[14,20]. These

fragments are referred to as nsp3.1 for the N-terminal fragment, nsp3.2 for the middle fragment, and nsp3.3 for the C-terminal fragment[21]. We expressed each fragment from each of the five viruses listed above (hCoV-229E, hCoV-OC43, MERS-CoV, SARS-CoV, SARS-CoV-2). We employed tandem mass tag (TMTpro 16plex) isobaric tagging technology, which enables highly multiplexed analysis for direct comparison of interactor abundances across homologs from all strains. Previously, we demonstrated the use of AP-MS and TMT technologies in comparing the interactomes of the coronavirus nsp2 and nsp4 proteins from three strains: SARS-CoV-2, SARS-CoV, and hCoV-OC43[22]. We now extend the analysis to the understudied nsp3 protein across additional viral strains. In particular, comparing host protein interactions for homologs from multiple coronavirus strains and genera may provide insight into how the molecular mechanisms of pathogenic coronaviruses differ from endemic ones, as well as the evolution of functions that nsp3 assumes across these strains.

Our study finds that very few interactors are shared among the five strains, although several interactors are common among the mostly conserved SARS variants. Several previously unknown pathways are discovered to be highly enriched with individual variants, such as ERAD processing for SARS-CoV nsp3.2 and nuclear import for 229E nsp3.2. In addition, we find that SARS-CoV-2 nsp3.1 interacts with the unfolded protein response (UPR) transcription factor ATF6 and suppresses the ATF6 pathway in both basal and activated conditions. These discoveries open the door for further work delineating the role of nsp3 in coronavirus infections, with a particular emphasis on the variation in roles between different CoV strains.

6.2 Results

6.2.1 Expression of nsp3 truncations and AP-MS of CoV nsp3

The orf1a and orf1b open reading frames encode for 16 non-structural proteins which perform crucial roles during the viral life cycle, including replication of the genome and formation of double-membraned vesicles. Non-structural protein 3 (nsp3) is the largest of the 16 non-structural

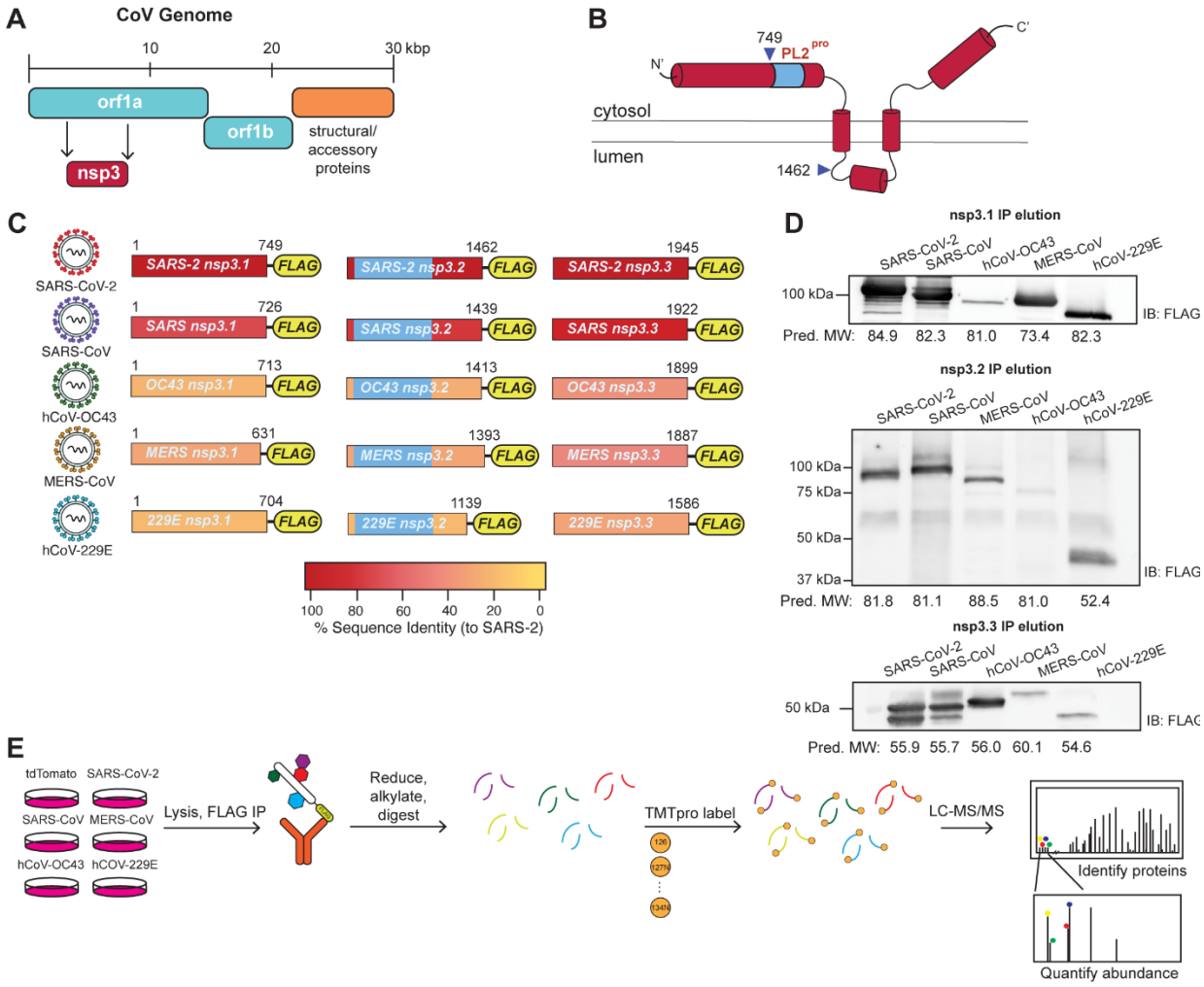

Figure 6.1. Design and expression of CoV nsp3 truncations for affinity-purification mass spectrometry (AP-MS).

A) Coronavirus (CoV) genome schematic indicating the regions encoding orf1a, orf1ab, and structural/accessory proteins. Nsp3 is encoded within orf1a.

B) General schematic of SARS-CoV-2 nsp3 protein topology. Nsp3 has two single-span transmembrane regions anchoring the protein in the ER membrane, with a small luminal domain and both N and C terminal regions in the cytosol. The conserved papain-like protease ($PL2^{pro}$) domain is on the N-terminal cytosolic portion. For this study, the nsp3 protein was truncated into three fragments: nsp3.1 (1-749), nsp3.2 (750-1462), and nsp3.3 (1463-1945), numbering corresponding to SARS-CoV-2 nsp3.

C) The nsp3 truncations for homologs from all five human coronaviruses used in this study. All fragments contain a C-terminal FLAG tag for affinity-purification. Percent sequence identity compared to SARS-CoV-2 is indicated. The $PL2^{pro}$ domain in nsp3.2 homologs is highlighted in light blue.

D) Western blotting of immunopurified nsp3.1, nsp3.2, and nsp3.3 homologs after transient transfection in HEK293T cells. Predicted MW of proteins is indicated below.

E) AP-MS workflow to identify virus-host protein interactions of nsp3 fragment homologs. HEK293T cells were transfected with corresponding homologs and lysates were

immunopurified using anti-FLAG beads to enrich for viral proteins in complex with host interactors. Proteins were reduced, alkylated, and digested with trypsin. Peptides were then labeled with tandem mass tags (TMTpro) and analyzed by tandem mass spectrometry (LC-MS/MS) to both identify and quantify host interactors.

proteins; the full-length protein is 1586–1945 amino acids long (177-217 kDa) (**Figure 6.1A**). While the domain organization is different among CoV variants, several domains are shared, including multiple ubiquitin-like-domains, at least one highly conserved papain-like protease ($PL2^{Pro}$) domain, and an ER luminal domain postulated to be important for nsp4 binding and double membrane vesicle (DMV) formation (**Figure 6.1B-C, Figure A6.1**).

Initial attempts at expression of the full-length construct for SARS-CoV-2 nsp3 were unsuccessful, likely due to the complex structure and topology of the full-length protein. To study the interactome, we thus divided the protein into three portions based on a prior interactome study carried out on similar truncations of the SARS-CoV nsp3 homolog[20]. The N-terminal fragment (nsp3.1), comprising the first ubiquitin-like-domain through the SARS unique domain, is expected to localize exclusively to the cytosol (**Figure 6.1C**, **Figure A6.1**). The second portion (nsp3.2), starting before the second ubiquitin-like domain and ending just after the first transmembrane region, includes the papain-like-protease ($PL2^{Pro}$) domain. The C-terminal fragment (nsp3.3) starts with the ER-localized 3Ecto-domain, includes the second transmembrane region and ends with the C-terminus of the protein. Based on multiple sequence alignments, similar N-terminal, middle, and C-terminal constructs were created for the SARS-CoV-2, MERS-CoV, hCoV-OC43, and hCoV-229E nsp3 homologs (**Figure A6.1**). Each construct contains a C-terminal FLAG tag for affinity purification (**Figure 6.1C**).

Constructs were transfected into HEK293T cells, and expression was confirmed by immunoprecipitation and immunoblotting for the FLAG tag and/or detection by mass spectrometry (**Figure 6.1D**). Overall, SDS-PAGE gel patterns matched with the expected molecular weights; the exception was the MERS nsp3.1 fragment, which ran larger than expected. In addition,

confocal immunofluorescence microscopy of transfected HEK293T cells shows that nsp3.2 and nsp3.3 homologs colocalize with PDIA4, an ER marker, while nsp3.1 exhibits cytosolic localization as expected (**Figure A6.2A-C**). Although kidney cells do not represent a primary tissue target of the virus, previous work has identified HEK293T cells as appropriate cell lines to recapitulate relevant CoV protein interactions with host factors[18,22]. While the constructs showed variable expression levels, all fragments were reproducibly detectable by mass spectrometry, and peptides coverage spanned the length of each fragment (**Figure 6.1D**). For native co-immunoprecipitations with host interactors, protein constructs were expressed, lysed in mild detergent buffer to maintain interactions, and co-immunoprecipitated from lysates using anti-FLAG beads. After confirmation of IP by silver stain, samples were reduced, alkylated, and trypsin digested. Samples were labeled using TMTpro 16plex reagents for MS2 quantification of peptides abundances[23] (**Figure 6.1E**). Between 2 and 4 co-immunoprecipitation replicates for each construct were pooled into a single TMTpro 16plex run, along with mock IPs from tdTomato transfected cells to establish the background signal. The final datasets consisted of 184 IPs across the 16 constructs (tdTomato & 15 viral protein constructs) (**Figure A6.3**). We quantified the abundance of nsp3 bait proteins across the biological replicates showing consistent enrichment compared to the mock control (**Figure A6.3G-I**).

After identification and quantification of interactors using Proteome Discoverer, a variable cutoff method was used to determine high- and medium- confidence interactors for each construct based on enrichments compared to the tdTomato background control.

6.2.2 Comparison of CoV nsp3.1-host interactors

The N-terminal fragments of nsp3 contain a conserved ubiquitin-like domain (Ubl1), a highly variable or acidic-rich region, a conserved macrodomain (Mac1), followed by strain-specific domains (**Figure 6.2A, Figure A6.1**). In hCoV-229E and hCoV-OC43, this fragment includes a papain-like protease domain (termed $PL1^{Pro}$). This first $PL1^{Pro}$ domain is absent from all viruses

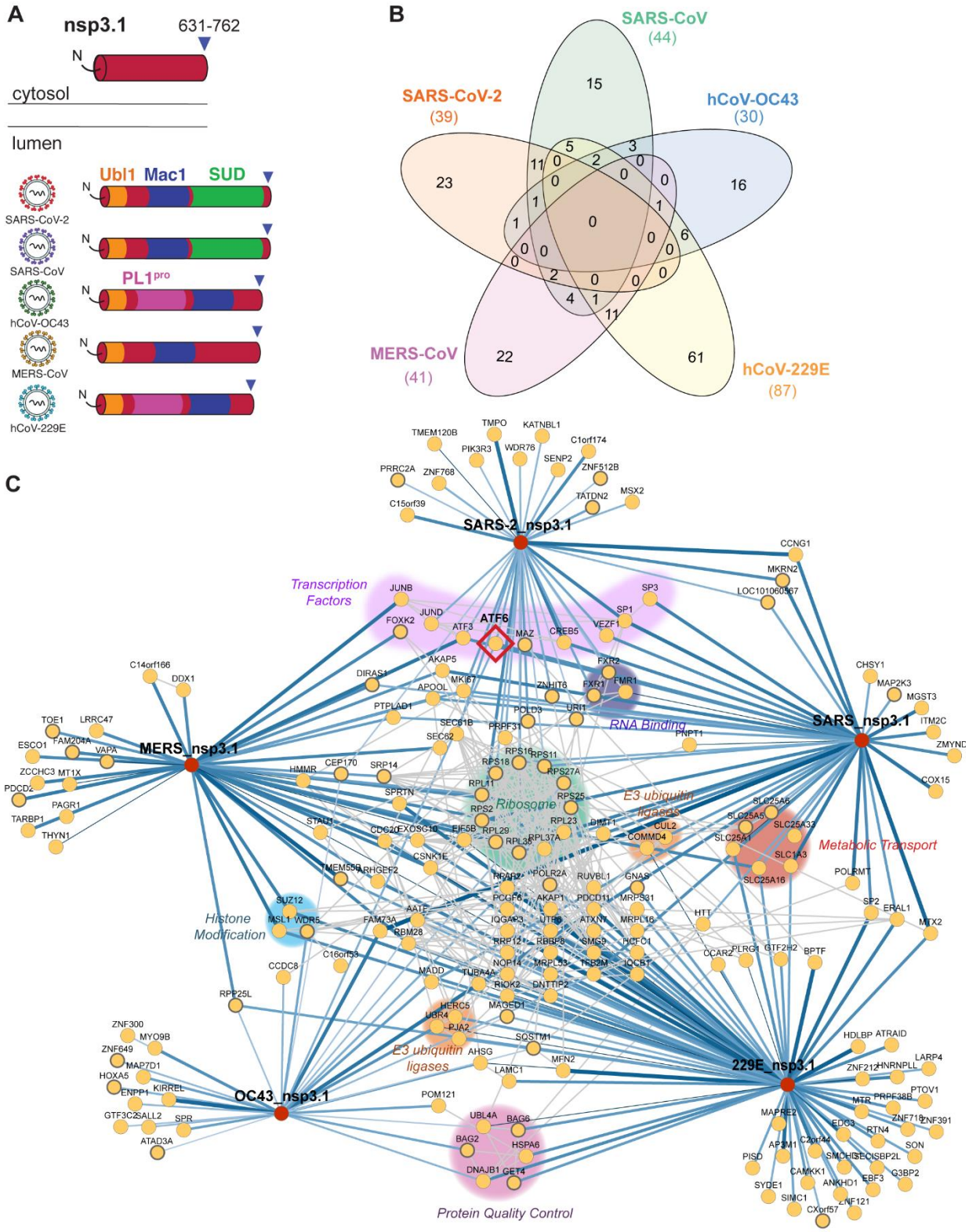
A
nsp3.1
631-762
N
cytosol
lumen
Ubl1 Mac1 SUD
SARS-CoV-2
SARS-CoV
PL1pro
hCoV-OC43
MERS-CoV
hCoV-229E
B
SARS-CoV
(44)
SARS-CoV-2
(39)
hCoV-OC43
(30)
MERS-CoV
(41)
hCoV-229E
(87)
15
23
16
22
61
11
C
SARS-2_nsp3.1
Transcription Factors
JUNB
JUND
FOXK2
ATF3
ATF6
MAZ
CREB5
SP3
SP1
VEZF1
RNA Binding
Ribosome
E3 ubiquitin ligases
Metabolic Transport
Histone Modification
MERS_nsp3.1
SARS_nsp3.1
229E_nsp3.1
OC43_nsp3.1
Protein Quality Control

Figure 6.2. Identification of CoV nsp3.1 host interactors.

A. Schematic of nsp3.1 topology for all five CoV homologs. Nsp3.1 is a cytosolic fragment, comprising residues from 1 to 631-762. All fragment homologs contain a ubiquitin-like domain (Ubl1, yellow) and a conserved macrodomain (Mac1, blue). SARS-CoV-2 and SARS-CoV contain a SARS-unique domain (SUD, green), while hCoV-OC43 and hCoV-229E contain a papain-like protease domain ($PL1^{pro}$, pink).
B. Venn diagram showing the number of unique and shared host interactors amongst all five CoV nsp3.1 homologs. Total interactors for each homolog are shown in parentheses.
C. Network plot of virus-host interactors. Individual nsp3.1 homologs are shown as red circles, while host interactors are shown as yellow circles. Blue lines indicate virus-host protein interactions, where line width and shade are wider/darker for more highly enriched interactions. Grey lines indicate known host-host protein interactions from the STRING database. Notable clusters of host proteins are highlighted. The transcription factor ATF6 (red diamond) interacts with SARS-CoV-2, SARS-CoV, and hCoV-OC43 and was subjected to later functional follow-up (**Figure 6.5**).

in clades B and C of the betacoronaviruses, hence its absence in MERS-CoV and the two SARS variants. In contrast, SARS strains contain a SARS-unique domain (SUD) consisting of 3 sequential macrodomains. Overall, this region of nsp3 is most variable from strain to strain, despite several of the predicted domains being conserved (**Figure 6.1B-C, Figure A6.1**).

The final dataset for the N-terminal fragment analysis combined 5 mass spectrometry runs containing 62 co-IP samples (tdTomato 15, SARS-CoV-2 13, SARS-CoV 9, OC43 9, MERS 8, 229E 8) (**Figure A6.2A**). We identified a robust set of high-confidence interactors for each fragment: 39 for SARS-CoV-2, 44 for SARS-CoV, 41 for MERS-CoV, 30 for hCoV-OC43, and 87 for hCoV-229E (**Figure A6.4**).

Of these high-confidence interactors, none were common across all 5 strains, and none were common to all betacoronaviruses (**Figure A6.2B**). Fourteen interactors were common between the two SARS variants, and 2 of these 14 interactors, MKI67 and ATF3, were also shared with the MERS fragment. MKI67 is required to maintain individual chromosomes in the cytoplasm during mitosis, and ATF3 is a cyclic AMP-dependent transcription factor which negatively regulates the cellular antiviral response. Lastly, we identified 25 high confidence interactors unique to SARS-CoV-2, 16 unique to SARS-CoV, 17 unique to hCoV-OC43, 62 unique to hCoV-

229E, and 23 unique to MERS-CoV. Notably contained in this fragment is the SARS-unique domain, which is exclusively found in SARS-CoV and SARS-CoV-2 nsp3. As noted, 14 proteins were identified as interactors of both fragments. Eleven of these interactors were exclusive to the SARS variants, including several ribosomal proteins (RPL38, RPS11, RPS2, RPS16) and assorted factors (FMR1, MKRN2, SP1, VEZF1, CREB5, CCNG1, and PEX11B).

We also identify 9 shared interactors between OC43 and 229E, both of which have a $PL1^{pro}$ domain (UBR4, TUBA4A, SQSTM1, RPP25L, MADD, DNAJB1, BAG6, AHSG, AATF). BAG6 and DNAJB1 are co-chaperones components involved in protein quality control [24,25], while UBR4 is an E3 ubiquitin ligase involved in membrane morphogenesis and SQSTM1 is an autophagy receptor[26,27]. These shared interactors may represent possible targets of the $PL1^{pro}$ domains in OC43 and 229E.

We performed the same filtering on proteins observed to be less enriched with the viral bait and more enriched with the tdTomato background, interpreting these largely to be proteins which bind non-specifically to the FLAG beads in the absence of viral bait and its interactors (**Figure A6.4**). To determine any overlap between our data set and contaminant interactors, we queried all identified high-confidence interactors in the Contaminant Repository for Affinity Purification (CRAPome) dataset for common contaminant proteins found in control AP-MS experiments[28]. Using a frequency threshold of 25%, only 34 of 186 unique high-confidence interactors overlapped with the CRAPome (**Figure A6.5**), emphasizing the specificity of host interactors for viral bait proteins. Many of these overlapping interactors are ribosomal and chaperone proteins with central roles in protein biogenesis and may be expected to be found in control AP-MS experiments.

As an alternative method to map shared and unique interactors for nsp3.1 from the different strains, we performed hierarchical clustering of the grouped protein abundance Z-scores for all identified high-confidence interactors (**Figure A5.6**). Consistent with the Venn diagram, we observed a cluster of shared interactors for the SARS construct (cluster 4), distinct interactors of

229 (cluster 5) and MERS (cluster 3). A large cluster (7) contained interactors present in four of the strains but absent in SARS-CoV-2.

To ascertain how these proteins cluster into cellular pathways with potential pro- or anti-viral roles, we grouped the high-confidence interactors into a network plot. To highlight connections between the binding partners, known protein interactions based on the STRING database were included (**Figure 6.2C**). Several groups of associated interactors emerged, including a large cluster of eleven ribosomal proteins (RPS2, RPS11, RPS16, RPS18, RPS25, RPS27A, RPL11, RPL23, RPL29, RPL37A, RPL38). Other notable clusters include factors involved in protein quality control (BAG2, BAG6, HSPA6, DNAJB1, UBL4A, GET4), metabolic transport (SLC1A3, SLC25A1, SLC25A5, SLC25A6, SLC25A16, SLC25A33), histone modification (SUZ12, MSL1, WDR5), RNA-binding proteins (FXR1/2, FMR1), and E3 ubiquitin ligases (CUL2, COMMD4, HERC5, UBR4, PJA2). Interactions between nsp3 and FXR1/2, as well as several ribosomal proteins were also prominently observed in a BioID proximity ligation data set[29]. Additionally, ten transcription factors were identified with at least one interaction to severely pathogenic betacoronaviruses. These include VEZF1, a transcription factor for IL-3[30], ATF3, a broad negative regulator of NF-κB, IL-4, IL-5, IL-13 expression[31], and ATF6, which turns on expression of the ATF6 branch of the unfolded protein response (UPR)[32].

As a last method to identified pathways represented by the interactors, we filtered the list of proteins through EnrichR to determine the most common gene ontology terms related to biological processes among each interactome (**Figure A5.7**). For both SARS variants, as well as MERS-CoV, we observed a strong enrichment for several ribosomal-related processes, including SRP-dependent cotranslational protein targeting, ribosome biogenesis, and rRNA metabolic processes. These processes were not observed in the less pathogenic hCoV-OC43 and hCoV-229E strains. For SARS-CoV, but not SARS-CoV-2, we also observed several mitochondrial related processes, such as mitochondrial transport, and mitochondrial RNA metabolic processes. hCoV-OC43 showed enrichment of factors associated with an upregulation of transcription from

RNA polymerase II factors. Lastly, despite having the highest overall number of high confidence interactors, no individual pathways showed enrichment at the high confidence interactor level for hCoV-229E.

6.2.3 Comparison of nsp3.2 CoV interactors

Next, we turned to the middle fragment of the nsp3 constructs, which includes the highly conserved $PL2^{Pro}$ domain, the protease responsible for the self-cleavage of several coronavirus non-structural proteins from the orf1a/b polypeptide[33]. This domain also has deubiquitination and de-ISGylation activity, an activity well-studied in the pathogenic coronaviruses, but less studied in the endemic strains[34,35]. The importance of this domain for both viral polypeptide processing and remodeling of host ubiquitination/ISGylation modifications make it an intriguing target for drug development. Also included in this fragment are the second ubiquitin-like domain UBL2, the first transmembrane domain, and the first portion of the ER ectodomain (**Figure 6.3A**).

The final dataset for the middle fragment analysis combined 3 mass spectrometry runs containing 59 co-IP samples (tdTomato 10, SARS-CoV-2 11, SARS-CoV 11, hCoV-OC43 10, MERS-CoV 10, hCoV-229E 7) (**Figure A6.3B,E**). In total, we identified 11 high confidence interactors for SARS-CoV-2, 23 for SARS-CoV, 11 for hCoV-OC43, 36 for MERS-CoV, and 35 for hCoV-229E (**Figure 6.3B, Figure A5.8**). Nine proteins were observed as high confidence interactors for both SARS-CoV and SARS-CoV-2. No proteins were observed to be common among all 5 strains at the high confidence level (6 at the medium confidence level), and no proteins were observed to be exclusive interactors of betacoronaviruses at the high confidence level (2 at the medium confidence level). Lastly, we identified 2 high confidence interactors unique to SARS-CoV-2, 11 unique to SARS-CoV, 3 unique to OC-43, 28 unique to 229E, and 34 unique to MERS. When querying the CRAPome dataset, we only found overlap in 14 of 93 idenfied proteins, supporting the specificity of the interactors for the nsp3.2 bait proteins (**Figure A6.5**).

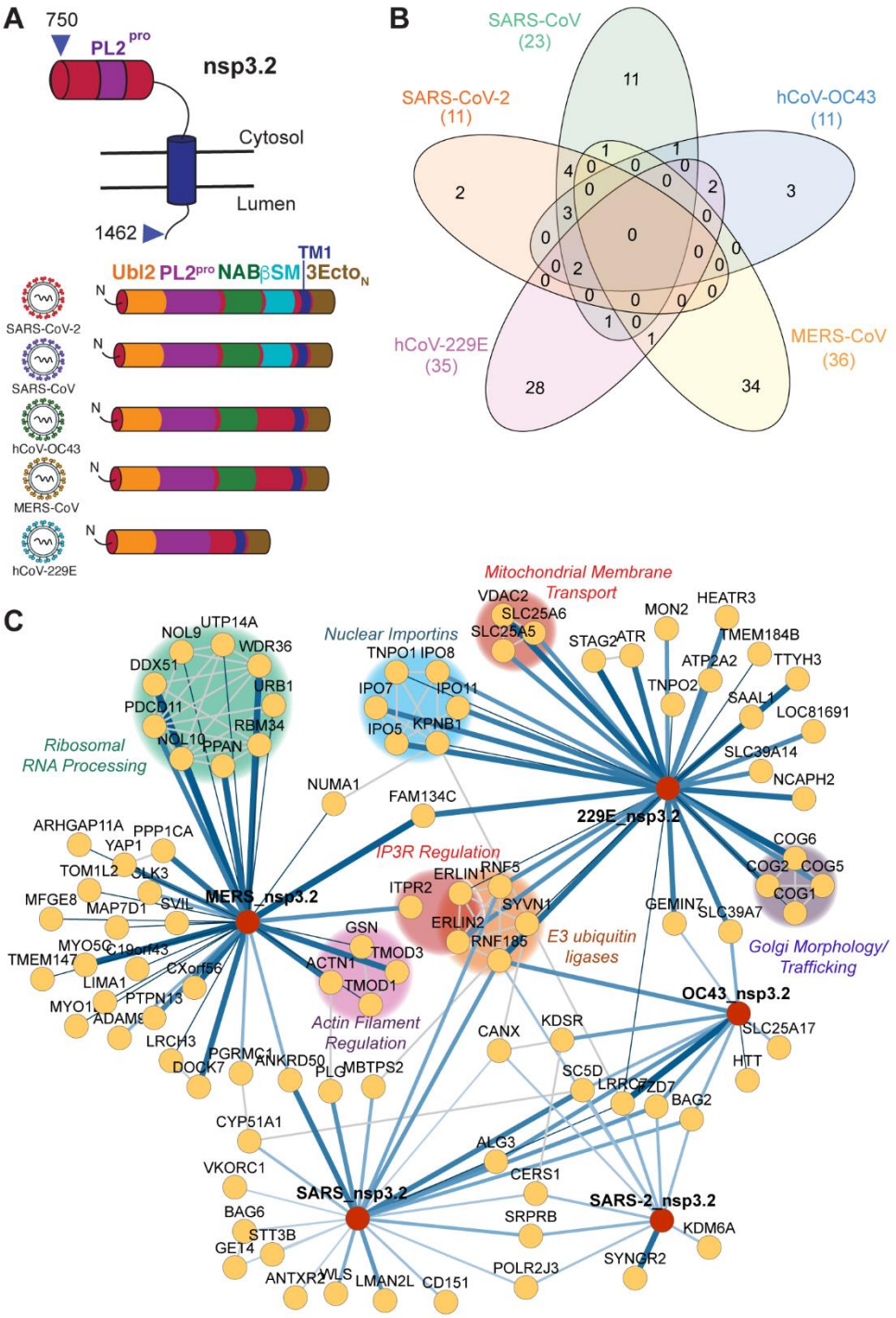

Figure 6.3. Identification of CoV nsp3.2 host interactors.

A. Schematic of nsp3.2 protein topology for all five CoV homologs. Nsp3.2 contains both cytosolic, transmembrane, and luminal regions. All homologs contain a ubiquitin-like domain (Ubl2, yellow), a papain-like protease domain ($PL2^{pro}$, purple), a transmembrane region (TM1, blue), and the N-terminal portion of the ectodomain ($3Ecto_N$, brown). Betacoronavirus homologs also contain a nucleic acid binding domain (NAB, green), while SARS strains also have a betacoronavirus-specific marker (βSM, light blue).

B. Venn diagram showing the number of unique and shared host interactors amongst all five CoV nsp3.2 homologs. Total interactors for each homolog are shown in parentheses.
C. Network plot of virus-host interactors. Individual nsp3.2 homologs are shown as red circles, while host interactors are shown as yellow circles. Blue lines indicate virus-host protein interactions, where line width and shade are wider/darker for more highly enriched interactions. Grey lines indicate known host-host protein interactions from the STRING database. Notable clusters of host proteins are highlighted.

We carried out hierarchical clustering of the grouped abundance Z-scores for all high-confidence interactors. The resulting heatmap (**Figure A5.9**) more clearly highlights a cluster of shared interactions for all five strains (cluster 2), although intensities vary, which could explain why not all may have passed our stringent high-confidence cutoff. Cluster 1 contains binding partners found in four of the strains, but absent in MERS. A striking observation were two large clusters of strain-specific interactors for 229E (cluster 3) and MERS (cluster 4) respectively.

We also grouped the high-confidence interactions into a network plot highlighting previously known interactions from String DB (**Figure 6.3C**). We identify several ER-associated degradation (ERAD) components as high confidence interactors of SARS-CoV nsp3.2. While some of these components were identified as high confidence interactors of SARS-CoV-2 as well, the number and magnitude were both much less. Analysis of GO terms associated with both the medium and high confidence interactors confirmed the enrichment of the ERAD machinery, as well as several related processes such as membrane proteolysis and cellular response to ER stress (**Figure A6.10**).

The 229E fragment revealed a high number of unique interactors related to nuclear importins and translocation of proteins into the nucleus (IPO5, IPO7, IPO11, IPO8, KPNB1, TNPO1). A recent report identified a role of MHV nsp3 in forming pores across the DMV membrane in coronavirus infection, potentially for the purpose of dsRNA export from the DMVs[36]. The nuclear importins could be additional host factors co-opted by 229E or alphacoronaviruses specifically for a similar purpose. Additional interactors of the 229E fragment include ERLIN1 and ERLIN2, which we

previously identified as being interactors of both SARS-CoV-2 and SARS-CoV nsp2 and nsp4. These proteins are also associated with ERAD, most notably in regulating ubiquitination and degradation of the inositol 1,4,5-triphosphate receptor IP3R[37]. Lastly, other unique interactor of hCoV-229E nsp3.2 included a cluster of mitochondrial membrane transporters (SLC25A6, SLC25A5, VDAC2), as well as a cluster of subunits of the conserved oligomeric Golgi (COG) complex involved in intra-Golgi mediated vesicle transport. COG6 was identified in a recent CRISPR screen as essential for hCoV-229E replication[38], and the intra-Golgi mediated vesicle transport was a pathway enriched only in our hCoV-229E nsp3.2 dataset, not appearing for the other strains (**Figure 6.10**).

Lastly, for MERS nsp3.2. we identified a complex of ribosomal RNA (rRNA) processing factors as highly unique interactors, including DDX51, NOL9, NOL10, UTP14A, WDR36, URB1, RBM34, PPAN, and PDCD11 (**Figure 6.3C**). Consistent with this finding, RNA processing and ribosome biogenesis were the most highly-enrichment GO terms specific to the MERS nsp3.2 fragment (**Figure A6.10**). Other viruses have been shown to target ribosomal biogenesis to facilitate infection, such as human cytomegalovirus (CMV) and HIV-1[39,40]. The specificity of these interactors for MERS nsp3.2 is striking and may represent a unique replication strategy to modulate host protein synthesis.

6.2.4 Comparison of nsp3.3 CoV interactors

The C-terminal fragments begin with the second half of the ER ectodomain, continuing through the second transmembrane region and Y domains, ending with the nsp3/nsp4 cleavage site. The Y domains, although one of the more conserved domains across the 5 strains, remains largely unstudied. In co-expression experiments of individual SARS-CoV-2 nsp3 fragments and nsp4, we observed co-immunoprecipitation of this C-terminal fragment with nsp4 (**Figure A6.11**). In contrast, the N-terminal and middle fragments did not co-immunoprecipitate with nsp4.

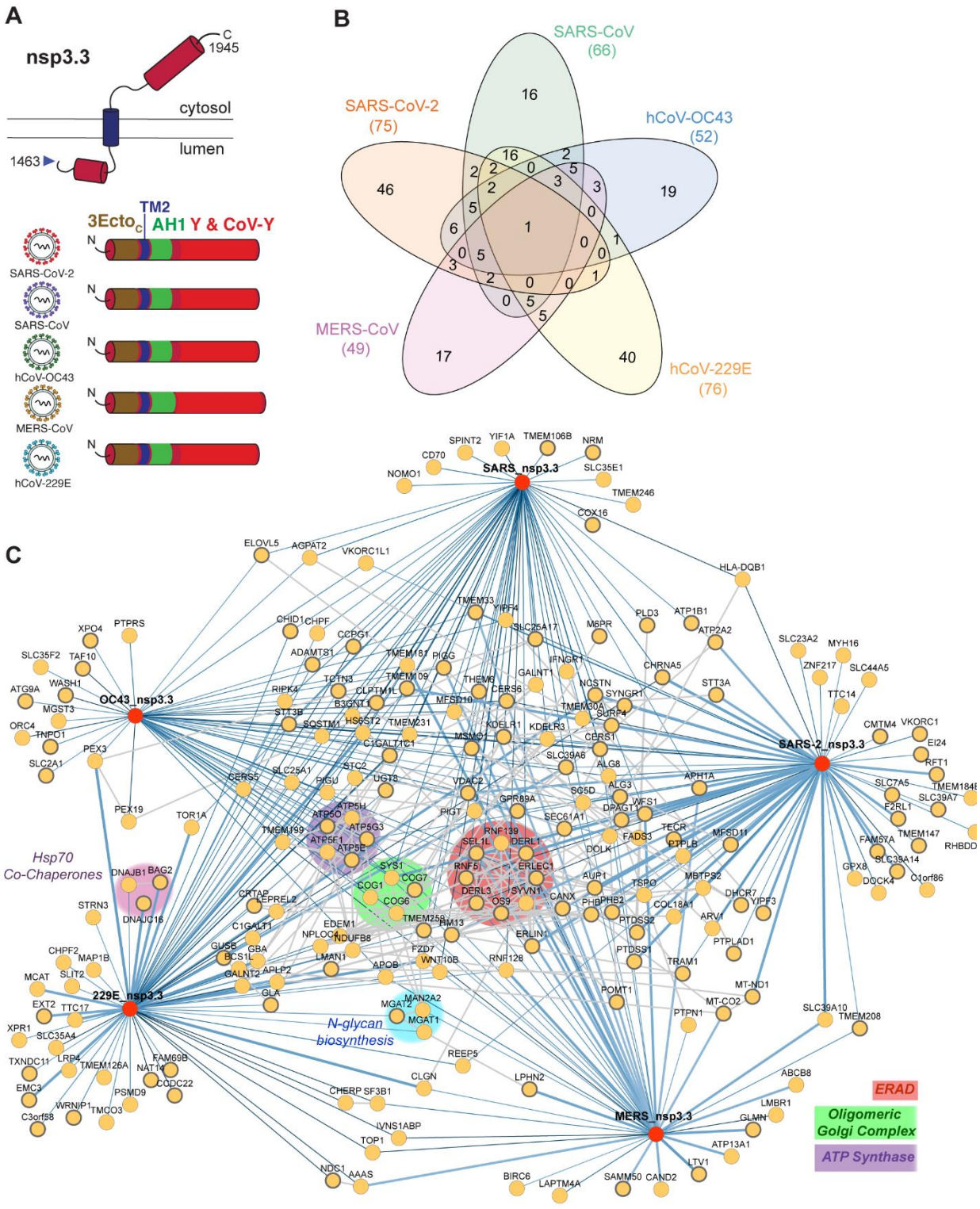

Figure 6.4. Identification of CoV nsp3.3 host interactors.

A. Schematic of nsp3.3 protein topology for all five CoV homologs. Nsp3.3 contains both cytosolic, transmembrane, and luminal regions. All homologs contain the C-terminal

portion of the ectodomain ($3Ecto_C$, brown), the second transmembrane region (TM2, blue), a likely amphipathic helix (AH1, green), and a Y&CoV-Y domain (red).

B. Venn diagram showing the number of unique and shared host interactors amongst all five CoV nsp3.3 homologs. Total interactors for each homolog are shown in parentheses.
C. Network plot of virus-host interactors. Individual nsp3.3 homologs are shown as red circles, while host interactors are shown as yellow circles. Blue lines indicate virus-host protein interactions, where line width and shade are wider/darker for more highly enriched interactions. Grey lines indicate known host-host protein interactions from the STRING database. Notable clusters of host proteins are highlighted.

The final dataset for the middle fragment analysis combined 5 mass spectrometry runs containing 63 co-IP samples (tdTomato 15, SARS-CoV-2 14, SARS-CoV 9, hCoV-OC43 9, MERS-CoV 8, hCoV-229E 8) (**Figure A6.3C,F**). In total, we identified 75 high confidence interactors for SARS-CoV-2, 66 for SARS-CoV, 52 for hCoV-OC43, 49 for MERS-CoV, and 76 for hCoV-229E (**Figure 6.4B**, **Figure A6.12**). One protein, SLC39A6, a zinc transporter, was observed as a high confidence interactor for all five strains (68 proteins observed as common medium confidence interactors). Five proteins, DERL3, TMEM33, SC5D, CERS1, and ALG8, were observed as high confidence interactors unique to the betacoronavirus strains. DERL3 is a functional component of the ERAD system, TMEM33 is involved in tubular ER network organization as well as being a component of the IRE1 and PERK stress response pathways, SC5D is involved in cholesterol biosynthesis, CERS1 is involved in lipid biosynthesis, and ALG8 is involved in N-glycan biosynthesis. Lastly, we identify 48 high confidence interactors unique to SARS-CoV-2, 17 unique to SARS-CoV, 20 unique to hCoV-OC43, 41 unique to hCoV-229E, and 18 unique to MERS-CoV (**Figure 6.4B**). As for the other nsp3 fragment, little overlap was identified with the CRAPome dataset (12 of 206 proteins), confirming the specificity of the interactions (**Figure A6.5**).

We carried out hierarchical clustering of the grouped abundance Z-scores for all high-confidence interactors. The resulting heatmap (**Figure A6.13**) highlights 6 clusters of interactors, including a cluster of shared interactors for all five strains (cluster 4), a cluster of shared betacoronavirus interactors (cluster 5), and a cluster of shared SARS interactors (cluster 6).

Despite these C-termini being the most conserved of the fragments across strains, there was a large divergence observed in the enriched pathways when searched for enriched GO-terms (**Figure A6.14**). In all strains except hCoV-OC43, ERAD was a highly enriched pathway. It has been postulated that nsp3, in tandem with nsp4 and nsp6, hijacks ERAD-tuning vesicles during double-membrane vesicle (DMV) formation, after ERAD factors EDEM1 and OS-9 were shown to co-localize with MHV-derived DMVs in infected cells[14,41]. Our results may provide insight into a role for nsp3 in modulating this machinery.

Unexpectedly, the biological process most enriched for the hCoV-229E fragment was protein N-linked glycosylation. N-linked glycosylation sites are localized at the N-terminus of the 3.3 fragment in the ectodomain. One of these interactors, MGAT1 (unique to the hCoV-229E interactome), was identified in the CRISPR screen as being an essential gene for hCoV-229E infection[38]. In addition, we identify STT3B, a catalytic component of the oligosaccharyl transferase complex, as a high confidence hCoV-229E nsp3.3 interactor.

The patterns observed in our GO term analysis were consistent with network plots of high-confidence interactors (**Figure 6.4C**). Multiple homologs shared interactors involved in ERAD (RNF139, DERL1, DERL3, ERLEC1, SYNV1, OS9, RNF5, SEL1L) and the oligomeric Golgi complex (COG1, COG6, COG7, SYS1). A cluster of five components of the mitochondrial ATP synthase complex (ATP5E, ATP5G3, ATP5H, ATP5F1, and ATP5O) was enriched for hCoV-OC43 nsp3.3, while clusters of Hsp70 co-chaperones (DNAJB1, DNAJC16, BAG2) and *N*-glycan biosynthesis factors (MGAT1, MGAT2, MAN2A2) were enriched for hCoV-229E nsp3.3. Interestingly, a large swath of identified high-confidence interactors are interconnected based on STRING analysis but do not cluster into distinct biological categories outside of those previously mentioned.

6.2.5 SARS-CoV-2 nsp3.1 interacts with ATF6 and suppresses the ATF6 branch of the Unfolded Protein Response (UPR)

An intriguing observation was the shared interaction of the nsp3.1 fragment from SARS-CoV-2, SARS-CoV and hCoV-OC43 with ATF6 (**Figure 6.2C**), a transmembrane protein located across the ER membrane serving as one of the sensors of the ER unfolded protein response (UPR). Upon activation by ER stress, ATF6 is trafficked to the Golgi apparatus, where site-1 and site-2 proteases (SP1 & MBTPS2) cleave the protein, releasing an active transcription factor that serves to upregulate chaperones and other proteostasis factors which aid in relieving ER stress[32]. Intriguingly, we also observed MBTPS2 as an interactor of SARS-CoV nsp3.2. MSTPS2 was found in a recent CRISPR to be an essential gene in the replication of SARS-CoV-2[38]. Coronaviruses are known to upregulate the UPR. Specifically, the SARS-CoV spike protein was

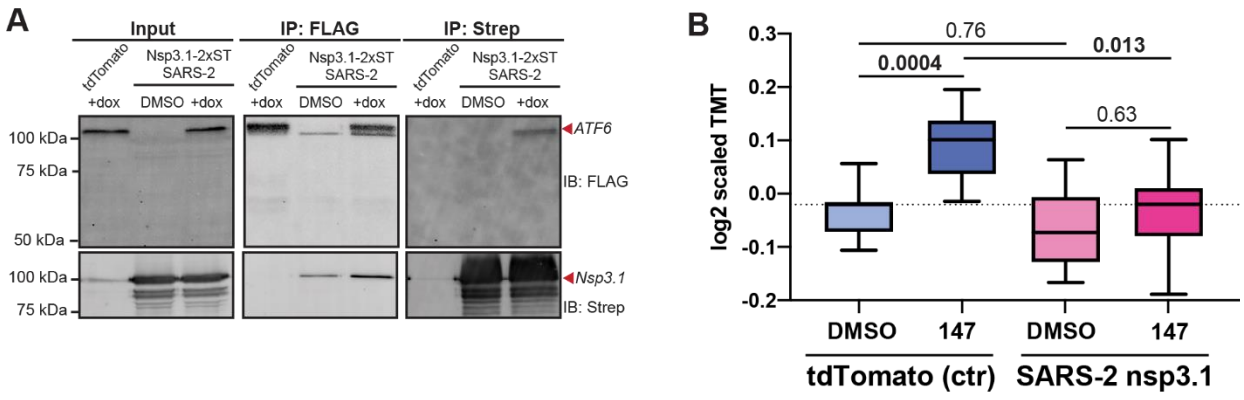

Figure 6.5. SARS-CoV-2 nsp3.1 interacts with ATF6 and suppresses the ATF6 branch of the Unfolded Protein Response (UPR).

A. Representative co-immunopurification (IP) western blots of 3xFT-ATF6 cells transfected with SARS-CoV-2 nsp3.1-2xST or tdTomato (control), lysed, and immunopurified for either FLAG or 2xStrepTag. Cells were treated with 100 nM doxycycline to induce 3xFT-ATF6 expression 24 h pre-harvest. Input and IP elution blots were probed with both anti-FLAG and anti-StrepTag antibodies. *n* = 3.
B. Box-and-whisker plots of ATF6-regulated protein abundance measured by quantitative proteomics. HEK293T cells were transfected with tdTomato (control) or SARS-CoV-2 nsp3.1-FT and treated with DMSO or 10 µM **147** for 16 h pre-harvest. Shown are the distribution of scaled log2 TMT intensities for ATF6-regulated proteins based on published genesets[45]. A one-way ANOVA with Geisser-Greenhouse correction and post-hoc Tukey's multiple comparison test was used to determine significance. Adjusted *p*-values are shown. *n* = 3 biological replicates in a single mass spectrometry run.

shown to be sufficient to upregulate transcription of factors such as GRP78/BiP and GRP94[42,43], both known to be downstream targets of ATF6[44,45]. Furthermore, SARS-1 Orf8 can activate ATF6 and promote UPR induction[46], but a role for nsp3 in UPR modulation during virus infection is not known.

As technical validation of the interaction of the N-terminal fragment of SARS-CoV-2 nsp3 with ATF6, Jonathan Davies, co-first author, used a HEK293T cell line expressing a doxycycline-inducible 3xFLAG-ATF6 construct[47]. The affinity tag of the nsp3 N-terminal construct was replaced with a 2x strep tag (2xST) to allow for complementary immunopurifications (IP) and detection. He observed reciprocal pulldown of SARS-CoV-2 nsp3.1 with ATF6, and vice-versa. After determining that nsp3.1 transfection did not upregulate the ATF6 branch of the UPR (by measuring downstream reporter gene levels), he tested UPR suppression by treating cells with 147, the compound discussed in chapter 3 that mildly upregulates ATF6 specifically in 293T cells. SARS-CoV-2 nsp3.1 was able to inhibit the activation by small molecules, suggesting its role in suppression of the UPR (**Figure 6.5 A-B**).

6.3 Discussion

As evidenced by its many domains, nsp3 likely serves a multitude of roles within the coronavirus replication cycle. Some of these roles are well characterized, such as the requirement of nsp3 for formation of double-membraned vesicles and the papain-like protease function in autocleavage of the orf1a polypeptide[14–17,51,52]. Other roles remain less defined, and the interactome of the individual nsp3 fragments contained herein may serve to help delineate the role of this protein across several CoV strains. Using tandem mass tags (TMTpro 16plex), we are able to directly identify and compare the abundance of interactors across five coronavirus strains, including two different genera and three different betacoronavirus clades. Given the frequent emergence of severely pathogenic coronavirus strains over the past 20 years, it is becoming increasingly apparent that a deeper knowledge of the molecular mechanisms of coronavirus replication is

needed to understand how we may better prepare therapeutics against potential future strains of these viruses.

The N-terminal portion of the protein (nsp3.1) is the only fragment lacking transmembrane domains and exclusively localizes to the cytosol. This could explain the high expression levels seen with this fragment, although there was still some variation among the expression efficiency for the homologs from different viral strains. An interesting divergence observed in the nsp3.1 dataset is the enrichment of pathways related to mitochondrial transport and metabolism in the SARS-CoV dataset that is absent in the SARS-CoV-2 dataset. Given the two fragments share high sequence identity, it is noteworthy when one pathway is so highly enriched in one fragment versus the other, pointing to rapid divergent evolution. Other SARS-CoV-2 proteins have been shown to interact with several components of the mitochondria[18,19], including our earlier nsp2/4 dataset that found both SARS-CoV and SARS-CoV-2 proteins interacting with mitochondria-associated membrane factors involved in controlling calcium flux between ER and mitochondria[22]. Interestingly, the most highly enriched pathways in both of the SARS variants are also enriched (to a similar magnitude) in the MERS-CoV nsp3.1 fragment pointing towards conserved functions among the pathogenic variants.

The C-terminal portion of the nsp3.1 fragment for SARS-CoV and SARS-CoV-2 consists of the SARS unique domain (SUD). While a definitive function of this domain has not been established in the coronavirus replication cycle, prior studies described a role for macrodomains within the SUD binding G-quadruplexes, strings of RNA containing multiple guanosines[51,53,54]. While no RNA-binding pathways were observed as enriched with either of the SARS nsp3.1 fragments, potentially related processes such as mRNA catabolism, rRNA metabolism, and ribosome biogenesis were significantly enriched. This pathway was also observed in the MERS-CoV nsp3.1 interactor set, potentially pointing to a broader role for pathogenic strains. The singular pathway shown to be enriched only in the two SARS variants was “positive upregulation of transcription in

response to ER stress", which prompted us to investigate the interactions and regulation of this fragment with the UPR sensor ATF6, which is discussed further below.

The middle fragment yielded the smallest number of overall interactors of the three fragments, across all five strains. Generally, expression levels of this fragment were also lower than the termini, which may have limited detection of interactors. However, all fragments and interactors were still reproducibly detectable by mass spectrometry. Surprisingly, we observed highly distinct pathway enrichment from the MERS-CoV and hCoV-229E fragments showing substantial interactions with ribosomal RNA processing proteins and nuclear import proteins, respectively. Interactions of other coronavirus proteins with nuclear transport machinery have been observed, for instance nsp9 with the nuclear pore complex and nsp1 with mRNA export machinery[18,55]. Orf6 of SARS-CoV and SARS-CoV-2 inhibits STAT1 signaling by blocking nuclear import of phosphorylated STAT1. Nuclear localization of SARS-CoV and SARS-CoV-2 orf3b has been shown, as well as for N proteins[56–58]. In contrast, no strains studied to date have observed interactions of nuclear transport pathways with nsp3. One possibility is the recruitment of nuclear transport proteins to 229E nsp3 to assist in the transport of viral components from double-membraned vesicles, which nsp3 is essential in helping to create[14–16]. A recent study showed that nsp3 from murine hepatitis virus (MHV) not only assists in initial formation of the DMVs, but subsequently forms the core of a pore-like structure that may aid in export of viral RNA[36]. The absence of these protein interactions between nsp3.1 homologs from betacoronavirus strains and nuclear importins points to evolution of functional divergence.

We also find that MERS nsp3.2 uniquely interacts with rRNA processing machinery involved in ribosome biogenesis. Several of these factors (WDR36, NOL10, URB1) were previously found to interact with SARS-CoV-2, SARS-CoV, and MERS-CoV nsp8 homologs[18,19]. Some viruses, such as HIV-1, have also been shown to down-regulate factors involved in rRNA processing during infection[40]. Given the dependence of all coronaviruses on host translation machinery, it is

interesting that MERS is the only CoV to maintain these interactions. This may represent a specialized avenue for MERS-CoV to modulate host translation through nsp3.

Viruses often modulate cellular stress responses in order to assist during replication and/or subvert the host immune system. Many groups of viruses, including coronaviruses and flaviviruses, have been shown to upregulate branches of the UPR[42,43,46,59–64], although exact roles of this activation for the viral life cycle are still debated. We were therefore particularly interested to find ATF6 as a high confidence interactor of the SARS-CoV and SARS-CoV-2 nsp3.1 fragments. ATF6 is a transmembrane sensor representing one of the most upstream portions of the ER unfolded stress response (UPR). As noted, coronaviruses replicate near the ER, and nsp3 possesses transmembrane domains that anchor the protein in the ER membrane. Given the localization of nsp3.1 to the cytosol, the protein is likely to interact with the cytosolic basic leucine zipper (bZIP) transcriptional activator domain of ATF6. Therefore, we sought to determine if the fragment could be regulating the ability of ATF6 to respond to stress. Jonathan Davies probed translational level of known ATF6 regulated genes after overexpression of nsp3.1 fragments. He showed that SARS-CoV-2 fully blocked the modest induction by the pharmacological activator **147**. It is likely that UPR activity has to be finely tuned during infection to prevent detrimental consequences from prolonged activation, such as apoptosis induction. Prior studies found that the IRE/XBP1s UPR branch was inhibited by the SARS-CoV E protein and that ATF6 gene targets were not upregulated during MHV infection despite ATF6 activation and cleavage[60,65]. These results suggest that coronaviruses employ strategies to attenuate distinct UPR signaling branches, but little is known about what viral proteins are responsible for tuning UPR activity. Our results indicate that the N-terminal regions of SARS-CoV-2 nsp3 directly acts on ATF6 to suppress activation. Further work is needed to understand the molecular mechanisms of this suppression and its role during SARS-CoV-2 infection.

Many studies have highlighted the utility of viral protein interactomes in identifying roles for host pathways in the life cycle of many viruses[38,66], and large-scale interactome studies with SARS-

CoV-2 demonstrated how these interactomes may be useful for identifying existing drugs to be repurposed to fight viral infections[18]. Despite the large body of work done in the past year on SARS-CoV-2, interactome studies of nsp3 have been limited to the $PL2^{pro}$ papain-like-protease domain[11]. In addition to presenting data for the full nsp3 interactome, our studies highlight the utility of using tandem mass tag technology to quantitatively compare the SARS-CoV-2 nsp3 interactome to the interactome of other known coronaviruses, both severely and mildly pathogenic. We find very divergent interactomes, suggesting that while there is a large conservation of domains, there may also be more specific roles for this protein in the context of each individual virus. One caveat is the use nsp3 fragments in our analysis, which may miss host interactions that require different region or domains of the protein to coordinate. Additionally, it would be intriguing to investigate the interactomes of nsp3 (fragmented or in full) with nsp4 and/or nsp6, as coordination between these viral proteins is required to form the double-membraned vesicles characteristic in CoV infection. In the future, it may be important to study the variations in host protein interactions that occur between specific SARS-CoV-2 variants that are rapidly emerging. This study was initially published during the rise of the B.1.1.7 (alpha) variant which possesses three mutations in nsp3[67,68]. Additionally, the B.1.351 (beta) variant contains one nsp3 mutation, and the P.1 (gamma) variant contains two. More recently, the B.1.617.2 (delta) and B.1.1.529 (omicron) variants of concern also possess mutations in nsp3[67]. This makes nsp3 protein variants relevant to study for better understanding how such evolutionary adaptations in non-structural proteins may impact virulence.

6.4 Materials and Methods

Construct design

The coding sequences for full-length nsp3 were obtained from GenBank (SARS-CoV-2 isolate Wuhan-Hu-1 MN908947, SARS-CoV Urbani AY279741, hCoV-OC43 NC006213, MERS-CoV JX869059, hCoV-229E AF304460).

Sequences for creating fragments of the SARS-CoV nsp3 were chosen based on Pan et al, 2008, PLoS One[21]. The amino acid sequences of full-length nsp3 for the remaining hCoV strains were aligned using ClustalOmega to the SARS-CoV fragments to determine the corresponding starting/ending positions for each fragment.

Full length SARS-CoV-2 nsp3 was codon optimized and cloned into a pcDNA-(+)-C-DYK vector (Genscript). Truncations were performed using primers listed in Table 1. All other nsp3 fragments were individually codon optimized and cloned into pTwist CMV Hygro vectors (Twist Biosciences). SARS-CoV and SARS-CoV-2 nsp3.1 strep-tagged constructs were created using primers listed in Table 1. Briefly, nsp3 fragment plasmids were amplified to exclude the FLAG tag. A pLVX vector containing a strep tag was used to amplify the insert. The two fragments were ligated using a DNA HiFi assembly kit (NEB). All plasmid constructs were confirmed by sequencing (Genewiz).

Cell culture and transfection

HEK293T and HEK293T-REx cells were maintained in Dulbeccos' Modified Eagle's Medium (high glucose) and supplemented with 10% fetal bovine serum, 1% penicillin/streptomycin, and 1% glutamine. Cells were kept at 37°C, 5% CO_2. For transfections, 2E6 cells were seeded into 10cm tissue culture dishes. 24 hours after seeding, cells were transfected using a calcium phosphate method with 5 µg nsp3 or tdTomato construct. Media was exchanged 16 hours post-transfection and cells were harvested 24 hours after media exchange.

FLAG immunoprecipitations

Immunoprecipitations were performed as reported previously[22]. Cells were collected from 10cm dishes via scraping, washed with PBS, and lysed by suspension in TNI buffer (50mM Tris pH 7.5, 150mM NaCl, 0.5% IGEPAL-CA-630) supplemented with Roche cOmplete protease inhibitor. Cells were left to lyse on ice for at least 10 minutes, followed by 10 minute sonication in a room temperature water bath. Lysates were cleared by centrifugation at 21.1xg for 20 minutes. Protein concentrations were normalized using 1x BioRad Protein Assay Dye, and normalized lysates were added to 15 µL pre-washed (4x in lysis buffer) Sepharose 4B beads (Sigma) and rocked at

4°C for 1 hour. Resin was collected by centrifugation at 400xg for 10 minutes, and pre-cleared supernatant was added to 15 µL G1 anti-DYKDDDDK resin (GenScript) and rocked at 4°C overnight. The next day, resin was collected by centrifugation at 400xg for 10 minutes. Resin was washed 4x with lysis buffer. Resin-bound proteins were eluted with the addition of modified 3x Laemelli buffer (6% SDS, 62.5mM Tris) for 30 minutes at room temperature, followed by 15 minutes at 37°C. A second elution was performed for 15 minutes at 37°C.

During the first IP for each construct, immunoprecipitation was confirmed by silver stain using a Pierce Silver Stain Kit (Thermo Fisher) and by western blotting with anti-FLAG antibody (Sigma-Aldrich, F1804)

Immunofluorescence confocal microscopy

HEK293T cells were transfected with nsp3 constructs as described in “Cell culture and transfection”. Two hours post-media change, $2x10^4$ transfected cells were seeded into glass-bottom culture dishes (MatTek, P35G-0-14-C). At 40 hours post-transfection, cells were fixed with 4% paraformaldehyde-PBS, washed with PBS three times, then permeabilized in 0.2% Triton-X (in PBS). After three PBS washes, cells were blocked in PBS with 1% BSA and 0.1% Saponin (blocking buffer) for 1 hour at room temperature. After blocking, cells were incubated with anti-PDIA4 primary antibody (Protein Tech, 14712-1-AP) in blocking buffer (1:1000 dilution) overnight at 4°C. After three PBS washes, cells were incubated with AlexFluor 488-conjugated anti-rabbit goat antibody (ThermoFisher, A-11008) in blocking buffer (1:500 dilution) at room temperature for 30 min. Cells were then stained with M2 FLAG primary antibody (SigmaAldrich, F1804) and AlexFluor 594-conjugated anti-mouse goat antibody (ThermoFisher, A-11005) using the same conditions. Cells were then mounted in Prolong Gold with DAPI stain (ThermoFisher, P36935) overnight. Cells were imaged using an LSM-880 or LSM-710 confocal microscope (Zeiss) and images were merged using Image J software.

Tandem Mass Tag sample preparation

Sample preparation was carried out as previously described[22]. Eluted proteins were precipitated via methanol/chloroform/water (3:1:3) and washed thrice with methanol. Each wash was followed by a 5 minute spin at 10,000xg. Protein pellets were air dried and resuspended in 1% Rapigest SF (Waters). Resuspended proteins were reduced (TCEP) for 30 minutes, alkylated (iodoacetamide) for 30 minutes, and digested with 0.5 µg trypsin/Lys-C (Thermo Fisher) overnight. Digested peptides were labeled using 16plex TMTpro (Thermo Scientific) and quenched with the addition of ammonium bicarbonate. Each TMT channel shown in **Figure A6.3A-F** represents an independent immunoprecipitation and biological replicate. Samples were pooled, acidified, and concentrated. Cleaved Rapigest products were removed by centrifugation at 17,000xg for 45 minutes.

MudPIT LC-MS/MS analysis

Triphasic MudPIT columns were prepared as previously described using alternating layers of 1.5cm C18 resin, 1.5cm SCX resin, and 1.5cm C18 resin[71]. Pooled TMT samples (roughly one-third of pooled IP samples and 20 µg of peptide from global UPR activation samples) were loaded onto the microcapillaries using a high-pressure chamber, followed by a 30 minute wash in buffer A (95% water, 5% acetonitrile, 0.1% formic acid). Peptides were fractionated online by liquid chromatography using an Ultimate 3000 nanoLC system and subsequently analyzed using an Exploris480 mass spectrometer (Thermo Fisher). The MudPIT columns were installed on the LC column switching valve and followed by a 20cm fused silica microcapillary column filled with Aqua C18, 3µm, C18 resin (Phenomenex) ending in a laser-pulled tip. Prior to use, columns were washed in the same way as the MudPIT capillaries. MudPIT runs were carried out by 10µL sequential injections of 0, 10, 20, 40, 60, 80, 100 % buffer C (500mM ammonium acetate, 94.9% water, 5% acetonitrile, 0.1% formic acid) for IP samples and 0, 10, 20, 30, 40, 50, 60, 70, 80, 90, 100% buffer C for global UPR activation samples, followed by a final injection of 90% C, 10% buffer B (99.9% acetonitrile, 0.1% formic acid v/v). Each injection was followed by a 130 min gradient using a flow rate of 500nL/min (0-6 min: 2% buffer B, 8 min: 5% B, 100

min: 35% B, 105min: 65% B, 106-113 min: 85% B, 113-130 min: 2% B). ESI was performed directly from the tip of the microcapillary column using a spray voltage of 2.2 kV, an ion transfer tube temperature of 275°C and a RF Lens of 40%. MS1 spectra were collected using a scan range of 400-1600 m/z, 120k resolution, AGC target of 300%, and automatic injection times. Data-dependent MS2 spectra were obtained using a monoisotopic peak selection mode: peptide, including charge state 2-7, TopSpeed method (3s cycle time), isolation window 0.4 m/z, HCD fragmentation using a normalized collision energy of 32 (TMTpro), resolution 45k, AGC target of 200%, automatic injection times, and a dynamic exclusion (20 ppm window) set to 60s.

Data analysis

Identification and quantification of peptides were performed in Proteome Discoverer 2.4 (Thermo Fisher) using the SwissProt human database (TaxID 9606, released 11/23/2019; 42,252 entries searched) with nsp3 fragment sequences (15 entries) manually added (42,267 total entries searched). Searches were conducted with Sequest HT using the following parameters: trypsin cleavage (maximum 2 missed cleavages), minimum peptide length 6 amino acids, precursor mass tolerance 20ppm, fragment mass tolerance 0.02Da, dynamic modifications of Met oxidation (+15.995Da), protein N-terminal Met loss (-131.040Da), and protein N-terminal acetylation (+42.011Da), static modifications of TMTpro (+304.207Da) at Lys and N-termini and Cys carbamidomethylation (+57.021Da). Peptide IDs were filtered using Percolator with an FDR target of 0.01. Proteins were filtered based on a 0.01 FDR, and protein groups were created according to a strict parsimony principle. TMT reporter ions were quantified considering unique and razor peptides, excluding peptides with co-isolation interference greater that 25%. Peptide abundances were normalized based on total peptide amounts in each channel, assuming similar levels of background in the IPs. For global UPR proteomics, protein abundances were also scaled. Protein quantification used all quantified peptides. Post-search filtering was done to include only proteins with two identified peptides.

Experimental Design and Statistical Rationale

Nsp3.1 analysis combined 62 co-IP samples distributed across 5 individual MS runs (biological replicates: 15x tdTomato (negative co-IP control), 13x SARS-CoV-2, 9x SARS-CoV, 8x MERS-CoV, 9x hCoV-OC43, 8x hCoV-229E). Nsp3.2 analysis combined 63 co-IP samples distributed across 4 individual MS runs (biological replicates: 15x tdTomato (negative co-IP control), 14x SARS-CoV-2, 9x SARS-CoV, 9x hCoV-OC43, 8x MERS-CoV, 8x hCoV-229E). Nsp3.3 analysis combined 63 co-IP samples distributed across 5 individual MS runs (biological replicates: 15x tdTomato (negative co-IP control), 14x SARS-CoV-2, 9x SARS-CoV, 8x MERS-CoV, 9x hCoV-OC43, 8x hCoV-229E). Pairwise ratios between conditions were calculated in Proteome Discoverer based on total protein abundance, and ANOVA was performed on individual proteins to test for change in abundances and report adjusted P-values. To filter interactors of individual nsp3 fragments, we used a variable cutoff method combining log2 enrichment and adjusted p-value according to a published method [22,72]. The histogram of log2 protein abundance fold changes for each construct vs the tdTomato control was fitted to a gaussian curve with a bin width of 0.1 using a nonlinear least square fit (excluding outliers) to determine the standard deviation σ of the scatter. For medium- and high-confidence interactors, the cutoff values were 1σ and 2σ respectively. To take into consideration the adjusted p-values, we used a hyperbolic curve $y > c/(x-x_0)$ where y is the adjusted p-value, x is the log2 fold change, and x_0 corresponds to the value of the 1σ or 2σ standard deviation. Negative medium- and high-confidence interactors were filtered using cutoff values of -1σ and -2σ respectively and the hyperbolic curve $y > -c/(x+x_0)$.

CRAPome overlap, geneset enrichment analysis, comparative heatmaps, and network plots

High-confidence interactors of all homologs for each nsp3 fragment were queried in the CRAPome "*Homo sapiens* Single Step Epitope tag AP-MS" dataset[28]. A frequency threshold of 25% of control experiments found in was used to qualify an interactor as overlapping with the CRAPome. A gene ontology (GO) enrichment analysis for biological processes was conducted in EnrichR. The analysis was conducted separately for the high (and/or medium) confidence

interactors for each fragment. GO terms were manually filtered for adjusted p-values <0.1. Redundant GO terms were grouped manually based on overlapping genes in related pathways. Network plots were generated in Cytoscape[73]; human protein interactions were validated based on the STRING database.

Data availability

The mass spectrometry proteomics data have been deposited to the ProteomeXchange Consortium via the PRIDE partner repository with the dataset identifier PXD024566. All other necessary data are contained within the dissertation.

6.5 References

(1) Ksiazek, T. G.; Erdman, D.; Goldsmith, C. S.; Zaki, S. R.; Peret, T.; Emery, S.; Tong, S.; Urbani, C.; Comer, J. A.; Lim, W.; Rollin, P. E.; Dowell, S. F.; Ling, A.-E.; Humphrey, C. D.; Shieh, W.-J.; Guarner, J.; Paddock, C. D.; Rota, P.; Fields, B.; DeRisi, J.; Yang, J.-Y.; Cox, N.; Hughes, J. M.; LeDuc, J. W.; Bellini, W. J.; Anderson, L. J. A Novel Coronavirus Associated with Severe Acute Respiratory Syndrome. *N. Engl. J. Med.* **2003**, *348* (20), 1953–1966. https://doi.org/10.1056/nejmoa030781.

(2) Drosten, C.; Günther, S.; Preiser, W.; van der Werf, S.; Brodt, H.-R.; Becker, S.; Rabenau, H.; Panning, M.; Kolesnikova, L.; Fouchier, R. A. M.; Berger, A.; Burguière, A.-M.; Cinatl, J.; Eickmann, M.; Escriou, N.; Grywna, K.; Kramme, S.; Manuguerra, J.-C.; Müller, S.; Rickerts, V.; Stürmer, M.; Vieth, S.; Klenk, H.-D.; Osterhaus, A. D. M. E.; Schmitz, H.; Doerr, H. W. Identification of a Novel Coronavirus in Patients with Severe Acute Respiratory Syndrome. *N. Engl. J. Med.* **2003**, *348* (20), 1967–1976. https://doi.org/10.1056/nejmoa030747.

(3) Zaki, A. M.; van Boheemen, S.; Bestebroer, T. M.; Osterhaus, A. D. M. E.; Fouchier, R. A. M. Isolation of a Novel Coronavirus from a Man with Pneumonia in Saudi Arabia. *N. Engl. J. Med.* **2012**, *367* (19), 1814–1820. https://doi.org/10.1056/nejmoa1211721.

(4) Wu, F.; Zhao, S.; Yu, B.; Chen, Y. M.; Wang, W.; Song, Z. G.; Hu, Y.; Tao, Z. W.; Tian, J. H.; Pei, Y. Y.; Yuan, M. L.; Zhang, Y. L.; Dai, F. H.; Liu, Y.; Wang, Q. M.; Zheng, J. J.; Xu, L.; Holmes, E. C.; Zhang, Y. Z. A New Coronavirus Associated with Human Respiratory Disease in China. *Nature* **2020**, *579* (7798), 265–269. https://doi.org/10.1038/s41586-020-2008-3.

(5) Zhou, P.; Yang, X. Lou; Wang, X. G.; Hu, B.; Zhang, L.; Zhang, W.; Si, H. R.; Zhu, Y.; Li, B.; Huang, C. L.; Chen, H. D.; Chen, J.; Luo, Y.; Guo, H.; Jiang, R. Di; Liu, M. Q.; Chen, Y.; Shen, X. R.; Wang, X.; Zheng, X. S.; Zhao, K.; Chen, Q. J.; Deng, F.; Liu, L. L.; Yan, B.; Zhan, F. X.; Wang, Y. Y.; Xiao, G. F.; Shi, Z. L. A Pneumonia Outbreak Associated with a New Coronavirus of Probable Bat Origin. *Nature* **2020**, *579* (7798), 270–273. https://doi.org/10.1038/s41586-020-2012-7.

(6) Letko, M.; Marzi, A.; Munster, V. Functional Assessment of Cell Entry and Receptor

Usage for SARS-CoV-2 and Other Lineage B Betacoronaviruses. *Nat. Microbiol.* **2020**, *5* (4), 562–569. https://doi.org/10.1038/s41564-020-0688-y.

(7) Fehr, A. R.; Perlman, S. Coronaviruses: An Overview of Their Replication and Pathogenesis. In *Coronaviruses: Methods and Protocols*; Springer New York, 2015; Vol. 1282, pp 1–23. https://doi.org/10.1007/978-1-4939-2438-7_1.

(8) Chan, Y. K.; Gack, M. U. A Phosphomimetic-Based Mechanism of Dengue Virus to Antagonize Innate Immunity. *Nat. Immunol.* **2016**, *17* (5), 523–530. https://doi.org/10.1038/ni.3393.

(9) Hou, Z.; Zhang, J.; Han, Q.; Su, C.; Qu, J.; Xu, D.; Zhang, C.; Tian, Z. Hepatitis B Virus Inhibits Intrinsic RIG-I and RIG-G Immune Signaling via Inducing MiR146a. *Sci. Rep.* **2016**, *6* (1), 1–12. https://doi.org/10.1038/srep26150.

(10) Shi, C.-S.; Qi, H.-Y.; Boularan, C.; Huang, N.-N.; Abu-Asab, M.; Shelhamer, J. H.; Kehrl, J. H. SARS-Coronavirus Open Reading Frame-9b Suppresses Innate Immunity by Targeting Mitochondria and the MAVS/TRAF3/TRAF6 Signalosome. *J. Immunol.* **2014**, *193* (6), 3080–3089. https://doi.org/10.4049/jimmunol.1303196.

(11) Shin, D.; Mukherjee, R.; Grewe, D.; Bojkova, D.; Baek, K.; Bhattacharya, A.; Schulz, L.; Widera, M.; Mehdipour, A. R.; Tascher, G.; Geurink, P. P.; Wilhelm, A.; van der Heden van Noort, G. J.; Ovaa, H.; Müller, S.; Knobeloch, K. P.; Rajalingam, K.; Schulman, B. A.; Cinatl, J.; Hummer, G.; Ciesek, S.; Dikic, I. Papain-like Protease Regulates SARS-CoV-2 Viral Spread and Innate Immunity. *Nature* **2020**, *587* (7835), 657. https://doi.org/10.1038/s41586-020-2601-5.

(12) Clementz, M. A.; Chen, Z.; Banach, B. S.; Wang, Y.; Sun, L.; Ratia, K.; Baez-Santos, Y. M.; Wang, J.; Takayama, J.; Ghosh, A. K.; Li, K.; Mesecar, A. D.; Baker, S. C. Deubiquitinating and Interferon Antagonism Activities of Coronavirus Papain-Like Proteases. *J. Virol.* **2010**, *84* (9), 4619–4629. https://doi.org/10.1128/jvi.02406-09.

(13) Báez-Santos, Y. M.; St. John, S. E.; Mesecar, A. D. The SARS-Coronavirus Papain-like Protease: Structure, Function and Inhibition by Designed Antiviral Compounds. *Antiviral Research*. Elsevier B.V. March 1, 2015, pp 21–38. https://doi.org/10.1016/j.antiviral.2014.12.015.

(14) Angelini, M. M.; Akhlaghpour, M.; Neuman, B. W.; Buchmeier, M. J. Severe Acute Respiratory Syndrome Coronavirus Nonstructural Proteins 3, 4, and 6 Induce Double-Membrane Vesicles. *MBio* **2013**, *4* (4). https://doi.org/10.1128/mBio.00524-13.

(15) Oostra, M.; Hagemeijer, M. C.; van Gent, M.; Bekker, C. P. J.; te Lintelo, E. G.; Rottier, P. J. M.; de Haan, C. A. M. Topology and Membrane Anchoring of the Coronavirus Replication Complex: Not All Hydrophobic Domains of Nsp3 and Nsp6 Are Membrane Spanning. *J. Virol.* **2008**, *82* (24), 12392–12405. https://doi.org/10.1128/jvi.01219-08.

(16) Oudshoorn, D.; Rijs, K.; Limpens, R. W. A. L.; Groen, K.; Koster, A. J.; Snijder, E. J.; Kikkert, M.; Bárcena, M. Expression and Cleavage of Middle East Respiratory Syndrome Coronavirus Nsp3-4 Polyprotein Induce the Formation of Double-Membrane Vesicles That Mimic Those Associated with Coronaviral RNA Replication. *MBio* **2017**, *8* (6). https://doi.org/10.1128/mBio.01658-17.

(17) Lei, J.; Kusov, Y.; Hilgenfeld, R. Nsp3 of Coronaviruses: Structures and Functions of a Large Multi-Domain Protein. *Antiviral Research*. Elsevier B.V. January 1, 2018, pp 58–74. https://doi.org/10.1016/j.antiviral.2017.11.001.

(18) Gordon, D. E.; Jang, G. M.; Bouhaddou, M.; Xu, J.; Obernier, K.; White, K. M.; O'Meara,

M. J.; Rezelj, V. V.; Guo, J. Z.; Swaney, D. L.; Tummino, T. A.; Hüttenhain, R.; Kaake, R. M.; Richards, A. L.; Tutuncuoglu, B.; Foussard, H.; Batra, J.; Haas, K.; Modak, M.; Kim, M.; Haas, P.; Polacco, B. J.; Braberg, H.; Fabius, J. M.; Eckhardt, M.; Soucheray, M.; Bennett, M. J.; Cakir, M.; McGregor, M. J.; Li, Q.; Meyer, B.; Roesch, F.; Vallet, T.; Mac Kain, A.; Miorin, L.; Moreno, E.; Naing, Z. Z. C.; Zhou, Y.; Peng, S.; Shi, Y.; Zhang, Z.; Shen, W.; Kirby, I. T.; Melnyk, J. E.; Chorba, J. S.; Lou, K.; Dai, S. A.; Barrio-Hernandez, I.; Memon, D.; Hernandez-Armenta, C.; Lyu, J.; Mathy, C. J. P.; Perica, T.; Pilla, K. B.; Ganesan, S. J.; Saltzberg, D. J.; Rakesh, R.; Liu, X.; Rosenthal, S. B.; Calviello, L.; Venkataramanan, S.; Liboy-Lugo, J.; Lin, Y.; Huang, X. P.; Liu, Y. F.; Wankowicz, S. A.; Bohn, M.; Safari, M.; Ugur, F. S.; Koh, C.; Savar, N. S.; Tran, Q. D.; Shengjuler, D.; Fletcher, S. J.; O'Neal, M. C.; Cai, Y.; Chang, J. C. J.; Broadhurst, D. J.; Klippsten, S.; Sharp, P. P.; Wenzell, N. A.; Kuzuoglu-Ozturk, D.; Wang, H. Y.; Trenker, R.; Young, J. M.; Cavero, D. A.; Hiatt, J.; Roth, T. L.; Rathore, U.; Subramanian, A.; Noack, J.; Hubert, M.; Stroud, R. M.; Frankel, A. D.; Rosenberg, O. S.; Verba, K. A.; Agard, D. A.; Ott, M.; Emerman, M.; Jura, N.; von Zastrow, M.; Verdin, E.; Ashworth, A.; Schwartz, O.; d'Enfert, C.; Mukherjee, S.; Jacobson, M.; Malik, H. S.; Fujimori, D. G.; Ideker, T.; Craik, C. S.; Floor, S. N.; Fraser, J. S.; Gross, J. D.; Sali, A.; Roth, B. L.; Ruggero, D.; Taunton, J.; Kortemme, T.; Beltrao, P.; Vignuzzi, M.; García-Sastre, A.; Shokat, K. M.; Shoichet, B. K.; Krogan, N. J. A SARS-CoV-2 Protein Interaction Map Reveals Targets for Drug Repurposing. *Nature* **2020**, *583* (7816), 459–468. https://doi.org/10.1038/s41586-020-2286-9.

(19) Gordon, D. E.; Hiatt, J.; Bouhaddou, M.; Rezelj, V. V.; Ulferts, S.; Braberg, H.; Jureka, A. S.; Obernier, K.; Guo, J. Z.; Batra, J.; Kaake, R. M.; Weckstein, A. R.; Owens, T. W.; Gupta, M.; Pourmal, S.; Titus, E. W.; Cakir, M.; Soucheray, M.; McGregor, M.; Cakir, Z.; Jang, G.; O'Meara, M. J.; Tummino, T. A.; Zhang, Z.; Foussard, H.; Rojc, A.; Zhou, Y.; Kuchenov, D.; Hüttenhain, R.; Xu, J.; Eckhardt, M.; Swaney, D. L.; Fabius, J. M.; Ummadi, M.; Tutuncuoglu, B.; Rathore, U.; Modak, M.; Haas, P.; Haas, K. M.; Naing, Z. Z. C.; Pulido, E. H.; Shi, Y.; Barrio-Hernandez, I.; Memon, D.; Petsalaki, E.; Dunham, A.; Marrero, M. C.; Burke, D.; Koh, C.; Vallet, T.; Silvas, J. A.; Azumaya, C. M.; Billesbølle, C.; Brilot, A. F.; Campbell, M. G.; Diallo, A.; Dickinson, M. S.; Diwanji, D.; Herrera, N.; Hoppe, N.; Kratochvil, H. T.; Liu, Y.; Merz, G. E.; Moritz, M.; Nguyen, H. C.; Nowotny, C.; Puchades, C.; Rizo, A. N.; Schulze-Gahmen, U.; Smith, A. M.; Sun, M.; Young, I. D.; Zhao, J.; Asarnow, D.; Biel, J.; Bowen, A.; Braxton, J. R.; Chen, J.; Chio, C. M.; Chio, U. S.; Deshpande, I.; Doan, L.; Faust, B.; Flores, S.; Jin, M.; Kim, K.; Lam, V. L.; Li, F.; Li, J.; Li, Y.-L.; Li, Y.; Liu, X.; Lo, M.; Lopez, K. E.; Melo, A. A.; Moss, F. R.; Nguyen, P.; Paulino, J.; Pawar, K. I.; Peters, J. K.; Pospiech, T. H.; Safari, M.; Sangwan, S.; Schaefer, K.; Thomas, P. V.; Thwin, A. C.; Trenker, R.; Tse, E.; Tsui, T. K. M.; Wang, F.; Whitis, N.; Yu, Z.; Zhang, K.; Zhang, Y.; Zhou, F.; Saltzberg, D.; Hodder, A. J.; Shun-Shion, A. S.; Williams, D. M.; White, K. M.; Rosales, R.; Kehrer, T.; Miorin, L.; Moreno, E.; Patel, A. H.; Rihn, S.; Khalid, M. M.; Vallejo-Gracia, A.; Fozouni, P.; Simoneau, C. R.; Roth, T. L.; Wu, D.; Karim, M. A.; Ghoussaini, M.; Dunham, I.; Berardi, F.; Weigang, S.; Chazal, M.; Park, J.; Logue, J.; McGrath, M.; Weston, S.; Haupt, R.; Hastie, C. J.; Elliott, M.; Brown, F.; Burness, K. A.; Reid, E.; Dorward, M.; Johnson, C.; Wilkinson, S. G.; Geyer, A.; Giesel, D. M.; Baillie, C.; Raggett, S.; Leech, H.; Toth, R.; Goodman, N.; Keough, K. C.; Lind, A. L.; Klesh, R. J.; Hemphill, K. R.; Carlson-Stevermer, J.; Oki, J.; Holden, K.; Maures, T.; Pollard, K. S.; Sali, A.; Agard, D. A.; Cheng, Y.; Fraser, J. S.; Frost, A.; Jura, N.; Kortemme, T.; Manglik, A.; Southworth, D. R.; Stroud, R. M.; Alessi, D. R.; Davies, P.; Frieman, M. B.; Ideker, T.; Abate, C.; Jouvenet, N.; Kochs, G.; Shoichet, B.; Ott, M.; Palmarini, M.; Shokat, K. M.; García-Sastre, A.; Rassen, J. A.; Grosse, R.; Rosenberg, O. S.; Verba, K. A.; Basler, C. F.; Vignuzzi, M.; Peden, A. A.; Beltrao, P.;

Krogan, N. J. Comparative Host-Coronavirus Protein Interaction Networks Reveal Pan-Viral Disease Mechanisms. *Science (80-.).* **2020**, *370* (6521), eabe9403. https://doi.org/10.1126/science.abe9403.

(20) Pan, J.; Peng, X.; Gao, Y.; Li, Z.; Lu, X.; Chen, Y.; Ishaq, M.; Liu, D.; DeDiego, M. L.; Enjuanes, L.; Guo, D. Genome-Wide Analysis of Protein-Protein Interactions and Involvement of Viral Proteins in SARS-CoV Replication. *PLoS One* **2008**, *3* (10), e3299. https://doi.org/10.1371/journal.pone.0003299.

(21) von Brunn, A.; Teepe, C.; Simpson, J. C.; Pepperkok, R.; Friedel, C. C.; Zimmer, R.; Roberts, R.; Baric, R.; Haas, J. Analysis of Intraviral Protein-Protein Interactions of the SARS Coronavirus ORFeome. *PLoS One* **2007**, *2* (5), e459. https://doi.org/10.1371/journal.pone.0000459.

(22) Davies, J. P.; Almasy, K. M.; McDonald, E. F.; Plate, L. Comparative Multiplexed Interactomics of SARS-CoV-2 and Homologous Coronavirus Nonstructural Proteins Identifies Unique and Shared Host-Cell Dependencies. *ACS Infect. Dis.* **2020**, *6*, 3189. https://doi.org/10.1021/acsinfecdis.0c00500.

(23) Li, J.; Van Vranken, J. G.; Pontano Vaites, L.; Schweppe, D. K.; Huttlin, E. L.; Etienne, C.; Nandhikonda, P.; Viner, R.; Robitaille, A. M.; Thompson, A. H.; Kuhn, K.; Pike, I.; Bomgarden, R. D.; Rogers, J. C.; Gygi, S. P.; Paulo, J. A. TMTpro Reagents: A Set of Isobaric Labeling Mass Tags Enables Simultaneous Proteome-Wide Measurements across 16 Samples. *Nat. Methods* **2020**, *17* (4), 399–404. https://doi.org/10.1038/s41592-020-0781-4.

(24) Mock, J. Y.; Chartron, J. W.; Zaslaver, M.; Xu, Y.; Ye, Y.; Clemons, W. M. Bag6 Complex Contains a Minimal Tail-Anchor-Targeting Module and a Mock BAG Domain. *Proc. Natl. Acad. Sci. U. S. A.* **2015**, *112* (1), 106–111. https://doi.org/10.1073/pnas.1402745112.

(25) Shi, Y.; Mosser, D. D.; Morimoto, R. I. Molecular Chaperones as HSF-1 Specific Transcriptional Repressors. *Genes Dev* **1998**, *12*, 654–666.

(26) Nakatani, Y.; Konishi, H.; Vassilev, A.; Kurooka, H.; Ishiguro, K.; Sawada, J. I.; Ikura, T.; Korsmeyer, S. J.; Qin, J.; Herlitz, A. M. P600, a Unique Protein Required for Membrane Morphogenesis and Cell Survival. *Proc. Natl. Acad. Sci. U. S. A.* **2005**, *102* (42), 15093–15098. https://doi.org/10.1073/pnas.0507458102.

(27) Bjørkøy, G.; Lamark, T.; Brech, A.; Outzen, H.; Perander, M.; Øvervatn, A.; Stenmark, H.; Johansen, T. P62/SQSTM1 Forms Protein Aggregates Degraded by Autophagy and Has a Protective Effect on Huntingtin-Induced Cell Death. *J. Cell Biol.* **2005**, *171* (4), 603–614. https://doi.org/10.1083/jcb.200507002.

(28) Mellacheruvu, D.; Wright, Z.; Couzens, A. L.; Lambert, J. P.; St-Denis, N. A.; Li, T.; Miteva, Y. V.; Hauri, S.; Sardiu, M. E.; Low, T. Y.; Halim, V. A.; Bagshaw, R. D.; Hubner, N. C.; Al-Hakim, A.; Bouchard, A.; Faubert, D.; Fermin, D.; Dunham, W. H.; Goudreault, M.; Lin, Z. Y.; Badillo, B. G.; Pawson, T.; Durocher, D.; Coulombe, B.; Aebersold, R.; Superti-Furga, G.; Colinge, J.; Heck, A. J. R.; Choi, H.; Gstaiger, M.; Mohammed, S.; Cristea, I. M.; Bennett, K. L.; Washburn, M. P.; Raught, B.; Ewing, R. M.; Gingras, A. C.; Nesvizhskii, A. I. The CRAPome: A Contaminant Repository for Affinity Purification-Mass Spectrometry Data. *Nat. Methods* **2013**, *10* (8), 730–736. https://doi.org/10.1038/nmeth.2557.

(29) Samavarchi-Tehrani, P.; Abdouni, H.; Knight, J. D.; Astori, A.; Samson, R.; Lin, Z.-Y.; Kim, D.-K.; Knapp, J. J.; St-Germain, J.; Go, C. D.; Larsen, B.; Wong, C. J.; Cassonnet, P.; Demeret, C.; Jacob, Y.; Roth, F. P.; Raught, B.; Gingras, A.-C. A SARS-CoV-2 – Host

Proximity Interactome. *bioRxiv* **2020**, 2020.09.03.282103. https://doi.org/10.1101/2020.09.03.282103.

(30) Koyano-Nakagawa, N.; Nishida, J.; Baldwin, D.; Arai, K.; Yokota, T. Molecular Cloning of a Novel Human CDNA Encoding a Zinc Finger Protein That Binds to the Interleukin-3 Promoter. *Mol. Cell. Biol.* **1994**, *14* (8), 5099–5107. https://doi.org/10.1128/mcb.14.8.5099.

(31) Jadhav, K.; Zhang, Y. Activating Transcription Factor 3 in Immune Response and Metabolic Regulation. *Liver Research*. KeAi Communications Co. September 2017, pp 96–102. https://doi.org/10.1016/j.livres.2017.08.001.

(32) Walter, P.; Ron, D. The Unfolded Protein Response: From Stress Pathway to Homeostatic Regulation. *Science (80-.).* **2011**, *334* (November), 1081–1086. https://doi.org/10.1152/physrev.00001.2011.

(33) Baez-Santos, Y. M.; Mielech, A. M.; Deng, X.; Baker, S.; Mesecar, A. D. Catalytic Function and Substrate Specificity of the Papain-Like Protease Domain of Nsp3 from the Middle East Respiratory Syndrome Coronavirus. *J. Virol.* **2014**, *88* (21), 12511–12527. https://doi.org/10.1128/jvi.01294-14.

(34) Barretto, N.; Jukneliene, D.; Ratia, K.; Chen, Z.; Mesecar, A. D.; Baker, S. C. The Papain-Like Protease of Severe Acute Respiratory Syndrome Coronavirus Has Deubiquitinating Activity. *J. Virol.* **2005**, *79* (24), 15189–15198. https://doi.org/10.1128/jvi.79.24.15189-15198.2005.

(35) Mielech, A. M.; Kilianski, A.; Baez-Santos, Y. M.; Mesecar, A. D.; Baker, S. C. MERS-CoV Papain-like Protease Has DeISGylating and Deubiquitinating Activities. *Virology* **2014**, *450–451*, 64–70. https://doi.org/10.1016/j.virol.2013.11.040.

(36) Wolff, G.; Limpens, R. W. A. L.; Zevenhoven-Dobbe, J. C.; Laugks, U.; Zheng, S.; de Jong, A. W. M.; Koning, R. I.; Agard, D. A.; Grünewald, K.; Koster, A. J.; Snijder, E. J.; Bárcena, M. A Molecular Pore Spans the Double Membrane of the Coronavirus Replication Organelle. *Science (80-.).* **2020**, *369* (6509), 1395–1398. https://doi.org/10.1126/SCIENCE.ABD3629.

(37) Wright, F. A.; Bonzerato, C. G.; Sliter, D. A.; Wojcikiewicz, R. J. H. The Erlin2 T65I Mutation Inhibits Erlin1/2 Complex-Mediated Inositol 1,4,5-Trisphosphate Receptor Ubiquitination and Phosphatidylinositol 3-Phosphate Binding. *J. Biol. Chem.* **2018**, *293* (40), 15706–15714. https://doi.org/10.1074/jbc.RA118.004547.

(38) Wang, R.; Simoneau, C. R.; Kulsuptrakul, J.; Bouhaddou, M.; Travisano, K. A.; Hayashi, J. M.; Carlson-Stevermer, J.; Zengel, J. R.; Richards, C. M.; Fozouni, P.; Oki, J.; Rodriguez, L.; Joehnk, B.; Walcott, K.; Holden, K.; Sil, A.; Carette, J. E.; Krogan, N. J.; Ott, M.; Puschnik, A. S. Genetic Screens Identify Host Factors for SARS-CoV-2 and Common Cold Coronaviruses. *Cell* **2020**. https://doi.org/10.1016/j.cell.2020.12.004.

(39) Bianco, C.; Mohr, I. Ribosome Biogenesis Restricts Innate Immune Responses to Virus Infection and DNA. *Elife* **2019**, *8*. https://doi.org/10.7554/eLife.49551.

(40) Kleinman, C. L.; Doria, M.; Orecchini, E.; Giuliani, E.; Galardi, S.; De Jay, N.; Michienzi, A. HIV-1 Infection Causes a Down-Regulation of Genes Involved in Ribosome Biogenesis. *PLoS One* **2014**, *9* (12), e113908. https://doi.org/10.1371/journal.pone.0113908.

(41) Reggiori, F.; Monastyrska, I.; Verheije, M. H.; Calì, T.; Ulasli, M.; Bianchi, S.; Bernasconi, R.; De Haan, C. A. M.; Molinari, M. Coronaviruses Hijack the LC3-I-Positive

EDEMosomes, ER-Derived Vesicles Exporting Short-Lived ERAD Regulators, for Replication. *Cell Host Microbe* **2010**, *7* (6), 500–508. https://doi.org/10.1016/j.chom.2010.05.013.

(42) Chan, C.-P.; Siu, K.-L.; Chin, K.-T.; Yuen, K.-Y.; Zheng, B.; Jin, D.-Y. Modulation of the Unfolded Protein Response by the Severe Acute Respiratory Syndrome Coronavirus Spike Protein. *J. Virol.* **2006**, *80* (18), 9279–9287. https://doi.org/10.1128/jvi.00659-06.

(43) Versteeg, G. A.; van de Nes, P. S.; Bredenbeek, P. J.; Spaan, W. J. M. The Coronavirus Spike Protein Induces Endoplasmic Reticulum Stress and Upregulation of Intracellular Chemokine MRNA Concentrations. *J. Virol.* **2007**, *81* (20), 10981–10990. https://doi.org/10.1128/jvi.01033-07.

(44) Shoulders, M. D.; Ryno, L. M.; Genereux, J. C.; Moresco, J. J.; Tu, P. G.; Wu, C.; Yates, J. R.; Su, A. I.; Kelly, J. W.; Wiseman, R. L. Stress-Independent Activation of XBP1s and/or ATF6 Reveals Three Functionally Diverse ER Proteostasis Environments. *Cell Rep.* **2013**, *3* (4), 1279–1292. https://doi.org/10.1016/j.celrep.2013.03.024.

(45) Grandjean, J. M. D.; Plate, L.; Morimoto, R. I.; Bollong, M. J.; Powers, E. T.; Luke Wiseman, R. Deconvoluting Stress-Responsive Proteostasis Signaling Pathways for Pharmacologic Activation Using Targeted RNA Sequencing. *ACS Chem. Biol.* **2019**, *14* (4), 784–795. https://doi.org/10.1021/acschembio.9b00134.

(46) Sung, S. C.; Chao, C. Y.; Jeng, K. S.; Yang, J. Y.; Lai, M. M. C. The 8ab Protein of SARS-CoV Is a Luminal ER Membrane-Associated Protein and Induces the Activation of ATF6. *Virology* **2009**, *387* (2), 402–413. https://doi.org/10.1016/j.virol.2009.02.021.

(47) Gallagher, C. M.; Garri, C.; Cain, E. L.; Ang, K. K. H.; Wilson, C. G.; Chen, S.; Hearn, B. R.; Jaishankar, P.; Aranda-Diaz, A.; Arkin, M. R.; Renslo, A. R.; Walter, P. Ceapins Are a New Class of Unfolded Protein Response Inhibitors, Selectively Targeting the ATF6α Branch. *Elife* **2016**, *5* (2016JULY), 1–33. https://doi.org/10.7554/eLife.11878.

(48) Jiang, X. S.; Tang, L. Y.; Dai, J.; Zhou, H.; Li, S. J.; Xia, Q. C.; Wu, J. R.; Zeng, R. Quantitative Analysis of Severe Acute Respiratory Syndrome (SARS)-Associated Coronavirus-Infected Cells Using Proteomic Approaches: Implications for Cellular Responses to Virus Infection. *Mol. Cell. Proteomics* **2005**, *4* (7), 902–913. https://doi.org/10.1074/mcp.M400112-MCP200.

(49) Plate, L.; Cooley, C. B.; Chen, J. J.; Paxman, R. J.; Gallagher, C. M.; Madoux, F.; Genereux, J. C.; Dobbs, W.; Garza, D.; Spicer, T. P.; Scampavia, L.; Brown, S. J.; Rosen, H.; Powers, E. T.; Walter, P.; Hodder, P.; Luke Wiseman, R.; Kelly, J. W. Small Molecule Proteostasis Regulators That Reprogram the ER to Reduce Extracellular Protein Aggregation. *Elife* **2016**, *5* (2016JULY). https://doi.org/10.7554/eLife.15550.

(50) Paxman, R.; Plate, L.; Blackwood, E. A.; Glembotski, C.; Powers, E. T.; Wiseman, R. L.; Kelly, J. W. Pharmacologic ATF6 Activating Compounds Are Metabolically Activated to Selectively Modify Endoplasmic Reticulum Proteins. *Elife* **2018**, *7*. https://doi.org/10.7554/eLife.37168.

(51) Thiel, V.; Ivanov, K. A.; Putics, Á.; Hertzig, T.; Schelle, B.; Bayer, S.; Weißbrich, B.; Snijder, E. J.; Rabenau, H.; Doerr, H. W.; Gorbalenya, A. E.; Ziebuhr, J. Mechanisms and Enzymes Involved in SARS Coronavirus Genome Expression. *Journal of General Virology*. Microbiology Society September 2003, pp 2305–2315. https://doi.org/10.1099/vir.0.19424-0.

(52) Harcourt, B. H.; Jukneliene, D.; Kanjanahaluethai, A.; Bechill, J.; Severson, K. M.; Smith, C. M.; Rota, P. A.; Baker, S. C. Identification of Severe Acute Respiratory Syndrome

Coronavirus Replicase Products and Characterization of Papain-Like Protease Activity. *J. Virol.* **2004**, *78* (24), 13600–13612. https://doi.org/10.1128/jvi.78.24.13600-13612.2004.

(53) Chang, Y.-S.; Ko, B.-H.; Ju, J.-C.; Chang, H.-H.; Huang, S.-H.; Lin, C.-W. SARS Unique Domain (SUD) of Severe Acute Respiratory Syndrome Coronavirus Induces NLRP3 Inflammasome-Dependent CXCL10-Mediated Pulmonary Inflammation. *Int. J. Mol. Sci.* **2020**, *21* (9), 3179. https://doi.org/10.3390/ijms21093179.

(54) Tan, J.; Vonrhein, C.; Smart, O. S.; Bricogne, G.; Bollati, M.; Kusov, Y.; Hansen, G.; Mesters, J. R.; Schmidt, C. L.; Hilgenfeld, R. The SARS-Unique Domain (SUD) of SARS Coronavirus Contains Two Macrodomains That Bind G-Quadruplexes. *PLoS Pathog.* **2009**, *5* (5), e1000428. https://doi.org/10.1371/journal.ppat.1000428.

(55) Zhang, K.; Miorin, L.; Makio, T.; Dehghan, I.; Gao, S.; Xie, Y.; Zhong, H.; Esparza, M.; Kehrer, T.; Kumar, A.; Hobman, T. C.; Ptak, C.; Gao, B.; Minna, J. D.; Chen, Z.; García-Sastre, A.; Ren, Y.; Wozniak, R. W.; Fontoura, B. M. A. Nsp1 Protein of SARS-CoV-2 Disrupts the MRNA Export Machinery to Inhibit Host Gene Expression. *Sci. Adv.* **2021**, *7* (6), eabe7386. https://doi.org/10.1126/sciadv.abe7386.

(56) Kopecky-Bromberg, S. A.; Martínez-Sobrido, L.; Frieman, M.; Baric, R. A.; Palese, P. Severe Acute Respiratory Syndrome Coronavirus Open Reading Frame (ORF) 3b, ORF 6, and Nucleocapsid Proteins Function as Interferon Antagonists. *J. Virol.* **2007**, *81* (2), 548–557. https://doi.org/10.1128/jvi.01782-06.

(57) Frieman, M.; Yount, B.; Heise, M.; Kopecky-Bromberg, S. A.; Palese, P.; Baric, R. S. Severe Acute Respiratory Syndrome Coronavirus ORF6 Antagonizes STAT1 Function by Sequestering Nuclear Import Factors on the Rough Endoplasmic Reticulum/Golgi Membrane. *J. Virol.* **2007**, *81* (18), 9812–9824. https://doi.org/10.1128/jvi.01012-07.

(58) Miorin, L.; Kehrer, T.; Sanchez-Aparicio, M. T.; Zhang, K.; Cohen, P.; Patel, R. S.; Cupic, A.; Makio, T.; Mei, M.; Moreno, E.; Danziger, O.; White, K. M.; Rathnasinghe, R.; Uccellini, M.; Gao, S.; Aydillo, T.; Mena, I.; Yin, X.; Martin-Sancho, L.; Krogan, N. J.; Chanda, S. K.; Schotsaert, M.; Wozniak, R. W.; Ren, Y.; Rosenberg, B. R.; Fontoura, B. M. A.; García-Sastre, A. SARS-CoV-2 Orf6 Hijacks Nup98 to Block STAT Nuclear Import and Antagonize Interferon Signaling. *Proc. Natl. Acad. Sci. U. S. A.* **2020**, *117* (45), 28344–28354. https://doi.org/10.1073/pnas.2016650117.

(59) Peña, J.; Harris, E. Dengue Virus Modulates the Unfolded Protein Response in a Time-Dependent Manner. *J. Biol. Chem.* **2011**, *286* (16), 14226–14236. https://doi.org/10.1074/jbc.M111.222703.

(60) Bechill, J.; Chen, Z.; Brewer, J. W.; Baker, S. C. Coronavirus Infection Modulates the Unfolded Protein Response and Mediates Sustained Translational Repression. *J. Virol.* **2008**, *82* (9), 4492–4501. https://doi.org/10.1128/jvi.00017-08.

(61) Fung, T. S.; Liu, D. X. Coronavirus Infection, ER Stress, Apoptosis and Innate Immunity. *Frontiers in Microbiology*. Frontiers Research Foundation June 17, 2014, p 296. https://doi.org/10.3389/fmicb.2014.00296.

(62) Minakshi, R.; Padhan, K.; Rani, M.; Khan, N.; Ahmad, F.; Jameel, S. The SARS Coronavirus 3a Protein Causes Endoplasmic Reticulum Stress and Induces Ligand-Independent Downregulation of the Type 1 Interferon Receptor. *PLoS One* **2009**, *4* (12), e8342. https://doi.org/10.1371/journal.pone.0008342.

(63) Carletti, T.; Zakaria, M. K.; Faoro, V.; Reale, L.; Kazungu, Y.; Licastro, D.; Marcello, A. Viral Priming of Cell Intrinsic Innate Antiviral Signaling by the Unfolded Protein Response. *Nat. Commun.* **2019**, *10* (1), 1–9. https://doi.org/10.1038/s41467-019-11663-2.

(64) Ke, P. Y.; Chen, S. S. L. Activation of the Unfolded Protein Response and Autophagy after Hepatitis C Virus Infection Suppresses Innate Antiviral Immunity in Vitro. *J. Clin. Invest.* **2011**, *121* (1), 37–56. https://doi.org/10.1172/JCI41474.

(65) DeDiego, M. L.; Nieto-Torres, J. L.; Jiménez-Guardeño, J. M.; Regla-Nava, J. A.; Álvarez, E.; Oliveros, J. C.; Zhao, J.; Fett, C.; Perlman, S.; Enjuanes, L. Severe Acute Respiratory Syndrome Coronavirus Envelope Protein Regulates Cell Stress Response and Apoptosis. *PLoS Pathog.* **2011**, *7* (10), e1002315. https://doi.org/10.1371/journal.ppat.1002315.

(66) Marceau, C. D.; Puschnik, A. S.; Majzoub, K.; Ooi, Y. S.; Brewer, S. M.; Fuchs, G.; Swaminathan, K.; Mata, M. A.; Elias, J. E.; Sarnow, P.; Carette, J. E. Genetic Dissection of Flaviviridae Host Factors through Genome-Scale CRISPR Screens. *Nature* **2016**, *535* (7610), 159–163. https://doi.org/10.1038/nature18631.

(67) Rambaut, A.; Holmes, E. C.; O'Toole, Á.; Hill, V.; McCrone, J. T.; Ruis, C.; du Plessis, L.; Pybus, O. G. A Dynamic Nomenclature Proposal for SARS-CoV-2 Lineages to Assist Genomic Epidemiology. *Nat. Microbiol.* **2020**, *5* (11), 1403–1407. https://doi.org/10.1038/s41564-020-0770-5.

(68) Rambaut, A.; Loman, N.; Pybus, O.; Barclay, W.; Barrett, J.; Carabelli, A.; Connor, T.; Peacock, T.; Robertson, D. L.; Volz, E. Preliminary genomic characterisation of an emergent SARS-CoV-2 lineage in the UK defined by a novel set of spike mutations https://virological.org/t/preliminary-genomic-characterisation-of-an-emergent-sars-cov-2-lineage-in-the-uk-defined-by-a-novel-set-of-spike-mutations/563.

(69) Gallagher, C. M.; Walter, P. Ceapins Inhibit ATF6α Signaling by Selectively Preventing Transport of ATF6α to the Golgi Apparatus during ER Stress. *Elife* **2016**, *5* (2016JULY). https://doi.org/10.7554/eLife.11880.

(70) Torres, S. E.; Gallagher, C. M.; Plate, L.; Gupta, M.; Liem, C. R.; Guo, X.; Tian, R.; Stroud, R. M.; Kampmann, M.; Weissman, J. S.; Walter, P. Ceapins Block the Unfolded Protein Response Sensor Atf6α by Inducing a Neomorphic Inter-Organelle Tether. *Elife* **2019**, *8*. https://doi.org/10.7554/eLife.46595.

(71) Fonslow, B. R.; Niessen, S. M.; Singh, M.; Wong, C. C. L.; Xu, T.; Carvalho, P. C.; Choi, J.; Park, S. K.; Yates, J. R. Single-Step Inline Hydroxyapatite Enrichment Facilitates Identification and Quantitation of Phosphopeptides from Mass-Limited Proteomes with MudPIT. *J. Proteome Res.* **2012**, *11* (5), 2697–2709. https://doi.org/10.1021/pr300200x.

(72) Wright, M. T.; Kouba, L.; Plate, L. Thyroglobulin Interactome Profiling Defines Altered Proteostasis Topology Associated With Thyroid Dyshormonogenesis. *Mol. Cell. Proteomics* **2021**, *20*, 100008. https://doi.org/10.1074/mcp.ra120.002168.

(73) Shannon, P.; Markiel, A.; Ozier, O.; Baliga, N. S.; Wang, J. T.; Ramage, D.; Amin, N.; Schwikowski, B.; Ideker, T. Cytoscape: A Software Environment for Integrated Models of Biomolecular Interaction Networks. *Genome Res.* **2003**, *13* (11), 2498–2504. https://doi.org/10.1101/gr.1239303.

CHAPTER 7: Conclusions and future directions

7.1 Summary of work

Viruses have been, and continue to be, a major threat to human health around the world. Over the course of this study, the world saw threatening outbreaks of a flavivirus (Zika) and a coronavirus (SARS-CoV-2) that caused significant social and economic impact worldwide. These events highlighted the need to better understand the pathogenesis of viruses, and how shared dependencies between strains or families may be exploited to allow us to prepare today for the public health emergencies of tomorrow.

Our group is not the first to have an interest in perturbing host-virus interactions to inhibit replication, and chapter 1 outlines some of the ways in which interactions, specifically those involving the host protein folding network, can be both identified and exploited. The ER protein folding network constitutes a swath of functions, from cotranslocation of ER targeted proteins to correct folding and glycosylation of those clients to degradation of misfolded substrates and more[1]. Given the interactions many viruses have with the ER, each of these steps in the protein folding process has been interrogated in some regard in an attempt to understand dependencies of many classes of viruses on the host cell[2,3]. Identifying these direct or indirect interactions can be performed in a variety of manners; affinity purification-mass spectrometry allows for identification of direct interactions by pulling down on a bait protein with its interactors after expression[4]. Genetic screens using CRISPR, RNAi, or overexpression constructs may help identify the role a protein has in enhancing or inhibiting viral replication without necessarily identifying a direct interaction[5–7].

The Plate lab was specifically interested in pharmacologic manipulation of the unfolded protein response, given the observation that dengue virus (DENV), a flavivirus related to Zika, is able to temporally control upregulation of each of the three branches; IRE1, ATF6, and PERK[8]. Specifically, we were interested in the effects that recently characterized modulators of the IRE1 and ATF6 pathways would have, given these two arms are largely responsible for controlling the

remodeling of the ER under conditions of protein folding stress[9]. In chapter 2, we find that neither inhibitor of the pathway has an effect on viral replication, either enhancing or inhibiting it. The activator of the IRE1 branch, **474**, initially showed some promising effects at enhancing viral replication, but these effects were not reproduced later. Compound **147**, an activator of the ATF6 branch, provided the largest effect, inhibiting viral replication up to 99% after 24 hours of infection. This compound was chosen as the basis for follow up in chapter 3.

Chapter 3 dives further into the mechanism of **147** as an antiviral[10]. We show that the compound is active up to at least 48 hours post-infection, and that it affects the total number of infectious virions released from the cell without affecting total viral protein secretion. Although designed as an activator of the ATF6 branch of the UPR, the antiviral activity of this compound is ATF6-independent, as measured by both small molecule cotreatment and chemical genetic methods. Instead, the compound relies on oxidation via P450 enzymes to create an active electrophile that covalently modifies free thiols, such as cysteine residues. Specifically, we use an alkyne labeled variant of **147** to show that it is predominantly ER resident proteins that are labeled, and even more specifically that the major targets are protein disulfide isomerases. Using small molecules specific for one or two PDIs, as well as RNAi, we were unable to find a single target whose inhibition or depletion resulted in a significant phenotypic change, indicating the effects of **147** are likely due to some polypharmacology. Encouragingly, we show that the compound **147** is able to inhibit several serotypes of dengue virus, which are antigenically distinct but genetically similar to one another. We also show the ability of the molecule to inhibit two strains of Zika virus, one ancestral and one from the 2015 outbreak.

After characterizing the activity of **147**, we wondered if a structurally and functionally similar molecule, **263**, would exhibit similar effects to **147**. Both groups possess an oxidizable motif to generate an active electrophile, and it was thought the potential electrophile on **263** could also covalently modify thiol groups. Chapter 4 explores our efforts to characterize this compound in the context of viral infection. While a lower dose of **263** had to be used due to toxicity, we were

encouraged when similar antiviral effects were seen, with infectious viral titers being lowered up to 90% 24 hours post infection. Contrary to **147**, **263** did cause a drop in total viral protein secretion, which was the first clue the mechanisms may be divergent. To support this point, a competition experiment using the alkyne labeled variant of **147** showed that **263** likely does not inhibit protein disulfide isomerases; many of the targets between the two molecules were different. The top target was the same between the two compounds, ALDH1A1, but shRNA experiments showed depletion of this gene does not have an effect on viral titers, suggesting it is not the target responsible for antiviral activity. Neither oxidation nor thiol modification are required for the antiviral activity either, positing this as a truly unique molecule compared to **147**. Encouragingly, we found that it is still active against several strains of dengue and Zika virus, further validating the utility of proteostasis modulation as an antiviral intervention point.

During these studies, SARS-CoV-2, the causative agent of COVID-19, emerged and immediately caused worldwide disruption socially, economically, and to the flavivirus research being done in the lab. This new virus, although genetically similar to SARS-CoV, marked a new starting line for science. Our lab chose to study the interactions that take place between viral proteins and host proteins using affinity purification-mass spectrometry, starting with non-structural proteins 2 and 4[11]. Using homologs from SARS-CoV-1, SARS-CoV-2, and hCoV-OV43, we showed that although some interactors are conserved among the strains, many interactors diverge. Among interactors, we observed an enrichment of mitochondria-associated ER membrane factors.

We were not the only groups interested in characterizing these interactions, and before and after we published our comparative study other groups used both AP-MS methods and proximity labeling methods to come up with lists of interactors of these viral proteins[12–16]. One nonstructural protein that was missing from all these studies was nonstructural protein 3, the largest and arguably most complex of the SARS-CoV-2 ORF1ab proteins. As outlined in chapter 6, we were unable to see the full length individual protein expressed, which suggests that it may be necessary to stabilize this protein with other members of the replication complex in order for stable

expression to occur[17]. To circumvent this problem, we divided the protein up into three fragments based on an intraviral interactome generated by Pan et al. for the SARS-CoV genome[18]. SARS-CoV-2 was aligned with these cut sites to create analogous fragments, and the same was done for coronaviruses MERS-CoV, hCoV-OC43, and hCoV-229E. These fragments all contained a FLAG affinity tag, which was used for immunoprecipitation of the bait proteins and their interactors. We identified and compared interactors among the N-terminal, middle, and C-terminal fragments for each strain (termed nsp3.1, nsp3.2, and nsp3.3 respectively). We find that almost no host interactors are conserved among all five strains for a given fragment, and that of the five strains SARS-CoV and SARS-CoV-2 generally share the most interactors. Surprisingly, we found interactions of the two SARS variants and hCoV-OC43 with ATF6, one of the transmembrane sensors involved in activation of the ER unfolded protein response. We reasoned two possibilities could result from this interaction, ATF6 activation or suppression. We found that SARS-CoV-2 nsp3.1 suppresses ATF6 activation, completely blocking it under mild activation conditions.

7.2 Ongoing experiments

7.2.1 Investigating perturbation of DENV structure by 147

One of the intriguing discoveries in chapter 3 was the observation that **147** does not reduce total viral protein levels secreted from the cell but does affect the infectious titer. This led to the hypothesis that **147** treatment results in the secretion of defunct virions. Given that **147** predominantly labels thioredoxin domain containing protein disulfide isomerases (PDIs), we further hypothesize that these virions are defunct because of aberrant disulfide bonding within or between envelope or premembrane protein monomers. The investigation of this question requires two methods to be optimized initially; a robust method of virus purification/concentration, and a method to quantify the number or concentration of free cysteines in one sample versus another.

A robust method of virus purification/concentration is needed to reproducibly isolate virus from the initial >10mL of viral supernatant into a concentrated solution for eventual detection by

western blot. While the method described in chapters 3 and 4 was sufficient for those experiments, going from ~10mL of virus to ~100µL of eventual resuspension rarely led to a concentration in virus titers, suggesting that much of the sample was lost during purification. To better isolate the virus, two options have been considered, one of which is under current investigation. Traditional methods use, as described, ultracentrifugation to pass viral particles through a sucrose cushion or gradient, while much of the remaining components of the media remain on top of the cushion. The virus pellets, allowing for removal of everything but the pellet, and resuspension in a smaller volume of liquid. The procedure used herein was a modified version of this protocol which used a shorter spin time. However, due to the mentioned concentration problems, an optimization of a full ultracentrifugation method may be needed for these purposes. In this case, a gradient is used to further separate components of the media, and each fraction is analyzed for the presence of virus. The relevant fractions are combined and subjected to a further spin to pellet the sample before resuspension in a chosen solution.

The second method of consideration is using centrifugal spin filters instead of a sucrose gradient to remove components of the media. The large advantage of spin filters is the ease of use; rather than needing a sucrose gradient and several hours to separate virus from solution, the spin filters easily allow cellular components smaller than the cutoff size of the membrane to pass through while retaining larger components. Viruses are larger than the typical extracellular protein, and so a 100kDa spin filter was chosen for the pilot experiments. The most crucial component of the media to remove is the bovine serum albumin from the added fetal bovine serum (FBS), which is approximately the same weight as the envelope protein monomer on DENV and extremely abundant in media samples run on SDS-PAGE gels; this abundance makes detection of the envelope protein difficult, and so the removal is important for any experiment on isolated virus. The 100kDa filter was intended to allow for the removal of this ~66kDa protein.

Initial experiments used DMEM with FBS to determine how efficiently the filter would remove the BSA. 4 mL DMEM plus 10% FBS was added to the top of an Amicon-4 100kDa spin filter, and

samples were spun at 4000xg for 20 minutes based on the suggested procedure given by EMD Millipore. Unexpectedly, a red buildup was observed in the bottom of the retentate; subsequent buffer exchanges using water did not relieve this buildup, and samples were unable to be run on a gel (**Figure A7.1**). Initially believing this to be a result of the phenol red in the DMEM complexing with BSA, the experiment was repeated using phenol red-free media. However, a buildup at the bottom of the retentate was still observed, with a color resembling that of BSA (**Figure A7.2**). In both cases, a freeze thaw of the samples left the retentate unable to be run on SDS-PAGE gels; the solution coagulated and would not return to a liquid state even after heating. The filtrates showed minimal presence of BSA based on stain-free gel imaging, supporting the hypothesis the BSA was being left behind in the retentate (**Figure A7.1, A7.2**). To attempt to subvert this problem, two additional attempts were made to pass BSA through the spin filter. A second attempt used 2% FBS medium instead of 10% FBS, as has typically been used in these experiments. With an infection time of 24 hours, the 2% FBS should only minimally affect the viability of the cells or virus. The same spin conditions were used, with repeated buffer exchanges of water after spins at 4000xg for 20 minutes. Unfortunately, the same buildup of BSA was observed, and

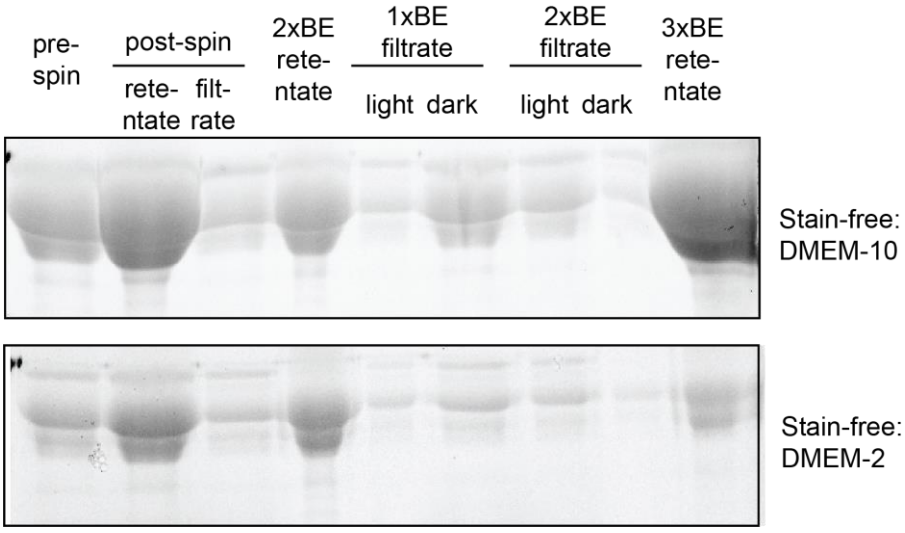

Figure 7.1 Stain-free gels of DMEM-10 and DMEM-2 before and after soft spin filtration. BSA, although below the 100kDa filter weight, accumulates in the retentate fraction. After 3 buffer exchanges (water), levels in the DMEM-2 sample were reduced to pre-filtration levels.

samples were still unable to be run on gels. Minimal BSA in the filtrate was also observed, suggesting most of the protein was in the retentate (**Figure A7.3**).

The third generation of the experiment used both 10% and 2% FBS media but decreased the spin time and intensity in an attempt to more gently concentrate the BSA. Spins were conducted for 5 minutes at 1500xg. Visible BSA concentration was still observed in all samples until three buffer exchanges had been performed in the 2% FBS media sample (**Figure 7.1**). While the BSA did not appear to be dilute relative to the initial media sample, under infection conditions the virus would be 20-30x concentrated. This ratio was posited to be enough to overcome any adverse effects from retaining the BSA.

To generate virus supernatant, 10cm dishes of Huh7 cells were treated for 16 hours with 10uM **147** or DMSO. Cells were infected for 3 hours with DENV2 16681 at MOI 3; inoculum was removed, and media with 2% FBS was replaced along with treatments. Media was collected 24 hours post infection. 8 mL media was divided among 2 4mL spin filters, and spin conditions as described in the last optimization experiment were repeated with five buffer exchanges into 5mM HEPES, pH 7.9. The final volumes for each sample were normalized to 288 µL, for an approximate concentration of 28x. It was observed that BSA still remained in the retentate, as observed by the buildup of a colored substance at the bottom of the filter even after repeated washes. This was confirmed by stain-free gel, where a darker band was observed in the retentate fractions compared to the filtrate. (**Figure A7.4**). Despite this, western blotting showed the concentration of DENV protein in the filtered samples compared to the initial media, indicating the goal of virus concentration was met. A focus forming assay to confirm this showed a 16x concentration in titer from pre-spin to post-spin, which is less than the 28x measured by volume but still more efficient than the ultracentrifugation methods used previously in this dissertation. It should be noted that no viral protein was observed in the post-spin **147** samples, whereas earlier results would indicate that the protein levels should have been the same between the two samples. The titer levels were still reduced by two orders of magnitude in both pre- and post-spin samples, but the equivalence

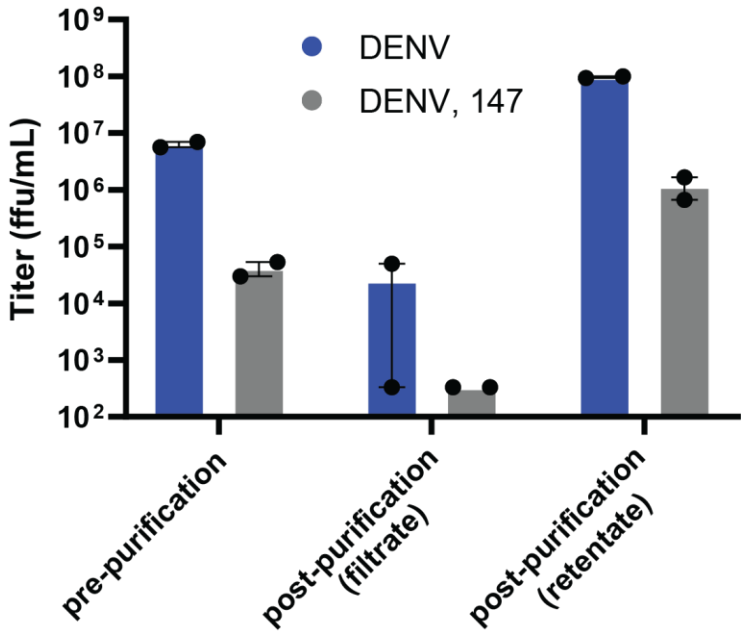

Figure 7.2. Titers increase in retentate after spin filter purification. Titers are increased approximately 15 fold in the DENV only retentate samples compared to the pre-purification, and approximately 30 fold in the **147** treated samples.

in protein intensities should form the basis of this experiment, indicating further follow up may be needed.

A second experiment was performed with virus containing media to confirm the results of the first spin. In this experiment, an aliquot was taken from the top layer of the retentate to determine if this layer contained most of the virus, in which case the BSA could be removed simply by leaving the bottom layer of the retentate in the filter. However, a titer approximately equal to that of the pre-filtrate was observed in the top layer of the retentate, while the bottom layer exhibited the increased titer expected after concentration (data not shown).

The second part of these follow-up experiments will consist of methodically footprinting the released virions to measure any structural changes that may occur between DMSO and **147** treated samples. Initially, we hypothesize that the structural changes are largely due to the disulfide bond arrangement, and so began seeking out reagents which would allow us to test this hypothesis. Initial experiments have used a PEG-maleimide reagent- the maleimide group is

electrophilic and cysteine-reactive, and thus will differentially label proteins involved in disulfide bonds compared to those with reduced residues. Only those free sulfhydryl groups will be available for covalent modification, and not those oxidized by disulfide bonds or otherwise modified. The long chain PEG substrate serves to alter the effective molecular weight of the compound, thus shifting it higher on an SDS-PAGE gel compared to an unmodified protein. The specific reagent used contained a photocleavable linker between the maleimide group and the PEG chain, allowing for separation by SDS-PAGE then cleavage of the PEG chain using UV light. Advantageously, removal of the PEG chain allows for better detection after transfer to a membrane for western blot.

Proof-of-concept experiments were performed on Huh7 cell lysates to measure proteins with known disulfide bonds or free cysteine residues. The first of these proteins measured was GAPDH, an enzyme involved in glycolysis which resides in the cytosol, a reducing environment, and thus has reduced disulfide bonds. Conditions were optimized using GAPDH, and it was determined that a concentration of approximately 0.5 mg/mL protein lysate with 0.5 mg/mL PEG-maleimide reagent at 37°C after 4 hours of exposure is sufficient to monitor labeling. In the labeled samples, two bands were seen above the unlabeled (**Figure A7.5**). GAPDH contains four cysteine residues including the active site, and thus a maximum of 5 bands would be expected. Still in protein lysates, the next set of experiments measured labeling of the protein disulfide isomerases under DMSO vs **147**. Identical conditions were used for labeling, and the various labeling states of PDIA1, PDIA4, and PDIA6 were measured by western blot. Of these, PDIA1 displayed the most complex labeling pattern. In all cases, the addition of **147** decreased the presence of higher molecular weight bands, supporting the data that **147** covalently modifies thiols; if these cysteine residues are labeled by **147**, they are unavailable for labeling by the maleimide reagent. This study is now able to be extended to intracellular viral proteins, and ultimately to the concentrated virus from an optimized purification scheme.

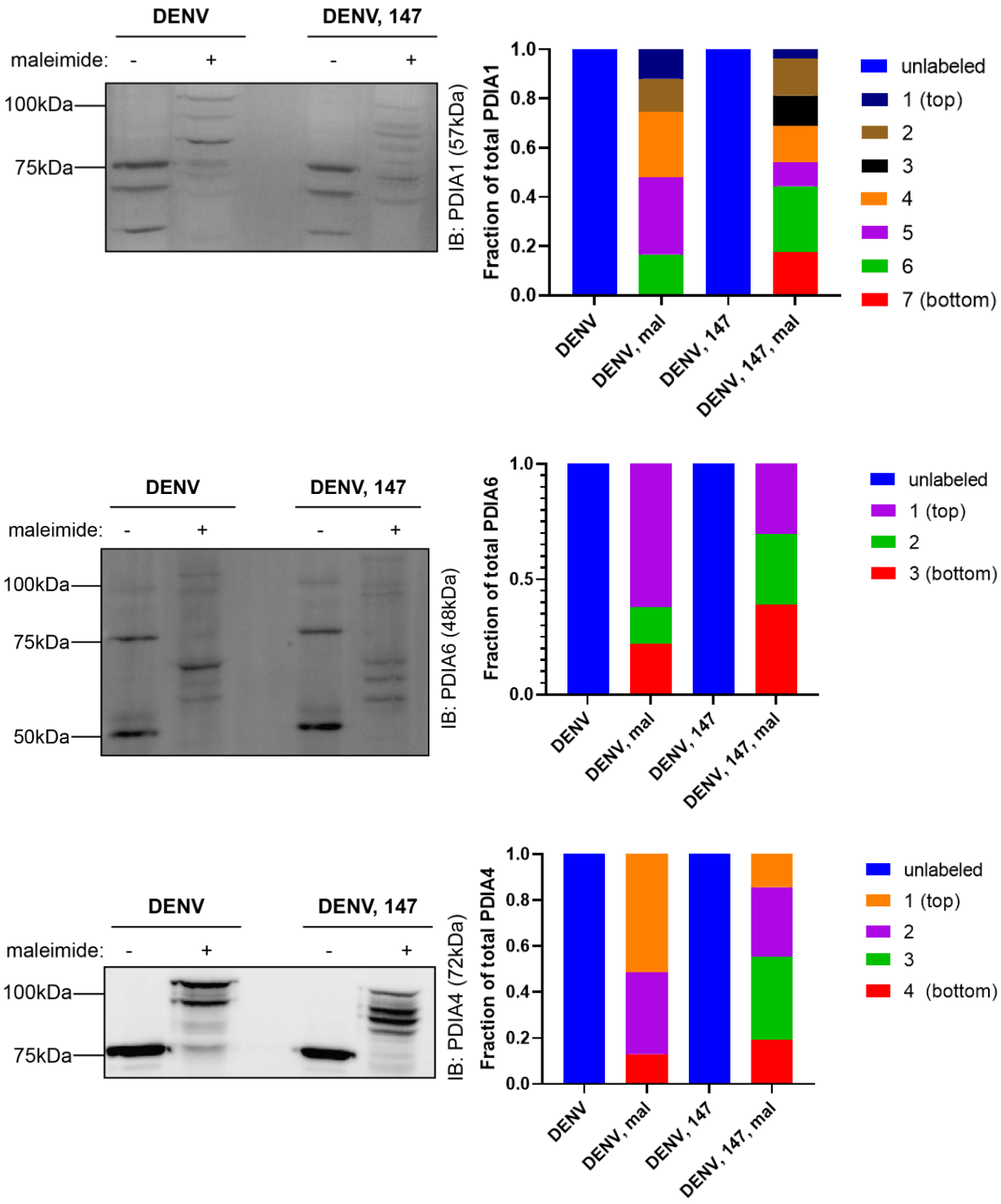

Figure 7.3. PC-PEGmal differentially labels 147 treated samples. DENV infected lysates with or without PC-PEG-maleimide compound for 4 hours at 37°C. Samples were separated by SDS-PAGE and visualized by western blot using antibodies for the proteins indicated. In general, the addition of **147** lowered the availability of cysteines to be labeled by the maleimide reagent, as indicated by the lowered intensity or disappearance of higher molecular weight bands compared to the non-**147** treated samples.

7.2.2 Target identification of 263 using thermal shift methods

Chapter 4 outlined our study of **263**, and how this molecule was initially posited to have a similar mechanism to **147** but in fact does not. This leaves the question of how **263** *does* work within the cell, both as an ER stress activator as well as its antiviral properties. We began answering the former by examining global proteome changes on **263** treatment, in addition to co-treatment with

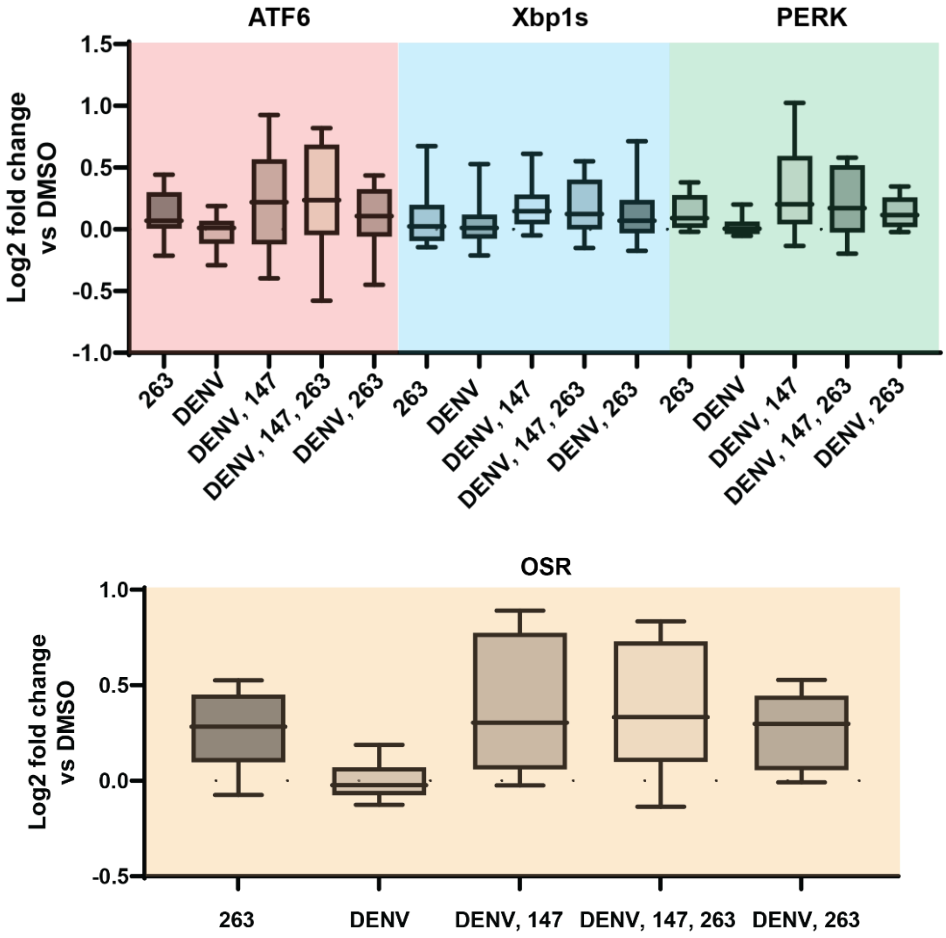

Figure 7.4. Stress pathway activation by combinations of DENV, 263, and 147. Samples were pre-treated with compounds where indicated, prior to infection with DENV at MOI 3 (where indicated) for 3 hours. After infection, inoculum was removed, cells were washed, and media and treatments were replaced for 24 hours. Samples were harvested and lysed, and 20 µg of each sample was precipitated, reduced, alkylated, and digested. Peptides were labeled using TMTpro reagents, combined, and run on an Exploris 480 using multidimensional peptide identification technology for on-line fractionation prior to MS analysis. Genesets for each stress pathway were taken from Grandjean et al. and changes relative to the DMSO control were calculated using TMT reporter ion intensities from Proteome Discoverer.

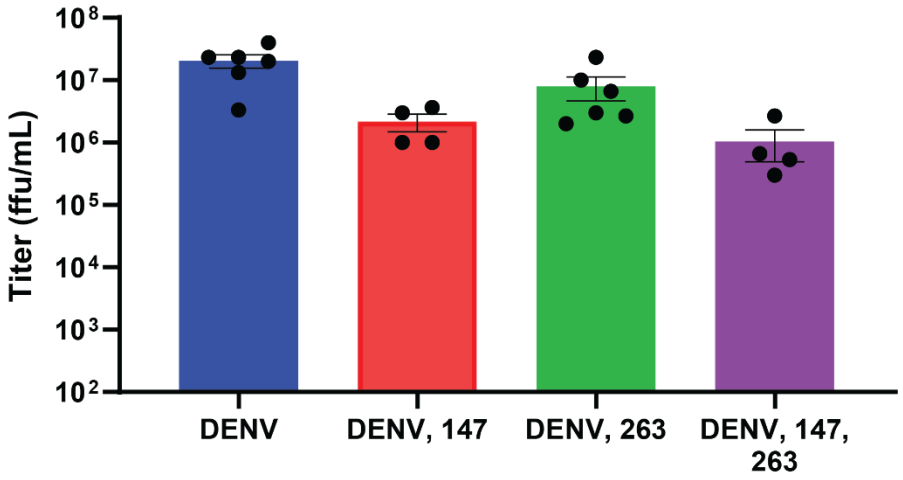

Figure 7.5. DENV titers after 263 and 147 treatement. Samples were pre-treated with compounds where indicated, prior to infection with DENV at MOI 3 (where indicated) for 3 hours. After infection, inoculum was removed, cells were washed, and media and treatments were replaced for 24 hours. Media samples were taken and analyzed by focus forming assay.

147. In initial studies, **263** was not examined further as a molecule because it did show slightly more promiscuous activity towards the other UPR branches, particularly IRE1. On treatment in Huh7 cells, it was clear that **263** did promiscuously activate branches of the UPR, though the gene profile was not typically as extreme in either direction as the samples with **147**.

Examining the targets of **263** requires a more intricate assay, because unlike **147**, there is little SAR data for the compound and no alkyne-labeled variant exists. Fortunately, recent methods have been developed to help identify the targets of small molecules not based on pulldown assays, but on the assumption that they confer thermal stability onto their targets and this stability can be measured. The initial method, the cellular thermal shift assay, developed by Norlund and colleagues, involved treating cells with compound and heating fractions of the lysate to different temperatures, followed by quantification of the soluble fraction of a protein of interest by western blot[19]. The quantification could be compared to a control lysate; a protein stabilized by a given drug would show a higher propensity to stay in solution as the melting curve progressed. This method has evolved into several related technologies, one of which is thermal proteome profiling[20]. The logic behind the method is the same, but this method takes advantage of

quantitative mass spectrometry to identify the melting curves of a high number of proteins at once in an unbiased manner. Using tandem mass tag technology, samples across a curve are combined into a single mass spectrometry run, and a melting curve is generated based on the TMT reporter ion intensity for each temperature.

We used this method to perform a pilot experiment to investigate some of the potential targets of **263**. Using **147** as a control (for which the targets are known as validated by pulldown in chapter 3), 15cm dishes of cells were treated with DMSO, 3 µM **147**, or 3 µM **263** for 4 hours. Cells were resuspended and aliquoted into 8 fractions, which were exposed to different temperatures as outlined in **Table 7.1** for 3 minutes. Cells were treated with benzonase and Igepal-CA-630 to disrupt membranes and precipitate nucleic acid, then subjected to freeze-thaw cycles to lyse. Lysates were cleared and aliquoted for mass spectrometry analysis or western blot.

The SDS-PAGE gels for each sample showed the expected indirect relationship between temperature and protein abundance; as the temperature in each set went up, the intensity of the lane (as a marker for total protein content) went down (**Figure A7.9**). To begin parsing whether the experiment may have worked, gels were transferred to PVDF membranes and two PDIs were blotted for. As targets of **147**, it was expected a difference would be seen in the melting curves of these proteins between the DMSO and **147** treated samples. However, the abundance curves did not look as expected, with noisy lines being produced and no distinction between the two conditions. In some samples, it was visible that the first heated sample (42°C) was higher in abundance compared to the control 37°C sample. It is possible that western blot may not be sensitive enough to detect subtle changes in abundance.

Temp (°C)
37
42
47.6
52
56.8
59.5
62.8
67

Table 7.1 Temperatures used for TPP.

The mass spectrometry run provides a higher sensitivity and throughput ability to measure changes in melting curves between conditions. With 8 temperatures for each condition in hand, a DMSO and treatment sample (for each drug) were labeled with TMTpro reagents, combined, and run on an Exploris480 instrument using MuDPIT. TMT reporter

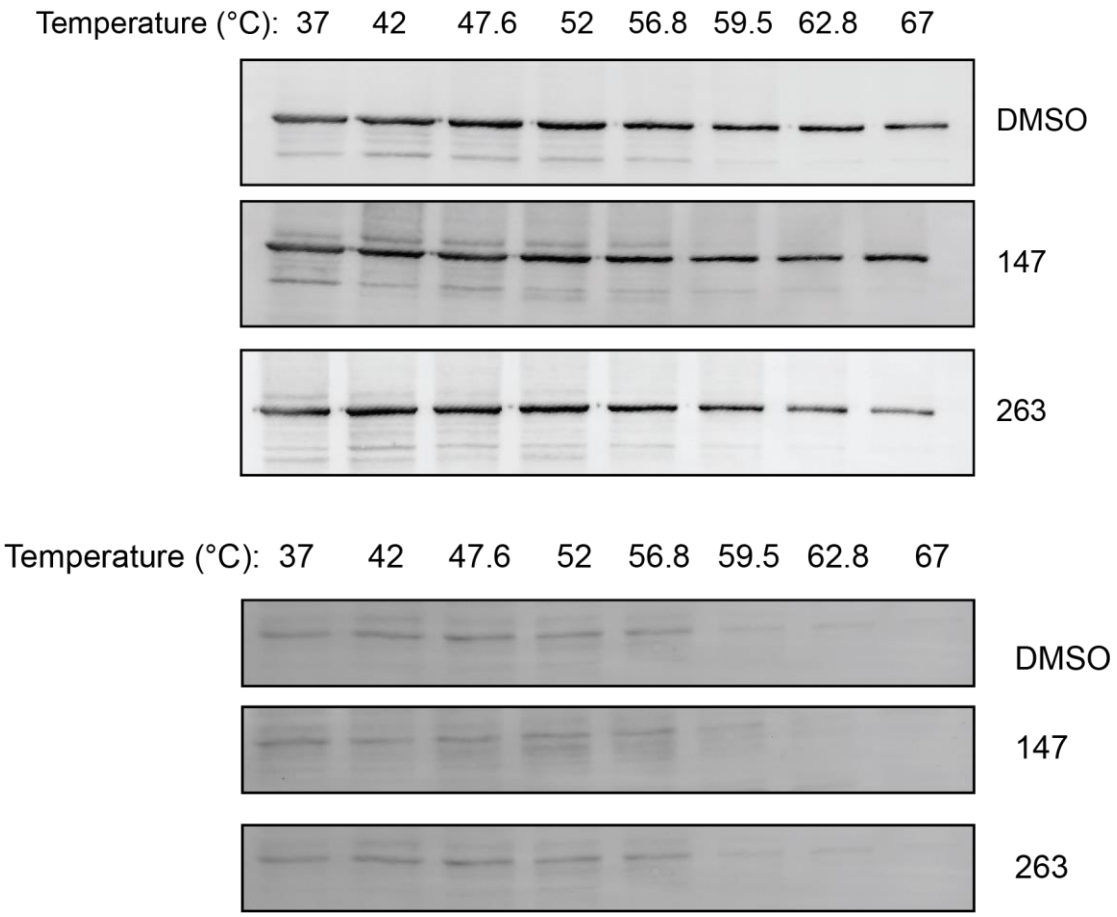

Figure 7.6. Western blots of select PDIs in thermal proteome profiling samples. After heating, samples were run on SDS-PAGE gels and transferred to PVDF membranes. PDIA4 (top) and PDIA6 (bottom) levels expectedly decreased in each of the samples as the exposure temperature increased.

intensities were quantified using Proteome Discoverer 2.4; after plotting the intensities observed in each channel, the same pattern as observed by western blot emerged. As the temperature rose in all three conditions, the total protein abundance (via TMT reporter ion intensity) decreased (**Figure A7.10**). Initial attempts to quantify the targets as measured by stabilization were not successful in identifying PDIs as the target group of **147.** Further data analysis as well as additional replicates of the experiments are needed.

7.2.3 Further exploration of coronavirus nsp interactomes

Chapter 4 relayed the story of our initial foray into viral interactomics using homologs of nonstructural proteins 2 and 4 from three different coronaviruses. While the interactome of a given viral protein provides useful information, it is more powerful when paired with functional data about the implications of these interactions. We observed in the nsp2/4 interactomes an enrichment of factors localized at mitochondria associated membranes, or MAMs. Jonathan Davies showed the nonstructural proteins to also localize to these MAMs, and he has since begun followup studies on how these proteins, and how coronavirus infection, may affect the morphology of mitochondria in cells. He is also interested in how calcium flux or mitochondrial function may change under these conditions. Lastly, he is using RNA to identify the pro- or anti-viral factors of these MAMs factors and other interactors during infection[2].

Chapter 5 explored the interactome of fragments of the coronavirus nsp3 interactome across five different strains by breaking the protein up in to three fragments per homolog. In the N-terminal portion, we observed an interaction between three variants (SARS-CoV-2, SARS-CoV, and OC43) with the ER unfolded protein response sensor ATF6. We showed that this interaction helps suppress the ability of ATF6 to respond to ER stress. This discovery raises several questions about how this suppression may be valuable in the context of the full viral replication cycle. The domain organization of nsp3 has been well documented, even if the specific roles of several domains are still unknown. It is pertinent to discover which of these domains interacts with ATF6, especially given that the N-terminus of nsp3 is not predicted to contain any membrane-associated domains and ATF6 is a membrane bound protein. To do so, domain truncations of nsp3 have been created, and similar immunoprecipitations are being performed to isolate which subfragments of nsp3 still retain the interaction with ATF6. In addition, a variant composed of both the N-terminal and middle fragments of nsp3 is being created to determine how the middle

[2] Work being done by Jonathan Davies, co-first author

fragment, which does contain a transmembrane domain that spans the ER membrane, affects localization of the fragment and binding to ATF6, as well as overall UPR activity[3]. In regard to the UPR activity, an observation was made that nonstructural protein 4, another component of the double membrane vesicle used for replication, activates the ATF6 and PERK branches of the UPR. Another question therefore is whether nsp3 is able to directly counteract ATF6 activation raised as a result of nsp4 expression. These experiments involve co-expression of nsp4 and nsp3.1, as well as individual expression[4].

Our initial paper noted mutations occurring in some of the early variants of SARS-CoV-2, including the alpha, beta, and gamma variants (at the time known as B.1.1.7, B.1.351, and P.1 or United Kingdom, South Africa, and Brazil variants respectively), that changed the amino acid sequence within nsp3 specifically[21]. Though the mutations within the spike protein received much of the attention, as they impact cell surface receptor binding and infectivity, we wonder how these mutations in nsp3 might impact the interactome of the protein. The corresponding mutations of the alpha, beta, gamma, delta, and omicron variants to date have been created within the appropriate fragments of SARS-CoV-2 nsp3, and the comparative interactome studies are currently being conducted[5].

7.3 Future directions

The work outlined herein increases our understanding of how viruses perturb host cellular function in order to facilitate their own replication cycles. This greater understanding has led to the characterization of two compounds which appear to have pan-flavivirus activity, reducing titers up to 99% after 24 hours of infection. These studies add to the versatility of compounds already

[3] Mutants created and tested by Joyce Karyuki, undergraduate.
[4] Experiments performed by Athira Sivadas, undergraduate.
[5] Mutants created and experiments performed by Valeria Garcia Lopez, graduate student.

under investigation for the treatment of other diseases, as the need for proteostasis regulators encompasses diseases far wider than viral infections.

147 has been tested in mouse models for protection against ischemia/reperfusion damage after cardiac injury, as well as in brain and kidney models. Given that the compound was a) effective and b) well tolerated by mice, it would be intriguing to test **147** against DENV and/or ZIKV in an infection-permissive mouse model. Other compounds, such as Hsp70 inhibitors, have been tested in such models[22,23]. A collaboration with the Dr. Judith Frydman research group at Stanford University has been discussed for this purpose. If these results continue to hold true, an antiviral purpose could be added to the potential clinical studies of **147**. Discussions about testing both the stress pathway and antiviral effects of **147** in mosquitos would also be intruiging; while likely more difficult due to the nature of handling infected mosquitos, a lab with this specialty could be identified for this purpose. It would also be interesting to test, either in cell culture or in mouse models, how the compound affects the efficacy and resistance development against other drugs that have failed as potential therapeutic candidates. The resistance development against **147** also needs to be examined. While we hypothesize that resistance will not develop due to the host proteins being targeted (which are less likely to develop mutations), this should be done through serial passaging of the virus in the presence of compound. Lastly, to further examine which targets of the compound may be responsible for the antiviral activity, literature comparisons could be made using existing RNAi or CRISPRi studies to determine how gene knockdown has affected flavivirus replication with the same proteins noted in chapter 4. A separate study could also be conducted using Huh7 cells in the lab to determine if **147** retains activity when each gene is knocked down.

Initial studies showed that **263**, but not **147**, may possess anti-coronavirus activity. While it is important to validate that the targets of the compounds are similar between cell lines (thus more of a reason to develop a **263** target ID method), further investigating the proteins responsible for these effects could lead to broader discoveries of what specific host-pathogen protein-protein

interactions are important for RNA virus infection, spanning multiple families. Contrarily, further understanding of the ways in which viral proteins interact with host proteins during infection would provide an alternative method of which targets of the compounds may be important. As outlined in chapter 1, affinity tagging of a specific viral protein in the context of a full genome can be difficult, especially in cases like these where multiple proteins are encoded by a single reading frame. However, the power these investigations would give surely yield a good return on investment in terms of understanding virus biology. Our lab has used FLAG, Strep, and GFP affinity handles for pulldowns in both single virus constructs and, in limited cases, full viral genomes. In published literature, transposon mutagenesis has often yielded the highest number of functional viruses with tags installed; doing this for flavivirus or coronavirus genomes with any of the named affinity tags would likely be the easiest method of obtaining replicons amenable to affinity pulldown.

A question that arose during our initial thermal proteome profiling (TPP) studies was how sensitive the technique would be for compounds that incompletely label their targets; **147**, for example, is known to only label up to 25% of PDIA4. Based on the premise of CETSA, this labeling would need to be enough to detect a shift in thermal stability in order to identify it as a ‘target’ of the compound. While the percentage of any given protein that **263** labels is unknown, a similar consideration may need to be made.

The importance of understanding viruses and being prepared for pandemics has arisen time and time again. However, we still largely lack the tools to prevent these outbreaks, and an understanding of how viruses perturb host cells and how therapeutics can manipulate the host back to inhibit viral replication is increasingly becoming an option for developing novel drugs. Host-centered therapeutics represent a new age in antiviral (or more generally, antimicrobial) discovery, and this work presents findings that expands on our understanding of the targets that may be relevant in coronavirus and flavivirus biology. Whether through drug repurposing or novel drug discovery platforms, science is developing towards being able to rapidly respond to public and global health threats.

7.4 References

(1) Schwarz, D. S.; Blower, M. D. The Endoplasmic Reticulum: Structure, Function and Response to Cellular Signaling. *Cell. Mol. Life Sci.* **2015**, *73* (1), 79–94. https://doi.org/10.1007/S00018-015-2052-6.

(2) Inoue, T.; Tsai, B. How Viruses Use the Endoplasmic Reticulum for Entry, Replication, and Assembly. *Cold Spring Harb. Perspect. Biol.* **2013**, *5* (1), a013250. https://doi.org/10.1101/CSHPERSPECT.A013250.

(3) Aviner, R.; Frydman, J. Proteostasis in Viral Infection: Unfolding the Complex Virus-Chaperone Interplay. *Cold Spring Harb. Perspect. Biol.* **2019**. https://doi.org/10.1101/cshperspect.a034090.

(4) Wright, M. T.; Plate, L. Revealing Functional Insights into ER Proteostasis through Proteomics and Interactomics. *Exp. Cell Res.* **2021**, *399* (1), 112417. https://doi.org/10.1016/J.YEXCR.2020.112417.

(5) Wang, R.; Simoneau, C. R.; Kulsuptrakul, J.; Bouhaddou, M.; Travisano, K. A.; Hayashi, J. M.; Carlson-Stevermer, J.; Zengel, J. R.; Richards, C. M.; Fozouni, P.; Oki, J.; Rodriguez, L.; Joehnk, B.; Walcott, K.; Holden, K.; Sil, A.; Carette, J. E.; Krogan, N. J.; Ott, M.; Puschnik, A. S. Genetic Screens Identify Host Factors for SARS-CoV-2 and Common Cold Coronaviruses. *Cell* **2021**, *184* (1), 106-119.e14. https://doi.org/10.1016/J.CELL.2020.12.004/ATTACHMENT/6132394D-27BB-4E30-92C2-8C0A4D8878CC/MMC5.XLSX.

(6) Jones, C. E.; Tan, W. S.; Grey, F.; Hughes, D. J. Discovering Antiviral Restriction Factors and Pathways Using Genetic Screens. *J. Gen. Virol.* **2021**, *102*, 1603. https://doi.org/10.1099/jgv.0.001603.

(7) Li, S.; Qian, N.; Jiang, C.; Zu, W.; Liang, A.; Li, M.; Elledge, S. J.; Tan, X. Gain-of-Function Genetic Screening Identifies the Antiviral Function of TMEM120A via STING Activation. *Nat. Commun.* **2022**, *13* (1), 1–12. https://doi.org/10.1038/s41467-021-27670-1.

(8) Peña, J.; Harris, E. Dengue Virus Modulates the Unfolded Protein Response in a Time-Dependent Manner. *J. Biol. Chem.* **2011**, *286* (16), 14226–14236. https://doi.org/10.1074/JBC.M111.222703/ATTACHMENT/26D81C6A-EC37-478A-8216-AE9671042F97/MMC1.PDF.

(9) Shoulders, M. D.; Ryno, L. M.; Genereux, J. C.; Moresco, J. J.; Tu, P. G.; Wu, C.; Yates, J. R.; Su, A. I.; Kelly, J. W.; Wiseman, R. L. Stress-Independent Activation of XBP1s and/or ATF6 Reveals Three Functionally Diverse ER Proteostasis Environments. *Cell Rep.* **2013**, *3* (4), 1279–1292. https://doi.org/10.1016/J.CELREP.2013.03.024/ATTACHMENT/835BC2E1-D13A-47AB-82E6-E52A9A6D36CF/MMC4.PDF.

(10) Almasy, K. M.; Davies, J. P.; Lisy, S. M.; Tirgar, R.; Tran, S. C.; Plate, L. Small-Molecule Endoplasmic Reticulum Proteostasis Regulator Acts as a Broad-Spectrum Inhibitor of Dengue and Zika Virus Infections. *Proc. Natl. Acad. Sci. U. S. A.* **2021**, *118* (3). https://doi.org/10.1073/PNAS.2012209118/-/DCSUPPLEMENTAL.

(11) Davies, J. P.; Almasy, K. M.; McDonald, E. F.; Plate, L. Comparative Multiplexed Interactomics of SARS-CoV-2 and Homologous Coronavirus Nonstructural Proteins Identifies Unique and Shared Host-Cell Dependencies. *ACS Infect. Dis.* **2020**, *6* (12), 3174–3189.

https://doi.org/10.1021/ACSINFECDIS.0C00500/SUPPL_FILE/ID0C00500_SI_007.XLSX
.

(12) Gordon, D. E.; Jang, G. M.; Bouhaddou, M.; Xu, J.; Obernier, K.; White, K. M.; O'Meara, M. J.; Rezelj, V. V.; Guo, J. Z.; Swaney, D. L.; Tummino, T. A.; Hüttenhain, R.; Kaake, R. M.; Richards, A. L.; Tutuncuoglu, B.; Foussard, H.; Batra, J.; Haas, K.; Modak, M.; Kim, M.; Haas, P.; Polacco, B. J.; Braberg, H.; Fabius, J. M.; Eckhardt, M.; Soucheray, M.; Bennett, M. J.; Cakir, M.; McGregor, M. J.; Li, Q.; Meyer, B.; Roesch, F.; Vallet, T.; Mac Kain, A.; Miorin, L.; Moreno, E.; Naing, Z. Z. C.; Zhou, Y.; Peng, S.; Shi, Y.; Zhang, Z.; Shen, W.; Kirby, I. T.; Melnyk, J. E.; Chorba, J. S.; Lou, K.; Dai, S. A.; Barrio-Hernandez, I.; Memon, D.; Hernandez-Armenta, C.; Lyu, J.; Mathy, C. J. P.; Perica, T.; Pilla, K. B.; Ganesan, S. J.; Saltzberg, D. J.; Rakesh, R.; Liu, X.; Rosenthal, S. B.; Calviello, L.; Venkataramanan, S.; Liboy-Lugo, J.; Lin, Y.; Huang, X. P.; Liu, Y. F.; Wankowicz, S. A.; Bohn, M.; Safari, M.; Ugur, F. S.; Koh, C.; Savar, N. S.; Tran, Q. D.; Shengjuler, D.; Fletcher, S. J.; O'Neal, M. C.; Cai, Y.; Chang, J. C. J.; Broadhurst, D. J.; Klippsten, S.; Sharp, P. P.; Wenzell, N. A.; Kuzuoglu-Ozturk, D.; Wang, H. Y.; Trenker, R.; Young, J. M.; Cavero, D. A.; Hiatt, J.; Roth, T. L.; Rathore, U.; Subramanian, A.; Noack, J.; Hubert, M.; Stroud, R. M.; Frankel, A. D.; Rosenberg, O. S.; Verba, K. A.; Agard, D. A.; Ott, M.; Emerman, M.; Jura, N.; von Zastrow, M.; Verdin, E.; Ashworth, A.; Schwartz, O.; D'Enfert, C.; Mukherjee, S.; Jacobson, M.; Malik, H. S.; Fujimori, D. G.; Ideker, T.; Craik, C. S.; Floor, S. N.; Fraser, J. S.; Gross, J. D.; Sali, A.; Roth, B. L.; Ruggero, D.; Taunton, J.; Kortemme, T.; Beltrao, P.; Vignuzzi, M.; García-Sastre, A.; Shokat, K. M.; Shoichet, B. K.; Krogan, N. J. A SARS-CoV-2 Protein Interaction Map Reveals Targets for Drug Repurposing. *Nature* **2020**, *583* (7816), 459–468. https://doi.org/10.1038/s41586-020-2286-9.

(13) Gordon, D. E.; Hiatt, J.; Bouhaddou, M.; Rezelj, V. V.; Ulferts, S.; Braberg, H.; Jureka, A. S.; Obernier, K.; Guo, J. Z.; Batra, J.; Kaake, R. M.; Weckstein, A. R.; Owens, T. W.; Gupta, M.; Pourmal, S.; Titus, E. W.; Cakir, M.; Soucheray, M.; McGregor, M.; Cakir, Z.; Jang, G.; O'Meara, M. J.; Tummino, T. A.; Zhang, Z.; Foussard, H.; Rojc, A.; Zhou, Y.; Kuchenov, D.; Hüttenhain, R.; Xu, J.; Eckhardt, M.; Swaney, D. L.; Fabius, J. M.; Ummadi, M.; Tutuncuoglu, B.; Rathore, U.; Modak, M.; Haas, P.; Haas, K. M.; Naing, Z. Z. C.; Pulido, E. H.; Shi, Y.; Barrio-Hernandez, I.; Memon, D.; Petsalaki, E.; Dunham, A.; Marrero, M. C.; Burke, D.; Koh, C.; Vallet, T.; Silvas, J. A.; Azumaya, C. M.; Billesbølle, C.; Brilot, A. F.; Campbell, M. G.; Diallo, A.; Dickinson, M. S.; Diwanji, D.; Herrera, N.; Hoppe, N.; Kratochvil, H. T.; Liu, Y.; Merz, G. E.; Moritz, M.; Nguyen, H. C.; Nowotny, C.; Puchades, C.; Rizo, A. N.; Schulze-Gahmen, U.; Smith, A. M.; Sun, M.; Young, I. D.; Zhao, J.; Asarnow, D.; Biel, J.; Bowen, A.; Braxton, J. R.; Chen, J.; Chio, C. M.; Chio, U. S.; Deshpande, I.; Doan, L.; Faust, B.; Flores, S.; Jin, M.; Kim, K.; Lam, V. L.; Li, F.; Li, J.; Li, Y. L.; Li, Y.; Liu, X.; Lo, M.; Lopez, K. E.; Melo, A. A.; Moss, F. R.; Nguyen, P.; Paulino, J.; Pawar, K. I.; Peters, J. K.; Pospiech, T. H.; Safari, M.; Sangwan, S.; Schaefer, K.; Thomas, P. V.; Thwin, A. C.; Trenker, R.; Tse, E.; Tsui, T. K. M.; Wang, F.; Whitis, N.; Yu, Z.; Zhang, K.; Zhang, Y.; Zhou, F.; Saltzberg, D.; Hodder, A. J.; Shun-Shion, A. S.; Williams, D. M.; White, K. M.; Rosales, R.; Kehrer, T.; Miorin, L.; Moreno, E.; Patel, A. H.; Rihn, S.; Khalid, M. M.; Vallejo-Gracia, A.; Fozouni, P.; Simoneau, C. R.; Roth, T. L.; Wu, D.; Karim, M. A.; Ghoussaini, M.; Dunham, I.; Berardi, F.; Weigang, S.; Chazal, M.; Park, J.; Logue, J.; McGrath, M.; Weston, S.; Haupt, R.; Hastie, C. J.; Elliott, M.; Brown, F.; Burness, K. A.; Reid, E.; Dorward, M.; Johnson, C.; Wilkinson, S. G.; Geyer, A.; Giesel, D. M.; Baillie, C.; Raggett, S.; Leech, H.; Toth, R.; Goodman, N.; Keough, K. C.; Lind, A. L.; Klesh, R. J.; Hemphill, K. R.; Carlson-Stevermer, J.; Oki, J.; Holden, K.; Maures, T.; Pollard, K. S.; Sali, A.; Agard, D. A.; Cheng, Y.; Fraser, J. S.; Frost, A.; Jura, N.; Kortemme, T.; Manglik, A.; Southworth, D. R.; Stroud, R. M.; Alessi, D.

R.; Davies, P.; Frieman, M. B.; Ideker, T.; Abate, C.; Jouvenet, N.; Kochs, G.; Shoichet, B.; Ott, M.; Palmarini, M.; Shokat, K. M.; García-Sastre, A.; Rassen, J. A.; Grosse, R.; Rosenberg, O. S.; Verba, K. A.; Basler, C. F.; Vignuzzi, M.; Peden, A. A.; Beltrao, P.; Krogan, N. J. Comparative Host-Coronavirus Protein Interaction Networks Reveal Pan-Viral Disease Mechanisms. *Science (80-.).* **2020**, *370* (6521). https://doi.org/10.1126/SCIENCE.ABE9403.

(14) Terracciano, R.; Preianò, M.; Fregola, A.; Pelaia, C.; Montalcini, T.; Savino, R. Mapping the SARS-CoV-2–Host Protein–Protein Interactome by Affinity Purification Mass Spectrometry and Proximity-Dependent Biotin Labeling: A Rational and Straightforward Route to Discover Host-Directed Anti-SARS-CoV-2 Therapeutics. *Int. J. Mol. Sci.* **2021**, *22* (2), 532. https://doi.org/10.3390/IJMS22020532.

(15) Samavarchi-Tehrani, P.; Abdouni, H.; Knight, J. D. R.; Astori, A.; Samson, R.; Lin, Z.-Y.; Kim, D.-K.; Knapp, J. J.; St-Germain, J.; Go, C. D.; Larsen, B.; Wong, C. J.; Cassonnet, P.; Demeret, C.; Jacob, Y.; Roth, F. P.; Raught, B.; Gingras, A.-C. A SARS-CoV-2 – Host Proximity Interactome. *bioRxiv* **2020**, 2020.09.03.282103. https://doi.org/10.1101/2020.09.03.282103.

(16) Liu, X.; Huuskonen, S.; Laitinen, T.; Redchuk, T.; Bogacheva, M.; Salokas, K.; Pöhner, I.; Öhman, T.; Tonduru, A. K.; Hassinen, A.; Gawriyski, L.; Keskitalo, S.; Vartiainen, M. K.; Pieti€ Ainen, V.; Poso, A.; Varjosalo, M. SARS-CoV-2–Host Proteome Interactions for Antiviral Drug Discovery. *Mol. Syst. Biol.* **2021**, *17* (11), e10396. https://doi.org/10.15252/MSB.202110396.

(17) Almasy, K. M.; Davies, J. P.; Plate, L. Comparative Host Interactomes of the SARS-CoV-2 Nonstructural Protein 3 and Human Coronavirus Homologs. *Mol. Cell. Proteomics* **2021**, *20*, 100120. https://doi.org/10.1016/J.MCPRO.2021.100120/ATTACHMENT/DC696480-9DA5-4D88-B4F1-9CCBDB68C498/MMC9.XLSX.

(18) Pan, J.; Peng, X.; Gao, Y.; Li, Z.; Lu, X.; Chen, Y.; Ishaq, M.; Liu, D.; DeDiego, M. L.; Enjuanes, L.; Guo, D. Genome-Wide Analysis of Protein-Protein Interactions and Involvement of Viral Proteins in SARS-CoV Replication. *PLoS One* **2008**, *3* (10), e3299. https://doi.org/10.1371/JOURNAL.PONE.0003299.

(19) Jafari, R.; Almqvist, H.; Axelsson, H.; Ignatushchenko, M.; Lundbäck, T.; Nordlund, P.; Molina, D. M. The Cellular Thermal Shift Assay for Evaluating Drug Target Interactions in Cells. *Nat. Protoc.* **2014**, *9* (9), 2100–2122. https://doi.org/10.1038/nprot.2014.138.

(20) Franken, H.; Mathieson, T.; Childs, D.; Sweetman, G. M. A.; Werner, T.; Tögel, I.; Doce, C.; Gade, S.; Bantscheff, M.; Drewes, G.; Reinhard, F. B. M.; Huber, W.; Savitski, M. M. Thermal Proteome Profiling for Unbiased Identification of Direct and Indirect Drug Targets Using Multiplexed Quantitative Mass Spectrometry. *Nat. Protoc.* **2015**, *10* (10), 1567–1593. https://doi.org/10.1038/nprot.2015.101.

(21) Rambaut, A.; Holmes, E. C.; O'Toole, Á.; Hill, V.; McCrone, J. T.; Ruis, C.; du Plessis, L.; Pybus, O. G. A Dynamic Nomenclature Proposal for SARS-CoV-2 Lineages to Assist Genomic Epidemiology. *Nat. Microbiol.* **2020**, *5* (11), 1403–1407. https://doi.org/10.1038/s41564-020-0770-5.

(22) Taguwa, S.; Maringer, K.; Li, X.; Bernal-Rubio, D.; Rauch, J. N.; Gestwicki, J. E.; Andino, R.; Fernandez-Sesma, A.; Frydman, J. Defining Hsp70 Subnetworks in Dengue Virus Replication Reveals Key Vulnerability in Flavivirus Infection. *Cell* **2015**, *163* (5), 1108–1123. https://doi.org/10.1016/J.CELL.2015.10.046/ATTACHMENT/DD2A8D18-BB22-

4E83-8D1D-06E377EAF788/MMC1.PDF.

(23) Taguwa, S.; Yeh, M. Te; Rainbolt, T. K.; Nayak, A.; Shao, H.; Gestwicki, J. E.; Andino, R.; Frydman, J. Zika Virus Dependence on Host Hsp70 Provides a Protective Strategy against Infection and Disease. *Cell Rep.* **2019**, *26* (4), 906-920.e3. https://doi.org/10.1016/J.CELREP.2018.12.095/ATTACHMENT/0C673173-7F84-4B6E-946B-0B1FFF72CE80/MMC1.PDF.

APPENDIX

Appendix 2 Supplementary figures and tables for chapter 2

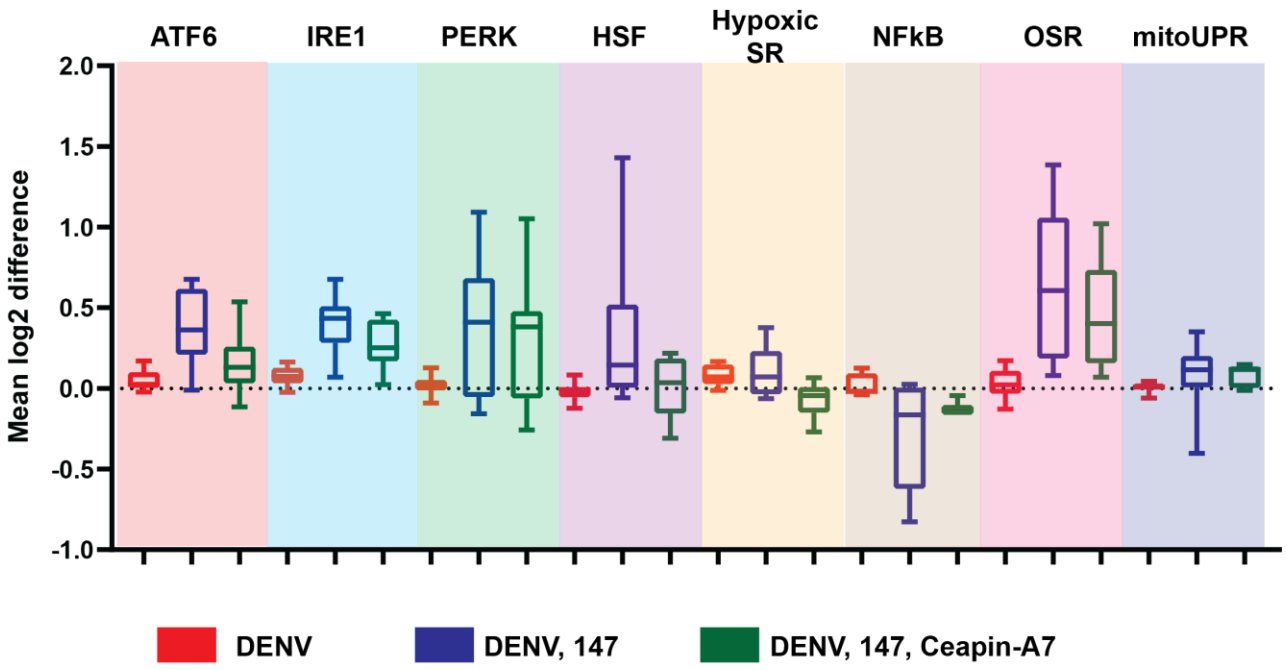

Figure A2.1 Stress pathway activation by DENV, 147, and Ceapin-A7. Stress pathway genesets based on characterization of Grandjean et al[1]. Cells were pre-treated with compounds where noted for 16 hours before infection with DENV BID-V533 at MOI 3 for 3 hours. Media and compounds were replaced for 24 hours before cells were harvested. 10 µg protein from each sample (quantified using BioRad 1x protein assay dye and BSA standards) was precipitated, reduced, alkylated, and digested. Peptides were labeled using TMT11plex reagents, combined, and run on a QExactiv HF instrument using multidimensional peptide identification technology (MudPIT) for separation. TMT reporter intensities were quantified using Proteome Discoverer.

Table A2.1. Key resources table for chapter 2

Reagent Type	Designation	Source	Sequence	Notes
Chemical	147	[2]		10 µM
Chemical	474	[3]		10 µM
Chemical	4µ8c	[4]		6 µM
Chemical	Kira6	[5]		10 µM
Chemical	Ceapin-A7	[6]		10 µM
Chemical	RP22	[2]		6 µM
Chemical	Ceapin-A5	[6]		10 µM
Chemical	Thapsigargin			0.5 µg/mL
Chemical	3-amino-5-ethylcarbazole	Sigma		
Antibody	Anti-pan-flavivirus 4G2	Millipore		1:1000
Antibody	Anti-mouse HRP			1:1000
Primer	Xbp1_F	Sigma	ccttgtagttgagaaccagg	For RT-PCR
Primer	Xbp1_R	Sigma	gagtcaataccgccagaatc	For RT-PCR
Primer	HspA5_F	Sigma	gcctgtatttctagacctgcc	For qPCR
Primer	HspA5_R	Sigma	ttcatcttgccagccagttg	For qPCR
Primer	ERDJ4_F	Sigma	ggaaggaggagcgctaggtc	For qPCR
Primer	ERDJ4_R	Sigma	atcctgcaccctccgactac	For qPCR
Primer	CHOP_F	Sigma	accaagggagaaccaggaaacg	For qPCR
Primer	CHOP_R	Sigma	tcaccattcggtcaatcagagc	For qPCR
Primer	RiboP_F	Sigma	cgtcgcctcctacctgct	For qPCR
Primer	RiboP_R	Sigma	ccattcagctcactgataaccttg	For qPCR

Appendix 3 Supplementary figures and tables for chapter 3

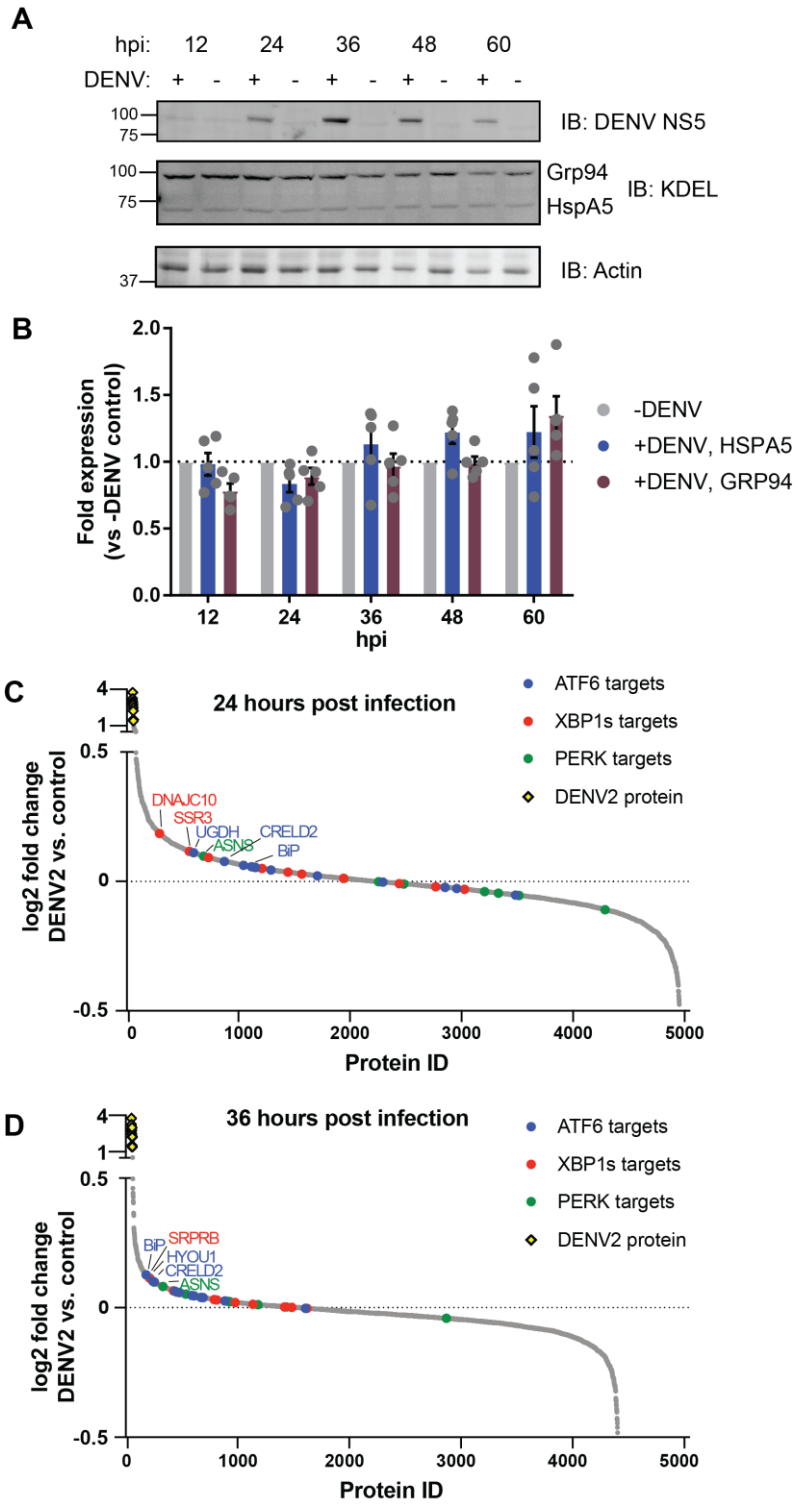

Figure A3.1. DENV infection induces the UPR.

Representative Western Blot (**A**) and protein quantification (**B**) showing time course of ATF6 upregulation over the course of DENV infection. Cells were infected with DENV-2 strain BID-V533 at MOI of 3 for 3 hours. Media was replaced and samples were taken at indicated timepoints post-

infection. Cells were lysed, and protein samples were run on SDS-PAGE gels and visualized using PVDF membranes. Actin is included as a loading control. Waterfall plots of proteomics data from samples infected with DENV-2 for 24 hours (**C**) and 36 hours (**D**), showing the presence of DENV proteins and upregulation of IRE1/XBP1s, ATF6, and PERK branches of the UPR. Cells were infected with DENV-2 strain BID-V533 at a MOI of 3 for 3 hours. Media was replaced and samples were collected at 24 or 36 hpi. Gene upregulation was quantified using TMT11plex reagents and comparison is between DENV-infected cells vs. noninfected cells. Graph represents 4-7 independent biological replicates.

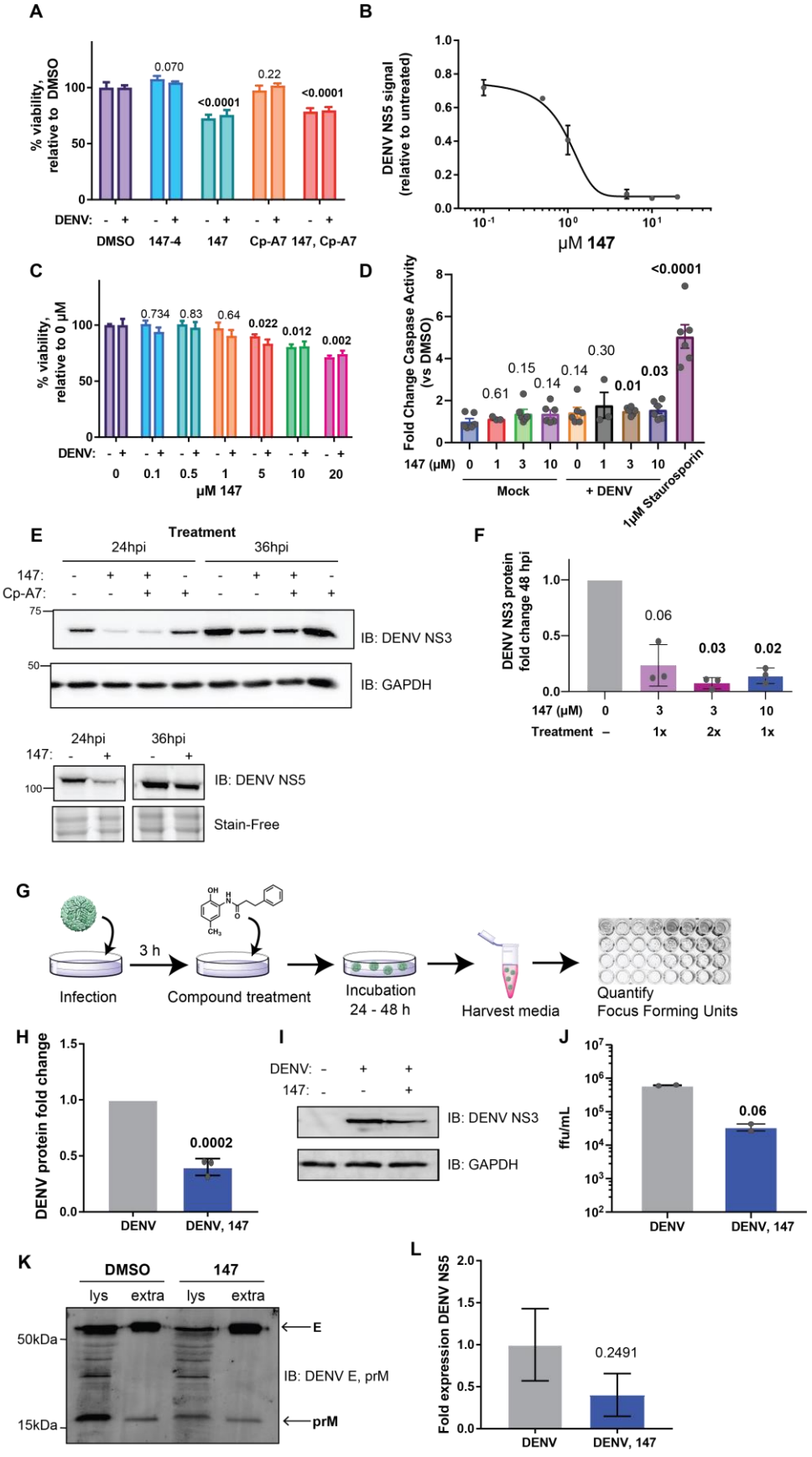

Figure A3.2. Treatment with small molecule 147 reduces DENV infection in a dose-dependent manner and only minimally impairs cell viability.

(A) **147** only modestly affects Huh7 cell proliferation over the course of treatment. No decrease in viability was seen with **147-4** or **Ceapin-A7** (**Cp-A7**). Cells were pretreated with 10 μM **147**, 6 μM **Cp-A7**, or both for 16h, then infected (where indicated) with DENV-2 strain BID-V533 at a MOI of 3 for 3 hours. Media and treatments were replaced, and proliferation was measured 24hpi using the Promega Cell Titer Glo reagent. Graphs represent six independent biological replicates across two days of measurement. Error bars represent SEM. Significance was determined using a one-sample t-test with a hypothesized mean of 100. A dose-response curve shows DENV is sensitive to **147** treatment with an IC50 of approximately 1 μM.

(B) Cells were treated with the indicated concentrations of **147** for 16 hours, then infected with DENV-2 strain BID-V533 at a MOI of 3 for 3 hours. Media and treatments were replaced, and cells were collected 24 hpi. Cells were lysed, and protein samples were run on SDS-PAGE gels and visualized using PVDF membranes. Western blot intensities were normalized to a GAPDH loading control. Graphs represent 2-4 independent biological replicates.

(C) Error bars represent SEM. Increasing **147** concentration causes decreasing cell proliferation. No decrease in cell growth was seen with **147-4** or Ceapin-A7 (**Cp-A7**). Cells were pretreated with the indicated concentrations of **147** for 16h, then infected (where indicated) with DENV-2 strain BID-V533 at a MOI of 3 for 3 hours. Media and treatments were replaced, and proliferation was measured 24 hpi using the Promega Cell Titer Glo reagent. Graphs represent three biological replicates. Error bars represent SEM.

(D) Bar graph quantifying caspase 3/7 activity in response to **147** treatment and DENV infection. Caspase activity is not significantly increased with up to 10 μM **147** treatment or with DENV treatment. **147** in combination with DENV infection causes a slight increase in caspase 3/7 activation; however, this activity is far less than the positive control staurosporin, a known activator of caspase 3/7.

(E) Representative western blot showing **147** attenuates DENV protein levels. Cells were pretreated with 10 μM **147**, 6 μM **Cp-A7**, or both for 16h, then infected with DENV-2 strain BID-V533 at MOI of 3 for 3 hours. Media and treatments were replaced, and cells were collected at indicated timepoints. Cells were lysed, and protein samples were run on SDS-PAGE gels and visualized using PVDF membranes. GAPDH is included as a loading control. No visualization of DENV protein could be seen at 12 hpi.

(F) Western blot quantification of DENV NS3 protein levels at an extended time point 48 hpi when treated with different dosing regimens of **147**. Huh7 cells were pretreated with **147** (3 or 10 μM) for 16 h, infected with DENV at MOI of 3 for 3 h, and media containing **147** was replenished (1x). For the 2x treatment, a fresh dose of 3μM **147** was added to the cells 24 hpi. Cells were harvested 48 hpi, lysed, proteins separated by SDS-PAGE, transferred to PVDF and blotted for NS3. The high dose of **147** is sufficient to lower viral protein levels at 48 hpi, while a single dose 3 μM **147** results in higher recovery of virus production 48 hpi. On the contrary, significant reduction can be achieved with the 2x repeated treatment of 3 μM **147**.

(G) Schematic showing the treatment regimen eliminating the pretreatment step, which will determine if **147** blocks viral entry. Cells are only treated post-infection with 10 μM **147**, and focus forming units are quantified 24 hpi.

(H) Quantification of western blots with treatment only post-entry shows similar phenotype to treatment pre- and post-entry. Cells were only treated post-infection with 10 μM **147**, and cells were harvested 24 hpi. Cells were lysed, and protein samples were run on SDS-PAGE gels and visualized using PVDF membranes. Graph represents three independent biological replicates. Error bars represent SEM and p-value from an unpaired t-test is shown.

(I) Representative western blot for **H** showing DENV NS3 levels decrease even when 10 μM **147** is only added to cells post-infection. Normalization to GAPDH was included as a loading control.

(J) Graph showing reduction in viral titers for only post-entry treatment. Cells were treated as in **G-H** and viral titers were determined by focus forming assay. Error bars represent SEM and p-value from a ratio paired t-test is shown.

(K) Representative western blot showing that extracellular viral structural protein levels are not affected by **147** treatment. Huh7 cells were pre-treated with **147**, infected with DENV at MOI of 3, and cells and media were harvested 24 h post infection. Cells were lysed to collect the total lysate protein sample (lys). Extracellular virions from the media were isolated and concentrated by ultracentrifugation (extra). 'Lys' and 'extra' samples were separate by SDS-PAGE, transferred to PVDF and probed for DENV structural proteins. As with the nonstructural protein levels, structural proteins E and prM show decreased levels in lysate with **147** treatment. On the other hand, no decrease in E and prM protein levels was observed for the purified extracellular virion fraction. Quantification of western blots is shown in **Fig. 3.2H**. This is in contrast to the observed decrease in infectious viral titers shown in **Fig. 3.2G** and **Fig. 3.2I**.

(L) qPCR data showing that **147** does not cause a significant decrease in the level of extracellular viral RNA. Cells were treated and infected as described in **K**, extracellular virions were isolated, and RNA was extracted from the same volume of samples and used to generate cDNA for qPCR. Bars represent the cumulative average of five biological replicates and error bars show SEM. P-value from unpaired t-test is shown.

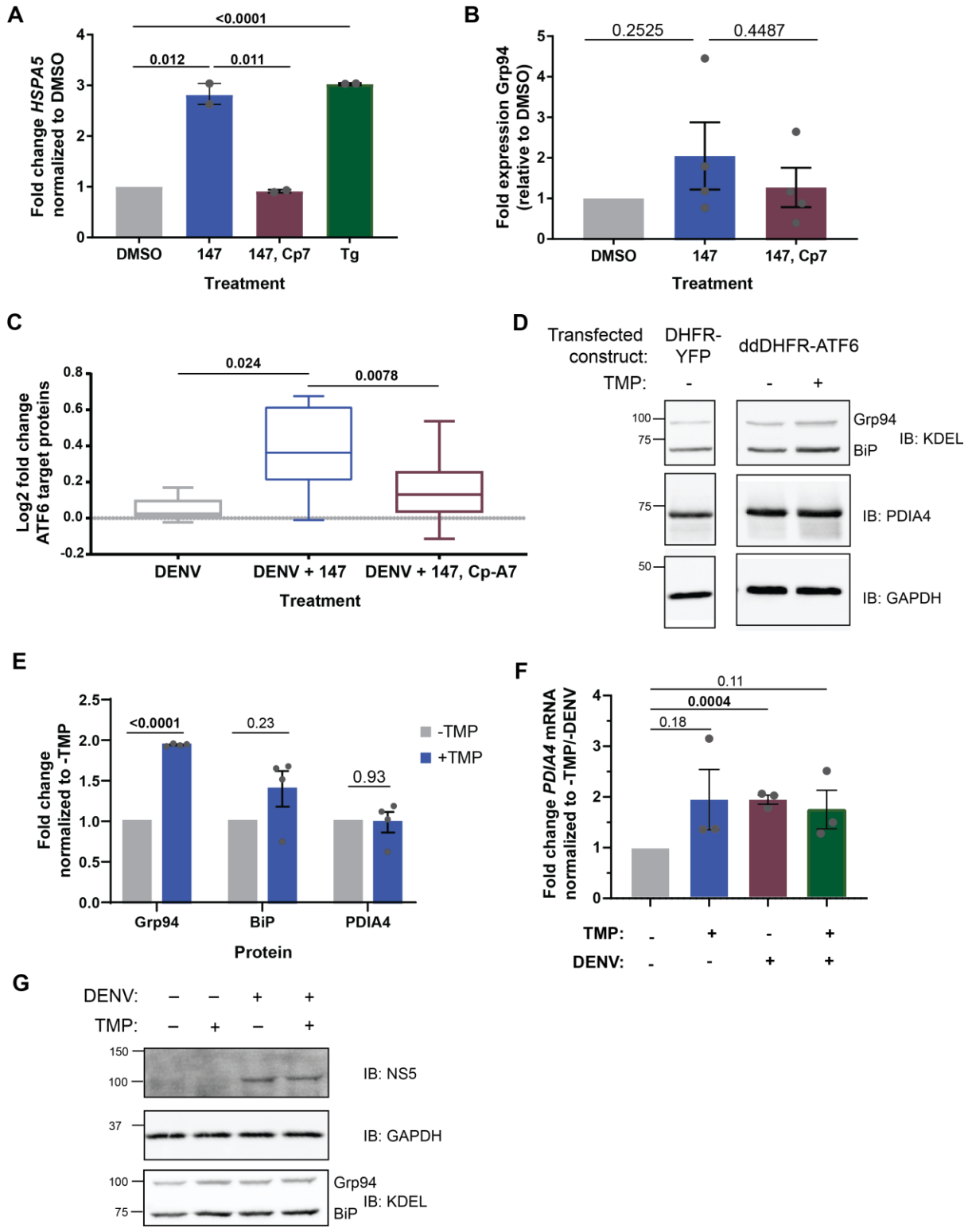

Figure A3.3. Ceapin-A7 blocks the 147-mediated ATF6 activation and ligand regulated DHFR.ATF6 activation in Huh7 cells.

(A) qPCR data showing **147** upregulates ATF6 target gene *HspA5/BiP*. Upregulation is reversed after cotreatment with **Cp-A7**. Thapsigargin (Tg), a global UPR stressor, is included as a positive control. Graphs represent two independent biological replicates, where each biological replicate

is the average of two technical replicates. Error bars represent SEM and p-values from unpaired t-tests are shown.

(B) Mild stimulation of ATF6 reporter gene GRP94 after **147** treatment, which is subsequently reversed by cotreatment with **147**. Cells were treated with 10 µM **147** or 10 µM **147** and 6 µM **Cp-A7**.

(C) Proteomics data showing **147**-mediated activation of ATF6 target proteins in DENV infected Huh7 cells. Huh7 cells infected with DENV were treated with 10µM **147** or a combination of 10µM **147** and 6µM **Cp-A7** and harvested 24 hpi. Control cells were DMSO treated and not infected. Cells were lysed and global protein abundances profiled by quantitative proteomics as outlined in the Materials and Methods. The box and whisker plot shows the cumulative activation for a previously defined geneset of ATF6 targets. Treatment of infected cells with **147** causes a significant increase in target protein expression. Co-treatment with **147** and **Cp-A7** reverses the ATF6 activation. p-values from two-tailed Wilcoxon signed rank tests are shown.

(D) Representative western blot shows upregulation of ATF6 targets BiP and GRP94 after transfection of ddDHFR-ATF6 construct AND treatment with TMP. A DHFR-YFP construct was used as a negative control.

(E) Quantification of western blots in **D** showing activation of ATF6 target proteins BiP and GRP94 in cells treated with TMP after transfection with the ddDHFR-ATF6 construct.

(F) qPCR shows upregulation of ATF6 target gene *PDIA4* after transient transfection of ddDHFR-ATF6 construct and treatment with trimethoprim (TMP). Treatment with DENV also shows upregulation of *PDIA4*. Combination TMP treatment and DENV infection does not appear to have a synergistic effect on *PDIA4* upregulation. Graphs represent 3 independent biological replicates, where each biological replicate is the average of two technical replicates. Error bars represent SEM and p-values from unpaired t-tests are shown.

(G) Representative western blot of **Fig. 3.3F** showing chemical genetic activation in cells transfected with the ddDHFR-ATF6 construct, activated with TMP, and infected with DENV show no significant change in viral protein levels compared to a -TMP control. 10cm dishes of Huh7 cells were transfected with ddDHFR-ATF6 using Lipofectamine 3000 reagent. Cells were then treated with TMP or DMSO as a mock control, infected with DENV where indicated. Cells were lysed and protein levels were measured by immunoblot.

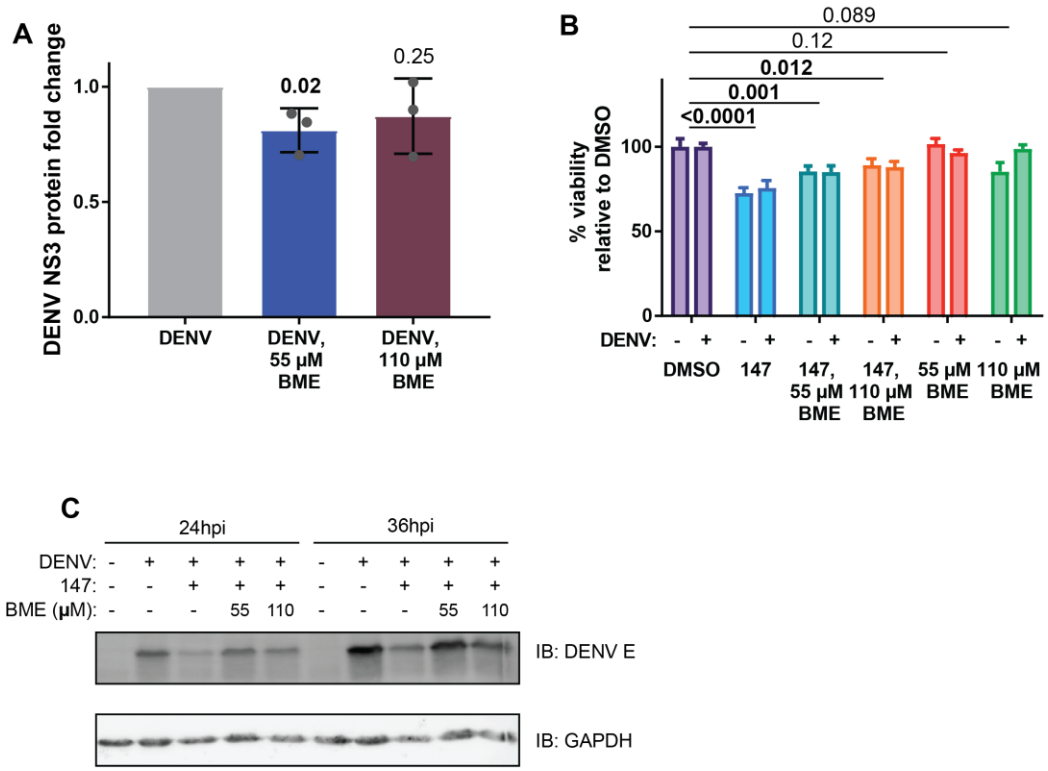

Figure A3.4. BME addition does not lower DENV infection or impair cell proliferation.

(A) Western blot data showing BME does not reduce DENV propagation in Huh7 cells. Cells were pretreated for 16h, then infected (where indicated) with DENV-2 strain BID-V533 at MOI of 3 for 3 hours. Media and treatments were replaced, and cells were collected 24hpi. Cells were lysed, and protein samples were run out on SDS-PAGE gels and visualized by immunoblot on PVDF membranes.

(B) Cell proliferation data showing **147**/BME treatment only modestly affects Huh7 cell viability over the course of treatment. Cells were pretreated for 16h, then infected (where indicated) with DENV-2 strain BID-V533 at MOI of 3 for 3 hours. Media and treatments were replaced, and proliferation was measured 24 hpi using the Promega Cell Titer Glo reagent. Graphs represent three to six biological replicates. Error bars represent SEM.

(C) Representative western blot for **Fig. 3.4B** showing attenuation of the antiviral effects of **147** on addition of BME at 55 µM or 110 µM. Cells were pretreated for 16h, then infected (where indicated) with DENV-2 strain BID-V533 at MOI of 3 for 3 hours. Media and treatments were replaced, and cells were collected 24 hpi. Cells were lysed, and protein samples were run out on SDS-PAGE gels and visualized using PVDF membranes.

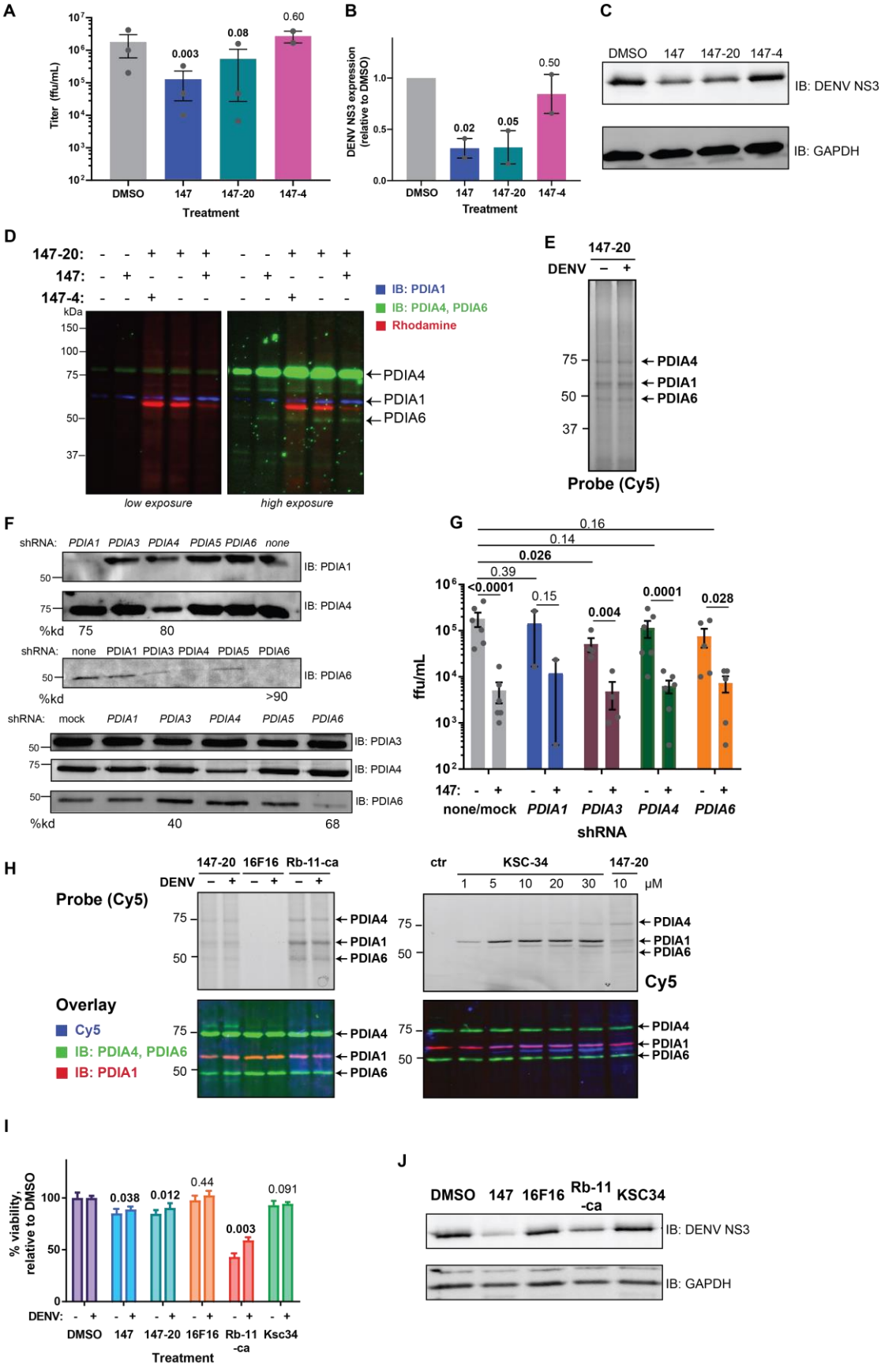

Figure A3.5. PDIs are covalent targets of 147 but knockdown or inhibition of PDIs does not recapitulate the reduction in DENV viral infection.

(A) Titer data showing **147-20** has a similar effect on virus replication as the parent compound **147**. In contrast, compound **147-4** has no observable effect on viral titer levels. Cells were pretreated with 10 μM of the respective compound for 16h, then infected with DENV-2 strain BID-V533 at MOI of 3 for 3 hours. Media and treatments were replaced and titer levels were measured 24 hpi. Error bars show SEM and p-values from ratio paired t-test relative to the DMSO treated control are shown.

(B) Western blot quantification of DENV NS3 levels after treatment with **147**, **147-20**, or **147-4**. Cells were pretreated with 10 μM respective compound for 16h, then infected with DENV-2 strain BID-V533 at a MOI of 3 for 3 hours. Media and treatments were replaced, and cells were collected at indicated timepoints. Cells were lysed, and protein samples were run on SDS-PAGE gels and visualized using PVDF membranes. Error bars show SEM and p-value from unpaired t-test relative to the DMSO treated control are shown.

(C) Representative weste**r**n blot of DENV NS3 levels after treatment with **147**, **147-20**, or **147-4** for data shown in **B**.

(D) Western blot showing overlay of TAMRA and probes for PDIs. Huh7 cells were treated with indicated compounds at 3 μM (for single compound treatments) or 3 μM **147-20** and 9 μM **147**/**147-4** (for double compound treatments) for 16-18 hours before harvest. Cells were lysed, protein concentration normalized, and Click chemistry was performed using a TAMRA-biotin-azide trifunctional probe for 1 hour at 37ºC. Samples were run on SDS-PAGE gels and targets were visualized on PVDF membranes.

(E) Representative western blot showing the addition of DENV does not result in additional target labeling of **147-20**. Huh7 cells were treated with 10 μM **147-20** for 16-18 hours before harvest, then infected with DENV2 strain BID-V533 at MOI of 3 for 3 hours. 24 hpi, cells were lysed, normalized to 1 mg/mL protein, and Click chemistry was performed using a Cy5 azide fluorophore for 1 hour at 37ºC. Samples were immediately run on SDS-PAGE gels and targets were visualized on PVDF membranes. No additional labeled protein bands were visible in DENV infected cells.

(F) Western blot validating the knockdown of PDIs in stable cell lines. Lentiviral vectors were produced using a pooled combination of 2 or 3 shRNAs in HEK293T cells. Lentiviruses were transduced into Huh7 cells, and knockdown cells were selected using puromycin. Polyclonal knockdown cells were maintained as normal Huh7 cells. Two independent batches of knockdown cell lines were produced; the top three panels represent the first, the bottom four panels represent the second. The knockdown % of each target protein is indicated below.

(G) PDI knockdowns cells exhibit a similar response to **147** as the parental Huh7 cell line or mock-transduced cells. Only PDIA3 knockdown results in a small but significant reduction. Cells were treated with **147** (where indicated) for 16 hours, then infected with DENV-2 strain BID-V533 at MOI 3 for 3 hours. Media and treatments were replaced, and media was harvested 24hpi. Titer assay was performed as described. Graphs represent 2-6 independent biological replicates. Error bars represent SEM and p-values from ratio paired t-tests are shown.

(H) Western blot showing overlay of Cy5 fluorophore (from Click chemistry) and antibody probes for PDIs. Huh7 cells were treated with indicated compounds (10 μM **147-20**, 10 μM **16F16**, 20 μM **Rb-11-ca**, or 5 μM **KSC34)** for 16-18 hours before harvest. Cells were lysed, normalized to 1 mg/mL protein, and Click chemistry was performed using a Cy5 azide fluorophore for 1 hour at 37ºC. Samples were immediately run on SDS-PAGE gels and targets were visualized using PVDF membranes. **16F16** lacks a click handle preventing fluorophore labeling.

(I) Cell proliferation data with PDI inhibitors. **147** only minimally reduced cell proliferation while **16F16** and **KSC34** do not impact cells, but **Rb-11-ca** leads to a greater than 50% reduction in ATP levels. Cells were pretreated with 10 μM **147**, 10 μM **16F16**, 20 μM **Rb-11-ca**, or 5 μM **KSC34** for 16h, then infected (where indicated) with DENV-2 strain BID-V533 at MOI of 3 for 3

hours. Media and treatments were replaced, and viability was measured 24hpi using the CellTiter-Glo reagent. Graphs represent three biological replicates. Error bars represent SEM.

(J) Representative western blot for **Fig. 5D** showing effects on DENV NS3 levels after treatment with 10 µM **147**, 10 µM **16F16**, 20 µM **Rb-11-ca**, or 5 µM **KSC34**. Cells were infected with DENV-2 strain BID-V533 at MOI of 3 for 3 hours. Media and treatments were replaced, and cells were lysed 24h post infection. Lysates were run on SDS-PAGE gels and proteins visualized by immunoblot on PVDF membranes.

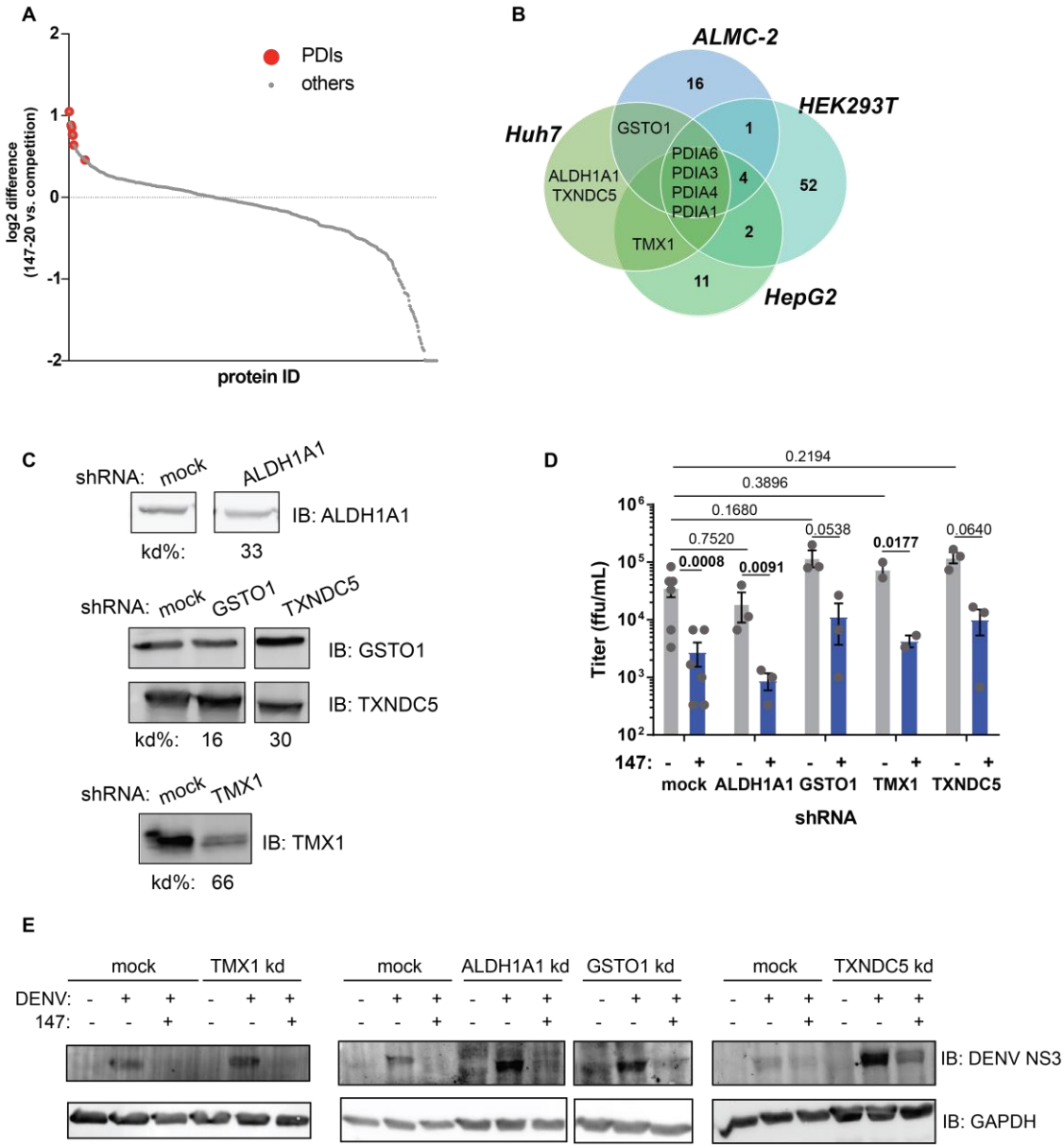

Figure A3.6. Identification of covalent protein target of 147 in Huh7 cells.

(A) Chemoproteomic target identification for **147-20** shows an enrichment of several PDIs compared to the **147**-competition control. Quantitative proteomics using TMT-11plex reagents was used to compare log2 intensities across 4 replicates of probe (**147-20** alone) versus probe in competition with excess parent compound **147**. Targets were ordered from most enriched (high log2 fold change) to least enriched (low log2 fold change). Protein disulfide isomerases (PDIs, highlighted as red dots) were among the most enriched targets identified.

(B) Venn diagram of highly enriched targets found in Huh7 cells in this study compared to HEK293T, HepG2, and ALMC-2 cells in a previous study. Previous target ID studies were comparable to the study conducted herein.

(C) Western blot validation of knockout of non-PDI targets in stable Huh7 knockout cell lines. Targets were selected based on top proteins identified in **Fig. 3.6C**. Lentiviral vectors were

produced using a pooled combination of 2 or 3 shRNAs in HEK293T cells. Lentiviruses were transduced into Huh7 cells, and knockdown cells were selected using puromycin. Polyclonal knockdown cells were maintained as normal Huh7 cells. The knockdown % of each target protein is indicated below.

(D) Knockdown cell lines of select targets exhibit a similar response to **147** as the mock-transduced cells. Cells were treated with **147** (where indicated) for 16 hours, then infected with DENV-2 strain BID-V533 at MOI 3 for 3 hours. Media and treatments were replaced, and media was harvested 24 hpi. Titer assay was performed as described. Graphs represent 2-5 independent biological replicates. Error bars represent SEM and p-values from ratio paired t-tests are shown.

(E) Representative western blot for **Fig. 3.6D** showing **147** is effective in reducing viral protein levels across all knockdown cell lines.

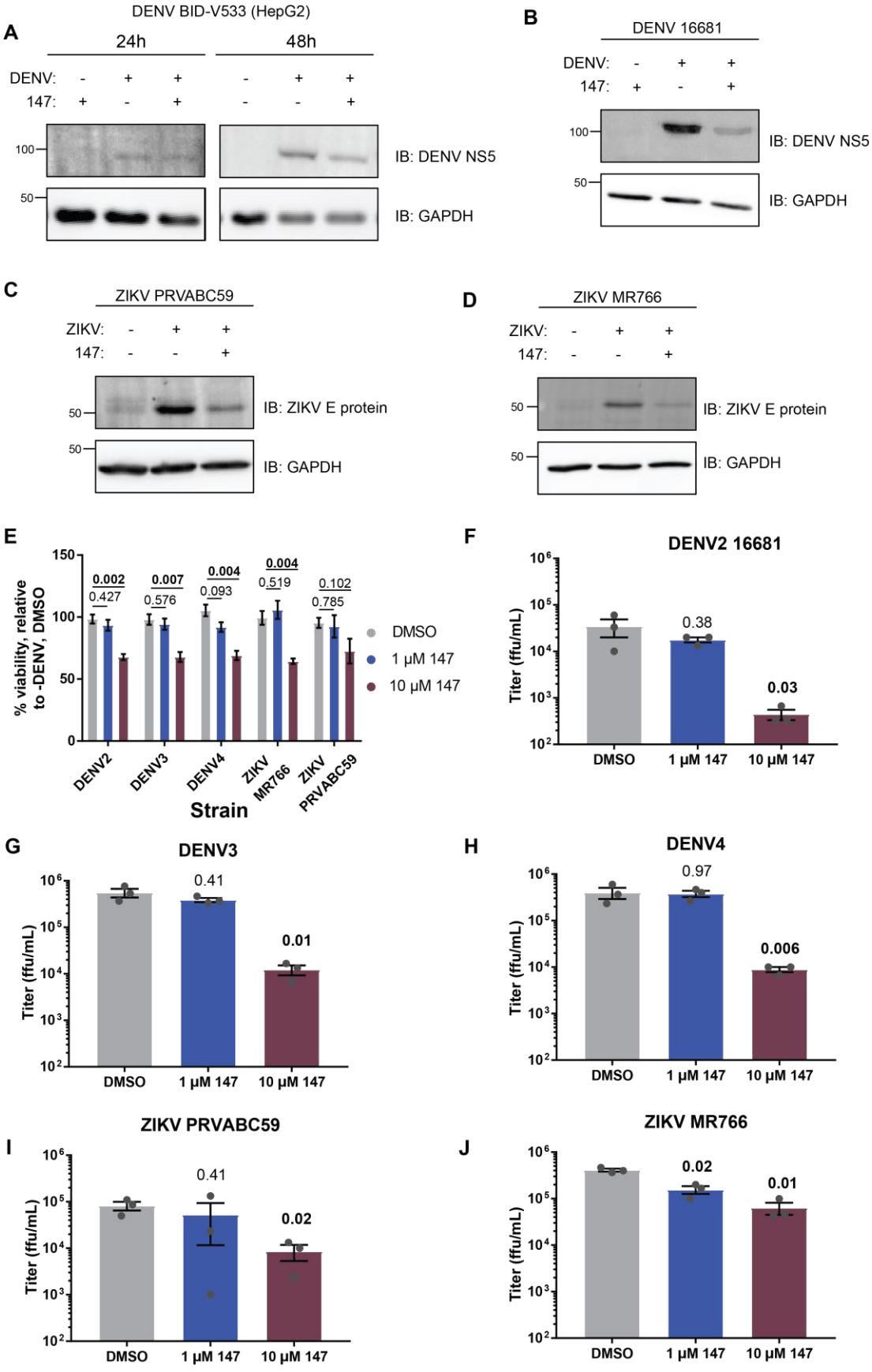

Figure A3.7. Reduction of viral proteins in DENV and ZIKV strains by compound 147.

(A) Representative western blot for **Fig. 3.7A** showing similar phenotype in HepG2 cells as in Huh7 cells. HepG2 cells were pretreated with 10 µM **147** for 16h, then infected with DENV-2 strain BID-V533 at MOI of 3 for 3 hours. Media and treatments were replaced, and cells were collected at 24 and 48 hpi. Cells were lysed, and protein samples were run on SDS-PAGE gels and visualized using PVDF membranes. GAPDH is included as a loading control.

(B) Representative western blot showing attenuation of DENV-2 16681 viral protein levels on treatment with **147**. Cells were pretreated with 10 µM **147** for 16h, then infected with DENV-2 strain 16681 at MOI of 3 for 3 hours. Media and treatments were replaced, and cells were collected at 24hpi. Cells were lysed, and protein samples were run on SDS-PAGE gels and visualized using PVDF membranes. GAPDH is included as a loading control.

(C) Representative Western Blot showing attenuation of ZIKV PRVABC59 viral envelope (E) protein levels on treatment with **147**. Cells were pretreated with 10 µM **147** for 16h, then infected with ZIKV strain PRVABC59 at MOI of 0.5 for 1 hour. Media and treatments were replaced, and cells were collected at 24hpi. Cells were lysed, and protein samples were run on SDS-PAGE gels and visualized using PVDF membranes. GAPDH is included as a loading control.

(D) Representative Western Blot showing attenuation of ZIKV MR766 viral E protein levels on treatment with **147**. Cells were pretreated with 10 µM 147 for 16h, then infected with ZIKV strain MR766 at MOI of 0.5 for 1 hour. Media and treatments were replaced, and cells were collected at 24hpi. Cells were lysed, and protein samples were run on SDS-PAGE gels and visualized using PVDF membranes. GAPDH is included as a loading control.

(E) Cell proliferation as measured by CellTiter-Glo for the panel of viruses when cells were treated with 1 or 10 µM of **147**. Cells were pretreated with **147** for 16h, then infected with the respective virus strains for 3 hours. Media and treatments were replaced, and ATP levels were measured 24 hpi using the Promega CellTiter-Glo reagent. Graphs represent six independent biological replicates across two days of measurement. Error bars represent SEM. Significance was determined using a one-sample t-test with a hypothesized mean of 100.

(F-J) Bar graphs showing reduction in viral titers of different DENV and ZIKV strains when cells were treated with low 1µM doses **147** or high 10µM dose of **147.** The 1µM concentration corresponds to the approximate IC50 value for **147** at inhibiting DENV-2 strain BID-V533 (**Fig. A3.2B**). Huh7 cells were pre-treated with the indicated concentrations of **147** or DMSO, infected with DENV-2 16681 (**F**), DENV3 (**G**), DENV4 (**H**), ZIKV PRVABC59 (**I**), or ZIKV MR766 (**J**). Media and treatments were replaced and viral titers were measured 24 hpi. Error bars correspond to SEM and p-values from ratio paired t-tests compared to the DMSO control are shown.

Table A3.1. Key resources table for chapter 3

Reagent type	Designation	Source or reference	Sequence	Usage notes
Chemical	147, 147-20, 147-4	[2,7]		10 µM
Chemical	Rb-11-ca	[8]		20 µM
Chemical	KSC-34	[9]		5 µM
Chemical	16F16	Sigma		10 µM
Chemical	Ceapin-A7	[6]		6 µM
Chemical	2-mercaptoethanol	Gibco		55 or 110 µM
Chemical	Thapsigargin	Sigma		0.5 µg/mL
Chemical	Trimethoprim	Research Products International		
Chemical	Cy5 azide	Click Chemistry Tools		
Chemical	TAMRA-desthiobiotin-azide	Click Chemistry Tools		
shRNA	PDIA1_1	Sigma (MISSION shRNA)	ccgggtgtggtcactgcaaacagttctcgagaactgtttgcagtgaccacacttttg	TRCN0000049194
shRNA	PDIA1_2	Sigma (MISSION shRNA)	ccggaggtgaaatcaagactcacatctcgagatgtgagtcttgatttcacctttttg	TRCN0000296675
shRNA	PDIA3_1	Sigma (MISSION shRNA)	ccgggcttactatgatgtggactatctcgagatagtccacatcatagtaagctttttg	TRCN0000147809
shRNA	PDIA3_2	Sigma (MISSION shRNA)	ccggcgatttgcacatacgaatgttctcgagaacattcgtatgtgcaaatcgttttttg	TRCN0000147738
shRNA	PDIA3_3	Sigma (MISSION shRNA)	ccggccaacactaacacctgtaatactcgagtattacaggtgttagtgttggttttttg	TRCN0000146965
shRNA	PDIA4_1	Sigma (MISSION shRNA)	ccggcctgagagaagattacaaattctcgagaatttgtaatcttctctcaggttttttg	TRCN0000289674
shRNA	PDIA4_2	Sigma (MISSION shRNA)	ccggcttggtcctaaatgatgcaaactcgagtttgcatcatttaggaccaagttttttg	TRCN0000289676
shRNA	PDIA4_3	Sigma (MISSION shRNA)	ccgggcttgtgttgaccaaagagaactcgagttctctttggtcaacacaagctttttg	TRCN0000289675

shRNA	PDIA6_1	Sigma (MISSION shRNA)	ccggccatcgaatttcaaccgagaactcgagttctcggttgaaattcgatggtttttg	TRCN0000049353
shRNA	PDIA6_2	Sigma (MISSION shRNA)	ccgggagattatcaacgaggacattctcgagaatgtcctcgttgataatctcttttg	TRCN0000049354
shRNA	PDIA6_3	Sigma (MISSION shRNA)	ccgggcagataagcatcattccctactcgagtagggaatgatgcttatctgcttttg	TRCN0000049355
shRNA	ALDH1A1_1	Sigma (MISSION shRNA)	ccgggccaaatcattccttggaattctcgagaattccaaggaatgatttggctttt	TRCN0000026498
shRNA	ALDH1A1_2	Sigma (MISSION shRNA)	ccgggctgatttaatcgaaagagatctcgagatctctttcgattaaatcagctttt	TRCN0000026415
shRNA	ALDH1A1_3	Sigma (MISSION shRNA)	ccgggctgatttaatcgaaagagatctcgagatctctttcgattaaatcagctttttg	TRCN0000276461
shRNA	GSTO1_1	Sigma (MISSION shRNA)	ccgggactaataagaagacgaccttctcgagaaggtcgtcttcttattagtctttttg	TRCN0000150913
shRNA	GSTO1_2	Sigma (MISSION shRNA)	ccgggcctgagtggttctttaagaactcgagttcttaaagaaccactcaggctttttg	TRCN0000152790
shRNA	GSTO1_3	Sigma (MISSION shRNA)	ccgggcttgccagaagatgatcttactcgagtaagatcatcttctggcaagctttttg	TRCN0000153150
shRNA	TXNDC5_1	Sigma (MISSION shRNA)	ccgggccaagcgaaagacgaactttctcgagaaagttcgtctttcgcttggctttttg	TRCN0000064354
shRNA	TXNDC5_2	Sigma (MISSION shRNA)	ccgggccaaagtctatgtggctaaactcgagtttagccacatagactttggctttttg	TRCN0000064355
shRNA	TMX1_1	Sigma (MISSION shRNA)	ccggcgtgccaagcaataagatttactcgagtaaatcttattgcttggcacgttttttg	TRCN0000150291
shRNA	TMX1_2	Sigma (MISSION shRNA)	ccggaggactgagtggacggtttatctcgagataaaccgtccactcagtccttttttg	TRCN0000338656

shRNA	TMX1_3	Sigma (MISSION shRNA)	ccgggctgaaagtaaagaaggaacactcgagtgttccttctttactttcagctttttg	TRCN0000338583
qPCR primer	DENV_NS5_F	Sigma	gagaaacggaccaccatgct	
qPCR primer	DENV_NS5_R	Sigma	gcaaccgagatccaccacct	
qPCR primer	PDIA4_F	Sigma	agtggggaggatgtcaatgc	
qPCR primer	PDIA4_R	Sigma	tggctgggatttgatgactg	
qPCR primer	HspA5_F	Sigma	gcctgtatttctagacctgcc	
qPCR primer	HspA5_R	Sigma	ttcatcttgccagccagttg	
qPCR primer	ERDJ4_F	Sigma	ggaaggaggagcgctaggtc	
qPCR primer	ERDJ4_R	Sigma	atcctgcaccctccgactac	
qPCR primer	GAPDH_F	Sigma	gtcggagtcaacggatt	
qPCR primer	GAPDH_R	Sigma	aagcttcccgttctcag	
qPCR primer	RiboP_F	Sigma	cgtcgcctcctacctgct	
qPCR primer	RiboP_R	Sigma	ccattcagctcactgataaccttg	
Antibody	Anti-DENV NS5	Genetex (GTX124253)		1:1000
Antibody	Anti-DENV NS3	Genetex (GTX124252)		1:1000
Antibody	Anti-GAPDH	Genetex (GTX627408)		1:1000
Antibody	Anti-KDEL	Enzo (ADI-SPA-827-F)		1:1000
Antibody	Anti-PDIA1	SantaCruz (SC-74551)		1:1000
Antibody	Anti-PDIA3	SantaCruz (SC-23886)		1:1000
Antibody	Anti-PDIA4	Proteintech		1:1000
Antibody	Anti-PDIA6	Genetex (GTX121275)		1:1000
Antibody	Anti-ALDH1A1	Santa Cruz Biotech		1:1000
Antibody	Anti-GSTO1	Genetex (GTX118439)		1:1000
Antibody	Anti-TXNDC5	Proteintech (19384-1-AP)		1:5000
Antibody	Anti-TMX1	Proteintech (24789-1-AP)		1:1000
Antibody	Anti-pan-flavivirus 4G2	Millipore-Sigma (MAB10216)		1:1000

Antibody	Anti-mouse HRP	Promega (W4021)		1:1000
Antibody	Anti-mouse Starbright 700	Bio-Rad (12004158)		1:10,000
Antibody	Anti-rabbit IRDye800	Li-Cor (926-32211)		1:10,000
Antibody	Anti-rabbit Starbright B520	Bio-Rad (12005869)		1:10,000
Antibody	hFAB rhodamine anti-actin	Bio-Rad (12004164)		1:10,000
Plasmid	pD2/ic-30p NBX	[10]		Used to generate DENV2 16681
Kit	CellTiter-Glo	Promega (G7572)		ATP-based cell proliferation assay
Kit	Caspase 3/7 assay	ThermoFisher (E-13184)		
Kit	MEGAScript T7 *in vitro* transcription kit	Invitrogen (AM1333)		
Kit	TransIT mRNA transfection reagent	Mirus (MIR2225)		

Appendix 4 Supplementary figures and tables for chapter 4

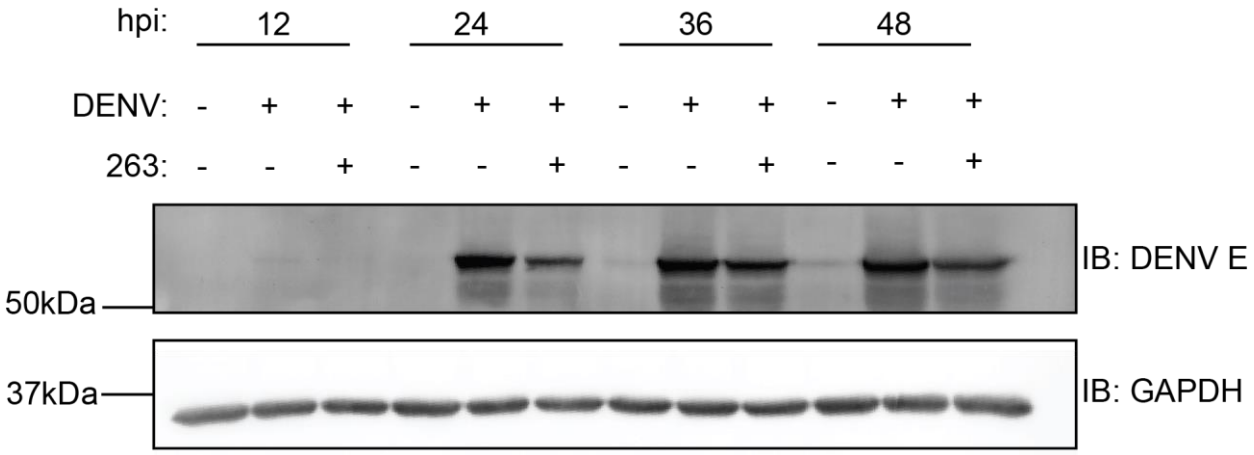

Figure A4.1. Representative western blot of timecourse with 263. Cells were pre-treated with **263** where indicated for 16 hours prior to infection, then retreated immediately after an infection with DENV2 (where indicated) at MOI 3 for 3 hours. Samples were harvested at the indicated timepoints, separated by SDS-PAGE, and immunoblotting was conducted on PVDF membranes. As shown, effects of **263** hold up to 48 hours post-infection (hpi).

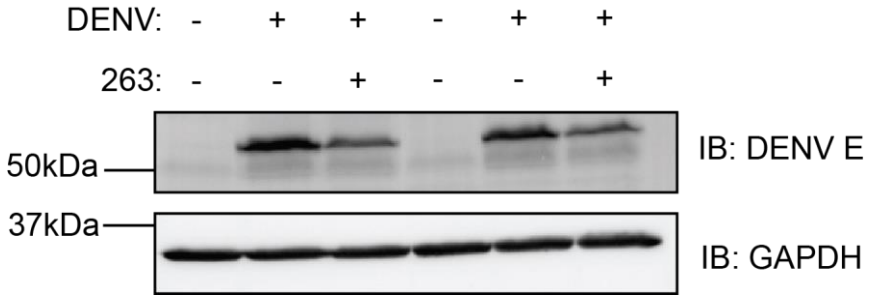

Figure A4.2. Representative western blot of eliminating pre-treatment with 263. Cells were infected where indicated, then treated where indicated with **263** only post-infection to determine if **263** affects viral entry. A reduction in viral protein levels is still seen when the pre-treatment step is eliminated.

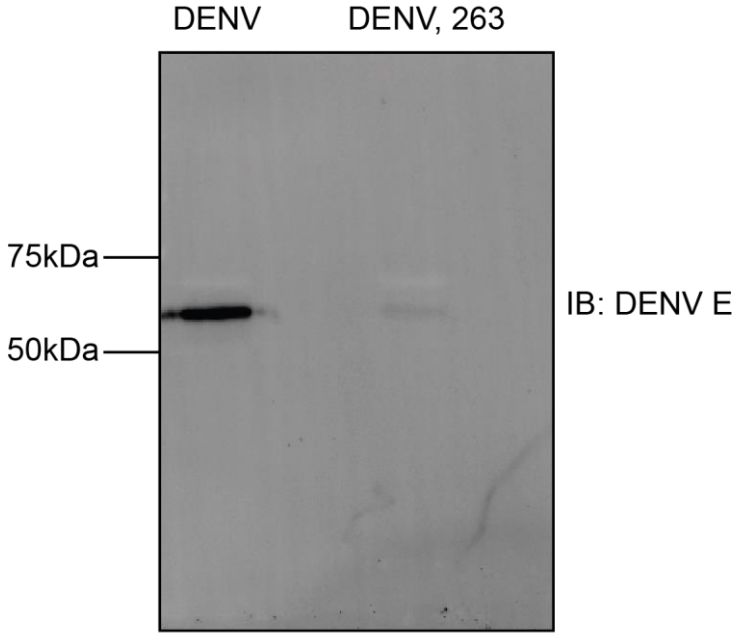

Figure A4.3. Representative western blot of purified virus. Media was harvested from infected 10cm dishes treated with either DMSO or **263**. Media was cleared for 45 minutes at 4000xg, then ultracentrifuged over a 20% sucrose cushion at 167,000xg for 3 hours to isolate virus. Purified virus was denatured in Laemelli buffer + DTT and run on SDS-PAGE gels. A reduction in total structural protein levels is observed in samples treated with **263**.

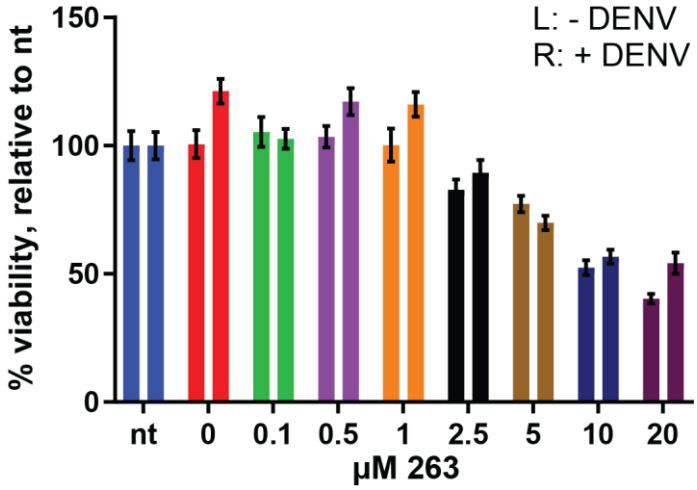

Figure A4.4. Cell viability as measured by CellTiter Glo (Promega) for varying concentrations of 263. Experiments were conducted in black-walled, clear-bottom 96 well plates. Cells were treated with the indicated concentrations of **263** (0 indicates DMSO vehicle control), then infected (for +DENV) samples for 3 hours at MOI 3. Inoculum was removed, treatments were replaced, and ATP levels were measured 24hpi. Viability percentages are compared to an untreated control. Bars indicated the average of 3 biological replicates, error bars indicate standard error of the mean. Concentration of 2.5µm for experiments was chosen based on combination of viability and response seen in **Figure A4.5**.

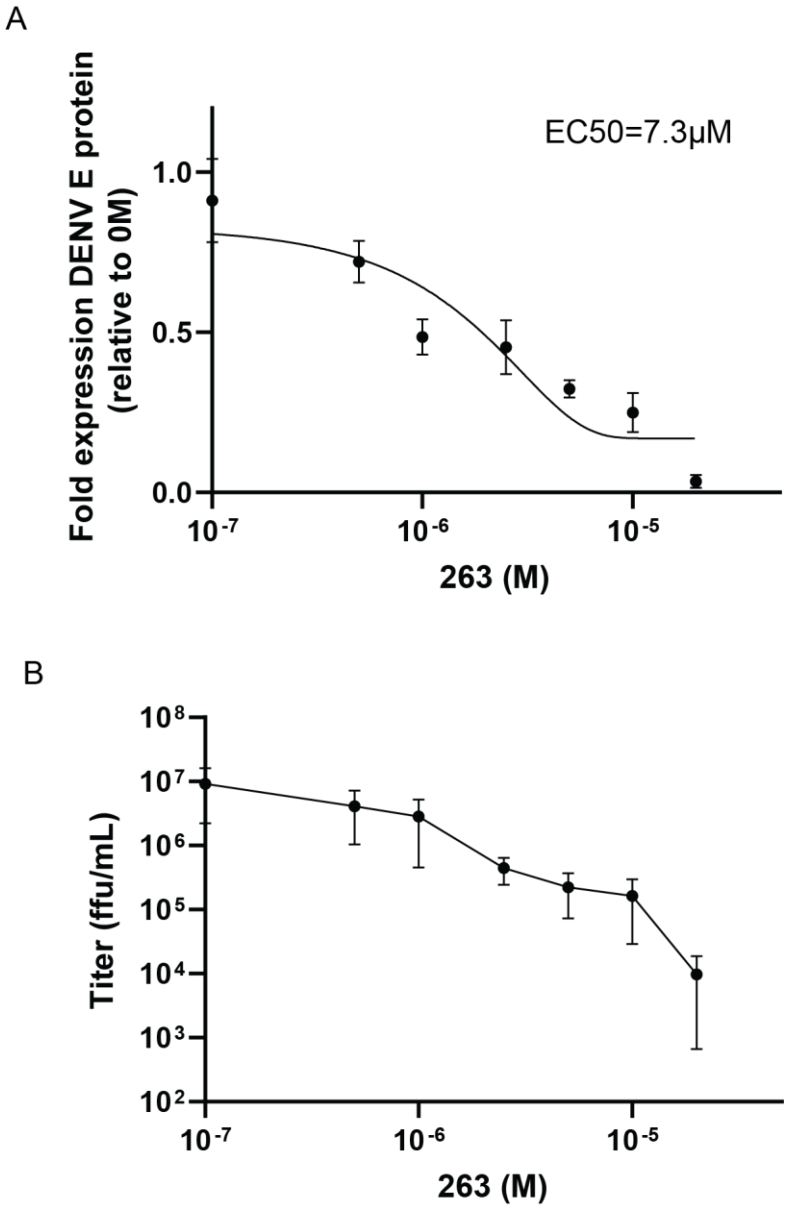

Figure A4.5. Dose-response curve of 263 effects. Cells were pre-treated with the indicated concentrations of **263**, infected with DENV for 3 hours at MOI 3, and re-treated. a) Protein samples were analyzed by western blot, and b) infectious titers were analyzed by focus forming assay. Protein samples are relative to an untreated control. EC50 was observed to be approximately 7.5µM.

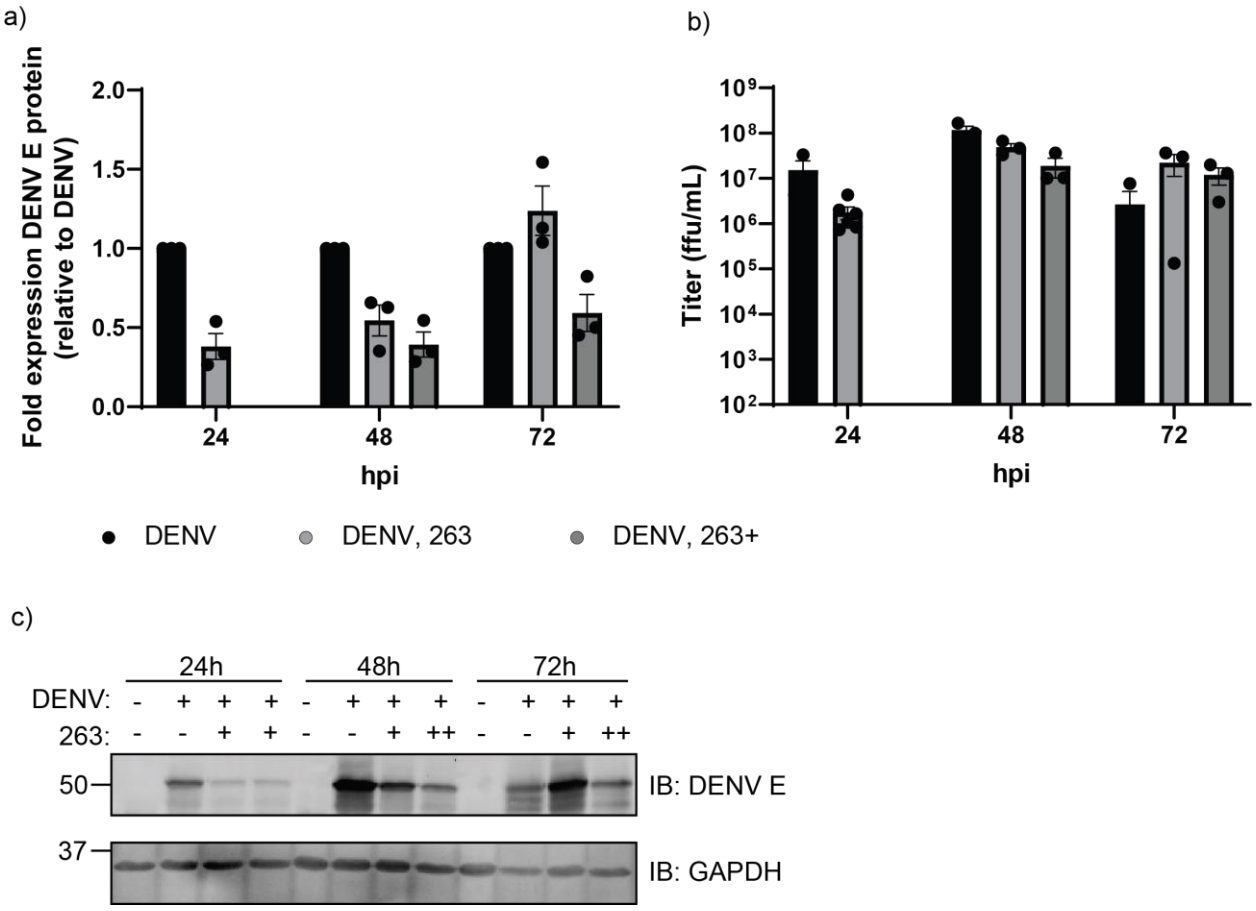

Figure A4.6. Repeated treatments increase effects of 263. Cells were pre-treated with the 2.5μM final concentration **263** for 16 hours, infected with DENV for 3 hours at MOI 3, and re-treated. Every 24 hours, samples were harvested, allowed to propagate without retreatment, or retreated.

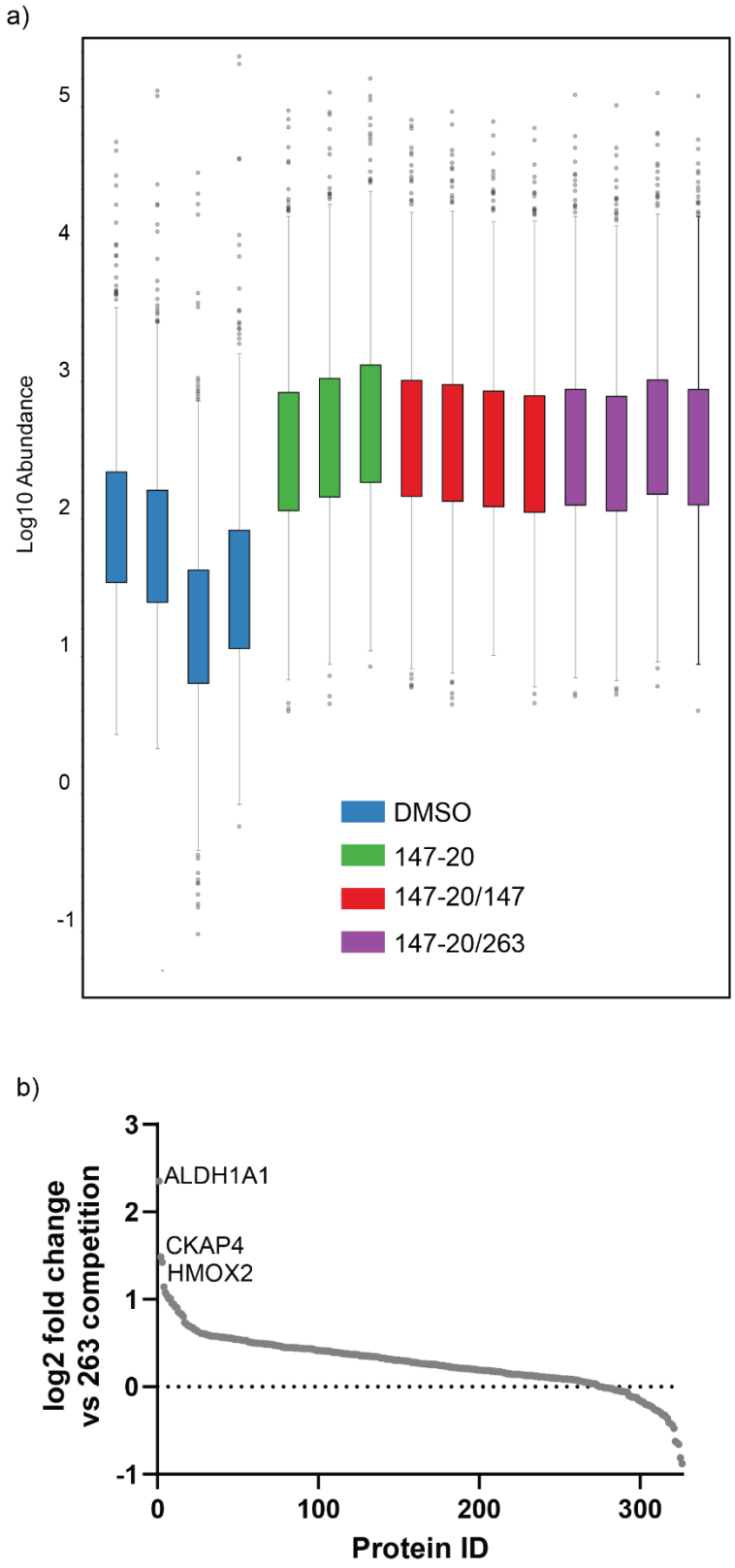

Figure A4.7. Mass spectrometry data for 147-20/147/263 pulldowns. (A) Absolute TMT intensities for 15 channels of TMTpro run. (B) Proteins ranked by enrichment in pulldown vs 263 competition.

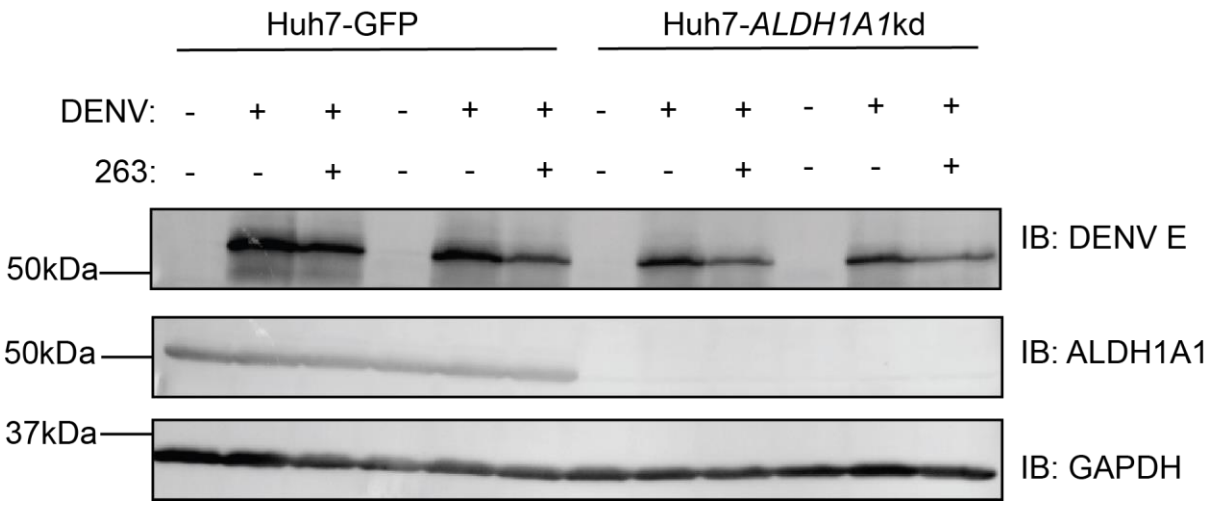

Figure A4.8. Representative western blot comparing Huh7-GFP and Huh7-*ALDH1A1*kd viral protein levels. Stable cell lines were produced by lentivirus transfection followed by blasticidin (GFP) or puromycin (*ALDH1A1* kd) selection. Cells were pre-treated with **263** where indicated, infected where indicated for 3 hours with DENV at MOI 3, and re-treated. Samples were collected 24hpi, lysed and separated by SDS-PAGE before western blot. Blotting for ALDH1A1 confirms high knockdown efficiency, but this does not significantly impact viral protein levels seen in samples.

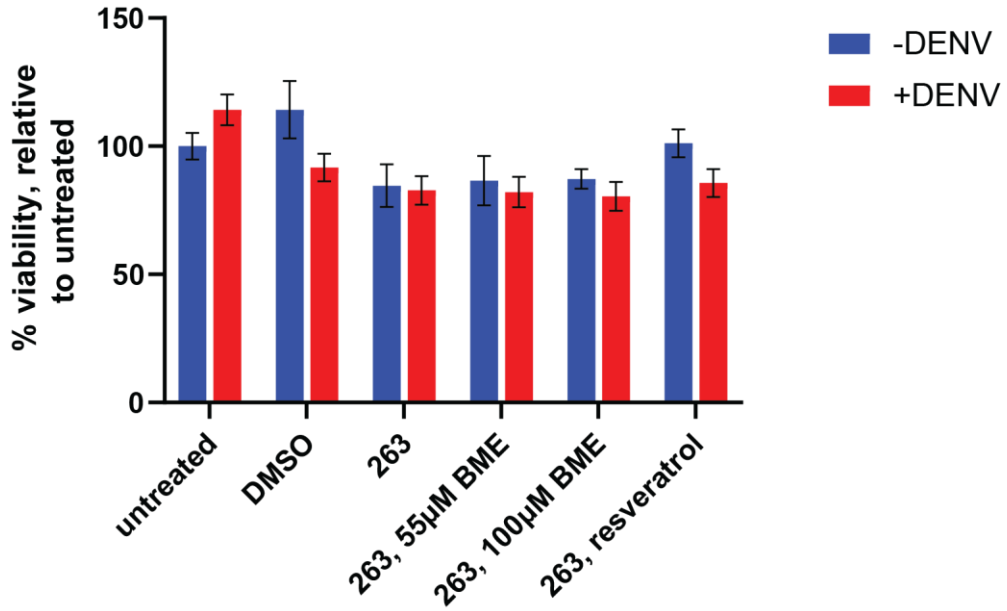

Figure A4.9. BME and resveratrol treatment do not affect cell viability. Cells were pre-treated with the indicated compounds and infected (where noted) for 3 hours with DENV at MOI 3. 24hpi, CellTiter Glo reagent was added and viability was calculated based on the uninfected or infected untreated control.

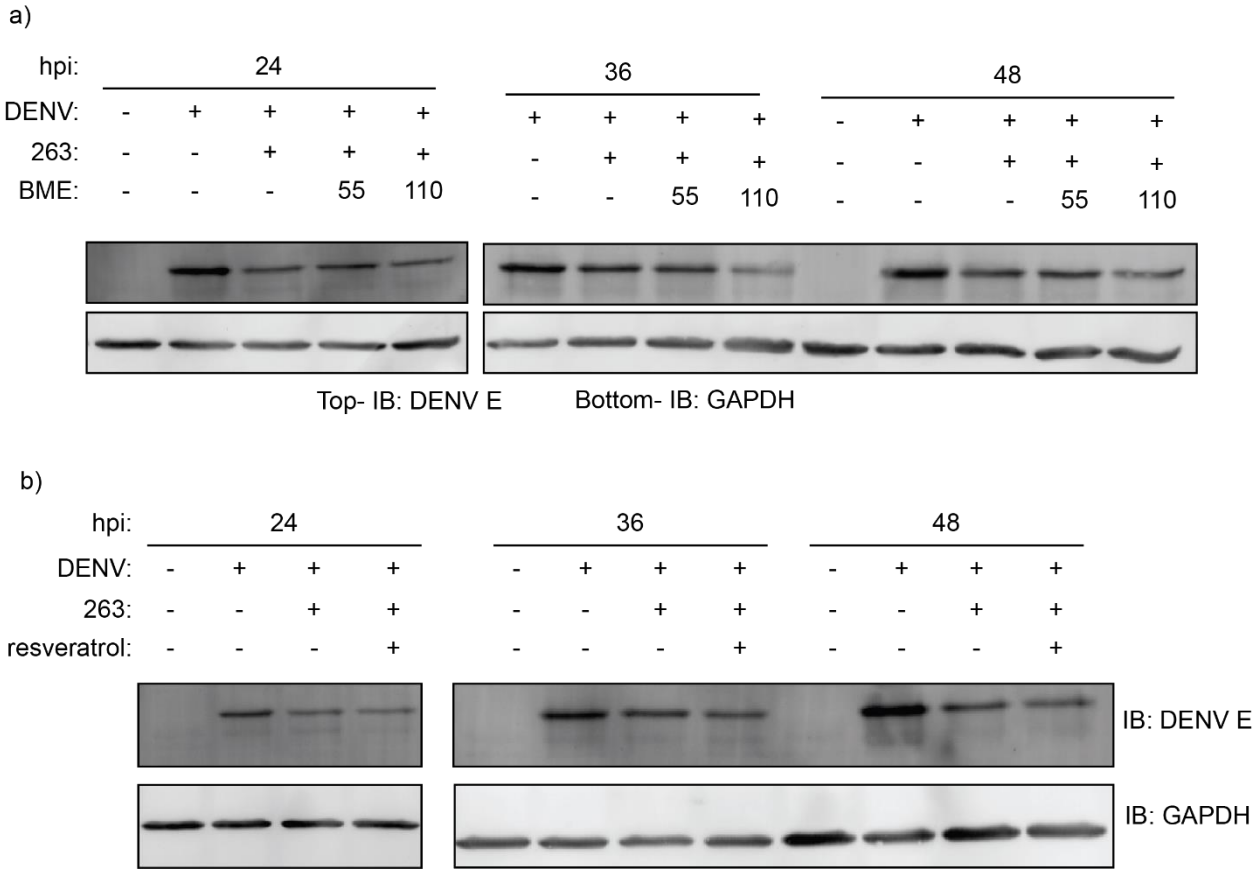

Figure A4.10. Representative western blots from BME and resveratrol co-treatments. Cells were pre-treated with the indicated compounds and concentrations for 16 hours.

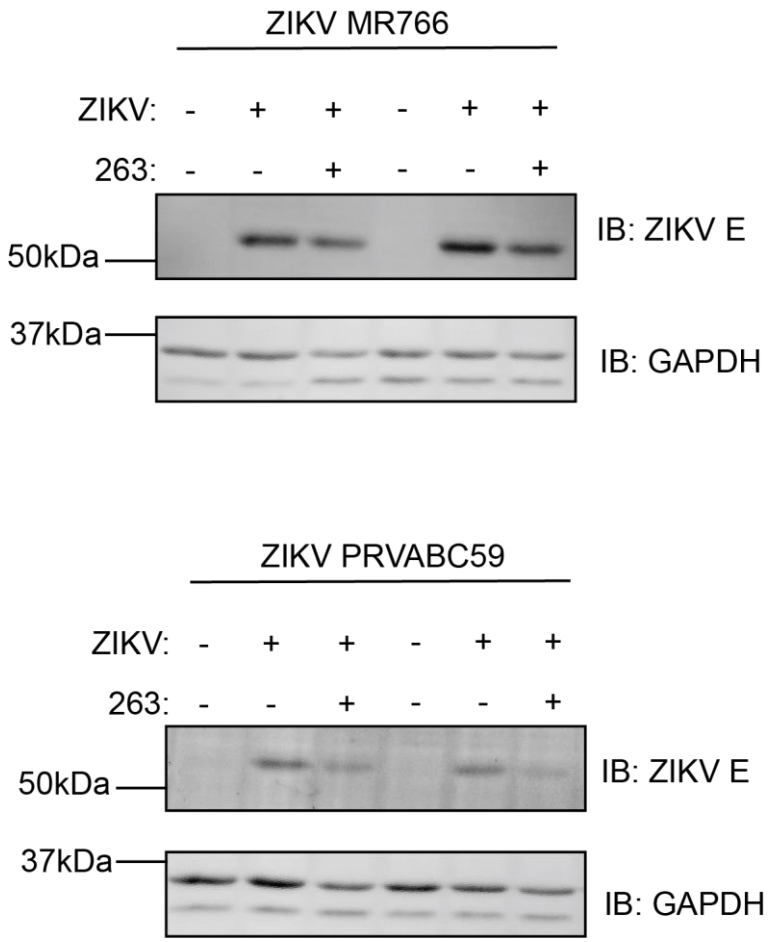

Figure A4.11. Representative western blots from samples infected with ZIKV MR766 and PRVABC59. Cells were pre-treated with **263** where noted, then infected with the indicated strain of ZIKV for 1 hour at MOI 0.5. Treatments were replaced and samples were harvested 24hpi.

Table A4.1 Key resources table for chapter 4

Reagent type	Designation	Source/Reference	Sequence	Usage notes
Chemical	263	[2]		2.5 µM, unless noted
Chemical	147	[2,7]		9 µM, unless noted
Chemical	147-20	[2,7]		3 µM, unless noted
Chemical	2-mercaptoethanol	Gibco		55 or 110 µM
Chemical	Resveratrol			10 µM
Chemical	TAMRA-desthiobiotin-azide	Click Chemistry Tools (1110)		100 µM
shRNA	ALDH1A1_1	Sigma (MISSION shRNA)	ccgggccaaatcattccttggaattctcgagaattccaaggaatgatttggctttttt	TRCN0000026498
shRNA	ALDH1A1_2	Sigma (MISSION shRNA)	ccgggctgatttaatcgaaagagatctcgagatctctttcgattaaatcagctttttt	TRCN0000026415
shRNA	ALDH1A1_3	Sigma (MISSION shRNA)	ccgggctgatttaatcgaaagagatctcgagatctctttcgattaaatcagctttttg	TRCN0000276461
qPCR primer	DENV_NS5_F	Sigma	gagaaacggaccaccatgct	
qPCR primer	DENV_NS5_R	Sigma	gcaaccgagatccaccacct	
qPCR primer	GAPDH_F	Sigma	gtcggagtcaacggatt	
qPCR primer	GAPDH_R	Sigma	aagcttcccgttctcag	
Antibody	Anti-DENV E	Genetex (GTX127277)		1:1000
Antibody	Anti-GAPDH	Genetex (GTX62708)		1:1000
Antibody	Anti-ALDH1A1	Santa Cruz Biotech (sc-374149)		1:1000
Antibody	Anti-pan-flavivirus 4G2	Millipore Sigma (MAB10216)		1:1000
Antibody	Anti-mouse HRP	Promega (W4021)		1:1000
Antibody	Anti-mouse Starbright 700	BioRad (12004158)		1:10,000
Antibody	Anti-rabbit Starbright B520	BioRad (12004164)		1:10,000
Kit	CellTiter Glo	Promega (G7572)		

Appendix 5 Supplementary figures and tables for chapter 5

Figure A5.1. Amino acid sequence comparison and MS sequence coverage of CoV non-structural protein homologs.

(A) Amino acid sequence alignment of nsp2 homologs from SARS-CoV-1 (SARS) and SARS-CoV-2 (Wuhan). Identical or similar residues are highlighted and color scheme corresponds to amino acid properties.
(B) Amino acid sequence alignment of nsp4 homologs from SARS-CoV-1 (SARS), SARS-CoV-2 (Wuhan) and hCoV-OC43. Identical or similar residues are highlighted and color scheme corresponds to amino acid properties.
(C) Tandem MS sequence coverage of SARS-CoV-2 (Wuhan) nsp4. Detected peptides are indicated in green.
(D) Tandem MS sequence coverage of SARS-CoV-1 (Urbani) nsp4. Detected peptides are indicated in green.
(E) Tandem MS sequence coverage of hCoV-OC43 nsp4. Detected peptides are indicated in green.

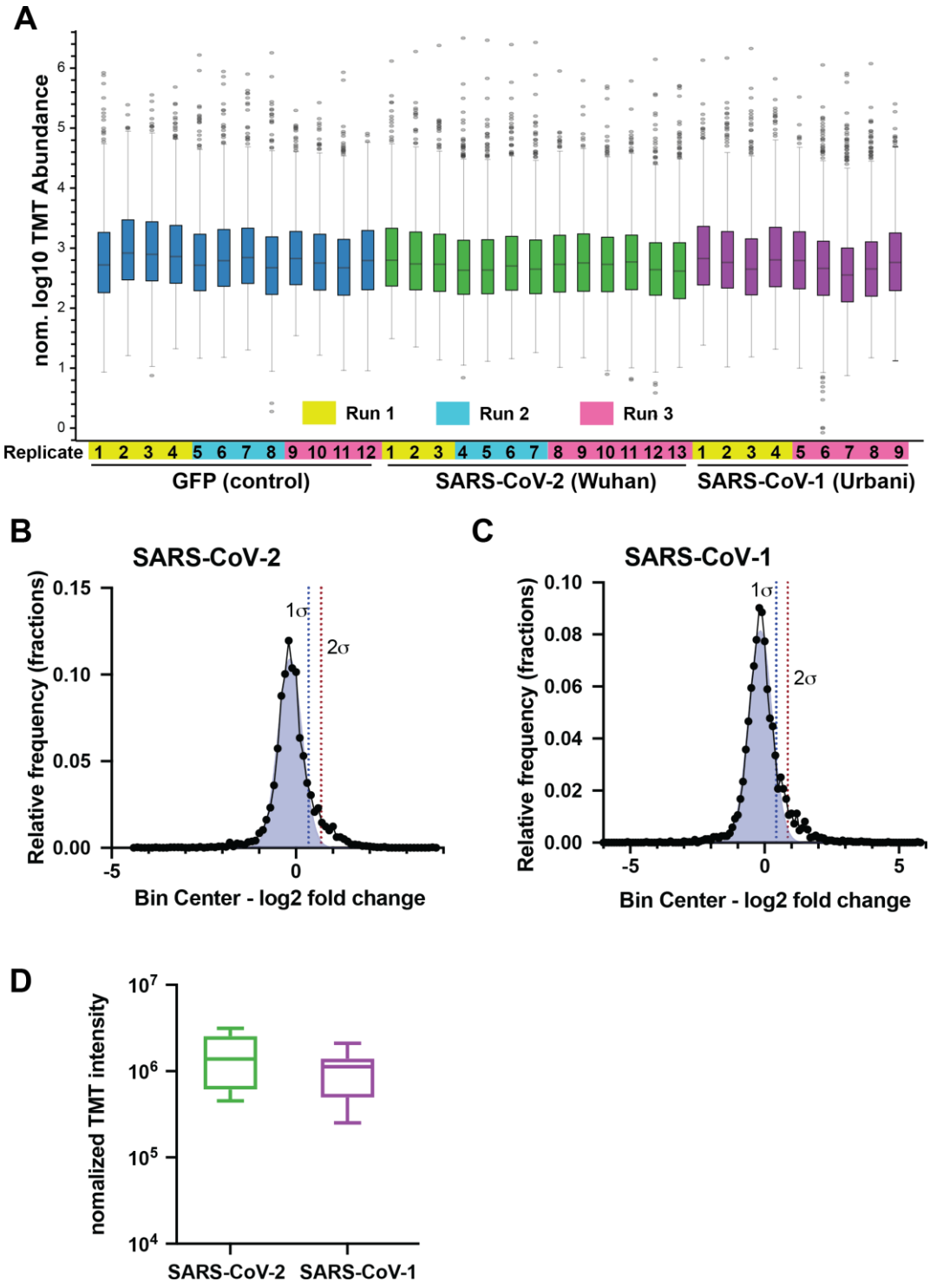

Figure A5.2. TMT normalization and filtering of nsp2 interactors.

(A) Normalized log10 TMT abundances of all proteins in the affinity purification samples expressing GFP control or nsp2 homologs as bait proteins. Pairing of individual samples into three separate mass spectrometry runs is indicated by the color bars.

(B-C) Histogram of log2 fold change enrichment of proteins in nsp2 affinity purification samples compared to GFP controls. A gaussian non-least square fit of the distribution is shown in light blue. The standard deviation of the distribution (σ) is indicated and 1σ and 2σ (dotted lines) were used for the variable cutoffs to define medium- and high-confidence interactors, respectively.
(B) shows the distribution for SARS-CoV-2 nsp2 with 1σ = 0.5.
(C) shows the distribution for SARS-CoV-2 nsp2 with 1σ = 0.43.
(D) Normalized TMT intensities comparing the abundances of SARS-CoV-2 and SARS-CoV-1 nsp2 homologs in the replicate samples.

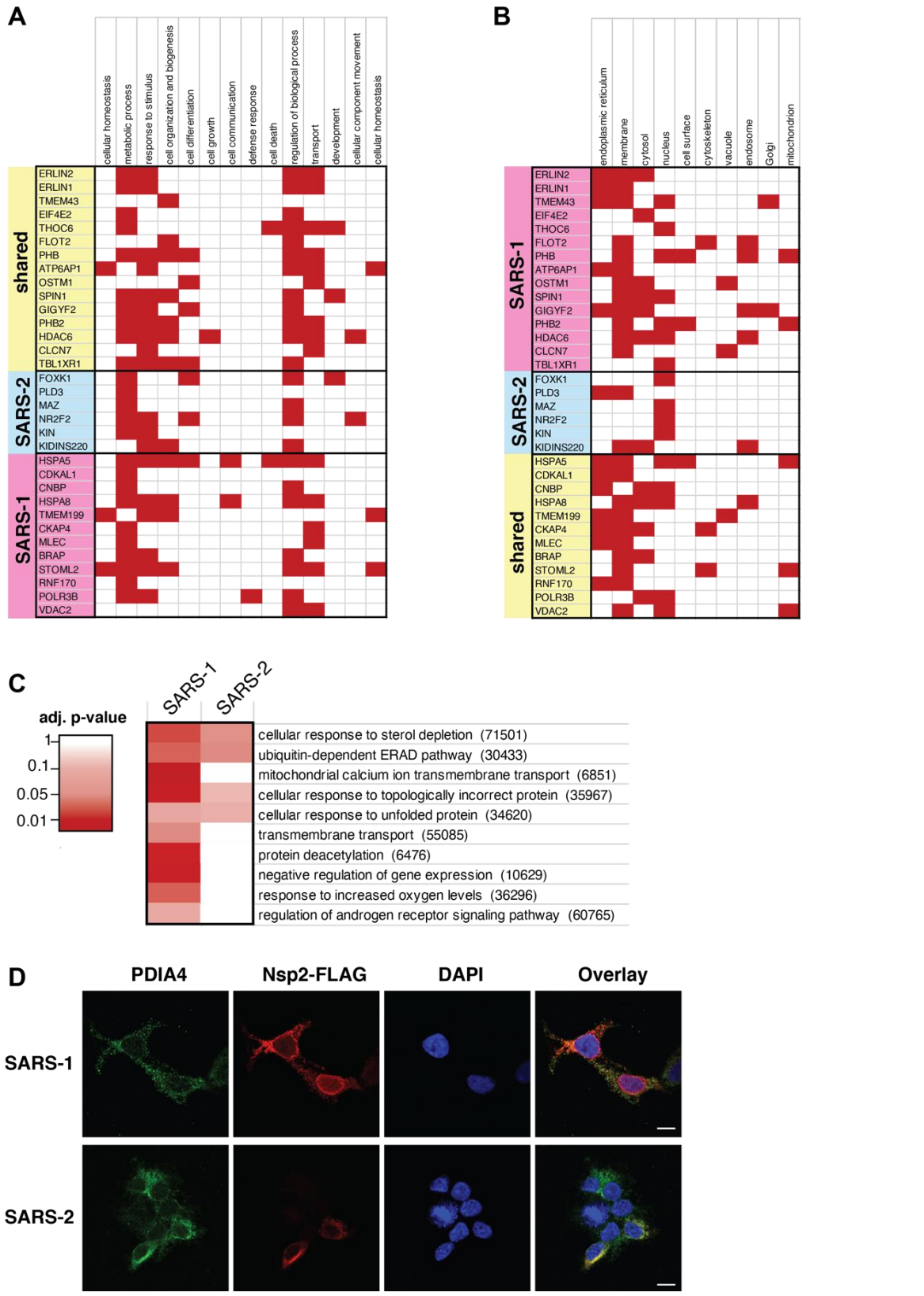

Figure A5.3. Gene ontology (GO) pathway analysis of interactors and cellular localization of nsp2 homologs.

(A-B) GO terms associated with the individual interactors of nsp2. Terms were assigned in the Protein Annotation node in Proteome Discoverer 2.4. Proteins were grouped according to the hierarchical clustering in Fig. 3B to distinguish shared and distinct interactors of SARS-CoV-1 and SARS-CoV-2 nsp2. (A) GO terms for biological processes. (B) GO terms for cellular components.

(C) Comparisons of pathways identified in gene set enrichment analysis of interactors of nsp2 homologs. Gene set enrichment analysis of high-and medium-confidence interactors was performed in Enrichr. GO terms for biological processes with adjusted p-values < 0.1 were included in the analysis and filtered manually to remove redundant terms containing similar genes. Non-redundant pathways are shown and color scheme indicates confidence of enrichment as represented by adjusted p-values of the Enrichr analysis.

(D) Confocal microscopy images of nsp2 homologs expressed in HEK293T cells, stained for PDIA4 (ER marker, green), FLAG-nsp2(red), and DAPI (blue). Scale bar is 10 µm.

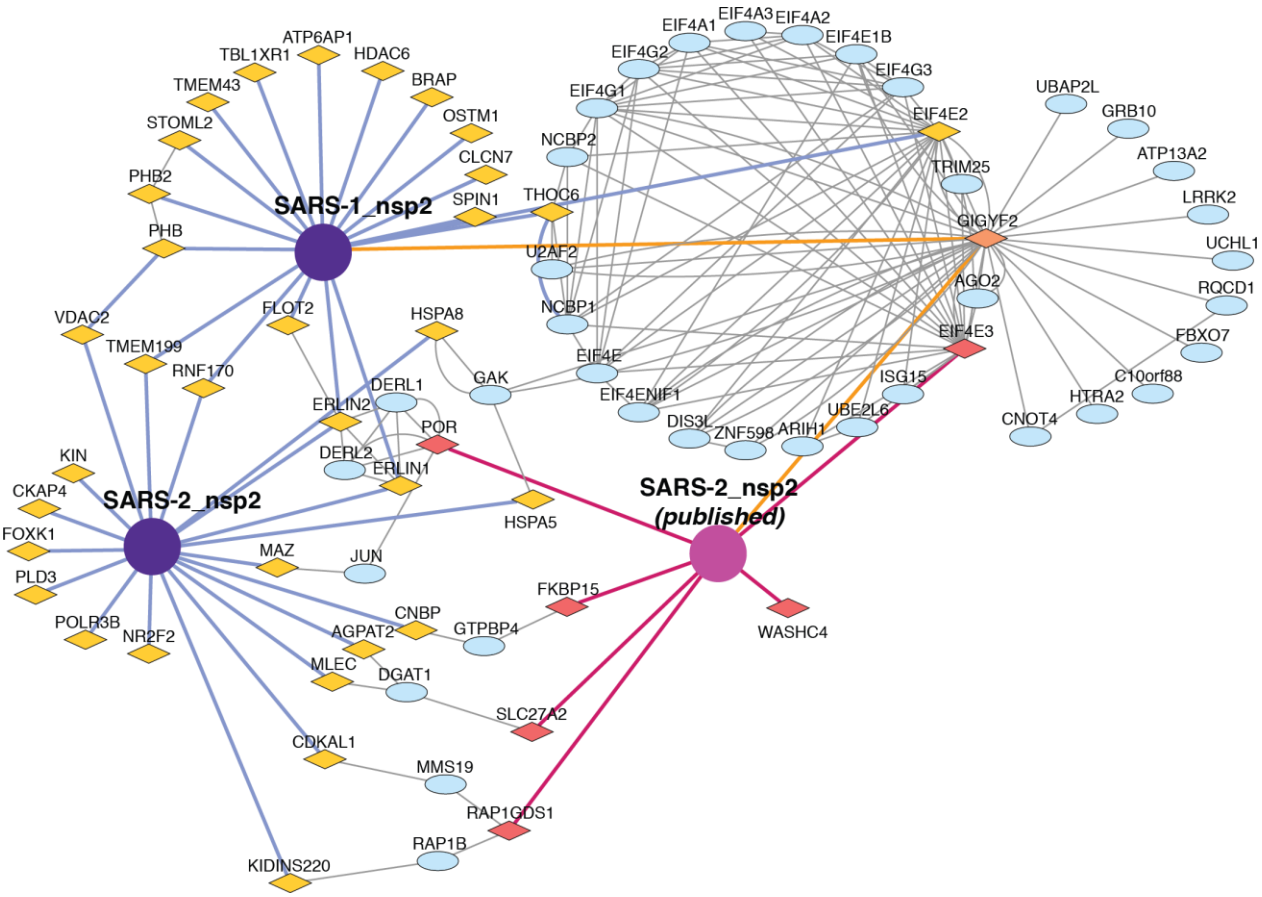

Figure A5.4. Nsp2 interactome overlap with published dataset.

Extended and overlapping interactors between our nsp2 dataset and previously published interactors of SARS-CoV-2 nsp2. Nsp2 proteins are shown as purple circles (our dataset) or pink circle (published dataset). Previously published primary interactors are shown as dark pink diamonds, novel primary interactors identified in this study are shown as yellow diamonds, overlapping primary interactors (GIGYF2) are shown as orange diamonds, and overlapping secondary interactors scraped from the STRING database are shown as blue ellipses. Previously identified primary interactions are shown with red edges, novel primary interactions identified in this study are shown with blue edges, overlapping primary interactors are shown with orange edges, and secondary interactions scraped from the STRING database are shown as grey edges between nodes.

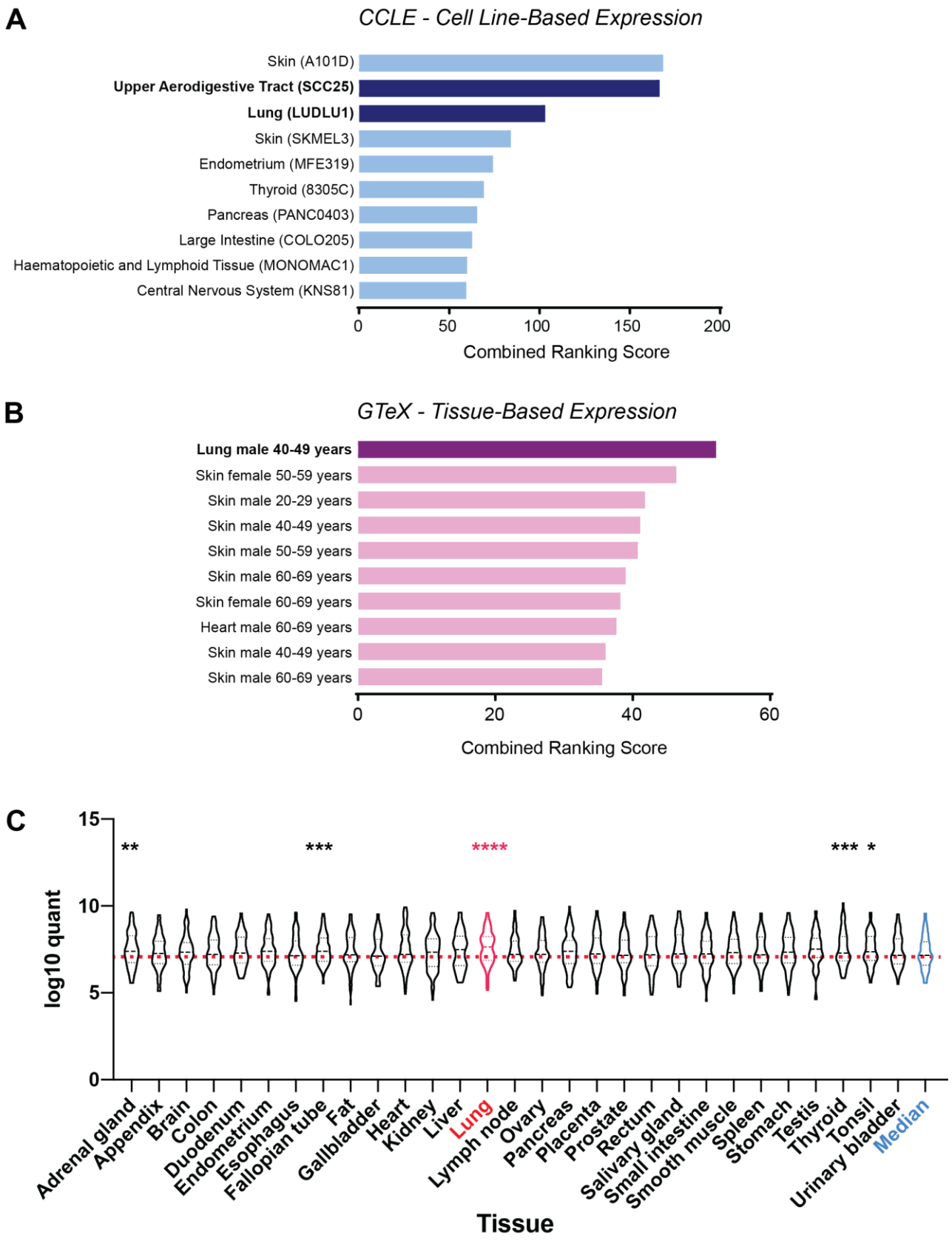

Figure A5.5. Tissue-specific expression of nsp2 and nsp4 interactors.

(A-C) Nsp2 and nsp4 interactors were cross-referenced with existing data sets on protein expression in cell lines and tissue-samples[11–13] to identify enrichment levels of interactors.
(A) Top ten cell lines enriched for interactors in the CCLE data set[11] based on analysis of combined ranking score using Enrichr[14].
(B) Top ten tissue samples enriched for interactors in the GTeX data set[12] based on analysis of combined ranking score using Enrichr[14].
(C) Violin plots showing $\log_{10}$ protein quantification values for the nsp2 and nsp4 interactions in 29 healthy human tissues based on the dataset published by Wang et al.[4] The median quantification across all tissues is shown on the right. Significance of expression difference was assessed in Graphpad Prism by mixed-effects analysis with the Geisser-Greenhouse correction and Holm-Sidak's multiple comparison test for each tissue compared to the median. * $p<0.05$; ** $p<0.01$, *** $p<0.001$; **** $p<0.0001$

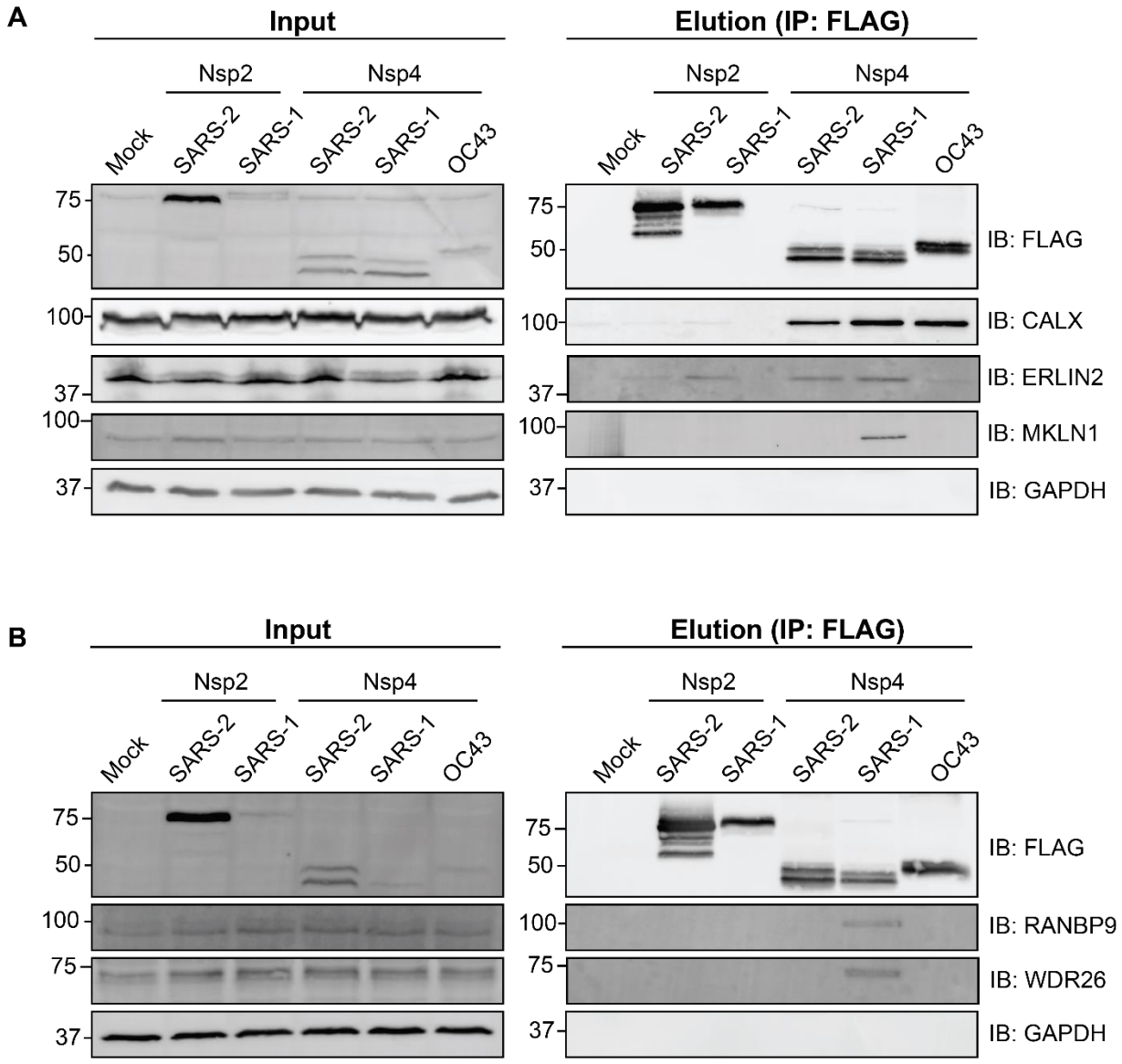

Figure A5.6. Co-immunoprecipitation of MAMs and proteostasis factors with CoV non-structural proteins.

(A-B) Lysates from HEK293T cells transfected with respective viral homologs of nsp2 or nsp2 were immunopurified using anti-FLAG sepharose beads and probed for MAMs factors (CANX, ERLIN2) and CTLH E3 ligase complex interactors (MKLN1, RANBP9, WDR26) by western blot. Representative blots for input and co-immunoprecipitations of are shown, n=3.

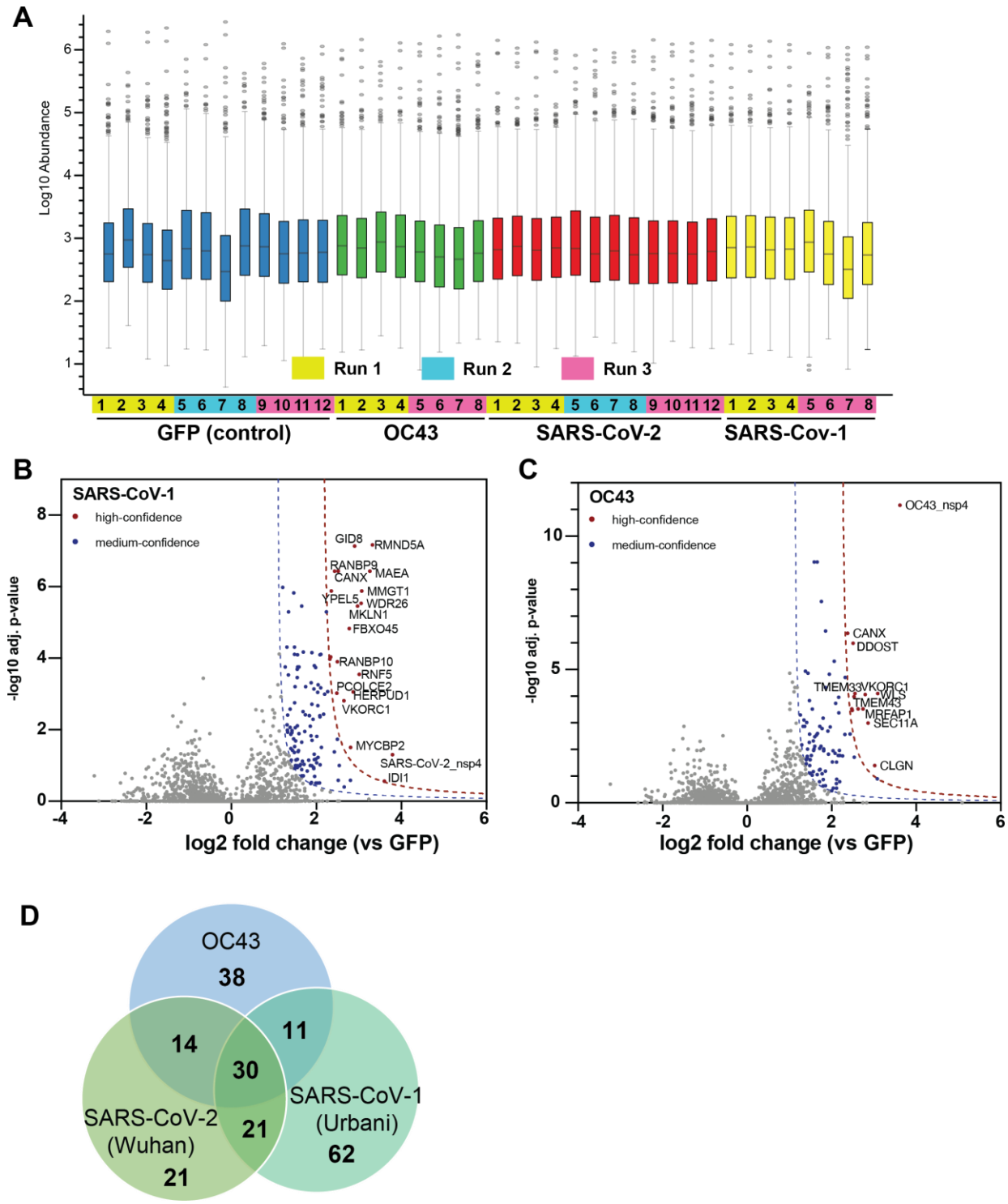

Figure A5.7. TMT normalization and filtering of nsp4 interactors.

(A) Normalized log10 TMT abundances of all proteins in the affinity purification samples expressing GFP control or nsp4 homologs as bait proteins. Pairing of individual samples into three separate mass spectrometry runs is indicated by the color bars.

(B-C) Volcano plot of SARS-CoV-1 (B) and OC43 nsp4 (C) interactors to identify medium- and high-confidence interactors. Plotted are log2 TMT intensity fold changes for proteins between nsp2 bait channels and GFP mock transfections versus -log10 adjusted p-values. Curves for the variable cutoffs used to define high-confidence (red) or medium confidence (blue) interactors are shown. $1\sigma = 0.4$ for (B), $1\ \sigma = 0.40$ for (C).

(D) Venn diagram comparing medium-confidence interactors of nsp4 homologs.

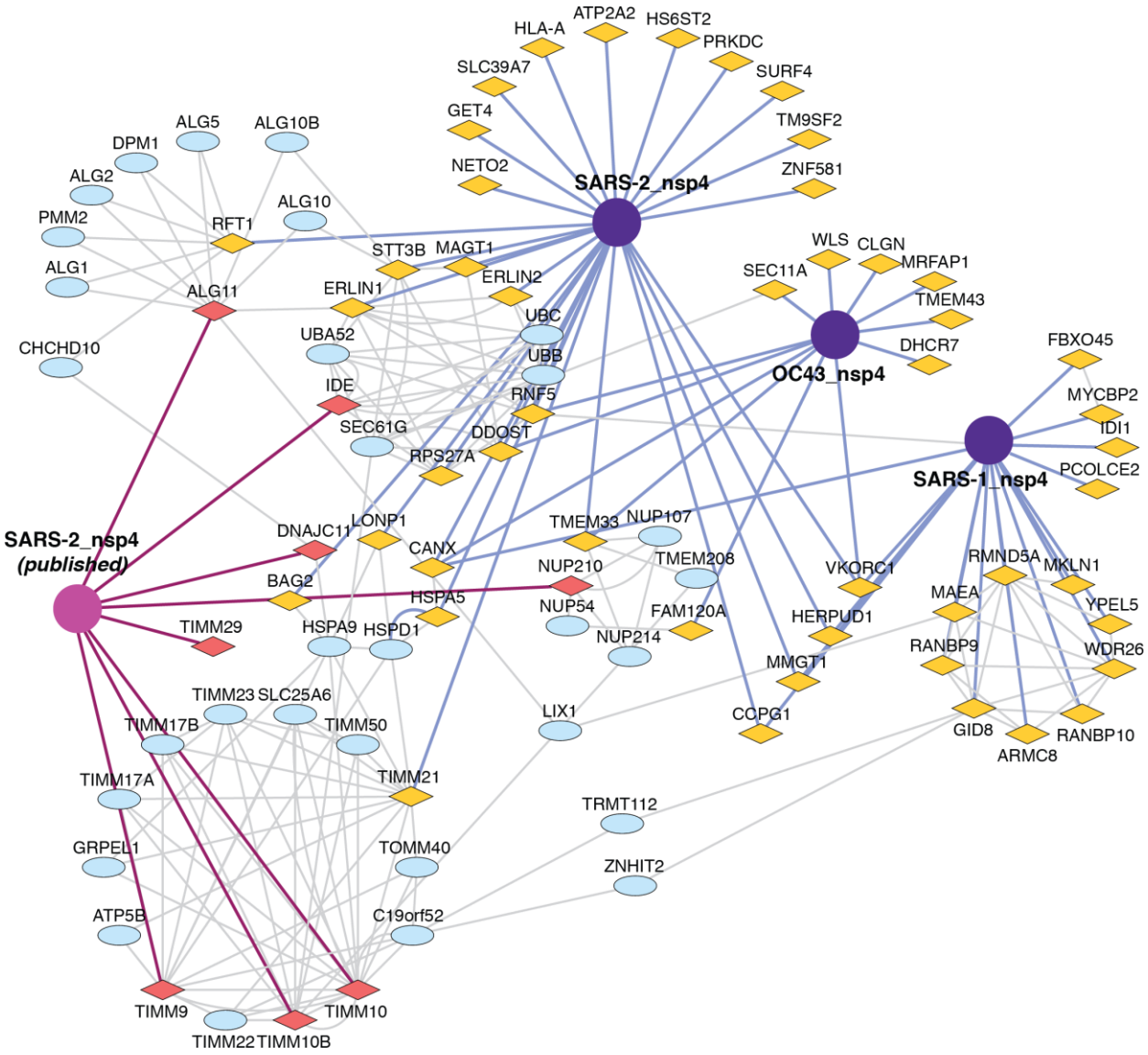

Figure A5.8. Nsp4 interactome overlap with published dataset.

Extended and overlapping interactors between our nsp4 dataset and previously published interactors of SARS-CoV-2 nsp4[15]. Nsp4 proteins are shown as purple circles (our dataset) or pink circle (published dataset). Previously published primary interactors are shown as dark pink diamonds, novel primary interactors identified in this study are shown as yellow diamonds, overlapping primary interactors are shown as orange diamonds, and overlapping secondary interactors scraped from the STRING database are shown as blue ellipses. Previously identified primary interactions are shown with red edges, novel primary interactions identified in this study are shown with blue edges, and secondary interactions scraped from the STRING database are shown as grey edges between nodes. The extended overlapping interactome reveals each Nsp4 protein uniquely plugs into clusters of proteins involved in the same pathway, which appear as circles of nodes such as the TIMM pathway involved in protein import into the mitochondria on the bottom left.

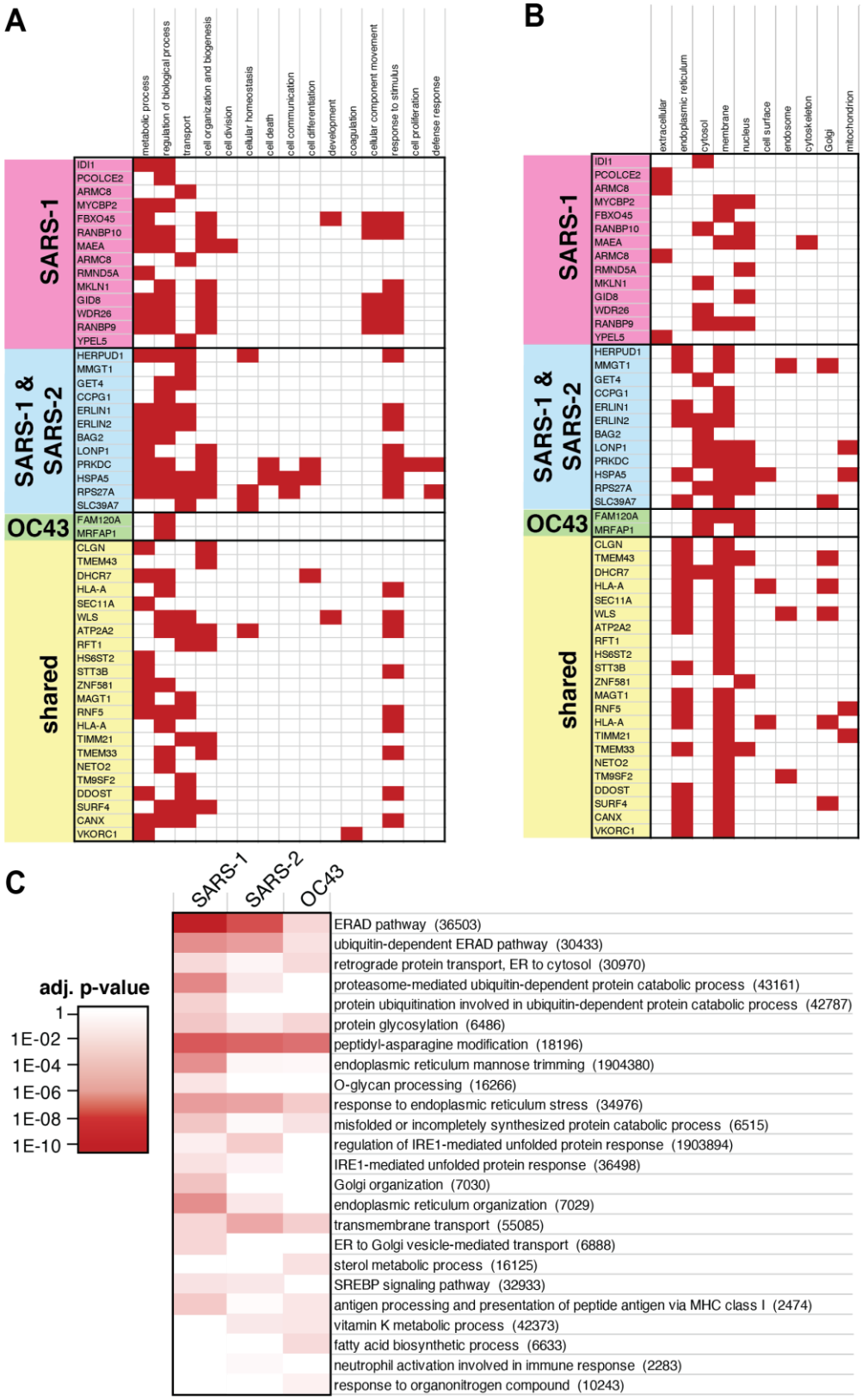

Figure A5.9. Gene ontology (GO) pathway analysis of nsp4 homolog interactors.

(A-B) GO terms associated with the individual interactors of nsp4. Terms were assigned in the Protein Annotation node in Proteome Discoverer 2.4. Proteins were grouped according to the hierarchical clustering in Fig. 4C to distinguish shared and distinct interactors of SARS-CoV-1, SARS-CoV-2, and OC43 nsp4. (A) GO terms for biological processes. (B) GO terms for cellular components.

(C) Comparisons of pathways identified in gene set enrichment analysis of interactors of nsp4 homologs. Gene set enrichment analysis of high-and medium-confidence interactors was performed in Enrichr. GO terms for biological processes with adjusted p-values < 0.1 were included in the analysis and filtered manually to remove redundant terms containing similar genes. Non-redundant pathways are shown and color scheme indicates confidence of enrichment as represented by adjusted p-values of the Enrichr analysis.

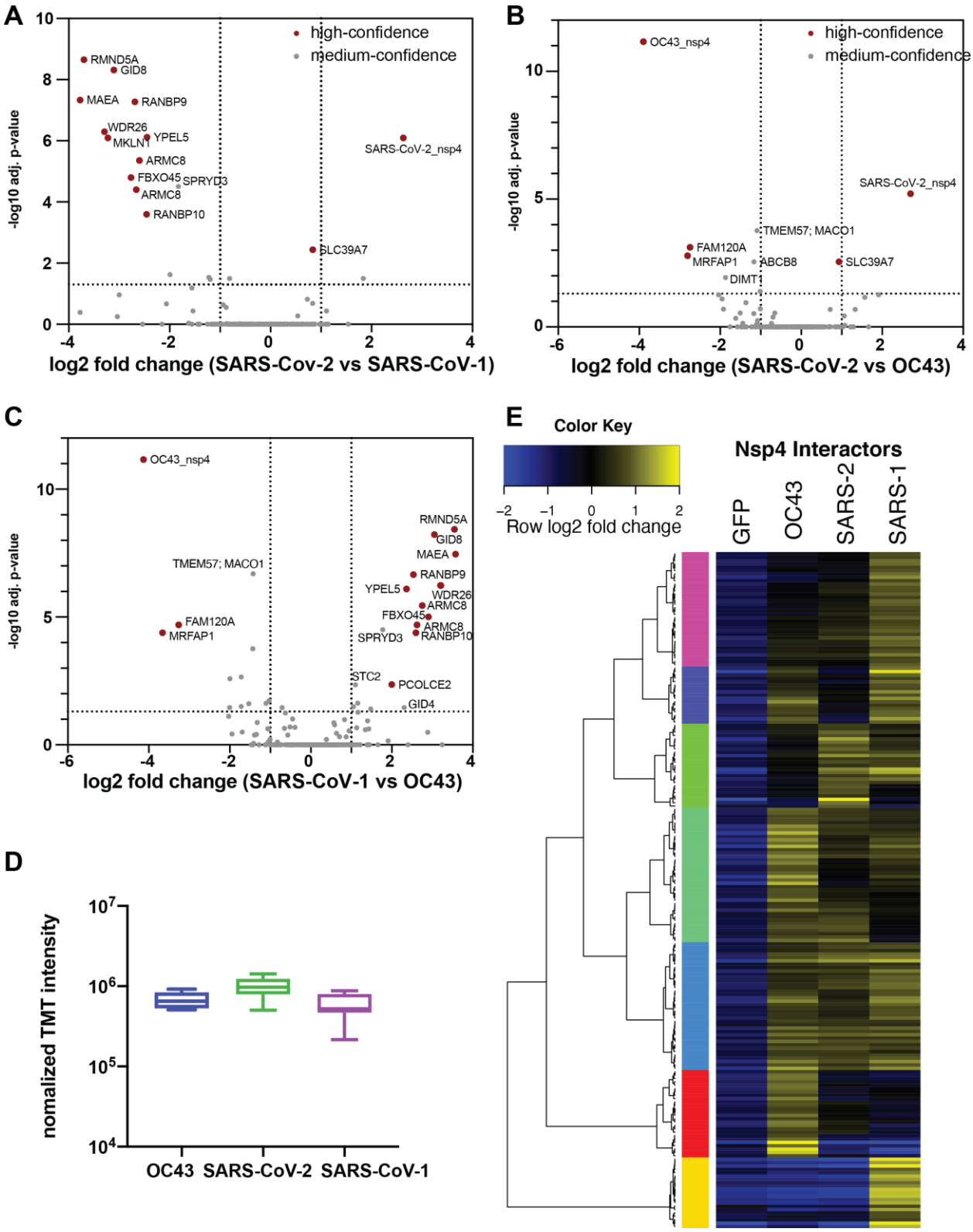

Figure A5.10. Comparative analysis of nsp4 homologs.

(A-C) Volcano plot comparing interactions between nsp4 homolog from SARS-CoV-1, SARS-CoV-2, and OC43. Only high- and medium confidence interactors of nsp4 are shown and high confidence interactors are highlighted in red. (A) Comparison of SARS-CoV-1 and SARS-CoV-2. (B) Comparison of SARS-CoV-2 and OC43. (C) Comparison of SARS-CoV-1 and OC43.

(D) Normalized TMT intensities comparing the abundances of SARS-CoV-2, SARS-CoV-1, and OC43 nsp4 homologs in the replicate affinity purification samples.

(E) Heatmap of high- and medium-confidence nsp4 homolog interactors compared to GFP control. log2 fold change is color-coded and centered by row (blue low, yellow high enrichment). Hierarchical clustering using Ward's method shown on the left was carried out on euclideanan distances of log2 fold changes scaled by row.

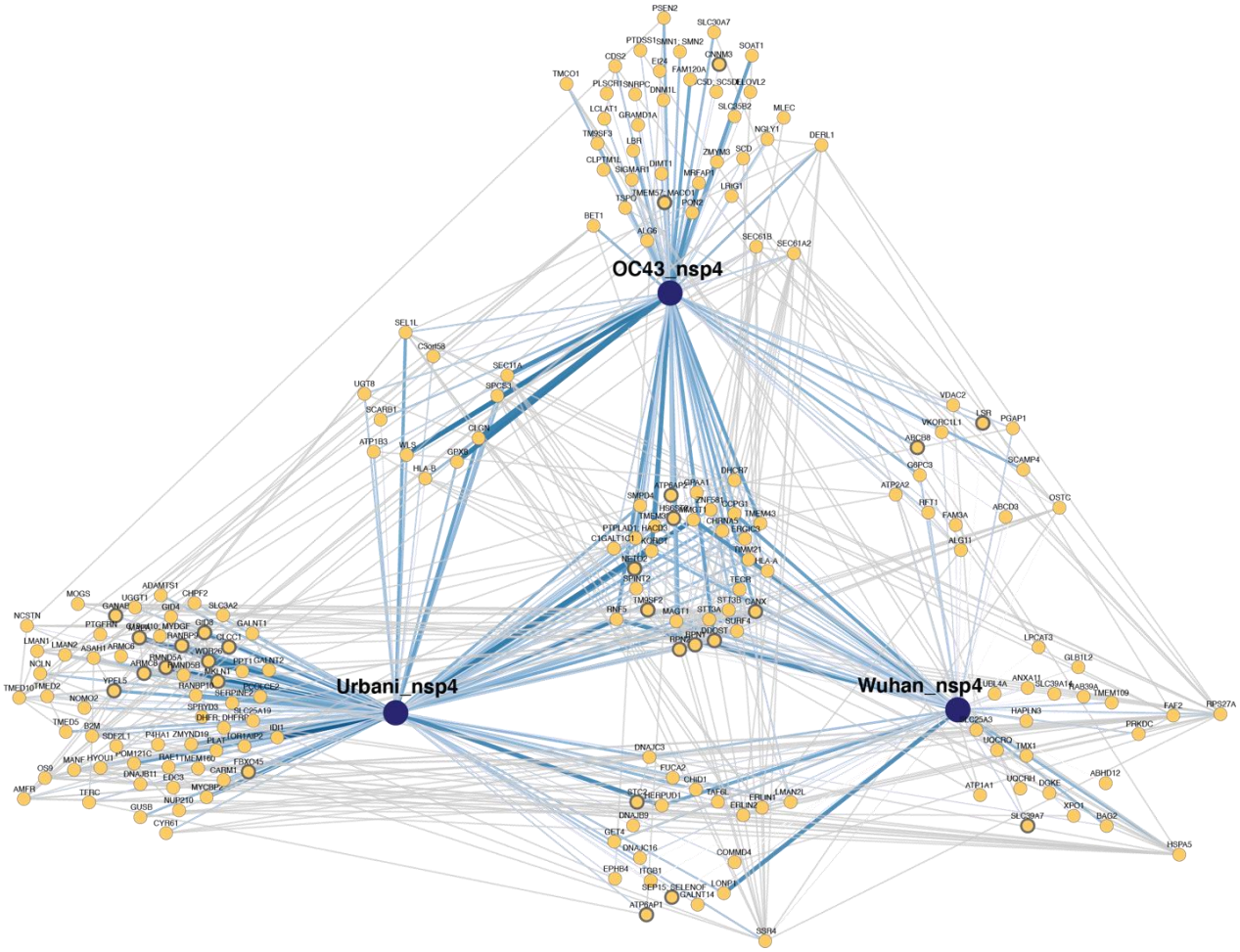

Figure A5.11. Network map of high- and medium-confidence nsp4 homolog interactors.

PPI network map of high- and medium-confidence interactors of nsp4 homolog. Blue lines indicate viral-host PPIs, where line width corresponds to fold enrichment compared to the GFP control. Grey lines indicate annotated host-host PPIs in STRING (score > 0.75).

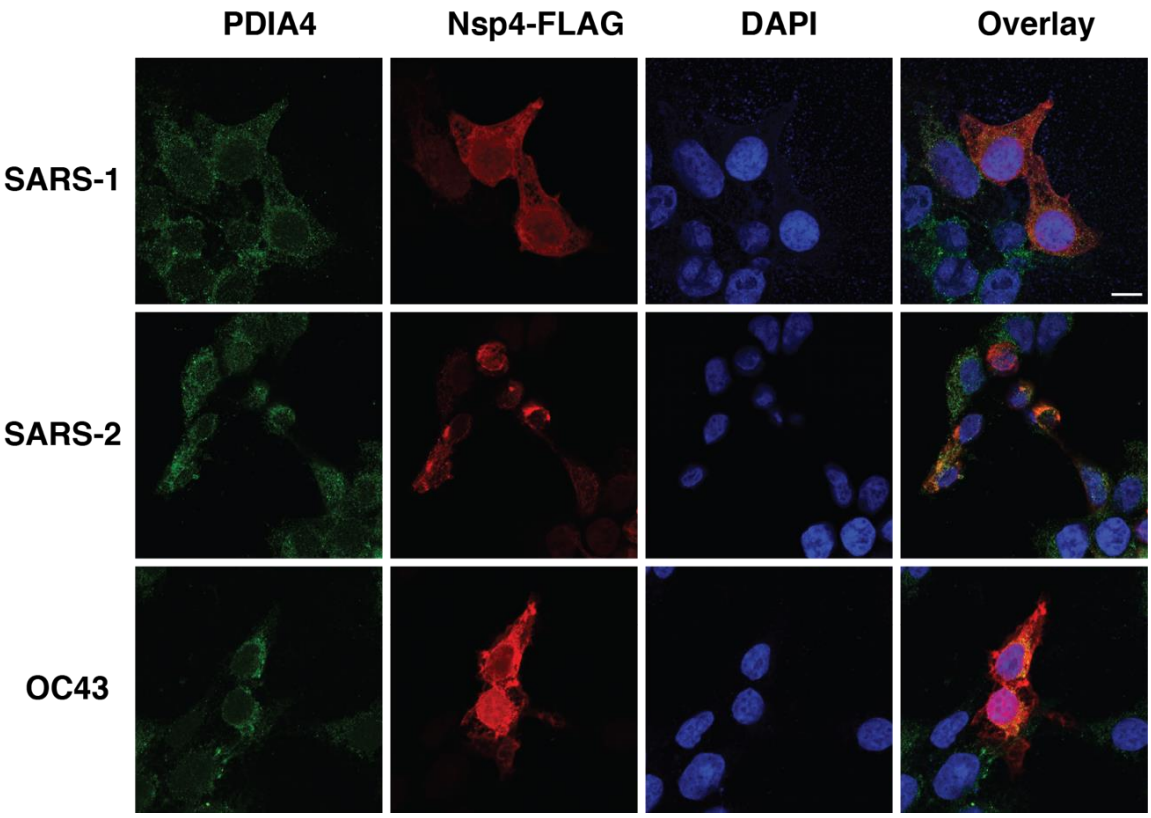

Figure A5.12. Subcellular localization of nsp4 homologs.

Confocal immunofluorescence microscopy images of nsp4 homologs expressed in HEK293T cells, stained for PDIA4 (ER marker, green), FLAG-tag (red), and DAPI (blue). Scale bar is 10 µm.

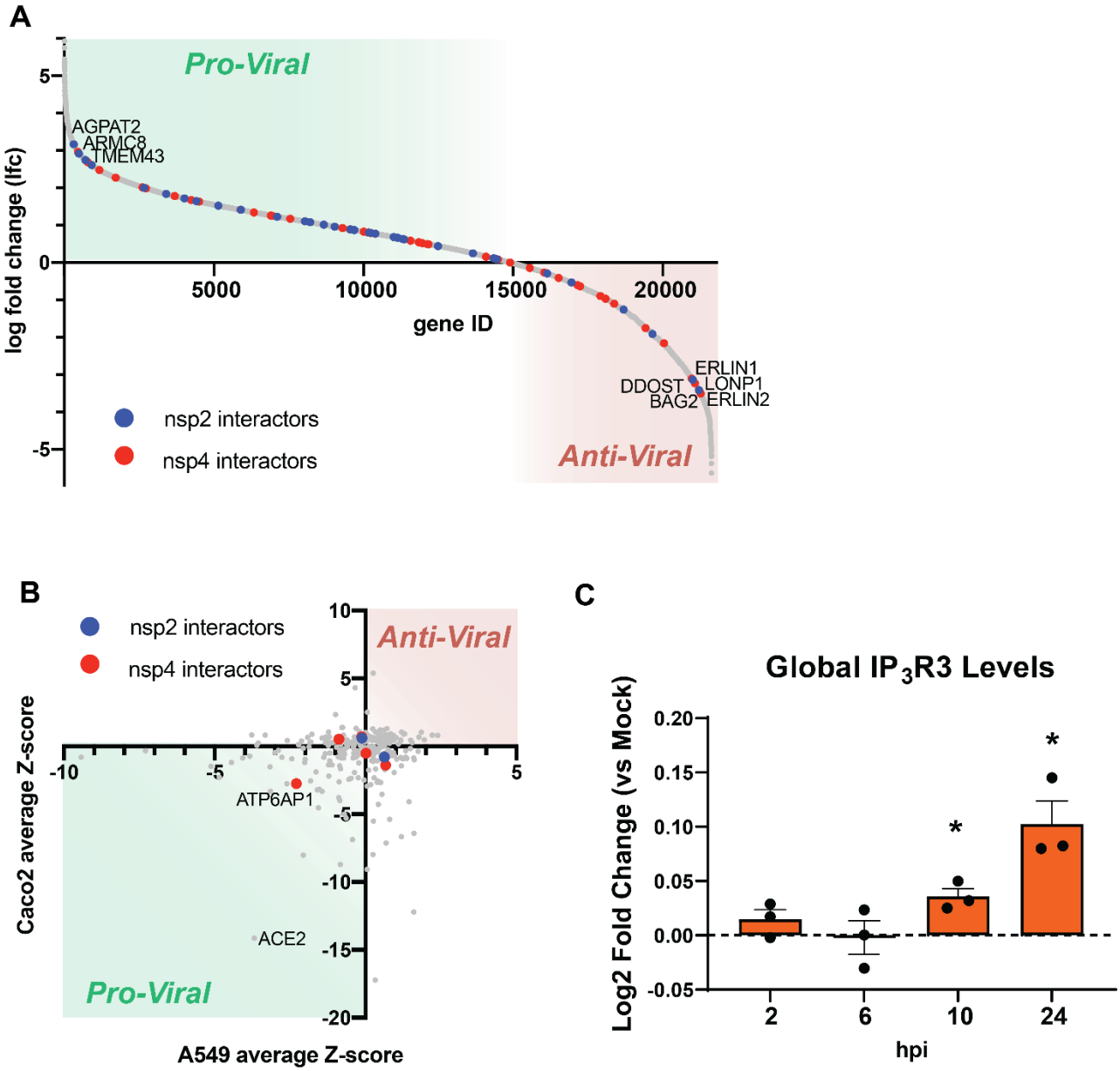

Figure A5.13. Functional genomic screens of interactors and global IP_3R3 protein levels in SARS-CoV-2 infection.

(A) Sorted enrichment of sgRNAs (lfc) in the genome-wide CRISPR screen of the GeCKO V2 library in A549-Cas9-ACE2 lung cancer cells infected with SARS-CoV-2 published by Heaton et al.[16] Interactors of nsp2 and nsp4 found in the dataset are highlighted in blue and red respectively.

(B) Correlation of Z-scores from functional genomics screens in A549-ACE2 and Caco-2 cells infected with SARS-Cov-2 published by Gordon et al.[17] The A549 cells were transduced with siRNA pools of prioritized SARS-CoV interactors and Caco2 cells contained CRISPR knockouts of the prioritized interactors. Z-score < 0 represents decreased infectivity upon

knockdown, while Z-score > 0 represents increased infectivity. Interactors of nsp2 and nsp4 found in the dataset are highlighted in blue and red respectively.

(C) Changes in the global proteome of Caco-2 cells during SARS-CoV-2 infection were measured via quantitative proteomics up to 24 hpi by Bojkova et al[18]. Mass spectrometry data was mined for log_2-fold changes in global IP_3R3 levels during infection. Significance was tested using unpaired two-sided students t-tests between infected and mock samples, *p<0.05.

Appendix 6 Supplementary figures and tables for chapter 6

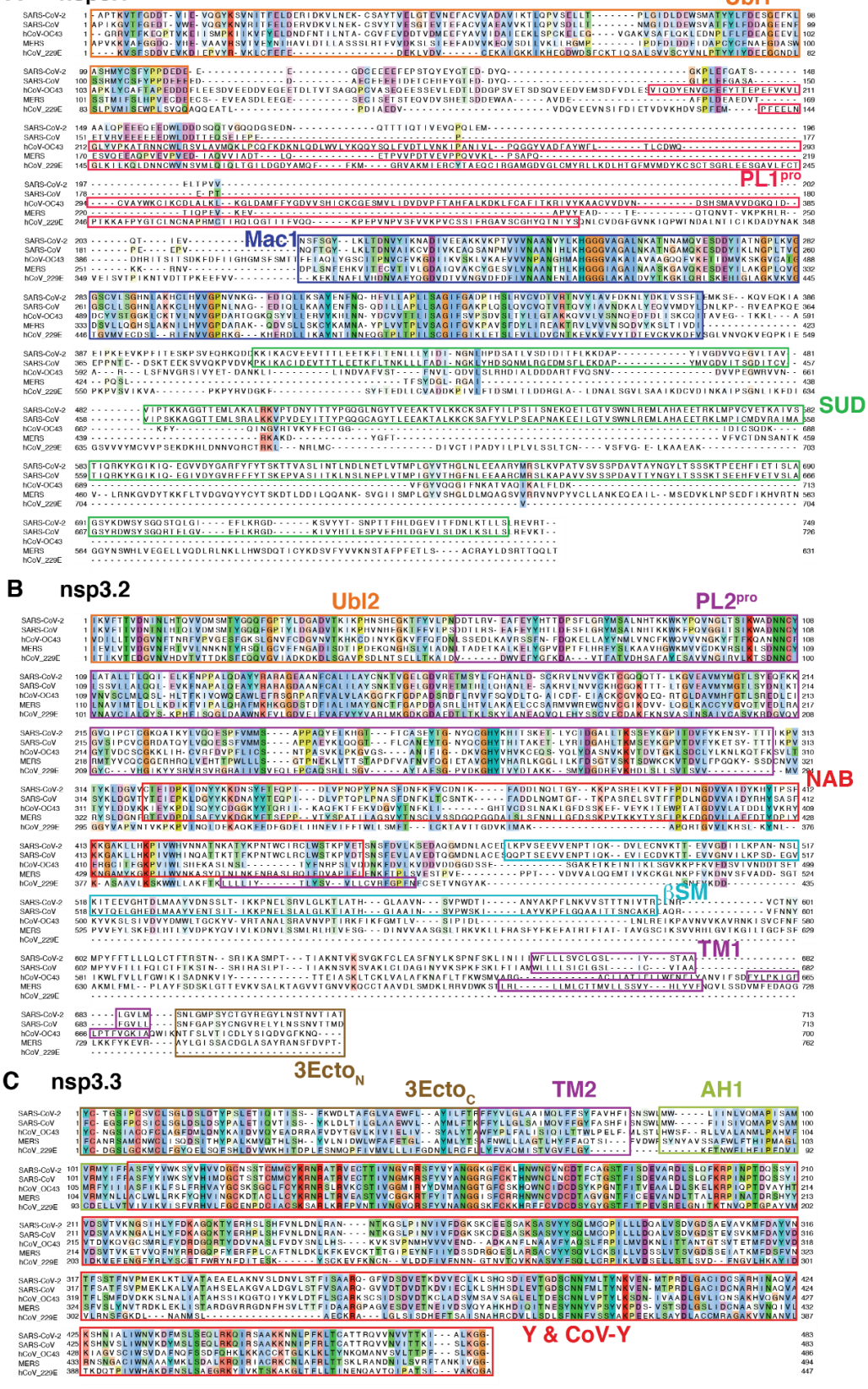

Figure A6.1. Multiple-sequence alignment and domain organization of amino acid sequences for nsp3 truncations from different coronavirus strains.

(A-C) Amino acid sequences of nsp3.1 (A), nsp3.2 (B), and nsp3.3 (C) homologs were aligned using Clustal Omega [19]. Domain organization is noted by colored boxes.

A.

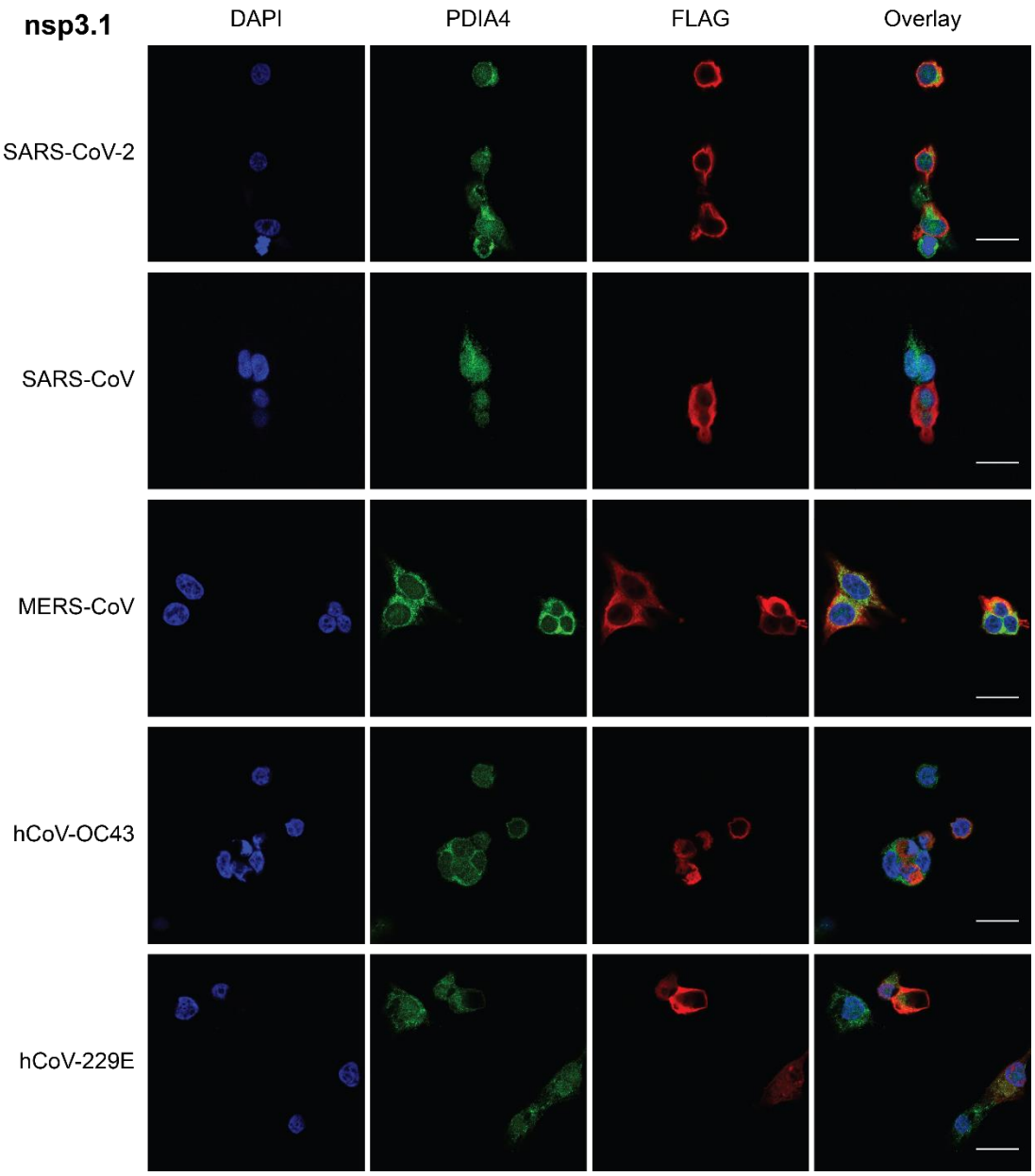
nsp3.1
DAPI
PDIA4
FLAG
Overlay
SARS-CoV-2
SARS-CoV
MERS-CoV
hCoV-OC43
hCoV-229E

B.

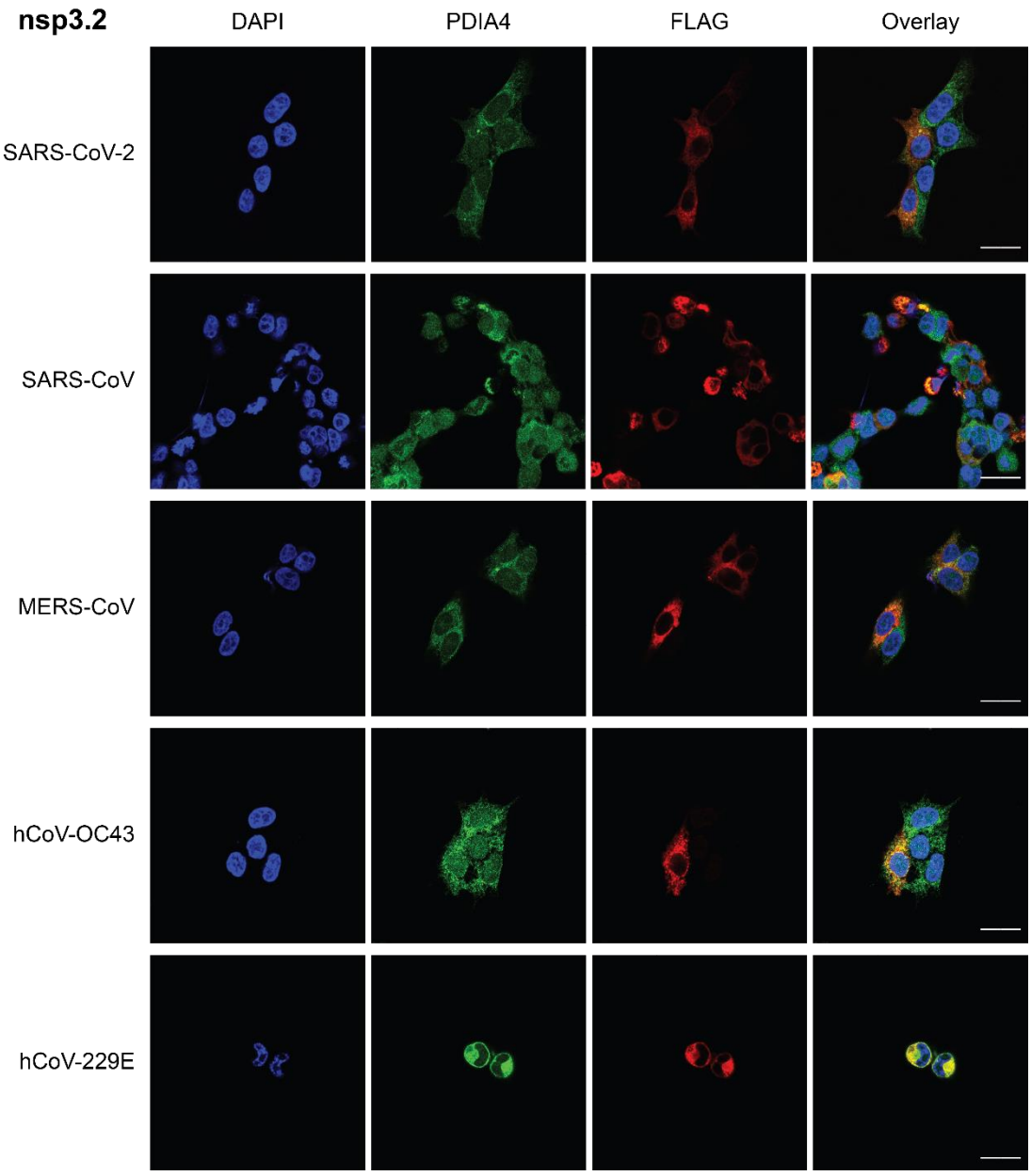
nsp3.2
DAPI
PDIA4
FLAG
Overlay
SARS-CoV-2
SARS-CoV
MERS-CoV
hCoV-OC43
hCoV-229E

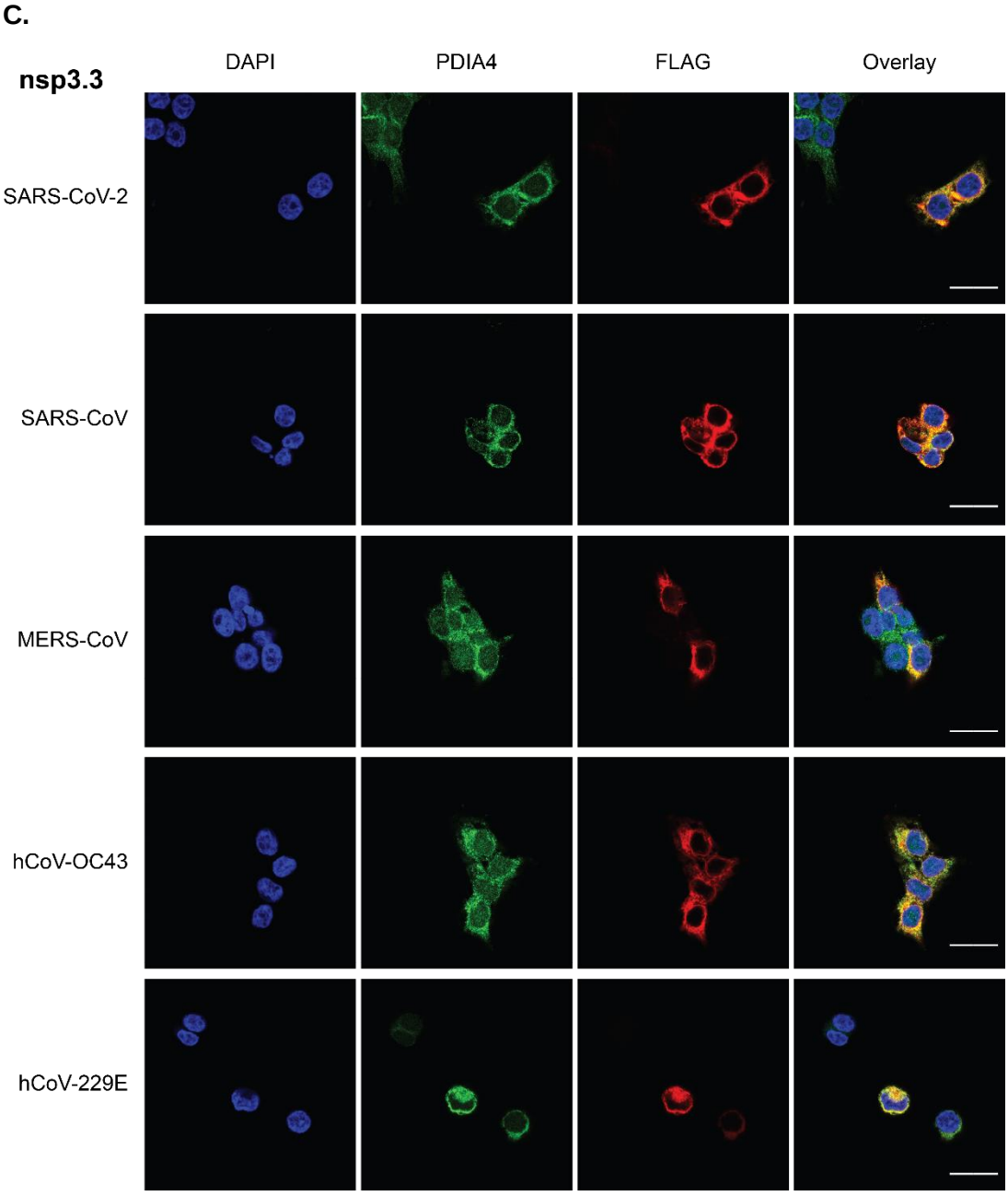

Figure A6.2. Immunofluorescence confocal imaging of nsp3 fragments.
(A-C) Colocalization of nsp3 fragment FLAG-tagged homologs (red) with the ER marker, PDIA4 (green), in HEK293T cells. Representative images shown. Scale bar is 20 µm. (A) nsp3.1 is predominantly localized diffusely cytosolic. (B) nsp3.2 and (C) nsp3.3 show greater co-localization with the ER maker PDIA4 confirming ER localization.

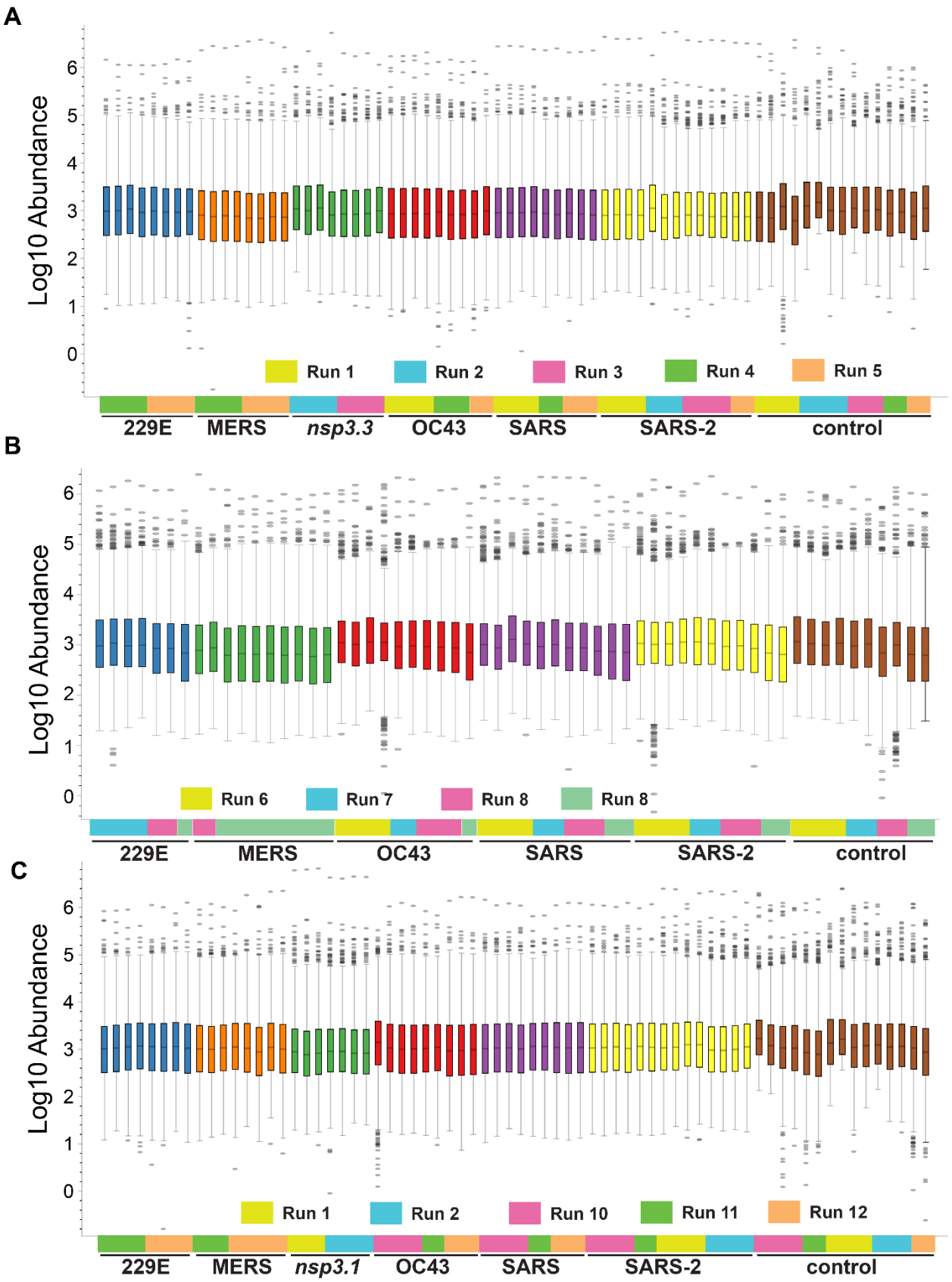
A
Log10 Abundance
0
1
2
3
4
5
6
Run 1
Run 2
Run 3
Run 4
Run 5
229E
MERS
nsp3.3
OC43
SARS
SARS-2
control
B
Log10 Abundance
0
1
2
3
4
5
6
Run 6
Run 7
Run 8
Run 8
229E
MERS
OC43
SARS
SARS-2
control
C
Log10 Abundance
0
1
2
3
4
5
6
Run 1
Run 2
Run 10
Run 11
Run 12
229E
MERS
nsp3.1
OC43
SARS
SARS-2
control

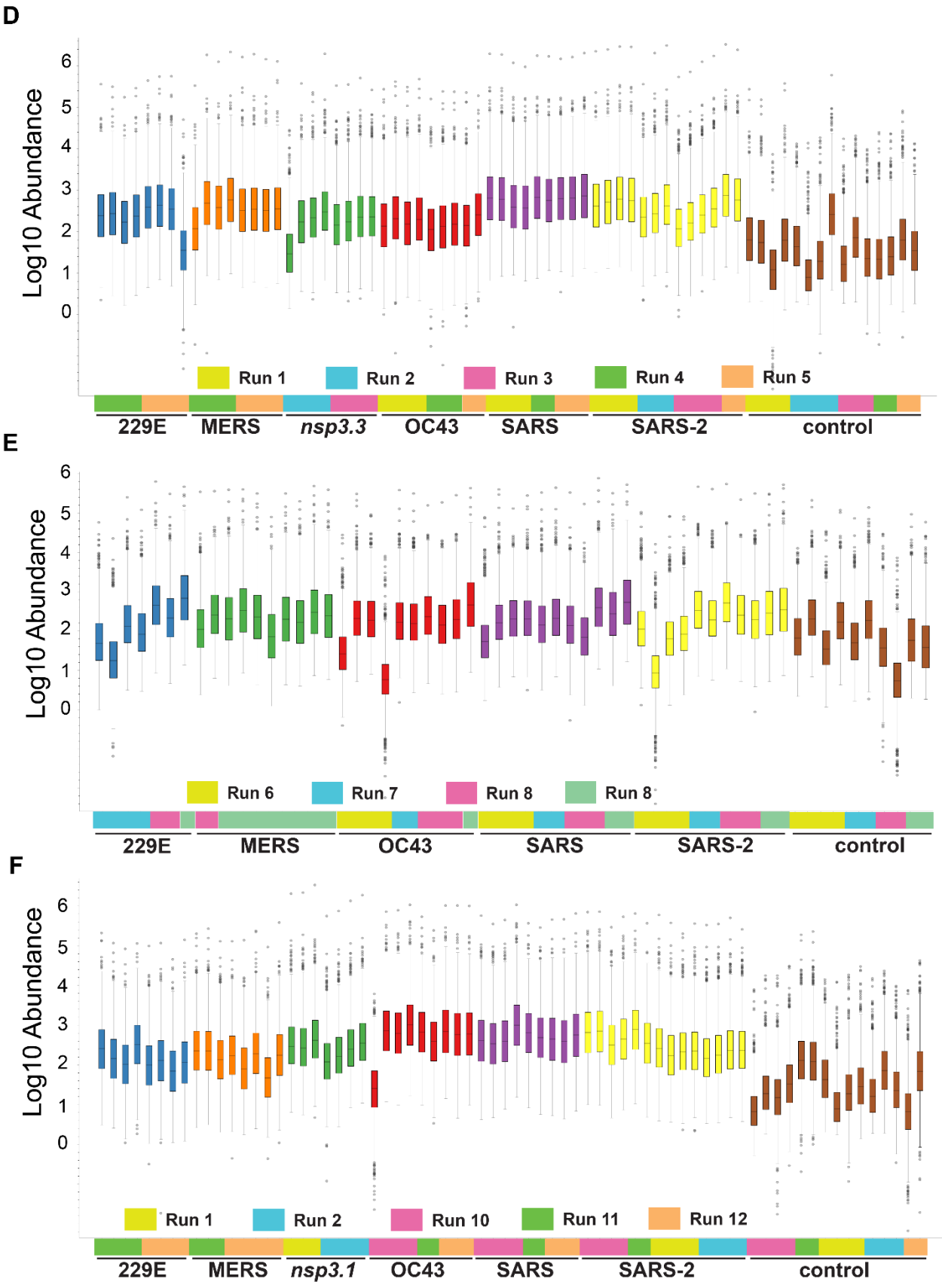
D
Log10 Abundance
0
1
2
3
4
5
6
Run 1
Run 2
Run 3
Run 4
Run 5
229E
MERS
nsp3.3
OC43
SARS
SARS-2
control
E
Log10 Abundance
0
1
2
3
4
5
6
Run 6
Run 7
Run 8
Run 8
229E
MERS
OC43
SARS
SARS-2
control
F
Log10 Abundance
0
1
2
3
4
5
6
Run 1
Run 2
Run 10
Run 11
Run 12
229E
MERS
nsp3.1
OC43
SARS
SARS-2
control

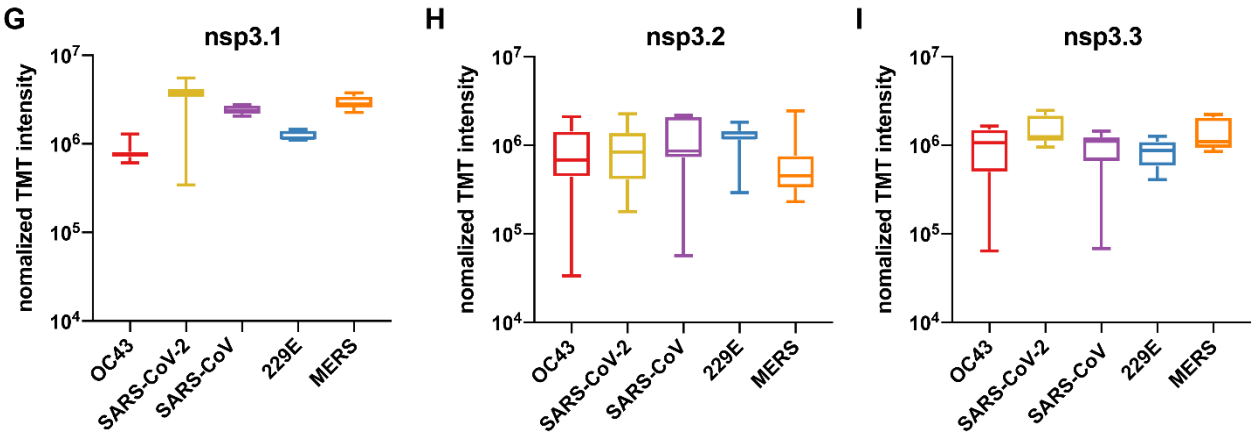

Figure A6.3. Nsp3 TMT intensity distribution.

(A-F) Box-and-whisker plot of the log10 TMT intensity abundance of all 11 mass spectrometry runs used in this study. Nsp3 homologs are grouped by same color box-and-whiskers while the identity of the corresponding mass spectrometry run is denoted by colored blocks below. TMT abundances were normalized based on total peptide amounts (A-C). See supporting dataset S8 for the layout of samples across TMT channels.

(A,D) Normalized (A) and unnormalized (D) TMT abundance distribution for nsp3.1 dataset. Channels denoted "*nsp3.3*" were used for the nsp3.3 dataset within the corresponding mass spectrometry run.

(B,E) Normalized (B) and unnormalized (E) TMT abundance distribution for nsp3.2 dataset.

(C,F) Normalized (C) and unnormalized (F) TMT abundance distribution for nsp3.3 dataset. Channels denoted "*nsp3.1*" were used for the nsp3.1 dataset within the corresponding mass spectrometry run.

(G-I.) Normalized TMT abundances of nsp3 bait proteins to compare the enrichment of fragments from the different strains. Box and whisker blots represent min. to max. values. (G) nsp3.1, (H) nsp3.2, (I) nsp3.3.

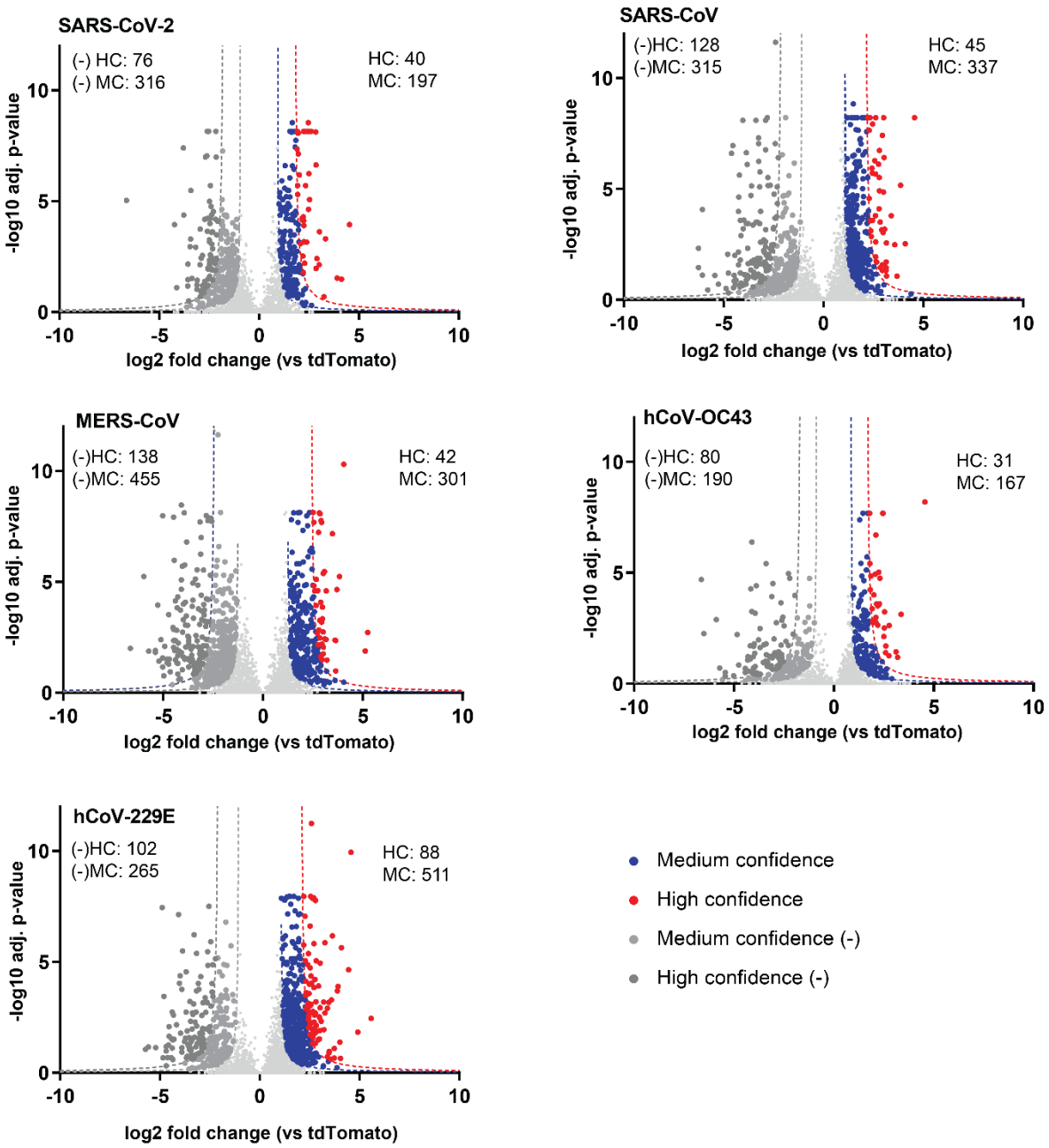

Figure A6.4. Volcano plots of nsp3.1 homolog high-confidence interactors enriched vs tdTomato control.

Host interactors of nsp3.1 homologs were identified by quantitative proteomics and graphed by log2 fold change compared to tdTomato control and -log10 adjusted *p*-value (based on ANOVA). Interactors were filtered for medium (blue) and high (red) confidence interactors based on a hyperbolic curve using 1σ (medium-confidence) or 2σ (high-confidence) standard deviations of the histogram of log2 protein abundance fold changes (refer to "Data analysis" in Methods). Negative medium- and high-confidence (MC, HC) interactors were calculated in a similar manner. Total MC and HC interactors for positive and negative fold change are indicated respectively.

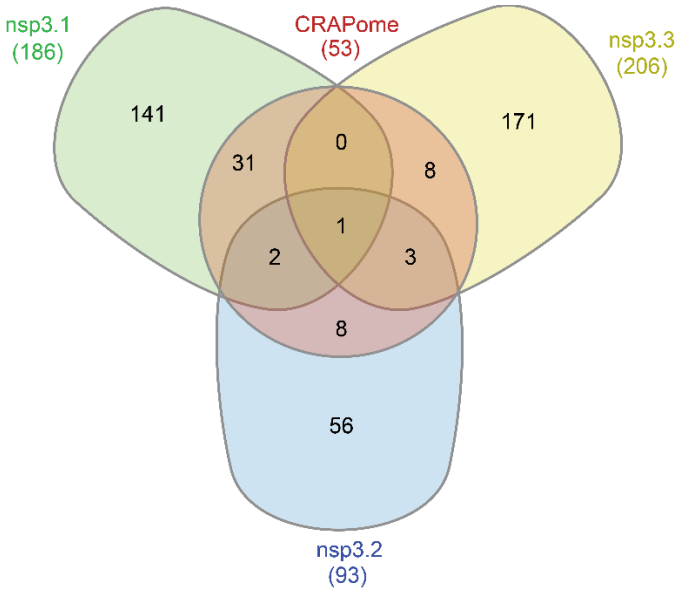

Figure A5.5. CRAPome overlap with nsp3.1, nsp3.2, and nsp3.3 homolog high-confidence interactors. All high-confidence interactors of nsp3 fragments were queried in the CRAPome *Homo sapiens* single step epitope tag AP-MS dataset to identify common contaminant proteins. Interactors with a frequency of 25% or higher in CRAPome control experiments qualified as overlapping with the CRAPome [20].

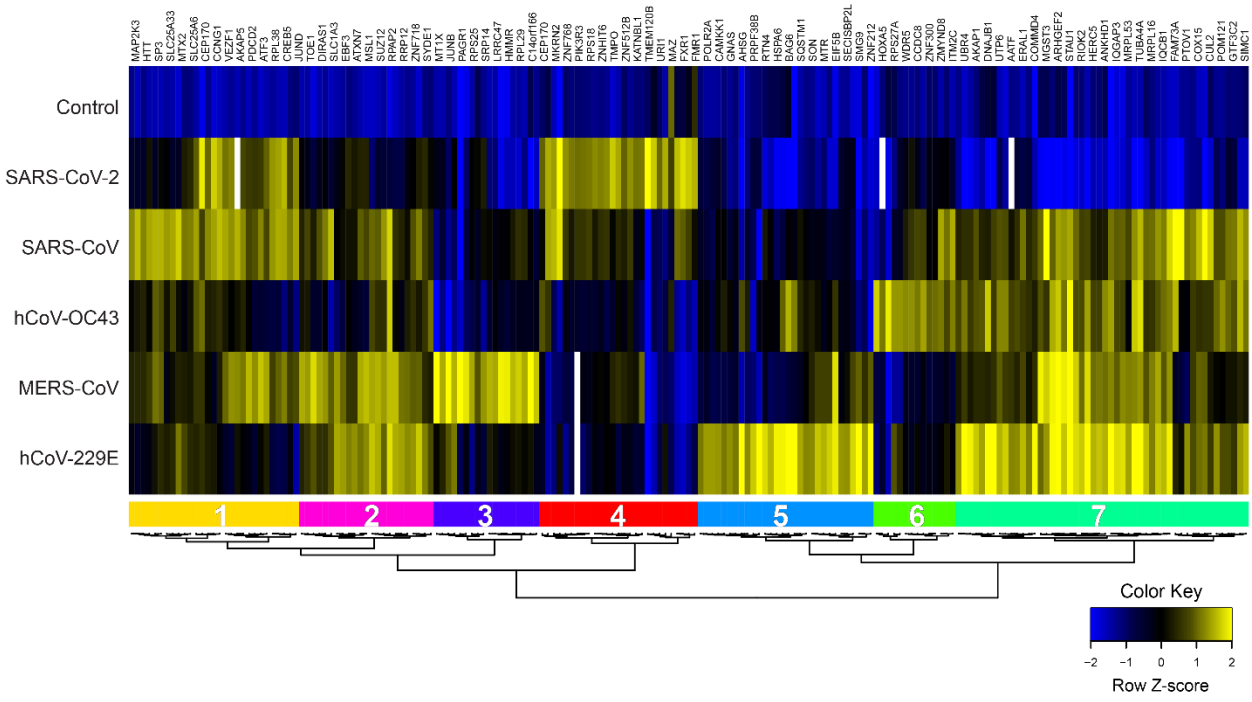

Figure A6.6. Comparative heatmap of nsp3.1 high-confidence interactors. Unbiased hierarchical clustering of log2 fold change for high-confidence interactors of nsp3.1 homologs yields 7 unique clusters.

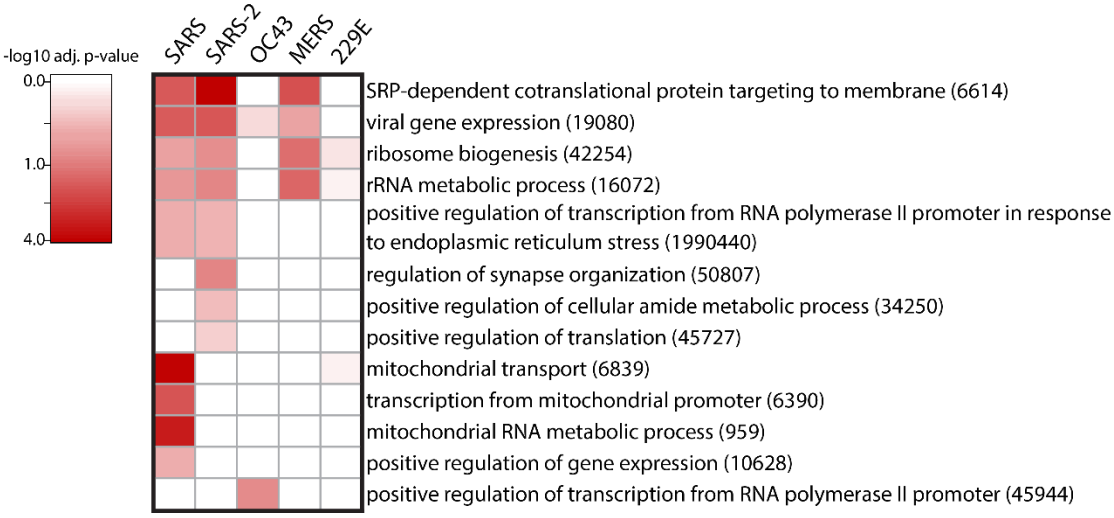

Figure A6.7. GO term analysis of nsp3.1 high-confidence interactors.
Heatmap of gene ontology (GO) term analysis of nsp3.1 high-confidence interactors for enriched biological processes. Selected terms are displayed with corresponding -log10 adjusted *p*-value for each homolog.

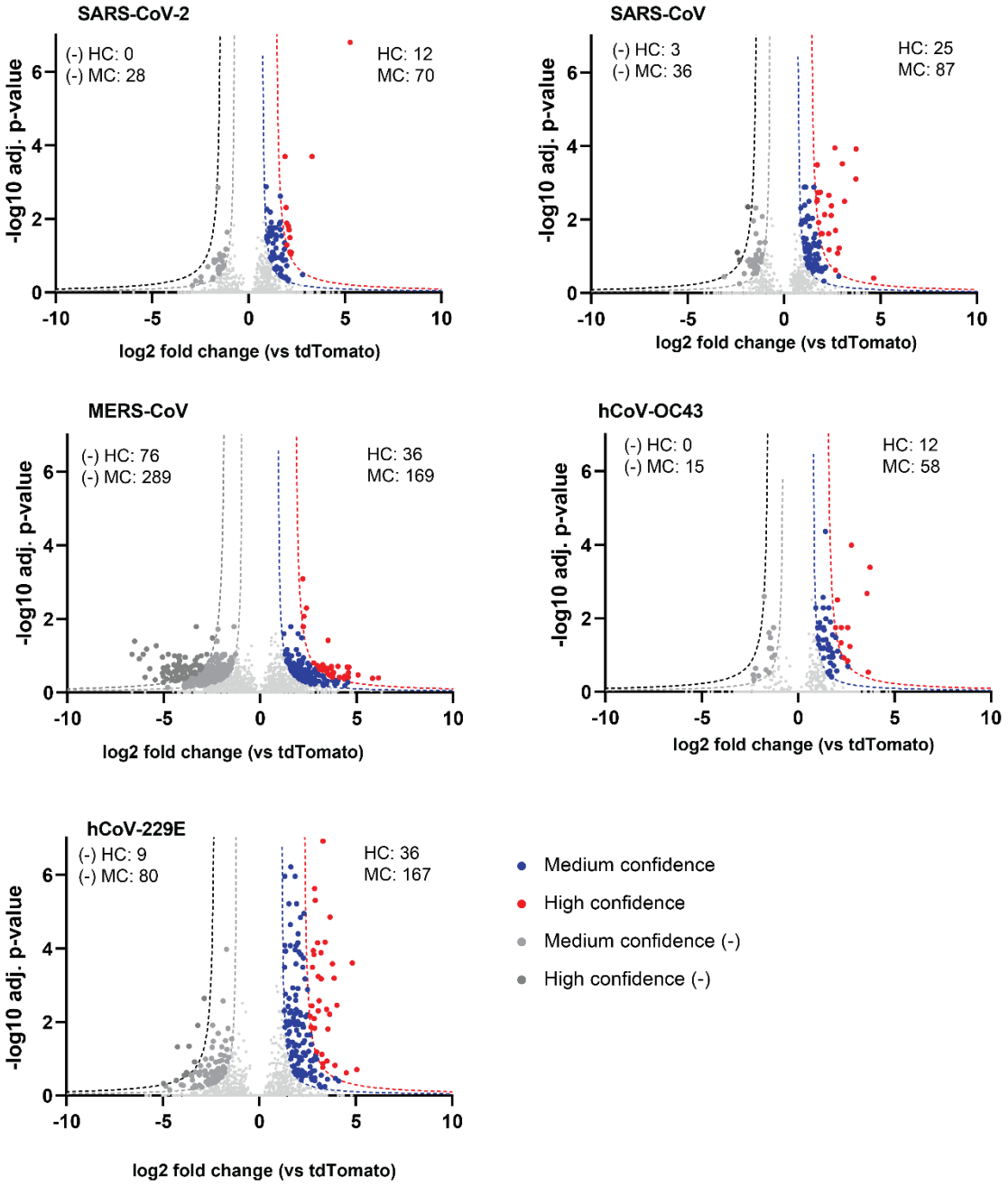

Figure A6.8. Volcano plots of nsp3.2 homolog high-confidence interactors enriched vs tdTomato control.

Host interactors of nsp3.2 homologs were identified by quantitative proteomics and graphed by log2 fold change compared to tdTomato control and -log10 adjusted *p*-value (based on ANOVA). Interactors were filtered for medium (blue) and high (red) confidence interactors based on a hyperbolic curve using 1σ (medium-confidence) or 2σ (high-confidence) standard deviations of the histogram of log2 protein abundance fold changes (refer to "Data analysis" in Methods). Negative medium- and high-confidence (MC, HC) interactors were calculated in a similar manner. Total MC and HC interactors for positive and negative fold change are indicated respectively.

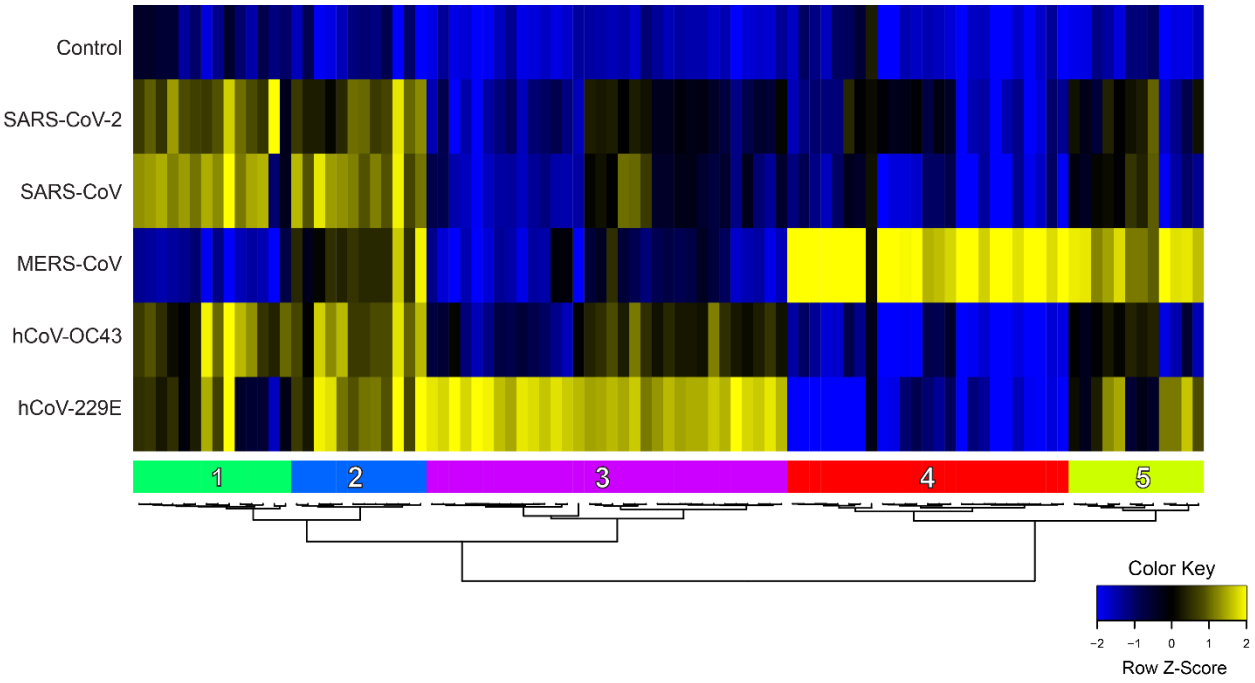

Figure A6.9. Comparative heatmap of nsp3.2 high-confidence interactors.
Unbiased hierarchical clustering of log2 fold change for high-confidence interactors of nsp3.2 homologs yields 5 unique clusters.

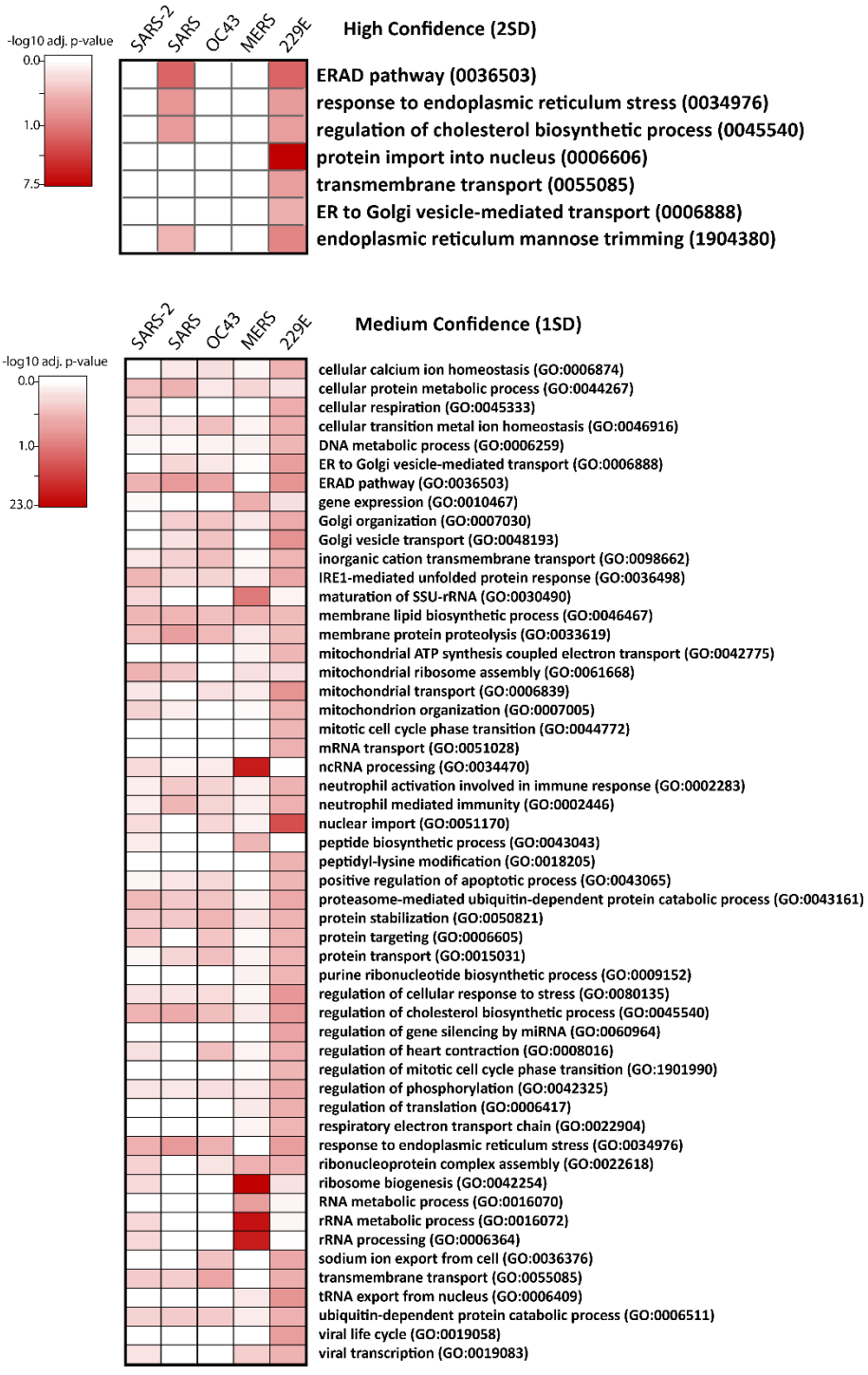

Figure A6.10. GO term analysis of nsp3.2 high-confidence interactors.
Heatmap of gene ontology (GO) term analysis of nsp3.2 high-confidence or medium-confidence interactors for enriched biological processes. Selected terms are displayed with corresponding -log10 adjusted *p*-value for each homolog.

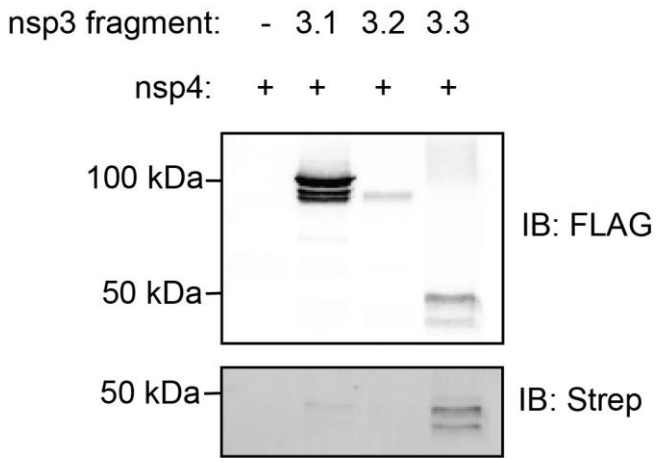

Figure A6.11. Nsp3 fragment co-immunoprecipitations with nsp4.
Samples were co-transfected with 2x-strep tagged SARS-CoV-2 nsp4 [15] and individual SARS-CoV-2 FLAG-tagged nsp3 fragments (nsp3.1, nsp3.2, nsp3.3) or tdTomato as a control, respectively. FLAG immunoprecipitations were performed to pull down on nsp3 constructs and immunoblotting was performed with an anti-FLAG antibody to confirm nsp3.3 expression and an FITC anti-Strep antibody to monitor nsp4 co-immunoprecipitation.

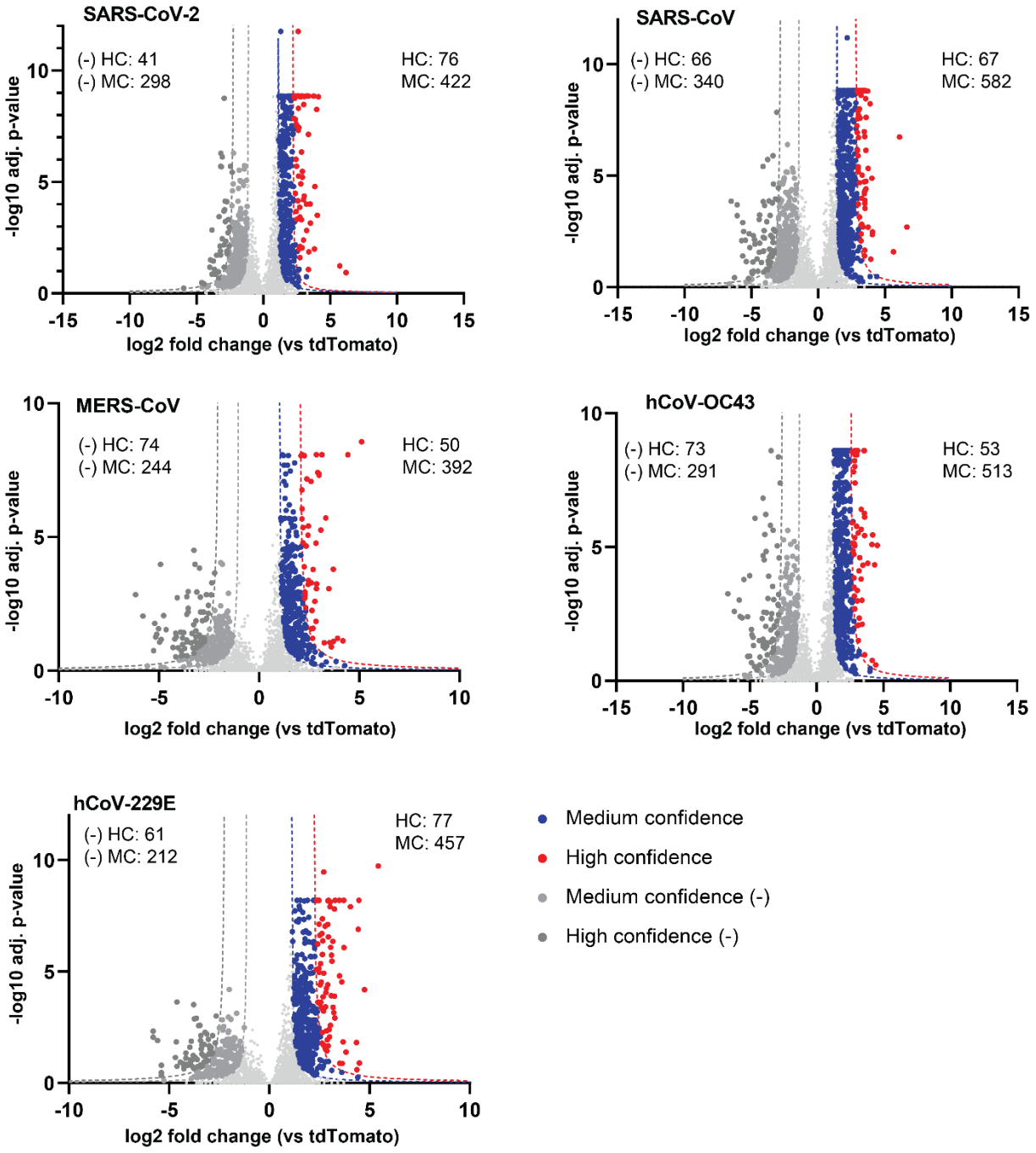

Figure A6.12. Volcano plots of nsp3.3 homolog high-confidence interactors enriched vs tdTomato control.

Host interactors of nsp3.3 homologs were identified by quantitative proteomics and graphed by log2 fold change compared to tdTomato control and -log10 adjusted *p*-value (based on ANOVA). Interactors were filtered for medium (blue) and high (red) confidence interactors based on a hyperbolic curve using 1σ (medium-confidence) or 2σ (high-confidence) standard deviations of the histogram of log2 protein abundance fold changes (refer to "Data analysis" in Methods). Negative medium- and high-confidence (MC, HC) interactors were calculated in a similar manner. Total MC and HC interactors for positive and negative fold change are indicated respectively.

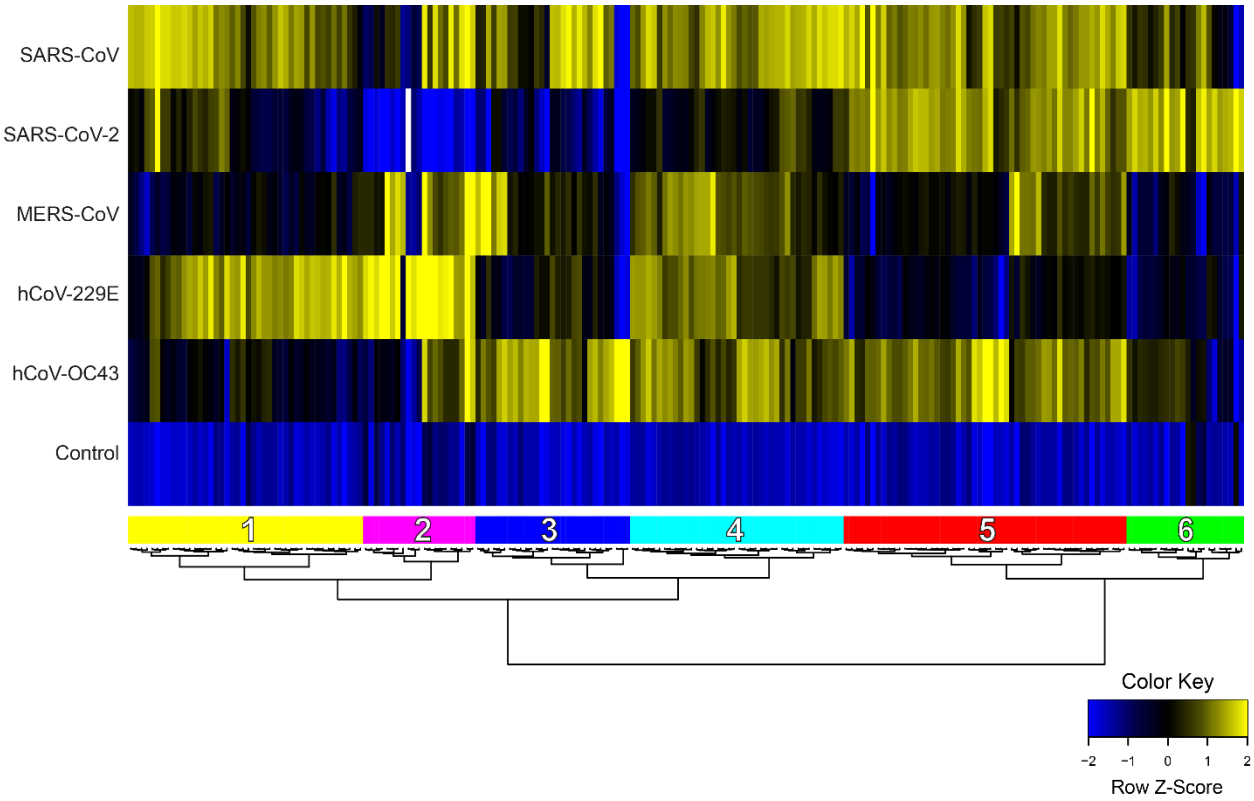

Figure A6.13. Comparative heatmap of nsp3.3 high-confidence interactors.
Unbiased hierarchical clustering of log2 fold change for high-confidence interactors of nsp3.3 homologs yields 6 unique clusters.

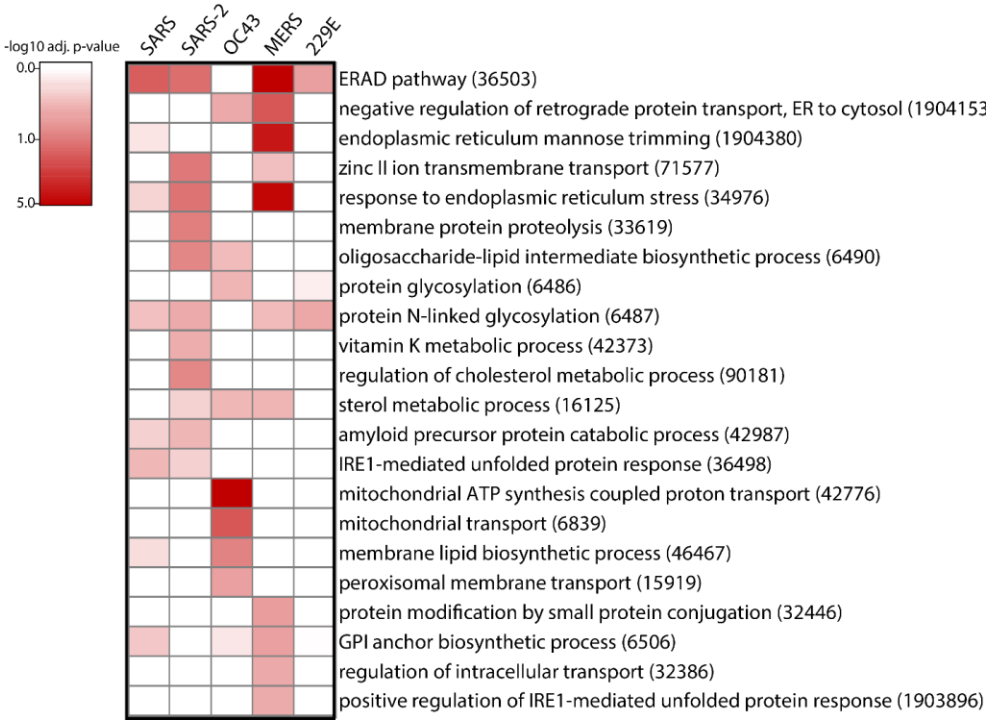

Figure A6.14. GO term analysis of nsp3.3 high-confidence interactors.
Heatmap of gene ontology (GO) term analysis of nsp3.3 high-confidence or medium-confidence interactors for enriched biological processes. Selected terms are displayed with corresponding -log10 adjusted *p*-value for each homolog.

Table A6.1 Key resources table for chapter 6

Reagent type	Designation	Source or reference	Sequence	Usage notes
Chemical	147	[2,7]		10 µM
Chemical	Tunicamycin (Tm)			
PCR primer	Nsp3_N_term_rem_F		atcaaggtgttcaccacagtg	Forward primer to remove N-terminus of Wuhan nsp3 (nsp3.2, 3.3 generation)
PCR primer	Nsp3_N_term_rem_R		catgctagccagcttggg	Reverse primer to remove N-terminus of Wuhan nsp3 (nsp3.2 generation)
PCR primer	Nsp3_middle_rem_F		tattgtacaggcagcatccc	Forward primer to remove middle fragment of Wuhan nsp3 (nsp3.3 generation)
PCR primer	Nsp3_middle_rem_R		ggttctcacctcccgcag	Reverse primer to remove middle fragment of Wuhan nsp3 (nsp3.1 generation)
PCR primer	Nsp3_C_term_rem_F		ctcgagtctagagggccc	Forward primer to remove C-terminus of Wuhan nsp3 (nsp3.1, 3.2 generation)
PCR primer	Nsp3_C_term_rem_R		ggtggcgattgtcacgttg	Forward primer to remove C-terminus of Wuhan nsp3 (nsp3.2 generation)
PCR primer	SARS2_nsp3.1_xFT_F		atccgcagtttgaaaagtaaacccgctgatcagcctcg	Removal of FLAG tag from Wuhan nsp3.1 fragment
PCR primer	SARS2_nsp3.1_xFT_R		catcccccgccgccttcgagggttctcacctcccgcag	Removal of FLAG tag from Wuhan nsp3.1 fragment
PCR primer	2xStrep_F		ctcgaaggcggcgggga	Amplification of 2xStrep tag from pLVX vector
PCR primer	2xStrep_R		ttacttttcaaactgcggatgtgaccatgatccac	Amplification of 2xStrep tag from pLVX vector
Antibody	Anti-M2 FLAG			
Antibody	Anti-STREP FITC			

Appendix 7 Supplemental figures and tables for chapter 7

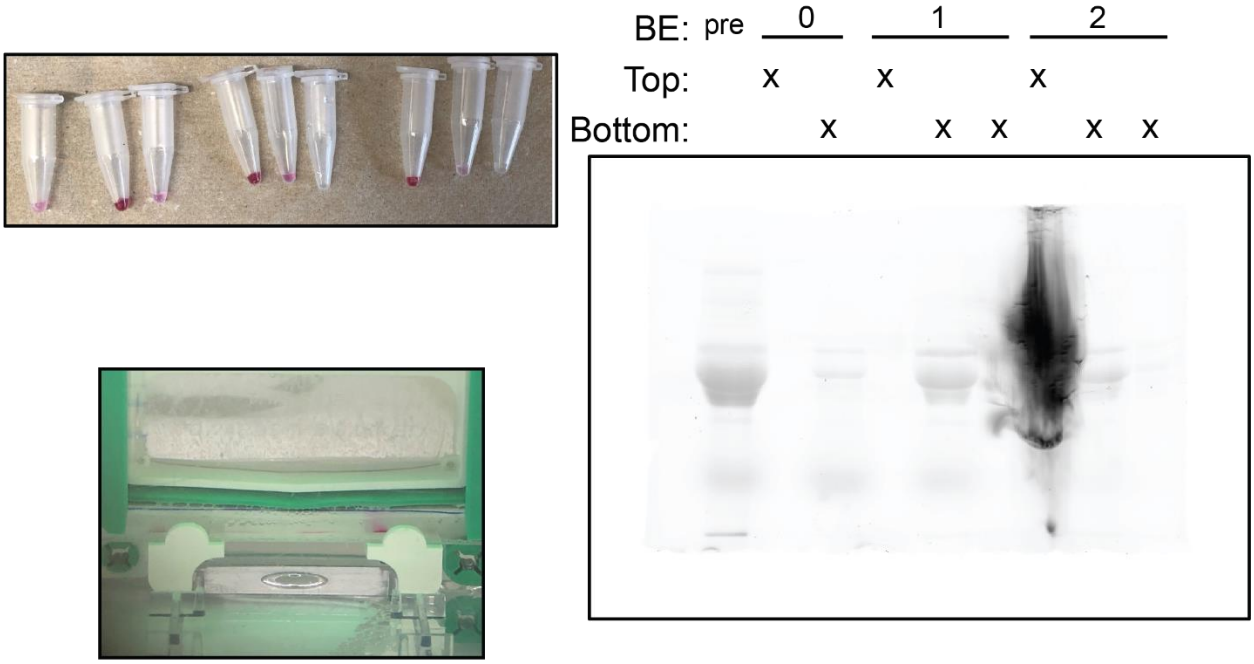

Figure A7.1. Spin filtration of DMEM-10 leads to BSA buildup in retentate.4 mL DMEM with 10% FBS was added to a 100kDa spin filter, with an aliquot reserved for SDS-PAGE ("pre"). Filtrate was spun for 20 minutes at 4000xg. Retentate was washed with water and spin was repeated. Process was repeated for a total of 2 washes. Aliquots of filtrate and retentate were reserved for SDS-PAGE gel after each spin. Samples were frozen before running on SDS-PAGE; 'top' fractions remained solid and did not thaw, thus were unable to be run on gel (2x 'top' sample liquified after extensive heating). Image is of stain-free gel; dark band assumed to be BSA. Little filtration of protein seen, much remains in retentate. Phenol red was also observed to be concentrated in gel samples (top left, in same order as SDS-PAGE gel samples), and formed a front line on the SDS-PAGE gel (pink line, bottom left).

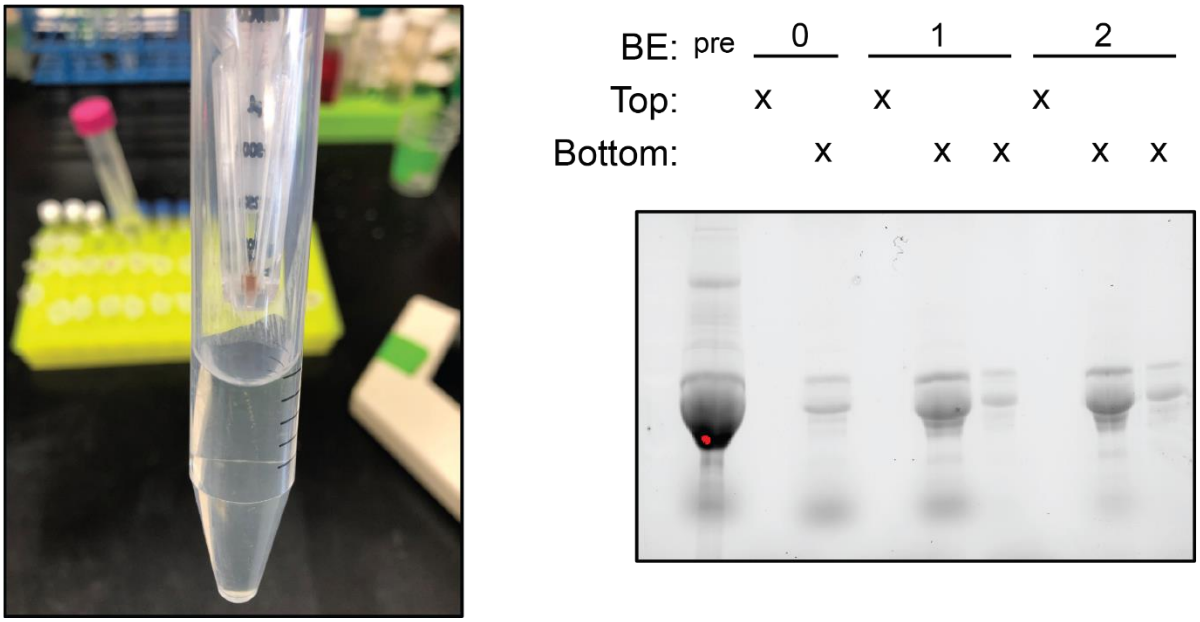

Figure A7.2. Spin filtration of DMEM-10 (no phenol red) leads to BSA buildup in retentate.4 mL DMEM with 10% FBS, without phenol red, was added to a 100kDa spin filter, with an aliquot reserved for SDS-PAGE ("pre"). Filtrate was spun for 20 minutes at 4000xg. Retentate was washed with water and spin was repeated. Process was repeated for a total of 2 washes. Aliquots of filtrate and retentate were reserved for SDS-PAGE gel after each spin. Samples were frozen before running on SDS-PAGE; 'top' fractions remained solid and did not thaw, thus were unable to be run on gel. Image is of stain-free gel; dark band assumed to be BSA. Little filtration of protein seen, much remains in retentate. Left panel shows apparent BSA buildup in filter based on color.

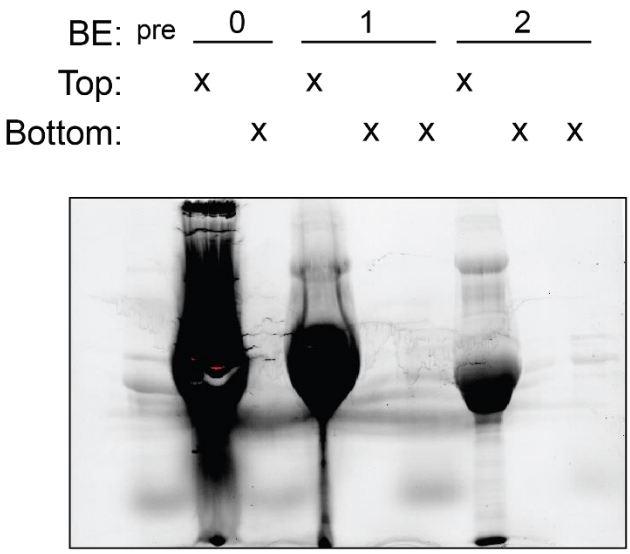

Figure A7.3. Spin filtration of DMEM-2 leads to BSA buildup in retentate.4 mL DMEM with 10% FBS was added to a 100kDa spin filter, with an aliquot reserved for SDS-PAGE (“pre”). Filtrate was spun for 20 minutes at 4000xg. Retentate was washed with water and spin was repeated. Process was repeated for a total of 2 washes. Aliquots of filtrate and retentate were reserved for SDS-PAGE gel after each spin. Image is of stain-free gel; dark band assumed to be BSA. Little filtration of protein seen, much remains in retentate.

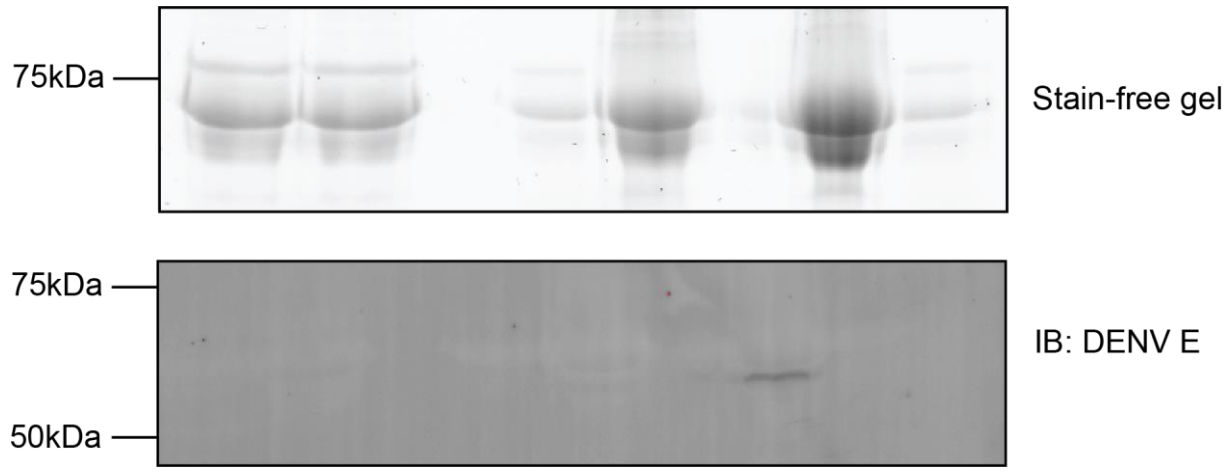

Figure A7.4 Spin filtration leads to enrichment of viral protein. Huh7 cells were infected with DENV2 strain 16681 at an MOI of 3 for 3 hours after pre-treatment with 147 for 16 hours (where indicated). After infection, DMEM-2 was added to cells, along with retreatment of 147 where appropriate. Infection proceeded for 24 hours, after which time media was collected and cleared for 10 minutes at 4000xg. Cleared media was divided into 2 spin filters and samples were spun at 1500xg for 5 minutes thrice, with the filter being replenished with 5mM HEPES. Samples were combined and protein levels in both the retentate and filtrate were measured. Stain-free gel (a) shows that BSA was retained in the filter, but western blot (b) shows the concentration of DENV E protein.

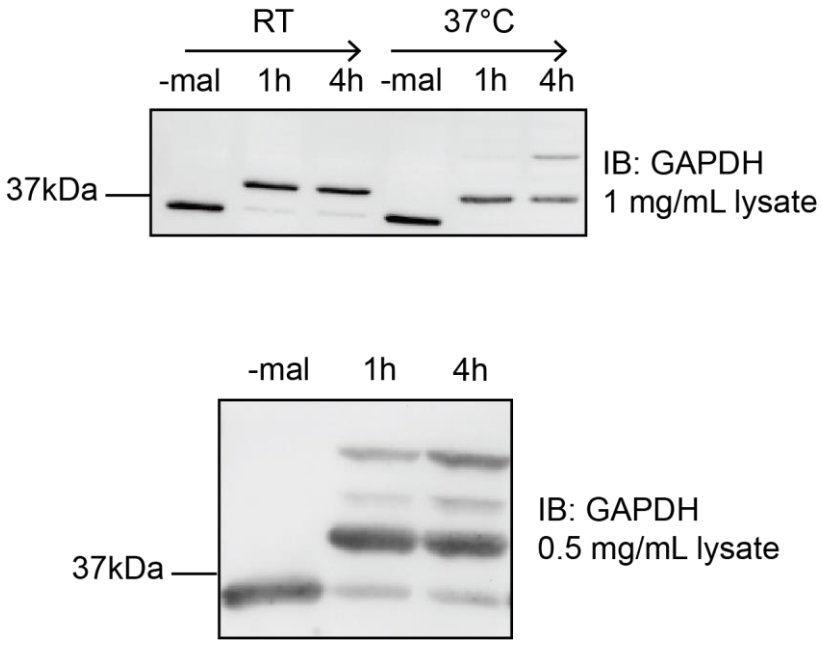

Figure A7.5 Labeling of GAPDH by PC-PEGmal reagent.

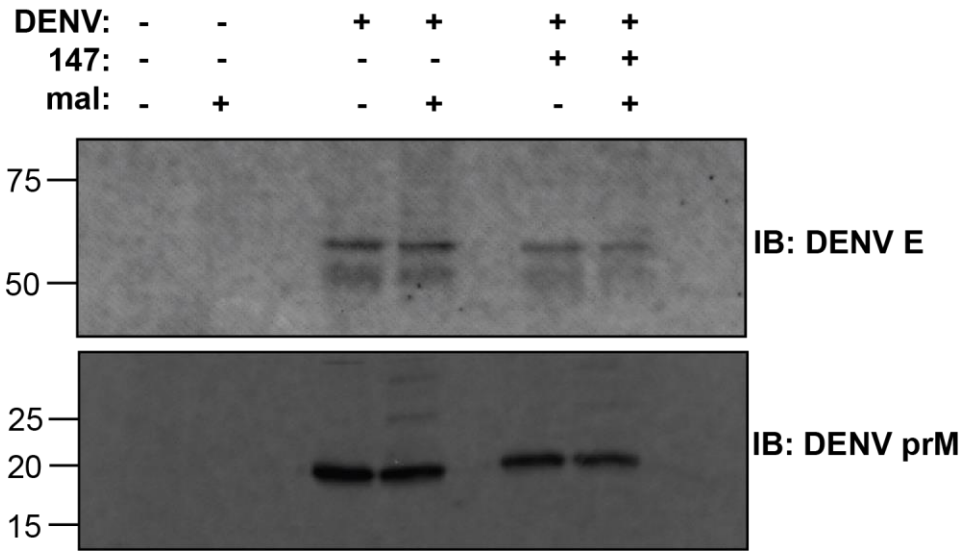

Figure A7.6. Significant labeling of intracellular DENV proteins not observed by western blot. Lysates were labeled at 0.5 mg/mL with photocleavable PEG-maleimide (mal) reagent for 4 hours at 37°C. Samples were prepared for SDS-PAGE gel and run on a 15% gel at 175V for ~1 hour. Gels were activated for 15 minutes using the 'stain-free gel' setting on a BioRad ChemiDoc imager to cleave the maleimide probe. Proteins were transferred to a PVDF membrane for western blot using mixed molecular weight settings on the Transblot Turbo. Primary antibodies for DENV E or prM were applied overnight, followed by a Starbright B520 secondary in milk for 30 minutes at room temperature. Notably, only weak labeling of the structural proteins by the maleimide reagent was seen in both the **147** treated and untreated samples. Because the **147** treated samples contain less viral protein, a quantitative comparison of the degree of labeling cannot be obtained without adjusting for this change. However, it appears that there are no significant changes in labeling between the two samples.

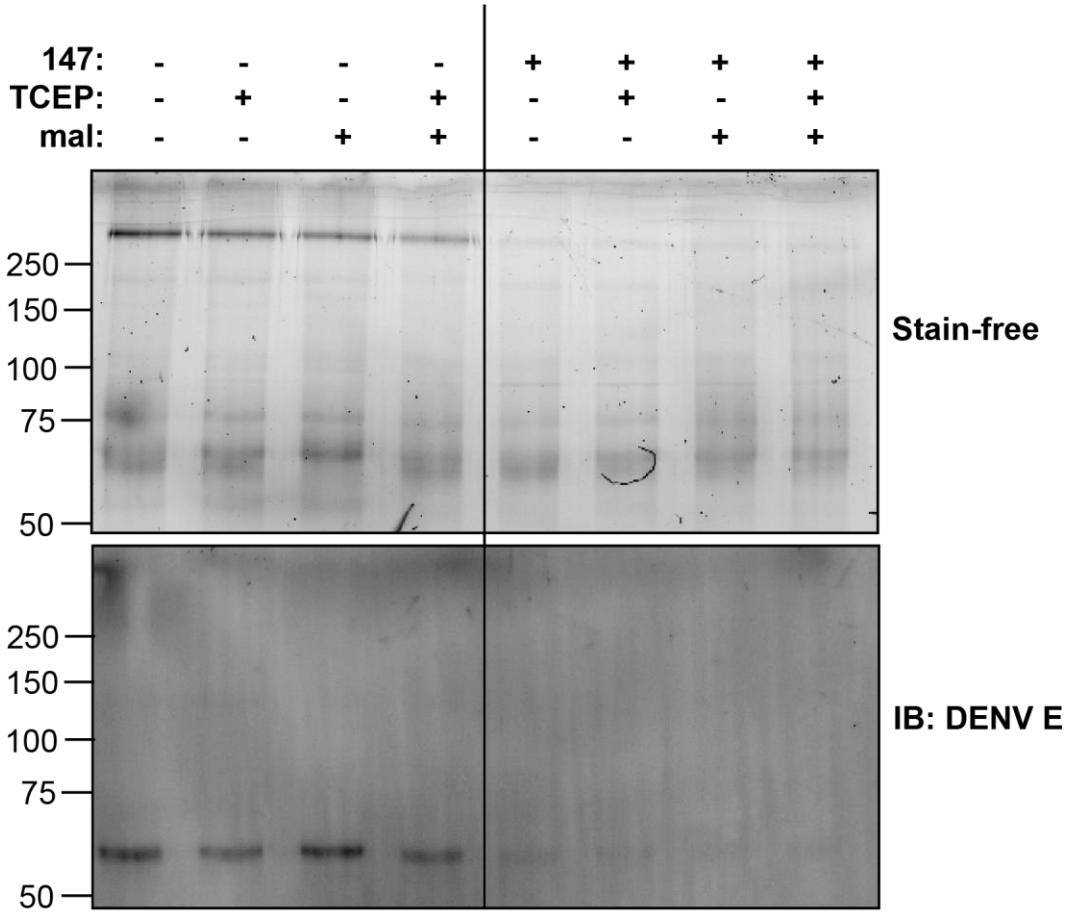

Figure A7.7. Labeling of purified virus not observed by western blot. Virus-containing supernatant (collected after 24 hours of infection with DENV2 16681) was purified by spinning at 4000xg for 45 minutes, followed by a 3 hour spin over a 20% sucrose cushion at 113,000xg. Supernatant was removed, and the viral pellet was dried and resuspended in 5 mM HEPES pH 7.9. Lowered titers were confirmed by FFA (not shown). Samples were treated as indicted with 10mM TCEP (in 0.5M HEPES) to denature disulfide bonds, then treated with maleimide as indicated. Samples were prepared for SDS-PAGE and run on a 10% gel at 175V for ~1 hour. Gels were activated for 15 minutes using the 'stain-free gel' setting on a BioRad ChemiDoc imager to cleave the maleimide probe. Proteins were transferred to a PVDF membrane for western blot using mixed molecular weight settings on the Transblot Turbo. Primary anti-DENV E antibody was added overnight at 4°C, secondary Starbright B520 was added in milk for 30 minutes at room temperature. It was expected the samples treated with both TCEP and maleimide would show a gel shift; this did not occur. Further experiments could use a pre-treatment of purified virus with SDS to increase the availability of disulfide bonds for reduction. Additionally, it was unexpected that the **147** samples showed less viral protein than the untreated samples.

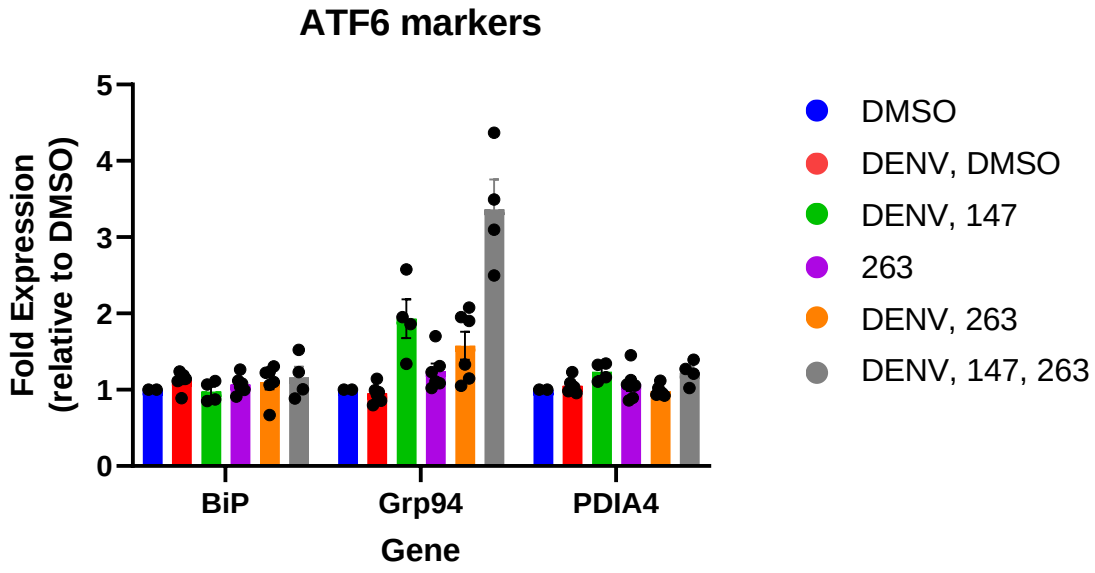

Figure A7.8. Western blot quantification of ATF6 markers after treatment with 263 or 147.

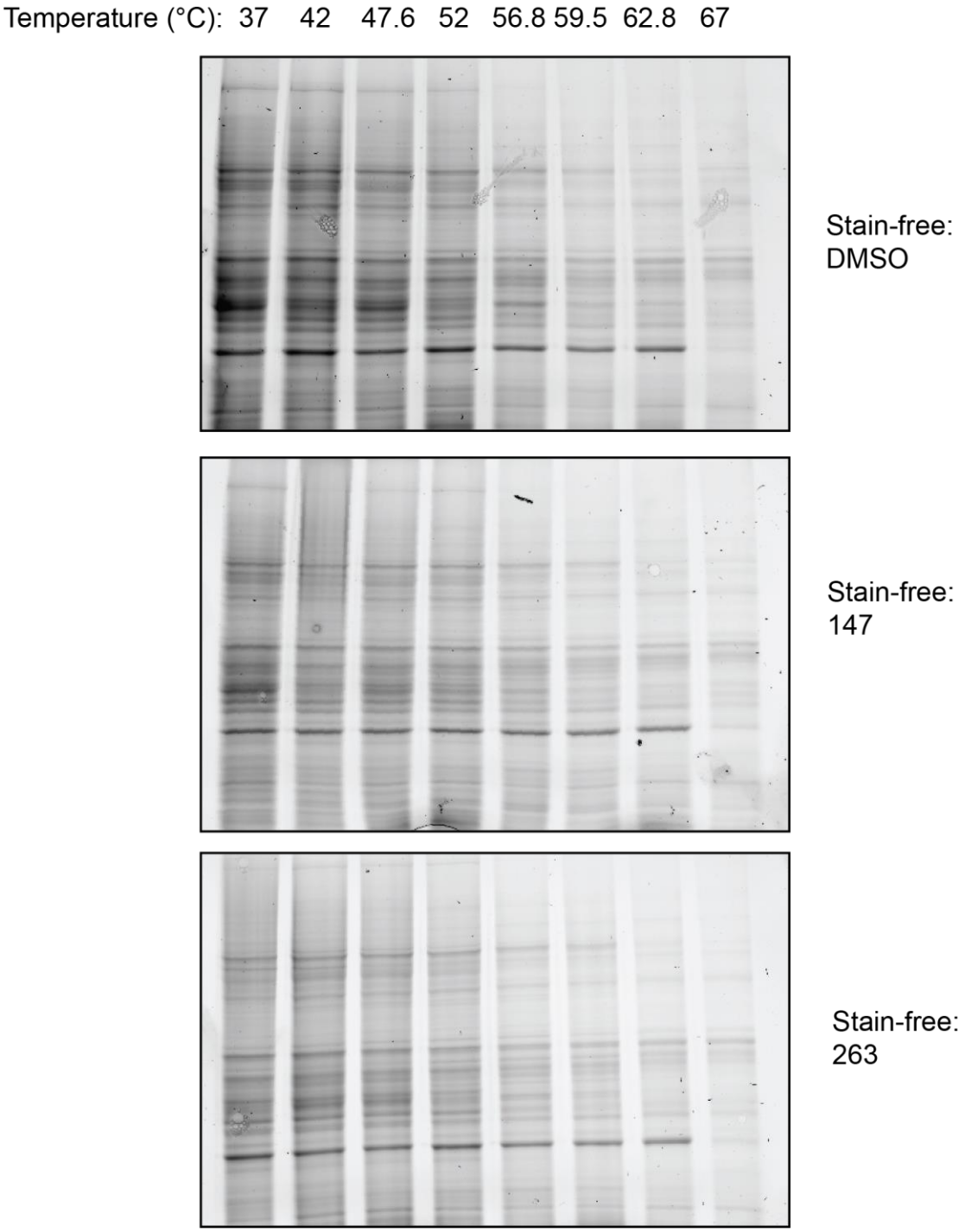

Figure A7.9. Thermal proteome profiling shows decreased protein abundance with increasing temperature. Protein samples were heated to the indicated temperatures for 3 minutes in a PCR thermocycler. Soluble protein fractions were isolated and run on an SDS-PAGE gel. The decrease in total protein signal matches the increase in aggregation (and thus decrease in soluble protein) expected as the temperatures increased. There do not appear to be significant changes in response to **147** or **263** treatment, which is also expected as most proteins should not alter in thermal stability based on treatment.

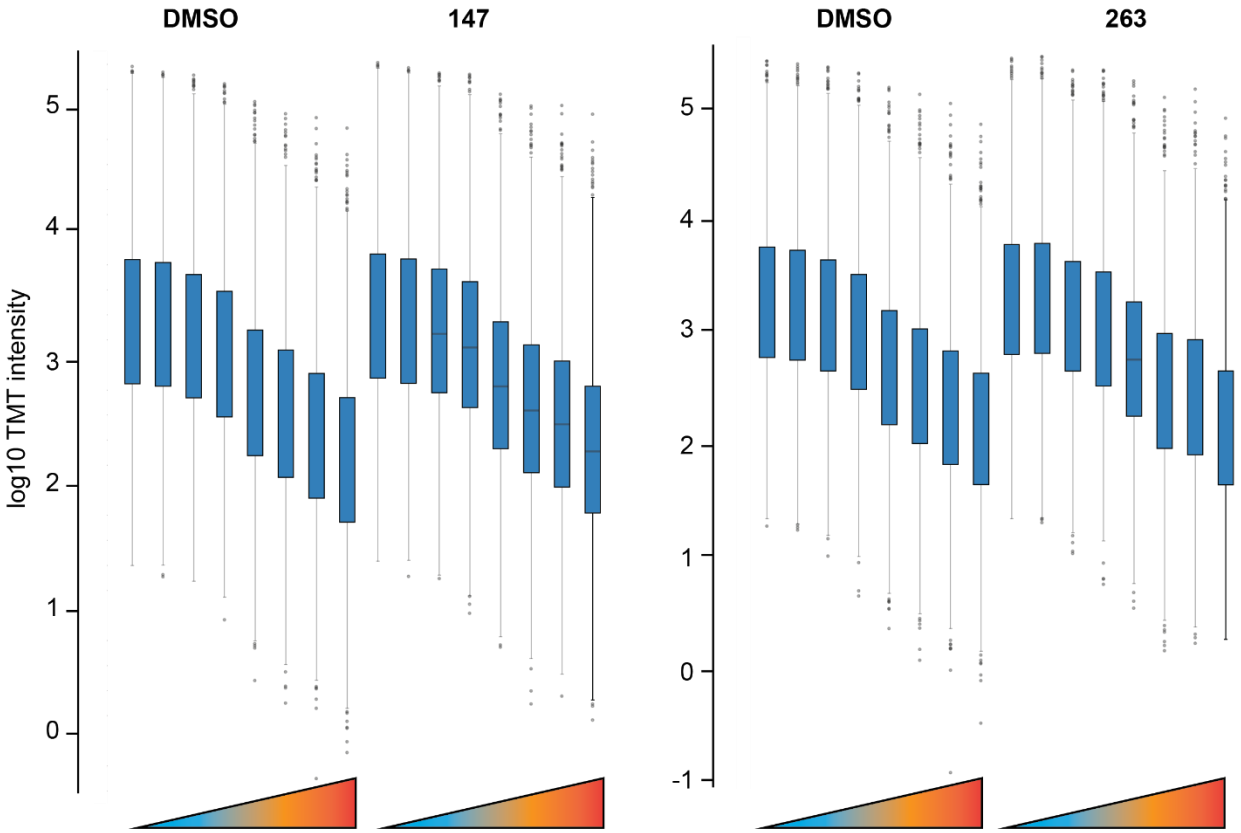

Figure A7.10. TMT intensity profiles of thermal proteome profiling samples. The same samples from **Figure A6.4** were subjected to MeOH/CHCl3 precipitation followed by resuspension in 1% Rapigest and reduction, alkylation, and digestion. Samples were labeled with TMTpro 16plex reagents and run on an Exploris 480 instrument. TMT intensities were plotted by Proteome Discoverer 2.4. From left to right in each sample set as indicated, the fractions were heated to increasing degrees, thus decreasing the soluble protein fraction. The drop in total protein intensity is thus expected.

Table A7.1 Key resources table for chapter 7

Reagent type	Designation	Source/reference	Sequence	Notes
Chemical	147	[2,7]		
Chemical	263	[2]		
Chemical	Photocleavable PEG-maleimide	Dojindo Molecular Technologies, Inc. (SB20)		
Antibody	Anti-PDIA4	Proteintech		1:1000
Antibody	Anti-PDIA1	SantaCruz (SC-74551)		1:1000
Antibody	Anti-PDIA6	Genetex (GTX121275)		1:1000
Antibody	Anti-DENV E	Genetex (GTX127277)		1:1000
Antibody	DENV prM	Genetex		
Antibody	Anti-pan-flavivirus 4G2	Millipore-Sigma (MAB10216)		1:1000
Antibody	Anti-mouse HRP	Promega (W4021)		1:1000
Antibody	Anti-mouse Starbright 700	Bio-Rad (12004158)		1:10,000
Antibody	Anti-mouse Starbright B520	Bio-Rad (12005866)		1:10,000

Appendix 7 References for appendices

(1) Grandjean, J. M. D.; Plate, L.; Morimoto, R. I.; Bollong, M. J.; Powers, E. T.; Luke Wiseman, R. Deconvoluting Stress-Responsive Proteostasis Signaling Pathways for Pharmacologic Activation Using Targeted RNA Sequencing. *ACS Chem. Biol.* **2019**, *14* (4), 784–795. https://doi.org/10.1021/ACSCHEMBIO.9B00134/SUPPL_FILE/CB9B00134_SI_004.XLSX.

(2) Plate, L.; Cooley, C. B.; Chen, J. J.; Paxman, R. J.; Gallagher, C. M.; Madoux, F.; Genereux, J. C.; Dobbs, W.; Garza, D.; Spicer, T. P.; Scampavia, L.; Brown, S. J.; Rosen, H.; Powers, E. T.; Walter, P.; Hodder, P.; Wiseman, L.; Kelly, J. W.; Wiseman, R. L.; Kelly, J. W. Small Molecule Proteostasis Regulators That Reprogram the ER to Reduce Extracellular Protein Aggregation. *Elife* **2016**, *5* (2016JULY), 1–26. https://doi.org/10.7554/eLife.15550.

(3) Grandjean, J. M. D.; Madhavan, A.; Cech, L.; Seguinot, B. O.; Paxman, R. J.; Smith, E.; Scampavia, L.; Powers, E. T.; Cooley, C. B.; Plate, L.; Spicer, T. P.; Kelly, J. W.; Wiseman, R. L. Pharmacologic IRE1/XBP1s Activation Confers Targeted ER Proteostasis Reprogramming. *Nat. Chem. Biol.* **2020**, *16* (10), 1052–1061. https://doi.org/10.1038/s41589-020-0584-z.

(4) Cross, B. C. S.; Bond, P. J.; Sadowski, P. G.; Jha, B. K.; Zak, J.; Goodman, J. M.; Silverman, R. H.; Neubert, T. A.; Baxendale, I. R.; Ron, D.; Harding, H. P. The Molecular Basis for Selective Inhibition of Unconventional MRNA Splicing by an IRE1-Binding Small Molecule. *Proc. Natl. Acad. Sci. U. S. A.* **2012**, *109* (15). https://doi.org/10.1073/PNAS.1115623109/SUPPL_FILE/SM02.MPG.

(5) Ghosh, R.; Wang, L.; Wang, E. S.; Perera, B. G. K.; Igbaria, A.; Morita, S.; Prado, K.; Thamsen, M.; Caswell, D.; Macias, H.; Weiberth, K. F.; Gliedt, M. J.; Alavi, M. V.; Hari, S. B.; Mitra, A. K.; Bhhatarai, B.; Schürer, S. C.; Snapp, E. L.; Gould, D. B.; German, M. S.; Backes, B. J.; Maly, D. J.; Oakes, S. A.; Papa, F. R. Allosteric Inhibition of the IRE1α RNase Preserves Cell Viability and Function during Endoplasmic Reticulum Stress. *Cell* **2014**, *158* (3), 534–548. https://doi.org/10.1016/J.CELL.2014.07.002.

(6) Gallagher, C. M.; Garri, C.; Cain, E. L.; Ang, K. K.; Wilson, C. G.; Chen, S.; Hearn, B. R.; Jaishankar, P.; Aranda-Diaz, A.; Arkin, M. R.; Renslo, A. R.; Walter, P. Ceapins Are a New Class of Unfolded Protein Response Inhibitors, Selectively Targeting the ATF6alpha Branch. *Elife* **2016**, *5*. https://doi.org/10.7554/eLife.11878.

(7) Paxman, R.; Plate, L.; Blackwood, E. A.; Glembotski, C.; Powers, E. T.; Wiseman, R. L.; Kelly, J. W. Pharmacologic ATF6 Activating Compounds Are Metabolically Activated to Selectively Modify Endoplasmic Reticulum Proteins. *Elife* **2018**, *7*. https://doi.org/10.7554/eLife.37168.

(8) Banerjee, R.; Pace, N. J.; Brown, D. R.; Weerapana, E. 1,3,5-Triazine as a Modular Scaffold for Covalent Inhibitors with Streamlined Target Identification. *J Am Chem Soc* **2013**, *135* (7), 2497–2500. https://doi.org/10.1021/ja400427e.

(9) Cole, K. S.; Grandjean, J. M. D.; Chen, K.; Witt, C. H.; O'Day, J.; Shoulders, M. D.; Wiseman, R. L.; Weerapana, E. Characterization of an A-Site Selective Protein Disulfide Isomerase A1 Inhibitor. *Biochemistry* **2018**, *57* (13), 2035–2043. https://doi.org/10.1021/acs.biochem.8b00178.

(10) Kinney, R. M.; Butrapet, S.; Chang, G. J. J.; Tsuchiya, K. R.; Roehrig, J. T.; Bhamarapravati, N.; Gubler, D. J. Construction of Infectious CDNA Clones for Dengue 2 Virus: Strain 16681 and Its Attenuated Vaccine Derivative, Strain PDK-53. *Virology* **1997**, *230* (2), 300–308. https://doi.org/10.1006/VIRO.1997.8500.

(11) Nusinow, D. P.; Szpyt, J.; Ghandi, M.; Rose, C. M.; McDonald, E. R.; Kalocsay, M.; Jané-Valbuena, J.; Gelfand, E.; Schweppe, D. K.; Jedrychowski, M.; Golji, J.; Porter, D. A.; Rejtar, T.; Wang, Y. K.; Kryukov, G. V.; Stegmeier, F.; Erickson, B. K.; Garraway, L. A.; Sellers, W. R.; Gygi, S. P. Quantitative Proteomics of the Cancer Cell Line Encyclopedia. *Cell* **2020**, *180* (2), 387-402.e16. https://doi.org/10.1016/j.cell.2019.12.023.

(12) Jiang, L.; Wang, M.; Lin, S.; Jian, R.; Li, X.; Chan, J.; Dong, G.; Fang, H.; Robinson, A. E.; Aguet, F.; Anand, S.; Ardlie, K. G.; Gabriel, S.; Getz, G.; Graubert, A.; Hadley, K.; Handsaker, R. E.; Huang, K. H.; Kashin, S.; MacArthur, D. G.; Meier, S. R.; Nedzel, J. L.; Nguyen, D. Y.; Segrè, A. V.; Todres, E.; Balliu, B.; Barbeira, A. N.; Battle, A.; Bonazzola, R.; Brown, A.; Brown, C. D.; Castel, S. E.; Conrad, D.; Cotter, D. J.; Cox, N.; Das, S.; de Goede, O. M.; Dermitzakis, E. T.; Engelhardt, B. E.; Eskin, E.; Eulalio, T. Y.; Ferraro, N. M.; Flynn, E.; Fresard, L.; Gamazon, E. R.; Garrido-Martín, D.; Gay, N. R.; Guigó, R.; Hamel, A. R.; He, Y.; Hoffman, P. J.; Hormozdiari, F.; Hou, L.; Im, H. K.; Jo, B.; Kasela, S.; Kellis, M.; Kim-Hellmuth, S.; Kwong, A.; Lappalainen, T.; Li, X.; Liang, Y.; Mangul, S.; Mohammadi, P.; Montgomery, S. B.; Muñoz-Aguirre, M.; Nachun, D. C.; Nobel, A. B.; Oliva, M.; Park, Y. S.; Park, Y.; Parsana, P.; Reverter, F.; Rouhana, J. M.; Sabatti, C.; Saha, A.; Skol, A. D.; Stephens, M.; Stranger, B. E.; Strober, B. J.; Teran, N. A.; Viñuela, A.; Wang, G.; Wen, X.; Wright, F.; Wucher, V.; Zou, Y.; Ferreira, P. G.; Li, G.; Melé, M.; Yeger-Lotem, E.; Barcus, M. E.; Bradbury, D.; Krubit, T.; McLean, J. A.; Qi, L.; Robinson, K.; Roche, N. V.; Smith, A. M.; Sobin, L.; Tabor, D. E.; Undale, A.; Bridge, J.; Brigham, L. E.; Foster, B. A.; Gillard, B. M.; Hasz, R.; Hunter, M.; Johns, C.; Johnson, M.; Karasik, E.; Kopen, G.; Leinweber, W. F.; McDonald, A.; Moser, M. T.; Myer, K.; Ramsey, K. D.; Roe, B.; Shad, S.; Thomas, J. A.; Walters, G.; Washington, M.; Wheeler, J.; Jewell, S. D.; Rohrer, D. C.; Valley, D. R.; Davis, D. A.; Mash, D. C.; Branton, P. A.; Barker, L. K.; Gardiner, H. M.; Mosavel, M.; Siminoff, L. A.; Flicek, P.; Haeussler, M.; Juettemann, T.; Kent, W. J.; Lee, C. M.; Powell, C. C.; Rosenbloom, K. R.; Ruffier, M.; Sheppard, D.; Taylor, K.; Trevanion, S. J.; Zerbino, D. R.; Abell, N. S.; Akey, J.; Chen, L.; Demanelis, K.; Doherty, J. A.; Feinberg, A. P.; Hansen, K. D.; Hickey, P. F.; Jasmine, F.; Kaul, R.; Kibriya, M. G.; Li, J. B.; Li, Q.; Linder, S. E.; Pierce, B. L.; Rizzardi, L. F.; Smith, K. S.; Stamatoyannopoulos, J.; Tang, H.; Carithers, L. J.; Guan, P.; Koester, S. E.; Little, A. R.; Moore, H. M.; Nierras, C. R.; Rao, A. K.; Vaught, J. B.; Volpi, S.; Snyder, M. P. A Quantitative Proteome Map of the Human Body. *Cell* **2020**, *183* (1), 269-283.e19. https://doi.org/10.1016/j.cell.2020.08.036.

(13) Wang, D.; Eraslan, B.; Wieland, T.; Hallström, B.; Hopf, T.; Zolg, D. P.; Zecha, J.; Asplund, A.; Li, L.; Meng, C.; Frejno, M.; Schmidt, T.; Schnatbaum, K.; Wilhelm, M.; Ponten, F.; Uhlen, M.; Gagneur, J.; Hahne, H.; Kuster, B. A Deep Proteome and Transcriptome Abundance Atlas of 29 Healthy Human Tissues. *Mol. Syst. Biol.* **2019**, *15* (2). https://doi.org/10.15252/msb.20188503.

(14) Kuleshov, M. V; Jones, M. R.; Rouillard, A. D.; Fernandez, N. F.; Duan, Q.; Wang, Z.; Koplev, S.; Jenkins, S. L.; Jagodnik, K. M.; Lachmann, A.; Mcdermott, M. G.; Monteiro, C. D.; Gundersen, G. W.; Ma'ayan, A. Enrichr: A Comprehensive Gene Set Enrichment Analysis Web Server 2016 Update. *Nucleic Acids Res.* **2016**, *44*. https://doi.org/10.1093/nar/gkw377.

(15) Gordon, D. E.; Jang, G. M.; Bouhaddou, M.; Xu, J.; Obernier, K.; White, K. M.; O'Meara,

M. J.; Rezelj, V. V.; Guo, J. Z.; Swaney, D. L.; Tummino, T. A.; Hüttenhain, R.; Kaake, R. M.; Richards, A. L.; Tutuncuoglu, B.; Foussard, H.; Batra, J.; Haas, K.; Modak, M.; Kim, M.; Haas, P.; Polacco, B. J.; Braberg, H.; Fabius, J. M.; Eckhardt, M.; Soucheray, M.; Bennett, M. J.; Cakir, M.; McGregor, M. J.; Li, Q.; Meyer, B.; Roesch, F.; Vallet, T.; Mac Kain, A.; Miorin, L.; Moreno, E.; Naing, Z. Z. C.; Zhou, Y.; Peng, S.; Shi, Y.; Zhang, Z.; Shen, W.; Kirby, I. T.; Melnyk, J. E.; Chorba, J. S.; Lou, K.; Dai, S. A.; Barrio-Hernandez, I.; Memon, D.; Hernandez-Armenta, C.; Lyu, J.; Mathy, C. J. P.; Perica, T.; Pilla, K. B.; Ganesan, S. J.; Saltzberg, D. J.; Rakesh, R.; Liu, X.; Rosenthal, S. B.; Calviello, L.; Venkataramanan, S.; Liboy-Lugo, J.; Lin, Y.; Huang, X. P.; Liu, Y. F.; Wankowicz, S. A.; Bohn, M.; Safari, M.; Ugur, F. S.; Koh, C.; Savar, N. S.; Tran, Q. D.; Shengjuler, D.; Fletcher, S. J.; O'Neal, M. C.; Cai, Y.; Chang, J. C. J.; Broadhurst, D. J.; Klippsten, S.; Sharp, P. P.; Wenzell, N. A.; Kuzuoglu-Ozturk, D.; Wang, H. Y.; Trenker, R.; Young, J. M.; Cavero, D. A.; Hiatt, J.; Roth, T. L.; Rathore, U.; Subramanian, A.; Noack, J.; Hubert, M.; Stroud, R. M.; Frankel, A. D.; Rosenberg, O. S.; Verba, K. A.; Agard, D. A.; Ott, M.; Emerman, M.; Jura, N.; von Zastrow, M.; Verdin, E.; Ashworth, A.; Schwartz, O.; d'Enfert, C.; Mukherjee, S.; Jacobson, M.; Malik, H. S.; Fujimori, D. G.; Ideker, T.; Craik, C. S.; Floor, S. N.; Fraser, J. S.; Gross, J. D.; Sali, A.; Roth, B. L.; Ruggero, D.; Taunton, J.; Kortemme, T.; Beltrao, P.; Vignuzzi, M.; García-Sastre, A.; Shokat, K. M.; Shoichet, B. K.; Krogan, N. J. A SARS-CoV-2 Protein Interaction Map Reveals Targets for Drug Repurposing. *Nature* **2020**, *583* (7816), 459–468. https://doi.org/10.1038/s41586-020-2286-9.

(16) Heaton, B. E.; Trimarco, J. D.; Hamele, C. E.; Harding, A. T.; Tata, A.; Zhu, X.; Tata, P. R.; Smith, C. M.; Heaton, N. S. SRSF Protein Kinases 1 and 2 Are Essential Host Factors for Human Coronaviruses Including SARS-CoV-2. *bioRxiv* **2020**, 2020.08.14.251207. https://doi.org/10.1101/2020.08.14.251207.

(17) Gordon, D. E.; Hiatt, J.; Bouhaddou, M.; Rezelj, V. V; Ulferts, S.; Braberg, H.; Jureka, A. S.; Obernier, K.; Guo, J. Z.; Batra, J.; Kaake, R. M.; Weckstein, A. R.; Owens, T. W.; Gupta, M.; Pourmal, S.; Titus, E. W.; Cakir, M.; Soucheray, M.; McGregor, M.; Cakir, Z.; Jang, G.; O, M. J.; Tummino, T. A.; Zhang, Z.; Foussard, H.; Rojc, A.; Zhou, Y.; Kuchenov, D.; Hüttenhain, R.; Xu, J.; Eckhardt, M.; Swaney, D. L.; Fabius, J. M.; Ummadi, M.; Tutuncuoglu, B.; Rathore, U.; Modak, M.; Haas, P.; Haas, K. M.; Zar Chi Naing, Z.; Pulido, E. H.; Shi, Y.; Barrio-Hernandez, I.; Memon, D.; Petsalaki, E.; Dunham, A.; Correa Marrero, M.; Burke, D.; Koh, C.; Vallet, T.; Silvas, J. A.; Azumaya, C. M.; Billesbølle, C.; Brilot, A. F.; Campbell, M. G.; Diallo, A.; Sasha Dickinson, M.; Diwanji, D.; Herrera, N.; Hoppe, N.; Kratochvil, H. T.; Liu, Y.; Merz, G. E.; Moritz, M.; Nguyen, H. C.; Nowotny, C.; Puchades, C.; Rizo, A. N.; Schulze-Gahmen, U.; Smith, A. M.; Sun, M.; Young, I. D.; Zhao, J.; Asarnow, D.; Biel, J.; Bowen, A.; Braxton, J. R.; Chen, J.; Chio, C. M.; Seng Chio, U.; Deshpande, I.; Doan, L.; Faust, B.; Flores, S.; Jin, M.; Kim, K.; Lam, V. L.; Li, F.; Li, J.; Li, Y.-L.; Li, Y.; Liu, X.; Lo, M.; Lopez, K. E.; Melo, A. A.; Moss III, F. R.; Nguyen, P.; Paulino, J.; Ishwar Pawar, K.; Peters, J. K.; Pospiech Jr, T. H.; Safari, M.; Sangwan, S.; Schaefer, K.; Thomas, P. V; Thwin, A. C.; Trenker, R.; Tse, E.; Kin Martin Tsui, T.; Wang, F.; Whitis, N.; Yu, Z.; Zhang, K.; Zhang, Y.; Zhou, F.; Saltzberg, D.; Moreno, E.; Patel, A. H.; Rihn, S.; Khalid, M. M.; Vallejo-Gracia, A.; Fozouni, P.; Simoneau, C. R.; Roth, T. L.; Wu, D.; Anisul Karim, M.; Ghoussaini, M.; Dunham, I.; Berardi, F.; Weigang, S.; Chazal, M.; Park, J.; Logue, J.; McGrath, M.; Weston, S.; Haupt, R.; James Hastie, C.; Elliott, M.; Brown, F.; Burness, K. A.; Reid, E.; Dorward, M.; Johnson, C.; Wilkinson, S. G.; Geyer, A.; Giesel, D. M.; Baillie, C.; Raggett, S.; Leech, H.; Toth, R.; Goodman, N.; Keough, K. C.; Lind, A. L.; Consortium, Z.; Klesh, R. J.; Hemphill, K. R.; Carlson-Stevermer, J.; Oki, J.; Holden, K.; Maures, T.; Pollard, K. S.; Basler, C. F.;

Vignuzzi, M.; Peden, A. A.; Beltrao, P.; Krogan, N. J. Comparative Host-Coronavirus Protein Interaction Networks Reveal Pan-Viral Disease Mechanisms. *Science (80-.).* **2020**, *22*, 14. https://doi.org/10.1126/science.abe9403.

(18) Bojkova, D.; Klann, K.; Koch, B.; Widera, M.; Krause, D.; Ciesek, S.; Cinatl, J.; Münch, C. Proteomics of SARS-CoV-2-Infected Host Cells Reveals Therapy Targets. *Nature* **2020**, 1–8. https://doi.org/10.1038/s41586-020-2332-7.

(19) Lei, J.; Kusov, Y.; Hilgenfeld, R. Nsp3 of Coronaviruses: Structures and Functions of a Large Multi-Domain Protein. *Antiviral Res.* **2018**, *149*, 58–74. https://doi.org/10.1016/J.ANTIVIRAL.2017.11.001.

(20) Mellacheruvu, D.; Wright, Z.; Couzens, A. L.; Lambert, J. P.; St-Denis, N. A.; Li, T.; Miteva, Y. V.; Hauri, S.; Sardiu, M. E.; Low, T. Y.; Halim, V. A.; Bagshaw, R. D.; Hubner, N. C.; Al-Hakim, A.; Bouchard, A.; Faubert, D.; Fermin, D.; Dunham, W. H.; Goudreault, M.; Lin, Z. Y.; Badillo, B. G.; Pawson, T.; Durocher, D.; Coulombe, B.; Aebersold, R.; Superti-Furga, G.; Colinge, J.; Heck, A. J. R.; Choi, H.; Gstaiger, M.; Mohammed, S.; Cristea, I. M.; Bennett, K. L.; Washburn, M. P.; Raught, B.; Ewing, R. M.; Gingras, A. C.; Nesvizhskii, A. I. The CRAPome: A Contaminant Repository for Affinity Purification–Mass Spectrometry Data. *Nat. Methods* **2013**, *10* (8), 730–736. https://doi.org/10.1038/nmeth.2557.